NASA SP-135
SCA VOL. 11

METEOR ORBITS AND DUST

THE PROCEEDINGS OF A SYMPOSIUM

SMITHSONIAN CONTRIBUTIONS to ASTROPHYSICS
Volume 11

Cambridge, Mass.
August 9-13, 1965

Sponsored by
NATIONAL AERONAUTICS AND SPACE ADMINISTRATION
and
SMITHSONIAN INSTITUTION

NASA SP-135
SCAVOL. II

METEOR ORBITS AND DUST

THE PROCEEDINGS OF A SYMPOSIUM

Edited by
Gerald S. Hawkins
Smithsonian Astrophysical Observatory

Results of a symposium held August 9-13, 1965, at Cambridge, Mass., and sponsored by the Smithsonian Institution and the National Aeronautics and Space Administration. This Publication is Volume 11 of ***Smithsonian Contributions to Astrophysics.***

Scientific and Technical Information Division
OFFICE OF TECHNOLOGY UTILIZATION 1967
NATIONAL AERONAUTICS AND SPACE ADMINISTRATION
Washington, D.C.

Preface

The ***Proceedings*** of ***the Symposium on Meteor Orbits and Dust*** is published simultaneously as a NASA Special Publication (SP–135) and as Volume 11 of the ***Smithsonian Contributions to Astrophysics.*** This single publication thus serves in a dual capacity to satisfy the requirements of both agencies for the published record of this international meeting.

The NASA Special Publications series, begun in 1962, makes available information derived from or of value to NASA activities, and includes such publications as conference proceedings, monographs, data compilations, handbooks, sourcebooks, and special bibliographies.

The ***Smithsonian Contributions to Astrophysics*** series was inaugurated in 1956 to provide a proper communication for the results of research conducted at the Astrophysical Observatory of the Smithsonian Institution. Its purpose is the "increase and diffusion of knowledge" in the field of astrophysics, with particular emphasis on the problems of the sun, the earth, and the solar system. Its pages are open to a limited number of papers by other investigators with whom the Observatory has common interests.

Additional information concerning this and other NASA scientific and technical publications can be obtained from the Scientific and Technical Information Division, National Aeronautics and Space Administration, Washington, D.C. 20546. Additional information concerning the publications of the Astrophysical Observatory can be secured from the Publications Department, Smithsonian Institution Astrophysical Observatory, 60 Garden Street, Cambridge, Mass. 02138.

Cambridge, Mass.

FRED L. WHIPPLE, ***Director,***
Astrophysical Observatory,
Smithsonian Institution

For Sale by the Superintendent of Documents,
U.S. Government Printing Office, Washington, D.C. 20402
Price $2.50 (paper cover)
Library of Congress Catalog Card Number 67-60003

Contents

Session 3

Session 4

Session 5

Session 5—Continued

Session 6

PROCEEDINGS OF THE SYMPOSIUM
ON
METEOR ORBITS AND DUST

Selected Results from Precision-Reduced Super-Schmidt Meteors

L. G. JACCHIA,[1] F. VERNIANI,[2] and R. E. BRIGGS[3]

Introduction

We recently completed a general analysis of the atmospheric trajectories of **413** precisely reduced Super-Schmidt photographic meteors (Jacchia, Verniani, and Briggs, **1965).** We studied the dependence of heights, lengths, decelerations, and magnitudes on such basic parameters as velocity, angle **of** incidence, **and** mass, as well as on derived parameters such as the ablation coefficient and the fragmentation index; the latter were in turn related to the other geometrical and physical characteristics, including the phenomena **of** wake and terminal blending. The results **of** the analysis are mainly concerned with physical characteristics of meteors; in this paper we shall limit ourselves to only a few points related to problems **of** orbits and distribution, namely, physical differences dependent on the type of orbit, peculiarities **of** individual showers, and the mass scale for photographic meteors.

Systematic differences between groups of meteors

Systematic differences in some physical characteristics between meteors in short-period and long-period orbits were first pointed out by Jacchia (1958, **1963).** He found that the beginning heights of meteors with aphelion distances greater than **7** a.u. were higher than the corresponding heights **of** meteors with aphelion distances smaller than **7** a.u. **All** meteors were, of course, reduced to the same brightness.

The present general analysis has confirmed the effect found by Jacchia: meteors with aphelion distance smaller than **6** a.u. appear **1.8** km lower than meteors in long-period orbits, reduced to the **same** velocity, mass, and zenith angle. The maximum light and end heights are correspondingly lower (fig. **1).** This effect is related to the different densities that we find for the two groups: on the average, meteors in short-period orbits appear to be about **1.4** times as dense as meteors in long-period orbits. In addition, for short-period meteors, the density increases as the aphelion distance decreases (fig. **2).** These systematic differences

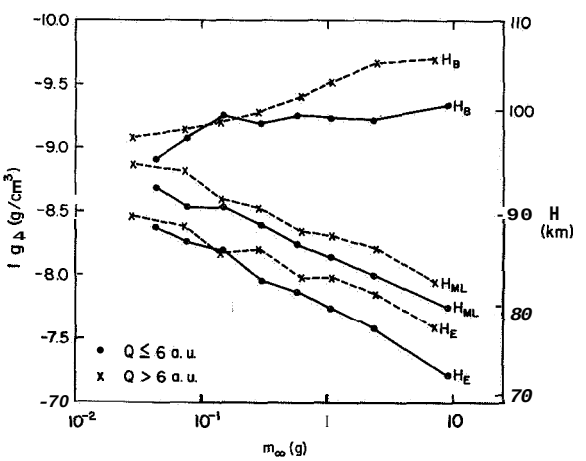

FIGURE 1.—Heights of the standard meteor when the mass is varied. Means for mass groups; all Super-Schmidt meteors, divided into two groups according to aphelion distance Q; H_B = beginning height; H_{ML} = height of maximum light; H_E = end height; ρ = atmospheric density (according to the U.S. Standard Atmosphere, 1962); a.u. = astronomical unit. The standard meteor has a velocity of **30** km/sec, a zenith angle Z_R such that log cos Z_R = —0.2, log σ = —11.20, and χ = 0.25. The ablation coefficient and the fragmentation index are σ and χ, respectively.

[1] Smithsonian Astrophysical Observatory and Harvard College Observatory, Cambridge, Massachusetts.

[2] Smithsonian Astrophysical Observatory and Harvard College Observatory; *on* leave from Centro Nazionale per la Fisica dell'Atmosfera e la Meteorologia del C.N.R., Rome, Italy.

[3] Smithsonian Astrophysical Observatory, Cambridge, Massachusetts.

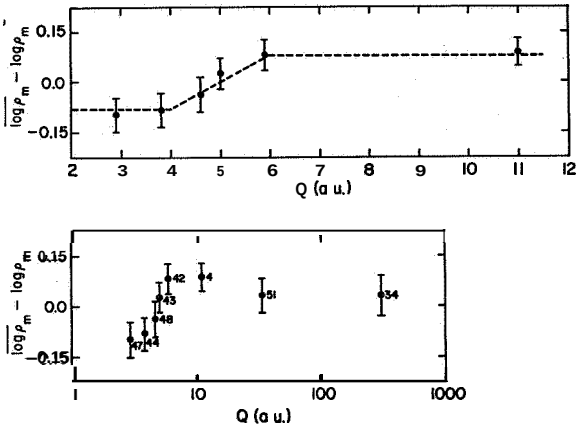

FIGURE 2.—The quantity $\overline{\log \rho_m} - \log \rho_m$ as a function of the aphelion distance Q, in natural values (top) and logarithms (bottom); ρ_m = meteor density in g/cm³; $\log \rho_m$ = mean logarithmic value of the density of all meteors.

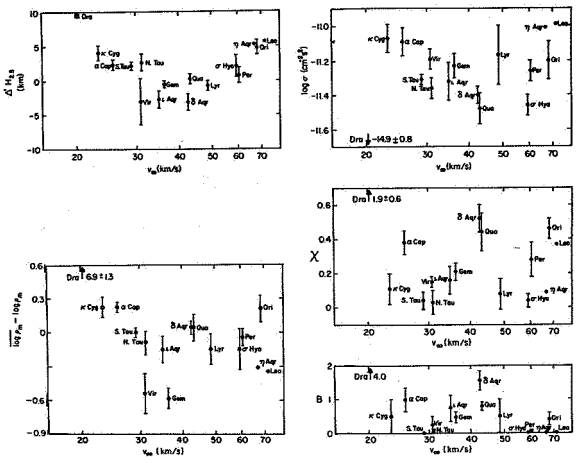

FIGURE 3.—Physical characteristics of individual meteor showers arranged in order of increasing velocity. $\Delta' H_{2.5}$ is the deviation of the height $H_{2.5}$ from the mean curve corresponding to sporadic meteors taking into account the aphelion distance Q. The height $H_{2.5}$ is the height of the point where the absolute photographic magnitude of the brightening meteor reaches the value +2.5; ρ_m = meteor density in g/cm³. The other parameters in the graphs are the logarithm of the ablation coefficient σ, the fragmentation index χ, and the blending index B. The standard deviations of the mean value of B for Southern Taurids (18 meteors) and σ Hydrids (3 meteors) are equal to zero.

in density could be ascribed to the different conditions in which the meteoroids were formed and to different resistance to destroying agents. Most of the meteors in short orbits may have originated in short-period comets that by now are completely evaporated; those that came from the inner core of Whipple's icy conglomerate should be denser because of the greater pressure to which they were subjected. Meteoroids with a loose structure are probably destroyed faster by collisions, erosion, and thermal effects.

Peculiarities of individual showers

Table 1 and figure 3 give a synoptic survey of the physical characteristics of those of our Super-Schmidt meteors that belong to major showers. The exceptional character of the Draconids shows up in all diagrams. The Geminids are 4 times as dense as the average meteor, i.e., about 1 g/cm³, but they crumble just as easily as any ordinary meteor. They have, in fact, a normal fragmentation index and normal blending; moreover, their heights are close to the average. The δ Aquarids are crumbly and have large fragmentation and blending indices; they appear 3 km lower than the average meteor with the same velocity and mass. The Southern Taurids have great tensile strength, as is shown by their fragmentation index equal to about zero and by the absence of terminal blending. Rather surprisingly, they are not denser than the average.

Mass scale for photographic meteors

MAGNITUDES AND MASSES.—The statistical analysis of the photographic magnitudes of our Super-Schmidt meteors has yielded the following relationship between magnitude, velocity, mass, and zenith angle of meteors in cgs units:

$$M_{pm} = 55.34 - 8.75 \log v_\infty - 2.25 \log m_\infty - 1.5 \log \cos Z_R.$$

We have adopted the luminous efficiency derived by Verniani (1964), $\tau_p = 1.0 \times 10^{-19} v$, where the velocity v is expressed in cm/sec and the intensity is expressed in zero magnitude units. From our results, the color index of a zero magnitude meteor is $-1^m.86$. Therefore the initial mass of a zero visual magnitude meteor with a velocity of 40 km/sec and a zenith angle of 50° is 0.76 g. This mass depends strongly on velocity and on zenith angle, as is shown in table 2.

FRAGMENTATION.—It has often been repeated in meteor literature that the abrupt increase in

brightness occurring in some photographic meteors—the so-called abrupt-beginning meteors—occurs at a point in the trajectory corresponding to a constant value of ρv_∞^2, where ρ is the atmospheric density. The point of abrupt beginning clearly marks the breakup of the meteor body. We used our material to see whether or not we could confirm such results.

Our Super-Schmidt material includes 26 meteors with an abrupt beginning, or about 6 percent of the total number. McCrosky (1955) estimates that 13 percent of all Super-Schmidt meteors belong to this category; the smaller percentage in our material is probably due partly to selection (many of the abrupt-beginning meteors are of too short duration to yield a good deceleration, which was the primary goal of our selection) and partly to a more stringent rule for classification. Even among our 26 meteors some have a less abrupt beginning than others; for 12 of them the rise is almost instantaneous.

If we take the atmospheric density ρ_{AB} corresponding to the abrupt beginning of all 26 meteors and put $\rho_{AB} v_\infty^K = \text{const}$, we find by least squares that $K = 3.6 \pm 0.3$. Using only the 12 ultra-abrupt meteors, we obtain $K = 3.0 \pm 0.5$. Taking the density ρ_B corresponding to the beginning heights of all Super-Schmidt meteors and putting $\rho_B v_\infty^K = \text{const}$, we find $K = 3.0 \pm 0.1$.

We see then that fragile meteors tend to break up at a point corresponding to a constant value of ρv_∞^3 rather than of ρv_∞^2, and that the power of v_∞ is not too different from that found from the beginning points of ordinary meteors. Abrupt meteors do, however, begin 4 km lower, on the average, than ordinary meteors, probably because, were it not for the breakup, we would not have photographed them.

The $\rho v_\infty^3 = \text{const}$ relation would suggest heat transfer rather than pressure as the trigger for the breakup of meteors. This could be the case if we have to deal with a body so porous that air molecules will penetrate deep inside to do their heating and melting, thus destroying the precarious cohesion of the body as a whole. In larger meteors the penetration of air molecules will be relatively smaller because of the shielding by the outer layers; this could explain why no meteors with abrupt beginnings are found among small-camera meteors. This process of flaking-off of large meteors and complete breakup of small meteors was already described by Jacchia (1955) in his first paper on fragmentation.

Cometary and asteroidal meteors

Since several major showers are associated with comets and since the heights, decelerations, and other physical characteristics of shower meteors, taken in their totality, do not differ from those of most sporadic meteors, we must conclude that the overwhelming majority of the photographic meteors are of cometary origin. A search for meteors of asteroidal origin has led to the conclusion that only 1 of our 413 meteors has all the requisites to qualify as an asteroidal meteor, in spite of the fact that the criteria employed for the selection of our meteors favor long, bright meteors. Individual meteor densities computed from decelerations generally have little meaning because of the scatter introduced by diversity in shape and fragmentation, by atmospheric variations, and by intrinsic deceleration errors. It is noteworthy, however, that 82 percent of the computed densities fall within a factor of 4 of the mean density—which, according to our calculations, is 0.26 g/cm^3—and that for only 14 meteors the computed density is larger than 2 g/cm^3. Even these 14, however, with the exception of the one mentioned above, are normal in other respects, such as heights and fragmentation, or have dubious decelerations or belong to cometary showers. The lone candidate for membership in the asteroidal group yields a density of 4 or 5 g/cm^3. While the objections to individual densities stand, we think this value is more reliable than the average in view of the exceptionally long trajectory of the meteor and the consistency of the decelerations.

The common occurrence of fragmentation, the behavior of abrupt-beginning meteors, the low density of nearly all meteors, and, in addition, the fact that most meteors are associated in streams and associations further confirm Whipple's theory of comets and of meteor origin.

TABLE 1.—*Physical characteristics of individual meteor showers*

Showers	v_∞ (km/sec)	cos Z_R	M_{pm}	H_B (km)	$H_{2.5}$ (km)	H_{ML} (km)	H_E (km)	D (sec)	ϵ_∞
All meteors	35.3±0.8	0.67f0.01	+0.0±0.1	L00.0±0.4	99.6±0.5	89.8±0.4	85.1±0.4	0.76f0.02	−0.42±0.02
Sporadic meteors	33.7f 1.0	0.66f0.01	+0.1±0.1	98.8±0.6	98.2±0.6	89.1-40.5	84.5±0.5	0.80±0.03	−0.44±0.03
Shower meteors	39.3f 1.2	0.69±0.02	−0.2±0.1	102.9±0.6	103.0±0.7	91.5±0.7	86.5±0.7	0.67±0.03	−0.36f0.05
Abrupt-beginning meteors	28.8±3.1	0.67±0.04	−0.1±0.2	92.5±2.1	92.4±2.3	87.6 f 1.7	81.5±1.4	0.62±0.04	−0.50±0.07
Short, flare-like meteors	36.8±4.2	0.78±0.04	−0.8±0.2	94.3±2.7	94.4±2.8	89.7±2.0	85.2±1.9	0.32±0.02	−0.52±0.10
Individual Showers:									
Quadrantids	43.1±0.2	0.61±0.05	+0.2±0.3	102.8±0.7	103.1±0.7	95.7f 1.5	90.6±1.6	0.48f0.03	−0.58f0.09
Virginids	30.8±3.7	0.73±0.02	−0.2±0.3	96.0±5.4	96.0±3.4	83.7±0.8	77.7f1.1	0.89±0.42	−0.31±0.31
Lyrids	48.8±1.1	0.93±0.05	−1.0±0.3	107.1f0.9	107.9±0.7	97.3±2.6	87.6±2.5	0.43±0.07	**−0.18±0.14**
η Aquarids	66.8	0.42	−0.7	115.6	119.6	102.1	99.7	0.58	−0.20
δ Aquarids	42.5±0.3	0.58±0.03	−0.1±0.3	99.8±1.1	99.8±1.2	93.0±0.7	88.4±0.8	0.49±0.06	−0.59f0.11
α Capricornids	25.6±0.4	0.69±0.03	+0.7±0.2	97.8±0.8	96.9±0.8	89.6±1.1	86.0f 1.3	0.70f0.08	−0.67 f 0.12
Southern ι Aquarids	34.4f 1.0	0.54±0.04	+0.540.4	96.3±1.9	95.7f 1.7	90.2±1.1	86.5f 1.1	0.58±0.12	−0.73±0.12
Northern ι Aquarids	35.9±1.7	0.70±0.08	+0.6±0.9	99.1±1.5	98.8±1.4	89.9±3.9	84.7f4.1	0.57±0.02	−0.63±0.24
Perseids	60.2±0.2	0.52±0.08	−1.4-10.4	114.1f1.1	114.8±1.1	99.0f 1.5	94.3f1.8	0.67±0.10	+0.16f0.20
κ Cygnids	23.2±0.4	0.68f0.13	+0.8±0.3	99.2±0.8	97.1±1.1	88.9±2.3	85.5±2.0	0.94±0.08	−0.65f0.05
Draconids	20.2±0.1	0.61±0.06	+0.1±0.0	103.6±0.2	102.6f0.2	96.7±0.4	91.0±0.4	1.22f0.12	−0.29±0.03
Orionids	68.0f 0.4	0.60±0.08	−1.1±0.3	117.0±0.5	119.6±1.0	105.9±1.7	99.3f 1.7	0.47±0.05	−0.14f0.10
Southern Taurids	29.9±0.4	0.73±0.03	+0.5±0.3	100.8f0.5	99.6±0.6	87.9±0.9	82.2±0.9	0.91±0.05	−0.45f0.10
Northern Taurids	31.1±0.5	**0.84**±0.07	−0.8±0.5	103.3±1.0	103.0f 1.2	83.2f 1.3	79.5f 1.4	0.97±0.16	+0.00±0.22
Leonids	71.7	0.89	−3.3	127.8	125.9	89.1	87.2	0.64	+0.72
σ Hydrids	59.2±0.6	0.84±0.02	−0.7±0.1	111.7±0.3	113.6±1.6	92.9±0.4	88.8±1.8	0.46±0.02	−0.29±0.08
Geminids	36.2±0.1	0.86±0.04	−0.8±0.3	100.4±0.3	101.3±0.5	85.6±1.5	80.0f 1.8	0.64±0.04	−0.18±0.13

	m_∞ (g)	log σ (cm^{-2} sec^2)	χ	$\overline{\Delta \log \rho_{corr}}$ (g/cm^3)	W	B	D/D_{th}	$\Delta' H_{2.5}$ (km)	No. obs.
All meteors	0.80f0.11	−11.19±0.01	0.27f0.01	0.00±0.01	0.74f 0.05	0.51±0.05	0.61±0.01	+0.3±0.5	413
Sporadic meteors	0.96±0.16	−11.16f0.01	0.27f0.02	0.00±0.02	0.77±0.06	0.47±0.05	0.60f0.01	0.0±0.6	290
Shower meteors	0.42±0.07	−11.25±0.02	0.27f0.03	0.00±0.02	0.67±0.08	0.63±0.08	0.65±0.02	+1.0±0.7	123
Abrupt-beginning meteors	0.65±0.12	−11.04±0.06	0.25±0.05	−0.18f0.08	0.59±0.13	1.35±0.24	0.45±0.03	−5.1±2.3	26
Short, flare-like meteors	0.32-40.09	−11.18±0.12	0.27f0.06	0.15±0.12	0.83±0.30	0.57f0.23	0.35f 0.04	−7.Of2.8	12
Individual Showers:									
Quadrantids	0.08±0.02	−11.48±0.09	0.44f0.11	0.03±0.08	0.40±0.19	0.80±0.11	0.61±0.03	+0.3±0.7	10
Virginids	0.59±0.47	−11.19±0.06	0.15f0.03	−0.36±0.12	1.15±1.15	0.25±0.25	0.67±0.17	−3.0±3.4	2
Lyrids	0.13±0.04	−11.17±0.17	0.08±0.09	−0.10±0.09	0.43±0.30	0.50f 0.50	0.64±0.11	−0.7±0.7	3
η Aquarids	0.04	−11.01	0.09	−0.21	0.0	0.0	0.63	+5.3	1
δ Aquarids	0.09±0.03	−11.4050.05	0.52f 0.08	0.03±0.04	0.21±0.12	1.55f0.27	0.50±0.05	−3.1f1.2	11
a Capricornids	0.53±0.24	−11.09±0.08	0.38±0.07	0.15f0.03	0.74f0.27	1.00f0.34	0.58±0.04	+2.4±0.8	14
Southern ι Aquarids	0.11±0.02	−11.27±0.12	0.18±0.09	−0.05±0.06	0.33f0.21	0.83±0.54	0.53±0.10	−3.2±1.7	*6*
Northern ι Aquarids	0.11±0.04	−11.48f0.25	0.10±0.26	−0.24±0.28	0.50±0.50	0.50±0.50	0.63f0.04	−1.2±1.4	2
Perseids	0.27±0.13	−11.26±0.06	0.28±0.10	−0.03±0.05	0.96±0.35	0.03±0.03	0.56±0.04	+0.8±1.1	11
κ Cygnids	0.39±0.06	−11.07±0.08	0.11±0.09	0.15±0.06	1.00±0.20	0.50±0.50	0.69±0.03	$4.1±1.1	4
Draconids	2.00±0.13	[−14.88±0.79]	1.89±0.57	4.61±0.85	0.00f0.00	4.00±0.00	0.50f0.02	+9.5±0.2	2
Orionids	0.06±0.02	−11.20±0.11	0.46±0.06	0.14f0.08	0.34±0.25	0.41f0.19	0.55±0.04	+4.8f1.0	8
Southern Taurids	0.48f0.13	−11.31±0.03	0.04f 0.05	−0.00±0.03	0.14±0.08	0.00±0.00	0.84±0.02	+2.2±0.6	18
Northern Taurids	1.01±0.32	−11.36±0.06	0.03±0.07	−0.06±0.07	0.72±0.43	0.06±0.06	0.77±0.05	+2.7±1.2	5
Leonids	0.29	−10.99	0.37	−0.23	4.0	0.0	0.44	+5.7	1
σ Hydrids	0.05±0.01	−11.46±0.06	0.04±0.04	−0.10f0.12	0.33±0.33	0.00±0.00	0.87±0.10	+2.1±1.6	3
Geminids	0.76±0.28	−11.23±0.07	0.21±0.05	−0.39f0.06	1.48±0.26	0.47±0.17	0.69±0.03	−0.5±0.5	20

TABLE 2.—*The mass (in g) of a zero visual magnitude meteoroid as a function of velocity* v_∞ *and zenith angle* Z_R

v_∞ (km/sec) / Z_R		20	30	40	50	60	70
0°	120	8. 13	1. 66	0. 55	0. 23	0. 11	0.062
30°	132	8. 91	1. 82	0. 63	0. 25	0. 12	0.068
45°	151	10. 2	2. 09	0. 69	0.29	0. 14	0.078
60°	191	12. 9	2. 63	0. 87	0. 36	0. 18	0. 098
75°	269	18. 2	3. 72	1. 23	0. 51	0. 25	0. 14
85°	617	41. 7	8. 51	2. 82	1. 17	0. 58	0. 32

References

JACCHIA, L. G.

1955. The physical theory of meteors, VIII: Fragmentation as a cause of the faint-meteor anomaly. Astrophys. Journ., vol. 121, pp. 521–527.

1958. On two parameters used in the physical theory of meteors. Smithsonian Contr. Astrophys., vol. 2, no. 9, pp. 181–187.

1963. Meteors, meteorites and comets; interrelations. *In* The Solar System, vol. IV, ed. by B. M. Middlehurst and G. E. Kuiper, Univ. of Chicago Press, pp. 774–798.

JACCHIA, L. G.; VERNIANI, F.; and BRIGGS, R. E.

1965. An analysis of the atmospheric trajectories of 413 precisely reduced photographic meteors. Smithsonian Astrophys. Obs. Spec. Rep. No. 175, 309 pp.; also Smithsonian Contr. Astrophys., vol. 10, no. 1, 139 pp., 1967.

MCCROSKY, R. E.

1955. Some physical and statistical studies of meteor fragmentation. Ph.D. thesis, Harvard University, Cambridge, Mass.

U.S. STANDARD ATMOSPHERE

1962. U.S. Standard Atmosphere 1962. Prepared under NASA, USAF, and USWB, Washington, D.C., 278 pp.

VERNIANI, F.

1964. On the luminous efficiency of meteors. Smithsonian Astrophys. Obs. Spec. Rep. No. 145, 62 pp.; also Smithsonian Contr. Astrophys., vol. 8, no. 5, pp. 141–172.

Abstract

The authors have recently completed a general analysis of the atmospheric trajectories of 413 precisely reduced Super-Schmidt photographic meteors; the results obtained mainly concern physical characteristics of meteors. This paper mentions only a few of the results as they relate to the subject of the Symposium, namely, physical differences dependent on the type of orbit, peculiarities of individual showers, and the mass scale for photographic meteors.

Meteors with abrupt beginnings appear at a height where the atmospheric density ρ is such that ρv^3 is a constant (v = meteor velocity); this result suggests that heating rather than aerodynamic pressure is the trigger mechanism in the breakup of such objects.

Explanation of table 1 symbols

v_∞ apparent velocity, corrected for atmospheric drag

Z_R zenith distance of apparent radiant

M_{pm} photographic absolute magnitude reached by meteor at maximum light

H_B height corresponding to beginning of photographic trajectory

$H_{2.5}$ height of point where absolute photographic magnitude of brightening meteor reached the value +2.5

H_{ML} height of point where meteor reached its maximum absolute brightness

H_E height corresponding to end of photographic trajectory

D duration of photographic trail from H_B to H_E

ϵ_∞ a measure of integrated brightness of meteor, defined by

$$\epsilon_\infty = \log_{10} \int_{-\infty}^{+\infty} I_p \, dt,$$

where I_p is absolute photographic brightness of the meteor expressed in zero-magnitude units

m_∞ photometric mass of meteor, computed using Verniani's (1964) luminous efficiency

σ ablation coefficient, defined by

$$\sigma = \frac{dm/dv}{mv}$$

χ progressive fragmentation index, defined by

$$\chi=\frac{d}{ds}\log\frac{\dot{v}}{\dot{v}_T},$$

where $\dot{v}$ is the observed deceleration, $\dot{v}_T$ is the theoretical deceleration, and

$$s=\log_{10}\left(\frac{m_\infty}{m}-1\right).$$

$\overline{\Delta \log \rho_{corr}}$ $\log\rho_{obs}-\log\rho_{st}-\chi s$, where ρ_{obs} is the atmospheric density deduced from the observed deceleration, and ρ_{st} is the density tabulated in the U.S. Standard Atmosphere (1962); s was defined in the explanation of χ; $\Delta \log \rho_{corr}$ is also equal to $\frac{2}{3}(\log\rho_m-\overline{\log\rho_m})$, where ρ_m is the meteor density and $\overline{\log\rho_m}$ is the mean logarithmic value of the density of all meteors

W, B wake and blending, respectively, expressed in an arbitrary scale from 0 to 4 (0=no wake or blending, 4=maximum)

D/D_{th} ratio between observed and theoretical duration

$\Delta' H_{2.5}$ difference between the average $H_{2.5}$ of a group of meteors and the overall mean of $H_{2.5}$

No. obs. number of observations used

Relation of Meteor Orbits to the Orbits of Comets and Asteroids

Ľ. KRESÁK[1]

Introduction

In the solar system, comets and asteroids are two potential sources of meteoroids. It has been demonstrated that both comets and asteroids are able to supply new meteor particles necessary to replace those being constantly removed by planetary perturbations, collisions with the planets, and interplanetary erosion and spiraling into the sun under the action of drag effects (Fesenkov, **1942;** Whipple, **1951;** Piotrowski, **1954).** No dependable quantitative information is available, however, either on the efficiency of the two sources or on the potential lifetimes of individual meteoric particles in circumsolar orbits.

With regard to a number of known comet-meteor shower associations and to the abundance of meteor orbits with both high inclinations and eccentricities, the cometary origin of a large proportion of meteors is beyond any shadow of doubt. On the other hand, there are very few, if any, convincing cases of asteroidal origin. Hence the fundamental question is not whether the source is cometary or asteroidal, but rather whether, and in what proportion, asteroidal meteors are present at all. According to Jacchia, Verniani, and Briggs (1965), only 1 of **413** precision-reduced Super-Schmidt meteors was of asteroidal nature.

Conceivably, the mass distributions of cometary and asteroidal meteoroids need not be the same, and a different proportional representation of the two components may be expected to appear at different levels of brightness. Curiously enough, Hawkins **(1959)** finds an increasing proportion of asteroidal meteors toward brighter objects, whereas Kresák **(1964)** suggests the same for fainter objects.

Insofar as there is no reliable device for discriminating between asteroidal and cometary meteors from their behavior during their interaction with the earth's atmosphere (the range of variability for shower meteors of cometary origin is even wider than that for sporadic meteors in general), the orbital characteristics appear to be the most suitable data for attempting to solve the problem. Unfortunately, the restriction of observations to the particles crossing the earth's orbit requires an extrapolation of the systems of cometary and asteroidal orbits rather than a direct comparison between them. Our statistics of these orbits are strongly, and in different ways, biased by the discovery conditions; also, when dealing with particles of meteoric size we must take into account the operation of nongravitational effects, which are practically negligible for their parent bodies, and the efficiency of which depends on a number of factors difficult to evaluate.

The main purpose of this paper is to represent the virtual distribution of the orbits of comets, asteroids, and meteors in a common diagram where, analogous to the Hertzsprung-Russell diagram, the main features of each distribution could be fixed and the evolutionary paths indicated. A two-dimensional diagram requires the choice of two characteristic elements out of the *six* defining a Keplerian orbit. Among these, the time of perihelion passage is obviously of no interest for our problem. The longitude of the node, although able to reveal some rela-

[1] Astronomical Institute of the Slovak Academy of Sciences, Bratislava, Czechoslovakia.

240–022 0—67 ——2

tion of evolutionary significance to Jupiter's orbit, can also be omitted. Incidentally, this is the only element that can be simply determined for individual meteors with high precision and that permits separate studies in terms of diurnal and annual variations of meteor rates. The argument of perihelion for meteors encountering the earth is bound to the semimajor axis and eccentricity by a strict condition. Neglecting the eccentricity of the earth's orbit, we have

$$\cos w = -\frac{1}{e}(a - ae^2 - 1), \qquad (1)$$

and we may discard one of these three elements without any ambiguity as far as meteor orbits are concerned. Thus it appears most reasonable to use a set of diagrams in which the semimajor axis is plotted against eccentricity, each diagram for a specific range of inclination. The position of every object in this diagram determines the size and shape of its orbit. The diagrams for higher inclinations will obviously include only orbits essentially different, by orientation, from those of asteroids and short-periodic comets of Jupiter's family.

The representation of the fundamental observational data by the a/e diagram—hespective of inclinations and inherent effects of selection—is shown in figure 1. In the system of asteroids (black dots) the fine structure of commensurability gaps is clearly visible, as well as the clustering of the Trojans and the Hilda group. All 1649 asteroids numbered up to the end of 1963 are indicated; in addition, six unnumbered asteroids of the Apollo group (Apollo, Adonis, Hermes, 1948EA, 194808, and 1950-DA), for which orbital elements of lower accuracy are available, are included. All 77 known periodic comets with periods not exceeding 20 years are indicated by open circles, only two cases of very inaccurate elements, P/Wilson-Harrington and P/Perrine, being omitted. The short-dashed ovals indicate the areas occupied by the members of five major short-periodic meteor showers (the Quadrantids, Northern and Southern Taurids, Geminids, and δ Aquarids); other showers, for which no dependable data on the dispersion of elements are available, are denoted by crosses. The broken heavy line delimits, to the right, the region in which the boundary condition of crossing the earth's orbit,

$$a(1-e) < 1 < a(1+e), \qquad (2)$$

is satisfied. Obviously, meteors observed from the earth's surface can fall only within this area, with some small overlapping due to the eccentricity of the earth's orbit.

The diagram may be supplemented by the scales of other significant quantities that are functions of a and e alone, either in general (period of revolution, mean daily motion, eccentricity angle, perihelion distance, aphelion distance) or for the particular case of bodies colliding with the earth (heliocentric velocity, argument of perihelion). The loci of equal perihelion distance q, aphelion distance Q, and argument of perihelion w are plotted in figures 2a, 2b, and 2c, respectively. Other quantities, depending on a, e, and i (such as the geocentric and no-atmosphere velocity or Whipple's "cosmic weight"), may be similarly indicated in the a/e diagrams designed for the proper values of inclination.

The apparent distribution of orbits shown in figure 1 is strongly biased by the discovery conditions. For periods of observation long compared with the periods of revolution ($<$20 years in fig. 1), the due correction factors may be visualized, too, as functions of the position within the diagram. The form of these functions is, obviously, different for different kinds of objects, and a discrimination according to the inclination is again necessary.

Empirical comet-asteroid criteria

In order to provide a sharp conventional distinction between the cometary and asteroidal meteor orbits, Whipple (1954) introduced the K criterion,

$$K = \log \frac{a(1+e)}{(1-e)} - 1 \gtrless 0, \qquad (3)$$

and demonstrated that K is positive for 96 percent of known comet orbits, and negative for all but 3 asteroid orbits. Since K is a function of a and e alone, the borderline $K=0$ may be indicated in the a/e diagram; this is done in figure 1 by the thinner full curve. It is evident that, unless there is physical

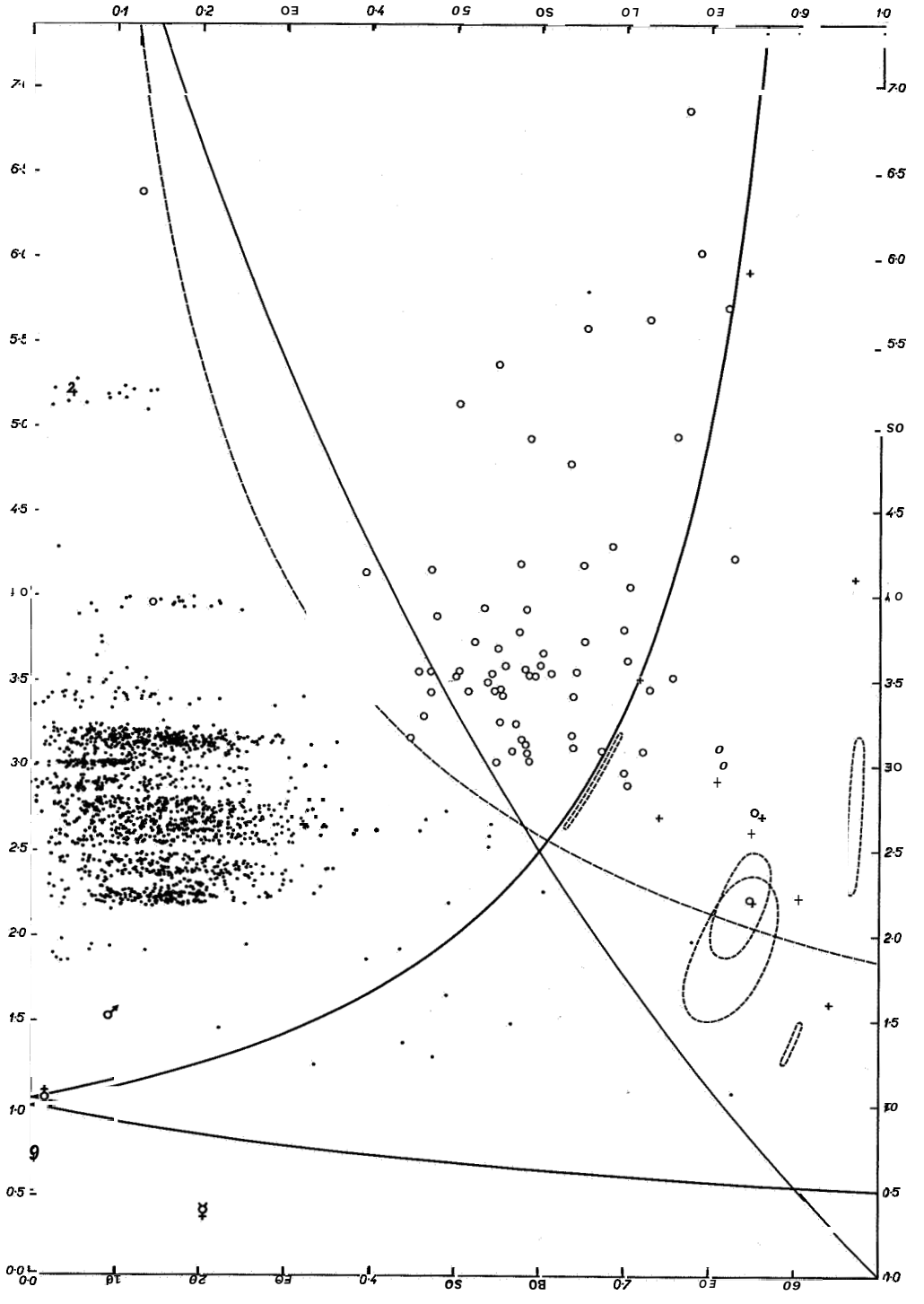

FIGURE 1.—Position of different objects in the *a/e* diagram. Astronomical symbols = major planets; dots = asteroids; open circles = comets; short-dashed ovals = dispersion of major meteor streams; crosses = mean orbits of other meteor streams; heavy line = boundary condition for crossing the earth's orbit; thinner line = Whipple's *K* criterion; dashed line = *Pe* criterion.

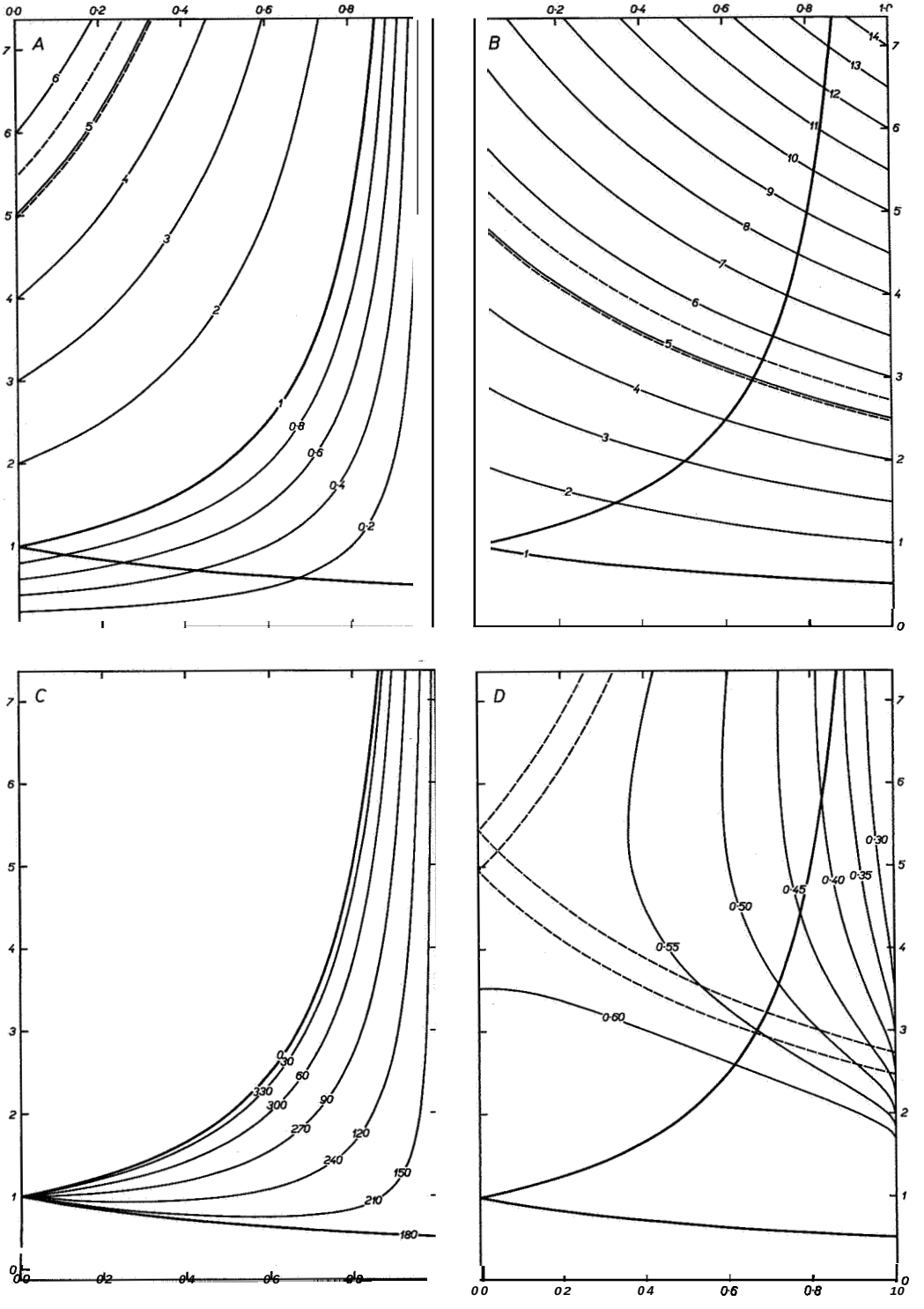

FIGURE 2.—a, Perihelion distances (heavy line= boundary condition for crossing the earth's orbit; dashed lines=perihelia at the distance of Jupiter's perihelion and aphelion, respectively); b, aphelion distances (dashed lines= aphelia at the distance of Jupiter's perihelion and aphelion, respectively); c, argument of perihelion for the orbits intersecting the orbit of the earth; d, Tisserand's invariant T_0 for Jupiter, $i=0$ (dashed lines= boundary conditions for crossing Jupiter's orbit at its perihelion and aphelion, respectively).

reasoning for formula **(3)** (which is not the case), a number of other functions of **a** and **e** may be chosen to suit the same purpose. The measure of suitability is the minimalization of the number of exceptions not obeying the criterion, and the simplicity of the function. Probably the best criterion from this point of view is

$$Pe=a^{3/2}e\gtrsim 2.5. \qquad (4)$$

In fact, there are **13** comets moving in asteroidal orbits according to **(3)** but only **1** according to **(4);** and 3 asteroids moving in cometary orbits according to **(3)** but only 1 according to **(4).** The fit is improved against the K criterion from **99.8** to **99.9** percent for the asteroids and from **97.8** to **99.8** percent for the comets. Also the a/e diagram (fig. 1), where the Pe criterion is indicated by the dashed curve, proves that the division is now as good as possible. The lists of exceptions from the K and Pe criteria, respectively, are given below (tables **1** and **2).** Again, the problematical case of P/Wilson-Harrington ($K=-0.377?$, $Pe=0.95?$) is omitted. Of the exceptions from (4), P/Oterma did not satisfy the Pe criterion for only three revolutions between **1937** and **1962,** and P/Schwassmann-Wachmann **1** was close to the limit at the time of discovery.

TABLE 1.—*Exceptions from the* K *criterion*

	K
944 Hidalgo	**+0.445**
Adonis	**+0.200**
1566 Icarus	**+0.055**
P/Schwassmann-Wachmann 2	**−0.106**
P/Whipple	**−0.098**
P/Johnson	−0.098
P/Schwassmann-Wachmann 1	**−0.081**
P/Kulin	**−0.081**
P/Holmes	**−0.076**
P/Ashbrook-Jackson	**−0.053**
P/Shajn-Schaldach	**−0.052**
P/Tempel 1	**−0.048**
P/Reinmuth 2	**−0.020**
P/Wolf 1	**−0.020** (+0.102 **before 1922)**
P/Spitaler	**−0.019**
P/Schorr	**−0.005**
P/Wolf-Harrington	(+0.066) **−0.075** in **1924**
P/Oterma	(+0.083) **−0.006 before 1937, −0.276 in 1958**

from

	Pe
944 Hidalgo	**9.15**
P/Schwassmann-Wachmann 1	**2.12 2.46 in 1925**
P/Oterma	**(4.92) 3.24 before 1937, 1.14 in 1958**

Nevertheless, while criteria **of** this type yield a practical orientation as to the general character of the orbit of a specific object, there are two reasons why we cannot rely upon them as indicators **of** meteor origin. One of these reasons, the operation of nongravitational evolutionary effects necessary to displace the orbits to crossing with that of the earth, has already been pointed out by Dycus and Bradford **(1964).** The other reason is that observational bias prevents the comets moving in asteroidal orbits from being discovered even if such exist. Only a high eccentricity ensures that a comet becomes bright enough around the perihelion and, at the same time, does not age too rapidly in the aphelion part **of** its orbit where it spends most of its time. This requirement is evidently not met in the asteroidal region ($K<0$, $Pe<2.5$). **A** comet located in the upper left part of this region would have to be of abnormal brightness (like P/Schwassmann-Wachmann 1) to be discovered, and a comet situated in the lower part of the diagram would disintegrate rapidly.

It is rather problematical whether comets can enter at all the lower part of the diagram. The perturbational capture process by Jupiter does not allow this and, in fact, with the exception of P/Encke, there is no comet having aphelion far inside Jupiter's orbit. The concentration of aphelia around Jupiter's orbit is undoubtedly a characteristic feature of short-periodic comets. Nevertheless, it is questionable whether the presence or absence of such concentration among meteor orbits can reveal anything about their origin: partly because the Trojan asteroids exhibit such concentration,

too, and partly because cometary meteors, which are subject to considerable nongravitational forces unlike the comets themselves, may much more easily pass Jupiter's perturbational barrier.

It must be pointed out that there may even be an essential difference between a cometary and an asteroidal orbit in spite of entirely identical angular elements, a and e (i.e., an identical position in the a/e diagram). This difference occurs at simple commensurabilities with the mean motion of Jupiter, where the asteroid orbits are relatively stable, due to interplay of perturbations preventing any closer approach to Jupiter (Öpik, 1963), whereas the comet orbits are highly unstable, due to the preceding capture process. A nice example of this difference is P/Oterma and the Hilda group of asteroids (Kresák, 1965a). In figure 1, Comet Oterma appears imbedded within the Hilda group, but this was the case only during three revolutions of the comet and two revolutions of Jupiter. The escape of the comet from this region (Marsden, 1961) is indicated in figure 5c.

If we want to establish the difference between comet and asteroid orbits, each object must be classified either as a comet or as an asteroid absolutely, regardless of the type of its orbit. In fact, the aspect of these two types of objects does not always differ sharply. On several occasions some asteroids (1 Ceres, 2 Pallas, 3 Juno, 14 Irene, 122 Gerda, 182 Elsa, 224 Oceana) have been observed surrounded by faint nebulosities. Although such observations are rare, unconfirmed, and doubtful (Putilin, 1953), the experience of observers such as Herschel, Hind, Schroter, or Comas Sola does not allow us simply to neglect them. On the other hand, some returns of periodic comets have been recorded during which no visible coma has developed and the comet was steadily of asteroidal appearance. The cometary character of P/Kulin has been recognized only after the determination of its orbit. Also the aspect of P/Arend-Rigaux was entirely stellar during its last two apparitions (Roemer, 1966); had the discovery occurred one revolution later than it actually did, we should have no reason for classifying this body as a comet, except for the form of the orbit. Of course, these are exceptional marginal cases that cannot affect the general character of the two distributions of orbits, but they are perhaps able to influence the degree of their overlapping.

When speaking about asteroidal orbits we must define precisely the meaning of this term. Unfortunately, this necessity is often overlooked and individual orbits (e.g., those of some meteorites and fireballs) are rather arbitrarily designated as cometary or asteroidal. Unless a sharp numerical criterion like (3) or (4) is applied, we can define asteroidal orbits crossing the orbit of the earth in three different ways: (1) as orbits of low inclination and eccentricity, constituting a direct continuation of the asteroidal ring at its inner side; (2) as orbits with aphelia situated within the main asteroidal belt; and (3) as orbits that could arise, by any evolutionary process, from typical asteroid orbits.

In fact, definitions (1) and (2) are not fulfilled by the asteroids of the Apollo group, the outstanding exception from (1) being 1566 Icarus, and from (2), 1620 Geographos. Exceptions are found in the outer region of the ring, too—such as 944 Hidalgo (from (1) and (2)), 279 Thule, the Trojans, and the Hilda group (from (2)). For investigating the origin of meteors, definition (3) is most reasonable; however, before applying it we must discuss the operation of all potential effects that are able to transform the original orbits.

Transformations of orbits

PLANETARY PERTURBATIONS.—The secular perturbations by major planets are of less significance for our problem. According to the well-known Poisson theorem, there are no secular terms of the first or second order in the perturbations of semimajor axes, and the perturbations of eccentricity are far from sufficient to displace the perihelia from the asteroidal belt to the earth's orbit.

Random perturbations at close encounters are of greater importance; however, an overwhelming majority of asteroids cannot appreciably approach major planets. The extreme outer asteroids, with the exception of Hidalgo, are prevented from that by the commensurability with Jupiter's mean motion; some of the innermost ones can encounter Mars, but its

mass is too small for efficient changes. For the comets, close approaches to Jupiter are frequent (they are responsible for the formation of short-periodic orbits) and the displacement in the a/e diagram is often drastic. Four striking examples of such a transformation (P/Oterma, P/Wolf 1, P/Kopff, and P/Pons-Winnecke) are plotted in dashed lines in figure 5c.

Owing to the equality of the planetocentric velocity at the moments of entering and leaving the sphere of action, the elements of the perturbed body before and after the appulse are bound by the condition known as the Tisserand criterion,

$$T=a^{-1}+2A^{-3/2}a^{1/2}(1-e^2)^{1/2}\cos I=\text{const}, \quad (5)$$

where A is the radius of the orbit of the perturbing planet, assumed circular, and I the inclination to its orbital plane. For a small original inclination of the perturbed body the orbital plane cannot change appreciably, keeping cos I very near to 1. Hence we have, for low inclined orbits, the approximate condition

$$T_0=a^{-1}+2A^{-3/2}a^{1/2}(1-e^2)^{1/2}=\text{const}. \quad (6)$$

The loci of equal T_0 for perturbations by Jupiter are plotted in figure 2d. They indicate the lines along which a body situated in the respective point of the diagram and revolving near the ecliptical plane would displace after the approach. Since there is an equal *a priori* probability that the nearest approach will occur ahead of or behind Jupiter, both directions of displacement are equally probable. A close approach to Jupiter may occur only within, or not far from, the area situated to the right of the double dashed lines; this refers to tangential orbits to Jupiter in perihelion and aphelion, respectively. In this area

$$a(1-e)<q_2<a(1+e) \quad \text{(lower line)}, \quad (7)$$

and

$$a(1-e)<Q_2<a(1+e) \quad \text{(upper line)}. \quad (8)$$

The probability of encounter increases toward this boundary.

Similar diagrams may be constructed for the perturbations by other planets, too, but the effect of Jupiter is definitely the predominant one.

ASTEROIDAL COLLISIONS.—If an asteroidal fragment should enter the terrestrial space after ejection from the main asteroidal belt as a consequence of collision, the resulting orbit must obviously fulfill two conditions: it must cross the region of collision, and the crossing velocity must be equal to the ejection velocity. For each original orbit from which the fragment has separated, the area accessible may be delimited in the a/e diagram. Furthermore, for each point within this area the required velocity of ejection may be determined.

A series of collisions may obviously occur before one of the fragments reaches the earth's orbit. Nevertheless, the probability of collision decreases rapidly with increasing separation from the main belt, because better conditions for the distribution of eccentricities cannot compensate for the decrease of particle density.

For a single collision, the velocity V_e at which the fragment must leave the original orbit, assumed circular with radius a_0 and situated in the plane of the ecliptic, will be

$$V_e=[3a_0^{-1}-a^{-1}-2a_0^{-3/2}a^{1/2}(1-e^2)^{1/2}\cos I]^{1/2} \quad (9)$$

in the units of the circular velocity of the earth (29.8 km/sec). The range of semimajor axes and eccentricities accessible for the fragment is obviously limited by the condition

$$a(1-e)\leq a_0\leq a(1+e). \quad (10)$$

Furthermore, unless the orbital inclination of the fragment is zero, the other node must be situated at the earth's distance from the sun. This condition is expressed by the relation

$$a(1-e^2)=2a_0(a_0+1)^{-1}. \quad (11)$$

Formulas (9) to (11) have been evaluated for three zones of collision, corresponding to the commensurability gaps 1:4 ($a_0=2.065$, conventional inner boundary of the main asteroidal belt), 1:2 ($a_0=3.278$, the outer region of the belt), and 1:1 ($a_0=5.203$, the region of the Trojans); and for two values of inclination, $i=0°$ and 30°. The results are represented in figures 3a, 3b, and 3c, with the proper velocities

V_e expressed in km/sec. Full curves apply to $i=0°$, dashed curves to $i=30°$. The fragments may enter only the area separated by the thin full envelope. With $i=0°$, an encounter with the earth is possible everywhere within the overlapping part of the two areas limited by the boundary conditions **(10)** and **(2)** (the full heavy curve), while with $i=30°$, only on the dashed-and-dotted line representing the additional condition **(11).**

It is evident from figures 3a to 3c that the ejection velocities required to bring the fragments from the asteroidal belt to the earth's orbit are much too high. For most of them a velocity of **10** to **15** km/sec is necessary, the absolute minimum amounting to about **4.5** km/sec. If we put, with Öpik **(1966),** the upper limit of this velocity at 1.0 to **1.5** km/sec, then even when allowing for a reasonable eccentricity of the original orbit we do not find regions of possible encounters with the earth. Even if we would admit ejection velocities of the order of **10** km/sec, we cannot explain the presence of asteroidal meteors in the lower left part of the a/e diagram by collisions within the main asteroidal belt.

DRAG EFFECTS.—Different nongravitational drag effects—the Poynting-Robertson effect, the effect of corpuscular radiation from the sun, and the Yarkovsky-Radzievsky effect—may be considered in common, as they all change the size and shape of the orbit in the same way. The evolutionary paths due to these effects may be plotted in the a/e diagram from the relation (Wyatt and Whipple, **1950)**

$$C=ae^{-4/5}(1-e^2)=\text{const.} \qquad (12)$$

The paths for different values of the invariant C, depending upon the initial elements, are plotted in figure 3d. The arrows indicate the direction of evolution that strongly predominates and is common to all the above-mentioned effects except the Yarkovsky-Radzievsky effect of the direct rotation; this may, however, play some role only for very rapidly rotating bodies. The speed of evolution, or the displacement in the a/e diagram, considerably accelerates downward and in the direction of the arrows.

Figure 3d demonstrates instructively the suggestion of Dycus and Bradford **(1964)** concerning the changes of Whipple's K criterion due to the Poynting-Robertson effect. From this figure the effect may be readily verified for individual objects without computation.

It is essential that the evolutionary paths are nearly perpendicular to the direction of Jupiter's perturbational barrier and to the prevailing direction of strong perturbations (fig. 2d). Also, the fragments formed by asteroidal collisions, which do not at once reach the boundary $a(1-e)=1$, will continue their evolutionary paths at large angles to the original displacement, and can eventually become observable in spite of a lower ejection velocity. Perturbations of the orbital plane will produce deviations from the nodal line condition **(11).** Thus the interplay of more effects may allow the particles of a given origin to enter also the regions of the a/e diagram otherwise forbidden.

Distribution in the a/e diagram

ASTEROIDS.—As seen from figure **1,** the distribution of the asteroids in the a/e diagram is strongly influenced by the commensurability effects, producing a fine vertical structure. This structure reflects in the smoothed equidensity lines shown in figure 4a, which depicts the apparent distribution of **1649** numbered asteroids. The heavy lines delimit the area occupied by one-half of the objects; each other line corresponds to a decrease of density by a factor of two per unit area of the diagram.

The sample of numbered asteroids is obviously biased by the discovery and recovery conditions, which depend, first of all, upon the mean opposition magnitude m_0. Owing to low orbital eccentricities of most asteroids, their short periods of revolution, and small amplitudes of brightness due to the rotation, the changes of apparent magnitudes from one opposition to another may be neglected in the first approximation in the main part of the asteroidal belt. The selection effect could be evaluated easily provided that the absolute magnitude distribution were known with sufficient accuracy; unfortunately, this is not the case.

At the boundary of the distribution, where the densities are low, other more intricate effects appear. Higher eccentricities, yielding considerable variations of discovery conditions at

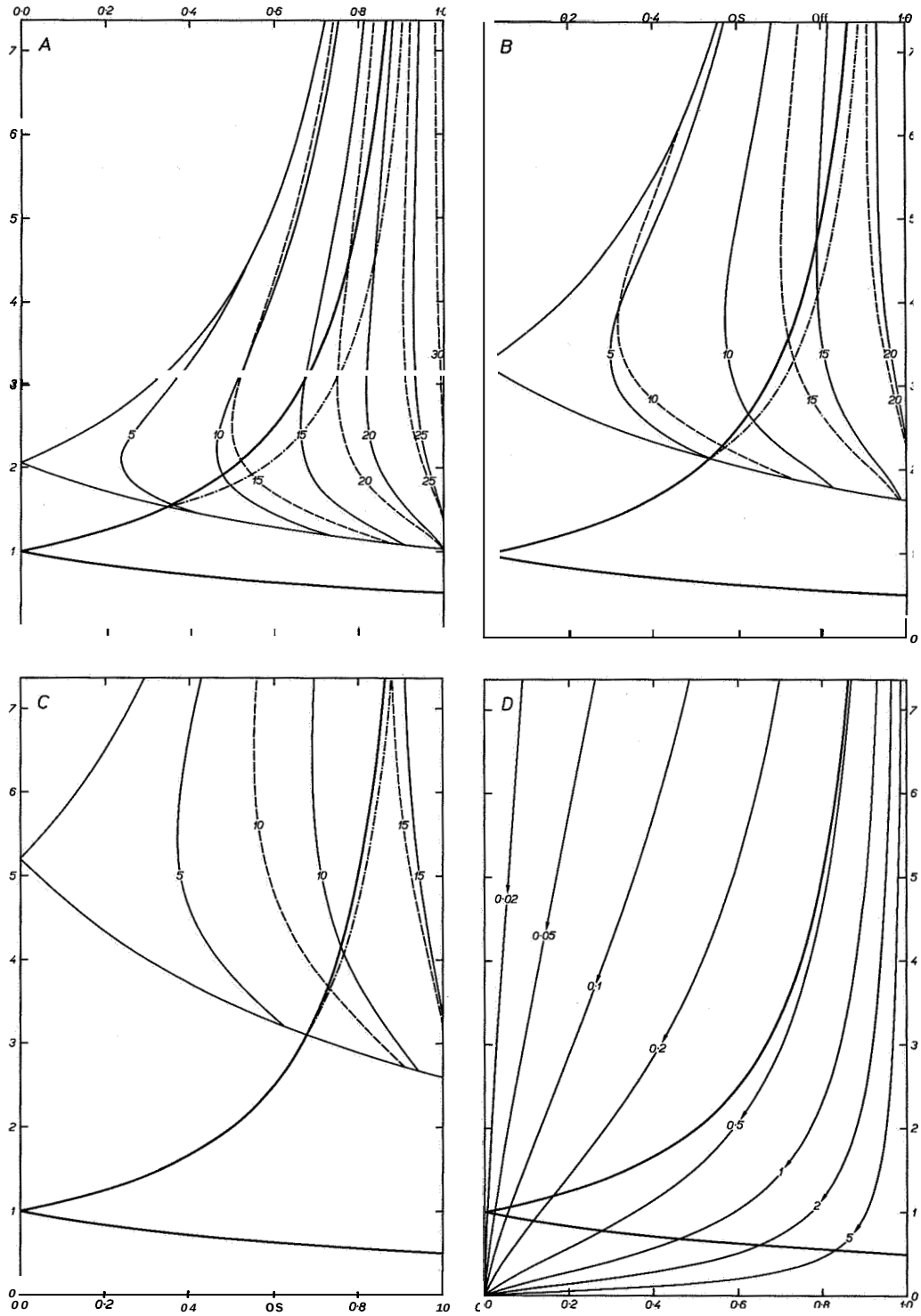

FIGURE 3.—Ejection velocities (in km/sec) referred to a circular orbit of: a, commensurability 1:4 (heavy line=boundary condition for crossing the earth's orbit; thinner lines= boundary condition for the orbits of ejected particles, ejection velocities for $i=0°$; dashed lines=ejection velocities for $i=30°$; dashed-anddotted line= nodal line condition for $i=30°$); b, commensurability 1:2; c, commensurability 1:1; d, operation of drag effects (constant C) (arrows=the predominant direction of evolution, common to the Poynting-Robertson effect, corpuscular effect, and Yarkovsky-Radzievsky effect of retrograde rotation).

different oppositions, deter the mean opposition magnitude from being a sufficient measure of the discovery probability. Systematic searches for new asteroids by Wolf and Metcalf's methods are intentionally suited to the bodies moving in the main part of the belt, as far as both the mean angular velocity and a small distance from the ecliptic are concerned. On the other hand, when an exceptional object happens to be discovered, the best efforts are made to follow it and eventually add it to the list of numbered objects. This applies to the Apollo group as well as to the Trojans, for which, in addition, special search programs have been accomplished.

If we restrict ourselves to the largest asteroids, which are presumably all known, no correction at all needs to be applied to the observed distribution. The list of numbered asteroids is essentially complete down to the absolute magnitude $g=10.0$; selecting 333 objects brighter than this limit from the revised catalog of asteroid magnitudes (Euiper et al., 1958), we obtain the distribution shown in figure 4b. The limiting absolute magnitude $g=10.0$ corresponds to a diameter of about 50 km.

The list of numbered asteroids is also essentially complete down to the mean opposition magnitude $m_0=15.0$; there are 796 objects brighter than this. We shall use them for extrapolating the distribution of asteroids in the a/e diagram down to $g=15.0$, or to the diameter of about 5 km. Since m_0 and g coincide at $A_0=1.618$ (where $a(a-1)=1$), correction factors of $F>1$ must be applied beyond this limit. They increase rapidly and become less and less reliable with increasing semimajor axis. Assuming the form of magnitude distribution

$$dN\sim\beta^g\,dg, \tag{13}$$

we have

$$\log F=a^2(a-1)'\log\beta. \tag{14}$$

The work of Kuiper et al. (1958) has shown that the value of the constant β varies considerably with the position within the asteroid ring. Extrapolating the correction factors F directly from the statistics of absolute magnitudes in the 3 zones delimited by Kuiper et al. (op. cit.) ($2.0<a<2.6$, $2.6<a<3.0$, $3.0<a<3.5$) and applying them to the sample of 796 asteroids brighter than $m_0=15.0$, we get the distribution shown in figure 4c. For the Hilda group, $\beta=3.6$ was adopted; for the Trojans the reduction was impossible because there are no objects brighter than $m_0=15.0$, and the magnitude interval covered by the known Trojans is too narrow to permit a reasonable estimate of β.

Comparing the figures 4b and 4c we see that the general picture radically changes when passing to objects with diameters 10 times smaller. Unfortunately, the values of β applied here are still rather uncertain, and the extrapolation has possibly been pushed too far. Nevertheless, the comparison is instructive at least in demonstrating the danger of applying the distribution function of larger bodies to the smaller ones. Since no asteroids crossing the earth's orbit appear in figure 4c, we have to search for another way of linking up the data on the Apollo group with those on the main asteroidal belt.

An attempt to do this is presented in figure 4d, which is constructed on a different principle. The absolute magnitude of the third brightest asteroid, g_3, was determined for elementary square areas in the a/e diagram ($\Delta a=0.2$, $\Delta e=0.04$), and smoothed loci of equal magnitudes g_3 have been drawn. Outside the central part of the belt, where less than three asteroids per sampling area have been found, or where it was guessed that the known asteroids do not represent the set of absolutely brightest ones, auxiliary tentative procedures had to be applied. Where the density gradient appeared low, the sampling area $\Delta a\Delta e$ was extended; in other cases it was necessary to introduce a subjective factor by estimating g_3 from an incomplete set of brightest objects. Here use was made of the probable sequence of g_i, which, for a given value of β in equation (13), yields

$$g_i-g_3=\frac{\log\,(0.4i-0.2)}{\log\,\beta} \tag{15}$$

For the Apollo group also this procedure fails because some of its members are probably too far from the top of the sequence. In this zone the estimates of the incompleteness (Öpik, 1963) have been applied. The respective equidensity lines are plotted in figure 4d in dashed

curves; all known asteroids falling within this region, whether numbered or unnumbered., are also inserted. The decrease of the asteroid density between two neighboring lines, which was 2:1 in figures 4a through 4c, is defined by an increment of 0.75 mag in g_3. This comesponds to a ratio of 2:1 for $\beta=2.5$, 2.5:1 for $\beta=3.4$, and 3:1 for $\beta=4.3$.

Even here the density ratios, in particular those overarching a number of equidensity lines, must be taken with much precaution. One important thing, however, becomes absolutely clear: the abrupt decrease of the asteroid population at the border of the central part of the distribution substantially slows down in the environment. The distribution of orbits in the Apollo group does not represent a smooth continuation of the distribution in the main asteroidal belt; there are, rather, two different systems superimposed: (1) a compact dense system, including all large asteroids and concentrated on a small area of the a/e diagram; and (2) a loose system with a low degree of concentration, stretching possibly over the whole area of the diagram between $a=1$ and $a=4$.

Unfortunately, nothing definite can be stated about the population in the upper right of the diagram. Unless Hidalgo is a peculiar, extinct cometary nucleus, its large separation from the central group would suggest that members of system (2) are also present here.

An essential improvement of the basic data on the orbits of faint asteroids may be expected from the results of the Palomar 48-inch Schmidt minor planet survey, which are now under elaboration at the Leiden and Cincinnati Observatories (Herget, 1964).

COMETS.—For the short-periodic comets the conversion of the observed distribution of orbits into the virtual one is even more difficult than for the asteroids: first, because of the considerable variations of discovery conditions from one return to another, and second, because of the rapid, irregular, and unpredictable variations of brightness with the heliocentric distance. We shall tentatively assume that for comets with $q>1$ the general discovery conditions are determined by the apparent brightness at the most favorable perihelion passage occurring in 50 years. With a random distribution of the earth's longitudes at the time of the comet's perihelion passage, there is a probability of 0.5 that at this optimum occasion the elongation of the comet from the earth, measured in radians from the sun in the ecliptical plane, will be less than ℓ :

$$\ell=0.01\pi a^{3/2}. \tag{16}$$

At the same time there is a probability of 0.5 that the angular distance of the comet from the ecliptical plane will be less than the median ecliptical latitude of the perihelion in the sample of comets concerned.

Short-periodic comets show a moderate increase of the mean perihelion latitude with increasing semimajor axis. A least-squares solution for all short-periodic comets falling within the limit of our diagram ($P<20$ years) yields the empirical relation

$$\cos b=1.011-0.004a. \tag{17}$$

Obviously, this relation holds good only within the interval of about $3<a<7$, and cannot be extrapolated outside it.

At the time of observation adopted, the heliocentric distance r and the geocentric distance of the comet A will be

$$r=q, \tag{18}$$

$$\Delta=(q^2-2q\cos\ell\cos b\ell)'". \tag{19}$$

Substituting (16) and (17) into (19), and considering that ℓ and b are small angles, we find, after some simplifications, that the geocentric distance expressed in terms of a and e will be

$$\Delta=[(a-ae-1)^2+(1-e)(0.0010a^4+0.008a^2-0.022a)]^{1/2}. \tag{20}$$

The first term in the brackets alone corresponds to the most favorable case possible of $\ell=0$, $b=0$ for each combination of a and e; the second term gives the correction on the average deviation from this for the best return in 50 years.

Obviously, the best discovery conditions need not occur exactly at the perihelion; on the other hand, there is no need for anybody to be searching for comets or observing the proper region just at the most favorable moment. Assuming that the brightness of the comet varies with

the second power of geocentric distance and with the fourth power of heliocentric distance—around the perihelion this appears more plausible than the sixth-power law (Kresák, 1965b)—we can compute the difference between the apparent magnitude m and the absolute magnitude h in the position defined above,

$$m-h=10 \log r+5 \log \Delta. \quad (21)$$

Again, we assume a distribution law of the form

$$dN \sim \gamma^h dh. \quad (22)$$

The distribution of absolute magnitudes of short-periodic comets suggests, despite the lack of data, $\gamma=2.0$ as the most plausible approximation. This figure may appear too low compared with the steeper incremental laws valid for the meteors and asteroids. It must be remembered, however, that the brightness of a meteor is approximately proportional to the cube of its radius, and that of an asteroid to the square of its radius, whereas for a comet it depends upon the quantity of gas and dust forming the coma. This should be roughly proportional to the square of the radius of the nucleus, too; however, a linear secular decrease of the diameters of the nuclei of short-periodic comets (Whipple, 1964) requires a reduction of the factory, analogous to the effect of sputtering of meteoroids (Kresák, 1960). Thus a lower value of γ does not indicate any outstanding difference between the mass distributions of the asteroids and the comets. It may be noted that Vsekhsviatskij (1958) estimates γ still lower.

Combining formulas (18), (20), (21), and (22), and putting $\log \gamma=0.30$, we obtain the correction factor F in an arbitrary point of the a/e diagram from

$$\log F=3 \log (a-ae)+0.75 \log [(a-ae-1)^2 + (1-e)(0.0010a^4+0.008a^2-0.022a)]. \quad (23)$$

The observed distribution of semimajor axes and eccentricities of short-periodic comets has been determined for two samples of orbits: (1) the orbits of all short-periodic comets (a total of 77) at their discovery apparitions; and (2) the orbits of those short-periodic comets (a total of 41) that have been observed during the last return to the sun.

The differences between these two samples, consisting, in particular, of a considerable enhancement of population below the commensurability gap of one-half, have been discussed elsewhere (Kresák, 1965a). Sample (2) evidently yields a better representation of the situation at a given moment; nevertheless, the comets entering the region below the gap are probably more efficient in ejecting meteoroids there than during other periods of their evolutionary history. The observed distributions, again with the smoothed equidensity curves indicating the loci of density ratios 1:2:4, etc., are shown in figures 5a (sample (1)) and 5c (sample (2)), the corresponding corrected distributions in figures 5b and 5d, respectively. The perturbational changes of the orbits of P/Oterma, P/Wolf 1, P/Kopff, and P/Pons-Winnecke, indicated by dashed lines in figure 5c, betray the frequent wandering of individual comets through the diagram.

Because of the lack of data, the corrected distributions cannot be extrapolated far to the left. In the upper left corner a concentration of comets with the perihelia grouping along Jupiter's orbit may be anticipated. The lower boundary of the distribution is fixed by Jupiter's perturbational barrier (fig. 2d), which does not allow the comets captured from outside to enter the inner region; however, meteoric particles that are ejected from the comets and that are small enough can do this under the action of drag effects, following the paths indicated in figure 3d.

METEORS.—The a/e diagram for meteor orbits may be supplemented by some quantities that are unambiguously defined only for the particular case of orbits intersecting the orbit of the earth. One such quantity, the argument of perihelion defined by equation (1), is shown in figure 2c. Other important quantities are the geocentric velocity and the no-atmosphere velocity, which, together with the elements a, e, and i, determine the probability of collision and the relation between the meteor's mass and brightness.

Neglecting the eccentricity of the earth's orbit and expressing all velocities in the units

of circular velocity of the earth, we have for the heliocentric velocity V_H at the moment of encounter:

$$V_H=(2-a^{-1})^{1/2}. \quad (24)$$

This, together with the velocity of the earth, results in the geocentric velocity V_G,

$$V_G=[3-a^{-1}-2a^{1/2}(1-e^2)^{1/2}\cos i]^{1/2}. \quad (25)$$

The attraction of the earth accelerates the approaching meteor; at the he'ght of about 100 km, where most meteors appear, the resulting no-atmosphere velocity V_∞ is related to the geocentric velocity by

$$V_\infty=(V_G^2+0.139)^{1/2}$$
$$=[3.139-a^{-1}-2a^{1/2}(1-e^2)^{1/2}\cos i]^{1/2}. \quad (26)$$

The values of V_∞ for $i=0°, 30°, 90°$, and $180°$, expressed in km/sec, are plotted in figure 6.

Just as for the asteroids and comets, the observed distribution of meteors in the a/e diagram will differ from the virtual distribution of meteoroid orbits in space. The selection effects include the geometric conditions of encounter (the probability of collision) and the conditions of recording the atmospheric phenomena, associated with the collisions, by a particular observing technique. For photographic observations, this includes the dependence of the brightness of a meteor upon its mass and no-atmosphere velocity, the dependence of the detectability of its image on the plate upon the brightness, distance, and angular velocity, and the mass (or magnitude) distribution law.

The dependence of the collision probability P upon orbital elements has been determined by Öpik (1951). Other effects mentioned above have been considered by Whipple (1954), who defined the proper correction factor, called "cosmic weight," as

$$C.W.\sim P^{-1}V_\infty^{-2}$$
$$=V_GV_\infty^{-4}[2-a^{-1}-a(1-e^2)]^{1/2}\sin i. \quad (27)$$

The cosmic weights have been computed for all meteors of the Harvard surveys (McCrosky and Posen, 1961; Hawkins and Southworth, 1961; Jacchia and Whipple, 1961).

There is some uncertainty as to whether the no-atmosphere velocity exponent, appearing in (27), correctly takes into account the mass-velocity and number-luminosity laws; however, with the data available at present a reasonable improvement of (27) may not be possible. Hence we have adopted this formula with two minor modifications: (1) we express the velocities in the units of circular velocity of the earth instead of the units of 100 km/sec adopted by Whipple, and (2) we omit the factor sin i. While the former modification is purely formal, equivalent to the introduction of a proportionality factor, the latter modification represents a reasonable adaptation of Whipple's "cosmic weights" for the application in the a/e diagram. In investigating the population in different parts of the diagram, we are driven to deal with meteor samples of limited range in inclination, and to presume that the distribution in a and e is the same everywhere within this range. If formula (27) is used, the meteors with inclinations near to 0° or 180° would be assigned very low weights, and the statistical importance of the sample would decrease. For instance, in the range of low-inclination orbits, $0°<i<30°$, the corrected distribution would essentially depend upon the meteors with orbits $15°<i<30°$, and reflect strongly all random fluctuations found in this less-populated range. For this reason we adopt the correction factor G:

$$G=V_GV_\infty^{-4}[2-a^{-1}-a(1-e^2)]^{1/2}, \quad (28)$$

which is in simple relation to Whipple's "cosmic weight,"

$$C.W.=37.8G\sin i. \quad (29)$$

Since P is the probability of collision per revolution of the particle, the factor G converts the observed distribution in the a/e diagram into the distribution of perihelion passages of individual meteoroids down to a uniform mass limit. To compare this with the distributions of the asteroids and comets (figs. 4 and 5), we must pass from the frequency of perihelion passages to the number of bodies in space, multiplying G by the period of revolution. Thus we obtain the correction factor G':

$$G'=V_GV_\infty^{-4}a^{3/2}[2-a^{-1}-a(1-e^2)]^{1/2}. \quad (30)$$

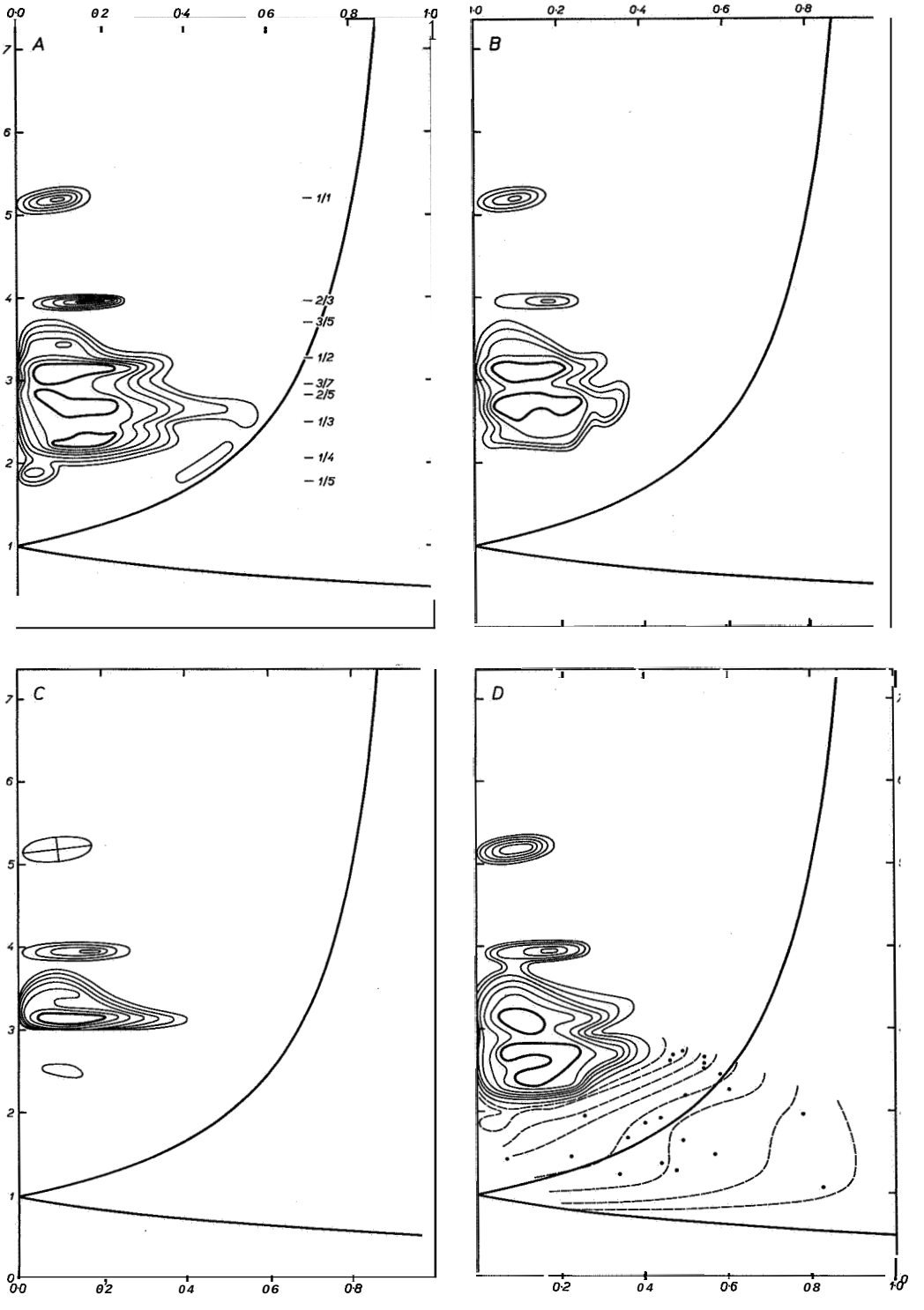

FIGURE 4.—Distribution of asteroids in the a/e diagram: a, observed distribution of **1649** numbered asteroids (cipher marks= commensurability ratios with respect to Jupiter); b, distribution of **333** asteroids brighter than $g = 10.0$ or larger than $D = 50$ km; c, distribution of asteroids brighter than $g = 15.0$ or larger than $D = 5$ km, extrapolated from the distribution of 796 asteroids brighter than $m_0 = 15.0$ using Kuiper's values of β; d, distribution extrapolated from the sequence of brightest asteroids in each region (heavy lines= boundary condition for crossing the earth's orbit, boundaries of the regions occupied by one-half of all objects). In diagrams a, **b,** and c each pair of neighboring lines corresponds to a change in the density by a factor of two; for the explanation of diagram d see the text.

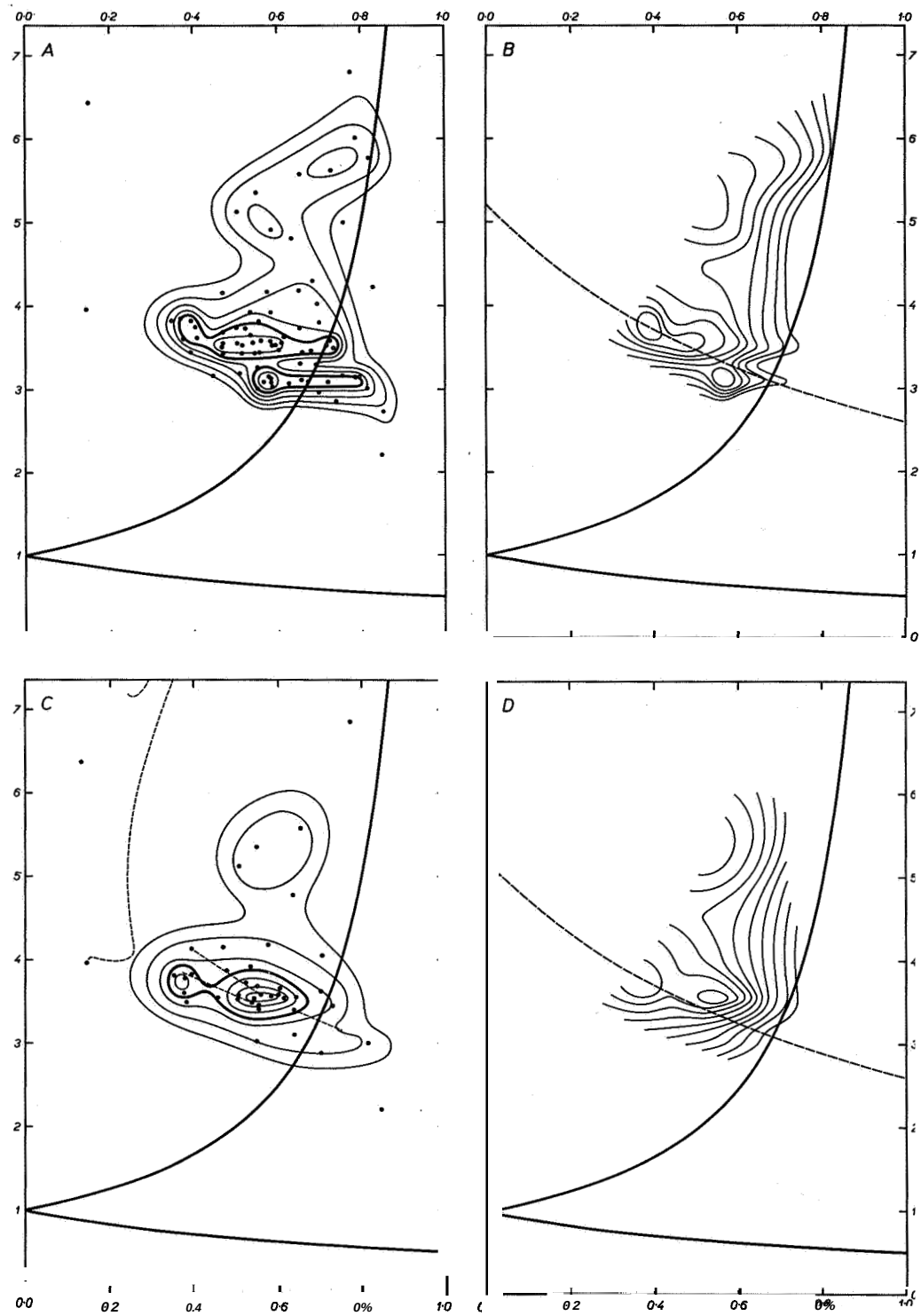

FIGURE 5.—Distribution of comets in the *a/e* diagram: a, observed distribution of 77 short-periodic comets at their discovery apparitions; b, same distribution corrected for the effect of selection; c, observed distribution of 41 short-periodic comets that have been observed during the last return to the sun; d, same distribution corrected for the effect of selection (heavy lines=boundary condition for crossing the earth's orbit, boundaries of the regions occupied by one-half of all objects; long-dashed lines= aphelia at the mean heliocentric distance of Jupiter; dots=individual comets; shortdashed lines= perturbational displacement of some strongly perturbed orbits. Each pair of neighboring equidensity lines corresponds to a change in the density by a factor of two).

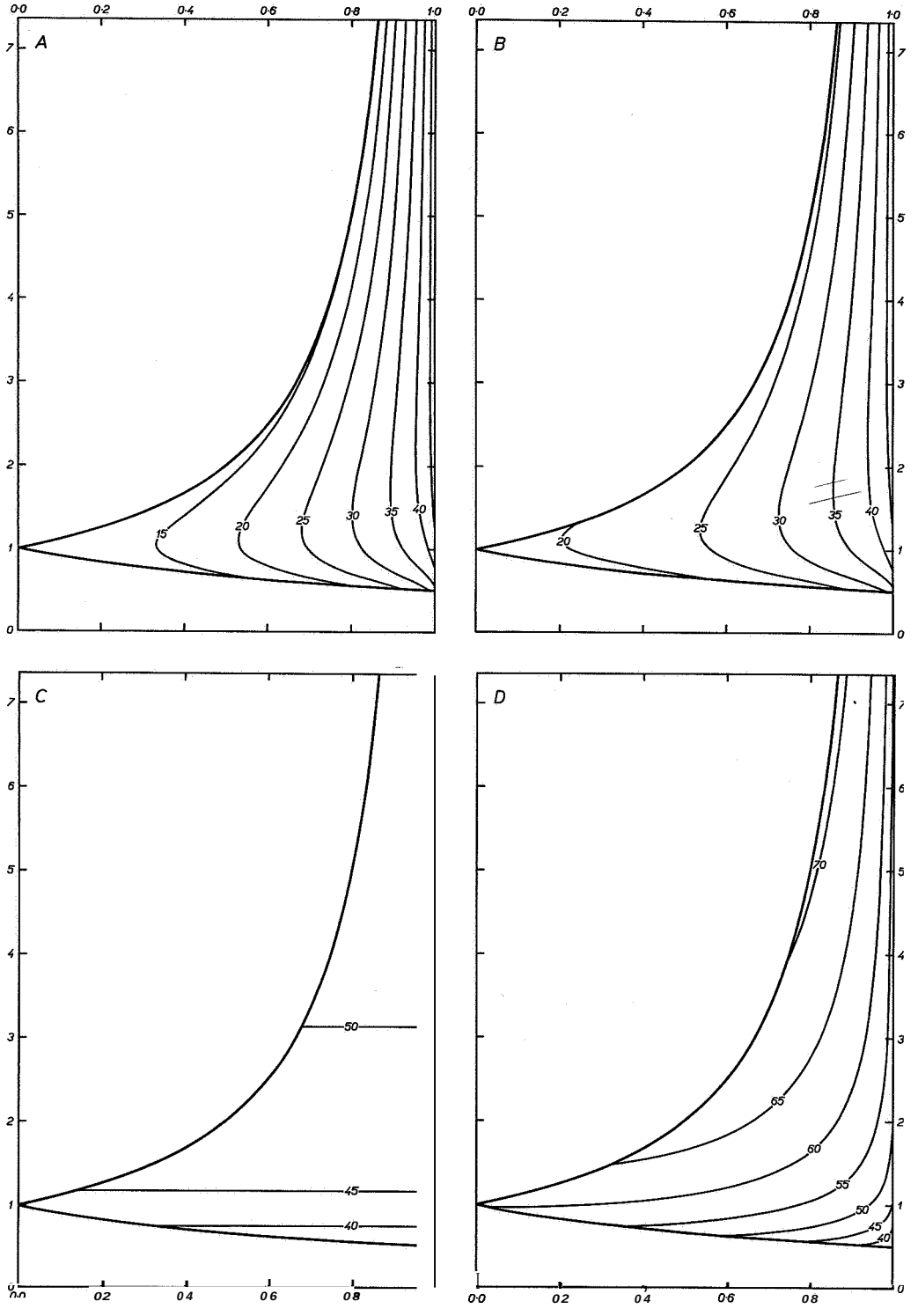

FIGURE 6.—No-atmosphere velocities V_∞ (in km/sec) of meteors in the a/e diagram: a, for $i=0°$; b, for $i=30°$; c, for $i=90°$; d, for $i=180°$ (heavy lines= boundary condition for crossing the earth's orbit).

Obviously, $C.W.$, G, and G' are not defined beyond the boundary set by equation (2).

The correction factors G and G' are plotted in figures 7 and 8 for four selected values of inclination, $i=0°$, 30°, 90°, and 180°. In our analysis we shall consider three groups of meteor orbits delimited by these boundary values: (1) low-inclination orbits ($0°<i<30°$); (2) direct high-inclination orbits ($30°<i<90°$); and (3) retrograde orbits ($90°<i<180°$).

It may be noted that the distribution of asteroids and short-periodic comets, treated above irrespective of inclination, referred practically to group (1). In fact, there are only 11, or 0.7 percent, numbered asteroids with inclinations exceeding 30° and merely 3, or 0.2 percent, with inclinations exceeding 35° (1580 Betulia, 52°.0; 944 Hidalgo, 42°.5; and 1373 Cincinnati, 38°.9). Also, there are only 6, or 8 percent, short-periodic comets ($P<20$ years) with inclinations exceeding 30° and merely 2, or 3 percent, with inclinations exceeding 32° (P/Tuttle, 54°.7; P/Pigott, 45°.1). For the meteors high inclinations are much more abundant even among short-periodic orbits, although low inclinations do prevail here, too.

In addition to the discrimination according to inclination, a discrimination between bright and faint meteors was also attempted. For faint meteors the extensive catalog of Super-Schmidt orbits by McCrosky and Posen (1961) is available; the lower precision of the graphical reduction methods used here appears sufficient for our purpose because of the homogeneity of the data. Photographic orbits of brighter meteors, although generally more accurate, are rather scarce, and the data had to be compiled from different sources. Even so a sample of some statistical importance could be obtained for only low-inclination orbits It consists of 70 orbits measured in Dushanbe (Eatasev, 1964; Babadzhanov, 1963), 47 orbits from the Harvard bright meteor photographic data (Whipple, 1954), and 17 orbits from the Ondfejov data (Plavcovd and Plavec, 1960; Ceplecha et al., 1964). To these data, obtained by conventional slow cameras, 43 orbits of the brightest Super-Schmidt meteors (Jacchia and Whipple, 1961) have been added. In order to avoid a bias in favor of high-velocity meteors and to ensure a relative homogeneity with the rest of the sample, the choice of these meteors was not based on the photographic magnitudes but on the probable rise above the plate limit, inferred from the absolute magnitude and no-atmosphere velocity (Hawkins and Upton, 1958; Kresák, 1964).

A rather difficult problem is the exclusion of the shower meteors (already not included in the numbers quoted above). According to Southworth and Hawkins (1963), about 36 percent of all photographic meteors belong to meteor streams and associations, the proportion being even higher among brighter and short-per odic meteors. It is practically impossible to distinguish between "sporadic" and "shower" meteors in individual cases, because of both a low spatial density of minor showers and a considerable dispersion of many major showers. It was considered reasonable to discard only the members of the five major showers indicated in figure 1—the Geminids, Northern and Southern Taurids from group (1), the 6 Aquarids from groups (1) and (2), and the Quadrantids from group (2). The possible interference by other showers has been checked additionally by comparing the angular elements of meteors forming clusters in the a/e diagrams.

In connection with the peculiar shape of the dispersion areas of meteor showers in figure 1, one important point may be emphasized. As a consequence of the condition denoted by equation (1), the dispersions within the a/e diagram do not indicate a general relation between the semimajor axis and the eccentricity in a meteor stream, but only in its part meeting the earth. By comparing figures 2a, c, we see that the loci of constant q and ω run almost parallel unless the aphelion distance is extraordinarily small. Now, for a shower of short duration, where Ω is practically equal for all meteors, a small dispersion of the lines of apsides, necessary to keep the stream compact at large heliocentric distance, requires a small dispersion in the argument of perihelion ($\omega=\pi-\Omega$). In this case only meteors falling within a narrow range of perihelion distances can collide with the earth. Thus the large disproportion between the dispersion of the perihelion and aphelion distances (e.g., $\delta q=\pm 0.006$ against $\delta Q=\pm 0.7$ for the Quadrantids, $\delta q=$

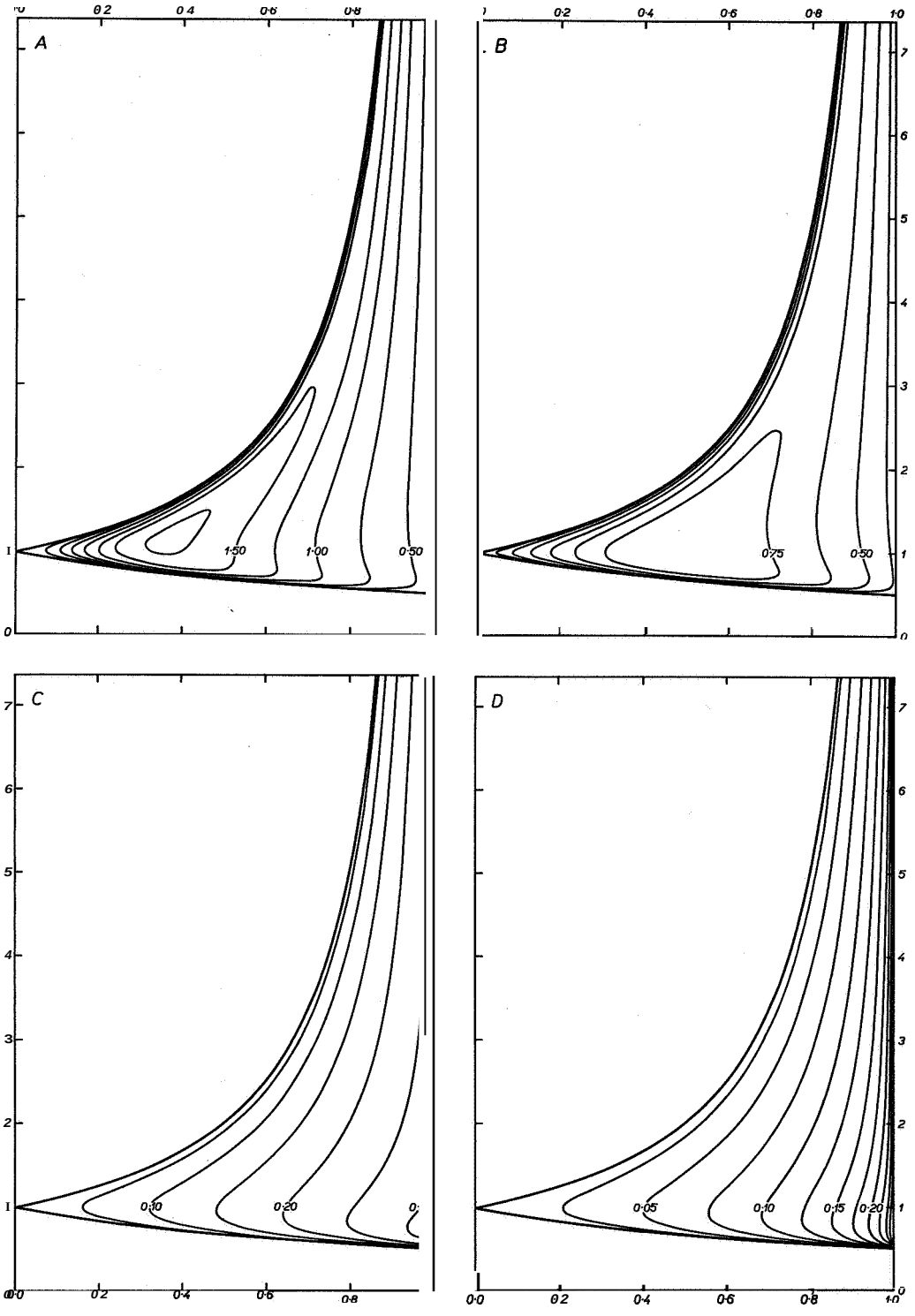

FIGURE 7.—Correction factors G for conversion of the observed frequency of meteors into the virtual frequency of perihelion passages in the *a/e* diagram: a, for $i=0°$; b, for $i=30°$; c, for $i=90°$; d, for $i=180°$ (heavy lines=boundary condition for crossing the earth's orbit).

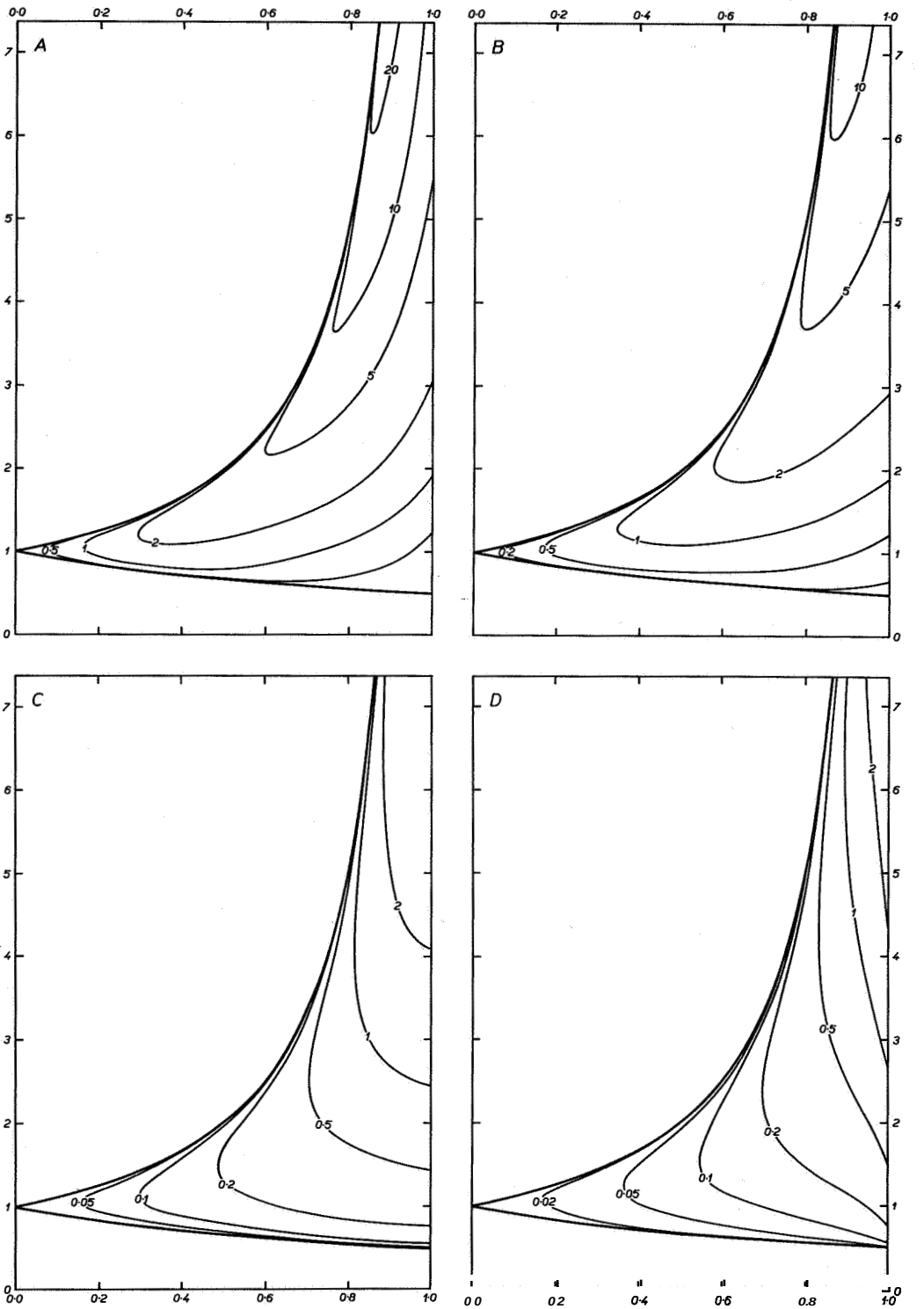

FIGURE 8.—Correction factors G' for conversion of the observed frequency of meteors into the virtual density in the a/e diagram: a, for $i=0°$; b, for $i=30°$; c, for $i=90°$; d, for $i=180°$ (heavy lines=boundary condition for crossing the earth's orbit).

± 0.015 against $\delta Q = \pm 0.7$ for the 6 Aquarids, or $\delta q = \pm 0.007$ against $\delta Q = \pm 0.15$ for the Geminids—all values determined from the catalog of McCrosky and Posen (1961)) is no definite characteristic of the stream's structure. The dispersion of perihelion distances is obviously underestimated because of the selection effect, whereas the dispersion of aphelion distances is overestimated because of the lower accuracy in determining this quantity from the velocity data.

The a/e diagrams for the low-inclination group (1) of nonshower meteors are shown in figure 9: for 176 bright photographic meteors above, for 1300 Super-Schmidt meteors below. The Příbram meteorite, with $a = 2.42$, $e = 0.674$, would fall into the lobe close to the left of the maximum occurrence in figure 9a. Again, the spacing of the equidensity lines corresponds to a change by a factor of two in the density per unit area, the heavy line delimiting the region occupied by one-half of the meteors. The observed distributions (figs. 9a, c) are converted into the respective virtual distributions (figs. 9b, d) by applying the correction factors G' plotted in figure 8. An interpolation between the correction factors for $i = 0°$ and $i = 30°$ was necessary; it proved sufficient to do this graphically by halving the angles formed by the loci of equal G' (0°) and G' (30°), and averaging the distances between two neighboring curves throughout the diagram. Analogous diagrams for the groups of high-inclination direct orbits (2) and retrograde orbits (3) are shown in figure 10. Here the random fluctuations in density are larger compared with figure 9c, because of the lower numbers of orbits included (226 and 125, respectively).

Minor irregularities in the distributions may be attributed to meteor showers in only two cases. The concentration of low-inclination orbits near $a = 1.5$, $e = 0.93$ (figs. 9c, d) is associated with a dispersed shower of extremely low perihelion distance, $q \simeq 0.10$, active around January 20. The radiant is situated near α Leo, at about $\alpha = 150°$, $\delta = +15°$, the orbits resembling those of the Geminids and 6 Aquarids. The belt of enhanced density of direct high-inclination orbits, stretching from $a = 1.9$, $e = 0.95$ to $a = 0.7$, $e = 0.80$ (figs. 10a, b), is associated with another stream of extremely short perihelion distance, $q \simeq 0.10$. The approximate radiant coordinates at the time of maximum activity (about July 17) are $\alpha = 325°$, $\delta = +5°$. These meteors are probably connected with the complex of Southern and Northern Aquarid streams meeting the earth a little later; a resemblance to the intricate system of Taurid-Arietids is apparent. The large dispersion in the semimajor axes and the occurrence of extremely short aphelion distances ($Q = 1.3$ for Meteors nos. 3356 and 8028) is of particular interest, insofar as the concentration approximately follows the evolutionary path anticipated for the drag effects. A similar prominence, ending near $a = 1.0$, $e = 0.50$, is found in the distribution of retrograde orbits (figs. 10c, d), but there is no orbital association among the bodies constituting this concentration.

The group of retrograde orbits exhibits, as expected, an increasing concentration toward longer semimajor axes, continuing over the upper edge of the diagram. A secondary maximum reveals a concentration of aphelia of high-eccentricity orbits to the orbit of Jupiter. This concentration extends downward to the left, in the proper direction of operation of the drag effects.

The main change in passing from the retrograde to the direct high-inclination orbits (fig. 10b) is that a concentration of orbits of the type of Jupiter's family of short-periodic comets (around $a = 3.5$, $e = 0.70$) begins to appear. This concentration becomes the predominant feature among the direct low-inclination orbits (figs. 9b, d). Here, in the region of $a > 2.5$, no distinction between brighter and fainter meteors is apparent. The concentration is not so sharp as for the short-periodic comets, which may be partially due to a lower accuracy in determining meteor orbits. At the lower side, the region of maximum occurrence of brighter meteors ends by a sharp cutoff, a decrease in the density by a factor of 10 within less than 0.5 a.u. in a. This cutoff is absent in the group of fainter meteors (fig. 9d), although even here the decrease is steeper than for the high-inclination orbits. It must be remembered that because of the brightness-velocity dependence we are

dealing with smaller particles in the high-inclination and retrograde groups. Thus the comparison of figures 9b with 9d, and 9d with 10b and 10d consistently suggests an increasing proportion of extremely short-periodic orbits, situated far inside Jupiter's perturbational barrier, with decreasing size of the particles.

In figures 9a and 9b, based on the most accurate elements, the separation of a very interesting group of eight low-eccentricity meteors, forming the secondary maximum at the extreme left, is clearly indicated. This concentration appears just in the region accessible to fragments ejected from the asteroidal belt at reasonable velocities, and subsequently decelerated by the drag effects. It is also essentially the same region where an anomaly of the magnitude distribution, suggesting a different origin of the particles, has been found previously (Kresák, 1964). It may be noted that **Cook,** Jacchia, and McCrosky (1963) suspected two distinct classes of orbits for four meteors considered asteroidal on the basis of their behavior in the atmosphere. In fact, two of these meteors (Halliday's iron meteor with $a=1.05$, $e=0.117$, and Harvard Meteor no. 1242 with $a=1.33$, $e=0.262$) fall just within this region, whereas the two others (Harvard Meteor no. 19816 with $a=2.24$, $e=0.662$, and the Příbram meteorite with $a=2.42$, $e=0.674$ (a chondrite)) together with the Harvard Meteor no. 7946 ($a=2.49$, $e=0.621$), classified as asteroidal by Jacchia, Verniani, and Briggs (1965), fall on the lower boundary of the region of maximum occurrence of low-inclination orbits. This is just the region where the orbits of the asteroids not belonging to the Apollo group (719 Albert: $a=2.59$, $e=0.541$; 887 Alinda: $a=2.52$, $e=0.540$; 1036 Ganymedes: $a=2.66$, $e=0.543$; 1953EA: $a=2.44$, $e=0.580$) approach most closely to the boundary condition (2), as is evident from figure 4d.

Conclusions

The application of the a/e diagram to the distribution of asteroid, comet, and meteor orbits suggests that there are probably five distinct classes of short-periodic meteors, each of which is generically related to a corresponding class of larger bodies:

1. Long-periodic comets supply meteors with a random distribution of orbital planes, which are spiraling to the sun under the action of drag effects. As pointed out by Whipple (1963), the Poynting-Robertson effect generally acts much more slowly than the interplanetary erosion, which prevents the aphelia of all but the very smallest cometary meteoroids from displacing appreciably toward the sun. Whipple also suggests, however, that just the high-inclination orbits are favored by the Poynting-Robertson effect because of the concentration of the eroding dust to Jupiter's orbital plane. Possibly the corpuscular component increases the efficiency of drag effects not to be entirely eliminated by the erosion. A relatively slow decrease in the number of high-inclination meteors with decreasing aphelion distance suggests that a drag is actually acting on them. The only alternative explanation, that these meteors belong to class (5), will be referred to below.

2. Jupiter's family of short-periodic comets supplies a class of meteoroids that reflects its characteristic features: the concentration of aphelia around Jupiter's orbit, and low inclinations. Not more than a few percent of the orbits have $i>30°$. For bright photographic meteors, Jupiter's perturbational barrier, combined with the erosion effects, prevents the aphelia from drifting toward the sun and produces a sharp cutoff in the semimajor axes. For fainter meteors, this boundary is less definite, either because of the diffusion of some particles inward, or because of an increased degree of overlapping with the orbits of class (5).

3. The system of minor planets is obviously associated with a similar system of smaller particles, but these are unobservable from the earth on account of their excessive perihelion distances. Individual marginal members of this system enter the region of observability, in particular as a continuation of the Albert group of asteroids, near $a=2.5$, $e=0.6$. They are hardly distinguishable by orbital elements from the cometary meteors of Jupiter's family; only their aphelion distances are generally somewhat shorter (about **4.0).**

4. The asteroidal fragments originating from the collisions in the central part of the asteroidal belt spiral to the sun in orbits of lower and decreasing eccentricity, until they

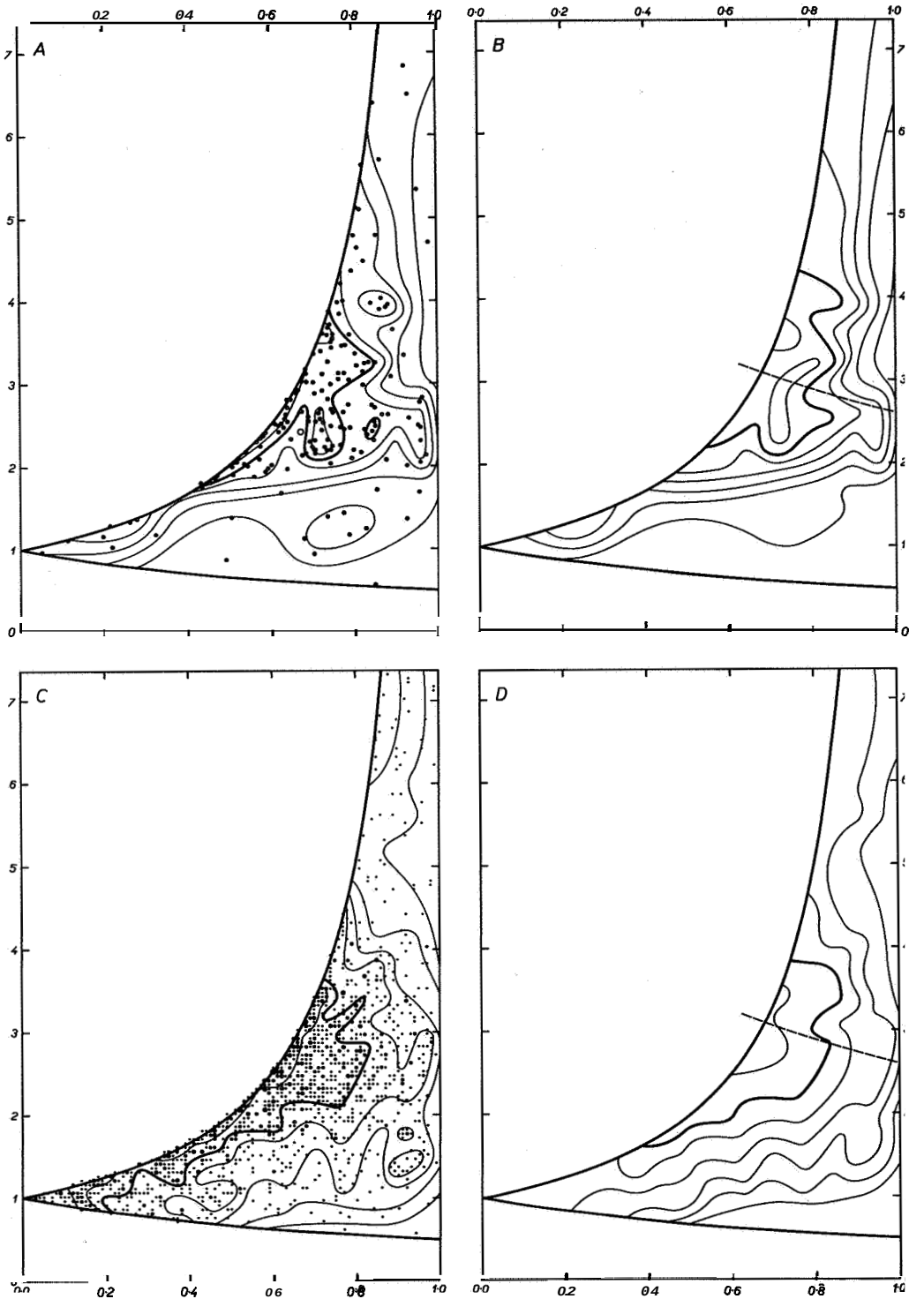

FIGURE 9.—Distribution of meteors in low-inclination orbits ($0° < i < 30°$) in the a/e diagram: a, observed distribution of **176** bright nonshower meteors; b, same distribution corrected for selection effects; c, observed distribution of 1300 faint nonshower meteors; d, same distribution corrected for selection effects (heavy lines = boundary condition for crossing the earth's orbit, boundaries of the regions occupied by one-half of all objects; dashed lines = aphelia at the mean heliocentric distance of Jupiter. Each pair of neighboring equidensity lines corresponds to a change in the density by a factor of **two).**

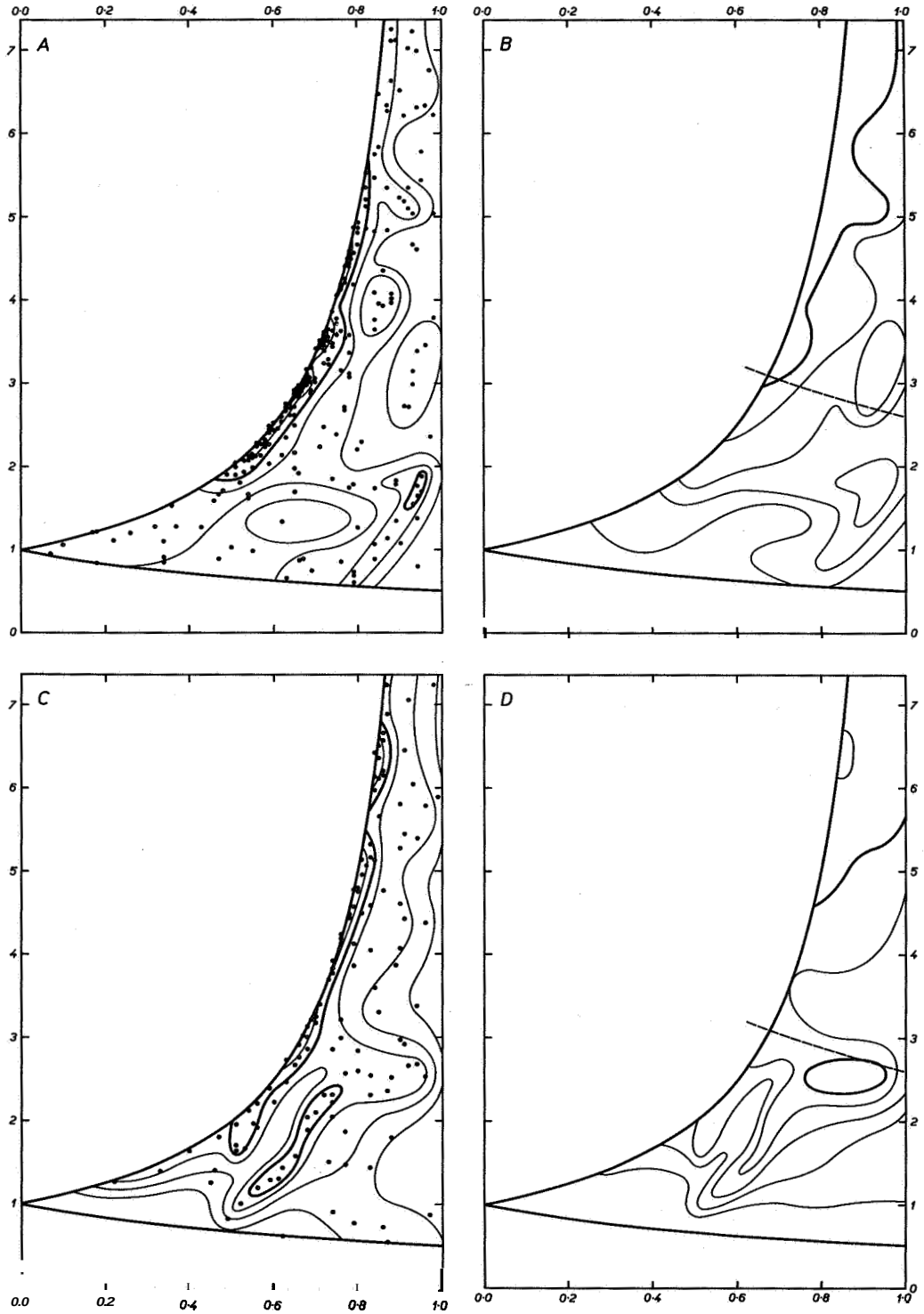

FIGURE 10.—Distribution of meteors in high-inclination orbits in the a/e diagram: a, observed distribution of 226 faint nonshower meteors in direct orbits ($30° < i < 90°$); b, same distribution corrected for selection effects; c, observed distribution of **125** faint nonshower meteors in retrograde orbits ($90° < i < 180°$); d, same distribution corrected for selection effects (heavy lines= boundary condition for crossing the earth's orbit, boundaries of the regions occupied by one-half of all objects; dashed lines=aphelia at the mean heliocentric distance of Jupiter. Each pair of neighboring equidensity lines corresponds to a change in the density by a factor of two).

become observable around $a = 1.2$, $e = 0.2$. Owing to a higher crushing strength they are much less affected by erosion than the cometary particles. This class shows a steeper increase in frequency with decreasing brightness than do the cometary meteors (Kresák, 1964), and may be rather abundant at the magnitudes below the present threshold of photographic techniques. In the range of fainter meteors a connection of this area with (3), running closely along $q = 1$, appears.

5. The fifth component is most difficult to interpret, because of insufficient information on the nature and distribution of orbits of the parent bodies. The largest bodies belonging to this class are members of the Apollo group of asteroids. It has been shown that these objects do not constitute a smooth continuation of the distribution of orbits within the main asteroidal belt (fig. 4d). It has also been demonstrated by Öpik (1963) that the perturbations by Mars are inadequate for supplying this region with the observed number of asteroids. Öpik's assumption that the members of the Apollo group have originated from residual nuclei of comets seems plausible. However, the diameters of these bodies, of the order of 1 km, are essentially the same as those of the nuclei of most short-periodic comets (Roemer, 1966), and the efficiency of the jet deceleration necessary to reduce the aphelion distances of the parent comets is problematical with regard to Jupiter's perturbational barrier. On the other hand, it is difficult to imagine how a meteor stream of the type of the Geminids might be of asteroidal origin; and the orbit of this stream is definitely more similar to that of 1566 Icarus than to the orbit of any comet.

Unfortunately, the virtual distribution of orbits in the Apollo group is rather indeterminate because of the inherent selection effects. Whipple (see Öpik, 1961, discussion) has pointed out the relatively small angular velocity of most known Apollo asteroids at the time of the nearest approach, which increases the chances of discovery of the bodies subject to heavier perturbations by the earth; however, the geocentric velocities of these bodies (18 km/sec on average) are considerably higher than the velocities of the bodies of class (4), which are not observed among asteroids. Note that there are no indications of perceptible perturbations by the earth in the parts of meteor streams intersecting the orbit of the earth (Kresák, 1954), but this may also be due to much shorter lifetimes.

Another possible bias, which appears even more serious, concerns the distribution in inclination. High-inclination orbits of the type of Apollo yield a much smaller probability of a close approach to the earth, and bodies moving in retrograde orbits would imply such rapid angular motion at the time of approach that they could hardly be discovered on photographs. In fact, we are not certain that the orbits of this type are actually of low inclination only, as indicated by the observations. A proof that there are also orbits of high inclination and retrograde motion would comply with the existence of similar meteor orbits. The origin of these meteors (class 1) in long-periodic comets and strong drag effects compared with the erosion effects would not be required in this case.

A dependable estimate of the relative abundances of these five classes of meteor particles from earth-based observations is practically impossible, because of the boundary condition (2). The relative abundances among the observable particles, and their general trend toward the unobservable region of the *a/e* diagram, may be estimated from figures 9 and 10. With regard to the strong velocity dependence of meteor phenomena and meteor observing techniques, the relative contributions to the total influx of meteors down to a uniform magnitude, or mass limit, essentially differ both from the virtual and from the observed states; they also change with the limiting values adopted.

Acknowledgments

Some computations used in this paper have been performed with the ZRA–1 electronic computer, by the courtesy of the Institute of Mechanics and Automation of the Slovak Academy of Sciences. Dr. A. Hajduk and Dr. J. Štohl kindly assisted in the programming, and Mrs. L. Ďurkovičová and Mrs. L. Smíšková in the statistical processing of the data. My sincere thanks are due to all of them.

References

BABADZHANOV, P. B.

1963. Results of photographic study of meteors of periods MGG and MGS Dushanbe. Bull. Inst. Astrofiz. Akad. Nauk Tad. SSR, no. 36, pp. 3–36.

CEPLECHA, Z.; JEŽKOVÁ, M.; NOVÁK, M.; RAJCHL, J.; SEHNAL, L.; and DAVIES, J. G.

1964. Ondfejov double-station meteors during the IGY and IGC. Bull. Astron. Inst. Czechoslovakia, vol. 15, pp. 144–155.

COOK, A. F.; JACCHIA, L. G.; and MCCROSKY, R. E.

1963. Luminous efficiency of iron and stone asteroidal meteors. *In* Proceedings of the Symposium on the Astronomy and Physics of Meteors. Smithsonian Contr. Astrophys., vol. 7, pp. 209–220.

DYCUS, R. D., and BRADFORD, D. C.

1964. The origin of meteors inferred from the orbital elements. Icarus, vol. 3, pp. 306–310.

FESENKOV, V. G.

1942. Asteroids and cosmic dust. Doklady Akad. Nauk SSSR, vol. 34, 163–167.

HAWKINS, G. S.

1959. The relation between asteroids, fireballs, and meteorites. Astron. Journ., vol. 64, pp. 450–454.

HAWKINS, G. S., and SOUTHWORTH, R. B.

1961. Orbital elements of meteors. Smithsonian Contr. Astrophys., vol. 4, no. 3, pp. 85–95.

HAWKINS, G. S., and UPTON, E. K. L.

1958. The influx rate of meteors in the earth's atmosphere. Astrophys. Journ., vol. 128, pp. 727–735.

HERGET, P.

1964. Report of commission no. 20 on the positions and movements of minor planets, comets, and satellites, pp. 241–250. [Trans. IAU XIIth Gen. Assembly.]

JACCHIA, L. G.; VERNIANI, F.; and BRIGGS, R. E.

1965. An analysis of the atmospheric trajectories of 413 precisely reduced photographic meteors. Smithsonian Astrophys. Obs. Spec Rep. No. 175, 309 pp.; also in Smithsonian Contr. Astrophys., vol. 10, no. 1, 139 pp., 1967.

JACCHIA, L. G., and WHIPPLE, F. L.

1961. Precision orbits of 413 photographic meteors. Smithsonian Contr. Astrophys., vol. 4, no. 4, pp. 97–129.

KATASEV, L. A.

1964. Photographic Methods in Meteor Astronomy. Trans. from Russian by Israel Program for Scientific Translations, Jerusalem, 114 pp.

KRESÁK, Ľ.

1954. On a criterion concerning the perturbing action of the earth on meteor streams. Bull. Astron. Inst. Czechoslovakia, vol. 5, pp. 45–49.

1960. The effect of solar corpuscular emission on the magnitude distribution of meteors. Bull. Astron. Inst. Czechoslovakia, vol. 11, pp. 1–9.

1964. A relation between the orbits and magnitude distribution of meteors. Bull. Astron. Inst. Czechoslovakia, vol. 15, pp. 190–201.

1965a. The effects of commensurability in the system of short-periodic comets. Bull. Astron. Inst. Czechoslovakia, vol. 16, pp. 292–296.

1965b. On the secular variations in the absolute brightness of periodic comets. Bull. Astron. Inst. Czechoslovakia, vol. 16, pp. 348–355.

KUIPER, G. P.; FUJITA, Y.; GEHRELS, T.; GROENEVELD, I.; KENT, J.; VAN BIESBROECIC, G.; and VAN HOUTEN, C. J.

1958. Survey of asteroids. Astrophys. Journ., suppl. no. 32, vol. 3, pp. 289–428.

MARSDEN, B. G.

1961. The orbit and ephemeris of periodic comet Oterma. Astron. Journ., vol. 66, pp. 246–248.

MCCROSKY, R. E., and POSEN, A.

1961. Orbital elements of photographic meteors. Smithsonian Contr. Astrophys., vol. 4, no. 2, pp. 15–84.

ÖPIK, E. J.

1951. Collision probabilities with the planets and the distribution of interplanetary matter. Proc. Roy. Irish Acad., vol. 54, sec. A, pp. 165–199.

1961. The survival of comets and cometary material. Astron. Journ., vol. 66, pp. 381–382.

1963. The stray bodies in the solar system, 1: Survival of cometary nuclei and the asteroids. Adv. Astron. Astrophys., vol. 2, pp. 219–262.

1966. Comet nuclei as the principal source of meteorites. Univ. Liège Inst. Astrophys. Coll. 8°, vol. 21, no. 510, pp. 575–580.

PIOTROWSKI, S.

1954. The collisions of asteroids. Acta Astron., vol. 5, ser. a, pp. 115–136.

PLAVCOVÁ, Z., and PLAVEC, M.
1960. Heliocentric orbits of six photographed sporadic meteors. Bull. Astron. Inst. Czechoslovakia, vol. **11,** pp. **226–227.**

PUTILIN, I. I.
1953. Minor Planets. Moscow, **412** pp.

ROEMER, E.
1965. The dimensions of cometary nuclei. Univ. Liège Inst. Astrophys. Coll. **8°,** vol. **21,** no. **510,** pp. **23–28.**

SOUTHWORTH, R. B., and HAWKINS, G. S.
1963. Statistics of meteor streams. *In* Proceedings of the Symposium on the Astronomy and Physics of Meteors. Smithsonian Contr. Astrophys., vol. **7,** pp. **261–285.**

VSEKHSVIATSKIJ, S. K.
1958. Physical Characteristics of Comets. Moscow, **575** pp.

WHIPPLE, F. L.
1951. A comet model, **11:** Physical relations for comets and meteors. Astrophys. Journ., vol. **113,** pp. **464–474.**
1954. Photographic meteor orbits and their distribution in space. Astron. Journ., vol. **59,** pp. **201–217.**
1963. Meteoric erosion in space. *In* Proceedings of the Symposium on the Astronomy and Physics of Meteors. Smithsonian Contr. Astrophys., vol. **7,** pp. **239–248.**
1964. Brightness changes in periodic comets. Astron. Journ., vol. **69,** p. **152.**

WYATT, S. P., Jr., and WHIPPLE, F. L.
1950. The Poynting-Robertson effect on meteor orbits. Astrophys. **Journ.,** vol. **111,** pp. **134-141.**

Abstract

The distribution of the orbits of asteroids, short-periodic comets, and meteors is investigated using a series of diagrams with semimajor axis plotted against eccentricity, designed for particular values of inclination. This kind of representation allows a number of significant quantities and conditions to be interrelated and compared with observations. Empirical comet-asteroid criteria are discussed, and the evolutionary paths in the a/e diagram, resulting from the perturbations by Jupiter, asteroidal collisions, and the drag effects of solar radiation, are computed.

The selection effects inherent in the discovery, or observation, of individual categories of objects are evaluated as functions of the position within the diagram, and the observing data are converted into the probable virtual distributions. All known orbits of the asteroids and short-periodic comets and all available photographic meteor orbits are used for this purpose.

The comparison of the corrected distributions and the consideration of potential evolutionary effects suggest that there are five distinct classes of meteor orbits, generically related to comets or asteroids as parent bodies, which are concentrated in different regions of the diagram.

Classification of Meteor Orbits

Z. CEPLECHA[1]

Introduction

This paper will try to answer two principal questions:

1. Do groups exist among sporadic meteor orbits that we can recognize?

2. If there are such groups, can we connect them with groups of the known bodies of the solar system?

These questions were partly answered by many authors, but complex answers in the general form that I shall attempt could be of great importance. My answers, however, are limited to a small mass region because of the necessity of dealing with relatively precise photographic orbits, which are at present available for meteors of photographic magnitude from +2 to −10, with the majority of the observational material between +1 and −5.

If we do not limit the questions to sporadic meteors only, the answers are quite clear. We know the meteor showers, which means "yes" for the first question. Hence our first question must be understood to apply to more of the meteor population than the groups similar to meteor showers, which are called associations by Jacchia and Whipple (1961). The second question applied to classical meteor showers yields the well-known answer that there is a direct connection between individual cometary orbits and individual meteor shower orbits. For the sporadic meteors we must exclude every partial case that is induced by meteor showers and associations.

Whipple's comet-asteroid criterion

Whipple (1954) postdated his K criterion for the investigation of the origin of short-period streams. Later, many authors applied this criterion to individual sporadic meteor orbits, thus implying positive answers to both our questions. To compare the present orbits of streams, which cross the earth's orbit, with the present orbital distribution of short-period cometary and asteroidal orbits, which usually do not cross the earth's orbit, is, of course, to some extent risky; but, to apply the same procedure to individual sporadic orbits is quite inadmissible, at least before we know the answers to both our questions.

Recently, Dycus and Bradford (1964) criticized the application of Whipple's K criterion to individual sporadic meteor orbits. I had similar thoughts before reading that paper and I fully agree with the criticism. In short, Whipple's criterion is an empirical boundary line between cometary and asteroidal orbits, which could hardly be extrapolated down to perihelion distances equal to and less than 1 a.u. It is possible to find other empirical expressions to distinguish between cometary and asteroidal origins, but the extrapolation down to the perihelion distances equal to and less than 1 a.u. differs considerably.

Composition of the meteor particles

Some years ago, I found a double maximum distribution of a parameter, denoted by k_B, which represents a measure of the heat conductivity, density, and specific heat of the meteoric particle (Ceplecha, 1958a). In that paper I implied a positive answer to our first question, and found it possible to connect the two maxima with the stony and iron meteorites. At the same time, I had insufficient data on the meteor orbits. Thus, the connection was based solely on the correspondence of theo-

[1] Astronomical Institute of the Czechoslovak Academy of Sciences, Ondrejov, Czechoslovak

retical k_B with observed values. Such an absolute scale of the k_B parameter derived from the beginning heights is very dubious, and my results were much criticized. The results of that paper on meteor composition are today inadmissible for me, at least before we know the answer to both our questions. On the other hand, I shall use the concept of the k_B parameter throughout this paper to clarify the problem of sporadic meteor orbits.

ADDITIONAL k_B PARAMETER.—In addition to the orbital elements of individual sporadic meteors, I shall use a parameter k_B, which is directly connected with the composition of the body. This idea is quite clear if we suppose that individual groups of sporadic meteors could have not only different orbits but also different compositions.

A simple one-dimensional solution of the heat-conductivity problem during the first part of the meteor trajectory, where the ablation and light production are quite negligible, yields the temperature τ on the surface of the particle as a function of the air density and other parameters. Thus,

$$\tau=\frac{\Lambda v_\infty^{5/2}\rho}{2(\lambda\delta c b\cos z_R)^{1/2}}, \qquad (1)$$

where A is the heat-transfer coefficient, λ the heat conductivity, δ the density, c the specific heat of the meteor material, z_R the zenith distance of the radiant, ρ the air density, b the air-density gradient, v_∞ the no-atmosphere velocity, and τ the temperature of the body before entering the atmosphere. If we now assume that the temperature at the beginning of the meteor light as recorded by the photographic emulsion is constant and equal to τ_B, we can use equation (1) to compute a certain value that will be strongly dependent on the material constants. Let us now define a logarithmic parameter k_B as

$$k_B=\log\frac{2\tau_B}{\Lambda}+\frac{1}{2}\log\lambda\delta c b, \qquad (2)$$

$$k_B=\log\rho_B+\frac{5}{2}\log v_\infty-\frac{1}{2}\log\cos z_R. \qquad (3)$$

First we shall deal with equation (2), i.e., the "theoretical" definition of k_B. The density gradient is changed very little, and the spread induced in equation (2) by b is hardly greater than 0.1. Almost all the energy is used in heating the surface at the first part of the trajectory of such small particles as we shall deal with. Thus A will be almost the accommodation coefficient, not far below one. In most cases A could hardly change from one meteor to another to such an extent that the induced statistical spread exceeds 0.3. The temperature at which we begin to observe the meteor was estimated by Levin (1961) to lie between 2000° and 3000°C. But even if we extend the temperature limits at the meteor beginning, we are still in the negligible range of spread, say 0.2, in equation (2).

The weakest point of the theoretical definition of k_B is the range of validity of equation (1). If the body has dimensions of, say, less than 1 mm, we proceed to a more complicated theoretical solution of the problem (Ceplecha and Padevět, 1961). Using the numerical results of such a solution with a meteor dimension as one of the parameters to compute k_B from equation (3), I found that the induced spread due to differences in dimensions is less than 0.1 in all the cases I will discuss in this paper.

Since we begin, however, to photograph the meteor not at the point that is theoretically the beginning of rapid ablation, the correspondence of equations (2) and (3) is not certain in advance. There may be three possible cases. If we photograph the meteor before the point of rapid ablation, equations (2) and (3) correspond with the temperature at this point. If we photograph the meteor just at the point of rapid ablation, both equations are exactly satisfied. At this point, theoretically speaking, there is a jump in brightness of 1 mag for meteors with small velocity and of 3 mag for meteors with great velocity. Thus the probability of coincidence of photographic and theoretical beginnings is not negligible. If we begin to photograph the meteor *after* it has started rapid ablation, equations (2) and (3) have no meaning and we must speculate qualitatively. If this point is not too far beyond the point of beginning of rapid ablation, we need only add to the logarithm of air density ($\log\rho_B$) a certain value dependent on many parameters to correct

equation (1). But the direction of the density correction is the same for all such meteors; thus the constant correction can be assumed as a first approximation. Equations (2) and (3) can, therefore, be used again, but with the additional uncertainty of an unknown positive constant.

Thus we can use equations (2) and (3) for the photographic meteors without a previous knowledge of the exact theoretical point at which we begin to photograph the meteors, if the observational material is homogeneous in the sense of limiting magnitudes and maximum brightnesses of the photographed meteors. These conditions are excellently fulfilled by the McCrosky and Posen (1961) meteors, which we shall use as our main observational material in this paper (42 percent of the meteors have a maximum magnitude between 0 and 1, and 67 percent a limiting magnitude between 3 and 4).

Equation (3) contains only values accessible for measurement. We can understand equation (3) so that k_B given by the beginning height density as the main factor is corrected by the velocity and zenith distance of the radiant. The influence of $\cos z_R$ on k_B from equation (3) is in almost all real cases very small. Thus the velocity is the only factor that can induce statistical groups of velocities into the statistical groups of k_B, and then there is a real danger that statistical groups of k_B can be wrongly identified as groups of different composition. We must first examine this velocity effect before considering the distribution found for k_B.

A very great advantage of the k_B value is the fact that it is obtained from data on beginning meteor heights. At this point the fragmentation of the meteor body is less than at any other observed point. Even if we assume that the beginning point is identical with the beginning of rapid fragmentation, we arrive at correct results by the following procedure.

Groups according to the k_B parameter

I will use the photographic Super-Schmidt meteors studied by McCrosky and Posen (1961) as my main observational material because (1) they give the most extensive photographic observational material for more than 2000 sporadic meteors with orbits and other data necessary to compute the k_B parameter; and (2) the limiting and maximum magnitudes of all these meteors have a statistical distribution that indicates a very good homogeneity of the material. The relatively greatest drawback of the McCrosky-Posen material is its lack of accuracy due to the graphical reduction method used. But in all the cases that I investigated, this inaccuracy resulted in an additional statistical spread only, which did not interfere with the main results.

The U.S. Standard Atmosphere (1962) was used to connect heights with air densities. If we now compute k_B for all the McCrosky-Posen sporadic meteors, we obtain the histogram given in figure 1. The interval of k_B, in which the numbers of meteors are plotted, was chosen as 0.1. (Throughout this paper I shall usually

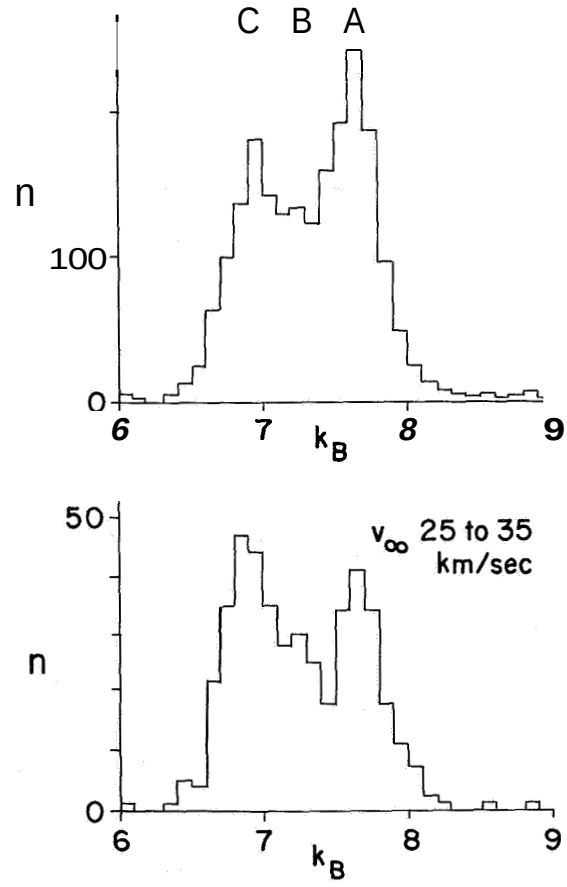

FIGURE 1.—Distribution of the k_B parameter for all sporadic meteors of the McCrosky-Posen Super-Schmidt meteors. The 25 to 35 km/sec interval of velocities is a good check that the positions of the maxima do not depend on the velocity.

denote intervals by their initial values; for example, $k_B=7.7$ contains values from 7.70 to 7.79, and so on.)

I must add that k_B is at first taken as a relative value only; thus we can say that the right-hand part of figure 1 contains denser particles with greater heat conductivity than the left, but what is the absolute value of the density we leave open for the present. At first sight we observe two maxima of k_B distribution, as I previously found from other data on bright meteors (Ceplecha, 1958a). The minimum between these two maxima lies higher than would be expected if the sample were composed of the two main groups only, thus indicating the possible presence of a third group. I denote these groups in order of decreasing density of the meteoroids: A group with maximum at $k_B=7.6$, B group with maximum at $k_B=7.2$, and C group with maximum at $k_B=6.9$. The difference of k_B between the A and the C groups is 0.7, which corresponds to a change in height of 8 to 10 km.

Now we must prove the influence of velocity on the total distribution. I divided all the material into groups of different velocities with 10 km/sec intervals. The distribution of k_B for each of these velocity intervals is plotted in figure 2. The interval of 30 km/sec (i.e., from 30 to 40 km/sec) compared with the total distribution is at first sight a good verification of the reality of all the three groups A, B, and C, quite independent of the velocity. The maxima are at exactly the same positions as for the total distribution. We see that the interval of velocity below 20 km/sec contains almost only the A group; on the other hand, almost all the meteors with $v_\infty>60$ km/sec belong to the C group. The 20 km/sec interval has all three groups with the main group A; the 30 km/sec interval has all three groups with the main group C; the 40 and 50 km/sec intervals contain relatively few meteors because of a minimum in the velocity distribution, but there is still an indication of the three groups in the 40 km/sec interval and a dominant C group in the 50 km/sec interval.

Summarizing, we see that the A group is well recognized up to the 40 km/sec interval, the B group from the 20 to the 40 km/sec interval, and the C group from the > 60 km/sec down to the 20 km/sec interval.

We can further prove the influence of differences in the meteor magnitudes and masses. We use the material divided into different velocity groups and make a further separation into different magnitude and mass intervals. The results are summarized in table 1.

The homogeneity of the material is well demonstrated in table 1, and the k_B parameter is thus confirmed as a very good criterion for investigating the McCrosky-Posen meteors.

Jacchia (1960) observed an effect similar to our groups (using the bright Super-Schmidt meteors), but his material, comprising about 400 meteors, was not sufficient for a detailed statistical study such as I present in this paper.

Distribution of orbital elements of the groups (preliminary classification)

If we wish at this stage to answer our first principal question, we must turn to the orbital elements. We are now in a position to recognize at least two, possibly three, groups of sporadic meteors according to their k_B parameters (i.e., their composition). Thus we can choose the representatives of each group: A group with k_B interval from 7.5 to 7.8 containing 719 members, C group with k_B interval from 6.7 to 7.0 containing 559 members, and B group with k_B interval 7.3. The B group is contaminated by A and C groups to the extent of about 70 percent, but we can "subtract" the A and C

TABLE 1.—*The change of k_B maxima between the lowest and the highest values of meteor mass and magnitude*

Velocity interval km/sec	k_B maximum shift					
	A		C		B	
	mass	mag-nitude	mass	mag-nitude	mass	mag-nitude
20	0.1	0.2	—	—	—	—
20 to 30	0.1	0.1	0.0	0.2	—	—
30 to 40	0.1	0.0	0.1	0.2	0.1	0.2
60	—	—	0.1	0.1	—	—

*The number of meteors in the 40 and 50 km/sec intervals is too small to permit a statistical investigation.

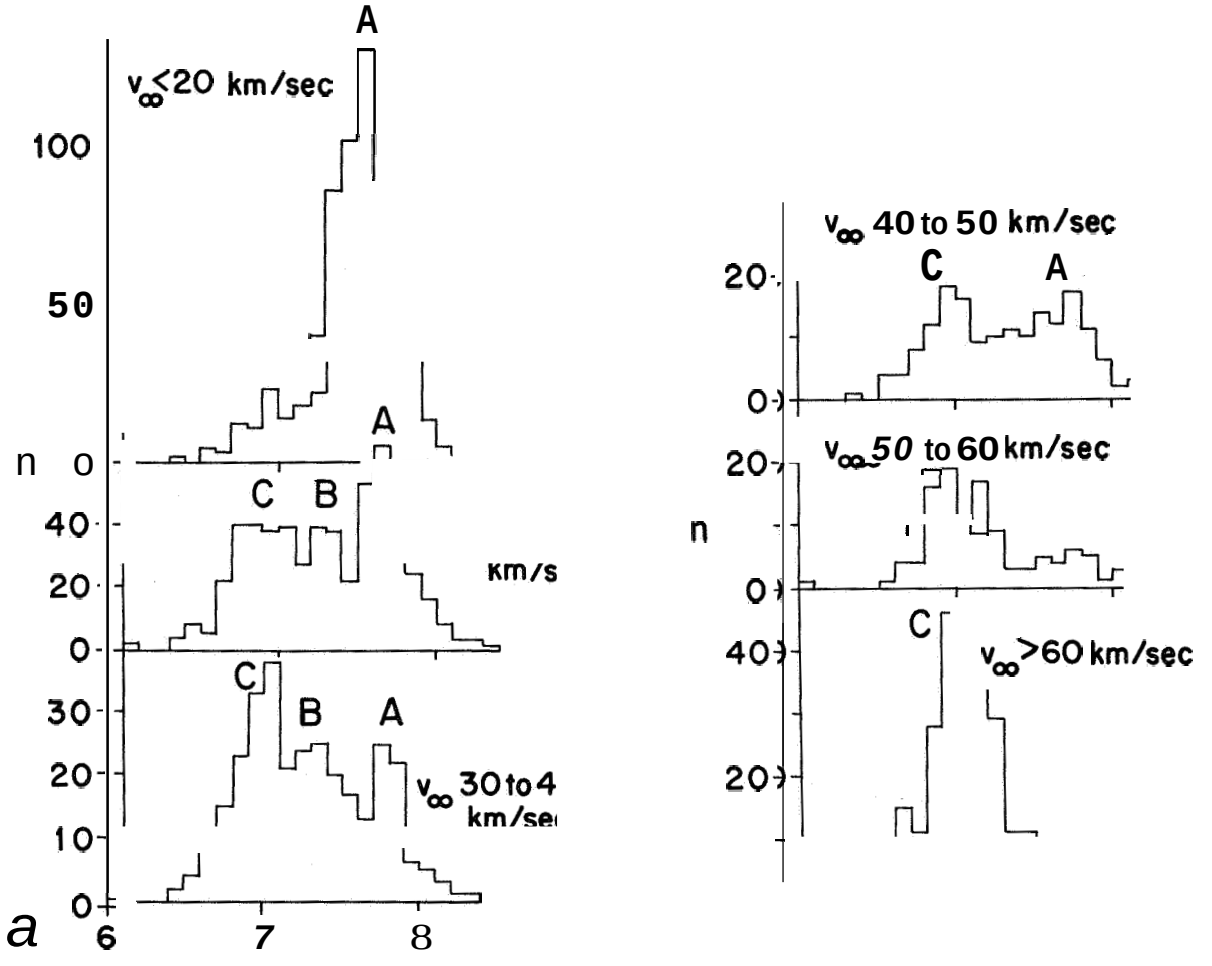

FIGURE 2.—Distribution of the k_B parameter for the same sample as in figure 1 but divided into different velocity intervals. The positions of the maxima do not depend on the velocity.

distributions and get some information on this smaller B group.

Figure 3 illustrates the distribution of orbital inclinations for all three groups. The A group shows a very strong ecliptical concentration with a negligible part of highly inclined orbits that can be explained by uncertainties in classification due to errors in the beginning heights. The C group also displays ecliptical concentration, but the highly inclined orbits are very frequent and cannot be explained by errors. The B group has ecliptical concentration of orbits with practically constant numbers between 0° and 30°. Before separating the observational material according to inclination, we will find it useful to look at the distribution of the semimajor axis. We observe in figure 4 that the A group has a maximum of a distribution between 1 and 2 a.u., the B group a flatter maximum between 1 and 3 a.u. On the other hand, the C group has a double maximum, the first one between 2 and 3 a.u., and the second one for $a \approx \infty$. (The many negative values of a are not surprising because of the approximate reduction method used by McCrosky and Posen (1961).)

Thus we see that the simple C group is now separated into two groups according to the orbit. To check this fact we use the orbital inclination 50° as a division. All orbits with

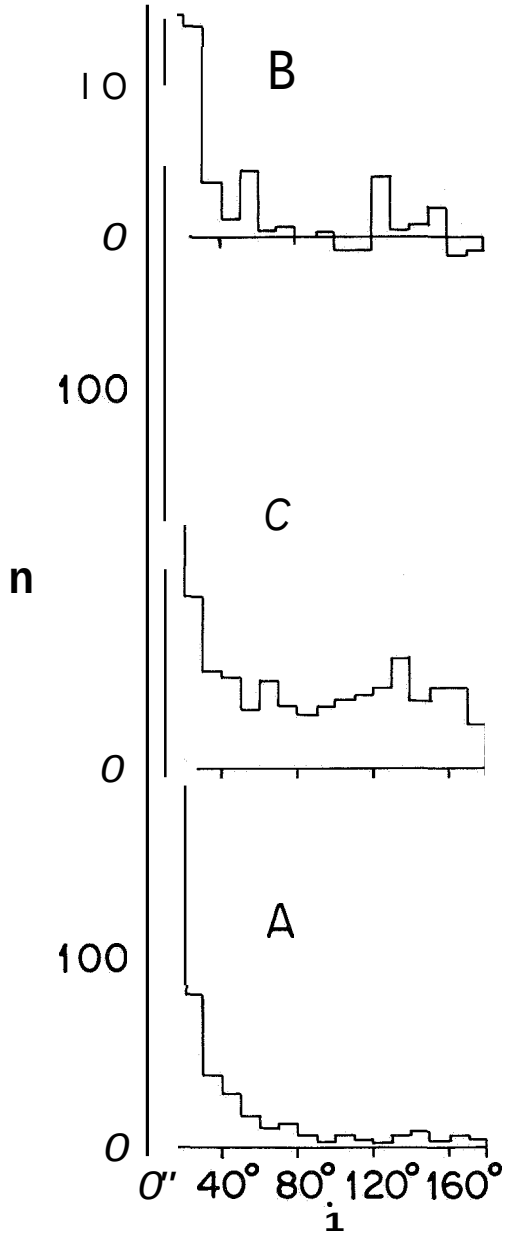

FIGURE 3.—Distribution of inclinations of the orbits of all the sporadic Super-Schmidt meteors divided into the groups A, B, C according to the preliminary classification.

$i \geq 50°$ represent the nonecliptic component, and with $i < 50°$ the ecliptic component. Such a separation for the **A** group is meaningless since almost all meteors would be in the ecliptic component. This confirms that wrongly classified meteors mainly are present.

The situation for the C group is quite different. The meteors with $i \geq 50°$ yield the maximum of $a \approx$ m, and the meteors with $i < 50°$ yield the maximum between **2** and **3** a.u. This is really a very good triple coincidence among the k_B parameter, semimajor axis, and inclination. Thus we can divide the C group into two groups according to inclinations. The ecliptical short-period group with $i < 50°$ I shall denote as the C_1 group, and the long-period group with arbitrary inclinations as the C_2 group (in practice I take $i \geq 50°$ as the criterion for the C_2 group).

The next element I consider is the eccentricity, using the 0.1 interval (fig. *5)*. The **A** group has more maxima, indicating statistical subgroups; the main maximum is in the **0.6** interval, and the majority of the **A** meteors have eccentricities below this maximum. The C_1 group has only one maximum at **0.7,** and the number of meteors with eccentricities below **0.6** is negligible. The C_2 group has a maximum at eccentricity= 1.

The perihelion distance distribution (fig. **6)** for the **A** group and the C groups is also quite different. The **A** group has a strong maximum in the interval 0.9, while the C_1 group has constant distribution starting with $q = 0.2$. The distribution of q for the B group points to a relatively great number at very small perihelion distances, less than *0.3,* in which the B group markedly differs from the **A** and C_1 groups.

In summary, we see that the **A** group contains denser bodies with smaller semimajor axes and smaller eccentricities than does the **C** group. Both these groups have ecliptical concentration and short-period orbits. The C_2 group contains particles of the same composition as the C_1 group, but with random inclinations and long-period orbits. The B group contains bodies with densities between the **A** and the C groups, with relatively eccentric orbits, ecliptical concentration, and small perihelion distances.

It is evident that the velocity can be used as an additional parameter for the classification. The **A** group has a strong maximum in the velocity interval $v_\infty < 20$ km/sec, the C_2 group has a maximum in the velocity interval $v_\infty > 60$ km/sec, the C_1 group in the interval *25* to *35* km/sec, and the B group in the interval

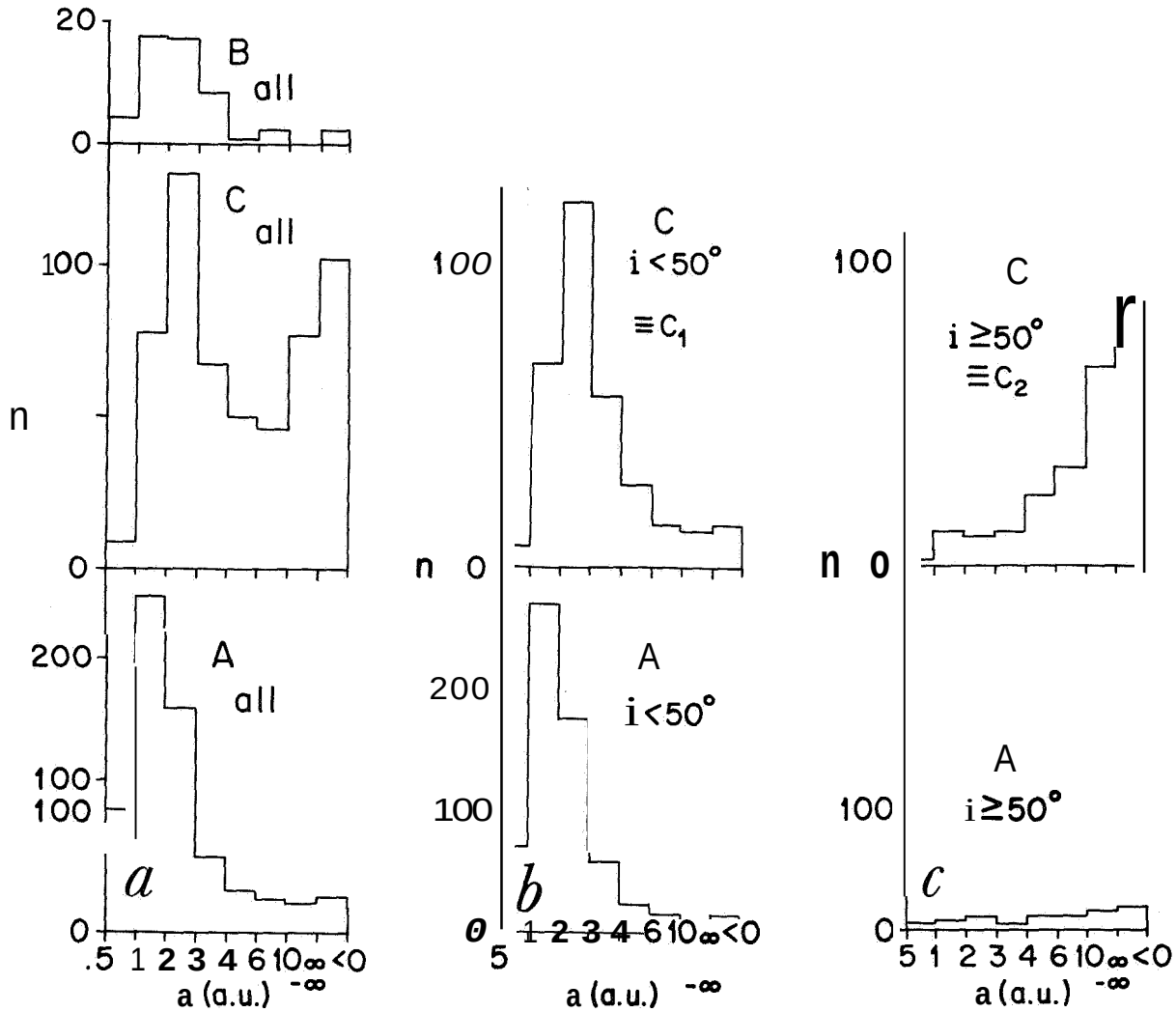

FIGURE 4.—Distribution of semimajor axes for the same material as in figure 3. The separation according to the inclinations yields the C_1 and C_2 groups.

from 30 to 40 km/sec. This was used throughout the investigation and yielded the same results I present in this section, except that the groups were more distinct and the results were clearer.

Groups in the *e–q* diagram (definitive classification)

The one-dimensionalhistograms of the preceding section show clearly the reality of the groups according to composition, and at the same time they are also distinct groups according to the orbital element distributions; however, if we wish to compare the orbital shape for different groups, we must turn to the two-dimensional histograms. I chose the eccentricity as the x axis'and the perihelion distance as the y axis, representing the oribtal shape. My choice of q instead of the usual a makes it possible to represent conveniently the short-period and long-period orbits together on one diagram.

I used the *e–q* diagram to plot the positions of all meteors of individual groups. As is expected on the basis of differences in one-dimensional histograms of individual groups, we can find statistical limits between the groups in our *e–q* diagram (fig. 7). The lower line is the limit where the meteor collides with the

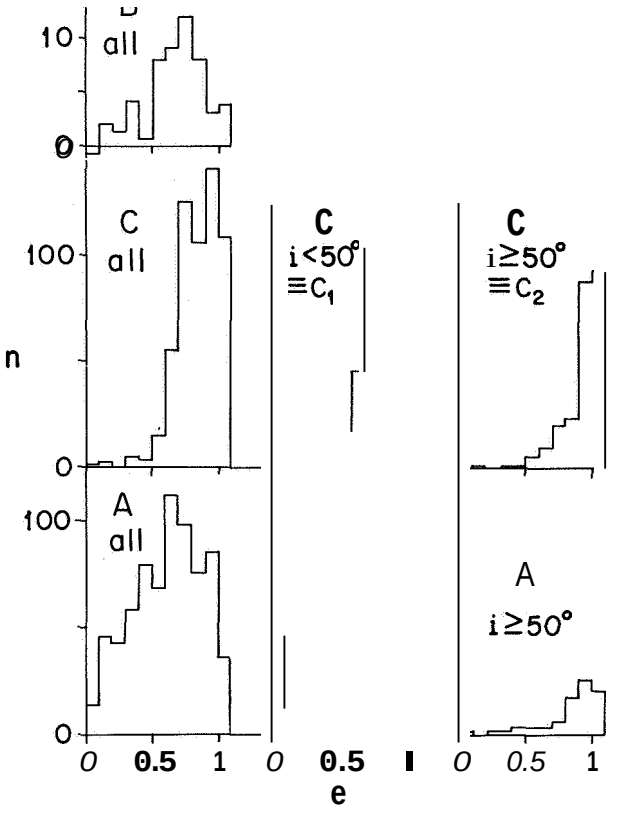

FIGURE 5.—Distribution of eccentricities for the same material as in figure 3.

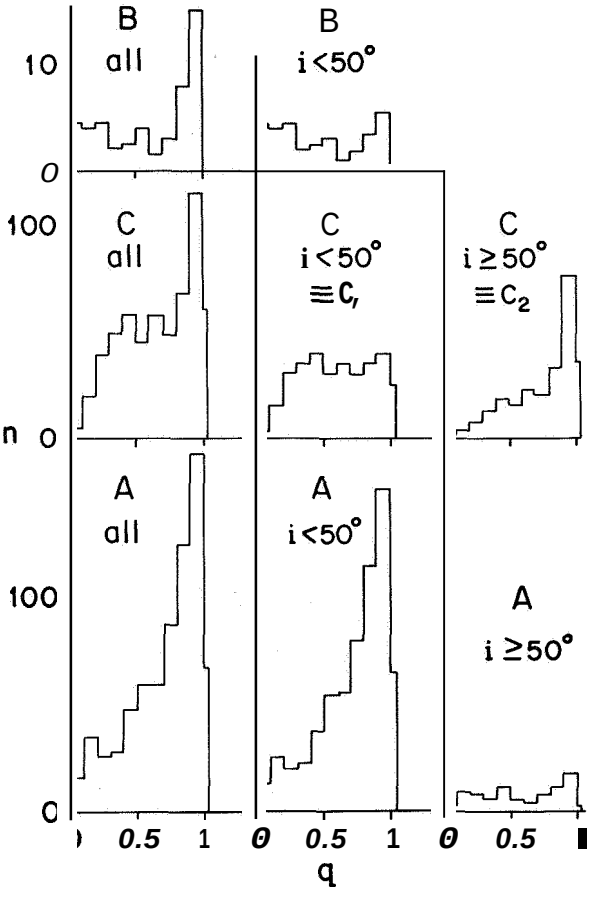

FIGURE 6.—Distribution of perihelion distances for the same material as in figure 3.

earth at aphelion, The straight line, with $q = 1$, is the limit where the meteor collides with the earth's orbit at perihelion. Real cases can, of course, be somewhat outside the limits because of'the eccentricity of the earth's orbit. Thus, the upper part of the diagram contains all observable orbits of meteors. The statistical limits given by the solid lines determine where the balance of observed numbers of meteors of different groups is attained. In reality, the interference of groups is present. We can conclude that meteors with $e < 0.6$ belong to the A group; meteors with $a > 5$ a.u. belong to the C_2 group; and meteors with $q < 0.2$ and $a < 5$ a.u. belong to the B group. The boundary region between the A and C_2 groups contains many instances of the C_1 group, but they are still less numerous than A or C_2. This is the reason why statistically the C_1 group is limited to lower values of q, where the C_1 meteors are more frequent relative to A and C_2. Thus a significant number of meteors of the C_1 group are in the region between the dashed lines, but A and C_2 groups prevail there. Other parts of the e–q diagram have stronger limits and the groups are sharply separated. The small contamination of these boundary regions is due mainly to the wrong classification and wrong orbit of individual cases.

We can prove the limits among groups of the e–q diagram by the following opposite procedure. We choose now the limits in figure 7 as the definition of the groups; to avoid misunderstanding, I denote these defined groups by A', B', C_1', C_2'. The k_B distribution for each group will show clearly the contamination of groups in the e–q diagram (fig. 8). It is not possible to separate the C_1 and C_2 interferences in this way, but both groups, mainly C_1, have a relatively high A-group contamination, which is mainly present in the upper region of the e–q diagram between the dashed lines.

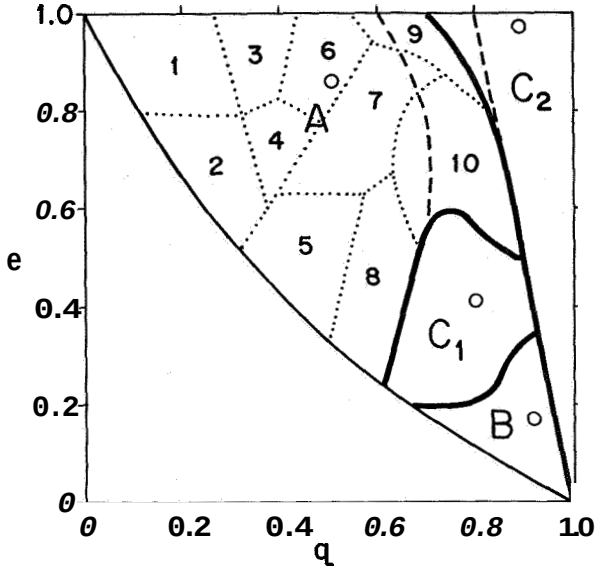

FIGURE 7.—Boundary lines among groups in the *e-q* diagram. The main groups are contained inside the full lines. The probable extension of the C_1 group superposed with the A and C_2 groups is marked by the dashed lines.

A small part of A', B', and C_1' meteors have orbits with inclinations greater than *40°*. Such orbits are denoted by A'I, B'I, C_1'I, and their k_B distribution in figure *8* clearly shows that these cases are present mainly because of errors in the basic material. The contamination of the A group by the C_2 group is well evident from the distribution of the A'I group.

We are now ready to use two criteria for the classification of sporadic meteors: the k_B value and the position in the *e-q* diagram. Thus the contamination of individual groups, when both criteria are used, becomes negligible. From figures *7* and *8*, I now define each group to be inside the limits given in figure *7* and with the following k_B interval: A group with k_B=7.40 to *7.89;* B group with k_B=7.10 to *7.29;* C_1 group with k_B=6.70 to *7.09;* and C_2 group with k_B=6.70 to *7.29.*

Characteristic orbits of the groups

We use the newly defined groups to investigate characteristic orbits. The results of one-dimensional histograms are summarized in table 2. The B and C_1 groups have a simple distribution of elements, and one characteristic orbit can be derived from the maxima of the distributions, which are in all cases close to median

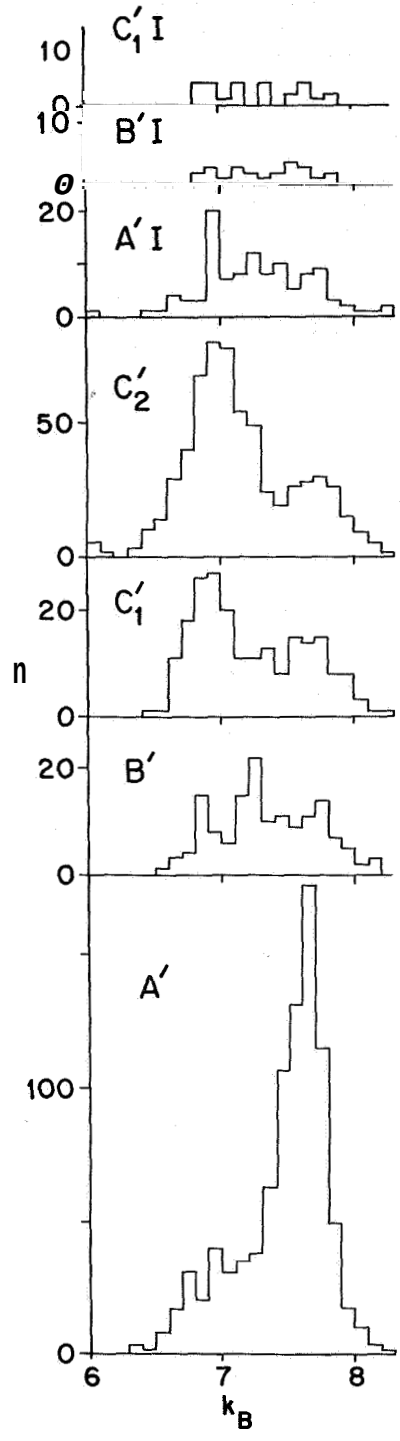

FIGURE 8.—Distribution of the k_B parameter, if the classification is made using the *e-q* diagram of figure 7. The groups are marked by "dashes" to be clear that a different definition of the groups is used from that in the preceding figures. The contamination of the groups is evident from this figure.

TABLE 2.—*Maxima* of the *one-dimensional* histograms of *orbital elements*. (The values a, e, and q are not quite consistent since they belong to independently determined maxima of the distribution of the three quantities connected with strong correlation $q=a(1-e)$.)

Group	A					B	C_1	C_2		
	Main max.	Second max.	Third max.	Fourth max.	Median			Main max.	Second max.	Median
a	2.29	1.82	1.31	1.14	1.69	2.45	2.17	$\approx\infty$ [c]	10.6	35
e	0.61	0.47	0.35	0.17	0.51	0.92	0.80	0.99	0.92	0.97
q	1.00	0.88	0.90	0.93	0.86	0.17	0.41 [b]	1.00	0.81	0.89
i	1°	1°	1°	2"	------	5° [a]	6"	------	64° [d]	-------
π	252"	91"	270"	164"	------	115"	124"	------	230"	-------
Corresponds to	A_9+A_7	A_6	A_3	A_1						

values. The C_2 group has one dominant maximum (fig. 9) close to the parabolic orbit with $q=1$, and one well-defined secondary maximum, which is probably caused by a shower not separated from the original material. This shower could in some way be connected with the Lyrids.

The A group covers a relatively large area in the e–q diagram; thus it is not surprising that a more complicated statistical distribution of elements is present. Figure 10 shows the distribution of eccentricity for the A group,

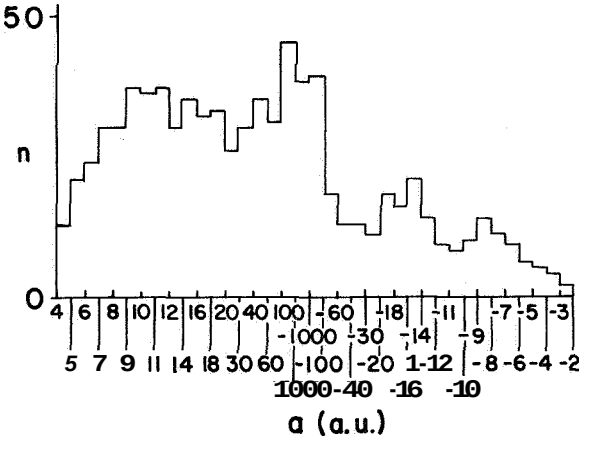

FIGURE 9.—Distribution of the semimajor axis of the C_2 group of definitive classification of the McCrosky-Posen Super-Schmidt meteors. The numbers of meteors are reduced to equal $1/a$ intervals.

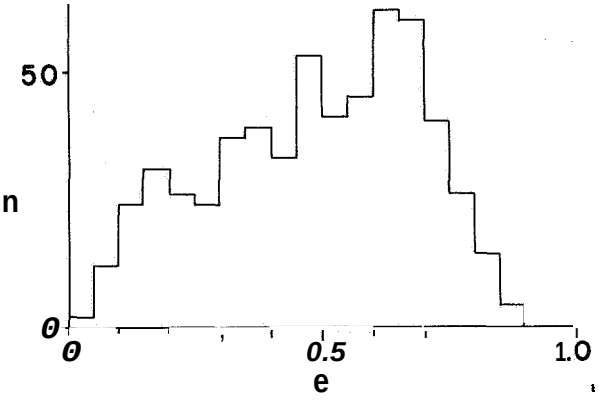

FIGURE 10.—Distribution of eccentricities for the A group of definitive classification.

and at least four groups are present. But some of these groups are further separated in the two-dimensional e–q histogram. If we look for areas of minimal number of meteors in the e–q histogram, we can find limits among 10 subgroups of the A group (fig. 7), and at the same time determine the characteristic orbits of these subgroups (table 3). Dividing lines in figure 7 are the "valleys," if the meteor numbers are plotted in the e–q diagram as heights.

The distribution of inclinations has the following characteristics (fig. 11):

	A_1	A_2	a	4	A_5	A_6	A_7	A_8	A_9	A_{10}
a	1.12	0.96	1.45	1.23	0.94	1.84	2.15	1.32	2.80	2.69
e	0.17	0.25	0.35	0.38	0.46	0.49	0.61	0.62	0.65	0.74
q	0.93	0.72	0.94	0.76	0.51	0.94	0.84	0.50	0.98	0.70
Number of meteors	88	41	59	17	36	68	88	22	78	84

A group: ecliptical concentration, two maxima at 1° and 11°, and a trace of a third maximum at 17".

B group: ecliptical concentration, flat maximum from 0° to 30°, then a drop from 30° to 40".

C_1 group: strong ecliptical concentration, one maximum at 5" followed by a drop. The cases with $i > 15°$ are negligible.

C_2 group: smooth distribution in the complete 0° to 180° interval. (The local increase at the 60" interval is explained in c of table 2.)

A subgroups (the maxima of inclination distribution are given in parentheses; the main maxima are italicized):

two maxima: A_1 (*2°*, 13°); A_2 (*1°*, 9"); A_3 (*2°*, 12°); A_7 (*2°*, 10°); A_4 (2°, *10°*); A_8 (5°, *12°*);

one flat maximum: A_5 (5°); A_6 (5");

three maxima: A_9 (*3°*, *9°*, 18°); A_{10} (*0° to 5°*, *10°*, 17°).

The distribution of inclination of the complete A group, and also of all subgroups, is quite different from the distribution of the C_1 group. Only the A_{10} subgroup is probably contaminated in the first maximum by the C_1-group distribution. The third maximum of the A_9 and A_{10} subgroups is probably caused by the C_2-group contamination.

The last element to be examined is the longitude of perihelion. The distributions with a 10° interval for different groups are given in figure 12.

A group has a big maximum in the interval 190° to 340°, with the greatest numbers in the interval from 230" to 280". A secondary maximum between 70° and 100" is well defined.

B group contains too few cases for the investigation of any reliable distribution of longitude of perihelion.

C_1 group has a well-defined maximum from 120" to 160".

C_2 group has no maximum, as is expected for orbits without any ecliptical concentration.

The distribution of longitude of perihelion is clearly different for the A and C_1 groups. The distribution of π for the A subgroups is given in table 4. All distributions of π for the A subgroups are different from the C_1-group distribution.

The characteristic orbits of groups are plotted in figure 13.

Relative number of meteors among the groups

The observed number of meteors n_{obs} for each group can be corrected for different observational effects. If we use the so-called cosmic weight (as defined by Whipple, 1954), we obtain the number of meteoroids n_p with constant mass that pass perihelion per unit time. The characteristic orbits of groups were used, and thus only a very rough estimation was obtained. The C_2 group with long-period orbits was seriously affected. The results are valid for the mass interval from about 1 to 10^{-4} g. The A group is dominant. The C-group space density is about eight times less than that of the A group. The B-group space density is about 50 times less than that of the A group (table 5).

A subgroups and associations

Southworth and Hawkins (1962) investigated the connection among elements of orbits of a random sample taken from the same material we use, but by quite a different method. As the probability of finding the meteor associations by their method is much higher in those

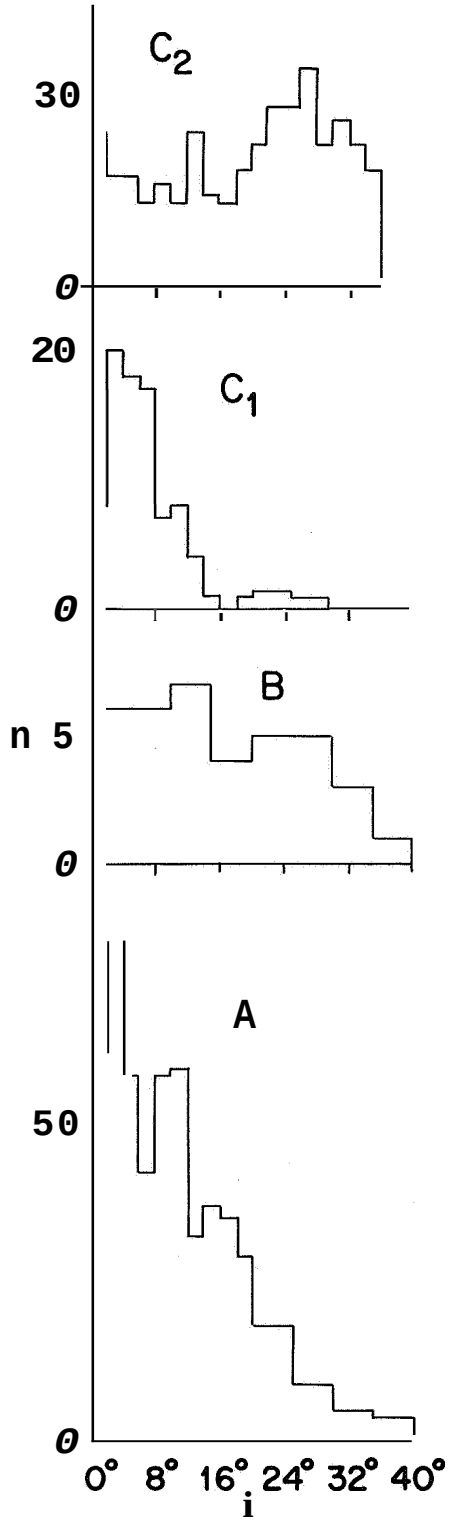

FIGURE 11.—Distribution of inclinations for the definitive classification.

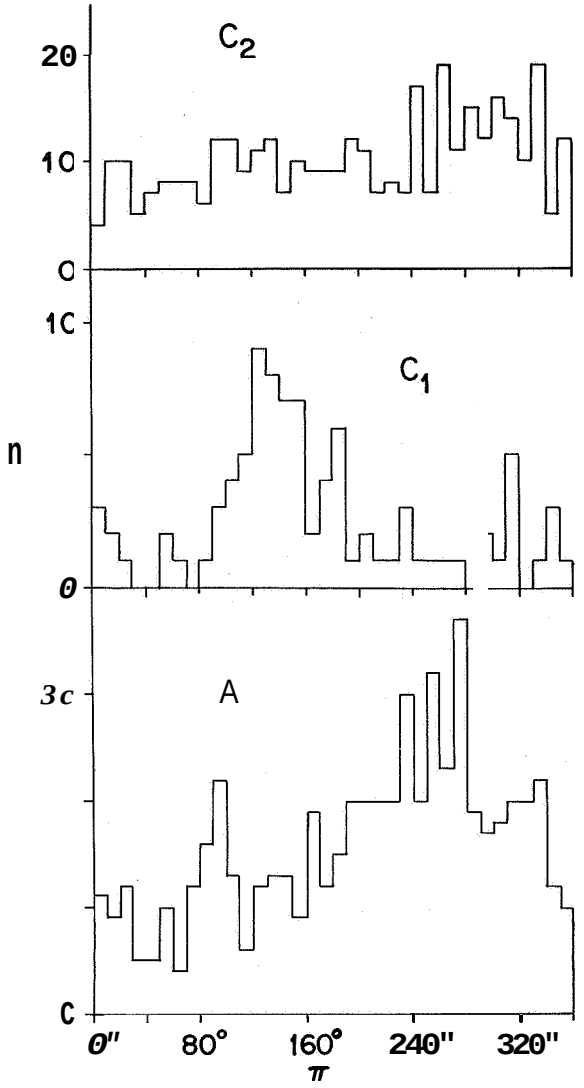

FIGURE 12.—Distribution of longitudes of perihelion for the groups of definitive classification.

TABLE 4.—*Maxima of distribution of* π for *A subgroups (the main maxima are underlined)*

Main maximum 230" to 280"	Secondary maximum	Other subgroup maxima
$\underline{A_1}$	A_1	A_1 (160°)
	A_2	$\underline{A_2}$ (140°)
$\underline{A3}$		$\underline{A_3}$ (140°)
$\underline{A_4}$?		
	$\underline{A_5}$	A_5 (320°)
$\underline{A_6}$	$\underline{A_6}$	
$\underline{A_7}$	A_7	
		$\underline{A_8}$ (330')
$\underline{A_9}$		
$\underline{A_{10}}$	A_{10}	

TABLE 5.—*Percentage number of meteors in the groups*

Group	n_{obs}	n_p
A	54	87
B	6	2
C_1	9	5
C_2	31	6

regions where the density of meteor numbers in the e–q diagram is higher, I was not surprised to obtain a distinct classification for almost all the Southworth and Hawkins associations. The only criterion in table 6 was the orbital shape.

We see that the associations belong mostly to the A group. On the contrary, as we shall see later, the classical meteor showers belong without exception to the B, C_1, and C_2 groups, the C group being the most frequent. Thus the associations found by Southworth and Hawkins have, on the whole, different characteristics from the classical meteor showers.

Classification of small-camera meteors

Before answering the principal questions in the Introduction, I shall try to repeat the same procedure as adopted above to the observational material of small-camera meteors. This is, of course, not so simple; first, because of the small number of meteors available from individual observatories, and second, if we summarize all the material, because of possible inhomogeneities. A further complication is the much greater number of shower meteors in the

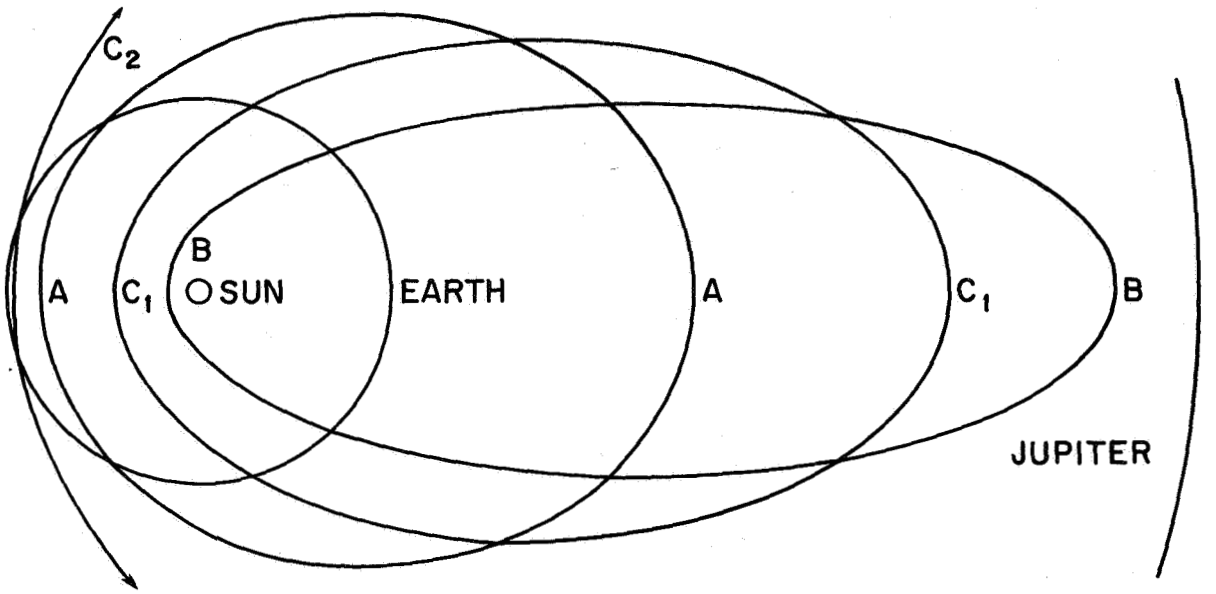

FIGURE 13.—Characteristic orbits of the groups.

Association	Group	Association	Group	Association	Group
χ Geminids	C_1	ϕ Bootids	A_3	ϕ Herculids	A_9
ρ Geminids	A_{10}	ξ Cepheids	A_1	β Cetids	A_8
ξ Orionids	A_6	ω Ursa Majorids	A_9	ξ Capricornids	A_3
ψ Ursa Majorids	A_6	Cgclids	A_1	a Pegasids	A_9, A_7
a Bootids	A_7, A_{10}	θ Ophiucids	C_1	λ Draconids	Ca
γ Bootids	A_9, A_{10}	μ Draconids	A_9	ε Geminids	Ca
δ Librids	B	τ Herculids	A_9	η Taurids	A_9
ν Draconids	C_2	μ Ophiucids	A_9	σ Leonids	

small-camera material compared with the Super-Schmidt meteors. I use the following published material of the small-camera meteors: Harvard (Whipple, 1954), Ondfejov (Ceplecha, 1952, 1953, 1957, 1958b; Ceplecha and Rajchl, 1959; Plavcová and Plavec, 1960; Ceplecha et al., 1964) (and some unpublished values), Dushanbe and Odessa (Babadzhanov and Eramer, 1963). There were altogether 645 meteors, of which 281 belong to showers in the classical sense. The remaining 364 sporadic meteors comprise less than 20 percent of the material we had at our disposal for the Super-Schmidt meteors.

We computed the k_B parameter for all these meteors. We checked the homogeneity of the material using the k_B distribution for the material from individual observatories. The maxima coincide quite well, even though the sharpness of the maxima is not so good due to the small number of meteors investigated. The only correction, which must be applied, is a small correction of $+0.1$ of k_B for Ondfejov meteors. But the results are practically the same without this correction.

If we now summarize meteors from all the observatories, we get the histogram for k_B in figure 14. The result is the same as for the Super-Schmidt meteors: two maxima of the distribution separated by exactly the same difference, 0.7. The third group between these two main maxima is present at the same relative place. Thus we can identify the same A, B, and C groups without any doubt among the sporadic meteors photographed by the small cameras.

The numerical values of k_B, at which the maxima occur, are of course slightly different, mainly because of the differences in the limiting magnitudes. The k_B values for the small-camera meteors are systematically higher by 0.3 than for Super-Schmidt meteors, which corresponds to systematically lower beginning heights (due to a decrease of the limiting magnitude) of 3 or 4 km.

The A group, relative to the C group, is much weaker for the small-camera than for the Super-Schmidt meteors. This is in good agreement with the fact that among the small-camera meteors many more shower meteors are present, and practically all these shower meteors belong to the C group, as we shall see later (table 7). The same holds for the B group, which is more prominent among the small-camera than among the Super-Schmidt meteors. (Some classical showers belong to the B group, but there is no clear case of the presence of the A group.)

The ratio of the observed numbers of meteors in the A and C groups is 0.92 for the small-camera and 1.35 for the Super-Schmidt meteors.

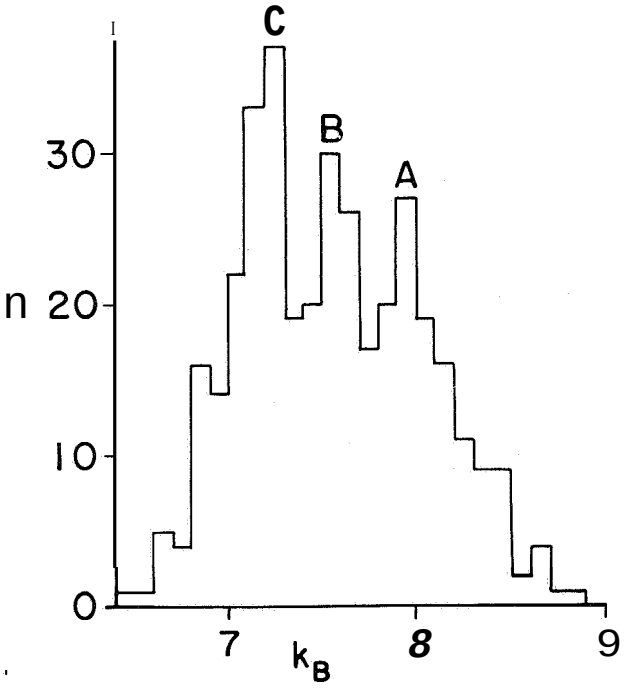

FIGURE 14.—Distribution of the k_B parameter for all sporadic small-camera meteors from four observatories. The main groups A, B, C, are well defined.

Shower	Classification	Shower	Classification
α Capricornids	C_1	Orionids	C_2
South Taurids	C_1	Quadrantids	B [a]
Geminids	B	χ Cygnids	C_1
South δ Aquarids	B	North Taurids	C_1
Lyrids	C_2	South Arietids	C_1
Perseids	C_2	γ Draconids	(C_1) [b]

[a] B group according to k_B but with highly inclined orbit with q near 1.
[b] k_B has a maximum at 6.9 of the small-camera scale, which could be caused by the smallest observed density 0.9 (with the extreme possibility 0.4).

The correction for the number of particles passing the perihelion per unit time could fully explain this difference. The resulting constant number ratio for meteors passing the perihelion per unit time and having the same mass is 8 for both the small-camera and Super-Schmidt meteors.

It is surprising that weaker meteors photographed by Super-Schmidt cameras contain more observed dense particles than the small-camera meteors. But if we suppose that shower meteors, which are clearly connected with comets, have small densities, then the relative absence of classical showers among the Super-Schmidt meteors could point also to the greater observed number of heavy particles among the Super-Schmidt meteors.

It is not possible to present a definition of the groups using the e–p diagram for the small-camera meteors because of the small number insufficient for the construction of two-dimensional histograms. Thus, I use the parameter k_B only for the group definitions: A group, k_B from 7.70 to 8.19 with 99 cases; B group, k_B from 7.40 to 7.59 with 50 cases; and C group, k_B from 6.80 to 7.29 with 122 cases.

meteors

The distribution of orbital elements for different groups of the small-camera meteors is given in histograms of figures 15, 16, 17, and 18. Though

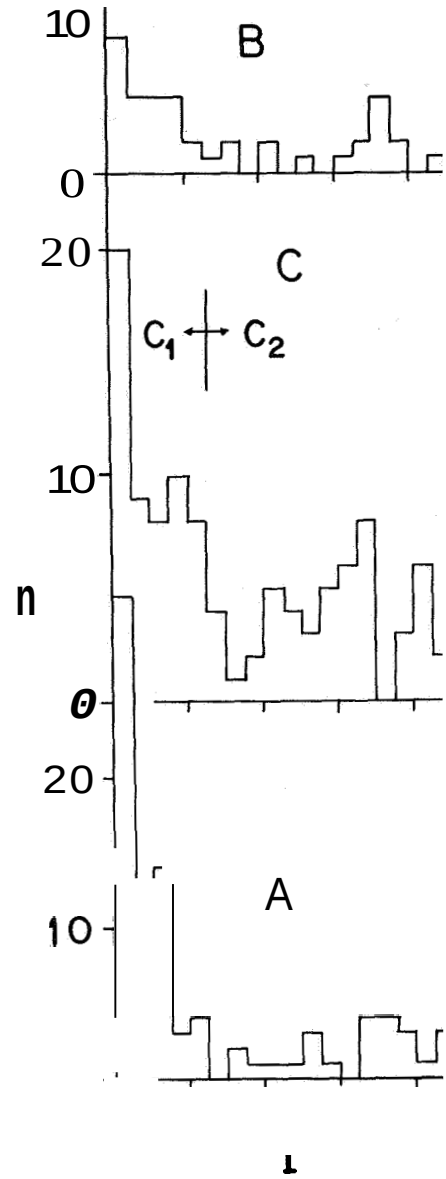

FIGURE 15.—Distribution of inclinations for small-camera meteor groups.

INCLINATIONS: A group: ecliptic concentration;
B group: ecliptic concentration with flat maximum;
C group: ecliptic concentration with many meteors of highly inclined orbits.

The distribution of inclinations is, for all groups, similar to that for the Super-Schmidt meteors. Thus the same dividing inclination of 50° was used to separate the C group into the C_1 and C_2 groups. This separation by inclinations also divides the short-period orbits from the long-period orbits; thus the double maximum of semimajor and eccentricity distributions for the whole C group is well separated into a single maximum distribution for the C_1 and C_2 groups.

SEMIMAJOR AXIS: A group: maximum of distribution in interval from 2 to 3 a.u.;
B group: maximum from 2 to 3 a.u.;
C_1 group: maximum from 3 to 4 a.u.;
C_2 group: maximum $\approx \infty$.

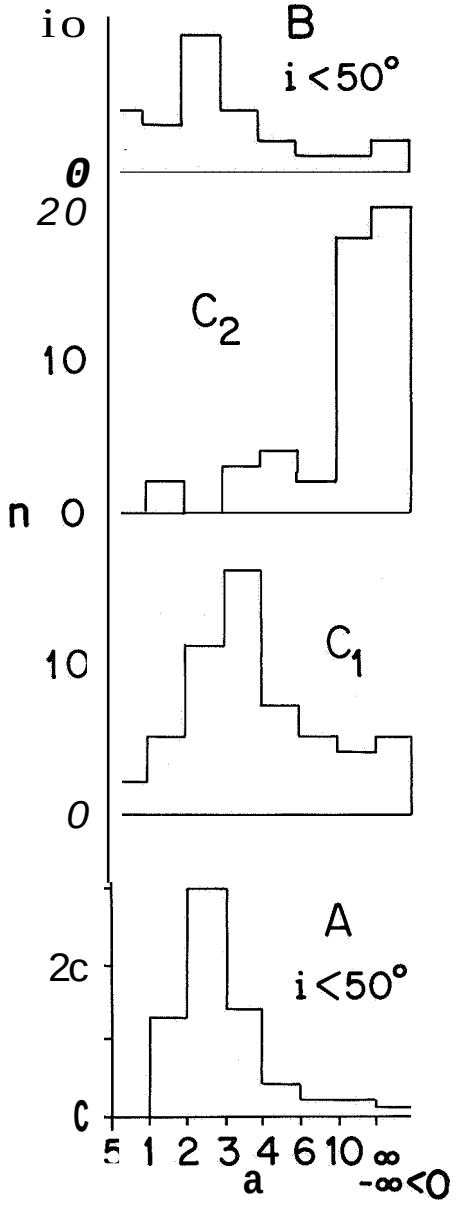

FIGURE 16.—Distribution of semimajor axes for small-camera meteor groups.

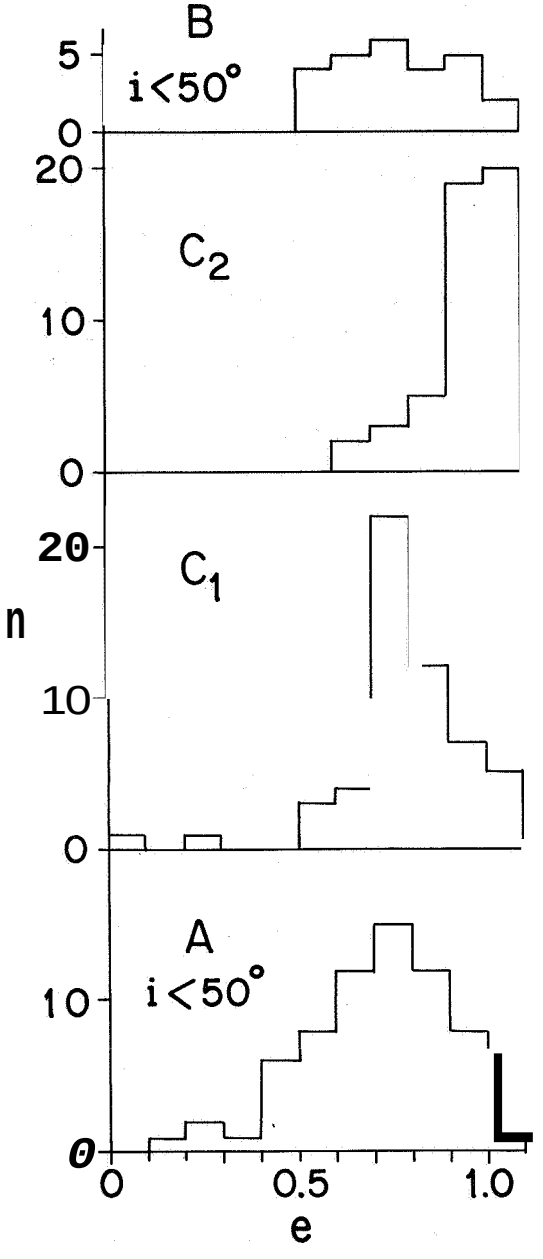

FIGURE 17.—Distribution of eccentricities for small-camera meteor groups.

The groups with ecliptical concentration have the maxima of distributions of semimajor axis about 1 a.u. greater than for the Super-Schmidt meteors. This we can explain by the greater average mass of the small-camera meteors, which are thus, because of the Poynting-Robertson effect, much nearer to the original starting orbits than the lighter Super-Schmidt meteors.

The C_2 group has relatively less negative values of a, if compared with the Super-Schmidt meteors. This, of course, is due to the more precise orbits of the small-camera meteors than of the McCrosky and Posen meteors. Also lower values, below 10 a.u., of the C_2 group can be explained by the higher accuracy of a.

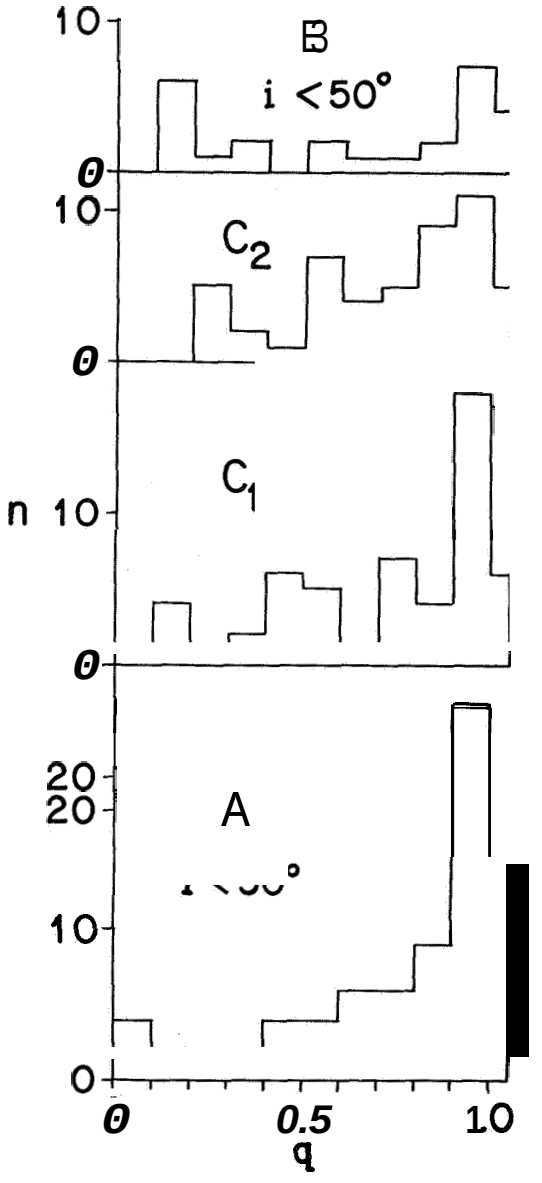

FIGURE 18.—Distribution of perihelion distances for small-camera meteor groups.

ECCENTRICITIES: A group: one maximum in the 0.7 interval is **0.1** higher, if compared with the main maximum for the Super-Schmidt meteors. The structure is not so complicated as that for the Super-Schmidt meteors;

B group: very flat maximum with no values below **0.5,** and relatively more values in the 0.8 and 0.9 intervals, if compared with the Super-Schmidt meteors;

C_1 group: one maximum in the **0.7** interval and a relatively lower number **of** meteors in the **0.6** interval, if compared with the Super-Schmidt meteors;

C_2 group: one maximum ≈1 and very small differences when compared to the distribution of the Super-Schmidt meteors.

The eccentricity distribution for the **A,** B, and C_1 groups confirms that the small-camera meteors are nearer to the original starting orbits.

PERIHELION DISTANCES: A and C_1 groups: more concentrated at q =**1** than for the Super-Schmidt meteors;

B group: more distinct maximum at q from **0.1** to **0.2** than the Super-Schmidt meteors, which show **only** a flat maximum at small perihelion distances.

Note that the **A** group contains more highly inclined orbits than for the Super-Schmidt meteors. This can be explained by the greater number **of** 'meteors of the C_2 group, which are wrongly classified as the **A** group in some cases, and so the contamination **of** the statistical **A** group by the C_2 group is expected to be higher for small-camera meteors; this is rarely observed.

The limits among groups in the e–q diagram (see fig. **7)** hold for the Super-Schmidt meteors and are not applicable to the small-camera meteors. Generally speaking, the limits for the small-camera meteors are shifted to the right and up (greater e and q).

Poynting-Robertson effect: age and origin

Results **for** the small-camera meteors, if compared with the Super-Schmidt meteors, point to the possibility of estimating the age of the ecliptical groups taking into account the Poynting-Robertson effect. **As** the material

for the B and C_1 groups is not too extensive, and both these groups seem to be connected with a cometary origin, I use the procedure of this section exclusively for the A group of the McCrosky and Posen meteors with $v_\infty < 20$ km/sec.

Wyatt and Whipple **(1950)** give the equations of changes of orbital elements due to the Poynting-Robertson effect as

$$a = \frac{Ce^{4/5}}{1-e^2}, \qquad (4)$$

where C is a constant given by a known pair of a, e, and

$$(t-t_0)_{\text{years}} = 1.13\times 10^7 r\delta C^2 \int_e^{e_0} \frac{e^{3/5}de}{(1-e^2)^{3/2}}, \qquad (5)$$

where r is the radius and 6 the density of the meteor particle.

The computation was made from the individual data on each meteor of the A group. The density 1 was assumed and also used for the computation of the meteor radius r from the mass m. The choice of density is equivalent to the choice of the time scale only and has no influence on the element distribution.

We first computed the C constant, and its histogram is shown in figure **19.** There is one great maximum at **2.2,** which is connected with the A_8 and A, subgroups. The **e-q** diagram is used to present the results of the distribution of A-group meteors today and **2, 5,** and **9** million years ago (see fig. **20).** The lines in the today diagram have the same C, i.e., the direction of the motion of the points due to the Poynting-Robertson effect.

If we now choose the statistical semimajor axis of a starting asteroidal orbit to be **2.8** a.u., we can follow individual groups back in time up to this limit and hence determine the age. Thus we have found at least five age groups of $<$1, **3, 4, 8,** and **12** million years. They correspond to the following **A** subgroups:

$<10^6$ years A_8+A_7
3×10^6 years A_5
4×10^6 years $A_2+A_3+A_4+A_6$
8×10^6 years A_1
12×10^6 years A_1

The subgroups A_{10} and **A,** are not present in this A-group sample because of the limitation imposed by $v_\infty < 20$ km/sec.

The time scale for the A group seems to be higher than previously supposed. But the absolute scale of time is dependent on the mass scale, and thus on the luminosity coefficient τ_0. As $r\delta \propto (\delta^2/\tau_0)^{1/3}$ and the value δ^2/τ_0 can be determined from the observations (Verniani, 1964), the time scale of equation **(5)** is estimated to be about by **30** percent less than the assumed value. On the other hand, the results in this paper on the meteor densities tend to increase the deduced ages. Even if we assume the results of Verniani, the ages are still too large and the original starting orbit can be not only asteroidal, but also subasteroidal. In particular,

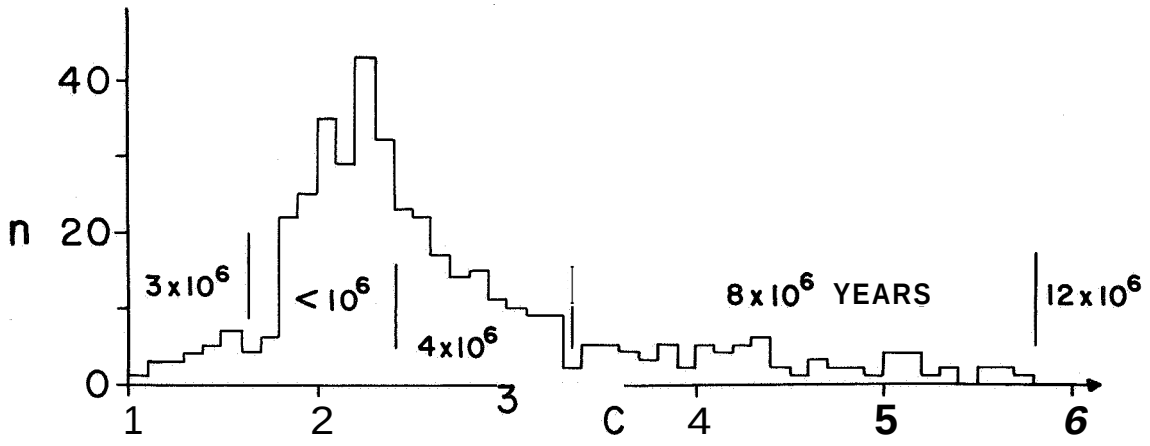

FIGURE 19.—Distribution of the Poynting-Robertson constant C for the sporadic meteors with $v_\infty < 20$ km/sec belonging to the A group of the Super-Schmidt meteors.

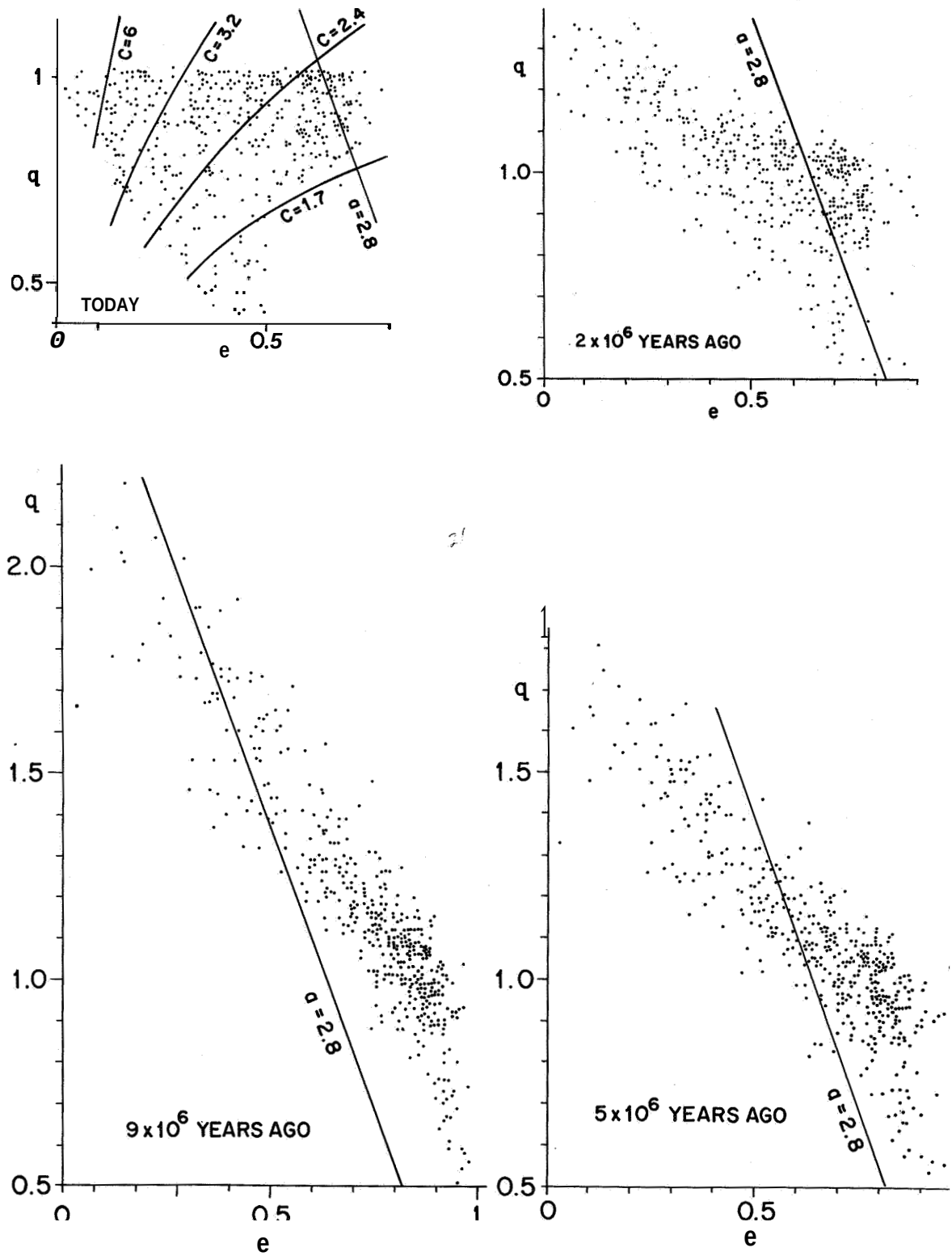

FIGURE 20.—Poynting-Robertson effect plotted as points for each meteor in the e–q diagram. The A group with $v_\infty < 20$ km/sec of sporadic Super-Schmidt meteors is used.

the orbits with observed eccentricities less than 0.30, which are very usual among the Super-Schmidt meteors, can hardly originate from an eccentric cometary orbit, since the Poynting-Robertson effect cannot change such orbits into observed orbits during periods shorter than some tens of million years.

Our starting asteroidal orbit with $a=2.8$ a.u. is chosen on the assumption that collisions with large asteroidal bodies change the semimajor axis in both directions. It would be difficult to find a collision mechanism that shortens only the semimajor axis. If we wish to reduce the ages, we must suppose the existence of a great number of small asteroidal bodies with semimajor axes between 1 and 2 a.u. It is interesting that the same assumption appears to be necessary for a stony meteorite origin (Anders, 1965). The asteroidal origin of the A group is not excluded on the basis of the Poynting-Robertson effect.

Absolute scale of the k_B parameter

The theoretical values of the k_B parameter from equation (2) are of no importance for the absolute scale of this parameter. On the other hand, if we know the absolute scale, we can obtain rough estimates of meteor-particle densities for our groups. We can calibrate the k_B scale from photographed meteors of known composition. I will use two meteors with pure iron spectra without any indication of sodium, calcium, and magnesium lines, and the McCrosky-Soberman (1963) artificial iron meteoroid. The fist grating spectrum with 12 lines and 340 A/mm was published by Halliday (1960). The second grating spectrum was recently photographed and reduced at the Ondfejov Observatory, and has 189 lines with 58 A/mm dispersion. The spectrum and the normal small-camera photographs of this meteor, taken from two stations, were obtained; thus, all the necessary data are at our disposal (Meteor no. 36221 and Spectrum no. S 912). There is no doubt that, with such a great dispersion, the Ondfejov S 912 spectrum is a pure iron spectrum with Fe I and Fe II lines and some clearly resolved Ni I lines. The lines for Na I, Ca I, Ca II, Mg I, Mn I, and Cr I, usual in normal meteor spectra, are absent. This confirms the iron composition of the meteor body.

The k_B parameter for this Ondfejov iron meteor was found to be 7.94. But this value must be corrected for the increase in brightness of the meteor over the average brightness of the small-camera meteors investigated in this paper. The average brightness magnitude m_{pg} (median of the distribution) of all the meteors in the small-camera samples is −4.2, and the brightness of Meteor no. 36221 is −11.0 m_{pg}. The change of k_B per magnitude can be estimated from the difference between the small-camera and Super-Schmidt meteors. The median of the limiting photographic magnitude for the Super-Schmidt meteors is +3.3, and for the small-camera meteors is −1.0. The change of k_B in this interval is 0.30; hence the ratio $\Delta k_B/\Delta m_{pg}=0.070$ mg^{-1}. Thus the correction for k_B is 0.48, and the corrected $k_B=8.42$. To check such a small correction, we can use the separation of the small-camera meteors into two groups according to magnitudes. The median photographic magnitudes of these groups with the same number of meteors are −2.9 and −5.6. Although the k_B distributions for both groups do not define the maxima as clearly as for the complete material, we can definitely conclude that the difference of k_B between these two groups is close to 0.10. This indicates that the correction of k_B used for Meteor no. 36221 could be somewhat overestimated but it could hardly be smaller than the real value.

The Halliday iron meteor has the great advantage that its magnitude has exactly the median value of our small-camera sample. The k_B parameter is 8.38, and no further correction is necessary. This value checks our correction 0.07 of k_B/m.

The most important data we use are those on the artificial iron meteoroid. The great advantage is the use of Super-Schmidt cameras for the records. Thus the k_B value can be directly compared with the main sample of the Super-Schmidt meteors we use. The only slight drawback is the very small velocity 9.8 km/sec. But the Super-Schmidt sample is so extensive that we can determine the A maximum of the k_B distribution for meteors with

$v_\infty < 12$ km/sec. The resultant value $k_B = 7.55$ is only **0.10** less than for the whole sample. (For meteors with $12 \leq v_\infty < 13$ km/sec, the k_B maximum is exactly the same as for the whole sample.) The resultant value of k_B, according to the whole sample of the Super-Schmidt meteors, is thus 8.05 for the artificial iron meteoroid.

All these three values of k_B are in good agreement. If we scale these values to correspond to the Super-Schmidt meteors we have **8.12, 8.08,** and **8.05.** The mean value $k_B = 8.08$ can be accepted for the iron body. The difference of this value from the maxima of the k_B distribution for the Super-Schmidt meteors determines the absolute scale of k_B, and thus the product $\lambda\delta c$.

Now we can use a rough dependence of $\lambda\delta c$ on 6 for the different materials examined (fig. **21).** If we use the data from Levin's book **(1961)** and the data on the stainless steel **304** from McCrosky and Soberman (1963), we get the following rough estimates of the density:

$$\text{A group } \delta = 4.0 \text{ g/cm}^3,$$

$$\text{B group } \delta = 2.2 \text{ g/cm}^3,$$

$$\text{C group } \delta = 1.4 \text{ g/cm}^3.$$

These estimates are not precise since no strict dependencies exist among λ, 6, and c. But there is a tendency for c to be constant and independent of the porosity, which could cause a low density for the C group. Thus we can reduce the problem to the δ–λ dependence only. If we assume for a porous body of stony composition

$$\lambda \propto \delta^n, \qquad (6)$$

then the value of **n** could be between **1** and **3,** with **2** as the most probable value. The value **2** corresponds to the data given by Levin **(1961).** Even if we use $n = 1$, we obtain $\delta = 0.9$ for the C group as the lowest acceptable limit.

Thus we see that the A group with the shortest semimajor axis and the smallest eccentricities has a density close to that of the average stony meteorite. On the other hand, the C group has a density not much greater than one, a value quite unknown among meteorites. At the same time, the separation of this

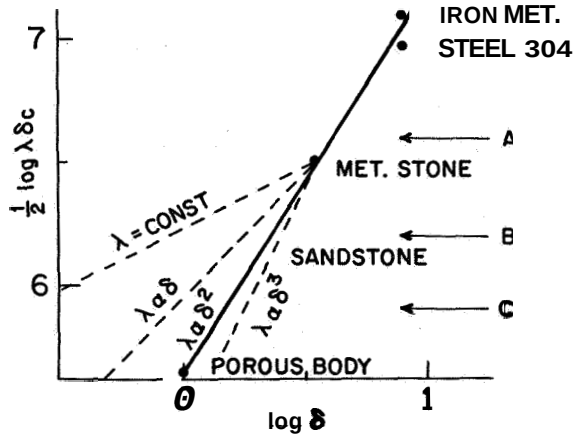

FIGURE 21.—Log δ is plotted against ½ log $\lambda\delta c$. Different materials (iron meteorite, steel 304, meteoric stone, sandstone, hypothetical porous body) are each represented by a point. The y axis is also the k_B parameter + constant. The constant is easy to determine as the observed values of k_B for three iron bodies must be at the place where iron meteorite and steel 304 are plotted. Thus the observed k_B parameter for the A, B, and C groups can be plotted in this figure (arrows). Thus a rough estimation of the density of the meteor material is possible.

C group into the C_1 group with ecliptical concentration and short-period orbits and the C_2 group without ecliptical concentration and with long-period orbits indicates that the C group is connected with comets.

The B group has a density close to two. As the orbits of the B group have very great eccentricities with aphelion distances near the Jupiter orbit, a cometary origin is highly probable. The increase of density could be caused during the close approach to the sun, as the perihelion distances are all below **0.35** a.u., with the most probable characteristic value of **0.17** a.u. The temperature of about **500°** C can join the individual grains of the conglomerate more closely together, thus increasing the heat conductivity. On this assumption the change in the density could be less than the given change of **0.8.** If n in equation **(6)** is **3,** then we proceed from the C-group density **1.4** to the B-group density **1.9** and to the heat conductivity 1.3×10^5. The increase in the heat conductivity of five times, due to the solar heating, seems quite reasonable. If no changes of density are present ($n = \infty$), the heat conductivity must change **10** times.

The iron particles among the Super-Schmidt meteors can be estimated from figure 1 in a maximum of 10 cases, i.e., 0.5 percent of the whole sample.

The results on the densities differ from the recent data given by Verniani (1964). The density of our C group is five times greater than the density of the whole Verniani sample. I shall present here some remarks on the meteor densities derived in the Verniani paper. I think that the absolute τ_0 value, which depends mainly on the McCrosky and Soberman experiment (1963), is quite acceptable. On the other hand, the absolute value of τ/δ^2 was determined from equation (11) of the Verniani paper, where the measured meteor deceleration, drag, and shape coefficients enter to the third power. As the fragmentation is effective, it is not quite clear to what particle the deceleration belongs. At the same time we must suppose knowledge of the drag and shape coefficients. I think that the '(absolute" values of τ/δ^2 determined in the Verniani paper could be systematically overestimated. The resulting density could be between the density of the particle, or dropcloud, and that of the main meteor body.

If the ratio $\Gamma A/(dv/dt)$ in Verniani's equation (11) is increased by only three times, the C-group density 1.4 will coincide with 0.25 given by Verniani for the complete sample. It is evident that systematic change due to all three quantities, Γ, A, and dv/dt, could be much greater than three.

If we suppose that the dimensions of fragments or drops do not depend too much on the main body dimension, then the fragmentation will change the decelerations more at the end of the trajectory, as is observed. But then the brighter meteors are less affected by the fragmentation, and it is quite clear why Verniani arrived at twice the density for the small-camera meteors than for the Super-Schmidt meteors. The Verniani meteoroid densities are not identical with the density of the main meteor body.

On the other hand, our results are based on the beginning heights, where the fragmentation is not so important as later, and no measurements or assumptions of decelerations were used at all. The absolute scale of our densities was obtained by direct comparison of three iron bodies with the sample. Thus I think my results on densities are closer to reality than Verniani's.

The question of the fragmentation of the A-group meteors can arise if they have stony densities. Fragmentation of meteors was well established by Jacchia (1955) to explain the faint meteor anomaly.. But if only our C group contains fragile meteors, then this contradicts the fact that the C group is relatively more numerous for brighter small-camera meteors than for the Super-Schmidt meteors. The same holds for shower meteors. But I think that the fragmentation necessary to explain the faint meteor anomaly must be understood quite generally, without assuming that the material leaves the body as solid particles only. The separation of drops is another form of "fragmentation." The study of meteor and wake spectra of very bright meteors (Ceplecha, 1964, 1965) shows such a great luminous volume where meteor light is produced at very small excitation temperatures that there must be a transport of meteor mass behind the body by means other than gas. "Fragmentation" of big bodies in the general sense is also present, but from the observational point of view has little importance for the measured decelerations, as the drops or fragments are much less than the body itself. The smaller the meteor body, the greater the effect on the measured velocity. This is the reason for deceleration anomalies for faint meteors and at the meteor ends. Thus we can conclude that fragmentation in this general sense is important for all the groups we have found, without strong dependence on the meteoroid density. The A group is no exception, even if its density and composition are those of the stony meteor.

Theoretical and observed beginning of the meteor

The small difference in the k_B values between the Super-Schmidt and the small-camera meteors points to a steep increase of the light curve just at or before the beginning of the photographed trail. The change of k_B by 0.30 is equivalent to the change of beginning height of about 3.5 km, and is accompanied by a change of the limiting magnitudes between the two

used samples of 4.3 m_{pg}. The resulting slope of the light curve at the meteor beginning is 1.2 m_{pg}/km, about seven times greater than is usually observed after the beginning. The majority of the observational material has maximum magnitudes in the interval from 2 to 4 m_{pg} above the plate limit equally for both samples. The sudden increase of brightness at the beginning could to some extent be related to the theoretical considerations of Levin (1961).

We can compute the ratio of the temperature to the heat-transfer coefficient from the theoretical equation (2). We get for iron bodies, which we use as the definition of the absolute k_B values:

$\log \tau_B/\Lambda = 3.60$ for the Super-Schmidt meteors,
$= 3.90$ for the small-camera meteors,

and thus,

Super-Schmidt meteors		small-camera meteors	
Λ	T_B	Λ	T_B
1	4300° K	1	8200° K
0.65	2800° K	0.65	5400° K

We see from the resulting temperature values that the theoretical beginning point of a meteor as defined by Levin (1961) is practically identical with the beginning photographed for an average meteor by the Super-Schmidt camera. The small camera is able to record the average meteor about 4 km lower than the corresponding theoretical beginning point.

Classification of shower meteors

There is not too much observational material for a statistical distribution of the k_B parameter for the shower meteors because of the dearth of observational material for the small-camera meteors and the small percentage of shower meteors among the Super-Schmidt sample. The Super-Schmidt sample is sufficient to classify, according to the k_B distribution, Orionids as C_2 group, Perseids as C_2 group, and Geminids as B group. The small-camera sample has enough cases for the Perseids, which are put into the same C_2 group. This is consistent with the cometary origin of the C group in general.

Only indications of the classification can be given for other showers, mainly based on the Super-Schmidt meteors (see table 7).

The classification of the showers corresponds well to the orbital characteristics except for the Quadrantids, which are classified according to k_B as the B group, but they have highly inclined orbits. It is interesting that among the classical showers no case with A-group classification is present. This supports the idea that the A group is not connected with comets.

As we know, γ Draconids are very young meteors recently separated from the parent comet. We can assume that the density of the cometary particles, when they leave the parent comet and lose their volatile material, is somewhat lower than they Draconid value of $\delta = 0.9$. This value is about twice Whipple's theoretical value (1955) derived on the basis of his cometary model. If all the volatile material is lost by the meteor body soon after leaving the comet, the results of this paper show that there could be some contrary process that makes the meteors more conductive for the heat flow and probably also somewhat denser. Heating by solar radiation could be the reason. Thus the evolution could proceed from γ A Draconids type to the C type and to the B type at close approach to the sun.

The k_B distribution for other sporadic meteor samples

Hawkins and Southworth (1958,1961) published all available data on a random sample of Super-Schmidt meteors taking every tenth meteor from the complete material. The precise reduction method was applied to these meteors. Thus we can use this sample of 285 sporadic meteors for checking the results on the k_B parameter distribution. The strong maxima at k_B intervals 7.5 and 6.9 and a weak maximum at 7.2 coincide almost exactly with the maxima obtained for the McCrosky and Posen meteors. It means that there is no systematic error, especially in the beginning heights. The A group is again the most prominent. Also the orbital elements have simiiar distributions in both samples.

Recently Verniani and Hawkins (1965) published data on 320 radio meteors available for computation of the k_B parameter. Even if the physical meaning of the beginning height for a radio meteor is different from that of an

optical meteor, some of the considerations of the second section of this paper still hold. It is interesting that the two strong maxima of k_B distribution are again present. The maximum at k_B=7.4 to 7.7 contains the majority of the material and could correspond to the A group. The maximum at k_B=6.9 could correspond to the C group. I do not have the orbits of individual meteors at my disposal, thus nothing final about the groups can be concluded. But statistics of radio meteor orbits as a whole (Hawkins, Southworth, and Rosenthal, 1964) give the distribution of semimajor axes, eccentricities, and inclinations similar to the A group of the Super-Schmidt meteors with more cases of smaller a and e than the A group of the Super-Schmidt meteors.

The ratio of meteor numbers in the groups A/C=3.8 for radio meteors indicates the continuing tendency of relative increase of the observed meteor numbers of the A group with the decrease of the meteor brightness ($m_{pg} \approx 8$ for the radio meteors).

Results

The main results of this paper answer the two principal questions in the introduction:

1. Four groups exist among sporadic meteor orbits. Three groups denoted A, B, C, can be separated using the k_B parameter, which represents to a good measure the product of heat conductivity, density, and specific heat. The A group has the greatest density, the C group the least. The C group can be further separated into the C_1 and C_2 groups by semimajor axes and orbital inclinations. Characteristics of the A group are the greatest meteoroid density, short-period orbits with small eccentricities, and ecliptical concentration; of the C_1 group, the lowest meteoroid density, short-period orbits, but with longer semimajor axis, and with greater eccentricities than the A group, ecliptical concentration; of the C_2 group, density identical with the C_1 group, long-period orbits with eccentricities near 1 and without any ecliptical or other concentration; and of the B group, density between the A and C groups, short-period orbits with great eccentricities, and ecliptic concentration, small perihelion distances. The A group is the most numerous among the observed Super-Schmidt meteors, and the C among the observed small-camera meteors.

2. The C_1 group is clearly connected with short-period comets and the C_2 group with the long-period "parabolic" comets. The B group is probably connected with the short-period comets. The A group as a whole is probably connected with asteroids, The A-group meteors with eccentricities below 0.30 are probably connected with smaller asteroidal bodies having orbits with semimajor axes between 1 and 2 a.u.

Further results of this paper are the following:

1. The distribution of the k_B parameter has two main maxima (A and C groups) independent of the observational material used (McCrosky and Posen, Hawkins and Southworth, small-cameras of four different observatories, radio meteors).

2. The independence of the k_B maxima on the velocity, mass, and magnitude was verified.

3. The parameter k_B defined by equations (2) and (3) is a very good relative measure of the meteoroid composition. The heating theory of the meteoroid before the rapid ablation is the most certain of all the meteor-phenomenon theories.

4. The absolute scale of the k_B parameter can be obtained using two meteors with pure iron spectra and the artificial steel meteoroid.

5. Using the absolute values of k_B, we get the probable average density 4.0 for the A group, 2.2 for the B group, and 1.4 for the C group. The lowest acceptable limit of the density for the C group is 0.9.

6. The absolute k_B values if compared with the theoretical values of equation (2) demonstrate that the observed beginning of the average Super-Schmidt meteor is almost identical with the theoretical beginning as defined by Levin (1961). This is not the case for the small-camera meteors.

7. A sudden increase of brightness is present at the meteor beginning, and is seven times greater than the normal slope of the first part of the light curve.

8. The extensive A group can be statistically separated into 10 subgroups using two-dimensional e–q histograms.

9. The differences in orbital elements for the small-camera meteors and for the Super-Schmidt meteors, if compared in A and C_1 groups, are quite consistent with the greater average mass of the small-camera meteors with orbits less changed by the Poynting-Robertson effect.

10. The different times of the origins of individual meteor subgroups of the A group are due to the Poynting-Robertson effect.

11. The results of Verniani (1964) on meteor densities are at least five times smaller than our results. Verniani uses meteor decelerations, and absolute values of the drag and shape coefficient, which I do not require. Also, meteor fragmentation affects my results much less than the results of Verniani.

12. Whipple's K criterion is an empirical boundary line between cometary and asteroidal orbits, which cannot be extrapolated down to perihelion distances equal to and less than 1 a.u.

13. My previous results based on theoretical values of k_B and connecting the two main groups of sporadic meteors (now denoted A and C) with iron and stony meteorites are incorrect. If there is some group of iron particles among the Super-Schmidt meteors, it contains less than 0.5 percent of all the sample.

14. Classical meteor showers studied by the k_B-parameter distribution belong mainly to the C group and some to the B group. No A group was found.

15. The associations of Southworth and Hawkins (1962) mainly belong to the A group.

16. The heating by solar radiation could be the reason for the change of C-group properties to the B-group properties.

17. The C group and the shower meteors dominate in the observed number of the small-camera sample. The A group dominates in the observed number of the Super-Schmidt sample, which has a distinct lack of the observed shower meteors. The ratio of meteoroid numbers passing the perihelion per unit time and having the same mass is A/C $\doteq$ 8 for both the samples.

Very recently Jacchia, Verniani, and Briggs (1965) published data on relatively brighter Super-Schmidt meteors, which can be used for the computation of the k_B parameter and fully confirm the results of this paper.

Acknowledgment

I am very much indebted to Miss M. Ježková for assistance with the numerical computations, which were mainly made with the ZUSE 2–23 electronic digital computer of the National Research Institute of Heat Engineering in Prague.

References

ANDERS, E.
1965. Tisserand's criterion: A link between meteorites and Mars asteroids. Enrico Fermi Institute for Nuclear Studies [preliminary draft].

BABADZHANOV, P. B., and KRAMER, E. N,
1963. Methods and some results of the photographic researches of meteors. *In* Ionosphere and Meteors, Sec. V of IGY Program, no. 12, Publ. House Acad. Sci. USSR, Moscow.

CEPLECHA, Z.
1952. Double photographed meteor, 1949 Apr. 21. Bull. Astron. Inst. Czechoslovakia, vol. 3, pp. 13-15.
1953. Meteor photographs, I: Air densities. Bull. Astron. Inst. Czechoslovakia, vol. 4, pp. 55–59.
1957. Photographic Geminids 1955. Bull. Astron. Inst. Czechoslovakia, vol. 8, pp. 51-61.
1958a. On the composition of meteors. Bull. Astron. Inst. Czechoslovakia, vol. 9, pp. 154–159.
1958b. Photographic Perseids 1956. Bull. Astron. Inst. Czechoslovakia, vol. 9, pp. 225–234.
1964. Study of a bright meteor flare by means of emission curve of growth. Bull. Astron. Inst. Czechoslovakia, vol. 15, pp. 102–112.
1965. Complete data on bright meteor 32281. Bull. Astron. Inst. Czechoslovakia, vol. 16, pp. 88–101.

CEPLECHA, Z.; JEZKOVA, M.; NOVAK, M.; RAJCHL, J.; SEHNAL, L.; and DAVIES, J. G.
1964. Ondfejov double-station meteors during the IGY and IGC. Bull. Astron. Inst. Czechoslovakia, vol. 15, pp. 144-155.

CEPLECHA, Z., and PADEVĚT, V.
1961. The beginning of rapid evaporation of meteors of different dimensions. Bull. Astron. Inst. Czechoslovakia, vol. 12, pp. 191-195.

CEPLECHA, Z., and RAJCHL, J.
1959. Photographic meteors 1955 and 1956. Bull. Astron. Inst. Czechoslovakia, vol. 10, pp. 133-135.

DYCUS, R. D., and BRADFORD, D. C.
1964. The origin of meteors inferred from orbital elements. Icarus, vol. **3,** pp. **306–310.**

HALLIDAY, I.
1960. The spectrum of an asteroidal meteor fragment. Astrophys. Journ., vol. **132,** pp. **482–485.**

HAWKINS, G. S., and SOUTHWORTH, R. B.
1958. The statistics of meteors in the earth's atmosphere. Smithsonian Contr. Astrophys., vol. **2,** no. **11,** pp. **349–364.**
1961. Orbital elements of meteors. Smithsonian Contr. Astrophys., vol. **4,** no. **3,** pp. **85–95.**

HAWKINS, G. S.; SOUTHWORTH, R. B.; and ROSENTHAL, S.
1964. Preliminary analysis of meteor radiants and orbits. Harvard Radio Meteor Project Res. Rep., no. 7, **32** pp.

JACCHIA, L. G.
1955. The physical theory of meteors, VIII: Fragmentation as a cause of the faint-meteor anomaly. Astrophys. Journ., vol. **121,** pp. **521–527.**
1960. Individual characteristics of meteor families. Astron. Journ., vol. **65,** pp. **53–54.**

JACCHIA, L. G.; VERNIANI, F; and BRIGGS, R. E.
1965. An analysis of the atmospheric trajectories of **413** precisely reduced photographic meteors. Smithsonian Astrophys. Obs. Spec. Rep. No. **175, 309** pp.; also in Smithsonian Contr. Astrophys., vol. **10,** no. 1, **139** pp., **1967.**

JACCHIA, L. G., and WHIPPLE, F. L.
1961. Precision orbits of **413** photographic meteors. Smithsonian Contr. Astrophys., vol. **4,** no. **4,** pp. **97–129.**

LEVIN, B. J.
1961. The Physical Theory of Meteors and Meteor Matter in the Solar System. Trans. by F. Bartel, ed. by N. Richter, Akademie-Verlag, Berlin, **130** pp.

MCCROSKY, R. E., and POSEN, A.
1961. Orbital elements of photographic meteors. Smithsonian Contr. Astrophys., vol. **4,** no. **2,** pp. **15–84.**

MCCROSKY, R. E., and SOBERMAN, R. K.
1963. Results from an artificial iron meteoroid at **10** km/sec. *In* Proceedings of the Symposium on the Astronomy and Physics of Meteors. Smithsonian Contr. Astrophys., vol. **7,** pp. **199–208.**

PLAVCOVÁ, Z., and PLAVEC, M.
1960. Heliocentric orbits of six photographed sporadic meteors. Bull. Astron. Inst. Czechoslovakia, vol. **11,** pp. **226–227.**

SOUTHWORTH, R. B., and HAWKINS, G. S.
1962. Statistics of meteor streams. Geophys. Res. Papers **75,** p. **261,** AFCRL **62–497,** May. *See* also, Proceedings of the Symposium on the Astronomy and Physics of Meteors. Smithsonian Contr. Astrophys., vol. **7,** pp. **261–285, 1963.**

U.S. STANDARD ATMOSPHERE
1962. U.S. Standard Atmosphere **1962.** Prepared under NASA, USAF, and USWB, Washington, D.C., **278** pp.

VERNIANI, F.
1964. On the luminous efficiency of meteors. Smithsonian Astrophys. Obs. Spec. Rep. No. **145, 62** pp.

VERNIANI, F., and HAWKINS, G. S.
1965. Masses, magnitudes, and densities of **320** radio meteors. Harvard Radio Meteor Project Res. Rep., no. **12, 34** pp.

WHIPPLE, F. L.
1954. Photographic meteor orbits and their distribution in space. Astron. Journ., vol. **59,** pp. **201–217.**
1955. On the mass-luminosity relation for meteors. Astron. Journ., vol. **60,** pp. **182–183.**

WYATT, S. P., Jr., and WHIPPLE, F. L.
1950. The Poynting-Robertson effect on meteor orbits. Astrophys. Journ., vol. **111,** pp. **134–141.**

Abstract

An additional k_B parameter proportional to log $\lambda\delta c$ of the meteoroid is used together with the orbital elements Four groups are found among sporadic meteors: the A group has the greatest density and short-period orbits with small eccentricities and ecliptical concentration; the C group has the least density and can be separated into a C_1 group of short-period orbits with ecliptical concentration but with longer semimajor axes and with greater eccentricities than the A group, and into a C_2 group with long-period orbits of eccentricities near one and without any ecliptical or other concentration. The B group has a density between that of the A and the C groups, and short-period orbits with great eccentricities, small perihelion distances and ecliptical concentration. The C_1 group is clearly connected with short-period comets, the C_2 group with the long-period "parabolic" comets. The B group could be connected with the short-period comets. The A group is probably connected with asteroids. The observed number of Super-Schmidt meteors is maximal in the A group, a little less in the C group (the C_2 group being a greater contributor than the C_1 group), and only small in the B group.

Comments on Ceplecha's Paper "Classification of Meteor Orbits"

F. VERNIANI[1]

In his paper "Classification of Meteor Orbits" *(supra)*, Ceplecha finds essentially the existence of two groups among sporadic meteors: One (A group) containing meteors with greater density and short-period orbits, and another (C group) containing meteors with lower density and long-period orbits. He then estimates the density of meteors of the A group to be about 4 g/cm^3 and hence infers that they are of asteroidal origin. In conclusion, he finds that 54 percent of the meteors observed photographically and about 90 percent of the true meteoric population should be considered as of asteroidal origin.

The existence of some physical differences between short-period and long-period meteors was first discovered by Jacchia (1958, 1960, 1963). A systematic difference in density was later explicitly pointed out by Verniani (1964a), and confirmed by Jacchia, Verniani, and Briggs (1965). The explanation of these differences was given on the basis of Whipple's theory of comets and meteors (1950, 1951). Therefore, while the existence of the two different groups found by Ceplecha confirms well-established facts, his conclusions about the asteroidal origin and the high density of most meteors differ from the generally accepted results and theory.

The present evidence shows that nearly all photographic meteors are of cometary origin. Referring for all details to Jacchia and Whipple (1961), Jacchia (1963), and Jacchia, Verniani, and Briggs (1965), I point out the following facts:

1. The orbits of many meteor showers and associations have been clearly identified with those of some comets.
2. The physical characteristics of sporadic and shower meteors not related to known comets do not show any systematic differences from those of the shower meteors connected with comets.
3. Fragmentation is of common occurrence, as is shown beyond any reasonable doubt by the deceleration anomalies, and by the blending of the exposed segments.
4. The average meteor density, directly computed by decelerations, is about 0.25 g/cm^3.
5. Among over 400 precisely reduced meteors, *only one* has all the expected characteristics of an asteroidal meteor, and this in spite of the fact that especially long trails were selected, thus favoring the inclusion of asteroidal meteors.

From all these facts we must conclude that the great majority of meteors are of cometary origin, and because they are also light, porous, and crumbly, they conform to Whipple's theory of comets and meteor production.

Ceplecha finds values of average meteor densities one order of magnitude larger than the currently accepted values (Whipple, 1963; Verniani, 1964a,b; Jacchia, Verniani, and Briggs, 1965). In particular, he criticizes the procedure used in my paper (1964a) to obtain meteor densities. He claims that, in the case of fragmenting particles, the meaning of decelerations is not clear, and quoting his own words, "it is evident that systematic changes due to (the drag coefficient) γ, (the shape factor) A, and (the deceleration) dv/dt could be much

[1] Smithsonian Astrophysical Observatory, Cambridge, Massachusetts; on leave from Centro Nazionale per la Fisica dell' Atmosfera e la Meteorologia del CNR, Rome, Italy.

greater than 3." I must remark, first of all, that the drag equation is sound, because it expresses the conservation of momentum; and as far as γ and A are concerned, there is indeed little danger of systematical error. The Super-Schmidt photographic meteors are small; free-molecule flow should occur in most cases, and therefore γ must be 1.1 or very close to it. In any case, γ could only be smaller than the assumed free-molecule-flow value; hence the computed densities would become even smaller than 0.25 g/cm³. It is also very difficult to see how, on the average, A could be different from 1.5 by more than 10 or 20 percent. Let us not forget that the increase in cross section due to fragmentation is properly taken into account by means of the fragmentation index.

For a good part of the precisely reduced photographic meteors used in my paper (1964a), the fragmentation index is close enough to 0 to make it useless to question the meaning of the decelerations, and consequently of the densities, which turn out to be about 0.25 g/cm³. The aforementioned asteroidal meteor has a deceleration 1 order of magnitude smaller than that of the other little-fragmenting meteors, and we do find for the former a density of about 4 g/cm³. Should we, for any reason, scale the density of the ordinary meteors to Ceplecha's value, we would find for the asteroidal meteor a density of the order of 50 g/cm³. As far as the most-crumbling meteors are concerned, the meaning of the measured decelerations may be rather obscure, but the use of the fragmentation index reduces their decelerations to a standard point in the trajectory where the effects of fragmentation are unimportant. Moreover, the resulting densities are in general agreement with those of meteors scarcely affected by fragmentation. Should we question the validity of the densities calculated for the severely fragmenting bodies, it is clear that those meteors could not in any case be stronger and denser than nonfragmenting bodies.

I must also point out that I have determined meteor densities using solely the heights of maximum light for 359 photographic meteors for which the decelerations were unknown (Verniani, 1964b). In spite of the different method employed, the results are in very good agreement with those obtained directly by decelerations.

It is natural now to ask ourselves why Ceplecha arrives at such different values. The discrepancy in Ceplecha's results is due mainly to the definition and use of his k_B parameter, not to mention the large uncertainties in heat conductivity, specific heat, and surface temperature of meteoric material. In fact, his equation (1), the basis for the definition of k_B, is at great variance with some well-established observational results. Ceplecha's equation (1) may be written as:

$$\log \rho_B = \text{constant} - 2.5 \log v_\infty + \frac{1}{2} \log (\rho_m \cos Z_R), \quad (1)$$

where ρ_B is the atmospheric density at the height of meteor beginning, v_∞ the apparent meteor velocity outside the atmosphere, ρ_m the meteor density, and Z_R the zenith angle. Now, the analysis of 413 precisely reduced Super-Schmidt meteors gives (Jacchia, Verniani, and Briggs, 1965):

$$\log \rho_B = \text{constant} - 3.5 \log v_\infty - 0.25 \log m_\infty \quad (2)$$

where m_∞ is the initial mass of the meteoroid, and the standard deviation of the coefficient of $\log v_\infty$ is ± 0.15. Accordingly, Ceplecha's k_B turns out to contain a term $(-\log v_\infty)$ that may explain why his average k_B for fast meteors ($v_\infty \simeq 60$ km/sec) is roughly 0.5 smaller than his average k_B for slow meteors ($v_\infty \simeq 20$ km/sec). Even if we divide the meteors into 2 groups of different orbital characteristics (long- and short-period), the coefficient of $\log v_\infty$ is still close to -3.5.

The lack of agreement between Ceplecha's theoretical equation (1) and the observational equation (2) is probably due to the effect of radiation cooling, neglected by Ceplecha. Incidentally, radiation cooling probably accounts also for meteors beginning some 6 km lower than expected on theoretical grounds (Jacchia, Verniani, and Briggs, 1965). If, for the sake of simplicity, we take a spherical body, the ratio R between the energy radiated by the meteor and the heat produced on the meteor

itself in the collisions with the atmospheric molecules is given by

$$R=\frac{8\epsilon\sigma T^4}{\Lambda v^3\rho}, \tag{3}$$

where ε is the emissivity, σ the Stefan-Boltzmann constant ($=5.67\times10^{-5}$ cgs), T the temperature, Λ the heat-transfer coefficient, v the velocity, and ρ the air density. Assuming, again for simplicity, that $\frac{\epsilon}{\Lambda}=1$, we find

$$R\simeq\frac{4.5\times10^{-4}T^4}{v^3\rho} \tag{4}$$

The average Super-Schmidt meteor with a velocity of 18 km/sec begins at 90 km (Jacchia, Verniani, and Briggs, 1965), where $\rho\simeq3.2\times10^{-9}$ g/cm³, while the beginning height of a meteor having a velocity of 70 km/sec is about 116 km, where $\rho\simeq4.0\times10^{-11}$ g/cm³. Assuming $T=$ 2000°K, equation (4) yields $R\simeq0.4$ and $R\simeq0.5$, respectively, which means that at meteor beginnings radiation is not at all negligible. With $T=3000$°K, we would find $R\geq2$; i.e., such a temperature cannot be reached. Incidentally, this shows also that the temperatures derived by Ceplecha in his section 13 (up to 8200°K) are physically impossible: a further proof of the unrealistic approach represented by his equation (1).

Acknowledgment

The author is grateful to Dr. Luigi G. Jacchia for discussions on several points touched on in this paper.

References

JACCHIA, L. G.
1958. On two parameters used in the physical theory of meteors. Smithsonian Contr. Astrophys., vol. 2, no. 9, pp. 181-187.
1960 Individual characteristics of meteor families (abstract). Astron. Journ., vol. 65, p. 53.
1963. Meteors, meteorites and comets; interrelations. *In* The Solar System, vol. 4, ed. by B. M. Middlehurst and G. P. Kuiper, Univ. of Chicago Press, Chicago, pp. 774-798.

JACCHIA, L. G.; VERNIANI, F.; and BRIGGS, R. E.
1965. An analysis of the atmospheric trajectories of 413 precisely reduced photographic meteors. Smithsonian Astrophys. Obs. Spec. Rep. No. 175, 309 pp.; also in Smithsonian Contr. Astrophys., vol. 10, no. 1, 139 pp., 1967.

JACCHIA, L. G., and WHIPPLE, F. L.
1961. Precision orbits of 413 photographic meteors. Smithsonian Contr. Astrophys., vol. 4, no. 4, pp. 97-129.

VERNIANI, F.
1964a. On the luminous efficiency of meteors. Smithsonian Astrophys. Obs. Spec. Rep. No. 145, 62 pp.; also in Smithsonian Contr. Astrophys., vol. 8, no. 5, pp. 141-172, 1965.
1964b. On the density of meteoroids, II: The density of faint photographic meteors. Nuovo Cimento, vol. 33, pp. 1173-1184.

WHIPPLE, F. L.
1950. A comet model, I: The acceleration of Comet Encke. Astrophys. Journ., vol. 111, pp. 375–394.
1951. A comet model, II: Physical relations for comets and meteors. Astrophys. Journ., vol. 113, pp. 464–474.
1963. On meteoriods and penetration. Journ. Geophys. Res., vol. 68, pp. 49294939.

Abstract

The present evidence pointing to a cometary origin and to a low density for the overwhelming majority of meteors is briefly reviewed. Account is given for some of the reasons leading Ceplecha to the wrong conclusion that most meteors are asteroidal and have a density of about 4 g/cm³.

Abstract of Ceplecha's Reply to Verniani's Comments

Verniani omitted the difference between the C_1 and C_2 groups.

The sporadic C group and shower meteors begin 9 km higher than the sporadic A group, and 15 km higher than each of the three iron meteors. These are observational values. Table 16.1 in Special Report 175 (Jacchia, Verniani, and Briggs, 1965) shows a systematic difference in log σ of at least 0.2 between the shower meteors and the sporadic A group, if the distribution is plotted instead of using the average values only. All three phases—solid, liquid, and gas—are transported behind the body. It is not necessary to explain the faint meteors anomaly as due only to fragmenting bodies produced by comets.

The 0.25-g/cm^3 density could be systematically shifted because of the unknown physical meaning of γ, A, and dv/dt in the free molecule flow drag equation, if applied to ablating meteors. I do not use any theoretical values of heat conductivity, specific heat, and surface temperature to derive the densities. My assumption could be shortly written: iron=iron.

The velocity exponent 2.5 is verified beyond any doubt from figures 1 and 2 of my paper. The velocity exponent 3.5 results if the two groups A and C are put together in one group and the difference of the beginning heights is explained by the velocity difference. But this is *not correct* (see figs. 1 and 2). The masses published for Super-Schmidt meteors are ***not direct*** *observational* values, but they are computed theoretically from the light curves.

As the meteor surface temperature rises in direct proportion to the air density ρ in the case of heat conductivity, and $\rho^{1/4}$ in the case of radiation, there exists some "reference height" not very much higher than the observed beginning, where radiation is negligible and my equation (1) holds. This "reference height" is strictly dependent on the heat conductivity, density, and specific heat, and it is to some extent related to the observed beginning height, though radiation could be the main process at the beginning.

My paper contains a more general view independent of any theoretical value (the only one is 2.5 log v_∞, which exactly corresponds to the observations). My densities are obtained by direct comparison of the relative k_B of three iron meteors with the relative values on the same scale for the whole sample.

Further Comments by F. Verniani

Among the **413** precisely reduced meteors of Jacchia, Verniani, and Briggs (1965), shower meteors begin on the average **3.1** km higher than sporadic meteors, mostly because of their greater velocities: after reduction to a standard velocity and mass, the difference in beginning height is about **1** km. These are observational values.

The small difference **(0.09)** in the average value of log σ between sporadic and shower meteors is, again, mostly due to the different mean velocity **(33.7** km/sec for sporadic and **39.3** km/sec for shower meteors). Moreover, **as** Jacchia, Verniani, and Briggs **(1965, p. 45)** state, there is no appreciable difference in log σ between short- and long-period meteors when groups of the same velocity are compared (ibid., table **17.1.2).**

The drag equation, the meaning of the deceleration, and the effect of the drag coefficient have been fully discussed in my previous comments.

Geplecha does assume theoretical (and very uncertain) values of the heat conductivity and specific heat of the meteoric material in order to derive his values of the density (see his eq. **2).**

I do not question Ceplecha's "reference height" where the atmospheric density ρ could be $\sim v_\infty^{-2.5}$, but it is obvious that these "reference heights" have very little to do with the observed beginning heights, which **follow** the law $\rho \sim v_\infty^{-3.5}$.

Reference

JACCHIA, L. G.; VERNIANI, F.; and BRIGGS, R. E. 1965. **An analysis of the atmospheric trajectories of 413 precisely reduced photographic meteors. Smithsonian Astrophys. Obs. Spec. Rep. No. 175, 309 pp.** Also **in Smithsonian Contr. Astrophys., vol. 10, no. 1, 139 pp., 1967.**

Orbits of Bright Photographic Meteors

P. B. BABADZHANOV [1] and E. N. KRAMER [2]

During the period 1957 to 1963, systematic photographic observations of meteors were carried out at the Astrophysical Institute of the Academy of Sciences of Tadjikistan (Dushanbe) and at the Odessa and the Kiev astronomical observatories. The photographs were taken with cameras NAFA 3C/25 (D=100 mm, F=250 mm, and field of vision 40°×50°); a panchromatic emulsion of 19-cm width with a sensitivity of 1100 to 1300 units of GOST (approx. 350–450 ASA) was used. The base lines between the stations at each observatory were from 20 to 40 km. The exposures, which were carried out automatically, had a duration of 30 to 60 minutes. Time signals were made on the star trails by a special transducer. The limiting magnitude of the system was approximately +1 mag. The precision of the determination of the coordinates of any points on the negatives was about 5 sec of arc.

The results are given for about 500 meteors photographed in Dushanbe and Odessa. Some of the results were published by Babadzhanov and Kramer (1963); those that include the observations of the period from 1960 to 1963 are given in table 1 (Dushanbe) and table 2 (Odessa); these tables consist of the following data:

No.	Meteor number. In table 1 the first two digits signify the year of observation minus 1900; the next three digits signify the number of exposures in the current year; and the last digit signifies the number of the camera. In table 2 the first column denotes the meteor number.
Year	Year of observation minus 1900.
Month	Number of the month of observation.
Day	Day of the month in Universal Time given to 0^{d}001.
Corr. rad.	Radiant (right ascension α and declination δ) after correction for the earth's attraction and diurnal aberration, in degrees and minutes. Equinox 1950.0.
Sin Q	Q is the angle between the great circles traced by the meteor, as seen from two stations.
cos Z_R	Z_R is the zenith distance of the radiant.
e	Elongation of the corrected radiant from the apex of the earth's motion, in degrees.
H_b	Height at beginning, in km.
H_{max}	Height at maximum light, in km.
H_e	Height at end, in km.
V_∞	Velocity outside the earth's atmosphere, in km/sec.
V_G	Geocentric velocity, in km/sec.
V_H	Heliocentric velocity, in km/sec.
a	Semimajor axis, in a.u.
e	Eccentricity.
4	Perihelion distance, in a.u.
4	Aphelion distance, in a.u.
ω	Argument of perihelion, in degrees. Equinox 1950.0.
Ω	Longitude of the ascending node, in degrees. Equinox 1950.0.
i	Inclination of the orbit plane to the ecliptic, in degrees. Equinox 1950.0.

[1] Astrophysical Institute of the Academy of Sciences of Tadjikistan, USSR.
[2] Odessa State University, USSR.

TABLE 1.—*Orbital elements of meteors (Dushanbe)*

No.	Year	Month	Day	Corr. radiant		Sin Q	Cos Z_r	e	H_b	H_{max}	H_e	V_∞	V_G	V_H	a
				α	δ										
600051	60	1	1.725	93°16′	−28°11′	0.171	0.394	90°1	88.2	78.9	77.5	26.2	23.6	38.4	2.70
600153	60	1	4.898	118 34	26 34	0.026	0.961	77.0	64.6	62.2	59.1	23.4	20.7	32.6	1.20
600165	60	1	4.924	228 53	4945	0.054	0.537	63.5	84.5	79.5	75.7	37.2	35.3	34.8	1.49
600185	60	1	4.877	229 55	49 17	0.053	0.635	63.7	92.9	68.6	67.8	37.4	35.5	35.0	1.53
630215	63	1	22.898	191 16	16 11	0.196	0.751	33.5	108.8	102.2	97.0	65.1	63.9	42.1	27.0
610592	61	2	13.885	258 06	5308	0.372	0.544	75.5	88.9	76.5	65.1	33.7	31.6	37.8	2.42
630521	63	2	17.658	97 15	840	0.942	0.909	137.8	74.8	59.5	48.8	14.2	8.9	37.3	2.18
630574	63	2	18.703	141 42	E 17	0.328	0.804	98.3	81.3	76.4	71.8	21.4	18.1	37.3	2.20
630584	63	2	18.783	159 45	502	0.190	0.788	79.1	95.7	93.0	76.6	32.5	30.4	38.6	2.88
630954	63	3	26.657	175 58	2 01	0.195	0.608	98.6	86.4	—	49.2	21.3	17.9	37.0	2.18
631512	63	6	16.804	271 33	−16 15	0.424	0.601	83.0	91.9	79.8	77.4	28.8	26.6	37.1	2.38
631712	63	6	22.890	343 27	953	0.375	0.662	19.4	110.4	106.0	101.9	59.2	57.8	31.7	1.20
611992	61	7	11.892	304 31	49 40	0.220	0.964	73.4	99.5	95.0	90.4	41.0	39.5	41.9	−78.2
631811	63	7	15.733	266 25	25 26	0.569	0.977	106.7	91.3	86.0	81.7	21.5	18.4	38.8	3.73
631996	63	7	20.846	34 38	45 32	0.111	0.512	35.8	113.0	110.2	106.5	62.5	61.3	41.3	1.98
632141	63	7	23.868	21 59	51 43	0.181	0.728	40.4	110.3	100.5	97.0	60.0	58.8	41.1	16.2
620384	62	7	25.787	25 51	51 50	0.066	0.487	39.7	111.5	84.3	82.5	60.1	58.8	40.8	10.5
601242	60	7	25.903	319 38	−9 12	0.184	0.656	73.9	102.0	96.0	80.2	37.6	36.0	39.6	5.02
601443	60	7	31.853	31 02	53 52	0.366	0.694	39.6	105.6	84.0	78.7	59.7	58.5	40.5	8.07
620511	62	8	2.734	47 34	83 35	0.244	0.583	68.8	100.7	94.0	92.5	42.5	41.0	40.9	11.6
620531	62	8	2.829	34 03	5448	0.193	0.619	40.0	110.4	89.4	87.2	60.7	59.5	41.5	33.8
620544	62	8	2.878	32 55	54 40	0.111	0.754	39.9	106.5	99.6	89.8	60.0	58.8	40.9	11.4
620581	62	8	3.788	342 34	−15 36	0.559	0.440	63.5	99.2	88.3	86.3	42.3	40.6	38.0	2.90
620605	62	8	3.874	332 49	−12 34	0.273	0.649	71.0	91.4	82.9	76.4	34.2	32.4	36.0	1.95
620652	62	8	4.818	36 36	56 50	0.401	0.594	41.4	112.3	101.3	96.2	59.8	58.6	41.4	22.2
620672	62	8	4.942	332 30	31 15	0.268	0.912	63.0	88.8	85.0	78.5	45.0	43.8	40.1	6.28
632341	63	8	10.681	276 45	42 51	0.194	0.995	103.6	94.4	88.5	74.6	21.9	18.9	38.5	3.31
620752	62	8	10.902	38 56	55 03	0.575	0.816	38.2	109.6	98.4	96.8	61.8	60.8	41.9	∞
612376	61	8	11.794	48 31	55 39	0.104	0.488	38.1	103.8	101.5	93.7	60.9	59.6	40.8	9.69
632395	63	8	12.773	4829	57 19	0.133	0.450	39.6	105.2	—	96.0	61.9	60.7	42.5	−17.3
612451	61	8	12.946	5823	55 58	0.246	0.809	38.9	103.0	92.0	89.0	57.3	56.1	38.0	2.86
632421	63	8	13.742	46 56	59 27	0.146	0.396	41.6	111.2	105.5	87.9	60.0	58.6	41.4	25.7
612474	61	8	13.750	41 22	58 25	0.051	0.460	40.7	113.4	95.0	93.8	63.9	62.7	44.8	−3.52
632432	63	8	13.776	47 56	58 11	0.272	0.474	40.3	109.3	92.0	89.2	60.8	59.6	41.7	83.2
632441	63	8	13.852	39 48	54 02	0.202	0.713	36.7	111.1	93.0	90.9	61.0	59.7	40.2	6.36
632494	63	8	14.849	47 26	54 40	0.075	0.660	36.5	104.5	87.5	82.9	59.0	57.8	38.4	3.16
632521	63	8	15.747	55 15	56 51	0.156	0.356	38.6	108.5	104.0	95.8	58.6	57.4	39.0	3.77
632552	63	8	15.867	49 35	57 18	0.629	0.701	38.8	108.9	99.0	94.4	60.8	59.6	41.0	13.0
632555	63	8	15.879	5024	59 17	0.143	0.726	40.8	107.7	102.2	97.6	59.2	58.0	40.6	8.45
632632	63	8	17.734	314 52	408	0.394	0.807	95.6	87.8	79.3	74.9	27.2	24.8	40.3	6.68
632725	63	8	18.875	22 13	34 46	0.067	0.898	31.6	108.0	92.0	90.2	64.5	63.4	41.3	18.8
632762	63	8	23.795	264 35	61 57	0.306	0.758	95.2	90.9	76.0	72.6	23.5	20.9	37.6	2.62
620886	62	8	24.717	36 56	69 56	0.201	0.558	51.2	105.4	98.0	95.7	50.1	48.7	38.0	2.84
620962	62	8	28.734	335 43	−5 08	0.641	0.668	89.9	95.4	84.8	82.1	27.9	25.4	38.9	3.63
621025	62	8	30.850	92 30	62 40	0.130	0.501	44.9	95.4	91.0	88.7	58.2	56.9	41.6	31.8
621105	62	8	31.912	58 07	26 24	0.172	0.801	9.2	109.4	96.6	95.9	72.7	71.6	42.8	−13.0
621134	62	9	1.774	91 35	56 29	0.092	0.289	38.8	107.0	98.5	90.2	60.9	59.7	41.1	12.8
621204	62	9	2.850	91 21	58 35	0.040	0.501	39.9	104.8	95.8	92.7	56.4	55.0	37.6	2.53
621234	62	9	3.688	276 17	4408	0.482	0.965	109.4	91.7	72.9	72.2	19.3	15.8	37.9	2.71
612992	61	9	9.902	101 13	40 00	0.226	0.516	27.0	100.3	98.2	92.4	67.0	65.8	41.7	31.8
621354	62	9	10.917	85 30	−10 34	0.168	0.311	34.4	114.7	—	84.2	64.0	62.7	41.8	58.0
621402	62	9	23.757	356 33	−2 37	0.625	0.761	95.2	83.5	61.0	58.2	23.5	20.6	37.6	2.51
621694	62	10	2.851	84 40	5033	0.157	0.740	30.2	112.0	94.5	87.6	66.6	65.4	42.4	−34.0
621892	62	10	6.898	79 37	33 17	0.704	0.892	24.8	110.8	94.3	94.1	68.9	67.9	42.7	−19.5
621973	62	10	9.915	110 39	−4 49	0.227	0.403	27.3	97.7	94.5	90.4	67.1	65.9	41.7	23.1
614003	61	10	16.878	37 46	10 20	0.255	0.875	75.2	104.0	74.2	68.7	32.3	30.4	36.8	2.07
600361	60	10	20.817	90 37	14 30	0.037	0.552	28.9	129.3	—	89.9	74.9	73.8	49.7	−1.29
622053	62	10	21.862	94 18	15 27	0.109	0.460	25.6	111.5	99.6	93.8	67.5	66.3	41.4	12.2
632943	63	10	23.940	96 20	15 29	0.194	0.884	25.5	106.2	93.5	91.8	67.9	66.9	41.9	28.0
622123	62	10	26.792	46 24	11 25	0.355	0.867	76.5	93.2	78.8	75.9	30.3	28.1	36.0	1.81
600522	60	10	28.939	52 38	038	0.083	0.684	77.0	98.6	85.0	80.9	34.4	32.8	39.1	3.47
622215	62	10	30.728	331 58	−12 55	a630	0.669	158.1	77.4	—	36.2	13.5	8.0	37.6	2.36
622372	62	11	1.989	5033	13 34	0.479	0.718	78.1	101.1	76.2	69.7	29.9	27.7	36.4	1.92
614554	61	12	3.662	99 17	27 34	0.298	0.996	63.4	94.6	75.6	69.9	41.0	39.2	37.3	2.15
622512	62	12	3.826	84 23	24 28	0.838	0.966	76.6	96.8	83.0	72.0	31.9	29.9	37.3	2.15
614715	61	12	8.925	72 43	−9 48	0.336	0.942	96.0	99.9	81.9	73.3	24.2	21.8	39.1	3.22
614713	61	12	8.957	151 33	21 05	0.405	0.909	22.5	66.3	60.3	58.6	28.6	26.3	11.7	0.533
614764	61	12	11.749	82 03	26 45	0.347	0.923	86.8	92.3	81.0	53.5	26.4	23.8	37.4	2.20
614794	61	12	11.880	81 37	16 33	0.275	0.881	87.9	89.9	76.9	72.8	24.6	22.1	36.8	1.98
622553	62	12	17.618	8348	24 50	0.206	0.575	90.9	98.8	89.6	77.9	25.9	23.1	38.4	2.68
622571	62	12	17.714	102 57	12 37	0.179	0.622	72.8	102.4	90.7	86.8	40.4	38.5	41.4	9.58
622713	62	12	22.796	274 50	71 51	0.573	0.409	91.5	86.8	85.3	82.9	26.1	23.6	38.9	3.04

TABLE 1.—*Orbital elements of meteors (Dushanbe)—Continued*

No.	Year	Month	Day	e	a	q'	ω	Ω	i	π	M_{max}	t	m_∞	Shower or parent comet
600051	60	1	1.725	0.728	0.736	4.66	6602	100°.2	14702	166°.4	−2.0	1.02	4.92	
600163	60	1	4.898	0.630	0.442	1.96	295.0	282.4	45	317.4	−4.2	0.30	2.65	
600165	60	1	4.924	0.343	0.979	2.00	169.0	282.4	65.2	91.4	−4.1	0.44	4.40	Quadr
600185	60	1	4.877	0.361	0.976	2.08	166.2	282.4	66.4	88.6	−5.7	1.02	38.6	Quadr
630215	63	1	22.898	0.980	0.633	53.5	265.8	302.0	137.3	207.8	−1.9	0.24	0.071	
610592	61	2	13.885	0.593	0.986	3.86	175.3	324.8	54.0	140.1	−0.9	1.36	1.49	
630521	63	2	17.658	0.558	0.962	3.40	22.2	148.1	3.5	170.3	−2.2	1.03	24.8	
630574	63	2	18.703	0.675	0.714	3.68	70.1	149.1	1.4	319.2	−0.2	0.55	0.955	
630584	63	2	18.783	0.874	0.362	5.40	111.0	149.2	4.0	260.2	—	0.76	—	1766 II
630954	63	3	26.657	0.668	0.725	3.64	251.3	5.2	0.1	256.5	—	2.92	—	
631512	63	6	16.804	0.812	0.448	4.32	284.3	847	7.2	9.0	−2.0	0.88	2.76	67
631712	63	6	22.890	0.386	0.738	1.66	259.2	90.5	148.3	359.7	−2.3	0.22	0.069	
611992	61	7	11.892	1.01	0.938	−157.2	212.3	109.2	63.4	331.5	−2.1	0.23	0.347	
631811	63	7	15.733	0.753	0.921	6.54	218.6	112.3	21.8	330.9	0.1	0.66	0.577	72(73)
631906	63	7	20.846	0.960	0.795	3.88	123.5	117.2	123.7	240.7	−1.5	0.21	0.036	1764
632141	63	7	23.868	0.941	0.958	31.4	152.1	120.1	112.6	272.2	−2.0	0.30	0.109	Per
620384	62	7	25.787	0.910	0.948	20.0	149.2	122.2	113.8	271.4	−6.8	0.49	3.06	Per
601242	60	7	25.903	0.954	0.229	9.81	305.9	122.8	11.4	68.7	−1.6	0.89	0.898	
601443	60	7	31.853	0.881	0.962	15.2	152.8	128.4	113.3	281.3	−4.0	0.66	1.14	Per
620511	62	8	2.734	0.921	0.914	22.4	142.4	129.8	67.9	272.2	−1.0	0.43	0.095	V
620631	62	8	2.829	0.972	0.957	66.6	151.9	129.8	113.6	281.8	−2.8	0.64	0.382	Per
620644	62	8	2.878	0.916	0.962	21.8	153.0	129.9	113.1	282.9	−2.4	0.37	0.210	Per
620581	62	8	3.788	0.970	0.087	5.71	148.7	310.8	25.9	119.5	r3.2	0.70	0.943	VII
620605	62	8	3.874	0.891	0.199	3.68	132.8	310.8	2.2	83.6	−2.7	0.66	1.40	Aqu
620652	62	8	4.818	0.957	0.951	43.4	150.6	131.8	111.2	262.4	−4.0	0.45	0.451	Per
620672	62	8	4.942	0.918	0.515	12.0	271.6	131.9	71.6	43.5	−1.0	0.26	0.088	
632341	63	8	10.681	0.704	0.978	5.64	203.9	137.1	27.1	341.0	−1.0	0.99	4.70	73(72)
620752	62	8	10.902	1.000	0.970	∞	161.8	137.6	116.4	299.4	−0.8	0.26	0.031	Per
612376	61	8	11.794	0.904	0.935	18.4	146.8	138.7	116.4	285.5	−2.7	0.30	0.330	Per
632395	63	8	12.773	1.054	0.943	−35.5	149.9	139.1	114.9	289.0	—	0.33	—	Per
612451	61	8	12.946	0.712	0.824	4.89	123.5	139.8	113.7	263.3	−2.8	0.30	0.366	Per
632421	63	8	13.742	0.963	0.956	50.4	152.1	140.1	110.8	292.2	−3.0	0.96	1.15	Per
612474	61	8	13.750	1.28	0.992	−8.04	164.4	140.6	114.1	305.0	−3.0	0.63	0.48	Per
632432	63	8	13.776	0.988	0.959	165.4	151.4	140.1	113.2	291.5	−2.4	0.71	0.379	Per
632441	63	8	13.852	0.843	0.999	11.7	165.9	140.2	117.5	306.1	−2.4	0.46	0.266	Per
632494	63	8	14.849	0.697	0.969	5.36	150.4	141.1	116.9	291.5	−2.8	0.55	0.461	Per
632521	63	8	15.747	0.760	0.902	6.63	138.4	142.0	114.3	280.4	−2.5	0.59	0.526	Per
632552	63	8	15.867	0.926	0.958	25.1	152.8	142.1	115.0	294.9	−1.9	0.34	0.121	Per
632555	63	8	15.879	0.888	0.949	16.0	150.2	142.1	111.4	292.3	−1.4	0.23	0.056	Per
632632	63	8	17.734	0.903	0.650	12.7	255.8	143.9	15.2	39.7	−1.7	0.55	1.28	
632725	63	8	18.875	0.961	0.739	36.8	243.2	145.0	134.4	28.2	−6.5	0.31	2.09	
632762	63	8	23.795	0.614	1.011	4.23	181.3	149.8	33.6	331.1	−0.7	1.12	2.15	κ Cyg
620886	62	8	24.717	0.645	1.009	4.67	175.0	150.9	91.5	325.9	−0.2	0.33	0.061	
620962	62	8	28.734	0.855	0.528	6.73	87.9	154.8	41.0	242.7	0.4	0.74	0.341	
621025	62	8	30.850	0.974	0.818	62.8	128.0	156.8	166.3	284.8	−1.4	0.23	0.059	IX
621105	62	8	31.912	1.08	0.973	−26.9	201.2	157.8	169.6	359.0	−2.9	0.24	0.089	186411
621134	62	9	1.774	0.938	0.784	24.8	124.1	158.7	117.2	282.8	−2.8	0.46	0.504	IX
621204	62	9	2.850	0.690	0.786	4.28	117.4	159.9	111.4	277.3	−2.4	0.43	0.216	IX
621234	62	9	3.688	0.633	0.997	4.44	194.0	160.5	22.8	354.5	−3.1	1.06	3.46	
612992	61	9	9.902	0.978	0.688	62.9	111.0	166.8	146.3	277.8	−1.6	0.22	0.029	17901
621354	62	9	10.917	0.983	0.985	115.0	343.3	347.5	122.2	330.8	—	0.76	—	
621402	62	9	23.757	0.748	0.632	4.38	82.2	0.1	0.7	82.3	−3.0	1.61	25.3	
621694	62	10	2.851	1.03	0.902	−69.0	216.3	189.0	132.1	45.3	−4.0	0.50	1.08	
621892	62	10	6.898	1.03	0.656	−39.6	251.2	193.0	159.6	84.2	−2.2	0.28	0.637	
621973	62	10	9.915	0.958	0.970	45.3	340.5	15.9	134.0	356.4	−1.9	0.27	0.069	1723
614003	61	10	16.878	0.862	0.286	3.85	122.7	23.1	6.0	145.8	−1.5		0.616	S. Ari
600361	60	10	20.817	1.48	0.617	−3.20	68.7	27.3	162.0	96.0	bolide	0.90		Ori
622053	62	10	21.862	0.953	0.571	23.8	82.8	28.1	163.2	110.9	−4.2	0.55	1.05	Ori
632943	63	10	23.940	0.979	0.583	55.4	80.7	29.6	163.6	110.3	−2.8	0.24	0.121	Ori
622123	62	10	26.792	0.818	0.328	3.29	119.3	32.7	7.0	152.0	−0.6	0.65	0.423	S. An
600522	60	10	28.939	0.894	0.354	6.57	111.1	35.4	25.8	146.5	−1.4	0.77	0.636	
622215	62	10	30.728	0.583	0.984	3.74	14.5	36.9	0.3	51.4	bolide	5.17	—	
622372	62	11	1.989	0.816	0.352	3.48	115.8	38.9	5.5	164.7		1.42		S. Taur
614554	61	12	3.662	0.958	0.091	4.21	31.2	251.1	13.6	282.3	−3.9	1.40	7.34	
622512	62	12	3.826	0.854	0.314	3.99	298.7	251.0	1.5	189.7	1.0	0.75	0.168	XV?
614715	61	12	8.925	0.774	0.728	5.72	66.3	76.4	19.7	142.7	−1.7	1.65	5.57	
614713	61	12	8.957	0.946	0.029	1.04	355.5	256.5	34.2	252.0	−1.4	0.29	0.668	
614764	61	12	11.749	0.768	0.513	3.90	276.0	259.3	2.9	175.3	−2.8	1.66	11.7	XV
614784	61	12	11.880	0.723	0 548	3.41	93.2	79.4	5.0	172.6	−1.9	0.77	1.68	XV
622553	62	12	17.618	0.788	0.569	4.79	267.6	264.9	1.1	172.6	−0.8	1.97	1.94	XV
622571	62	12	17.714	0.977	0.219	18.9	235.1	85.1	20.1	320.2	−2.2	0.62	0.413	19171
622713	62	12	22.796	0.678	0.979	5.10	188.4	269.6	37.3	98.0	−0.8	0.42	0.480	

TABLE 2.—*Orbital elements of meteors (Odessa)*

No.	Year	Month	Day	Corr. radiant		Sin Q	Cos Z_r	e	H_b	H_{max}	H_e	V_∞	V_G	V_H
				α	δ									
197	61	3	20.057	237°51′	1°12′	0.581	0.700	3803	101.5	98.3	94.1	66.1	54.6	36.3
198	61	4	8.836	195 07	−9 45	0.444	0.528	91.9	97.0		77.5	26.1	23.4	38.5
200	61	4	15.801	207 07	19 40	0.990	0.722	96.3	101.0	93.0	83.2	28.4	25.9	41.5
201	61	4	16.862	156 44	−0 03	0.576	0.713	158.5	87.8		82.0	16.3	12.2	41.3
202	61	5	9.924	202 11	−9 27	0.182	0.578	115.6	95.2		79.2	18.9	15.4	38.7
203	61	5	9.958	289 10	42 28	0.110	0.841	64.7	108.0	76.6		47.7	46.1	42.8
205	61	6	15.883	222 16	65 36	0.278	0.937	108.2	83.3	65.2	59.3	14.4	9.5	33.5
206	61	6	21.979	260 43	−4 38	0.892	0.574	99.2	91.4	85.5	78.2	22.5	19.8	37.9
207	61	6	22.974	265 12	16 00	0.186	0.807	95.3	79.8	70.8	69.0	35.5	33.8	46.8
162	60	6	29.994	272 33	−1 37	0.451	0.609	94.9	90.0	78.3	75.5	23.7	21.1	37.6
208	61	7	11.998	264 11	62 11	0.668	0.842	94.0	98.5	87.6	85.6	29.2	27.3	41.4
209	61	7	20.996	14 31	5346	0.229	0.865	43.6	107.3		96.3	62.5	61.3	45.0
164	60	7	23.847	370 10	44 04	0.328	0.997	111.3	940			22.3	19.4	38.2
209a	61	8	1.849	306 02	1 57	0.055	0.677	79.3	84.7	78.2	76.9	40.2	38.6	44.0
210	61	8	3.986	343 11	−14 15	0.996	0.605	61.9	98.8	89.3	86.0	41.9	40.4	37.1
212	61	8	6.852	39 44	57 22	0.238	0.503	41.2	111.5	88.0	79.0	60.2	58.8	41.5
215	61	8	7.002	47 29	55 25	0.015	0.785	39.1	107.6		98.2	60.3	59.0	40.7
214	61	8	7.035	30 34	56 46	0.268	0.884	41.4	109.0	97.0	93.2	60.2	59.0	41.8
213	61	8	7.053	40 27	55 22	0.256	0.912	39.0	109.2	81.6	77.0	60.9	59.7	41.2
219	61	8	7.871	311 35	542	0.147	0.772	89.7	83.8	78.4	75.6	24.1	21.3	36.2
221	61	8	9.032	42 10	57 32	0.237	0.880	40.8	105.7	98.3	93.9	61.5	60.3	42.6
222	61	8	9.036	43 32	47 12	0.128	0.836	30.4	104.6		88.0	63.2	62.0	39.5
220	61	8	9.037	12 42	62 58	0.132	0.952	51.0	97.0		83.4	53.6	52.4	40.9
224	61	8	9.826	41 35	55 32	0.201	0.424	38.6	111.2	98.5	93.0	60.6	59.3	40.7
226	61	8	9.890	44 55	57 35	0.125	0.424	40.6	107.7	97.2	90.9	60.9	59.6	41.8
223	61	8	9.972	325 01	−7 06	0.914	0.605	82.6	99.5	94.2	86.6	31.5	29.6	39.0
227b	61	8	9.989	4456	59 39	0.194	0.796	42.6	106.1		97.6	60.8	59.5	42.8
227	61	8	9.990	4446	56 26	0.284	0.854	39.4	115.0	93.0	89.4	60.8	59.5	4 t 3
227a	61	8	10.015	42 52	57 27	0.123	0.855	39.4	106.0		97.5	60.6	59.3	41.1
225	61	8	10.023	45 27	60 49	0.641	0.854	43.8	108.4	99.5	94.7	58.6	57.3	41.4
229	61	8	10.024	48 12	56 53	0.309	0.848	39.9	108.1	96.4	92.5	61.1	59.8	41.8
188	60	8	10.901	47 20	57 18	0.078	0.602	39.9	104.8		87.9	59.9	58.5	40.6
232	61	8	10.955	45 44	58 30	0.147	0.727	41.2	103.3	98.5	95.7	59.6	58.3	41.4
233	61	8	10.977	352 36	−12 09	0.576	0.526	59.3	95.0	89.9	89.0	40.6	39.0	348
228	61	8	10.981	343 34	−0 36	0.413	0.685	64.0	98.0	89.0	85.1	41.5	39.9	37.8
230	61	8	11.000	343 35	−11 16	0.761	0.550	60.6	99.6		86.4	40.2	38.7	35.3
231	61	8	11.051	50 54	58 16	0.125	0.880	41.1	102.2	91.9	90.7	59.6	58.3	41.0
236	61	8	11.794	47 13	59 17	0.379	0.398	41.7	107.3		90.0	61.1	59.8	42.6
168	60	8	11.827	44 19	59 05	0.021	0.472	41.5	109.6		97.5	60.8	59.5	42.2
235	61	8	11.834	46 00	57 46	0.279	0.461	40.2	108.0	99.6	93.9	60.5	59.2	41.4
166	60	8	11.864	50 45	57 04	0.220	0.492	39.5		93.0	92.0	58.1	56.7	38.8
165	60	8	11.881	48 22	57 52	0.122	0.561	40.2	112.5		80.0	60.4	59.0	41.2
169	60	8	11.881	45 54	57 40	0.210	0.564	40.0	110.7	102.6	96.4	60.4	59.0	41.1
190	60	8	11.881	47 15	5658	0.059	0.552	39.3	113.0			59.9	58.5	40.3
238	61	8	11.882	50 34	56 17	0.201	0.523	38.8	104.9		98.0	62.5	61.2	42.5
173	60	8	11.922	44 47	61 30	0.098	0.651	43.9	102.5	84.0	83.0	62.6	61.3	45.0
170	60	8	11.926	41 04	59 26	0.246	0.705	42.0	109.5	101.1	97.0	61.5	60.2	43.0
234	61	8	11.935	342 06	−13 16	0.562	0.500	69.9	98.6	81.5	74.5	38.7	37.0	38.5
167	60	8	11.935	45 10	58 41	0.837	0.696	41.0	107.5		92.0	62.2	60.9	43.2
239	61	8	11.965	46 20	5808	0.217	0.756	40.6	113.0	83.1	79.3	61.0	59.6	41.9
172	60	8	11.983	49 04	55 10	0.099	0.765	35.5	104.0		84.3	60.1	58.8	39.7
241	61	8	12.000	4609	57 19	0.224	0.819	39.7	110.0	101.0	95.4	60.3	59.0	40.9
240	61	8	12.010	47 17	5600	0.319	0.833	40.4	104.1	90.4	88.6	60.6	59.3	41.5
243	61	8	12.014	328 15	5339	0.810	0.950	69.3	106.2	96.0	85.8	43.1	41.8	41.8
249	61	8	12.044	4803	60 31	0.290	0.917	42.6	108.0	95.0	92.0	59.0	57.8	41.3
237	61	8	12.054	347 33	48 16	0.177	0.968	56.8	103.9	88.5	86.4	46.6	45.4	38.2
252	61	8	12.841	50 40	57 37	0.186	0.451	39.5	106.5		99.3	60.9	59.6	41.4
251	61	8	12.846	37 38	59 24	0.186	0.556	42.2	105.5	98.0	95.5	60.2	58.8	42.0
177	60	8	12.852	47 12	58 47	0.110	0.508	40.9	105.6		93.0	60.2	58.9	41.4
178	60	8	12.874	4646	5808	0.406	0.554	40.2	110.8	99.7	925	61.4	60.0	42.1
176	60	8	12.895	45 42	56 45	0.091	0.598	38.9	107.9	98.5	94.9	60.9	59.6	41.1
253	61	8	12.919	47 40	5823	0.157	0.649	40.6	111.3	101.5	95.6	60.1	58.8	41.1
179	60	8	12.981	5003	58 14	0.372	0.764	40.3	110.6	86.7	79.1	60.8	59.4	41.6
244	61	8	13.007	45 40	57 56	0.268	0.840	40.1	110.0	92.5	84.0	60.2	58.9	41.1
248	61	8	13.007	49 31	5650	0.100	0.819	39.0	104.5	87.0	86.3	60.3	59.0	40.6
250	61	8	13.018	4308	55 37	0.386	0.872	39.8	107.5	98.0	93.5	63.4	62.1	43.0
245	61	8	13.019	49 18	5800	0.638	0.841	40.2	112.0	81.4	80.0	61.1	59.8	41.9
244a	61	8	13.037	51 35	57 38	0.174	0.860	39.8	106.2		99.0	58.4	57.1	39.3
246b	61	8	13.045	48 27	57 14	0.470	0.891	39.4	108.9	90.9	90.8	60.1	58.9	40.7
255	61	8	13.957	53 00	56 47	0.202	0.699	39.0	109.5	91.2	89.0	60.8	59.5	41.0
256	61	8	14.017	56 17	61 41	0.221	0.813	43.8	105.3	100.0	95.6	57.8	56.4	40.7
257	61	8	14021	51 11	59 16	0.951	0.844	41.3	111.8	95.0	84.5	59.9	58.6	41.3
269	61	8	14.037	51 51	58 57	0.995	0.876	40.9	106.5	100.3	96.7	59.6	58.4	40.9

TABLE 2.—*Orbital elements of meteors (Odessa)—Continued*

No.	Year	Month	Day	a	e	q	q'	ω	Ω	i	π	M_{max}	m_∞	Shower or parent comet
197	61	3	20.057	1.90	0.828	0.328	3.47	298°8	359°1	122°8	297°9			
198	61	4	8.836	3.03	0.813	0.566	5.50	271.8	198.6	2.4	110.4	—5.1		1834
200	61	4	15.801	19.85	0.964	0.716	39.03	245.5	25.4	20.7	270.9	—2.2	2.57	
201	61	4	16.862	13.67	0.927	1.004	26.34	177.8	206.5	6.2	243	—1.1	5.67	
202	61	5	9.924	3.40	0.751	0.848	5.95	308.7	228.8	0.0	177.5	—3.6	50.8	
203	61	5	9.958	11.70	1.085	0.996		193.2	48.9	76.6	242.1	—6.7	1424	
205	61	6	15.883	1.42	0.287	1.014	1.83	172.9	84.4	15.6	257.3			
206	61	6	21.979	2.86	0.743	0.733	498	249.4	90.2	10.9	339.5	—2.6	6.62	
207	61	6	22.974	−2.01	1.371	0.746		237.4	91.1	33.4	328.5	—2.5	0.85	
162	60	6	29.994	2.64	0.739	0.690	460	255.9	98.1	142	354.0	—2.5	6.89	
208	61	7	11.998	27.32	0.963	1.015	53.56	184.4	109.2	41.1	293.6	—3.1	2.00	ξ Dra
209	61	7	20.996	3.18	1.310	0.985		161.1	117.8	110.5	279.0			
164	60	7	23.847	3.09	0.684	0.979	5.20	204.4	120.8	28.5	325.2	—2.6	6.97	III
209a	61	8	1.849	−4.82	1.077	0.372		77.2	129.2	31.9	206.3			
210	61	8	3.986	2.38	0.967	0.079	466	151.1	311.2	23.4	102.3			
212	61	8	6.852	32.87	0.971	0.950	64.77	150.6	1340	111.6	284 5	—6.7	20.45	Per
215	61	8	7.002	9.14	0.901	0.901	17.38	220.1	134 1	115.4	354.2			Per
214	61	8	7.035	147.30	0.993	1.003	293.90	192.2	134.1	111.1	326.3	—4.6	0.97	Per
213	61	8	7.053	18.13	0.947	0.960	35.26	207.1	134.2	115.3	341.3			Per
219	61	8	7.871	2.02	0.690	0.627	3.41	265.7	134.9	15.8	40.6			1457II
221	61	8	9.032	14.83	1.064	0.956		152.8	136.0	113.3	288.8			Per
222	61	8	9.036	4.72	0.797	0.958	8.48	161.0	136.0	126.4	287.1	—2.8	0.094	
220	61	8	9.037	11.49	0.912	1.014	21.97	182.9	136.0	95.0	318.9			
224	61	8	9.826	9.04	0.893	0.964	17.11	153.7	136.8	115.1	290.5	—3.7	1.05	Per
226	61	8	9.890	23.1	1.000	0.943	4618.02	149.4	136.9	113.0	286.3	—4.4	1.32	Per
223	61	8	9.972	3.77	0.894	0.398	7.14	73.4	137.0	7.5	210.3	—2.0	1.31	
227b	61	8	9.989	11.15	1.090	0.944		150.3	137.0	110.3	287.3			Per
227	61	8	9.990	18.35	0.948	0.945	35.76	149.3	137.0	1145	280.3	—4.6	1.42	Per
227a	61	8	10.015	13.86	0.931	0.957	26.76	152.2	137.0	114.1	329.2			Per
225	61	8	10.023	22.4	0.958	0.935	43.9	147.3	137.0	107.4	284.3	—3.3	0.24	Per
229	61	8	10.024	105.72	0.991	0.921	210.52	144.6	137.0	114.3	281.6	—5.2	1.04	Per
188	60	8	10.901	8.84	0.894	0.933	16.74	146.4	138.1	113.2	284.4	—3.5	0.47	Per
232	61	8	10.955	21.27	0.956	0.944	41.60	149.3	137.9	111.6	287.2			Per
233	61	8	10.977	1.65	0.954	0.076	3.22	206.6	317.9	29.6	164.4			Aqu
228	61	8	10.981	2.75	0.968	0.088	5.42	328.9	137.9	19.6	106.8	−4 1	2.83	VII
230	61	8	11.000	1.74	0.922	0.137	3.35	323.5	137.9	48.0	101.6	—2.3	0.90	VII
231	61	8	11.051	12.06	0.925	0.905	23.22	140.9	138.0	111.8	278.9	—5.9	3.18	Per
236	61	8	11.794	13.6	1.070	0.946		150.6	138.7	111.6	289.3	—5.9	7.24	Per
168	60	8	11.027	27.59	1.035	0.964		154.9	139.0	111.5	293.9			Per
235	61	8	11.834	21.20	0.955	0.951	41.45	151.0	138.7	119.1	289.8	—3.9	0.91	Per
166	60	8	11.864	3.62	0.750	0.905	6.34	138.6	139.0	112.6	277.6	−4.6	1.86	Per
165	60	8	11.881	16.99	0.944	0.951	33.02	156.9	135.0	112.9	289.9	—8	25.05	Per
169	60	8	11.881	14.15	0.933	0.954	27.36	151.5	139.0	113.1	290.6	—3.5	0.52	Per
190	60	8	11.881	6.99	0.865	0.943	13.04	148.2	139.0	113.8	287.2			Per
238	61	8	11.882	16.74	1.055	0.926		146.2	138.8	116.6	285.0			Per
173	60	8	11.922	−3.31	1.292	0.965		156.2	139.0	109.6	295.2			Per
170	60	8	11.926	−8.56	1.115	0.981		160.1	139.1	111.0	299.1	—3.7	0.26	Per
234	61	8	11.935	3.30	0.946	0.179	6.42	226.0	318.8	11.3	1749	—3.3	6.95	δ Aqu
167	60	8	11.935	−7.58	1.127	0.563		155.1	139.1	112.9	294 2	—3.5	0.45	Per
239	61	8	11.965	27.32	1.W4	0.952		151.5	138.9	112.9	290.4	—6.4	19.24	Per
172	60	8	11.983	5.09	0.818	0.929	9.26	144.6	139.1	116.6	283.7	—4.6	1.58	Per
241	61	8	12.000	11.40	0.917	0.951	21.85	150.7	138.9	113.6	289.6	—4.5	1.25	Per
240	61	8	12.010	29.04	0.968	0.945	57.14	149.6	138.9	113.0	288.5	—2.8	0.28	Per
243	61	8	12.014	07.2	0.992	0.878	213.5	223.0	138.9	68.1	1.9			
249	61	8	12.044	18.68	0.949	0.946	36.41	149.6	139.9	109.0	289.5	—3.3	0.24	Per
237	61	8	12.054	3.06	0.752	0.761	5.36	245.2	138.9	82.6	24.1			
252	61	8	12.841	25.138	0.963	0.929	49.35	146.2	139.7	114.2	285.8			Per
251	61	8	12.846	73.85	1.014	0.996		165.1	139.7	109.8	304.8	—3.3	0.36	Per
177	60	8	12.852	22.44	0.958	0.954	43.93	151.6	140.0	111.9	291.6	—4.1	1.20	Per
178	60	8	12.874	42.65	1.022	0.959		153.5	140.0	113.4	295.5	—3.4	0.66	Per
176	60	8	12.895	13.83	0.930	0.965	26.69	154.4	140.0	1149	294 4	—3.7	0.54	Per
253	61	8	12.919	1445	0.934	0.949	27.95	150.2	139.8	112.4	290.0	—4.8	1.46	Per
179	60	8	12.981	45.80	0.980	0.938	90.53	157.8	140.1	113.2	297.9	—7.4	11.75	Per
244	61	8	13.007	13.39	0.928	0.962	25.82	153.6	139.9	112.9	293.5	—4.0	1.12	Per
248	61	8	13.007	8.45	0.889	0.936	15.96	147.0	139.9	114.7	286.9	—5.2	3.88	Per
250	61	8	13.018	−9.46	1.104	0.984		161.0	139.9	117.5	300.8	—2.9	0.14	Per
245	61	8	13.019	162.20	0.999	0.942	3723.	149.2	139.9	113.6	288.1			Per
244a	61	8	13.037	4.25	0.786	0.911	7.59	140.5	139.9	112.4	280.5			Per
246b	61	8	13.045	9.16	0.897	0.944	17.38	148.9	139.9	114.0	288.8			Per
255	61	8	13.957	1238	0.926	0.915	23.84	143.0	140.3	115.3	283.3			Per
256	61	8	14017	9.18	0.903	0.894	17.46	138.9	140.8	106.9	279.7			Per
257	61	8	14.021	17.58	0.947	0.935	34.20	147.3	140.8	111.5	281.1			Per
259	61	8	14.037	11.27	0.918	0.929	21.61	145.7	140.8	111.8	286.6			Per

TABLE 2.—*Orbital elements of meteors* (Odessa)—Continued

No.	Year	Month	Day	Corr. radiant a	Corr. radiant δ	Sin Q	Cos Z_r	ϵ	H_b	H_{max}	H_e	V_∞	V_G	V_H
268	61	8	14.040	22 58	−11 00	0.433	0.520	38.9	105.6	98.1	96.9	60.7	59.6	41.1
261	61	8	14.928	6369	60 14	0.655	0.646	42.0	109.1	95.3	90.1	60.4	59.1	42.1
263	61	8	14.976	53 24	57 53	0.488	0.748	39.6	107.5	94.0	91.4	Bo. 1	58.8	40.7
264	61	8	16.937	356 02	−13 47	0.438	0.465	64.0	98.6	92.9	88.4	38.9	36.8	35.5
265	61	8	16.971	6600	59 01	0.173	0.743	40.3	111.8	97.2	94.8	Bo. 2	58.9	41.1
181	60	8	17.787	52 49	57 23	0.367	0.363	38.3	103.0	90.6	89.6	65.0	63.8	44.6
185	60	8	19.799	57 20	58 17	0.297	0.385	38.8	113.4	86.3	84.7	61.0	69.8	41.2
184	60	8	19.882	22 32	24 41	0.081	0.558	30.5	117.4	86.4	83.4	64.9	63.6	41.0
267	61	8	19.897	10 21	21 45	0.380	0.690	41.6	96.3	92.5	90.0	61.0	59.7	42.4
268	61	8	21.961	219 33	63 30	0.291	0.525	95.4	84.4	83.5	77.0	24.2	21.7	38.2
269	61	8	21.968	286 45	61 31	0.375	0.808	89.4	92.1	87.1	81.3	29.9	28.0	40.5
271	61	8	22.041	65 11	58 26	0.560	0.848	38.9	106.2	99.5	96.0	61.0	59.8	41.2
270	61	a	22.071	4 10	−13 17	0.447	0.497	61.8	98.0	89.3	86.0	46.0	44.5	40.2
187	60	8	25.971	261 10	64 53	0.526	0.682	87.1	89.1	86.2	82.6	25.0	22.8	38.2
273	61	9	1.812	296 31	51 04	0.186	0.994	95.5				24.9	22.3	38.7
272	61	9	1.824	298 50	12 17	0.838	0.833	119.6	80.5		70.7	31.5	29.5	51.0
274	61	9	4.036	349 28	3 41	0.550	0.616	80.2	81.7	76.3	73.2	27.7	25.2	35.4
194	60	19	19.818	335 38	−0 40	0.342	0.708	110.2	89.9	84.7	79.3	22.0	18.9	40.3
196	60		20.871	36 39	9 48	0.755	0.762	78.9	93.4	81.9	79.4	28.9	26.5	36.0

π Longitude of perihelion $(\omega+\Omega)$, in degrees.

M_{max} Maximum photographic absolute magnitude of the meteor's trail.

t Duration of photographed trails, in seconds of time.

m_∞ Initial mass of meteor body, in grams.

Shower or parent comet Meteor shower, association, or parent comet.

The meteors that belong to the associations discovered from observations in the USSR are designated by Roman numerals and those discovered by Jacchia and Whipple **(1961)** by Arabic numerals.

Determination **of** the instant of the meteor was made either by reduction of meteor photographs obtained at one **of** the stations by both driven and undriven cameras or by using a moving-blade shutter (Kramer, **1953).**

The velocity of the meteor outside the atmosphere was computed on the basis of the interpolation formula $V=V_\infty+kce^{kt}$. Reduction methods **for** meteor photographs have been described in detail by Babadzhanov and Kramer **(1963).**

From the distribution of maximum luminosity of all meteors (fig. **1)** it follows that on the whole they refer to the class of bright meteors ($M<1$ mag), the maximum being **—3** mag. For comparison, figure **1** also shows the distribution of maximum luminosity of faint meteors photographed by Baker Super-Schmidt cameras (McCrosky and Posen, **1961).** The distributions partly overlap; hence the results given

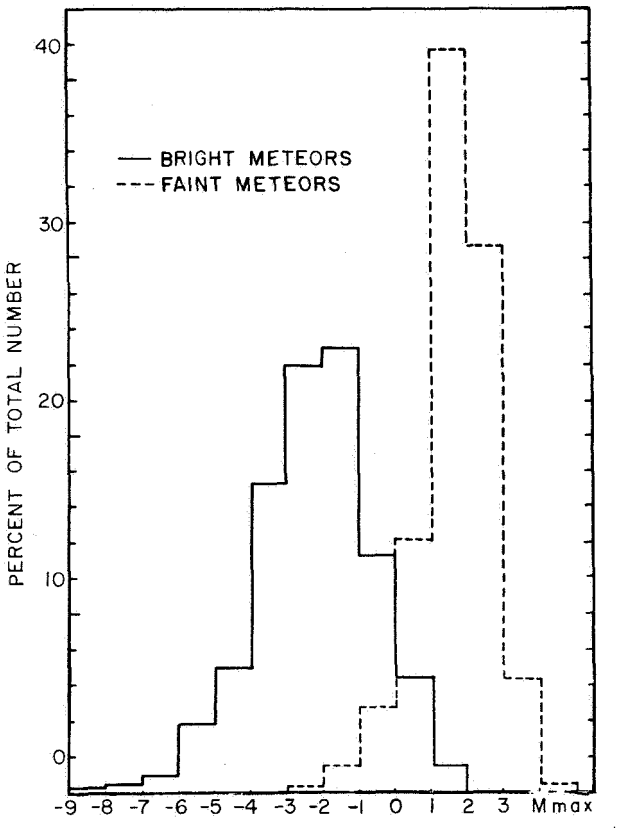

FIGURE 1.—Distribution of maximum magnitudes of meteors.

TABLE 2.—*Orbital* elements of meteors (Odessa)—Continued

No.	Year	Month	Day	a	e	q	q′	ω	Ω	i	π	M_{max}	m_∞	Shower or parent comet
258	61	8	14.040	13.64	0.971	0.399	26.91	356.6	320.8	131.6	317.5			
261	61	8	14.926	−43.68	1.021	0.928		146.4	141.7	110.9	288.1			Per
263	61	8	14.976	9.25	0.900	0.926	17.56	146.1	141.8	113.8	286.8			Per
264	61	8	16.937	1.80	0.927	0.131	3.46	144.0	323.6	28.3	107.7	−2.6	1.26	VII
265	61	8	16.971	13.90	0.933	0.929	26.89	146.1	143.7	112.9	289.8			Per
181	60	8	17.787	−3.73	1.260	0.970		157.8	144.7	118.2	302.5	−4.5	0.91	Per
185	60	8	19.799	14.50	0.934	0.951	28.03	151.0	146.6	115.3	297.6			Per
184	60	8	19.882	12.92	0.959	0.531	25.P	268.4	146.7	148.8	55.0	−5	1.82	VI
267	61	8	19.897	−18.99	1.015	0.292		65.7	146.5	133.8	212.2	−3.5	0.26	VI?
268	61	8	21.961	3.02	0.679	0.968	5.07	153.4	148.5	32.7	301.9			73?
269	61	8	21.968	7.44	0.866	0.997	13.88	1943	148.5	43.6	342.8			73?
271	61	8	22.041	15.77	0.942	0.914	30.60	143.3	148.5	115.5	291.8			Per?
270	61	8	22.053	6.52	0.984	0.102	12.96	144.4	328.6	53.7	113.0	−4.0	3.62	
187	60	8	25.971	2.95	0.658	1.010	4.89	177.4	152.6	36.5	330.0	−2.0	1.70	κ Dra
273	61	9	1.812	3.38	0.717	0.958	5.81	208.4	158.9	33.5	7.3			κ Cyg
272	61	9	1.824	−1.05	1.834	0.878		216.9	159.0	19.8	15.9			
274	61	9	4.036	1.76	0.767	0.410	3.10	68.4	161.1	7.6	229.5	−2.7	7.45	1907 IV
194	60	9	19.818	6.20	0.873	0.787	11.60	237.6	176.7	4.6	54.3	−2.0	2.76	
196	60	10	20.871	1.81	0.778	0.403	3.22	248.9	27.3	4.7	276.2	−2.8	2.55	A Cet

below supplement the results obtained for faint meteors.

Distribution of orbits

The distributions of orbital elements for bright meteors were studied in order to show how they differ from corresponding distributions for faint meteors. For sporadic meteors we considered only the semimajor axis, eccentricity, inclination, and aphelion distance. Cosmic weight was not included in our data, which were thus uncorrected for this factor.

Semimajor axis

The distribution of orbits of all sporadic meteors in reciprocal semimajor axis $1/a$ is given in figure 2. For comparison the distributions for faint photographic and radar meteors are also given. For $1/a<0.6$(a.u.)$^{-1}$, in all three distributions brighter meteors prevail; for $1/a>0.6$ (a.u.)$^{-1}$, the faint meteors become predominant. In the distribution of all meteors the maxima are at $a\approx2.5$ a.u. The second maximum for bright meteors is observed near the parabolic limit.

The percentage of orbits of sporadic meteors with $1/a<0.2$(a.u.)$^{-1}$ is given in table 3. The bright meteors were photographed in Dushanbe and Odessa, the faint meteors in the USA, and the radar meteors were observed in Eharkov (Kashcheyev, Lebedinets, and Lagutin, 1965). In spite of the fact that the data in this table are distorted by different observational selection, we may consider that among faint meteors the short-period orbits are predominant.

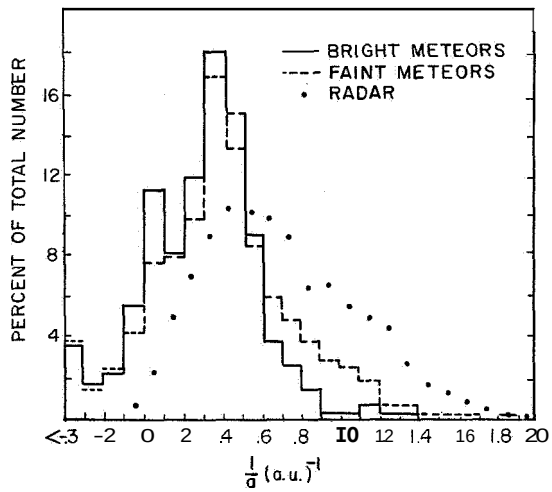

FIGURE 2.—Distribution of orbits of sporadic meteors in reciprocal semimajor axis $1/a$(a.u.)$^{-1}$.

TABLE 3.—*Orbits* of sporadic meteors

Meteors	Photographic magnitude	Percentage of orbits with $1/a$ <0.2 (a.u.)$^{-1}$
Bright photographic	≈ −3	34.7
Faint photographic	+0.8	27.4
Radar	≈ +6 to +7	7.8

It is necessary to note the existence of a considerable percentage of hyperbolic meteors, whereas among radar meteors it is low. This may be explained by the specific character of radar observations of meteors moving at great velocity. There is no reason to believe that all hyperbolic orbits could be explained as due to observational errors.

Inclination

The distribution of inclinations of sporadic meteors (fig. 3) shows that among faint meteors orbits with small inclination (less than 20°) predominate. The maximum in the distributions falls at $i=140°$ both for bright and for faint meteors. In addition, the second maximum for bright meteors can be observed at an inclination of about 180°.

Eccentricity

The distributions of the eccentricity of bright and faint sporadic meteors are given in figure 4, which shows that bright meteors move on more eccentric orbits than faint, meteors. Orbits with an eccentricity less than 0.65 are found more often among faint meteors, while those with a large eccentricity are found more often among bright meteors. A strongly pronounced maximum at $e=1$ for bright meteors should be noted. There is no such maximum for faint meteors (McCrosky and Posen, 1961). Here the relative number of meteors from $e=0.65$ to $e=1$ is nearly stable.

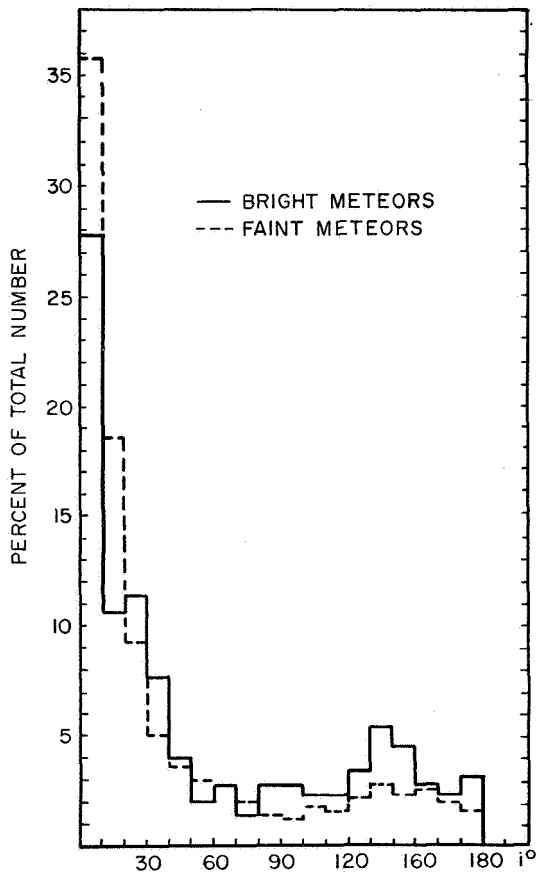

FIGURE 3.—Distribution of orbits of sporadic meteors in inclination i.

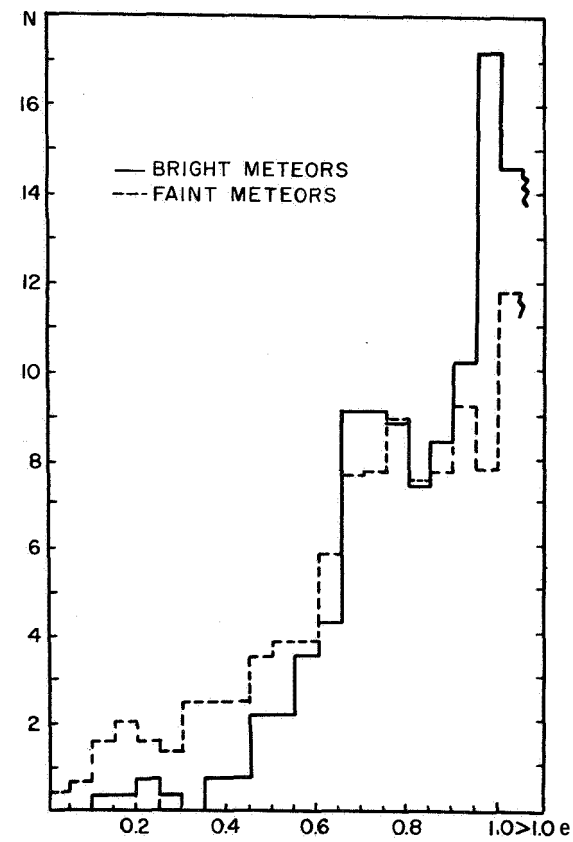

FIGURE 4.—Distribution of orbits of sporadic meteors in eccentricity e.

Aphelion

The distribution of meteor orbits in aphelion distance up to $q'=10$ a. u. is given in figure 5. The maxima at $q'=1.5$ a. u. and 4 a. u. may be noted in the distribution of aphelion of faint sporadic meteors. Bright meteors have one maximum at $q'=3.5$ a.u. Small aphelion distances ($q'<3$ a. u.) are found among faint meteors relatively more often. The percentage of orbits with aphelion distances of more than 10 a. u. ($q'>10$ a. u.) is higher for bright than for faint meteors.

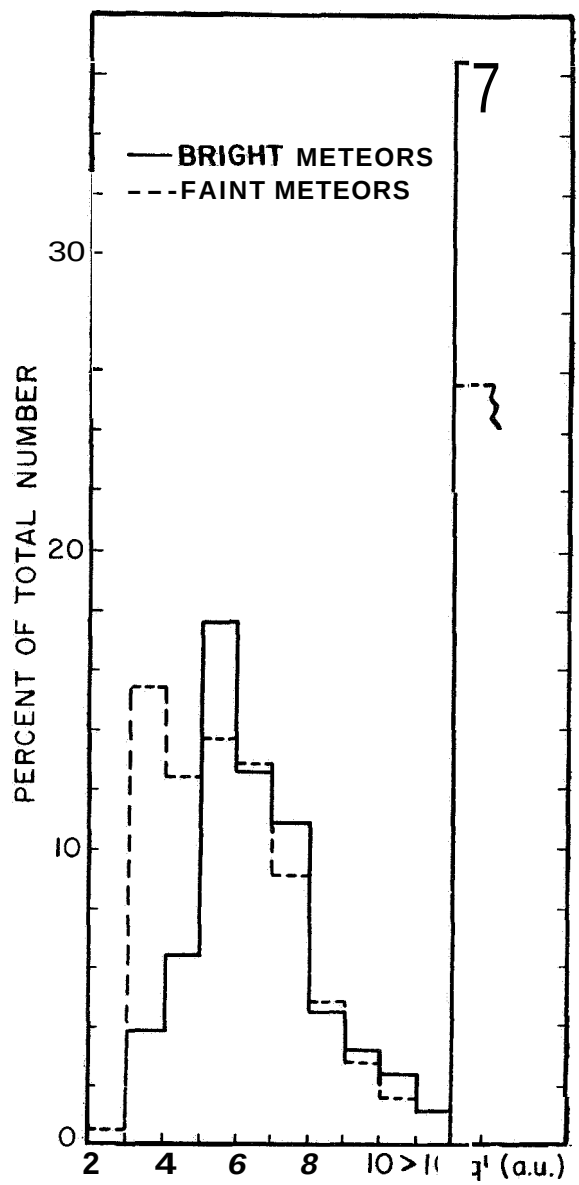

FIGURE 5.—Distribution of orbits of sporadic meteors in aphelion distance q'(a.u.).

The relation between all the other orbital elements for both bright and faint meteors is the same.

From the above we see that bright meteors move in more eccentric orbits than faint meteors and that the inclinations of the orbits of bright meteors are on the average larger than those of faint meteors. It is possible that the differences between bright and faint meteors are due to the Poynting-Robertson effect and the perturbations of the planets.

Meteor associations

In addition to the meteors belonging to showers, there is a separate class of meteor associations which occupies an intermediate position between sporadic and shower meteors. It would be simpler to identify them as weak showers. The data on the associations discovered mainly from the observations in Dushanbe and Odessa are given in table 4. The Harvard observations were also used in the identification of some associations. The first column of table 4 gives the ordinal number of the association; the second column gives the meteor number (D, O, and H corresponding to observations in Dushanbe, Odessa, and according to the Harvard Meteor Program, respectively); the remaining columns give the date of observation, radiant coordinate, meteor velocity, and the identification of associations with meteor showers (the number is from the list published by Astapovich (1962)). Table 4 contains 16 associations, 4 of which coincide with weak showers in Astapovich's list. The Soviet observations also support the associations discovered by Jacchia and Whipple (1961) (see tables 1 and 2).

Perseids

Among the orbits of meteors observed in Dushanbe and Odessa there are 167 Perseids, which constitute more than 60 percent of all known photographic Perseid orbits. On the basis of 188 orbits of Perseid meteors observed in the USA, the USSR, and Czechoslovakia, the dependence of the radiant on the solar

TABLE 4.—*Meteor* associations

No.	Meteors		Year	Month	Day	α	δ	V_∞ km/sec	Associations
I	D	590541	59	3	6.7	159°	78"	19	
	O	39	58	3	18.8	176	65	20	
II	O	121	59	6	29.9	285	−17	30	
	D	591987	59	7	1.9	287	−20	30	
III	D	570673	57	7	26.7	280	49	31	
	D	570706	57	7	26.8	278	51	28	
	D	570774	57	7	27.8	278	48	27	
	D	592351b	59	7	12.9	278	49	30	
	D	592524	59	7	27.8	280	51	31	
	H	8089	53	7	20.4	281	51	31	
	O	130	59	7	29.9	291	49	28	
	D	641623	64	8	8.8	284	46	25	
	D	641872	64	8	12.8	281	46	25	
IV	O	1	57	7	30.0	15	35	65	β Andromeda
	H	3377	52	7	24.3	10	37	65	(No. 177)
V	D	620511	62	8	2.7	48	84	42	
	H	8215	53	8	5.4	60	83	44	
VI	D	582652	58	8	13.9	17	30	58	
	O	64	58	8	12.9	20	27	60	
	O	184	60	8	19.9	22	25	65	
	O	267	61	8	19.9	10	22	61	
VII	O	228	61	8	11.0	343	−1	41	γ **Aquarids**
	O	230	61	8	11.0	344	−11	40	(No. 163)
	O	264	61	8	16.9	356	−14	38	
	D	620581	62	8	4.8	342	−16	42	
VIII	O	237	61	8	12.0	348	48	47	λ Andromeda
	O	243	61	8	12.0	328	54	43	(No. 181)
IX	D	621025	62	8	31.8	92	63	58	
	D	621134	62	9	2.8	92	56	61	
	D	621204	62	4	3.8	91	59	56	
X	O	19	57	8	28.8	10	62	52	
	H	3861	52	8	30.5	17	61	52	
	O	220	61	8	9.0	13	63	54	
XI	D	583464	58	9	17.9	9	7	33	
	D	583587	58	9	22.9	15	11	32	
XII	D	572181	57	9	25.7	0	−9	26	
	D	572182	57	9	25.7	0	−9	24	
	D	572384	57	9	27.8	2	−9	21	
	H	4657	52	9	27.5	3	−8	24	
XIII	O	87	58	10	13.0	20	4	24	η Arietids
	H	9030	53	10	10.4	16	12	24	(No. 246)
XIV	D	573027	57	10	28.9	102	38	71	
	O	90	58	10	19.1	106	32	71	
	O	104	58	10	23.1	102	27	70	
XV	D	622553	62	12	17.6	84	25	26	
	D	614764	61	12	11.7	82	27	26	
	D	614794	61	12	12.9	82	17	25	
XVI	D	614715	61	12	9.9	73	−10	24	
	H	5557	52	12	9.3	68	−10	23	

longitude was computed (Kramer and Roudenko, 1965) and found to be:

$$\alpha = -126.^\circ32 + 1.^\circ25(\pm 0.^\circ01)\lambda_\odot,$$
$$\delta = 29.^\circ67 + 0.^\circ20(\pm 0.^\circ01)\lambda_\odot.$$

Thus, the daily motion of the radiant in right ascension is 1.°20 and in declination 0.°20.

Computed heliocentric orbits of Perseids change within wide limits. The distribution of heliocentric velocities of photographic Per-

seids is given in figure 6. The solid curve corresponds to the observations made up to 1959, and the broken curve corresponds to the meteors given in tables 1 and 2. The maximum of these two distributions falls on 41.5 km/sec, which is about 0.3 km/sec less than the parabolic limit. A number of orbits are hyperbolic, in all probability partly due to observational errors; however, we can give some definite data about the existence of hyperbolic orbits in the Perseid shower. Meteors with strongly pronounced hyperbolic orbits were found by different observers, for example, Meteors nos. 9792, 14581, 16091, and 21232 from observations at Ondfejov (Ceplecha et al., 1964); nos. 1910, 1918, 2578, 8136, 8666, 8725, 8761, 10570, 11752, etc., from observations at Harvard (Whipple, 1954; Hughes, 1959); nos. 159, 167, 173, 181, 207, 209, 272, etc., from observations at Odessa; and Meteors nos. 582514, 582561, 583191, 592964, 594472, etc., from observations at Dushanbe. Many of them are Perseids, since the date of observation and the radiant and orbital elements, except for a and e, are close to the average data for the Perseid shower. The orbital elements of meteors are computed on the basis of the earth's coordinates and the vector of the meteor velocity at the moment of observation. When obtained in this way, the orbit is osculating, i.e., we know the motion of the meteor particle at the time of its collision with the earth, but the original orbit is usually unknown. The calculation of the original orbit for each meteor is very difficult indeed, since it is connected, for example, with the effect of various physical factors on the orbit of meteor particles.

Since meteor particles are usually small in size, they are subjected to the Poynting-Robertson and Yarkovsky-Radzievsky effects (Radzievsky, 1952). The forces connected with these effects may considerably change the initial orbit over a long period of time.

To explain the origin of the hyperbolic orbit of individual meteors, we must emphasize once again that these orbits are hyperbolic at the place of collision of a meteor particle with the earth, and that even among the meteors of known elliptic showers, such as the Perseids, individual meteors moving in hyperbolic orbits

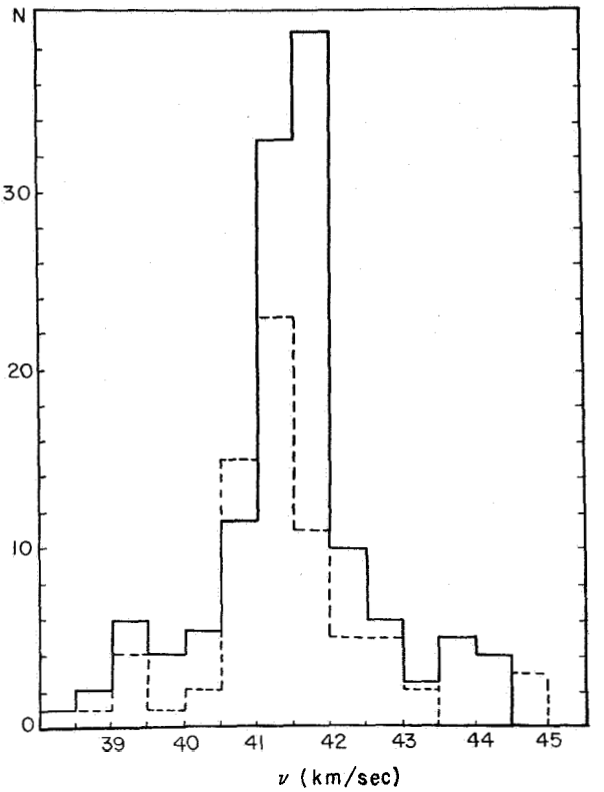

FIGURE 6.—Distribution of Perseid orbits in heliocentric velocity V_H (km/sec).

are observed. On the other hand, meteors whose orbits are smaller than the mean orbit are observed in the same shower (Babadzhanov, 1958). The considerable dispersion of the semimajor axis of shower meteor orbits cannot be explained by observational errors. Hence the force that causes a great scatter of orbits in space remains unknown. In any case, it is clear that the hyperbolic nature of some meteor orbits does not necessarily mean that the meteors are of interstellar origin. It is necessary to note that hyperbolic orbits are found more often among bright meteors. It is possible that the distinguishing feature of bright meteors is that some of them move in hyperbolic orbits. We are inclined to believe that hyperbolic orbits can originate within the solar system as the result of physical processes to which some meteor bodies are

exposed during their "last" approach to the sun (Kramer, Vorobyeva, and Roudenko, **1963;** Babadzhanov and Eramer, **1963;** Ceplecha et al., **1964).**

There is no doubt that more precise observations are needed to reveal the hyperbolic orbits, and it is also necessary to investigate the mechanisms that are capable of transferring a meteor particle from an elliptical to a hyperbolic orbit.

Relation between meteor bodies and other bodies of the solar system

Photographic observations of bright meteors confirm their relation to comets. In the last columns of tables **1** and **2** the names of the known showers as well as the parent comets are indicated. Sometimes they are individual sporadic meteors. Their relation to comets may be purely formal, but according to their general orbital characteristics (e.g., eccentricity, inclination) bright meteors appear to be connected with comets. It can be remarked that Whipple's K criterion for these orbits suggests a cometary relationship. However, the identification of meteors for which $K<O$ with asteroids does not seem to have sufficient basis, since orbital characteristics alone are insufficient to draw conclusions regarding the "generic" connection between meteors and asteroids or comets.

In **1964** experiments were made in the USSR on the photography of meteors by the method of instantaneous exposure. Photographs with an exposure of **0.5** msec were obtained by Babadzhanov and Eramer **(1965).** Meteor images on these photos were very little distorted by the motion of the meteor on the emulsion. Por slow meteors these images may be considered instantaneous. From such photographs the instantaneous structure of 'meteors can be studied. The photographs presented here illustrate instantaneous images of some meteors. The first (Meteor no. **641541,** plate **la)** belongs to a Perseid, and the second (Meteor no. **641872,** plate **lb)** to a weak shower (association III, table **4).** It is interesting to note that the photographs of all Perseids are nearly the same as in plate **la,** i.e., they have short tails. Meteor no. **641623,** according to its orbital characteristics, belongs to the same association III as does Meteor **no. 641872** according to its instantaneous image (plate **1c).** The tails of Meteors nos. **641872** and **641623** are similar in size and shape. Thus, the luminosity characteristics of these two meteors confirm their common origin and the reality of meteor associations.

References

ASTAPOVICH, I. S.
1962. Astronomical Calendar. Permanent section, pp. **616–637.**

BABADZHANOV, P. B.
1958. Photographic observations of Perseids. Astrophys. Inst. Acad. Sci. Tadjikiszan, no. **26,** pp. **13–20.**

BABADZHANOV, P. B., and KRAMER, E. N.
1963. Methods and some results of the photographic researches of meteors. *In* Ionosphere and Meteors, Sec. V of IGY Program No. **12,** Publ. House Acad. Sci. USSR, Moscow.
1965. Instantaneous meteor photography — preliminary results. Astron. Journ. USSR, vol. **42,** pp. **660–665.**

CEPLECHA, Z.; JEŽKOVA, M.; NOVÁK, M.; RAJCHL, J.; SEHNAL, L.; and DAVIES, J. G.
1964. Ondfejov double-station meteors during the IGY and IGC. Bull. Astron. Inst. Czechoslovakia, vol. **15,** pp. **144–155.**

HUGHES, R. F.
1959. Meteor trains. Smithsonian Contr. Astrophys., vol. **3,** no. 8, pp. **79–94.**

JACCHIA, L. G., and WHIPPLE, F. L.
1961. Precision orbits of **413** photographic meteors. Smithsonian Contr. Astrophys., vol. **4,** no. **4,** pp. **97–129.**

KASHCHEYEV, B. L.; LEBEDINETS, V. N.; and LAGUTIN, M. F.
1965. The motion of small meteoric bodies. Doklady Akad. Nauk SSSR, vol. **164,** pp. **1256–1259.**

KRAMER, E. N.
1953. On the determinat'on of flash times of meteors by means of a chopping shutter. Astron. Circ. USSR, no. **135,** pp. **10–12.**

KRAMER, E. N., and ROUDENKO, O. A.
1965. Photographic observations of the Perseids. Astron. Journ. USSR, vol. **42,** pp. **416423.**

KRAMER, E. N.; VOROBYEVA, V. A.; and ROUDENKO, O. A.
1963. The experiences of the Astronomical Observatory of Odessa in meteor surveillance during the International Geophysical Year. Astron. Obs. Odessa, vol. **5,** pp. **5–63.**

McCrosky, R. E., and Posen, A.
1961. Orbital elements of photographic meteors. Smithsonian Contr. Astrophys., vol. 4, no. 2, pp. 15–84.

Radzievsky, V. V.
1952. On the effect of an isotropic reemission of solar radiation on the orbital motion of asteroids and meteorites. Astron. Journ. USSR, vol. 29, pp. 162–170.

Whipple, F. L.
1954. Photographic meteor orbits and their distribution in space. Astron. Journ., vol. 59, pp. 201–217.

Abstract

The distributions of orbital elements of bright meteors ($M<1$ mag), which were photographed in 1957–1963 in Dushanbe and Odessa, are studied. It is concluded that bright meteors move in more eccentric orbits than faint meteors, which were photographed by Baker Super-Schmidt cameras. The inclinations of orbits of bright meteors are on the average larger than those of faint meteors. The reality of hyperbolic meteor orbits is discussed. Photographic observations of meteors made by the method of instantaneous exposure show that meteors belonging to different showers or associations have respectively different luminosity and fragmentation characteristics. Data about orbital elements of meteors photographed in 1960 to 1963 in Dushanbe and Odessa are presented.

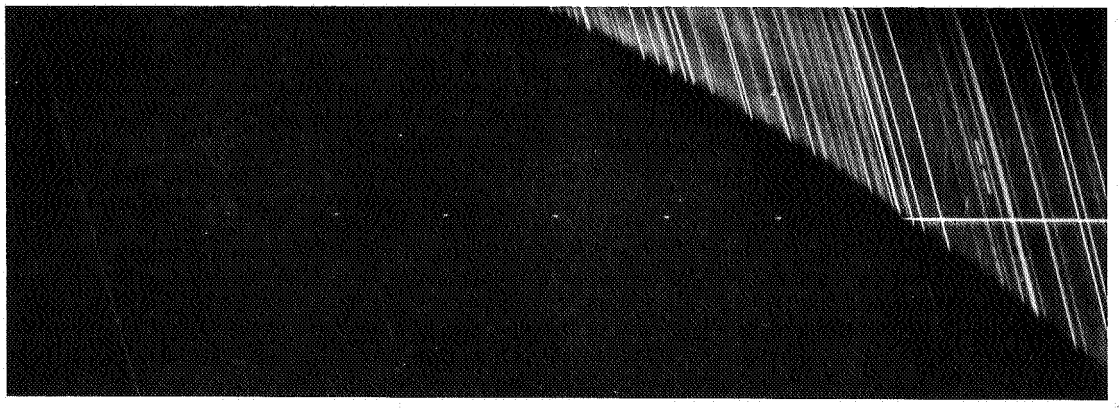

a

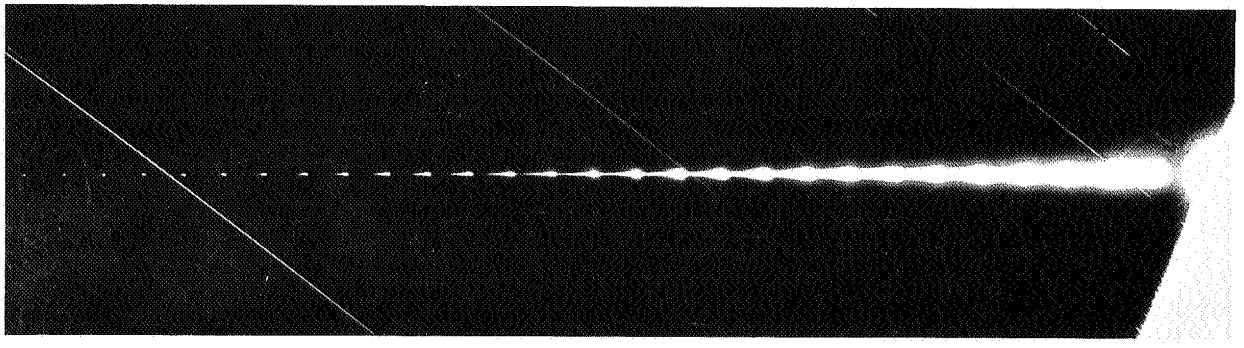

b

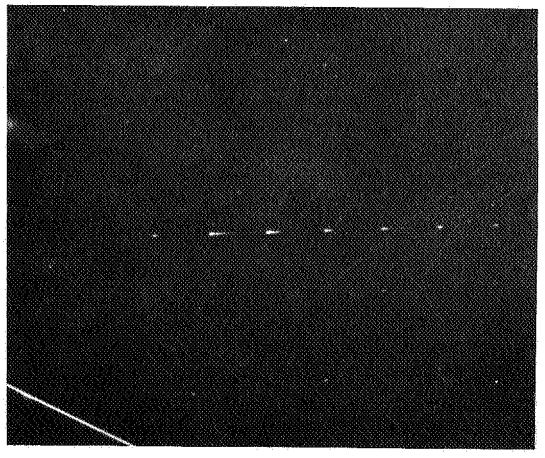

c

PLATE 1

a, Meteor no. 641541, which belongs to the Perseid shower, observed August 6, 1964. b, Meteor no. 641872, observed August 12, 1964. *c*, Meteor no. 641623, observed August E, 1964.

Inferences from Photographic Meteors

C. C. DALTON[1]

The masses of a random sample of **285** sporadic photographic meteors (Hawkins and Southworth, **1958, 1961)** mere recalculated according. to the physical theory of Öpik **(1958)** with rescaled mass. Weighting functions mere derived for the minimization of the effects of several sources of physical selectivity. A five-variable statistical analysis was made for log mass, log velocity, arithmetic celestial latitude of radiant, eccentricity, and radiant full-angular displacement from the apex of the earth's way. (For a detailed analysis, see Dalton (1965).)

Table 1 shows the top-of-the-atmosphere level-surface mean cumulative flux formulas that were found by comparing the weighted-sample cumulative distributions with the results of Hawkins and Upton **(1958)** for the cumulative flux with respect to absolute photographic magnitude for similar photographic meteors. The spatial weighting factor was used for a population of meteoroids in space, and it is proportional to the terrestrial weighting factor divided by Öpik's **(1951)** earth-encounter probability.

The construction of the spatial weighting factor is illustrated in figure **1.** After weighting inversely with the square of meteor height at maximum brilliance, the **3/2** power of the air-entry velocity, the apparent fraction of the circle of celestial latitude through the meteor radiant, and the earth-encounter probability, we found that weighting inversely with exp **(0.182)** gave maximum symmetry. Because the meteors more than **42°** below the ecliptic were obscured by the horizon, the meteors

TABLE **1.—Summary** *o j results*

2.24 g mass for zero absolute visual magnitude meteor at **30** km/sec

$\log F_{M_p} = 0.537\ Mp - 13.81 \pm 0.15$

$\log F_m = -1.34 \log \mathbf{m} - 14.24 \pm 0.60$

$\log F_{mv} = -1.09 \log (mv) - 12.62 \pm 0.60$

$\log F_{mv^2} = -0.92 \log (mv^2) - 13.78 \pm 0.60$

$\log F_{mv^{3/2}} = -\log (mv^{3/2}) - 12.00 \pm 0.06$

Partial correlations

Terrestrial weighting f_t	Spatial weighting f_s
0.097 for log **m** vs log **v**	**0.107** for log m vs $\lvert\beta_e\rvert$
0.103 for log **m** vs $\lvert\beta_e\rvert$	**−0.200** for log **m** vs e
−0.403 for log **v** vs $\lvert\beta_e\rvert$	**0.516** for $\lvert\beta_e\rvert$ vs e
0.882 for log **v** vs **λ**	**−0.799** for **λ** vs e

[1] Aero-Astrodynamics Laboratory, Marshall Space Flight Center, National Aeronautics and Space Administration, Huntsville, Ala.

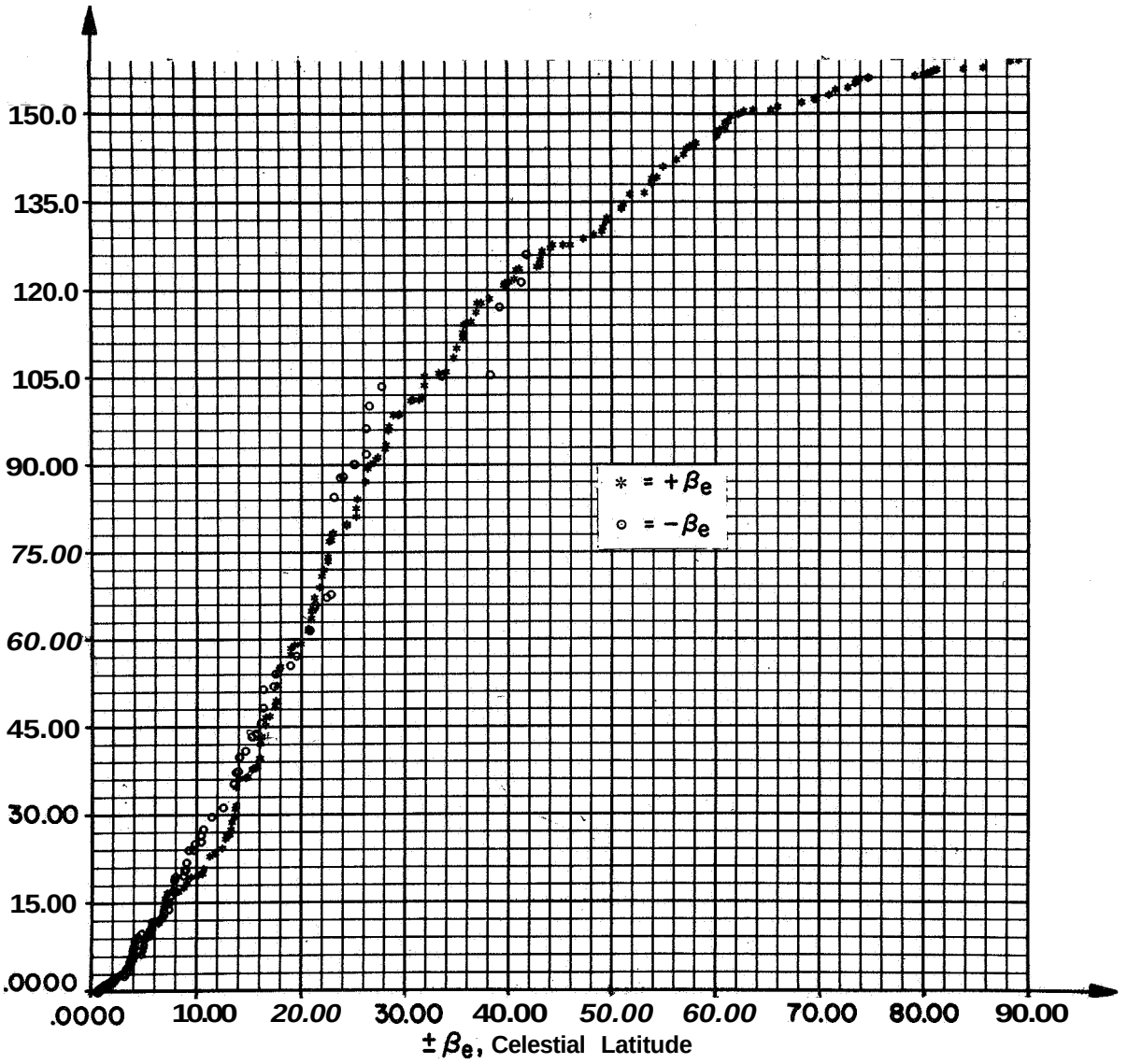

FIGURE 1.—Cumulative distributions of celestial latitude, for either positive or negative β_e separately, of radiant weighted exp (—0.182) for zenith angle Z.

more than 42° above the ecliptic were subsequently given double weight for arithmetic consideration of celestial latitude.

Figure 2 shows separate cumulative distributions of radiant celestial latitude over two regimes of mass. Each regime has half the sample weight.

A similar treatment for log velocity appears in figure 3; but the correlation with log mass is not so apparent as in the preceding figure.

It can be seen in figure 4 that the cumulative concentration of meteoroids in space has unit negative slope when the smaller meteoroids are ignored because of the lack of any magnitude-above-plate-limit weighting. Beard's (1963) results for the slope of cumulative concentration with respect to particle dimension, from zodiacal light and solar 3'-corona data, support this result.

When the earth-encounter probability is removed, the slope in figure 5 is the same as in Hawkins and Upton (1958).

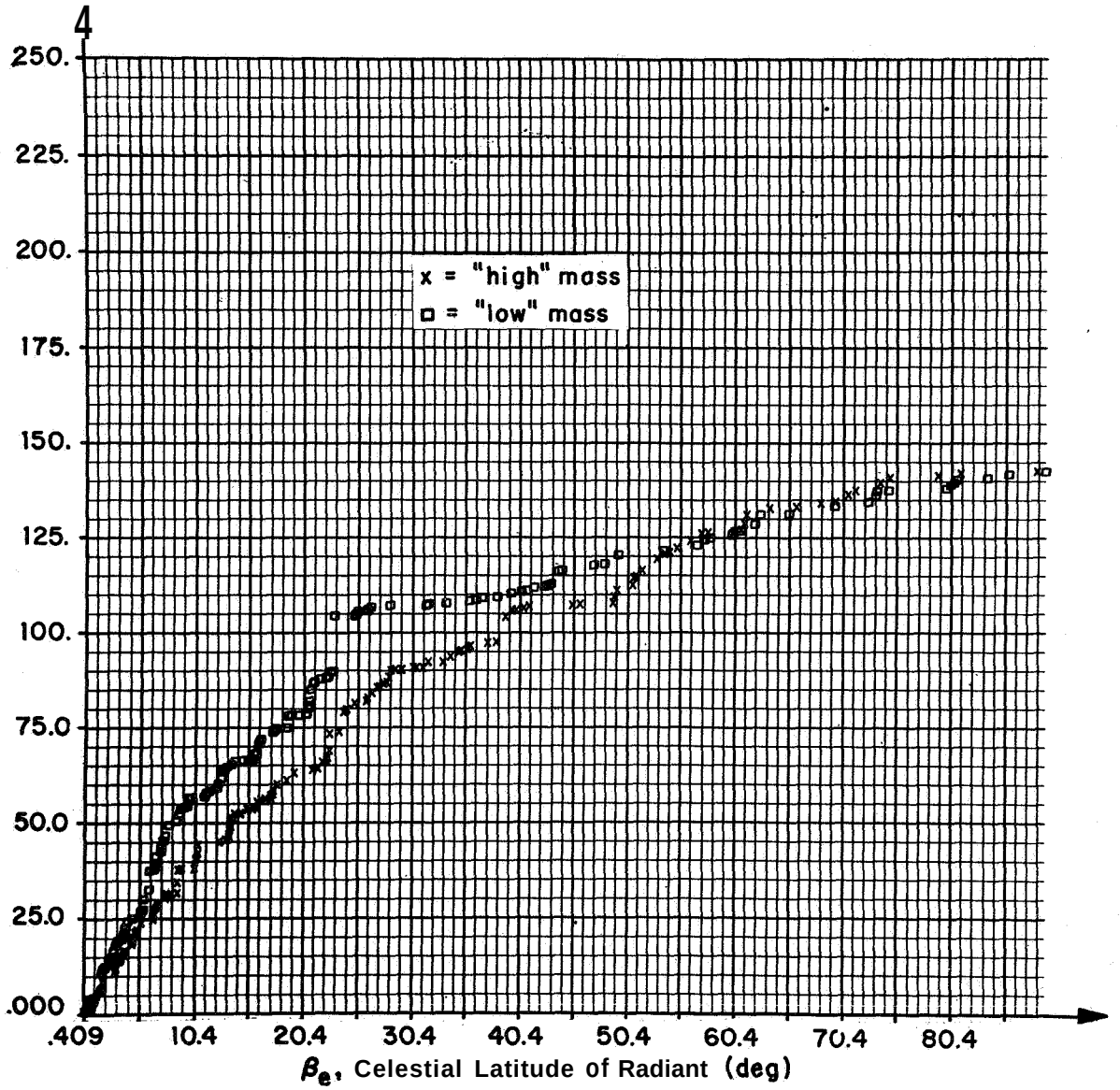

FIGURE 2.—Sample cumulative distributions of celestial latitude of radiant, separately for "high-" and "low-" mass regimes with terrestrial weighting f_t.

Figure 6 shows the same slope for absolute photographic magnitude as reported by Hawkins and Upton.

The slope of the cumulative flux with respect to momentum, as shown in figure 7, is not so steep as in the preceding figure with respect to mass; and figure 8 shows this tendency to be even more pronounced for kinetic energy. A unit negative slope for cumulative flux with respect to the geometric mean of momentum and energy is given in figure 9.

The mass values tabulated by Hawkins and Southworth (1961) give 40 percent partial correlation between log mass and log velocity instead of 10 percent; but they give the same slope, −1.34, for log-cumulative flux versus log mass, log momentum, and log energy.

References

BEARD, D. B.
1963. Comets and cometary debris in the solar system. Rev. Geophys., vol. 1, no. 2, pp. 211–229.

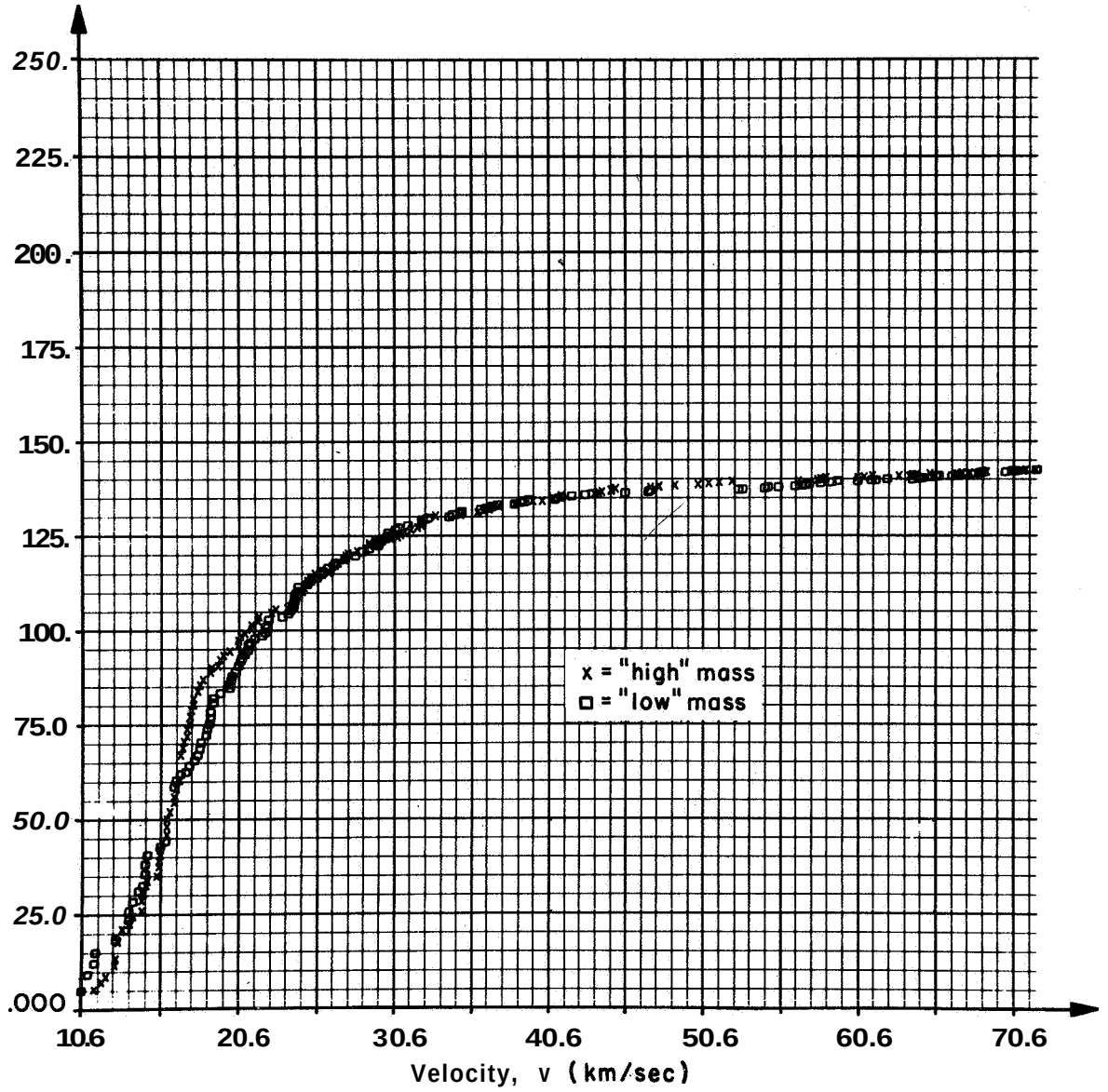

FIGURE 3.—Sample cumulative distributions of air-entry velocity, separately for "high-" and "low-" mass regimes with terrestrial weighting f_t.

DALTON, C. C.
1965. Statistical analysis of photographic meteor data, I: Öpik's luminous efficiency and supplemented Whipple weighting. NASA Tech. Memo. **X-53325.**

HAWKINS, G. S., and SOUTHWORTH, R. B.
1958. The statistics of meteors in the earth's atmosphere. Smithsonian Contr. Astrophys., vol. 2, no. **11,** pp. **349–364.**
1961. Orbital elements of meteors. Smithsonian Contr. Astrophys., vol. **4,** no. **3,** pp. **85–95.**

HAWKINS, G. S., and UPTON, E. K. L.
1958. The influx rate of meteors in the earth's atmosphere. Astrophys. Journ., vol. **128,** pp. **727–735.**

ÖPIK, E. J.
1951. Collision probabilities with the planets and the distribution of interplanetary matter. **Proc.** Roy. Irish Acad., vol. **54,** A, pp. **165–199.**
1958. Physics of meteor flight in the atmosphere. *In* Interscience Tracts on Physics and Astronomy, no. 6, Interscience Publ., New York.

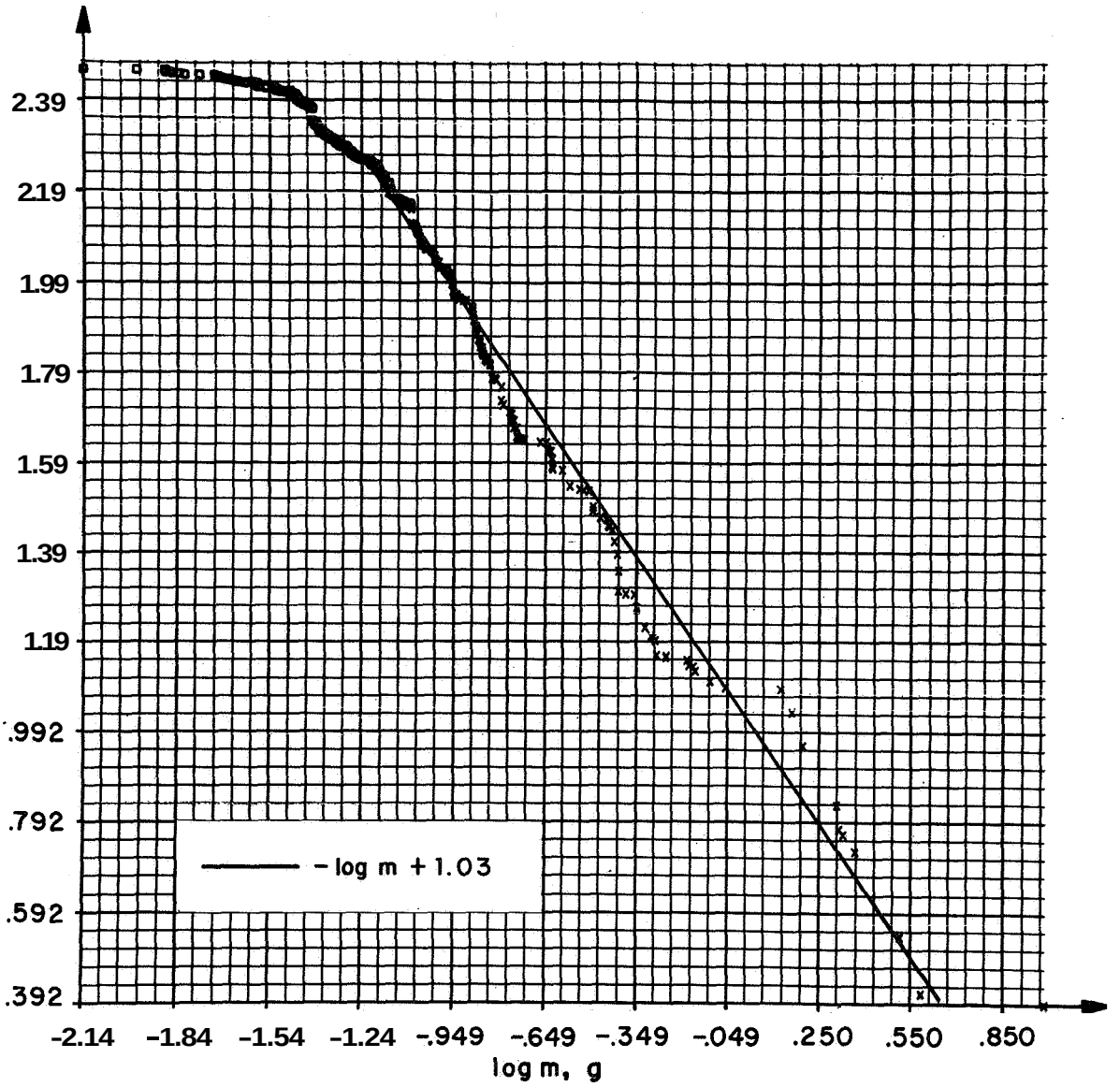

FIGURE 4.—Logarithm of sample cumulative spatially weighted distribution f_s of meteoroid mass.

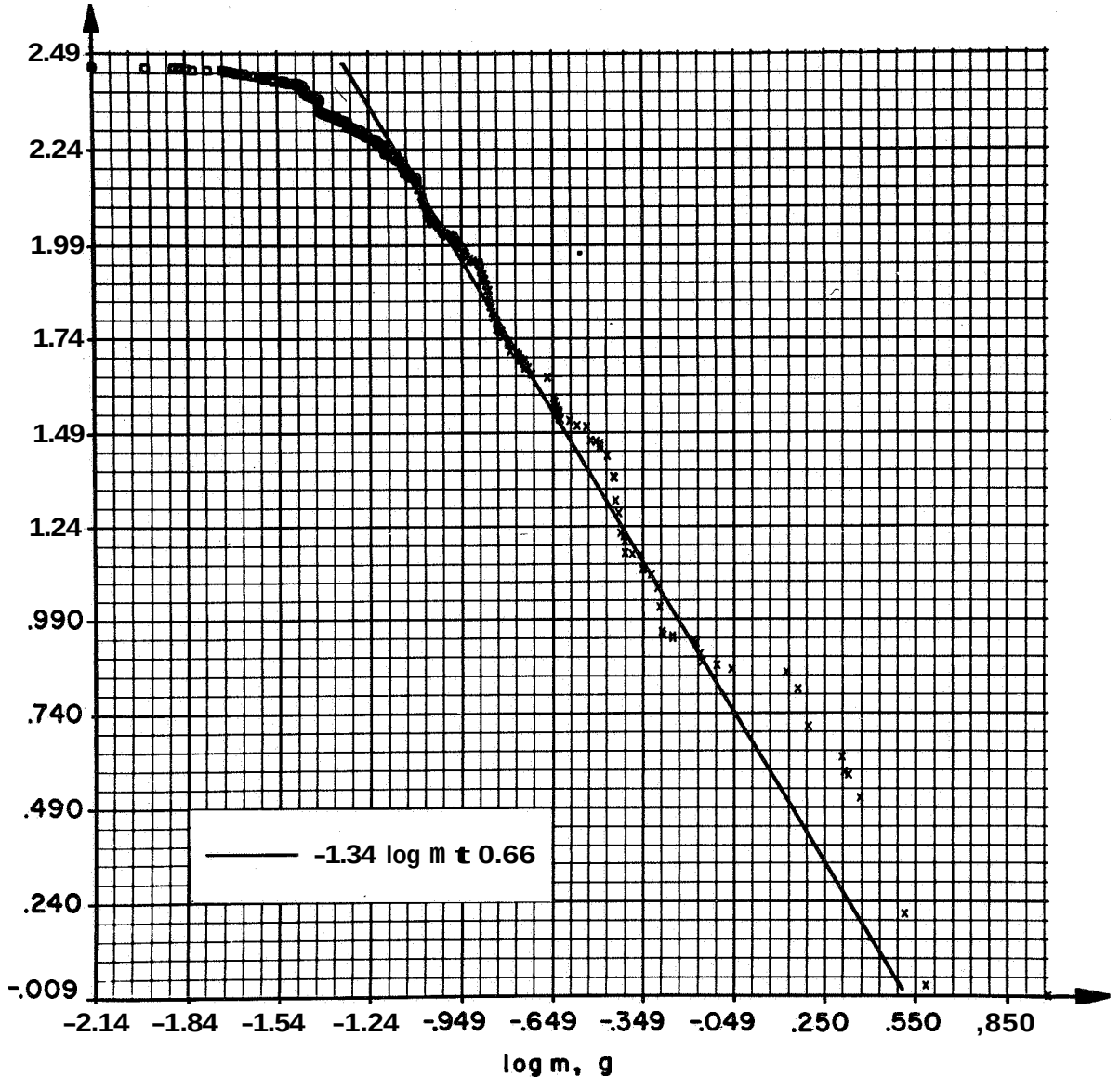

FIGURE 5.—Logarithm of sample cumulative terrestrially weighted distribution f_t of meteoroid mass.

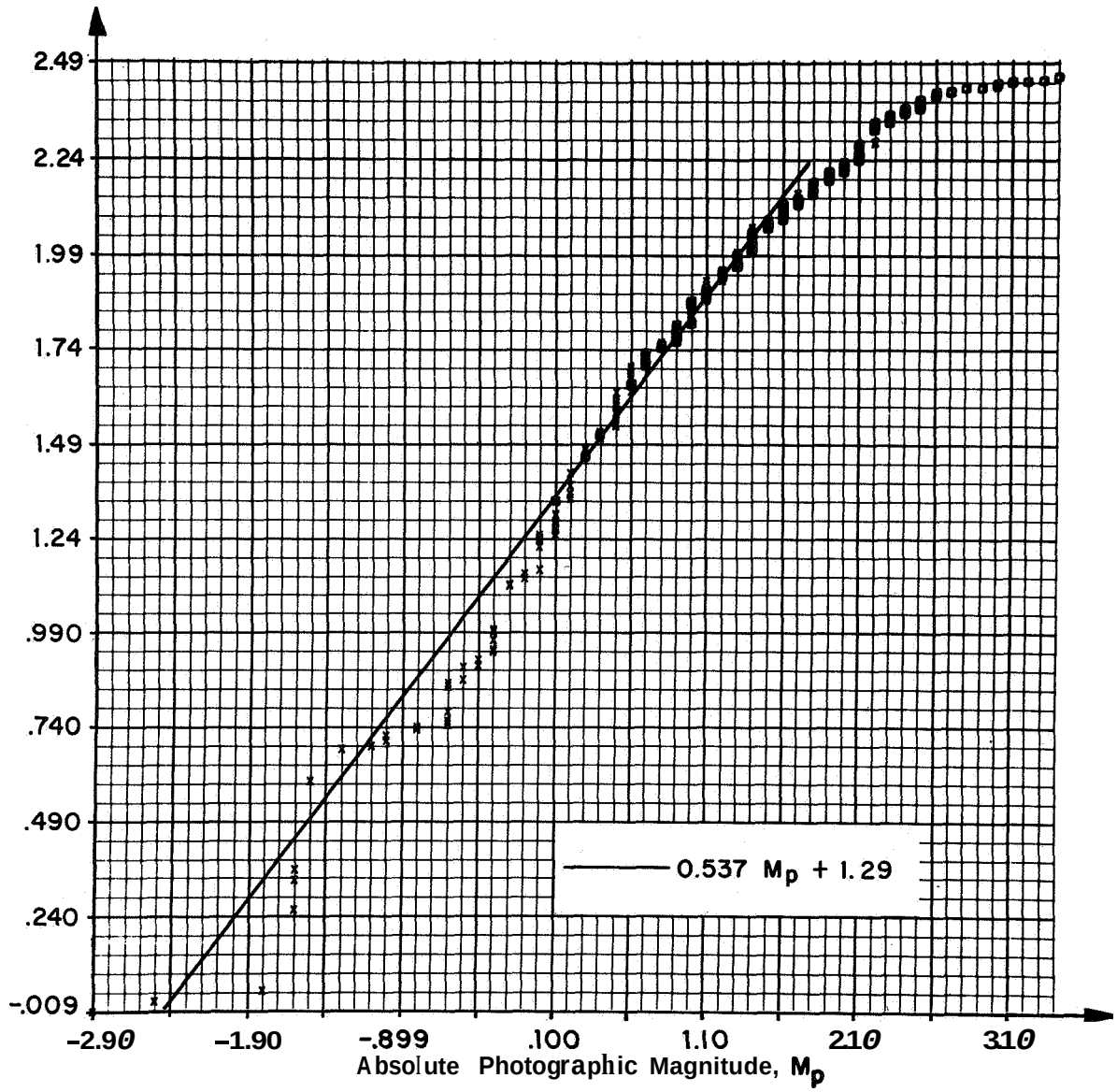

FIGURE 6.—Logarithm of sample cumulative terrestrially weighted distribution f_t of absolute photographic magnitude.

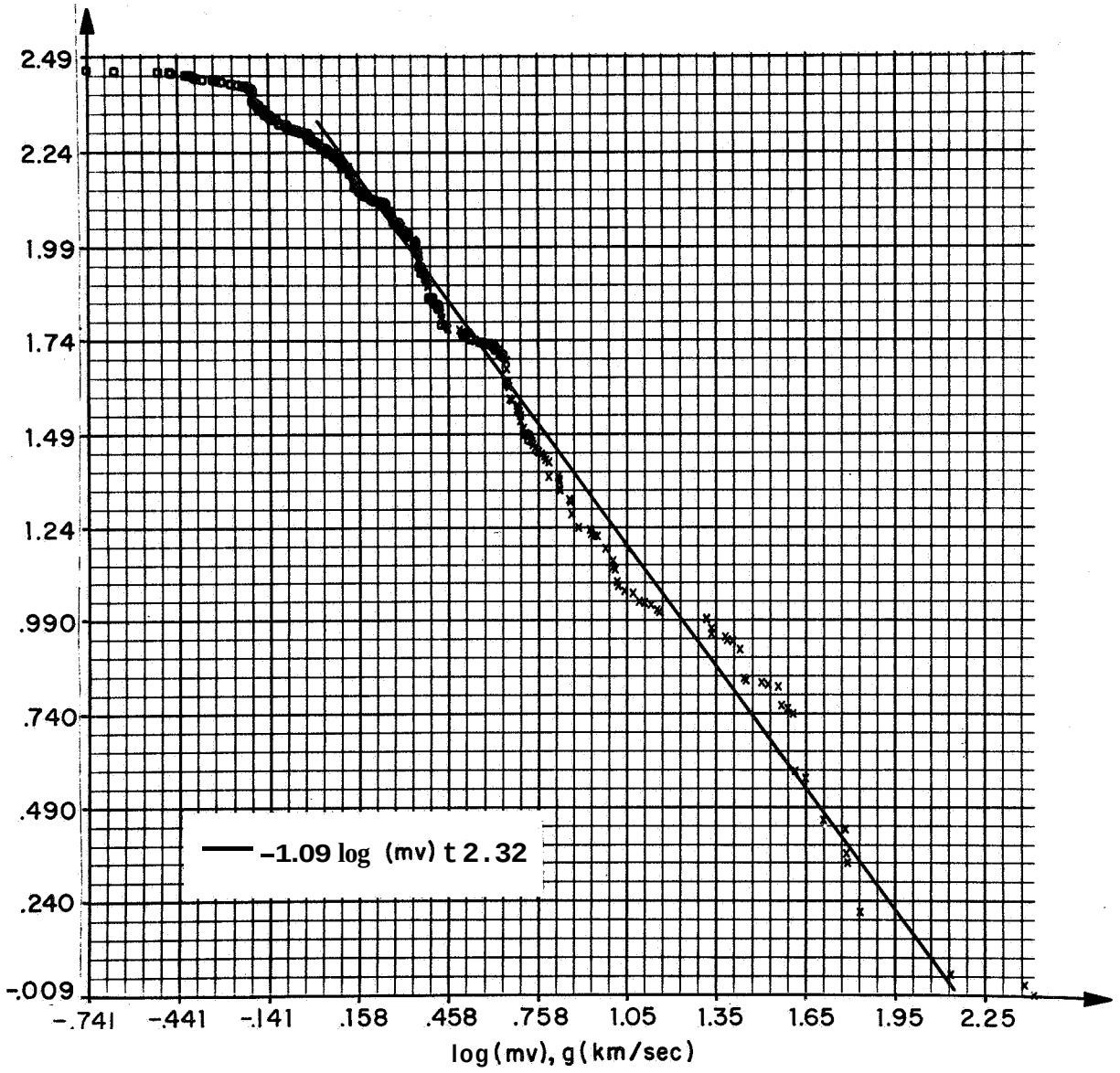

FIGURE 7.—Logarithm of sample cumulative terrestrially weighted distribution f_t of meteoroid air-entry momentum.

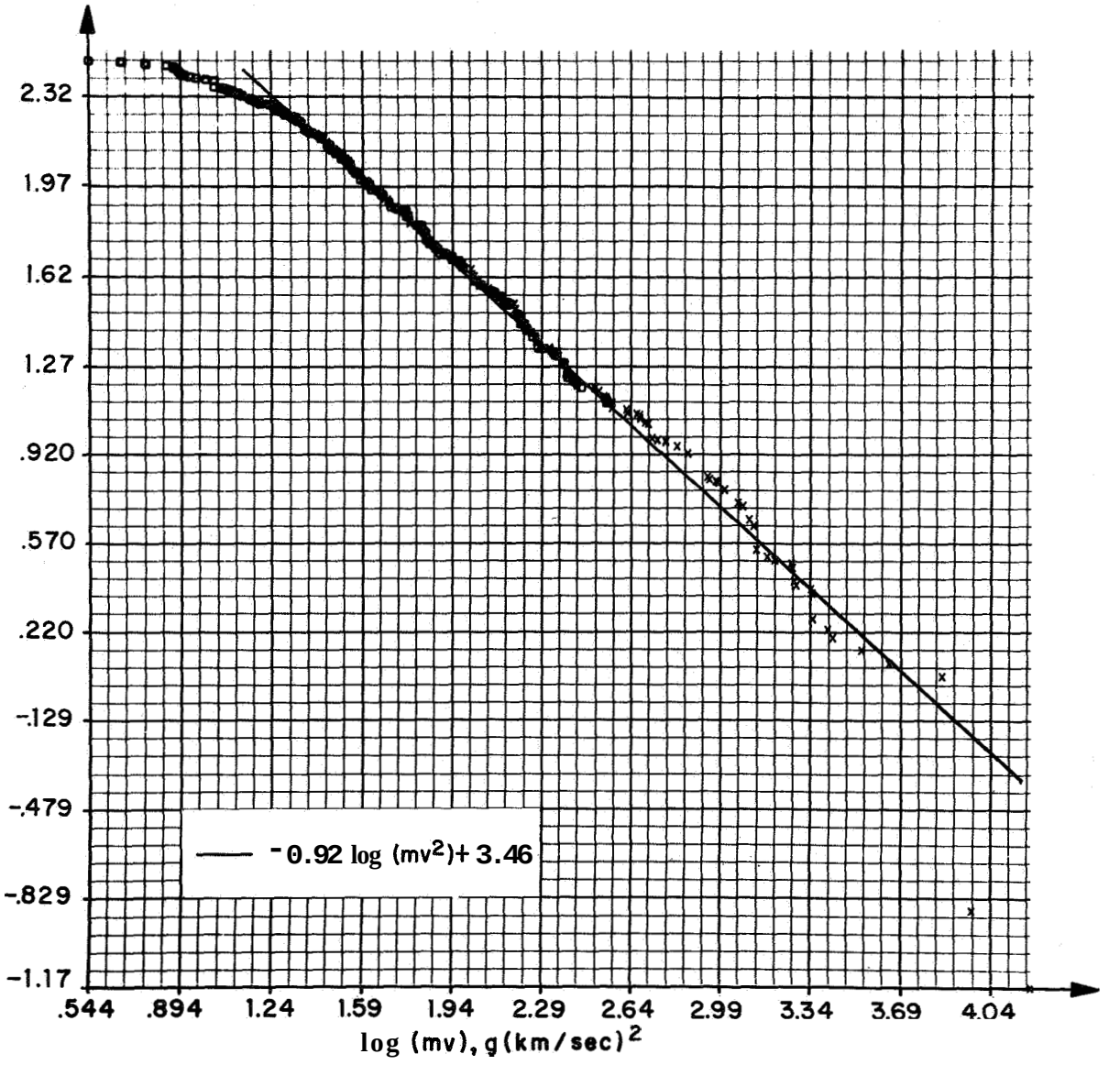

FIGURE 8.—Logarithm of sample cumulative terrestrially weighted distribution f_t of meteoroid air-entry kinetic energy.

240-022 O—67——7

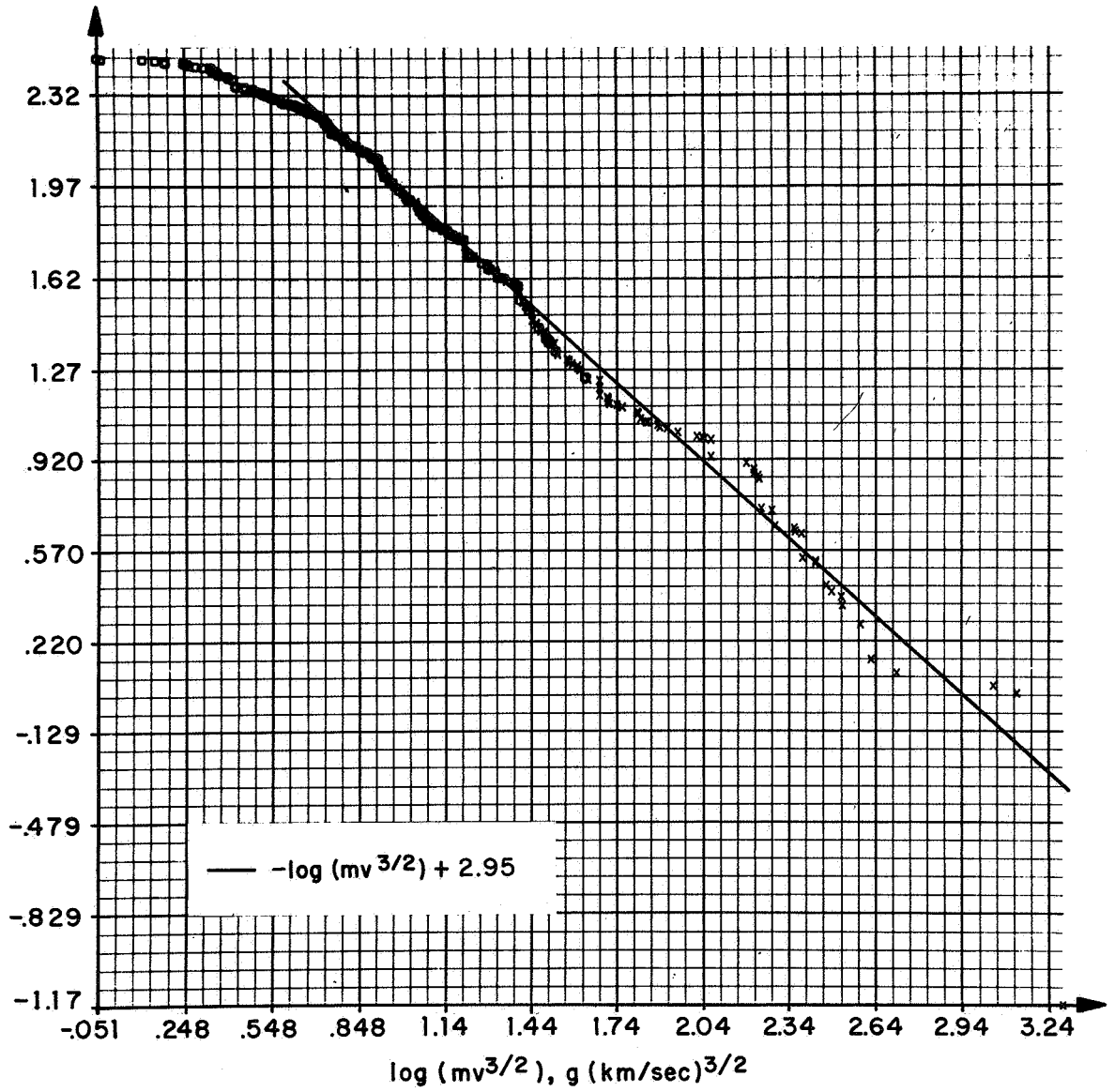

FIGURE 9.—Logarithm of sample cumulative terrestrially weighted distribution f_t of the geometric mean of meteoroid air-entry momentum and kinetic energy.

Equipment for the Observations of Meteor Trails[1]

J. DELCOURT[2]

Last year a program of radioelectrical observations of meteoric trails was undertaken by the CNET. A 40-MHz forward-scatter path was used. In August 1965, a new program was begun with a 30-MHz forward-scatter path and a 30-MHz radar.

An accurate localization of the reflection point on each meteor trail is obtained from an angle-measuring system from which one component of the meteor speed vector can be deduced. These data can be obtained easily for a great number of meteor echoes (some tens/hour).

The forward-scatter path is 1000 km long, in the north-south direction, between the Hague (Netherlands) and Toulon (France). The bistatic radar transmitting and receiving stations are 30 km apart, in the west-east direction.

Measurement of angle of arrival

To determine the direction $\vec{D}$ of a meteoric echo, the same equipment is used in both forward-scatter path and radar: the phase difference Φ between the field received by two antennas A_1 and A_2 is measured. The angle

$$\alpha' = (\overrightarrow{A_1A_2}, \vec{D})$$

is deduced from the Φ measurement by the expression

$$\Phi = \frac{2\pi d}{\lambda} \cos \alpha',$$

where λ is the wavelength and d the distance A_1A_2.

Let A_1A_2 be perpendicular to the path axis, and A_3 be a third antenna, A_1A_3 being aligned along the path axis. When the latter pair of antennas is used, the angle

$$\beta' = (\overrightarrow{A_1A_3}, \vec{D})$$

can be determined in the same way as α'. The azimuth α and the elevation β of the direction $\vec{D}$ are given by

$$\cos \alpha' = \cos \alpha \cos \beta,$$

$$\cos \beta' = \sin \alpha \cos \beta.$$

The two waves with phase difference Φ enter two receivers R_1 and R_2 and are mixed with a wave arising from a common local oscillator. The IF waves thus obtained have the same phase difference Θ. These signals, $E_1 \cos \Omega t$ and $E_2 \cos (\Omega t + \Phi)$, enter a modulator which yields a voltage proportional to $E_1 \cos \Phi$. Similarly, after changing one of the phases by $\pi/2$, the same signals enter a second modulator which yields a voltage proportional to $E_1 \sin \Phi$. The voltages $E_1 \cos \Phi$ and $E_1 \sin \Phi$ are applied to the plates of an oscillograph, producing a polar diagram (E_1, Φ).

The various possible errors in α' and β' are:

Reading error: Φ can be read from a film record with a precision of the order of 2°.

Phase shifts due to variations in a circuit element: it is necessary to verify frequently the zero position of the phase comparator.

Noise superimposed on the echo: the phase comparator introduces an error $\Delta\Phi$ which gives rise to the errors $\Delta\alpha'$ and $\Delta\beta'$ between 0°.3 and 0°.7 for a SNR of 30 db, and between 0°.2 and 0°.4 for a SNR of 25 db.

[1] This work is supported by the Centre National d'Études Syatiales (CNES) and the I.Q.S.Y.

[2] Centre National d'Études des Telecommunications (CNET), Issy-les-Moulineaux (Seine), France.

Frequency variations in the transmitter or in a local oscillator: supposing A+= 1°, it would be necessary for the transmitter and the fist receiver oscillator to have a relative stability of the order of 10^{-7}.

Errors due to tropospheric and ionospheric refractions are negligible compared to the preceding errors.

Doppler measurement

The two origins of doppler frequency shifts are doppler effects due to (1) movement of the meteor: its duration is of the order of 0.1 sec—the frequency shift is very high, a few hundred Hz; and **(2)** winds after the formation of the trail. This shift is much lower than that of (1).

The meteor speed is deduced from the doppler shift Δf, by using the relation

$$\Delta f(t) = \frac{2}{\lambda} \sin \frac{\gamma}{2} \vec{V} \cdot \vec{N},$$

where γ is the scattering angle, $\vec{V}$ is the speed vector of the meteor, and $\vec{N}$ is the inner normal to the equiphase surface.

Forward-scatter path

The phase difference $\Phi(t)$ is measured between the reflected wave and the wave generated by an oscillator. In the cylindrical approximation of the Fresnel ellipsoid we have

$$\Phi(t) = \frac{2\pi}{\lambda r} \sin \frac{\gamma}{2} (V_\perp t)^2,$$

where r is the cylinder radius, and $V_\perp$ is the speed component orthogonal to the axis.

Radar

The phase difference $\Phi(t)$ is measured between the reflected wave and the wave directly transmitted through a ground link. We have

$$\Phi(t) = \frac{2\pi}{\lambda r} (Vt)^2,$$

where r is the radar distance, and V is the speed.

The error in Φ is composed of the errors in (1) the phase of the echo, and **(2)** the phase of the reference wave. It can be shown that in the measurement of a speed component of the meteorite, the errors that, dominate are due to the noise.

The errors in V_r are $\Delta V_r = 2$ m/sec for SNR = 10 db, and $\Delta V_r = 1$ m/sec for SNR = 20 db.

Preliminary experimental results

Plate 1 shows a sample of meteoric echo record. The scope on the upper left corner gives the amplitudes as a function of time. The two other scopes on the right give polar diagrams of amplitude and angles of arrival also as a function of time: elevation (upper right scope) and azimuth (lower right scope). Time is marked every 10 msec, with a larger mark every 100 msec.

From the elevation and azimuth values so obtained, and from an approximate value of altitude, the geographic distribution of the echoes can be determined. Figure 1 shows an example of such a distribution (at 11 a.m.); it can be seen that the echoes only appear in the eastern half of the region where the antenna diagrams overlap, indicated by a dashed line. Figure 1 also shows the location of the radar relative to the forward-scatter path.

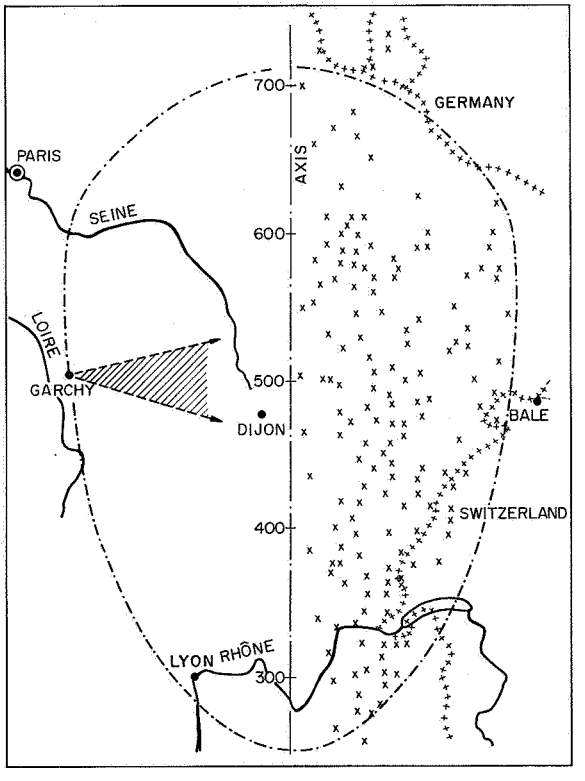

FIGURE 1.—Geographic distribution of echoes.

The velocity component orthogonal to the axis $\vec{V}_\perp$ is completely determined: the amplitude $V_\perp$ is known from the doppler-effect measurement, and the angle θ between $\vec{V}_\perp$ and the horizontal is deduced from the values of a' and β'. Figure 2 shows such a distribution of θ as a function of local time, established for a few days of 1964. It can be seen that most of the meteors come from the west in the morning and around midday, and from the east in the evening and around midnight, following the movement of the apex.

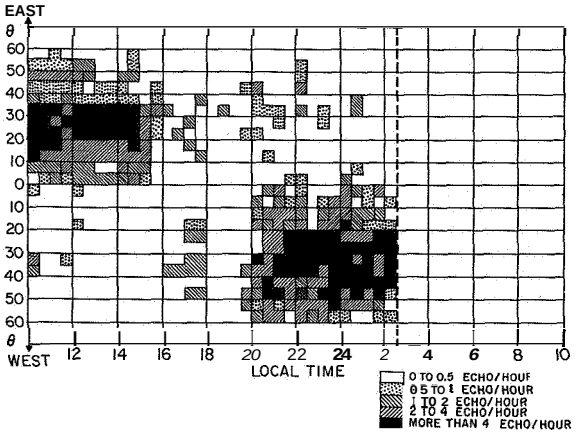

FIGURE 2.—Variation in the direction of meteoric trails as a function of time.

Acknowledgment

I am indebted to MM. Giraud, Masseboeuf, Revah, and Spizzichino for their work on the described apparatus.

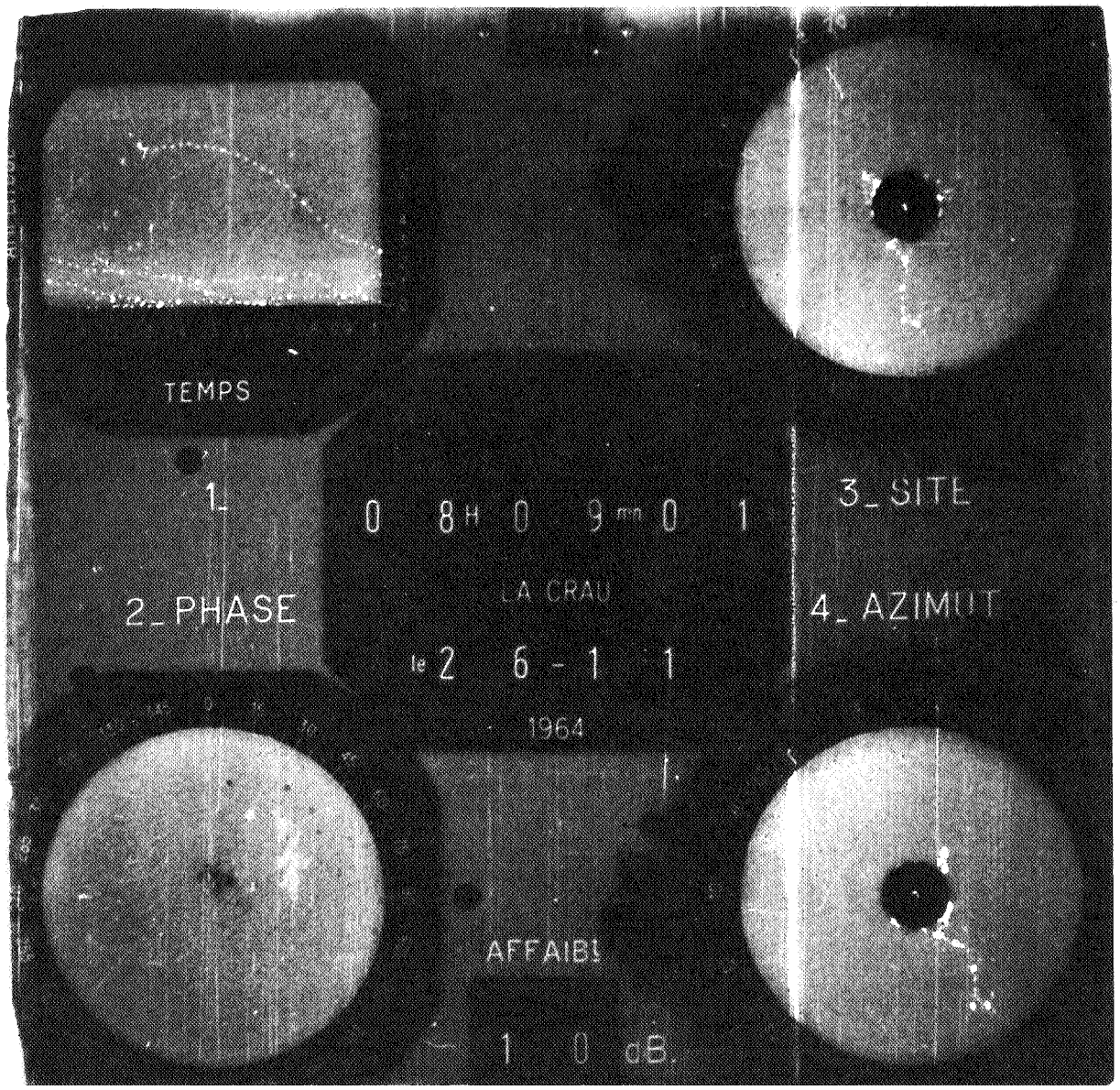

PLATE 1
Sample meteoric echo record.

Meteor Photography with an Image Orthicon System

G. T. HICKS,[1] G. G. BARTON, JR.,[1] and W. J. DAMBECK[1]

Introduction

For the past several years, we at the U.S. Naval Research Laboratory have been interested in the application of electronic imaging techniques at night under starlight conditions to view, and if necessary to photograph, an otherwise invisible scene. At the same time, we have also been interested in viewing and recording objects that might appear in a clear night sky. The objects that we have photographed include satellites, auroral phenomena, and meteors.

As an example of our earlier work, plate 1 shows successive 16-mm frames of a meteor photographed at 24 frames/sec from an image orthicon television monitor. The field of view of this system is approximately 15° in diameter, and this particular meteor had an apparent angular velocity of 15 deg/sec. The meteor reached its peak brightness in the 9th frame and "disappeared" in the 14th frame, leaving residual ionization along the trail, which persisted throughout the 28th frame. It should be pointed out that there is an inherent property of an image orthicon tube that does not permit complete erasure of information recorded on the tube target from one frame to the next. Consequently, for meteor work involving persistent ionization trails the image orthicon tube must be calibrated for moving targets of various brightnesses and speeds in order to get a correct measure of the ionization along a meteor trail. At its brightest this meteor is estimated to have been about +2 mag. The ionization trail is estimated to be down to approximately +8 or +9 mag near the last frame.

[1] E.O. Hulburt Center for Space Research, U.S. Naval Research Laboratory, Washington, D.C.

Equipment

Plate 2 shows a military version of an image orthicon system with a 105-mm lens and a focal ratio of 0.75. We still use the same lens but with a much smaller portable system. Figure 1 is a schematic presentation of an image orthicon camera tube, which is the heart of the system. The object of interest is focused by the lens to form an image on the photoelectric surface of the tube, This surface has a quantum efficiency of approximately 10 percent. Photoelectrons are accelerated by a potential of 500 volts to the target, where for each striking the target 5 or 6 secondary electrons are emitted and collected by a positive voltage on the mesh, which is variable with respect to the target. The target has the property of extremely low lateral leakage of charge compared with its leakage perpendicularly. Consequently, an electronic charge image is left on the target. This image, which corresponds to the optical image formed originally on the photoelectric surface, is scanned with a scanning beam of electrons from the

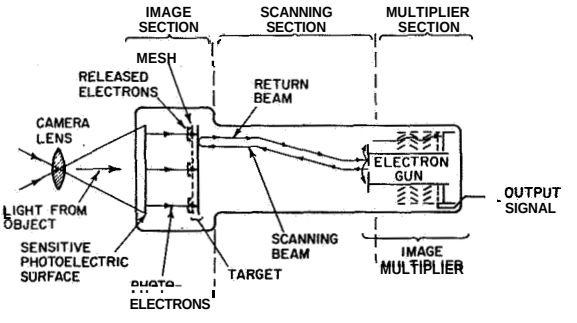

FIGURE 1.—Schematic drawing of image orthicon camera tube.

image orthicon tube. The return beam is a modulated signal as determined by the amount of charge seen at a particular point on the target. This modulated beam is amplified approximately 1000 times by a 5-stage electron multiplier and then coupled into the video amplifiers.

We have recently developed a new method of recording meteors with the image orthicon system.

1. A timing comb (see fig. 2) is now impressed on the photocathode so as to suppress photoelectric emission during preselected intervals. These pulses occur on the 1 sec, ⅝ sec, ⅒ sec, and 1/60 sec, and have a duration of approximately 10 msec, 5 msec, 200 psec, and 100 psec, respectively, thereby establishing by comparison four breaks occurring in the photographed meteor trail where the meteor was at some particular point in real time. The meteor trail can now be measured and the velocity determined for each 60-sec interval in its evanescent life.

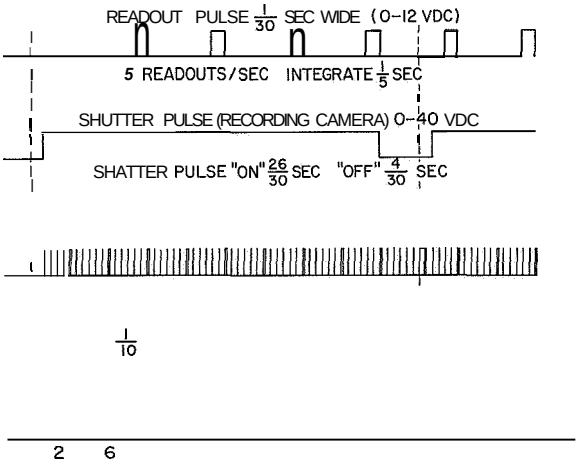

2. A shutter-driving amplifier and logic circuit synchronized to the circuit above opens a recording camera shutter for 26/30 sec and cycles the shutter in 4/30 sec.

3. An integrating network and amplifier, which turns the scanning beam on and off in synchronism with the above-mentioned circuits, allows storage of information on the target for 5/60 sec and subsequent readout in the 5/60-sec interval. This circuit and the shutter are so synchronized that the shutter is open during five readouts and cycled between the fifth and sixth readouts so as to allow photographic recording of the total information falling on the photocathode. This last circuit can be disconnected so as to allow normal scanning of the image orthicon tube. In this mode of operation approximately 90 percent of the information appearing on the kinescope is recorded and 10 percent is lost during the shutter cycle.

Some preliminary results obtained July 30, 1965, with this system for meteor photography are shown in plates 3 to 7. Time breaks at ⅒-sec intervals are noticeable in these meteor tracks, but the breaks at 1/60 sec are not so definite as they need to be for data reduction

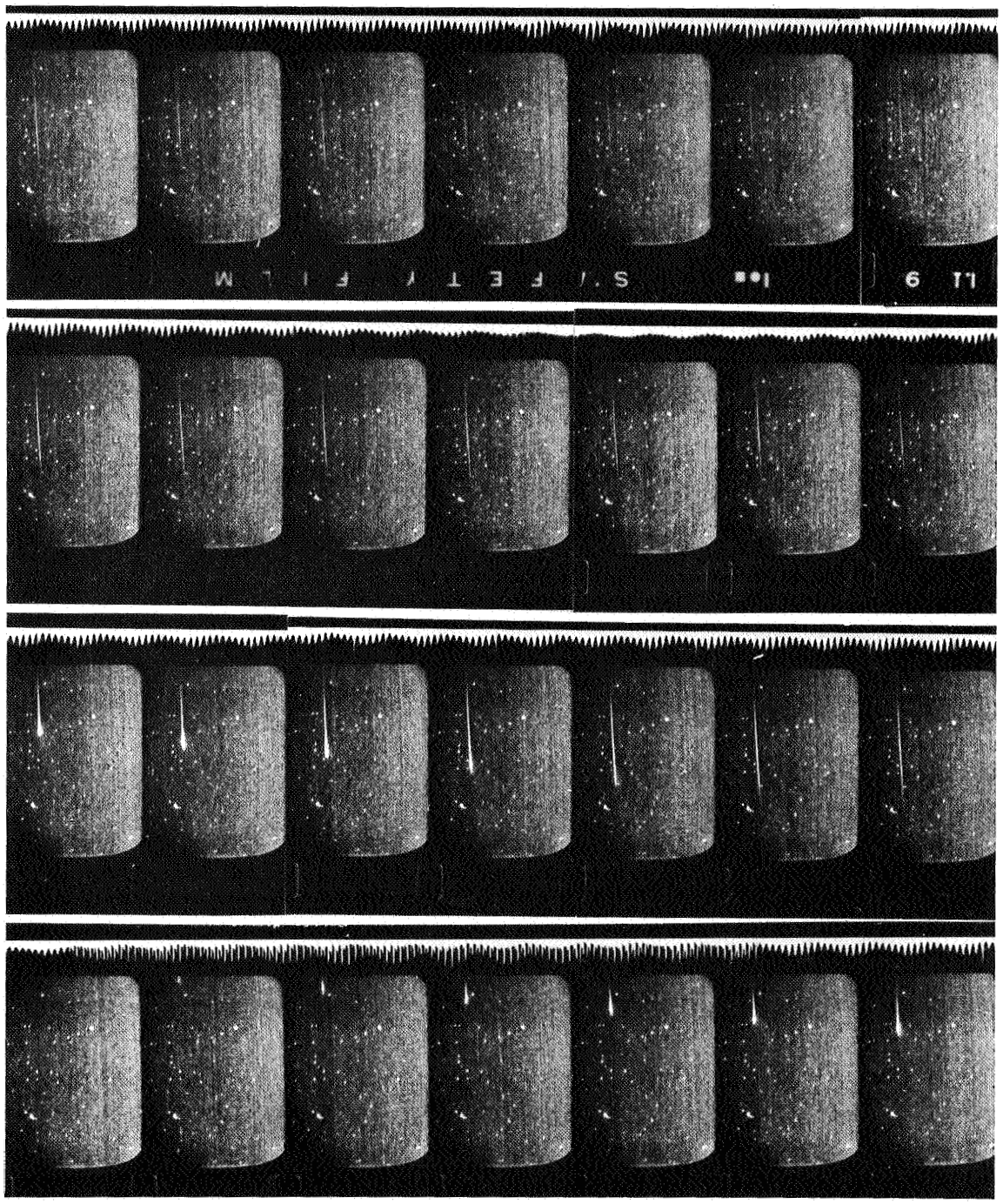

PLATE 1
Meteor photographed at 24 frames/sec from television monitor.

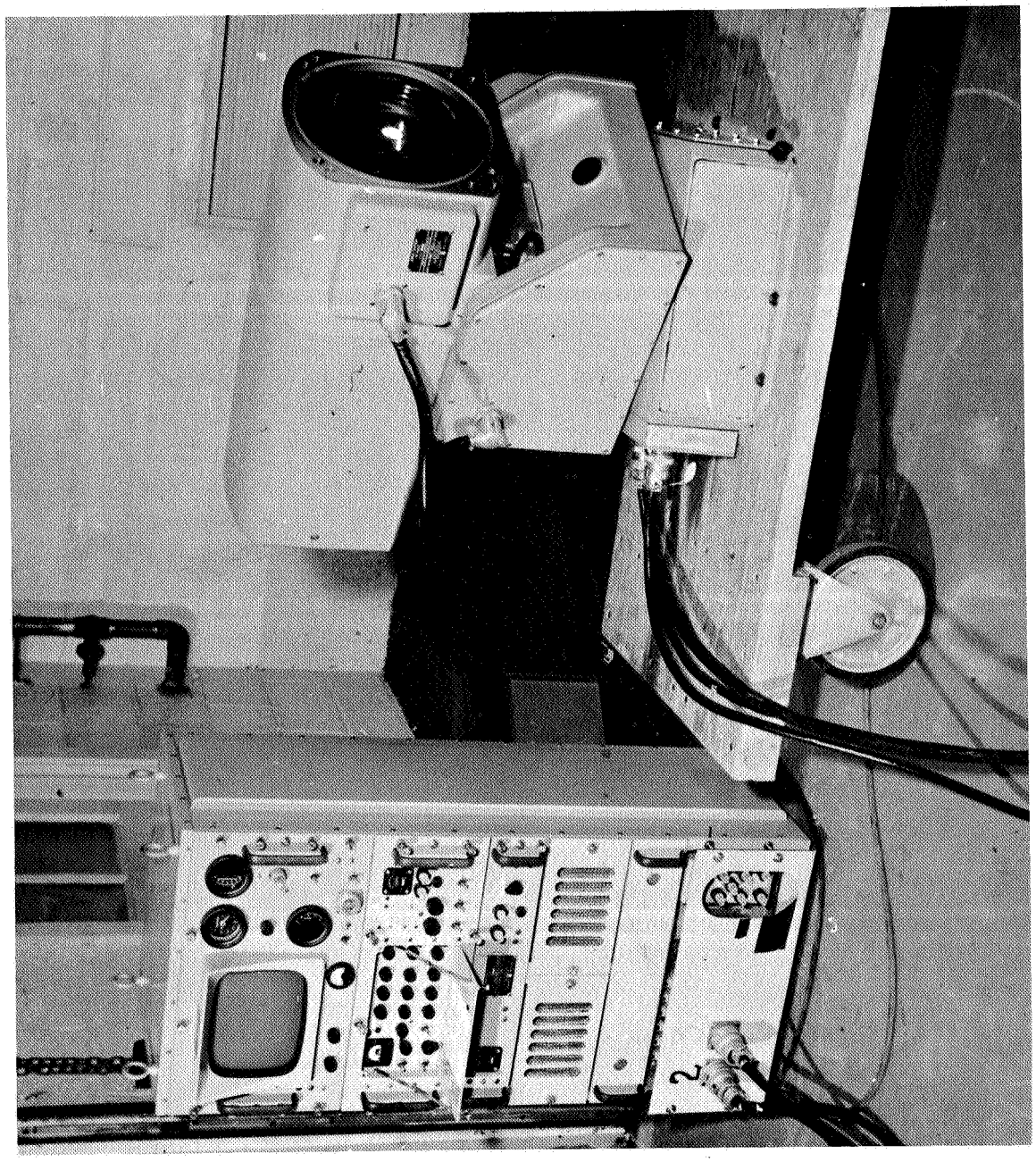

PLATE 2

AN/SXQ-3 image orthicon television system.

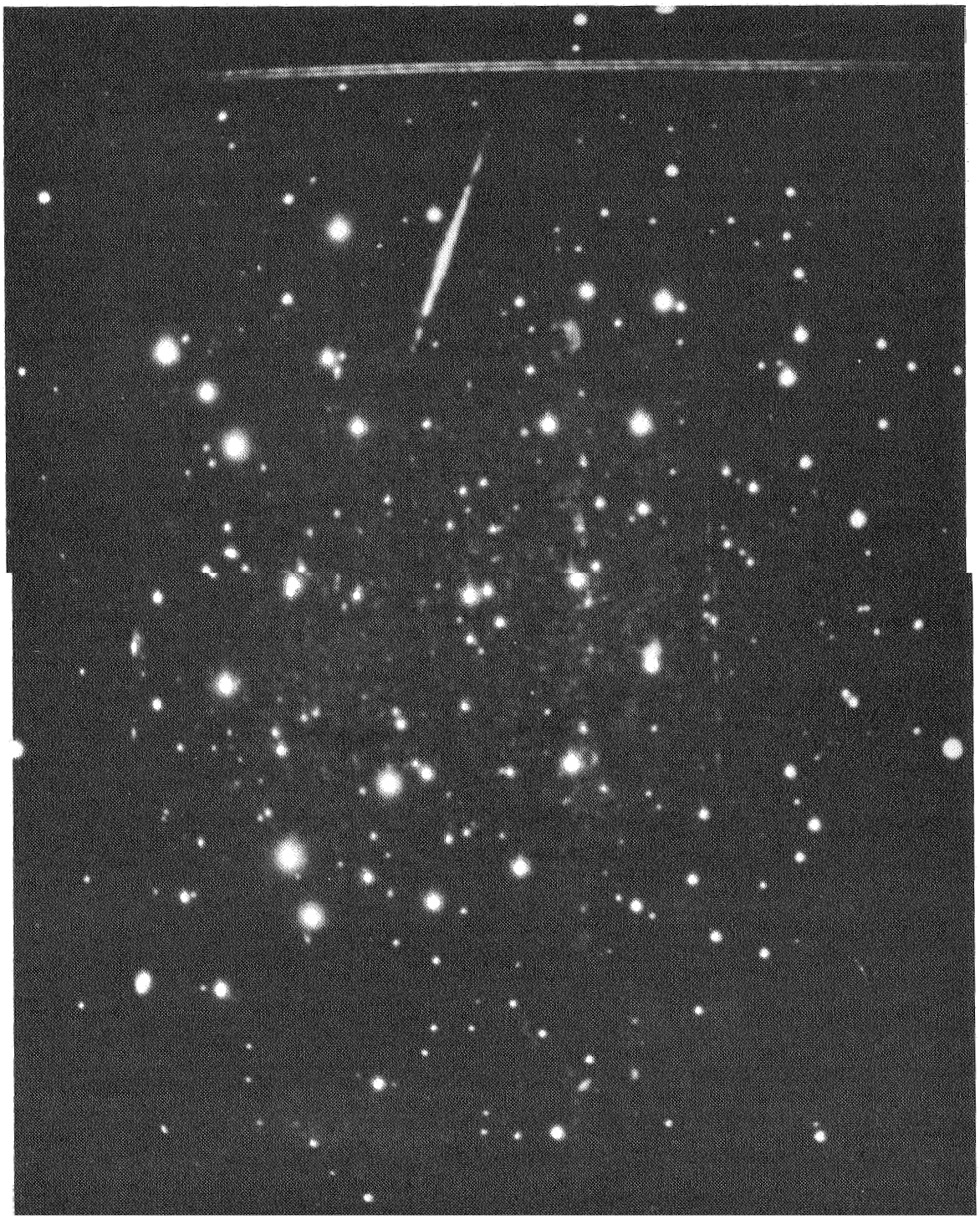

PLATE 3

Meteor photographed with new electronic shutter technique.

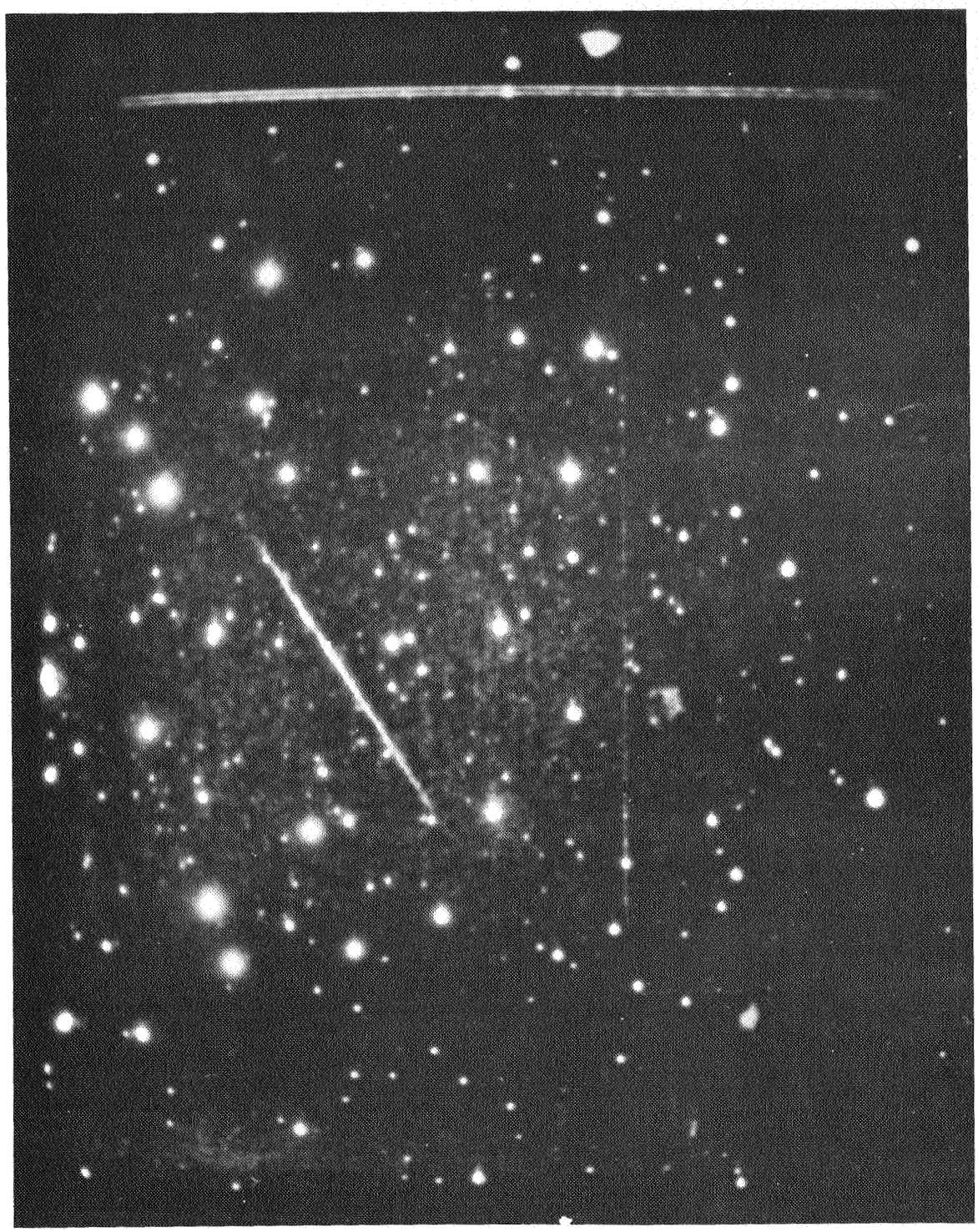

PLATE 4
Meteor photographed with new electronic shutter technique.

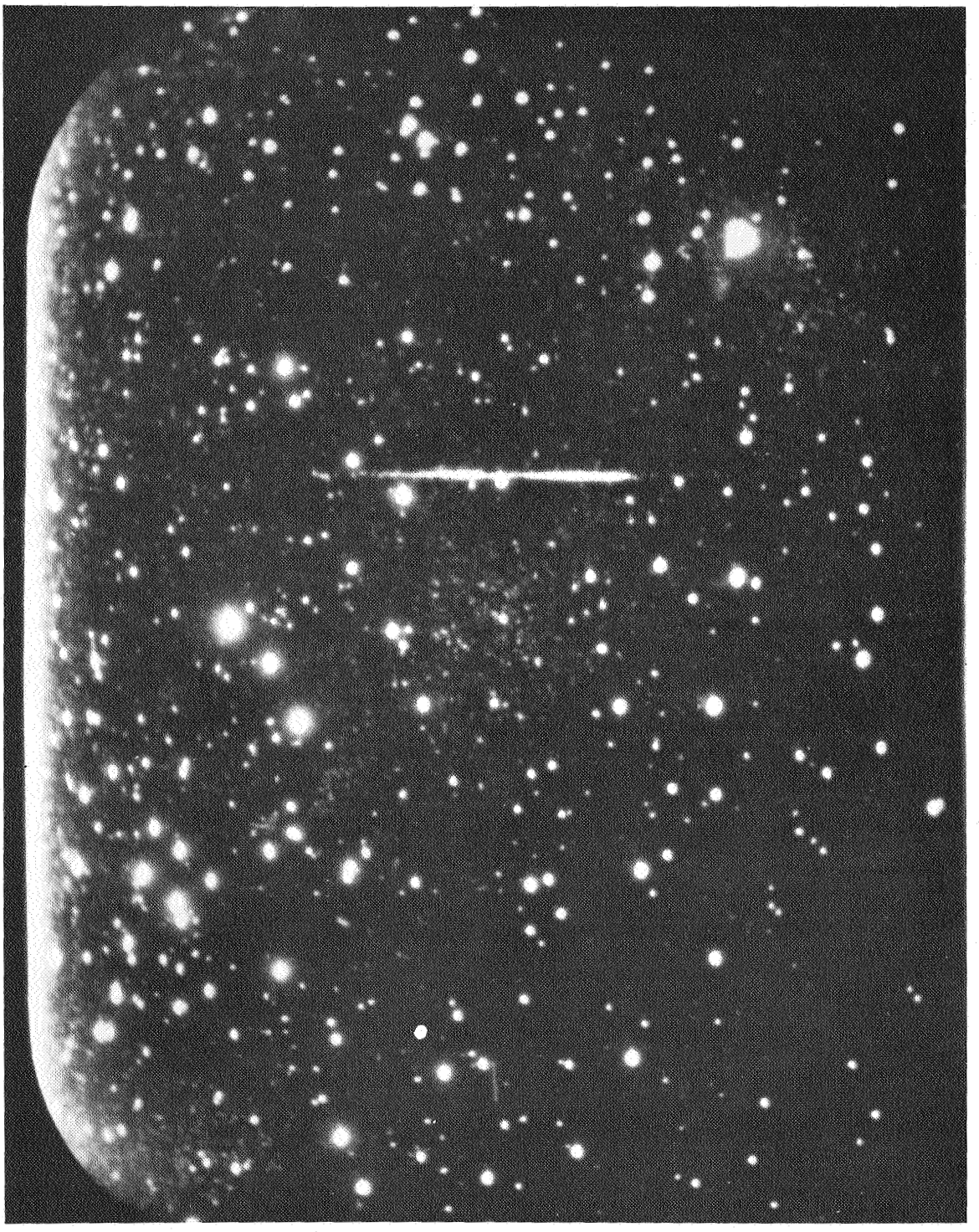

PLATE 5

Meteor photographed with new electronic shutter technique.

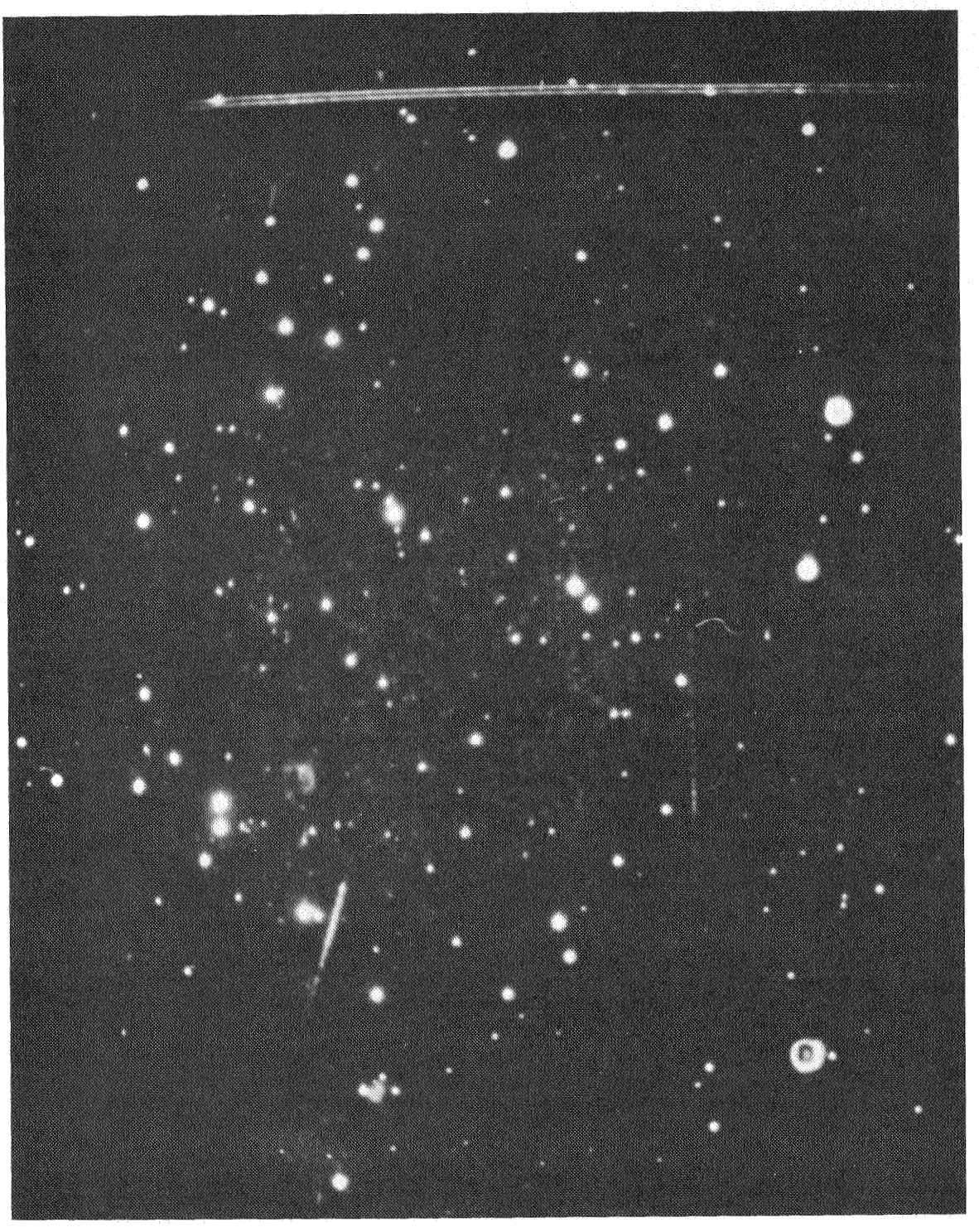

PLATE 6
Meteor photographed with new electronic shutter technique.

PLATE 7
Meteor photographed with new electronic shutter technique.

Some Characteristics of the Major Meteor Showers

P. M. MILLMAN [1]

The various physical parameters of meteors are determined by widely different methods that make use of a number of observational techniques. A selection was made here of some of those quantities that are likely to show correlation with the physical nature of the original meteoroid. The average values of these selected parameters, for meteors belonging to the major showers, were reduced to a simple qualitative index ranging from *0* to 10 and are listed in table **1.** These indices are plotted in figure 1, where the relationships among the various showers can be seen at a glance.

The first three parameters listed, ΔH, χ, and σ, were taken directly from a recent paper by Jacchia, Verniani, and Briggs **(1965).** The parameter ΔH is the average height difference in kilometers between the shower meteors and the nonshower meteors of the same geocentric velocity, and all heights are taken at the point near the beginning of the trail where the meteor reaches a photographic absolute magnitude of $+2.5$. For heights greater than the nonshower average, ΔH is positive. The index was taken as **10** for the greatest heights (Giacobinids), and *0* for the lowest (**6** Aquarids).

The parameter χ represents the degree of fragmentation of the meteoroid, determined from the variation in deceleration along the meteor trajectory. The value of χ is zero for virtually no fragmentation and increases as the tendency to fragment increases. For its derivation, see Jacchia, Verniani, and Briggs **(1965).** The index was graded from *0* to 10 in the same sense as the χ values.

The ablation coefficient σ is defined by $dm = \sigma m v \, dV$, the mass equation in basic meteor theory (m is meteoroid mass, and v its velocity in the atmosphere). From this it can be shown that $\sigma = A/2\Gamma\zeta$, where A is the heat transfer coefficient, Γ the drag coefficient, and ζ the effective latent heat of vaporization of the material in the meteoroid. When σ is large, the ablation from the meteoroid surface is relatively high. As is pointed out in the paper already referred to, there is no marked correlation between σ and χ, although each tends to cluster for any given group of meteors. A mean σ for the entire trajectory was used for each meteor, and only the meteors with fairly standard light curves were considered in compiling the mean σ and χ for the various showers. The σ index used here was taken in the reverse sense, i.e., 10 for the lowest σ value.

The meteoroid densities ρ were taken from Verniani **(1964),** who used the observational data from the Harvard program of meteor photography (Hawkins and Southworth, **1958).** The index was given high values corresponding to the lowest densities. If the density variations listed in Jacchia, Verniani, and Briggs **(1965)** are used, the only marked change in the ρ index would be almost an interchange of the values for the δ Aquarids and the Geminids. This point has to be investigated further.

The ratio between the numbers of meteors in successive whole magnitudes is designated r. The various determinations of this parameter from visual data show a wide range, and it has been difficult to arrive at satisfactory values. The values listed are my tentative estimates, and I used, in the main, unpublished material from the Ottawa visual meteor program, supplemented by various published results (Levin, **1965;** Öpik, **1955, 3958;** Millman and

[1] National Research Council, Ottawa, Canada.

240-022 O—67——8

TABLE 1.—*Physical parameters and corresponding qualitative indices for meteor showers.* (The qualitative indices plotted in figure 1 are given in parentheses following the corresponding value of the parameter. A colon between the parameter and the index suggests uncertainty due to small quantities of observational data or other causes. Where two values are listed for nonshower meteors, the first corresponds to the first **half** of the year, the second to the second half of the year.)

		AH (km)	χ	Log σ (sec²/cm²)	ρ (gm/cm³)	r	S (sec⁻¹)
Nonshower	(N)	0.0 (2½)	0.27 (2½)	−11.16 (1½)	0.22 (5)	3.0 (4)	1.05 (0) 0.75 (2%)
Quadrantid	(Q)	4-0.3 (2½)	0.44 (4)	−11.48 (5)	0.27 (5)		**0.50** (4%)
Lyrid	(Y)	−0.7:(2)	0.08:(½)	−11.17:(½)			0.40 (5½)
Arietid, ζ Perseid	(AZ)						0.60 (4)
δ Aquarid	(D)	−3.1 (0)	0.52 **(5)**	−11.40 (4)	0.49 :(0)	3.2:(2)	0.60:(4)
Perseid	(P)	4-0.8 (3)	0.28 (2%)	−11.26 (2%)	0.14 (7)	3.0:(4)	0.25 (7)
Giacobinid	(J)	+9.5 (10)	1.89:(10)	−14.9 :(10)	0.001:(10)	2.5 (10)	
Orionid	(O)	+4.8 (6½)	0.46 (4½)	−11.20 (2)	0.18 (6)		0.40 (5½)
Taurid	(T)	+2.3 (4½)	0.04 (0)	−11.32 (3)	0.17 (6)	2.6:(9)	
Geminid	(G)	−0.5 (2)	0.21 (1½)	−11.23 (2½)	0.32 :(4)	2.8:(6)	0.45 (5)

		Log T_A (sec)	N_R	N_V	D (days)	q (a.u.)	q_1 (a.u.)
Nonshower	(N)	−0.95 (0)	6 (½)	7 (½)	(0)		
		−1.37 (3)	12 (1½)	13 (1½)	(0)		
Quadrantid	(Q)	−1.33 (2½)	33 (3½)	40 (4)	1 (5½)	0.98 (10)	5.2 (2)
Lyrid	(Y)	−1.23 (2)	7 (1)	5:(0)	2.5 (4)	0.92 (9)	55 (10)
Arietid, ζ Perseid	(AZ)	−1.02 (½)	23 (2½)		24 :(1½)	0.22 (2)	3.0 (1)
δ Aquarid	(D)	−1.20:(2)	8 (1)	20:(2)	20 :(1)	**0.07** (1)	5.6 (2)
Perseid	(P)	−1.95 (7)	26 (3)	50 (5)	5 (3)	0.95 (9½)	55 (10)
Giacobinid	(J)		(10)	(10)	0.05 (10)	0.99 (10)	6.0 (2)
Orionid	(O)	−1.61 (4½)	8 (1)	25 (3)	6 (2½)	0.57 (6)	30 (7)
Taurid	(T)				30 :(½)	0.34 (4)	4.0 (1½)
Geminid	(G)	−1.12 (1)	46 (5)	50 (5)	5 (3)	0.14 (1)	2.6 (1)

Burland, 1961). All values of r listed here should be considered as tentative. The index was chosen with high values corresponding to low r.

The next two parameters, S and T_A, were taken from a paper by Millman and McIntosh (1964, 1966): S is the slope between log N and log T, where N is the number of meteor echoes, and T the echo duration in seconds. Since the larger and brighter meteors produce, on the average, echoes of longer duration, S will be larger where the number ratio between successive magnitudes is high. The S index was chosen high for low S and, since no comparable radar records are available for the Giacobinid shower, the peak S index was set at 7 to allow for the possibility of still lower S values.

The parameter T_A is the equivalent average duration of meteor echoes at the faint threshold of the records produced with the Ottawa meteor patrol radar (Millman and McIntosh, **1963).** This value was found by extending the log N vs log T curve to the T that corresponds to N for all echoes recorded. Here again, high values of the T_A index correspond to low values of T_A.

It will be noted in table 1 and in figure 1 that, commencing with the parameter S, two values are given for the nonshower meteors. The first of these corresponds to the period through February, March, and the first part of April, and is typical of nonshower meteors encountered during the first half of the year. The second corresponds to the last part of August, September, and the first part of October, and is typical of the nonshower meteors recorded during the second half of the year.

The parameter N_R is the hourly echo rate of shower meteors at shower maximum, as deter-

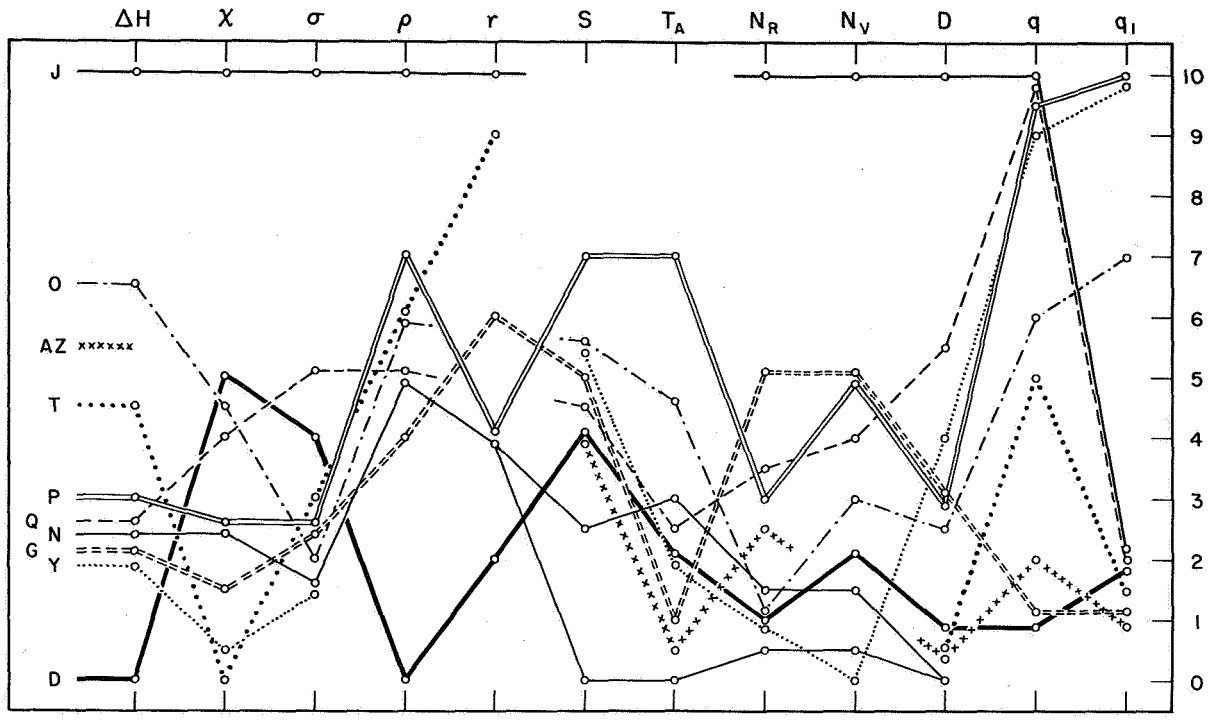

FIGURE I.—Plot of the qualitative indices for various physical characteristics of meteor showers. J=Giacobinid; O=Orionid; AZ=Arietid, ζ Perseid; T=Taurid; P=Perseid; Q=Quadrantid; N=Nonshower, lower line first half of year, upper line last half of year; G=Geminid; Y=Lyrid; D=δ Aquarid. The physical parameters are defined in the text. The index increases with increasing values of the parameters for AH, χ, N_R, N_V, q, and q_1 and with decreasing values of the parameters for σ, ρ, r, S, T_A, and D.

mined from the Ottawa patrol radar for echoes of duration 2 sec or greater. High index values correspond to high rates. Maximum index for the Ottawa records was set at 5, and the index for the Giacobinid shower was arbitrarily taken as 10.

The visual hourly rate for a single observer for shower meteors at shower maximum is represented by N_V, taken from a table published by Millman and McKinley (1963). High index values correspond to high rates, and again the index for the Giacobinid shower was taken arbitrarily as 10, with a maximum index for the regular annual showers as 5.

The shower duration D is measured between points where the hourly rate for the shower meteors is one-quarter the maximum rate. The values of D listed in table 1 are the average between those listed in the table by Millman and McEinley (1963) and measures made from the radar rates of echoes with durations 2 sec or greater (Millman and McIntosh, 1964, 1966). The D index is high for short duration.

The range of distances from the sun experienced by any group of meteors can be very significant in relation to their past history and current physical makeup. The last two parameters included in this summary are the perihelion distance q and the aphelion distance q_1. These values come from the orbital elements listed by Jacchia (1963). In both cases, high index corresponds to large values of distance.

The most striking feature in figure 1 is the exceptional character of the Giacobinid shower on the basis of almost every parameter. There is some tendency for the δ-Aquarid shower to lie at or near the other extreme. Additional points to note are the high indices of the Perseid shower for both S and T_A, the difference in these same two parameters between nonshower meteors appearing in the two halves of the year, and, except for the Giacobinids, the

apparent lack of correlation between fragmentation and low density. It must be remembered that the density values are still in some doubt, as was noted earlier, particularly in the case of the Geminids and the δ Aquarids. The ρ and r values used here are probably the least reliable when the differences found for the various showers are considered.

In summary, it may be concluded that the picture is far from simple, and there is evidence for a wide variety of basic physical characteristics even within the members of a single shower. When we remember the great diversity found in asteroidal fragments, it is not surprising that there should be a similar diversity in cometary fragments.

References

HAWKINS, G. S., and SOUTHWORTH, R. B.
1958. Statistics of meteors in the earth's atmosphere. Smithsonian Contr. Astrophys., vol. **2,** no. **11,** pp. **349–364.**

JACCHIA, L. G.
1963. Meteors, meteorites, and comets; interrelations. *In* The Solar System, vol. IV, ed. by B. M. Middlehurst and G. P. Kuiper, Univ. of Chicago Press, Chicago, pp. **774–798.**

JACCHIA, L. G.; VERNIANI, F.; and BRIGGS, R. E.
1965. An analysis of the atmospheric trajectories of **413** precisely reduced photographic meteors. Smithsonian Astrophys. Obs. Spec. Rep. No. **175, 309** pp.; also in Smithsonian Contr. Astrophys., vol. **10,** no. **1, 139 pp., 1967.**

LEVIN, B. J.
1965. Physical theory of meteors and the study of the structure of the complex meteor bodies on the basis of visual meteor observations. *In* Meteors, ed. by T. R. Kaiser, Spec. Suppl. Journ. Atmos. Terr. Physics, vol. **2,** Pergamon Press, New York, pp. **131–143.**

MILLMAN, P. M., and BURLAND, M. S.
1961. Meteor magnitude distributions. Astron. Journ., vol. **66,** pp. **291–292.**

MILLMAN, P. M., and MCINTOSH, B. A.
1963. A preliminary report on radar meteor counts. *In* Proceedings of the Symposium on the Astronomy and Physics of Meteors. Smithsonian Contr. Astrophys., vol. **7,** pp. **45–51.**
1964. Meteor radar statistics. **I.** Canadian Journ. Phys., vol. **42,** pp. **1730–1742.**
1966. Meteor radar statistics. II. Canadian Journ. Phys., vol. **44,** pp. **1593–1602.**

MILLMAN, P. M., and MCKINLEY, D. W. R.
1963. Meteors. *In* The Solar System, vol. IV, ed. by B. M. Middlehurst and G. P. Kuiper, Univ. of Chicago Press, Chicago, pp. **674–773.**

ÖPIK, E. J.
1955. The masses of meteors. Mém. Soc. Roy. Sci. Liège, ser. **4, vol. 15,** pp. **125–146.**
1958. Statistical results from the Arizona Expedition for the study of meteors. Contr. Armagh Obs., no. **26,** pp. **1–82.**

VERNIANI, F.
1964. On the density of meteoroids, **11:** The density of faint photographic meteors. Nuovo Cimento, vol. **33,** pp. **1173–1184.**

Abstract

Twelve physical parameters, found for the major meteor showers, were reduced to simple qualitative indices, which were plotted in relation to the indices for nonshower meteors. The general lack of correlation among these indices suggests a wide spread of physical characteristics within the members of any given meteor shower.

Research on Orbits of Minor Meteor Streams

A. K. TERENTJEVA [1]

Already in the 19th century the classical founders of meteor astronomy, G. V. Schiaparelli, G. A. Newton, and F. A. Bredikhin, suspected that meteor streams did exist in large quantities. The streams characterized by high meteor rates, duration of activity, and ease of observation were the first to be studied. The best known of these streams, 10 in number, are usually called major streams.

In recent years the development of instrumental techniques has made it possible to investigate the less numerous, but no less significant, minor streams.

The author has made a detailed analysis of the published data on the photographed orbits [about 3600) of individual meteor bodies and on numerous visual observations made in the second half of the 19th and the first half of the 20th centuries. The most reliable data concerning visual weak shower radiants (about 2000), whose velocities had been determined, were used. A study of this material resulted in the finding of 374 minor meteor streams. A monograph discussing the most authentic of these streams (154) will be published in Russian (Terentjeva, in press); brief reports have appeared (Terentjeva, 1963; 1964a, b; 1965a). The remaining 220 streams, which are less certain, as a rule include those that have no more than 2 photographic orbits (or 1 photographic orbit if a visual radiant exists).

Generally, the existence is accepted of several hundred minor meteor showers with a duration of not less than 3 to 7 days and an average rate not exceeding 2 meteors per hour. However, more observational material of high quality is needed in order to recognize these showers.

[1] Kiev State University, USSR.

We found a curious phenomenon of radiants located in symmetrical positions with respect to the ecliptic: several geocentric radiants (sometimes groups) are symmetrically located to the north and south of the ecliptic at a distance of up to 50°; the elements of corresponding orbits are the same, except for the 180° difference in ω and Ω. Therefore, the orbital planes, which cut across a common line of nodes, are symmetrical with respect to the ecliptical plane. Perhaps this phenomenon should be considered as a regular feature and be studied by means of celestial mechanics.

Ten of the minor streams are said to have a northern (N) and a southern (S) branch. As an exception, the 6-Arietids stream (8–17 December) has three clearly defined branches — northern (N), ecliptic (&), and southern (S) (Terentjeva, 1965b).

The great number of homogeneous visual observations of minor meteor showers, carried out by I. S. Astapovich in 1942–1945, show that their radiants near the ecliptic possess a considerable area of radiation. Some ecliptic minor showers have several small secondary radiation centers located within this large area (for example, Scorpionids, Virginids, Sagittarids, Librids). The position and relative activity of these centers change during the period of one night and from night to night. It is as if the meteor stream is dispersed into filaments. Because of the relative shortness of these filaments, the radiation center disappears after several hours or days and is replaced by other radiation centers in the same large radiation area. As a rule the radiation area of a minor shower, located at a distance from the ecliptic, is small.

Other meteor showers have a more homogeneous radiation area; their secondary centers of radiation are not as distinct (in some cases owing to the weakness of the shower), and the radiation area is more or less uniformly filled with individual radiants.

In some cases the activity of every secondary radiation center varies during its diurnal displacement, so that during the displacement from west to east the intensity increases in western and decreases in eastern radiant centers, respectively. This effect could produce the phenomenon of a stationary or even a backward-moving radiant, but, in reality, this does not occur.

The activity of minor showers is an extremely complicated and intricate dynamic problem to solve. It will take many years of investigation to obtain an approximate answer. One of the reasons is the rapid evolution of minor streams. Even Super-Schmidt meteor cameras are incapable of obtaining the necessary data because of the deficiency in or the total absence of bright meteors in minor showers. Many streams vary so rapidly that it is impossible to determine their structures before they assume a new form. Sometimes a shower can appear, reach its maximum, and then disappear for a period of some 10 years (for example, the Bootids of the Comet Pons-Winnecke). Other minor showers, which are little perturbed by major planets, exist for hundreds and thousands of years, making apparitions every year, just as Perseids, Geminids, and other major showers do.

Approximately half of the 374 recognized streams were visually observed in the 19th century. Reobservations of radiants of the end of the 19th and of the beginning of the 20th centuries, carried out by A. M. Bakharev in 1938 and by I. S. Astapovich in 1926, 1933, and 1942 to 1945, show that during approximately half a century, one-third of the old radiants were replaced by new ones; one-third noticeably changed their positions, visibility epochs, and activity; and only the remaining one-third of the radiants underwent a minimum of change. The last third, in the main, include long-periodic streams with significant orbital inclinations that are little influenced by planetary perturbations.

When analyzing the orbits of meteoric bodies not associated with any streams, we see that sporadic meteor matter shows traces of original homogeneity.

To determine the connection between the meteor streams under study and other minor bodies of the solar system, the author calculated the value of Tisserand's criterion $C=(1/a)+(2/a_j^{3/2})\sqrt{p}\cos i$ (perturbed planet Jupiter) for all comet orbits (except hyperbolic orbits) in Porter's catalog (1961), which number 738 (502 comets) in all; for orbits of 154 minor meteor streams (Terentjeva, in press); and for the orbits of the 1650 asteroids listed in 1965 (Institute of Theoretical Astronomy, Acad. Sci., USSR, 1964). The C distribution is shown in intervals of $d=0.02C$, and is illustrated in figure 1. For comets that had several perihelion passages, C was taken as the arithmetical mean of the values of every observed return; and for meteor streams, as the arithmetical mean of the values of every individual stream orbit.

The maximum overall distribution for meteor streams, short-periodic comets, and asteroids falls on the modal value $C\approx 0.6$. The long-periodic and parabolic comets with the modal value $C\approx 0$ differ greatly from the former and stand in a group by themselves.

The similarity of distribution for long-periodic and parabolic comets is evidence that parabolic comets can be considered to have elongated elliptic orbits.

In the course of a consistent transition from asteroids to comets and then to meteor streams, the overall range of values of C increases (see fig. 1). The distribution of asteroids is more compact as compared with that of comets; meteor streams have the greatest C dispersion and reveal their main maximum between $+0.55$ and $+0.58$ in the region of the maximum short-periodic comets of Jupiter's group. A deviation of the main mode is observed for streams with respect to comets at $+0.02$ in the direction of the higher values of C, which apparently is the result of a general evolution of meteor particles due to the action of various physical factors (corpuscular and photon radiation, interstellar medium, etc.).

If we compare the C-distribution graph for minor streams with the graphs for short-

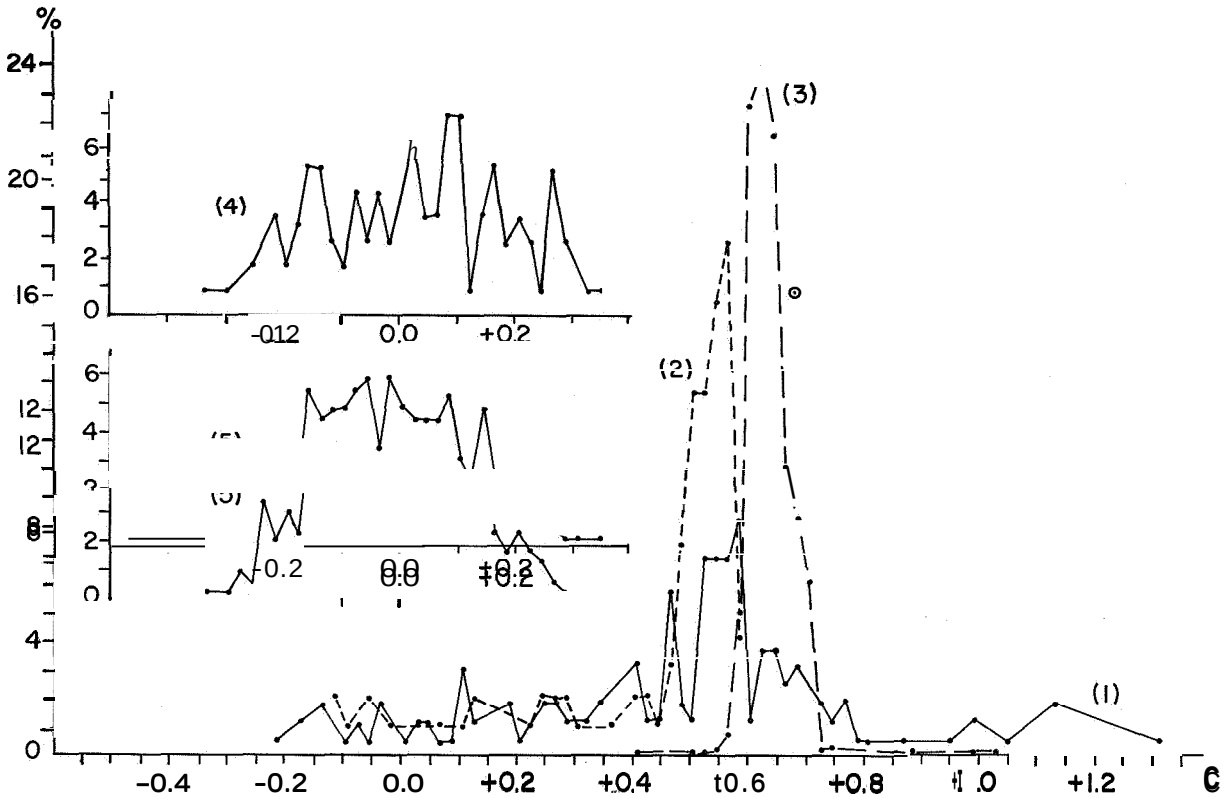

FIGURE I.—Distribution of minor bodies according to Tisserand's criterion: (1) minor meteor streams (N=154); (2) short-periodic (P <200 years) comets (N=95); (3) asteroids (N=1650); (4) long-periodic comets (N= 117); (5) parabolic comets (N=290). The encircled dot belongs to curved line (4).

periodic comets and asteroids on corresponding parts of the abscissa (fig. 1), we see a noticeable similarity, even to the smallest details. In several cases the secondary maxima coincide, and this is hardly fortuitous. The same holds true if we carefully compare the distributions of long-periodic and parabolic comets with the distribution of minor streams.

More precise structural details of the C distribution can be seen in figure 2, where the interval chosen (d=0.01C) is smaller. The general character of the distribution remains the same as in figure 1.

Hence, meteor streams can be connected with all the indicated minor bodies; the majority, however, with comets. If we interpret this connection from the standpoint of meteor streams originating from other minor bodies, the proportion of the asteroid component with, possibly, the meteorite component (Terentjeva, 1964c) will be not less than 23 percent, and that of the comet component not more than 74 percent, most of which is comprised of short-periodic comets of Jupiter's group. Some streams may have come directly from long-periodic and parabolic comets.

An insignificant portion of minor streams (3 percent) is found in the region of $C>1$ (fig. 1). They are streams with small eccentricity (in the main, e=0.15 to 0.24) and with large semimajor axes (a=0.87 to 1.18). If we calculate C for the particles in the zodiacal cloud, they will be located in the region of $C>>1$. Here, apparently, the influence of physical effects is present (Poynting-Robertson, etc.) and increases with the growth of dispersion of meteor matter. In the process of evolution the particles, apparently undergoing disaggregation, grow smaller and gradually approach the sun in spiral orbits. This evolutionary process, which is connected with secular variations of a and e, leads to "secular" variations in the values of C, and is consistent with the decrease of full particle energy.

At present the search for connections between streams and comets on the basis only of their

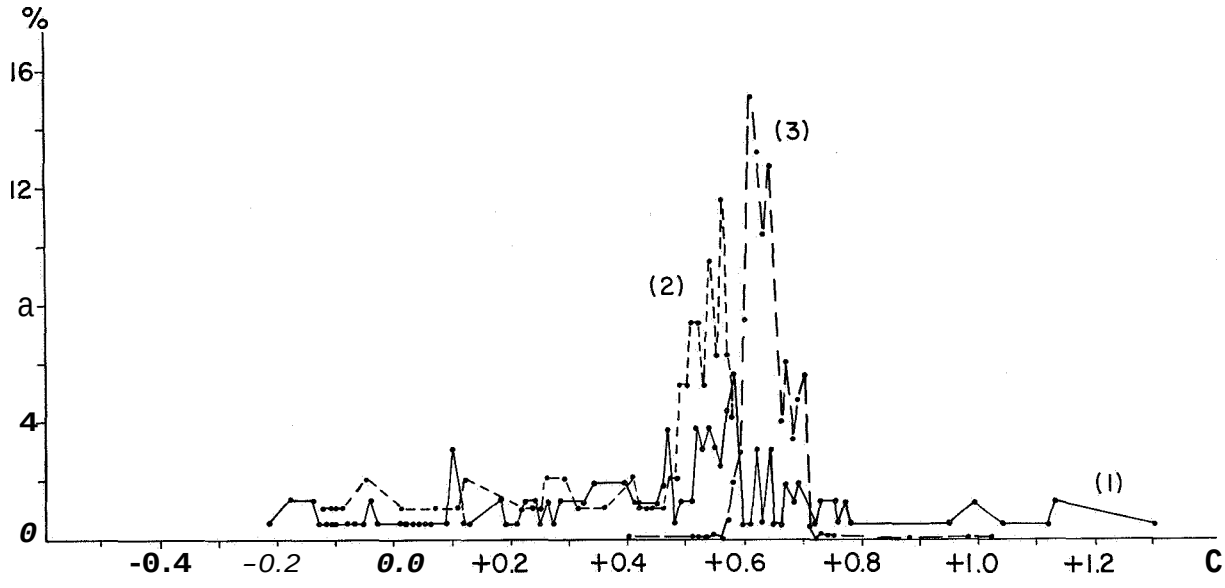

FIGURE 2.—Distribution of (1) minor meteor streams, (2) short-periodic comets, (3) asteroids, according to Tisserand's criterion.

orbits coinciding (as is frequently done) is limited and inadequate; this is particularly true for minor streams. If we consider the catalog of theoretical comet radiants (Kramer, 1953), it is possible to find a connection with comets for only 18 minor streams out of 154 (Terentjeva, 1964b), i.e., 12 percent. It is most likely that the remaining 88 percent can be related to: (1) minor streams of comet origin that have lost contact with the comet because of perturbations, (2) streams (also of comet origin) whose parent comet disintegrated or was lost sight of for some reason or another, (3) streams resulting from the disintegration of other greater streams and having lost contact with the parent stream (possibly as a result of partial perturbation), (4) possible streams of asteroid-meteorite origin, and (5) streams of other possible origin. If we make a comparison with major streams, we see that the parent comet is evident in approximately 80 percent of the cases. This may be due to a more favorable location of their orbits in the solar system at a great distance from perturbed planets. The greater portion of minor streams are less well located. They undergo frequent and greater perturbations, and in the entire process of evolution have progressed much further than major streams; apparently the minor streams are in a relatively later stage of evolution (although in reality they might be younger). This is affirmed by the greater number of cases of considerable radiation area as compared with that of major showers.

From the above discussion we must conclude that it is becoming more and more difficult to find connections between minor streams and comets. A careful study should be made of the history of the stream and of its associated comet; they certainly are not identical. It is necessary to utilize celestial-mechanical criteria (e.g., those of Tisserand, Callandreau) in order to judge whether the individual orbit of a given stream of the past could correspond to the orbit of one or another comet, and to what extent the conclusion of their genetic connection is probable. By such an approach the author was able to discover more stream-comet associations and, in part, the connection between separate comets and groups of meteor streams, in spite of the great differences today in their dates of visibility and radiant positions (simultaneously with a general similarity of physical properties of such meteors). There also possibly exists a family of minor streams connected with a comet, which, in turn, is a member of a comet family that originated from a parent-comet, i.e., the presence of complex comet-meteor systems is observed.

Data on possible families of meteor streams associated with Comet Pons-Winnecke 1951 VI and Comet Helfenzrieder 1766 II are given in

TABLE 1.—*Possible families of meteor streams associated with Comet Pons-Winnecke 1951 VI and Comet Helfenzrieder 1766 II*

Comet and meteor streams	a (a.u.)	e	q (a.u.)	π deg.	Ω deg.	i deg.	P (years)	C	n
Pons-Winnecke 1961 VI	—	0.653	1.161	264.6	94.4	21.7	**6. 12**	0.5125 ±0. 0016	15
17 Virginids (41) April 6–12	2.90	'0.722	0.795	258.7	19.5	**4. 8**	—	0. 54 **±0. 02**	4
71 Virginids (46) April 7–21	2. 95	0.758	0.716	271.9	21.8	10.8	—	0. 525 ±0.0003	2
ζ Draconids (88) May 22–June 13	3. 27	0.690	1.00	267.5	72.5	39.5	—	0. 48 ±0. 03	2
Bootids (90) June 13–July 2	2. 67	0.620	1.010	276.0	85.5	19.8	—	0. 58 ±0. 03	4
ζ Draconids (91) June 16–25	2. 56	0.603	1.015	265.0	90. 0	33. 1	—	0. 57 ±0. 02	3
Helfenzrieder 1766 II	—	0.852	0.403	254.3	76.1	7.9	**4. 51**	0.5107	1
ℓ Cancrids (9) January 13–19	2. 53	0.837	0.420	220.7	115.7	2.7	—	0.542 ±0. 006	3
η Leonids (17) February 3–6	2. 54	0.838	0.407	242.6	315.7	2.5	—	0. 54 ±0. 05	3
40 Leo Minorids (21) February 12–17	2. 36	0.770	0.525	240.0	325.5	13.0	—	0. 59 ±0. 07	2
ν Virginids (29) March 1–18	2. 65	0.800	0.527	262.7	349.4	3.4	—	0. 55 ±0. 04	5

table **1** (see also figs. **3** and **4).** The duration **of** activity of showers is noted in the first column **of** the table, and its number (Terentjeva, **1963)** is shown in brackets. The values of the orbital elements **of** the comets are taken from Porter's catalog. The last two columns list the mean values and mean absolute deviations **of** Tisserand's criterion C in n returns **of** the comet or in n individual orbits **of** the meteor stream.

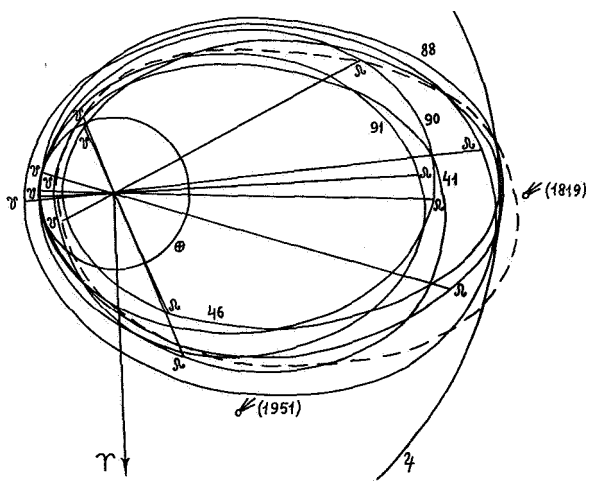

FIGURE 3.—Possible family of meteor streams associated with Comet Pons-Winnecke 1951 VI (projection on the ecliptic plane).

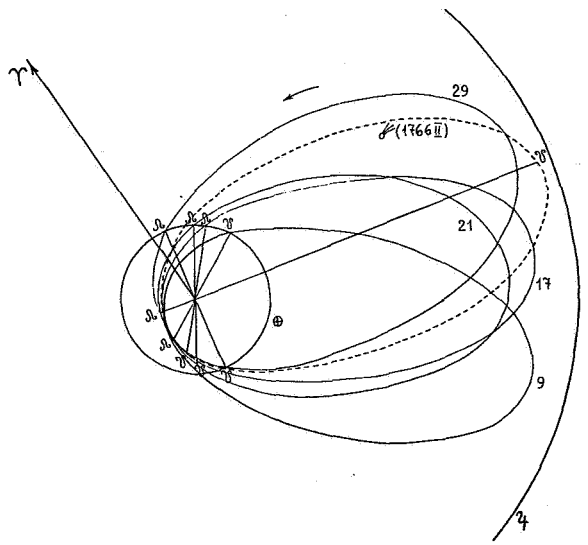

FIGURE 4.—Possible family of meteor streams associated with Comet Helfenzrieder 1766 II (projection on the ecliptic plane).

The short-periodic Comet Pons-Winnecke, after returning to the perihelion not fewer than 15 times, was systematically perturbed by Jupiter, which gradually increased the comet's perihelion distance (Porter, 1961). Figure 3 depicts two orbits of this comet in its returns of 1819 and 1951. During this period the absolute brightness of the comet decreased by 5.3 mag (Vsekhsvyatskii, 1958).

Special attention should be paid to the need for studying the connection between Comet Pons-Winnecke 1951 VI and Comet Helfenzrieder 1766 II. Possibly these two comets are in some way related to Comet van Biesbroeck 1954 IV ($C=0.5102$) and Comet Neujmin (3) 1951 V ($C=0.5054\pm0.0006$).

Naturally only a detailed investigation of gravitational perturbations, as well as light-pressure and corpuscular perturbations, can really substantiate the author's assumptions regarding comet-meteor families discussed in this article and earlier.

Do minor showers of telescopic and ultra-telescopic meteors exist? Yes, they do, but it is very difficult to observe them. For example, 6 days a year the activity of telescopic meteors is enormous (Skalnate Pleso, Ashkhabad). This means that every year the earth meets six minor streams of telescopic meteors. For July 20 to 24, this stream may be a "big" stream of telescopic meteors. It is necessary to find (by means of radar) the coordinates of the radiants and the velocity of these streams and to determine their orbits in the solar system. The orbits of telescopic and especially ultra-telescopic meteor streams are unknown.

If we consider that the general evolution of meteor matter in the solar system is accompanied by the disaggregation of meteor systems and meteor bodies themselves, we may conclude that among telescopic and weaker meteors the fraction organized into meteor streams as compared with the sporadic fraction will be much less than among ordinary and bright meteors, where this ratio is near to 1.

References

INSTITUTE OF THEORETICAL ASTRONOMY, ACAD. SCI., USSR
1964. Ephemerides of minor planets for 1965. Nauka, Moscow-Leningrad, pp. 1342.

KRAMER, E. N.
1953. Cometary radiants and the connection of meteor showers with comets. Izv. Astron. Obs. Odessa State University, vol. 3, pp. 163-247.

PORTER, J. G.
1961. Catalogue of cometary orbits, 1960. Mem. BAA, vol. 39, no. 3, 97 pp.

TERENTJEVA, A. K.
1963. Orbits of minor meteor streams. Astron. Circ. Acad. Sci. USSR, Moscow, no. 249, pp. 14; no. 264, pp. 1-8.
1964a. Some peculiarities and properties of minor meteor streams. Astron. Circ. Acad. Sci. USSR, Moscow, no. 277, pp. 1-3.
1964b. On the interconnection between minor meteor streams and comets. Astron. Circ. Acad. Sci. USSR, Moscow, no. 307, pp. 4-7.
1964c. On the interrelation of minor bodies of the solar system. Informational Bull. ("Materials International Geophysical Year" Geophysical Committee of the Ukrainian SSR), Kiev, no. 6, pp. 11-15.
1965a. On the space structure of some meteor streams. Astron. Circ. Acad. Sci. USSR, Moscow, no. 313, pp. 7-8.
1965b. Concerning the space structure of δ-Arietids and Leonids. Bull. Comm. Comets and Meteors, Acad. Sci. USSR, no. 11, pp. 33-35.
1966. Minor Meteor Streams. Collection of works "Meteor Investigation," no. 1, from series "Investigation Results According to International Geophysical Projects," Nauka, Moscow.

VSEKHSVYATSKII, S. K.
1958. Physical characteristics of comets. Fizmatgiz, Moscow; trans. from Russian by The Israel Program for Scientific Translations, Jerusalem, 1964.

On Two Problems of Sporadic Meteor Activity

J. Štohl [1]

The seasonal and diurnal variations of meteor rates obtained at different locations and by different methods of observation have been analyzed. The results will appear in extenso elsewhere (Contr. Astron. Obs. Skalnaté Pleso). Only two problems of broader interest, concerning the comparison of the Northern and Southern Hemisphere data, are discussed here: the dependence of the seasonal variation upon the geographiclatitude, and interstellar meteors.

Seasonal variation of sporadic radiant distribution

The model distribution of apparent radiants of sporadic meteors consisting of three constant sources—apex, helion, and antihelion (Hawkins, 1956; Hawkins and Prentice, 1957)—is a reasonable approximation to the mean whole-year distribution only, subject to considerable seasonal variations. As Keay (1963) has shown for the Southern Hemisphere, the actual strength varies from 0.8 to 3.7 for the helion, and from 1.1 to 4.0 for the antihelion sources, referred to the apex source. This variation is evidently connected with the changes of distribution of meteor orbits along the earth's orbit.

On the basis of the available observations, in particular of the extensive radar data from Ottawa (Millman and McIntosh, 1963), it is possible to estimate the variation of the individual source strength for the Northern Hemisphere. If we adopt a model of the radiant distribution with three point sources (apex, $\lambda_\odot - 90°$; helion, $\lambda_\odot - 30°$; antihelion, $\lambda_\odot - 150°$), strengths f_i, and a continuous sporadic background with the uniform strength f_0, then the observed frequency f_s of the sporadic meteors in each time interval can be expressed by the sum

$$f_s = \sum_{i=1}^{3} f_i \cos^n z_i + f_0, \qquad (1)$$

where we assume $n=1$. The mean zenith distances z_i of individual sources can be calculated for arbitrary time intervals. The strengths f_i and f_0 are considered constant throughout the day. Deriving an equation of the form (1) for each hour of the day, we obtain 24 equations of condition for 4 unknowns f_i and f_0, which can be evaluated by the method of least squares. By the solution of the equation systems for a number of the year's intervals, we obtain the seasonal variation of the strength of individual sources.

The numerical calculation was carried out by means of the electronic computer ZRA–1, on the basis of the Ottawa radar observations ($\phi = +45°.4$) for 12 monthly intervals. The contribution of shower meteors, included in the radar observations, has been considered qualitatively in the discussion of the results. Figure 1 shows the calculated seasonal variation of activity of the sources (in units of the mean Ottawa frequency). The mean errors, which are also indicated, have been calculated from the residuals in the equations of condition. Keay's results for the Southern Hemisphere ($\phi = -43°.6$) are shown in figure 2.

A comparison of the results for the Northern and Southern Hemispheres leads to the following conclusions:

1. The helion source in the Northern Hemisphere (H_N) exhibits an extensive maximum in the first half of the year, with an extreme activity in June. The activity of this

[1] Astronomical Institute of the Slovak Academy of Sciences, Bratislava, Czechoslovakia.

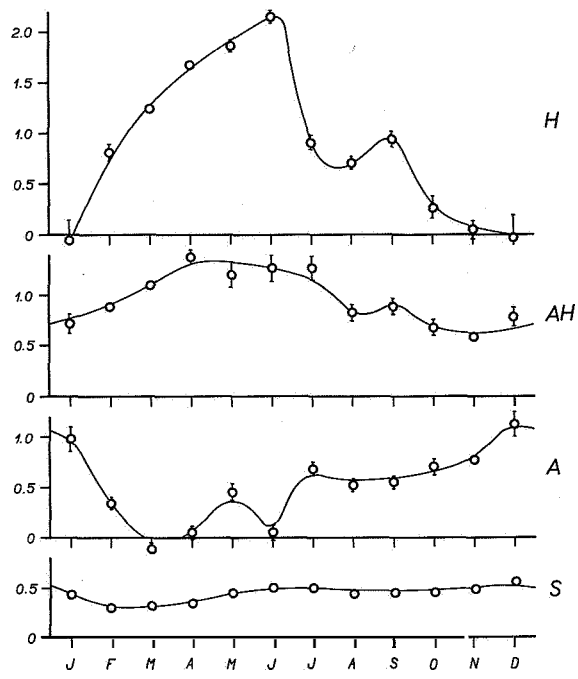

FIGURE 1.—Seasonal variation of the radiant sources in the Northern Hemisphere (Ottawa). H=helion, AH= antihelion, A=apex, S=sporadic background.

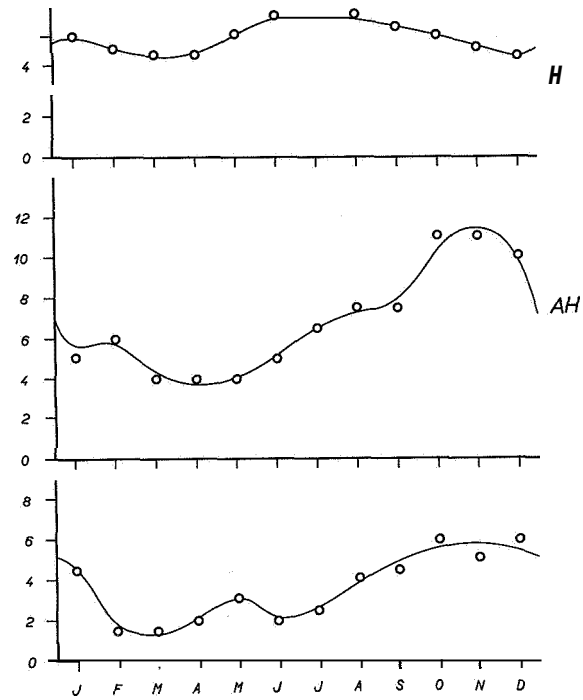

FIGURE 2.—Seasonal variation of the radiant sources in the Southern Hemisphere (Christchurch). H=helion, AH= antihelion, A= apex, S=sporadic background.

source in the Southern Hemisphere (H_S) is relatively constant, with a slight maximum in the summer months. On the contrary, in the Northern Hemisphere the antihelion source (AH_N) shows a relatively constant activity, whereas in the Southern Hemisphere (AH_S) an extensive maximum from October to December appears. The agreement in the strengths of the sources H_N–AH_S and AH_N–H_S in amplitude, combined with a phase displacement of 180° between H_N–AH_S and 90° between AH_N–H_S, suggests the activity of two extraordinarily Muse streams of meteors. These may be tentatively identified with the northern summer daytime showers and the southern complex of Velaid-Puppids; the radiants of these intricate systems are so diffuse that they can hardly be separated from the sporadic background.

2. The activity of the apex source has, both in the Northern and Southern Hemispheres, the same trend with a maximum in the second half of the year and a minimum in April-May. This can be attributed to a real variation of the meteor density. The activity of the sporadic background is practically constant throughout the year, with a moderate decline in February-March; this result is in complete agreement with the variation of the telescopic meteor activity (Kresák and Kresáková, **1963).**

3. The total annual strengths of individual sources of sporadic meteors are equal in both hemispheres. The integrated relative strengths are as follows: apex, **18** percent; helion, **31** percent; antihelion, 35 percent; uniform background, 16 percent.

Interstellar meteors

One of the main objections to the existence of interstellar meteors is the fact that no geocentric velocities in excess of 80 km/sec have been measured by radio methods. It can be shown that this objection is not entirely justified. McEinley **(1961)** has already pointed out that the heliocentric velocity of interstellar particles is given by the energy equation for their velocities in the earth's distance from the sun, rather than by the vectorial composition of the velocities. Hence, assuming a velocity of **20** km/sec with respect to the sun, the maxi-

mum geocentric velocity is not 92 km/sec, but only 76.5 km/sec.

This velocity obviously applies only to meteors with heliocentric radiants situated exactly in the earth's apex; however, this case is not representative for interstellar particles, at least not for the overwhelming majority of them. The sun's motion relative to the medium of interstellar particles is about 20 km/sec in the direction toward the point with equatorial coordinates $\alpha=276°$, $\delta=+37°$. The heliocentric radiant of the main source of interstellar meteors would shift from this point in the direction of the antihelion point by an effect analogous to the zenith attraction. The geocentric radiant, resulting from the vectorial composition of the heliocentric meteor velocity and the earth's orbital velocity, would displace during the year, with the position of the earth in its orbit. As the numerical computation shows, the elongation of the geocentric radiant from the earth's apex can acquire the values from 39°.5 to 78°.10 only. The corresponding geocentric velocities are surprisingly low, never exceeding the value of 65.5 km/sec, and with a lower limit of 42.5 km/sec.

The random dispersion of individual velocities of the interstellar particles results in a dispersion of the above-mentioned values of the geocentric velocity. Nevertheless, even in this case the geocentric velocities should group predominantly within the velocity interval quoted above. It is obvious that interstellar meteors are rare, if they do exist. Thus it is not surprising that there are no velocities in excess of 72 km/sec, even if some interstellar meteors actually exist. Perhaps there is another, more promising procedure for verifying the presence of interstellar meteors. If they actually exist, there must be some excess of the velocities 43 to 65 km/sec in the northern velocity distribution compared with the southern one, since the northern declination of the solar apex is high. Comparable and representative velocity data from both hemispheres would obviously be required for this purpose, and meteor showers with geocentric velocities falling within the interval in question would have to be discarded carefully.

References

HAWKINS, G. S.
1956. Variation in the occurrence rate of meteors. Astron. Journ., vol. **61,** pp. **386–391.**

HAWKINS, G. S., and PRENTICE, J. **P. M.**
1957. Visual determination of the radiant distribution of sporadic meteors. Astron. Journ., vol. **62,** pp. **234–240.**

KEAY, C. S. L.
1963. The annual variation in the radiant distribution of sporadic meteors. Journ. Atmos. Terr. Phys., vol. **25,** pp. **507–513.**

KRESÁK, Ľ., and KRESÁKOVÁ, **M.**
1963. The density distribution of telescopic meteors around the earth's orbit. *In* Proceedings of the Symposium on the Astronomy and Physics of Meteors. Smithsonian Contr. Astrophys., vol. **7,** pp. **253–258.**

MCKINLEY, D. W. **R.**
1961. Meteor Science and Engineering. McGraw-Hill Book Co., New York, **309** pp.

MILLMAN, P. M., and MCINTOSH, **3.** A.
1963. A preliminary report on radar meteor counts. *In* Proceedings of the Symposium on the Astronomy and Physics of Meteors. Smithsonian Contr. Astrophys., vol. **7,** pp. **45–51.**

Abstract

Seasonal changes of the sporadic radiant distribution are investigated on the basis of Ottawa radar records using a simplified four-source model. The results are compared with the Southern Hemisphere data from Christchurch. Low amplitude and parallel variations of the apex source and of the uniform sporadic background contrast with peculiar changes of the helion and antihelion source; the possible reasons of this effect are discussed.

It is shown that the observed absence of geocentric velocities exceeding 73 km/sec does not exclude the existence of some hyperbolic orbits. The comparison of the geocentric velocity distribution in the Northern and Southern Hemispheres is suggested as a potential check of the reality of the hyperbolic component.

Remark on a Cosmic-Probe Investigation of Meteor Showers with Retrograde Motion

V. GUTH [1]

Up to the present it has been possible to study the structure of meteor showers only once, or perhaps twice, a year, when the earth crosses the shower. If it were possible to send a cosmic probe along the meteor shower orbit, with the same heliocentric velocity but in the opposite direction, this probe could continuously collect the necessary data on the density of the dust and the micrometeoroids in the stream, as a function of the distance from the parent comet and the sun during a half period of the stream. Several probes with slightly different inclinations and launched at different times could measure the function of the density inside the shower. The launch into showers with retrograde motion is somewhat easier, since smaller velocities than for directly moving showers are needed. Studies of this kind would be especially valuable for showers where the matter is not yet uniformly distributed along the whole comet orbit as, say, for the Leonids (the return of the richer part of which we are now expecting) and for Halley's comet showers. The latter case is more important, since we expect the return of Halley's comet in 1986, and by this time we shall probably have rockets efficient enough to reach the required velocity.

Let us suppose that such a probe will be launched on May 5, 1986 (the date when the earth reaches the shortest distance from the comet's orbit), first on the parking orbit, and later on the orbit with apogee 0.064 a.u. to reach the comet's orbit at the closest point. At this moment it is necessary to accelerate the probe at the geocentric velocity $0.97V$ (earth), that is, at the heliocentric velocity $1.40V$ but in the opposite direction to the comet's motion. If we suppose (according to Prof. Kempinski) that the passage of Halley's comet will be on November 18, 1986 (1986.88), the probe will then be 4 a.u. distant from the comet at the time of launch. The probe will pass the perihelion on June 13 (0.8 a.u. from the earth), and on the last day in August it will meet Halley's comet with the true anomaly 106°.7 at a distance of 1.60 a.u. from the sun and 1.56 a.u. from the earth. Later, in mid-October, the comet will approach the earth at a distance as near as 0.16 a.u., just at the beginning of the Orionids' activity. At the time of the comet's perihelion passage the probe will be 2.7 a.u. from the sun. This probe could therefore measure the dust in parts of the orbit preceding and following the comet, and elucidate some processes of disintegration of comets. Naturally the given data are only tentative, as the return orbit in 1986 is not yet precisely known. (See fig. 1.)

[1] Astronomical Institute of the Czechoslovak Academy of Sciences, Ondřejov, Czechoslovakia.

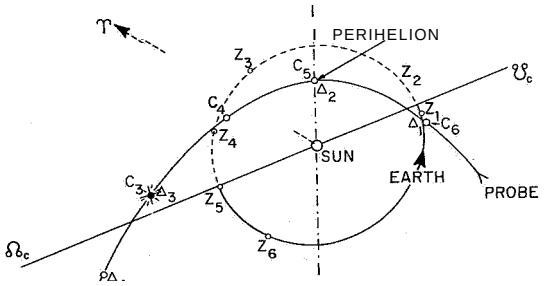

Point	Date 1986	Earth Z L	Earth Z R	Probe A v	Probe A r	Comet C v	Comet C r	Remark
1	May 5	22309	1.009	−8100	1.00	13008	3.14	launch
2	June 13	261.4	1.016	0.0	0.59	125.8	2.67	probe perihelion
3	August 31	337.0	1.009	106.7	1.60	106.7	1.60	probe meets comet
4	Oct. 19	25.0	0.996	120.7	2.28	69.4	0.86	Orionids
5	Nov. 18	55.1	0.988	125.8	2.67	0.0	0.59	comet perihelion
6	Dec. 27	94.6	0.983	130.8	3.14	−81.0	1.00	

Incidence of Meteors on the Earth Derived from Radio Observations

W. G. ELFORD [1]

1. Introduction

Radio observations of meteors have been used to investigate the incidence of meteors over a wide range of magnitudes. From hourly rate counts made with equipment operating on wavelengths between 4 and 18 m and at pulse power levels ranging from tens of kilowatts to several megawatts, data are now available on the flux of meteors between 0 and +13 mag.

Meteors are counted by radio equipment in terms of the electron density or the equivalent radio brightness (see equation (1)). A meteor trail formed within the radiation pattern of a radar system will be detected if the orientation of the trail satisfies the geometrical conditions of specular reflection and if the echo exceeds the threshold level for the system. Although the determination of meteor-echo rates is precise and objective, the brightness counts are not necessarily simply related to the total influx of meteors above a prescribed limiting brightness or to the total influx above a prescribed limiting mass. The transformation of rates to fluxes above a limiting brightness requires assumptions concerning the distribution of ionization along a meteor trail, the ablation process, and, in the case of sporadic meteors, a knowledge of the geocentric radiant distribution. Further, the extension of the transformation to determine the influx of meteors above a prescribed limiting mass requires a knowledge of the ionizing probability, a parameter still subject to considerable uncertainty. It is not surprising, therefore, that relatively few workers have attempted to reduce their rate observations to incident fluxes.

Earlier results have been summarized by Kaiser (1963), who also compared the radio results with those of optical observations. Kaiser has shown that over the magnitude range −5 to +10 the estimates of the incident flux of meteoroids capable of producing trails brighter than a given magnitude vary by about a factor of 10. The major part of this variation between estimates is almost certainly due to the difficulty in accurately allowing for the severe selection effects imposed by the various methods of observation.

In this paper we are chiefly concerned with the fluxes of meteors that produce line densities in excess of prescribed limiting values. The effect of the meteor velocity on the probability of detection is severe, and the brief discussions in sections 4 and 6 on the flux of shower and sporadic meteors in terms of a limiting value of mass have been introduced mainly to indicate the order of magnitude of the corrections.

A meteor radar system of a given wavelength has an effective height ceiling due to a combination of the effects of the initial radius of the trail and the diffusion of the ionized column on the strength of the returned echo (McEinley, 1961). A number of workers have claimed, on theoretical grounds, that the reduction in the true echo rate due to this height ceiling is severe. However, in order to make reliable corrections to the echo rates and hence to the flux estimates, we require experimental evidence concerning the magnitude of these effects. No corrections for this radio ceiling

[1] Department of Physics, University of Adelaide, Adelaide, South Australia.

240-022 O—67——9

have been attempted in the following discussions, but the problem is further examined in section 6.

It is convenient to introduce a scale of radio magnitude by the definition

$$M_R = 40 - 2.5 \log_{10} q_z, \quad (1)$$

where q_z is the zenithal line density in electrons/m. We assume that the maximum electron line density q in a trail is proportional to the cosine of the zenith angle χ of the path, so that $q_z = q/\cos \chi$.

It is of interest to note that the radio magnitude defined by equation (1) differs by only 0.6 mag from the photographic magnitude M_p, according to a recent analysis by Verniani and Hawkins (1964), who find that

$$M_p = 39.40 - 2.5 \log_{10} q_z.$$

2. Detection of meteor fluxes from radio meteor rates

In order to relate the rate of detection of meteors with a radar system to the absolute rate of influx of meteoroids into the atmosphere we must determine the fraction of the incident meteor population detectable by the radar system. The factors on which the rates of detection of meteor trails depend are: (1) the number distribution of meteors as a function of maximum electron line density, (2) the geocentric radiant distribution, (3) the distribution of ionization along the trail and the nature of the radio reflection process, and (4) the parameters of the radar system. The main sources of uncertainty arise in factors (2) and (3). These are discussed in sections 5 and 6.

The first step in solving the problem is to determine the response of the radio system to meteors from an element of the celestial sphere of unit radiant density, producing trails with line densities in excess of a prescribed limiting value. The description of the echo rate for all positions of the element in the altitude-azimuth coordinate system is termed the response function of the system. Graphical methods for determining the response function for any system have been given by Eaiser (1960, 1961a), and a computer method suitable for either coincident or spaced transmitting and receiving stations has been developed by Elford (1964). In general, the response function of any system will be a function of both elevation and azimuth of the radiant. However, for an omnidirectional antenna system such as used at Ottawa and Christchurch for surveys of meteor activity, the response function varies only in elevation.

The incident flux of meteors whose radiants lie within an element of the celestial sphere of solid angle $d\Omega$ and which produce zenithal line densities greater than q_z can be written as $N(q_z)d\Omega$. This is the flux across a plane normal to the meteor paths. It is assumed that the cumulative distribution function $N(q_z)$ can be represented by a simple power law of the form

$$N(q_z) = Kq_z^c. \quad (2)$$

Alternatively, the distribution function can be defined in terms of the number of meteors $dN(q_z)$ that produce line densities between q_z and $q_z + dq_z$. It is customary to write this incremental distribution function as a simple inverse power law with exponent s, i.e.,

$$dN(q_z) \propto q_z^{-s} dq_z. \quad (3)$$

The two exponents in equations (2) and (3) are related by the expression $c = 1 - s$. The exponent s is not constant but in general varies slowly with magnitude. Its value lies between 1.4 and 2.7. In calculating the response function of a system we usually assume a constant mean value for s (and hence for c) appropriate to that portion of the meteor population near the limiting magnitude of the system. This is justified by the fact that the radar echo rate is determined predominantly by those meteors whose radio brightness is within 2 or 3 mag of the limiting magnitude. However, it is shown later that the use of a mean value for s and c breaks down for shower meteors brighter than $+3$ mag.

For narrow-beam meteor radar systems the form of the response function is relatively insensitive to the value of c. In the case of radar systems that use antennas with broad polar diagrams, the response function can vary significantly with changes in the value of c. This is illustrated in figures 1 and 2, where the response functions for the omnidirectional

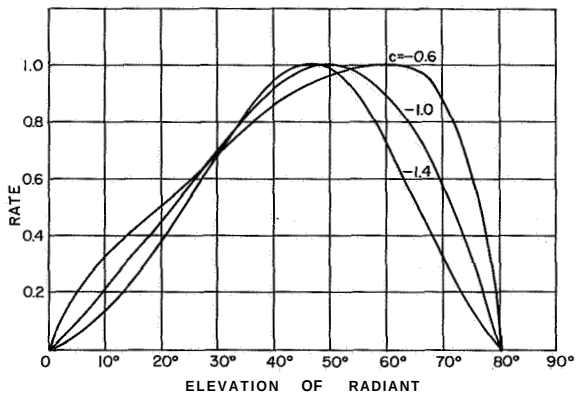

FIGURE 1.—Response functions for the 33 Mc/sec-meteor patrol radar at the Springhill Meteor Observatory, Ottawa. The functions have been calculated for several values of the exponent c in the cumulative distribution relation $N(q_z) = Kq_z^c$.

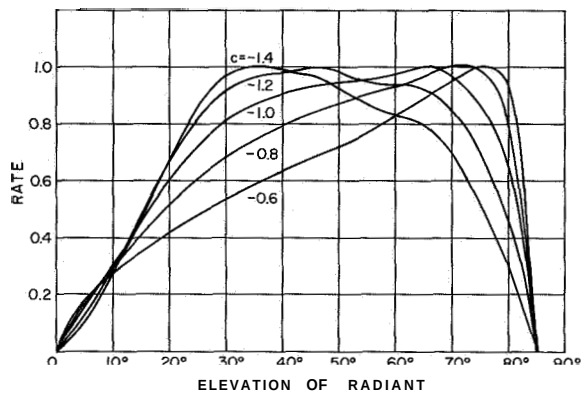

FIGURE 2.—Response functions for the 70 Mc/sec-meteor patrol radar at Christchurch, New Zealand. The functions have been calculated for several values of the exponent c in the cumulative distribution relation $N(q_z) = Kq_z^c$.

meteor radars at Ottawa (Neale, 1958) and Christchurch (Ellyett and Eeay, 1963) have been calculated for a number of possible values of c. Thus the radiant elevation at which a broad-beam system has its peak response will depend on the value of c. This effect must be taken into account when the rates of shower and sporadic meteors observed with such systems are compared.

The value of the exponents in the incremental distribution function for sporadic meteors has been estimated by various workers. From a detailed analysis of photographic meteors Hawkins and Upton (1958) obtained a value of 2.34 for sporadic meteors brighter than +4 mag. For fainter meteors the most direct method of estimating s is from a comparison of radio echo rates obtained at two different levels of transmitter power or minimum detectable signal level. The results of a number of estimates of s for sporadic meteors are summarized in figure 3. Estimates of error are available only for data marked (2), (5), and (6); it is therefore not possible to assess whether all the data are consistent. It appears, however, that there is a change in s of about 0.5 in going from meteors of 0 mag to meteors of +9 mag, and that in the magnitude range +9 to +13 the value is 2.0 ±0.05.

In the case of meteor showers the value of s has been determined only for those showers whose echo rate is such that they can readily be distinguished from the sporadic background. The distributions of maximum line density for six meteor streams have been determined by Browne et al. (1956), Weiss (1961), and Kaiser (1961b). As in the case of sporadic meteors, it was assumed that over a limited range of magnitudes the incremental distribution function could be represented by a simple inverse power law with exponent s. The combined results of these studies extend from 0 to +10 mag and are summarized in figure 4. The variation of s with magnitude is much greater than in the case of sporadic meteors, and for

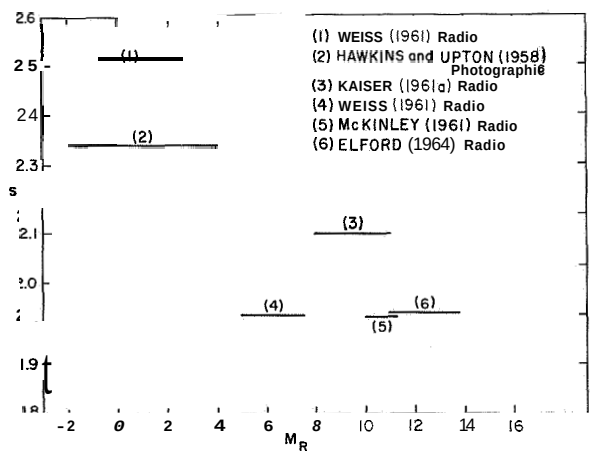

FIGURE 3.—Values of the exponent s in the incremental distribution function of sporadic meteors, determined by optical and radar methods. The length of the line indicates the range of radio magnitudes appropriate to each determination.

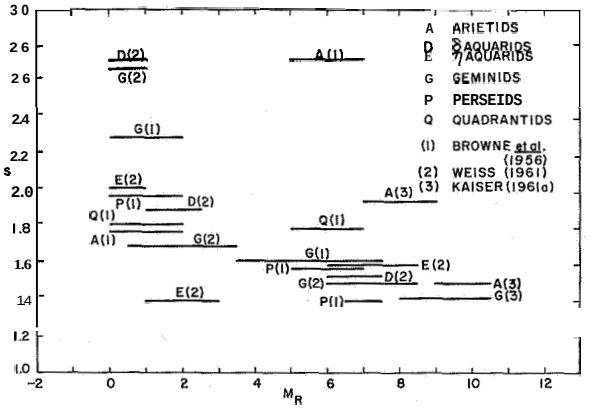

FIGURE 4.—Values of the exponent s in the incremental distribution function for six meteor showers. The length of the line indicates the range of radio magnitudes appropriate to each determination.

meteors brighter than \$3 mag the assumption of an inverse power-law distribution is clearly not justified even over a limited range of magnitudes. For the Geminid and δ-Aquarid streams the increase in s for meteors brighter than +1.5 mag is so steep that it effectively amounts to a cutoff of meteors larger than those corresponding to 0 mag. The same argument applies to the Arietid stream, which is composed mainly of meteors fainter than \$4 mag. For $M_R \geq +8$ all the showers have a value of s well below the value of 2.0 for sporadic meteors, and thus these showers must eventually become swamped by the sporadic background as the magnitude limit is extended to fainter meteors.

3. Sporadic meteor flux

Estimates of the flux of sporadic meteors that produce trails with zenithal line densities above prescribed limiting values have been made by a number of workers. Kaiser (1961a) has used sporadic meteor rates obtained with a 17 Mc/sec radar system at Sheffield to determine the sporadic flux down to a liiting line density of $5\times10^{11}\mathrm{m}^{-1}$ ($M_R=10.8$). The mean influx at this limit was estimated as $1.9\times10^{-10}\mathrm{m}^{-2}\mathrm{sec}^{-1}$, and the value of the exponent s in the distribution law was found to be 2.17 over the magnitude range +8 to +11. From observations carried out at a frequency of 27 Mc/sec at Adelaide, Weiss (1957a) estimated the sporadic flux down to a limiting line density of $10^{14}\mathrm{m}^{-1}$ as $3.8\times10^{-13}\mathrm{m}^{-2}\mathrm{sec}^{-1}$, and the value of s for meteors between +5 and +7 mag to be **2.0.** Lebedinets (1964) has discussed observations made at Eharkov with a 38 Mc/sec radar system that could detect meteors above a limiting zenithal line density of $10^{12}\mathrm{m}^{-1}$. When the estimates of the sporadic flux were extrapolated to the liiting line density of $5\times10^{11}\mathrm{m}^{-1}$ quoted by Kaiser for the Sheffield system, Lebedinets arrived at an incident flux of $2.6\times10^{-10}\mathrm{m}^{-2}\mathrm{sec}^{-1}$. This is in close agreement with the Sheffield result. A recent analysis (Elford and Hawkins, 1964) of observations carried out with the Harvard-Smithsonian 41 Mc/sec meteor radar system at Havana, Illinois, during March 1963 has extended the estimate of the flux of sporadic meteors down to a radio magnitude **of** \$13.4. The mean influx of meteors estimated from these observations was $1.0\times10^{-8}\mathrm{m}^{-2}\mathrm{sec}^{-1}$.

The various estimates of sporadic influx are shown in figure 5. There is general agreement among the results derived from the observations made at Adelaide, Kharkov, and Sheffield, which together extend over the magnitude range \$4 to +11. However, when the Harvard-Smithsonian and Sheffield results are

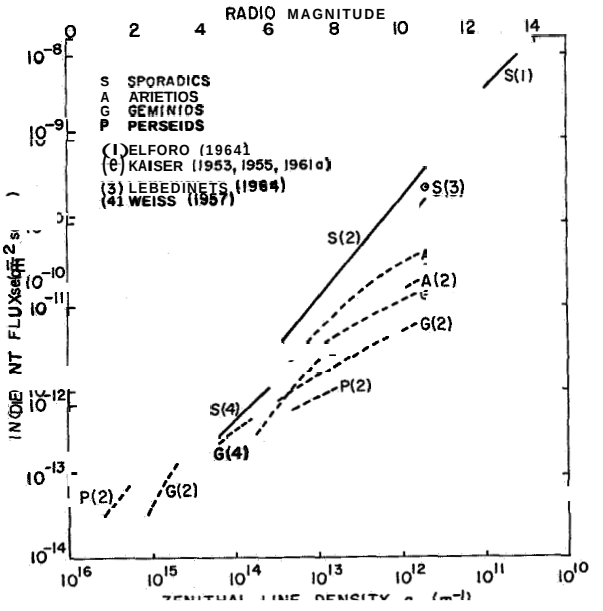

FIGURE 5.—Mean incident flux over the whole earth of meteoroids capable of producing meteors with zenithal electron line density greater than q_z. Solid lines, sporadic flux; broken lines, shower flux.

compared by extrapolating each to +11.5 mag, there is a discrepancy in the incident flux of a factor of 4, the higher flux being predicted by the observations of the fainter meteors. This discrepancy is too large to be explained by uncertainties in the radiant distribution or the response functions for the systems. Further, the single-body ablation theory predicts the reverse effect, i.e., as the radio observations are extended to fainter meteors there should be a decrease in the proportion of the meteor population detected. On the other hand, there is experimental evidence (Hawkins, 1964) that meteors fainter than +5 mag occur at progressively lower heights, an effect that has been attributed to a decrease in the degree of fragmentation of the meteoroid for meteors fainter than +5 mag. Thus the disparity between the estimates of the flux based on the 10th- and 13th-mag observations may be the result of a change in the degree of fragmentation of the meteoroids over this magnitude range.

4. Shower meteor fluxes

The incident flux for eight showers has been estimated by Weiss (1957a) for meteors with zenithal line densities in excess of $10^{14}\mathrm{m}^{-1}$, using data on hourly rates obtained at Jodrell Bank and Adelaide. From observations made at Sheffield and Jodrell Bank, Kaiser (1953, 1955, 1961a) has determined the incident flux for the three showers, Geminids, Arietids, and Perseids, over a considerable range of limiting line densities. The results of these various determinations are summarized in table 1, together with estimates of the sporadic flux made by Weiss and Kaiser. It can be seen from the table that for meteors fainter than $M_R=+5 (q=10^{14}\mathrm{m}^{-1})$ the sporadic background dominates over any of these major streams.

In order to obtain the rate of incidence of particles above a limiting mass, Weiss (1957a) applied a velocity correction of the form v^{4c}. For meteors whose mass exceeds that equivalent to a zenithal line density of $10^{14}\mathrm{m}^{-1}$ at a velocity of 60 km/sec, the three showers—Arietids, ξ Perseids, and δ Aquarids—all have a simiiar flux, which is about 40 percent of the sporadic background. In contrast, the contribution from the three high-velocity showers, Perseids, η Aquarids, and Orionids, is in each case only 1 to 2 percent of the sporadic background.

In figure 5 the variation with magnitude of the incident flux of the three showers, Arietids, Geminids, and Perseids, is compared with the variation for sporadic meteors. Here again we consider the mean flux over a sphere. The graphs emphasize the dominant role played by sporadic meteors fainter than radio magnitude +5. For meteors brighter than +10 mag sporadics outnumber any one of the three showers by a factor of 10 or more, and the trend of the graphs suggests that if the magnitude limit were +13 the sporadics would outnumber any of these showers by a factor of the order of 10^2.

Type of meteor	Flux ($\mathrm{m}^{-2}\ \mathrm{sec}^{-1}$) above limiting zenithal line density*				Reference
	$10^{15}\ \mathrm{m}^{-1}$	$10^{14}\ \mathrm{m}^{-1}$	$10^{13}\ \mathrm{m}^{-1}$	$10^{12}\ \mathrm{m}^{-1}$	
Sporadic		35×10^{-14}	56×10^{-13}	90×10^{-12}	(1), (2)
Germinid	45×10^{-15}	30×10^{-14}	12×10^{-13}	5×10^{-12}	(2)
Perseid	100×10^{-15}	15×10^{-14}	8×10^{-13}		(1), (2)
Arietid		25×10^{-14}	20×10^{-13}	13×10^{-12}	(1), (2)
Quadrantid		20×10^{-14}			(1)
ξ Perseid		18×10^{-14}			(1)
δ Aquarid		37×10^{-14}			(1)
η Aquarid		18×10^{-14}			(1)
Orionid		23×10^{-14}			(1)

*To facilitate comparison between shower and sporadic fluxes the values for the former are given as the mean flux over a sphere (i.e., one-quarter of the flux through a plane normal to the radiant direction).

References: (1) Weiss (1957a), (2) Kaiser (1953, 1955, 1961a).

It should be noted that the ratios of sporadic-to-shower fluxes discussed above refer to the total sporadic flux compared to the flux of an individual shower. The ratio of the total incidence per year of sporadic meteors to the total incidence per year of shower meteors will depend on the number of meteor showers per year and their strength and duration. An objective method of defining a meteor stream in terms of the degree of similarity of meteor orbits has been developed by Southworth and Hawkins (1963), and has been applied to 3000 orbits determined from observations made with the Harvard-Smithsonian meteor radar system during the period January to August 1962 (Hawkins, Southworth, and Rosenthal, 1964). The radio magnitude limit for these orbital data was estimated as +11. It was found that 24 percent of the orbits associated into streams (value of association parameter $D=0.1$). A somewhat similar analysis (Nilsson, 1964) has been carried out on 2200 orbits determined from observations of meteors brighter than +6 mag, made at Adelaide during 1961. From an examination of real and chance associations of orbits Nilsson concluded that 17 percent of the total orbits could be classed as definite streams, while a further 8 percent could probably be classed as members of minor streams. An examination of Nilsson's data using the method of Southworth and Hawkins (Elford; unpublished) gave essentially the same result as obtained by Nilsson if the association parameter D was chosen as 0.10 to 0.15. It would thus appear that over the radio magnitude range +6 to +12.5 the ratio of the total annual incidence of sporadic-to-shower meteors is about 3:1.

For meteors brighter than visual magnitude +5, Hawkins (1964) has stated that approximately 50 percent of the meteor flux comes from the major and minor streams. If the stream activity is defined in terms of the sporadic rate by the expression $N_s=kN \cos \chi$, where N_s is the shower rate, N the sporadic rate, and χ the zenith distance of the shower radiant, Hawkins gives values of k as high as 5.5.

Eeay and Ellyett (1961) have pointed out that hourly rates obtained from radio observations of meteor showers are strongly dependent on the geographical latitude of the observing station and, in general, do not give a reliable indication of the relative fluxes from different meteor showers. They have developed a simple method of determining the relative significance of meteor showers, and have shown that when applied to the shower rates determined at Adelaide, Christchurch, and Jodrell Bank, there is general agreement concerning the relative strengths of showers. They find that the δ-Aquarid shower is the strongest of the regular meteor showers.

The latitude variation in optical observations of 24 meteor showers has been investigated by Kresák (1964), who has determined the relative number of meteors from a given shower that penetrate the atmosphere at different geographic latitudes. The proportion of these that can be observed optically has also been determined. It is of interest to note that the fractional influx into the equatorial zone ($\pm 10°$ latitude) for 17 of the 24 major showers varies by only ± 4 percent. Only those showers with radiants of high declination show a distinct deficiency at the equator, and even among these the effect of zenithal attraction on showers with low geocentric velocity can partially compensate for the high declination.

5. Annual variation in the incidence of meteors on the earth

The daily echo rate of meteors observed at any point on the earth's surface varies throughout the year. Observations carried out at mid-northern latitudes (Hawkins, 1956; Vogan and Campbell, 1957; Evans, 1960; Millman and McIntosh, 1963) have shown that the daily echo rate has a maximum between June and September and a minimum during February and March. In the Southern Hemisphere the daily echo rate, as determined at Christchurch, 43°.5 S (Ellyett and Keay, 1961), and at Adelaide, 35° S (Weiss, 1957b), has a maximum in December and a minimum between June and September. Some features of these annual variations in daily rate can be explained by the occurrence of the major meteor showers. However, even when the effect of the major showers is removed, Hawkins (1956) and Weiss (1957b) have shown that there remains a significant annual variation.

It is generally accepted that the radiants of sporadic meteors are concentrated in a number of groups. For meteors brighter than $M_R \sim 6$ three groups lying on the ecliptic are recognized, one at the apex and two centered on points lying about 70° in longitude from the apex (Hawkins, 1956; Weiss and Smith, 1960; Davies and **Gill,** 1960). The last two groups, generally referred to as the sun and antisun groups, have diameters—60' to 70'. At fainter magnitudes there is increased activity from regions lying about 60° north and south of the apex (Davies and **Gill,** 1960; Hawkins, 1962). **For** 10th- to 12th-mag meteors the average strength of this high-latitude activity is about **50** percent of the sun and antisun concentrations (Elford, Hawkins, and Southworth, 1964).

Over a period of 1 year the declinations of the various sources **of** sporadic radiants, as viewed from one locality, vary in a cyclic manner, and it would be expected that the observed echo rate would be a maximum when the apex lies highest in the sky, that is, during March in the Southern Hemisphere and during September in the Northern. The observed rates for the Northern Hemisphere in general follow this pattern. However, the Southern Hemisphere observations contradict the expected annual variation. Weiss (1957b) interpreted these facts to mean that there is a real variation in the space density of meteors around the earth's orbit, and he derived an annual variation in relative density that was very similar to the results **of** telescopic studies of meteors by Kresáková and Kresák (1955). These results indicated that the incidence of meteors on the earth during the second half of the year is about **50** percent greater than during the first half.

This variability in the space density of meteors encountered by the earth during the course of the year has been confirmed by precise hourly rate observations carried out over a period of 1 year at Christchurch, 43°.5 S (Ellyett and Eeay, 1963; Keay, 1963). These observations were made with a 70-Mc/sec-wide aperture system that could detect meteors down to +8.2 mag. The response function for this system has already been discussed and is given in figure 2. From a comparison of the observed echo rate and the expected echo rate based on a triple-source radiant distribution (apex, sun, and antisun), Eeay (1963) has shown that the increase in meteor **flux** in the second half of the year is due primarily to an increase in the strength of the antisun group and, to a lesser extent, to an increase in the strength of the apex group. The strength of the sun group remains essentially constant throughout the year. In a recent investigation of meteor streams based on measurements made at Adelaide (35° S) of orbits of meteors of +6 mag **or** brighter, Nilsson (1964) has shown that the antisun group predominates during the 6 months July to December, in agreement with the conclusion reached by Eeay for somewhat fainter meteors. Moreover, as shown in figure 6, the predominance of the antisun group during these months is due to a large number of **minor** streams through which the earth passes during the second half **of** the year. When meteors that are members of these streams are removed, the strengths

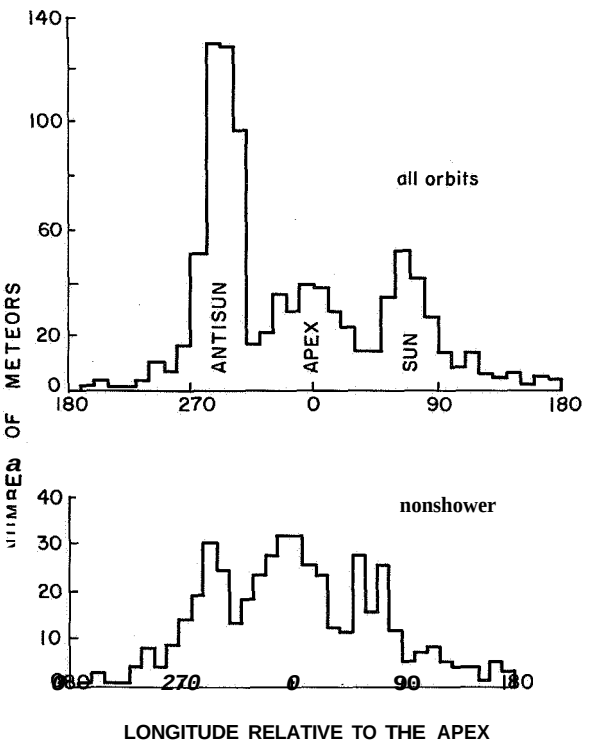

FIGURE 6.—The distribution of meteors with ecliptic longitude as observed at Adelaide (35° S) for 4 months, July–October 1961 (Nilsson, 1964).

of the sun and antisun groups over this period are essentially the same. If it is assumed that there is no marked change in the radiant distribution as the limiting magnitude is lowered from \$6 to +8, the increase in the incidence of meteors of \$8 mag or brighter during the second half of the year is most likely due to the occurrence of a large number of unresolved meteor showers.

Additional evidence for the presence of minor showers during the second half of the year comes from the results of an extensive investigation of hourly echo rates carried out at the Springhill Meteor Observatory, Ottawa (45° N) over a period of 5 years 1958 to 1962 (Millman and McIntosh, 1963). These observations were made with a 33-Mc/sec-wide aperture system omnidirectional in azimuth. The response function for this system has already been given in figure 1. There is no published information on the minimum signal that can be detected with this equipment, but, if it is assumed that the equipment will just detect a signal equal to the average cosmic noise, it is estimated that the radio brightness threshold for the equipment is \$7.5. This is very close to the threshold level for the Christchurch equipment. Thus it appears that the two precise echo-rate surveys carried out at Ottawa and Christchurch have investigated essentially the same portions of the meteor population. Further, these two surveys have been made from two points almost equally spaced either side of the equator, 45° N and 43°.5 S. In publishing the statistics of the survey, Millman and McIntosh have compared the daily rate of all echoes with the daily rate of echoes with duration greater than 8 sec. The percentage of echoes with durations ≥ 8 sec shows strong correlation with the major meteor showers, the percentage for the Perseids and Geminids rising to as much as 10 percent compared with a nonshower value of 1 to 2 percent. It is of interest to note that the average value of the percentage of long-duration echoes during February and March is 1.22 ± 0.20 percent, and the average value during September and the first half of October is 1.76f0.20 percent. If it is assumed that the percentage of long-duration echoes is an index of meteor shower activity, this result adds weight to the suggestion made earlier that during the second half of the year the earth passes through a large number of minor meteor streams.

Since the Christchurch and Ottawa surveys refer to essentially the same portion of meteor population, it is of interest to compare the meteor influx deduced from the two sets of observations. The average meteor influx for each month of the year has been determined from the Ottawa hourly rate data by a comparison of the observed diurnal rates with those predicted when the radiant distribution is approximated by a triple-source model and the response function is that given in figure 1 for $c = -1.0$. The three sources, each of diameter 65°, were centered on the ecliptic, one at the apex and the other two at points $\pm 70°$ from the apex. The relative strengths of the sources and the uniform background were adjusted to give the best match between the predicted and the observed diurnal rates. Using a similar procedure, Keay (1963) has deduced the average meteor flux for each month of the year from the Christchurch data. The radiant-distribution model assumed by Keay consisted of three point sources on the ecliptic and a uniform background. The strength and position of the sources were as follows: Source of strength 1 unit at the apex, two sources each of strength 2 units at points $\pm 60°$ from the apex, a uniform background of integrated strength 1 unit. The results are shown in figure 7 together

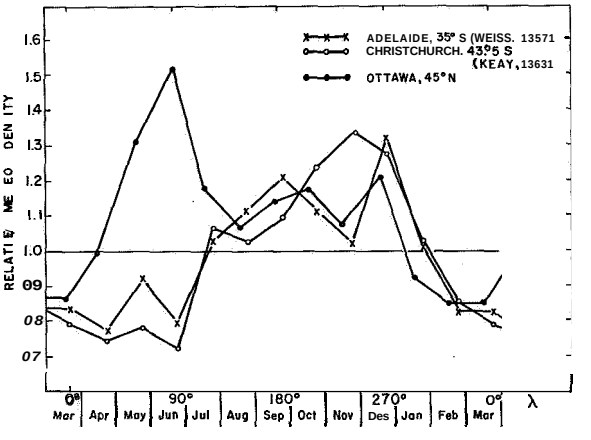

FIGURE 7.—The incidence of meteors on the earth as a function of ecliptic longitude; observed at mid-northern and mid-southern latitudes.

with an earlier result obtained by Weiss (1957b) from observations made at Adelaide. No attempt was made to remove the effect of meteor showers from the original rate data for either Christchurch or Ottawa. Keay justified this approach for the Christchurch data on the basis that for wide-aperture systems the ratio of shower to sporadic rates is greatly decreased as compared with observations made when narrow-beam antennas are used, and that faint shower meteors are swamped by the sporadic background. However, the Ottawa observations (Millman and McIntosh, 1963) do not support the latter contention. During May and June the echo rate from the daytime streams is comparable to the sporadic rate, and as a result the flux estimates based on the Ottawa data show an anomalous peak in June. The absence of a similar peak in the Christchurch result is due to the fact that the response functions of the Ottawa and Christchurch systems for shower meteors ($c=-0.4$ to -0.6) are markedly different from the response functions for sporadic meteors ($c=-1.0$). As a consequence, the probability of detecting Arietid and ζ-Perseid meteors at Ottawa is enhanced compared with sporadics, while the reverse is true at Christchurch.

With the exception of the 3 months, April, May, and June, there is good agreement between the three estimates of the relative meteor influx throughout the year as shown in figure 7. It is therefore of interest to compare the absolute values of the meteor flux determined from the Ottawa and Christchurch data. This has been carried out for the month of March 1960. The limiting zenithal line density of the Ottawa system was estimated by assuming that the minimum detectable echo power was 7.0×10^{-14} watts. This gave a limiting density of $8.9\times10^{12}\mathrm{m}^{-1}$, or radio magnitude $+7.5$. The incident flux was determined from a comparison of observed and predicted diurnal rates with the use of the triple-source radiant distribution discussed earlier. It was assumed that all trails were uniform in electron density along their length and that the difference in heights between the beginning and the end of the trails was 6 km. A similar analysis was carried out with the Christchurch data, and the results are shown in table 2. The Christchurch result is very close to the previous estimates shown in figure 5, but the Ottawa result is a factor of 2 higher. Since the response functions for these two systems can be calculated accurately and the assumed model radiant distribution is the same for the two calculations, this discrepancy between the two estimates of flux reflects either an incorrect estimate of the limiting zenithal line density for the Ottawa system or the failure to account properly for the effect of wavelength on the echo rate. This point should be examined further when the actual value of the minimum detectable echo power for the Ottawa system is known.[2]

TABLE 2.—*Sporadic* meteor *flux*

Station	λ (m)	Limiting q_z	Limiting M_R	Flux (m^{-2} sec^{-1}) (March 1960)
Ottawa, 45° N	9.2	8.9×10^{12}	+7.5	1.25×10^{-11}
Christchurch, 43°.5 S	4.3	5.1×10^{12}	+8.2	1.08×10^{-11}

In comparing measurements of meteor flux made by different workers at different times one should note that the maximum in the diurnal echo rate averaged over 1 month can show year-to-year variations of as much as 50 percent (Millman and McIntosh, 1963; Ellyett and Keay, 1964; McIntosh and Millman, 1964).

6. Selection effects due to meteor velocity, trail diameter, and diffusion

Estimates of meteor fluxes down to a given limiting mass from radio echo-rate data are subject to considerable error due to the severe selection effect of velocity and to uncertainties in the dependence of the ionizing probability β on velocity. In a recent review of the ionizing efficiency of meteors, Verniani and Hawkins (1964) conclude that $\beta\propto v^{4.0}$ with an uncertainty in the exponent of about ±0.5. A velocity correction of v^4 was applied to shower fluxes by Weiss (1957a), and it was shown in section 4 that this greatly reduces the significance of the high-velocity showers.

[2] Recently B. A. McIntosh (private communication) has pointed out that the minimum detectable echo power for the Ottawa system is probably closer to 2×10^{-14} watts. This would bring the Ottawa and Christchurch fluxes into closer agreement.

Recently (Elford, Hawkins, and Southworth, 1964), an estimate has been made of the mass limit for sporadic meteors observed in March 1963 with the Harvard-Smithsonian meteor radar system. From the observed velocity distribution and the value of the ionizing probability given by Verniani and Hawkins, it was estimated that the flux of sporadic meteors with mass greater than 1.3×10^{-6} g is $1.0\times10^{-8}m^{-2}$ sec^{-1}.

The effect of diffusion and finite initial trail radius on the radar echo rate of meteors has been discussed by a number of workers (Peregudov, 1958; Fialko, 1960; Greenhow and Hall, 1960; Lebedinets, 1964), who have predicted that equipment operating on short wavelengths (<10 m) will detect only a fraction of the meteor population. Lebedinets estimates that for equipment operating on a wavelength of 8 m and at an effective minimum detectable line density of $10^{12}m^{-1}$, the true sporadic rate is about a factor of 30 greater than the observed echo rate. Greenhow and Hall (1960) estimate that the percentage of the true influx of meteors detected by a radio system varies from 1.5 at 4-m wavelength to 40 at 17 m. However, the estimates of sporadic flux discussed in section 5, which have been derived from observations at frequencies of 70, 38, and 17 Mc/sec, do not differ by more than a factor of 2 to 4. The lack of agreement between the predicted and the observed variations in rate as a function of wavelength has been attributed to the effect of a decrease in fragmentation among meteors fainter than +5 mag (Hawkins, 1964).

References

BROWNE, I. C.; BULLOUGH, K.; EVANS, S.; and KAISER, T. R.
1956. Characteristics of radio echoes from meteor trails, II: The distribution of meteor magnitudes and masses. Proc. Phys. Soc. London, vol. 69B, pp. 83–97.

DAVIES, J. G., and GILL, J. C.
1960. Radio echo measurements of the orbits of faint sporadic meteors. Monthly Notices Roy. Astron. Soc., vol. 121, pp. 437–462.

ELFORD, W. G.
1964. Calculation of the response function of the Harvard Radio Meteor Project Radar System. Harvard Radio Meteor Project Res. Rep., no. 8.

ELFORD, W. G., and HAWKINS, G. S.
1964. Meteor echo rates and the flux of sporadic meteors. Harvard Radio Meteor Project Res. Rep., no. 9.

ELFORD, W. G.; HAWKINS, G. S.; and SOUTHWORTH, R. B.
1964. The distribution of sporadic meteor radiants. Harvard Radio Meteor Project Res. Rep., no. 11.

ELLYETT, C., and KEAY, C. S. L.
1961. All-sky meteor rates in the Southern Hemisphere. Journ. Geophys. Res., vol. 66, pp. 2590–2591.
1963. Southern Hemisphere meteor rates. Monthly Notices Roy. Astron. Soc., vol. 125, pp. 325–346.
1964. Meteors: An unexpected increase in 1963. Science, vol. 146, p. 1458.

EVANS, G. C.
1960. Radio echo observations of meteor activity between 1954 December and 1958 December. Astron. Contr. Univ. Manchester (1), Jodrell Bank Ann., vol. 1, pp. 280–337.

FIALKO, E. I.
1960. The dependence of the mean hourly rates of recorded meteors on the parameters of meteoroids, the atmosphere, and the radar system. Sov. Astron.—AJ., vol. 4, pp. 711–721.

GREENHOW, J. S., and HALL, J. E.
1960. The importance of initial trail radius on the apparent height and number distributions of meteor echoes. Monthly Notices Roy. Astron. Soc., vol. 121, pp. 183–196.

HAWKINS, G. S.
1956. A radio echo survey of sporadic meteor radiants. Monthly Notices Roy. Astron. Soc., vol. 116, pp. 92–104.
1962. Radar determination of meteor orbits. Astron. Journ., vol. 67, pp. 241–244.
1964. Interplanetary debris near the earth. Ann. Rev. Astron. Astrophys., vol. 2, pp. 149–164.

HAWKINS, G. S.; SOUTHWORTH, R. B.; and ROSENTHAL, S.
1964. Preliminary analysis of meteor radiants and orbits. Harvard Radio Meteor Project Res. Rep., no. 7.

HAWKINS, G. S., and UPTON, E. K. L.
1958. The influx rate of meteors in the earth's atmosphere. Astrophys. Journ., vol. 128, pp. 727–735.

KAISER, T. R.
1953. Radio echo studies of meteor ionization. Adv. Phys., Phil. Mag. Suppl., vol. 2, pp. 495–544.
1955. The incident flux of meteors and the total meteoric ionization. In Meteors, ed. by T. Kaiser, Pergamon Press, New York, pp. 119–130.

KAISER, T. R.—Continued
1960. The determination of the incident flux of radio-meteors. Monthly Notices Roy. Astron. Soc., vol. 121, pp. 284–298.
1961a. The determination of the incident flux of radio-meteors, II: Sporadic meteors. Monthly Notices Roy. Astron. Soc., vol. 123, pp. 265–271.
1961b. The incidence of interplanetary dust. Ann. Geophys., vol. 17, pp. 50–59.
1963. Meteors and the abundance of interplanetary matter. Space Sci. Rev., vol. 1, pp. 554–575.

KEAY, C. S. L.
1963. The distribution of meteors around the earth's orbit. Monthly Notices Roy. Astron. Soc., vol. 126, pp. 165–176.

KEAY, C. S. L., and ELLYETT, C. D.
1961. The latitude dependence of radar meteor shower observations. Journ. Geophys. Res., vol. 66, pp. 2337–2343.

KRESÁK, Ľ.
1964. The latitude variation of the meteor shower influx. Bull. Astron. Inst. Czechoslovakia, vol. 15, no. 2, pp. 53–62.

KRESÁKOVÁ, M., and KRESÁK, L.
1955. On the activity of telescopic meteors and some related problems. Contr. Astron. Obs. Skalnaté Pleso, vol. 1, pp. 40–77.

LEBEDINETS, V. N.
1964. Density of meteoric matter in the vicinity of the earth's orbit, from radar observations of meteors. Sov. Astron.—AJ, vol. 7, pp. 549–558.

MCINTOSH, B. A., and MILLMAN, P. M.
1964. Radar meteor counts: Anomalous increase during 1963. Science, vol. 146, p. 1457.

MCKINLEY, D. W. R.
1961. Meteor Science and Engineering. McGraw-Hill Book Co., New York, 309 pp.

MILLMAN, P. M., and MCINTOSH, B. A.
1963. A preliminary report on radar meteor counts. *In* Proceedings of the Symposium on the Astronomy and Physics of Meteors. Smithsonian Contr. Astrophys., vol. 7, pp. 45–51.

NEALE, M. J.
1958. A low-power continuously-operating meteor radar. Bull. R. and E. E. Div. Nat. Res. Counc. Canada, vol. 8, no. 3.

NILSSON, C. S.
1964. A Southern Hemisphere radio survey of meteor streams. Australian Journ. Phys., vol. 17, pp. 205–256.

PEREGUDOV, F. I.
1958. On the effect of meteor velocities on the hour number in radio-echo detection of meteors. Sov. Astron.—AJ, vol. 2, pp. 833–838.

SOUTHWORTH, R. B., and HAWKINS, G. S.
1963. Statistics of meteor streams. *In* Proceedings of the Sympasium on the Astronomy and Physics of Meteors. Smithsonian Contr. Astrophya., vol. 7, pp. 261–285.

VERNIANI, F., and HAWKINS, G. S.
1964. On the ionizing efficiency of meteors. Astrophys. Journ., vol. 140, pp. 1590–1600.

VOGAN, E. L., and CAMPBELL, L. L.
1957. Meteor signal rates observed in forward-scatter. Canadian Journ. Phys., vol. 35, pp. 1176–1189.

WEISS, A. A.
1957a. The incidence of meteor particles upon the earth. Australian Journ. Phys., vol. 10, pp. 397–411.
1957b. The distribution of the orbits of sporadic meteors. Australian Journ. Phys., vol. 10, pp. 77–102.
1961. The distribution of meteor masses for sporadic meteors and three showers. Australian Journ. Phys., vol. 14, pp. 102–119.

WEISS, A. A., and SMITH, J. W.
1960. Southern Hemisphere survey of the radiants of sporadic meteors. Monthly Notices Roy. Astron. Soc., vol. 121, pp. 5–16.

Abstract

Published estimates of the average flux over the earth of meteors with line densities in excess of prescribed limiting values are compared. The results for sporadic meteors are shown to be consistent within a factor of 2 over the radio magnitude range 0 to +10 and within a factor of 4 between radio magnitude +10 and +13.5. The annual variation in flux is deduced from the precise echo-rate observations made at Ottawa (45° N) and compared with the annual variation determined from a similar survey at Christchurch (43°.5 S). The 40 to 50 percent increase in the incidence of meteors during the second half of the year is confirmed. The results of a Southern-Hemisphere orbit survey suggest that this increase is due to a large number of minor showers.

For meteors fainter than +5 mag the sporadic flux dominates over any of the major showers, a sporadic/shower ratio of 10:1 being typical for 10th-mag meteors. However, over the range +6 to +12 mag the integrated flux of all shower meteors is about 30 percent of the sporadic flux.

The reduction from electron density to mass is still subject to considerable uncertainty. A preliminary study of 13th-mag meteors suggests that the flux of sporadics with mass greater than 1.3×10^{-6} g is 1.0×10^{-8} $m^{-2}sec^{-1}$.

Radar Observations of Meteor Deceleration

J. V. EVANS [1]

Introduction

In a previous paper (hereafter referred to as paper 1) Evans (1965) has described observations of sporadic and shower meteors at a radar wavelength of 68 cm. In these measurements the meteors were seen when traversing the antenna beam at right angles. The mean rate of sporadic meteors observed per hour at night was 40, and for shower meteors the hourly rates occasionally rose to well over 100. In view of these high rates it was considered possible that, by directing the antenna at the radiant point of a strong shower, a small number of meteors might be seen approaching the radar directly down the beam. This was successfully accomplished during the 1961 Geminid and Perseid and the 1962 Quadrantid showers, and very precise determinations of velocity and deceleration were achieved.

In this paper we review briefly the theory for the behavior of the velocity of a meteor when it encounters atmospheric drag. In subsequent sections the experimental observations are presented and a comparison made between theory and experiment.

Theory

Contributions to the theory of the deceleration of a meteor in the earth's atmosphere have been made by a number of authors over the last 40 years. Contemporary reviews of this work have been given by Whipple (1943), Hawkins and Southworth (1958), Whipple and Hawkins (1959), McKinley (1961), and Verniani (1961). The most useful treatise on the whole subject is that by Öpik (1958). In view of this large body of literature we will not do more than outline the development of the basic equations in this paper.

The physical assumptions employed in the derivation of an expression for the deceleration are as follows. It is generally assumed that the dimensions of the meteoroid are small compared with the mean free path of the air molecules. At a height of 100 km the mean free path λ in the air is 16 cm (U.S. Standard Atmosphere, 1962), and since most meteors probably have dimensions measured in millimeters, this assumption is almost certainly valid. At a 80-km height, however, λ has become 0.40 cm and this assumption probably no longer holds. The air molecules impinging on the surface of the meteor do so individually, and if the mean free path is very much larger than the size of the meteoroid no air cap will be formed. If the mean free path becomes comparable with the dimensions of the meteoroid then air molecules that have collided with the advancing meteor cannot escape freely. Instead, they suffer a collision with other air molecules before they have traveled far from the meteor. Thus, air becomes trapped in front of the meteoroid and this reduces the rate of heating of the meteor. It is probable that cap formation commences in the middle of the meteor region. This complication is ignored in many reviews and, of those listed, only Öpik (1958) has treated the problem in detail.

The next assumption that is widely made concerns the mechanics of the impact of the air molecules. It seems probable that most of the air molecules are occluded onto the surface of the meteor and liberated a short time later.

[1] Lincoln Laboratory (operated with support from the U.S. Air Force), Massachusetts Institute of Teohnology, Lexington, Mass.

Most theories simply assume that the collisions are largely inelastic and, on the average, the angle through which the air molecule will be scattered is that of specular reflection. During 1 sec the meteor will encounter a total air mass of up, where σ is the physical cross section of the meteor, ρ the air density, and v the meteor velocity. Because it is widely thought that the collisions are mostly inelastic, an amount of kinetic energy $\frac{1}{2}\sigma\rho v^3$ is given up by the meteor each second, and some fraction A of this goes toward heating the meteor. The quantity A is called the heat-transfer coefficient and is the net coefficient of transfer, i.e., the difference between the kinetic transfer and the loss through radiation and sputtering.

The heat given to the meteoroid is usually presumed to be distributed initially only over the surface. Thus the heat is assumed to be expended in vaporizing the surface layers and not in heating the meteor as a whole. If ℓ is the heat of ablation (the heat required to ablate 1 g of the material), then from conservation of energy it follows that

$$\ell\frac{dm}{dt}=-\frac{1}{2}\Lambda\sigma\rho v^3, \tag{1}$$

where dm/dt is the rate of loss of mass by the meteor. The velocity v is, of course, not constant. However, since $v\propto(dm/dt)^{1/3}$, v may be taken as constant until a very large fraction of the meteor mass has been ablated. Equation (1) is generally known as the mass equation.

A second equation of importance can be obtained by considering conservation of momentum. The momentum given in unit time to the air molecules in completely inelastic collisions would be the air mass ($\sigma\rho v$) times the velocity (v), i.e., $\sigma\rho v^2$. However, the final velocity of the air molecules may be somewhat less than v, and hence the meteor momentum destroyed per unit time can be written as $\gamma\rho\sigma v^2$, where γ is a dimensionless drag coefficient. Hence, we have

$$m\frac{dv}{dt}=-\gamma\rho\sigma v^2. \tag{2}$$

This is the drag equation. The meteor height will change at a rate $dh/dt=v\cos\chi$ km/sec, where χ is the angle between the meteor path and the zenith, and h is the height. It follows that (2) can be written

$$\frac{dv}{dh}=-\frac{v\gamma\rho\sigma\sec\chi}{m}. \tag{3}$$

The observations of the deceleration of the meteors presented in later sections give v, dv/dh, and sec χ as functions of time. Thus, provided that γ can be estimated theoretically, the variation of $\sigma\rho/m$ as a function of time can be obtained.

By combining the drag and the mass equations we obtain

$$\frac{1}{2\xi}vdv=\frac{dm}{m}, \tag{4}$$

where $\xi=\gamma\ell/\Lambda$ is the effective ablation energy for unit mass. The observations described here permit the value of this constant to be estimated. By integrating (4) we obtain

$$m=m_\infty\exp\left[\frac{v^2-v_\infty^2}{4\xi}\right], \tag{5}$$

where v_∞ and m_∞ are the initial velocity and mass of the meteor, respectively. This has a solution

$$v=v_\infty\left[1+\frac{12\xi}{v_\infty^2}\ln\left(\frac{1-\rho}{3\rho_{\max}}\right)\right]^{1/2}, \tag{6}$$

where $\rho_{\max}$ is the atmospheric density at the height of maximum ablation rate. We shall not continue the development of the various other possible equations, as these may all be found in the paper by Verniani (1961). Equations (5) and (6) are only approximately correct. Verniani (1961) shows that an exact value for the velocity can be obtained by solving

$$\rho=\frac{2}{3}\frac{\delta g r_\infty}{\gamma F}\cos\chi\exp\left[\frac{-v_\infty^2}{12\xi}\right]\cdot\left[E\left(\frac{v_\infty^2}{12\xi}\right)-E\left(\frac{v^2}{12\xi}\right)\right], \tag{7}$$

where δ is the density of the meteoroid, g is the acceleration due to gravity, $E(x)$ indicates the logarithmic integral, and F is a shape factor employed by Verniani and defined by

$$\sigma=F\pi r^2, \tag{8}$$

where r is the equivalent radius of the meteor.

The difference between the solution of (7) for a meteor with initial velocity v_∞=40 km/sec and equation (6) is illustrated in figure 1; the difference in the behavior of the equivalent radius r for the two solutions is illustrated in figure 2.

In equation (3) we developed an expression containing the meteor mass m and cross section. The mass m depends upon both the size and the density of the meteor, whereas the cross section σ depends upon the shape and the size. One of these variables can be removed if assumptions are made concerning the shape of the meteor. Thus, Öpik (1958) introduces the equivalent radius r defined in

$$m=\frac{4}{3}\pi r^3\delta, \tag{9}$$

where δ is the meteor density. The cross section may then be expressed as

$$\sigma=4J\pi r^2, \tag{10}$$

where J is a shape factor that would have a value of 0.25 if the particle were in fact a sphere. For an average solid meteoroid of not-too-unusual shape, Öpik adopts a value

$$J=0.5\pm0.1. \tag{11}$$

We also need to know the drag coefficient y in equation (3). Öpik (1958) adopts a value

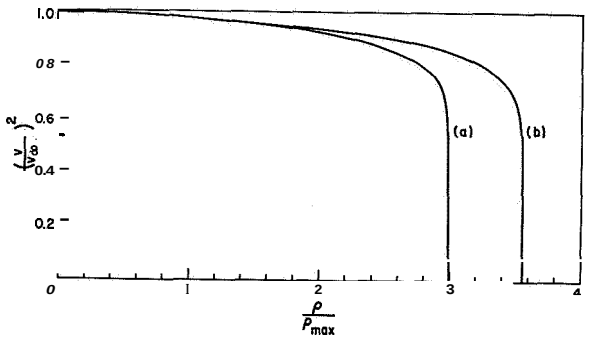

FIGURE 1.—Theoretical variation of velocity of a meteor with initial velocity 40 km/sec as a function of atmospheric density ρ normalized to density ρ_{max} at point of maximum ablation rate: a, the approximate solution of equation (6); b, the full solution of equation (7), after Verniani (1961).

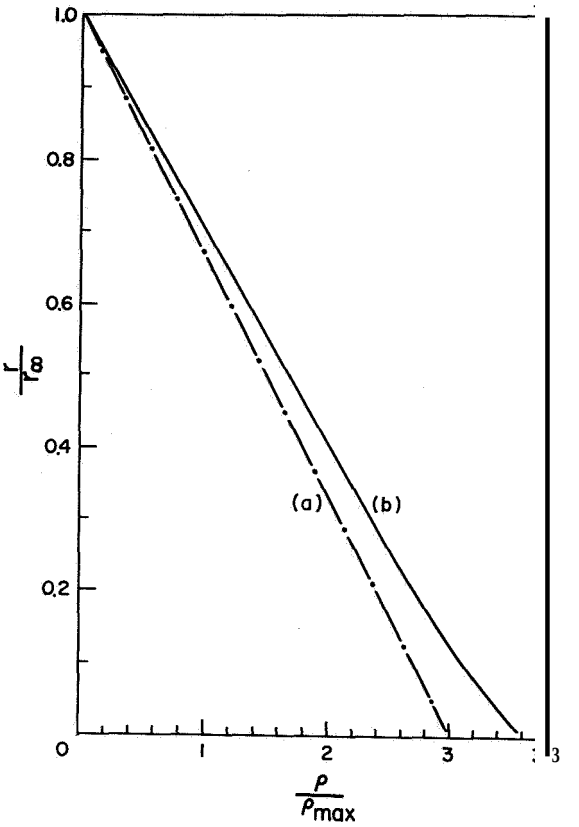

FIGURE 2.—Theoretical variation of equivalent meteor radius r as a function of atmospheric density ρ: a, the approximate solution given in equation (21); b, the more rigorous solution (Verniani, 1961).

of unity for small meteors in which no air cap is formed. Thus, the product $\gamma\sigma$ becomes

$$\gamma\sigma=2\pi r^2=6.28r^2. \tag{12}$$

We have adopted this value in the calculations that follow. We note, however, that different assumptions have been made by Hawkins and Southworth (1958), Whipple and Hawkins (1959), and McKinley (1961); the last has followed the formulation of Whipple and Hawkins. In this treatment the cross section of a sphere is written as

$$\sigma=\left(\frac{9\pi}{16}\right)^{1/3}\delta^{-2/3}m^{2/3}, \tag{13}$$

thereby removing the equivalent radius r as one of the parameters. Any object other than a sphere has a cross section that may be written

$$\sigma=A\delta^{-2/3}m^{2/3}, \tag{14}$$

where **A** is a dimensionless shape factor having a value $(9\pi/16)^{1/3}(=1.2)$ for a sphere. For a cube entering the atmosphere face on, $A=1.0$; for a cube with one edge leading, **A= 1.4.** When a cube moves with one corner leading, $A=2.5$. Thus, there is a very approximate relationship between the shape factor J used by Öpik and **A,** namely, $J\sim A/4$.

The drag coefficient γ will have a value of **1.0** for free molecular flow, but will be reduced to about **0.4** when an air cap is completely formed. Whipple and Hawkins (1959), therefore, favor values of $A>1$ and $\gamma<1$ and consequently adopt for an average value, $\gamma A=1.0$. (Jacchia **(1955)** employed **1.0** for the value of the product $\gamma A\delta^{-2/3}$.) Thus, from (14), according to Whipple and Hawkins (1959), we have

$$\gamma\sigma=\delta^{-2/3}m^{2/3}. \tag{15}$$

When expressed in terms of Öpik's equivalent radius r, **(15)** yields

$$\gamma\sigma=\left(\frac{4\pi}{3}\right)^{2/3}r^2=2.6r^2. \tag{16}$$

We see then that Öpik's value for $\gamma\sigma$ is **—2.4** times that suggested by Whipple and Hawkins **(1959).**

Combining equations (3), (10), and **(11)** we obtain (following Öpik)

$$\frac{dv}{dh}=\frac{3}{2}\frac{1}{\delta}\left(\frac{v\rho\sec\chi}{r}\right)_h, \tag{17}$$

in which all the quantities in parentheses are functions of height. It follows that if dv/dh, ρ, sec χ, and v are known, we may obtain $r\delta$ as a function of height. Had we chosen to follow Whipple and Hawkins (1959), the values of $r\delta$ would be uniformly reduced by **2.4.**

Observations

The equipment has been described in some detail in paper **1.** During the operations described here, in which a search was made for meteors traveling along radial paths toward the radar, the receiver must be detuned from the transmitter frequency (by as much as **179** kcps in the case of the Perseids). This is required in order to bring the center filter of the receiver filter bank to the expected doppler-shifted frequency of an approaching meteor for the particular shower being odserved.

During the course of the **1961** Geminids, attempts were fist made to observe meteors traveling directly toward the radar by pointing the antenna beam at the meteor radiant. These observations were attempted only for the Quadrantids, Perseids, and Geminids. With a narrow (2°) beam, directed at an elevation of only 3°, the amount of sky through which a shower meteor may pass and give rise to an echo is reduced in the "radiant" tracking position by about a factor of **10** from that in the "right-angle" point position (paper **1).** At elevations greater than 3°, the useful area is still further reduced, and it was considered worthwhile to direct the antenna at the radiant only when the radiant elevation was below about 20° to 30°. An additional reduction in the rate could be expected to arise as a result of the reduced cross section of the meteors when observed "head on." (The rates observed for these three major showers were in fact reduced to the order of **2** shower meteors/hour.) Thus, for successful observations of meteors traveling toward the radar, one requires a strong shower having a radiant whose declination is substantially different from the latitude of the observer. The radiant will then rise and set slowly, thus spending a long period of time at low elevations.

The separation of the meteors traveling directly down the beam from those that traverse it at an angle proved less difficult than anticipated. In the first place, the receiver, which employs a bank of doppler filters, is sensitive only to meteors having **a** radial component of velocity in the range ±9 km/sec. Thus, with the receiver detuned so that the center filter of the receiver filter bank corresponds to the frequency of an approaching shower meteor (with velocity V_s), meteors traveling through the antenna beam can be detected only if they possess a radial component of velocity in the range $v_s\pm 9$ km/sec. That is, any meteor with velocity v (measured in km/sec) traversing the beam at an angle ϕ to the axis will be detected only when the relation

$$\cos^{-1}\left(\frac{v_s+9}{v}\right)\leq\phi\leq\cos^{-1}\left(\frac{v_s-9}{v}\right) \tag{18}$$

is satisfied. From geometrical considerations alone one would expect to observe more meteors for which $v > v_s$ than for $v < v_s$. Yet, because the available number of sporadic meteors decreases as $V \geq 40$ km/sec (paper 1), the net effect will be an extremely large reduction in the rate of sporadic meteors when the receiver is detuned. Three tests are then applied to select meteors traveling toward the radar: (1) the duration should be large—a minimum value of about **0.5** sec was taken; **(2)** the velocity computed on the assumption that the meteor is traveling directly toward the radar should be close to the known velocity **of** the shower in question; and **(3)** the mean rate of change of radial velocity must be small (<2 km/sec^2).

In figure **3** the mean radial velocity is plotted against the mean derivative of the radial velocity, and there is a distinct group of meteors with long durations centered on a mean radial velocity of **35.5** km/sec and a mean deceleration of **1** km/sec^2. The members of this group were

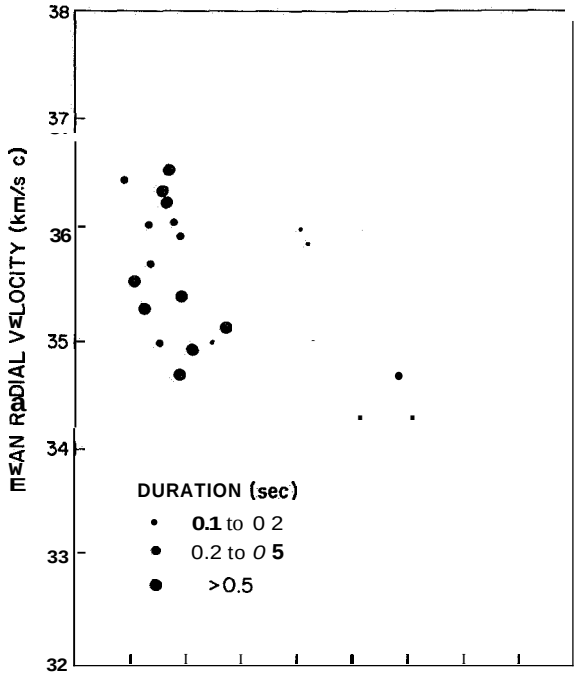

accepted as Geminids and all others rejected, although in fact some **of** those shown in figure 3 might also have been Geminids. **A** similar selection procedure was employed for the Quadrantids and Perseids, although here the problem was made much easier by the higher value of v_s and correspondingly lower number of sporadic meteors observed.

These selection procedures will not preclude the acceptance of a meteor traveling at a small angle (less than, say, 5°) to the axis. Thus, the angular extent of the radiant will play some part in limiting the accuracy obtained by this technique. We can, however, show that meteors traveling at angles larger than 5" to the axis cannot remain within the beam long enough to give rise to the observed durations. For a 5° difference between the meteor direction and the beam, the radial velocity observed will be only 99.4 percent of the true meteor velocity. The finite width of the beam (2°) precludes the aspect of the meteor changing by more than 2°. It follows that, though the meteor velocities may be systematically low (by as much as **0.6** percent), the amount of this error will not change significantly during the course of the observation. There was evidence of fragmentation in **40** percent of the sporadic meteors observed traveling through the beam at right angles (paper **1).** Since meteors with durations of more than **0.5** sec have been selected, however, we shall have largely excluded from this sample cases where the meteor fragmented. Obviously the exclusion of fragmenting meteors should improve the likelihood of agreement between theory and observation.

Results

VELOCITIES.—Tables 1 to **4** summarize the results **of** these observations. In the case of the Perseids (table **2)** the durations were mostly shorter than the Geminids (table **3)** and Quadrantids (table **4).** In general, the Perseid meteors showed little or no evidence of deceleration, but instead seemed to exhibit wider scatter of values **for** the radial velocity than did the Geminids or Quadrantids. **An** example of this is presented in figure **4,** where the radial velocity is plotted as a function **of** time for Perseid **7.** Thus, the extrapolated velocities

TABLE 1.—Comparison *of initial velocities of shower meteors*

	Geminids (km/sec)	Quadrantids (km/sec)	Perseids (km/sec)
Mean of first six returns (this paper)	42.25	35.98	60.03
Extrapolated value v_∞ (this paper)	42.42	36.55	260.26
v_∞ obtained by curve fitting (this paper)	42.46	36.73	—
v_∞ (Whipple and Hawkins, 1959)	42. 7	36. 5	60. 4
Mean value of v_∞ from Hawkins and Southworth (1958)	42. 6	36. 2	60. 6

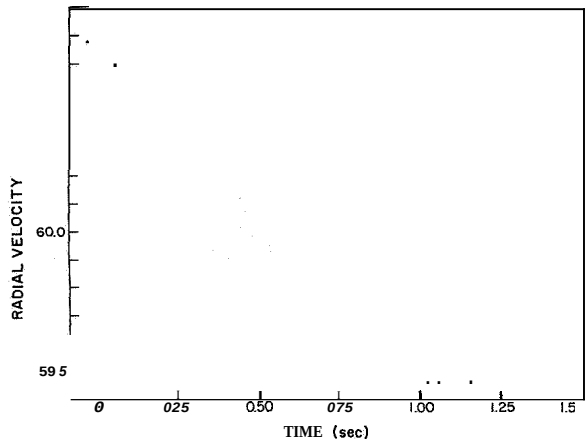

FIGURE 4.—Observations of radial velocity vs time for Perseid 7 (1961).

v_∞ for these meteors cannot reliably be obtained. We attribute this behavior to the apparent ability of the Perseids to fragment readily. The initial observed velocity has been computed from the mean of the first six returns, and the averages for the three showers are listed in table 1.

For most of the Geminids and Quadrantids, the radial velocity showed a smooth uniform decrease with time. Representative examples axe given in figures 5 to 10. Where the duration exceeded about 0.75 sec, a smooth curve was fitted to the points and extrapolated backward in time until the gradient of the curve became zero. The velocity at which this occurred is given in column 5 of tables 2 to 4 as v_∞ together with an estimate of the accuracy of this value, Weighted mean values for v, are given in table 1. The mean velocity given in column 4 of table 2 has been taken as the lower limit of v_∞ for the Perseids. From table 1 it can be seen that these values are in close agreement with values for v, obtained from photographic observations by means of the Super-Schmidt meteor cameras. We are forced to conclude, therefore, that though the reflec-

TABLE 2.—*Perseids (1961)*

Number	Date	Start time (EST)	Observed initial velocity*	v_∞ (extrapolated)	Duration (sec)
1	Aug. 13	1536.56	60.003	60.003	0. 59
2	Aug. 13	1546.27	59.953		0. 30
3	Aug. 13	1607.28	60.469		0. 74
4	Aug. 13	1620.56	60.089		0. 34
5	Aug. 13	1733.51	59.317		0. 24
6	Aug. 13	1835.52	59.503		0. 52
7	Aug. 13	1841.25	60.534		1. 37
8	Aug. 13	1844.20	59.812		0. 32
9	Aug. 13	1905.15	60.693		0. 58
10	Aug. 13	1912.32	59.848		0. 28
11	Aug. 13	1917.16	60.134	—60.53	0. 49
		Mean values =	60.032	60.26	

*Mean of first six returns.

Number	Date	Start time (EST)	Observed initial velocity*	v_∞ (extrapolated)	Duration (sec)
1	Dec. 12	0819.23	35.028		0.40
2	Dec. 12	0825.26	35.605	35.70f0.05	1.08
3	Dec. 12	0827.25	34.921		0. 56
4	Dec. 12	0827.28	35.840	36.6 ±0.20	0. 92
5	Dec. 12	0844.28	35.723		0. 55
6	Dec. 12	1006.41	36.731	36.72 ±0.05	0. 85
7, 8	†Dec. 12	1829.34	36.209		1.06
9	Dec. 12	1907.17	36.781	36.80 ±0.05	1.39
10	Dec. 13	0917.31	35.396		0. 62
11	Dec. 13	1801.47	36.475	37.2 ±0.20	1.97
12	Dec. 13	1833.40	36.41		0. 53
13	Dec. 13	1904.48	36.936	37.0 ±0. 05	1.17
14	Dec. 13	1927.16	36.441		0. 27
15	Dec. 14	1941.21	'35. 217	35.80 ±0.20	2. 78
		Mean values=	35.979	36.55	

*Mean of first six returns.
†This meteor appears to have fragmented into two pieces.

TABLE 4.—*Quadrantids (1962)*

Number	Date	Start time (EST)	Observed initial velocity*	v_∞ (extrapolated)	Duration (sec)
1	Jan. 2	1714 02	42.357	42.90f0.10	0. 72
2	Jan. 2	1839.00	42.598	42.64f0.05	0. 87
4	Jan. 2	2047.54	43.189	43.32 ±0.05	1.08
5	Jan. 2	2145.46	42.407	42. 82 ±0. 10	1.62
6	Jan. 2	2151.10	42.673	42.90 ±0. 10	1.96
7	Jan. 2	2159. 10	42.785		0. 50
8	Jan. 2	2254.14	42.121	42. 44 ±0. 10	2. 17
9	Jan. 2	2303.34	42.962	43.52 ±0.10	1.65
10	Jan. 2	2309. 19	41.092	41, 68 ±0. 10	0. 67
11	Jan. 2	2314.05	41.766	41.90 ±0. 10	1.00
12	Jan. 2	2337.19	42.225	42.24f0.05	0.96
13	Jan. 3	1735. 17	41.040	41, 16±0.05	1.25
14	Jan. 3	1745.54	41.975	42.20 ±0.10	1.75
15	Jan. 3	1753.30	41.940	42.00 ±0.10	1.20
16	Jan. 3	2017.12	41.935		0.31
17	Jan. 3	2316.25	42.970		0. 41
18	Jan. 3	2340.08	40.755		0. 34
		Mean values=	42.252	42. 416	

*Mean of first six returns.

tions come from electrons surrounding the meteoroid, the echoing region has the same velocity as the meteor itself.

In photographic observations the quantity measured is the angular distance traveled by the meteor. The fist derivative with respect to time is, of course, the velocity; the second derivative is the deceleration. A reduction procedure required to determine velocity and deceleration from photographic plates has been

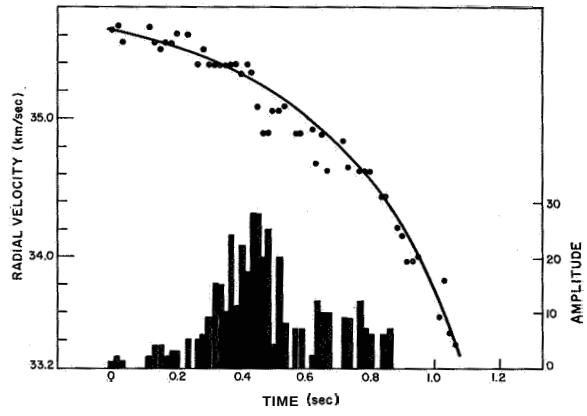

FIGURE 5.—Observations of radial velocity vs time for Geminid 2 (1961).

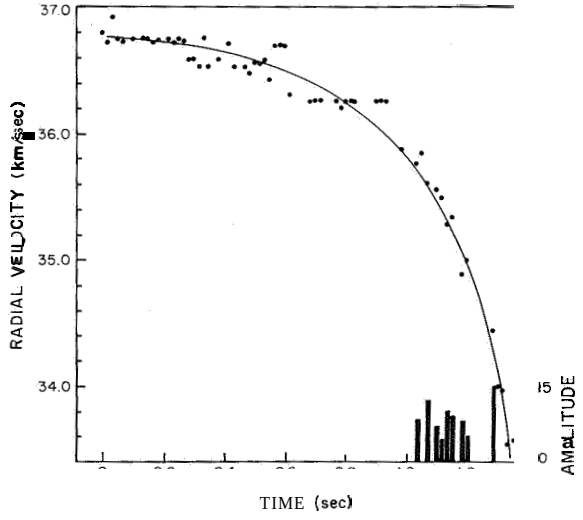

FIGURE 6.—Observations of radial velocity vs time for Geminid 9 (1961).

given by Whipple and Jacchia (1957), who emphasize the care that must be taken in the process. In these radio measurements the velocity is measured directly and deceleration is the first derivative. It seems, therefore, that the values of deceleration obtainable from these plots of velocity vs time, e.g., figures 5 to 10, are the best now available.

Unfortunately, even with an accurate plot of velocity vs time (such as obtained here), we cannot compute from theory unambiguous values for the mass of the meteor without assuming either its radius or its density. The principal difficulty is simply that there are too

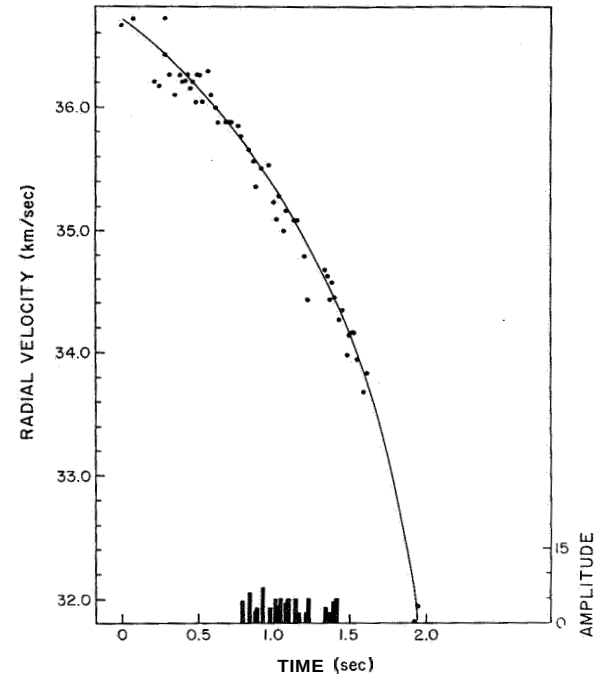

FIGURE 7.—Observations of radial velocity vs time for Geminid 11 (1961).

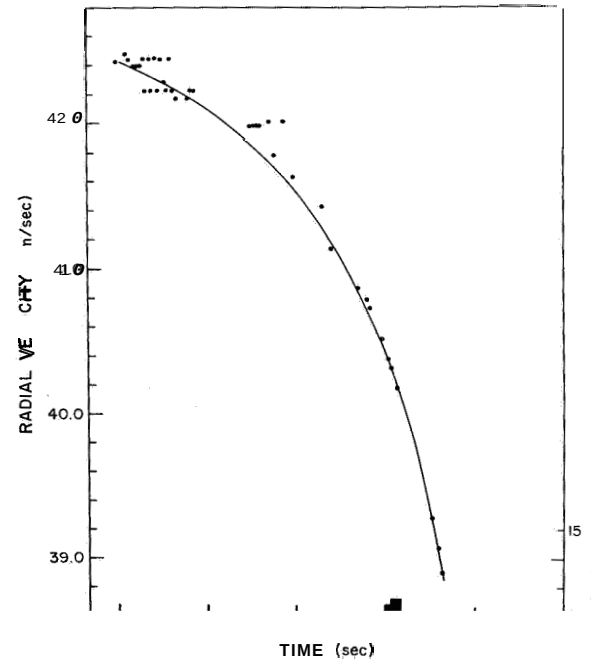

FIGURE 8.—Observations of radial velocity vs time for Quadrantid 5 (1962).

many unknowns in the equations. It is possible, however, by comparing these results with theory, to estimate the effective ablation energy for unit mass and the product of the

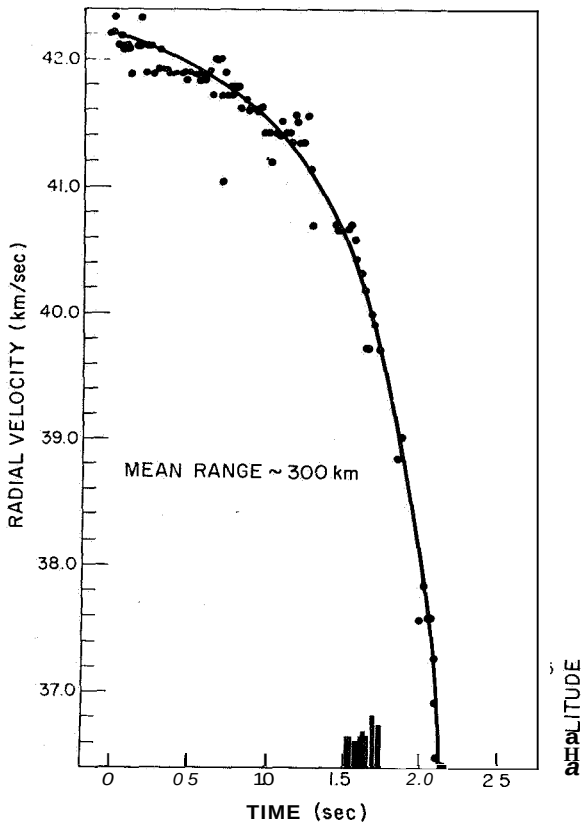

FIGURE 9.—Observations of radial velocity vs time for Quadrantid 8 (1962).

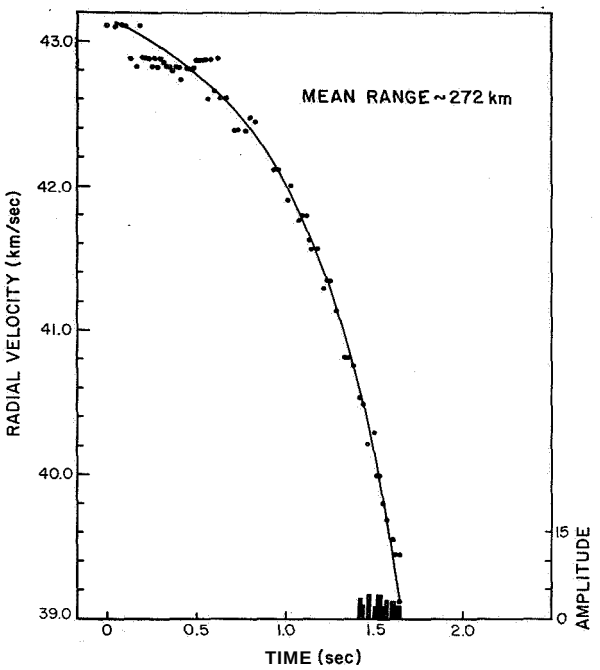

FIGURE 10.—Observations of radial velocity vs time for Quadrantid 9 (1962).

radius and density for most of the meteors. These results are presented on pp. 142–146.

AMPLITUDE.—We have enumerated earlier (in paper 1) the difficulties encountered in measuring echo amplitude. Problems arise because the basic detection scheme (which employs the filter bank) provides an output that is not linearly related to the input. For the observations of meteors traveling radially toward the radar, echo-power measurements were made with a separate IF channel having a bandwidth of 5 kcps. A larger filter would have been desirable to accommodate the wide range of doppler shifts encountered. This was not practical because the signal-to-noise ratio of most of the returns was very low and a larger filter would cause all but a few returns to be undetectable. The output from a 5-kcps-wide IF channel was connected to a detector having a logarithmic law, which gave as its output a voltage proportional to the received power expressed in db. This voltage was sampled by an analog-to-digital converter on command. The command to "sample" was derived from the trigger pulse generated at the output of the filter bank on receipt of an echo. The digital word representing the echo power, together with the other information pertinent to each echo (time, range, doppler, etc.) was stored in the CG24 computer, which is an integral part of the radar system (paper 1). This recording system provided a large dynamic range (better than 30 db), but unfortunately this precaution proved unnecessary as most of the returns were near the lower limit of detectability. The undesirable consequence of using the narrow (5 kcps) filter is that only a fraction of the amplitude data (lying within ±2 kcps of the center frequency) can be regarded as valid. The logarithm of the power of these returns is plotted on an arbitrary scale (labeled amplitude) in figures 5 to 10. The system was calibrated by means of a pulsed signal generator connected to the receiver via a directional coupler. The conversion of these values of signal power is shown in table 5. The majority of the returns lie between 5 and 10 on the

Amplitude value	Signal power (dbm)	
	Geminids	Quandrantids
1	−129	−127
10	−115	−113
100	−98	−96

about 200 and 400 km, and hence there is an uncertainty in the absolute height of as much as ±1 scale height (7 km). This is unfortunate and in principle could have been overcome by the use of a split-beam technique. It was not practicable to employ such a procedure at the time.

The values for the height at subsequent times were computed with the assumption that the meteor continues to travel toward the radar along the axis of the beam, and that it travels a linear distance of $0.05\bar{v}$ km in each 0.05-sec interval (where $\bar{v}$ is the mean of the velocities at the beginning and the end of this interval). The tables of velocity vs height constructed in this manner have been published (Evans and Brockelman, 1964).

The aforementioned tables provide a smooth variation of velocity vs height and do not reflect the large errors in the individual range measurements. The absolute height of the whole meteor is, however, uncertain by as much as 1 scale height. Errors in the velocity curve due to the meteor intersecting the antenna beam at a small angle cannot, of course, be corrected. As we have seen, the effect of assuming that the meteor is traveling radially toward the radar will tend to cause a small but systematic underestimate in the absolute meteor velocity. Unfortunately, it can introduce a far larger error in the computed height. Because the meteors are all observed at large zenith angles ($\chi \geq 70°$), a small error in the assumed value of χ can cause the height scale to be considerably altered. For example, in the worst case when the meteor is descending either more or less steeply than assumed by the maximum allowable amount ($\sim 5°$), the computed height scale may be as much as 40 percent in error. Thus, it is possible for the beginning height of the meteor to be −1 scale height in error, and in the worst possible case the difference between the beginning and the end heights may be in error by as much as a scale height also. These errors could in principle be reduced if an even narrower pencil beam were used, but unfortunately the meteor rate could be expected to vary as the square of the beam diameter, and might, therefore, become exceedingly low.

Attempts have been made to compare the observed deceleration with that predicted theoretically, with the assumption of free molecular flow (i.e., no air cap). Curves of v/v_∞ were prepared for different values of the effective ablation energy ξ (=6, 10, 14, 18, and 22 km²/sec²) for both the Geminids and Quadrantids (with v_∞=36.0 and 42.5 km/sec, respectively) from the approximate expression given in equation (6). These curves were plotted on a height scale marked off in kilometers, with respect to the height h_{max} at which the maximum rate of ablation occurs. To do this it was necessary to assume that the scale height H is independent of altitude, and a value H=6.5 km was employed. Because we have no way of determining h_{max} from our observations, the observed velocity ratios v/v_∞ were plotted against an arbitrary height scale and the two graphs were then adjusted for best alignment between the observed and any one of the theoretical curves. In practice, it was also necessary to adjust the graphs vertically to correct for errors in the estimated value of v_∞. It is easy to show that the first-order effect of a small error Δv in estimating the true value of v_∞ alters all the values of v/v_∞ by the same amount ($\Delta v/v_\infty$). Hence, the true value of v_∞ together with ξ and h_{max} can be obtained by this fitting procedure. The results of this work are summarized in table 6.

In some cases the duration of the meteor was insufficient to distinguish between different theoretical curves. An example of this is provided in figure 11, where Quadrantid 13 can be seen to fit the curves for ξ=14 km²/sec² and ξ=18 km²/sec². In these cases both solutions are given in table 6. In a small number of cases only one solution seemed possible—Geminid 9, for example (fig. 12). In six cases no proper fit could be obtained to any of the curves because the deceleration was not sufficiently rapid toward the end of the event. Examples of this behavior are shown in figures 12 and 13 by Geminid 11 and Quadrantids 5 and 8. Two of these cases might be attributed to the use of the approximate solution for the velocity (eq. (6)) in place of the more rigorous one (eq. (7)). The difference in predicted behavior for these two solutions is

TABLE 6.—*Down-the-beam meteors*

Estimated v_∞			First solution			Second solution			Comments	Assumed v_{max}	Mean $r\delta$	Mean height	Mean $\cos\chi$
			ξ	v_∞	h_{max}	ξ	v_∞	h_{max}					
Geminid.	2	35.7 ±0.05	14	35.89	94.8	18	35.92	93.2	Fits both solutions equally	34.76	0.088	96.48	0.3368
	4	36.6f0.2	18	36.42	91.6	22	36.47	90.75	Fits both solutions equally	34.98	0.123	92.66	0.3363
	6	36.72M.05	(appears to have fragmented)						Fits no solution		0.784	89.10	0.1683
	9	36.80±0.05	8	36.92	101.0				Fits this value only*	36.33	0.064	101.35	0.2876
	11	37.2 ±0.2	18	37.20	96.4				Poor fit below 96 km	35.86	0.127	93.65	0.1969
	13	37.0 ±0.05	18	37.18	96.95	14	37.15	98.0	Fits both solutions equally	36.98	0.054	101.03	0.2974
Mean value		†36.55	Mean of all solutions v_∞=36.73							36.68	0.207	95.7	
Quadrantid	1	42.9 f0.2	10	42.60	101.65				Fits this value only	42.00	0.056	102.13	0.2687
	2	42.64±0.05	6	42.79	106.3	10	42.79	103.8	Fits these and other solutions	42.31	0.059	108.33	0.2015
	4	43.32±0.1	6	43.47	85.75	10	43.47	83.2	Fits these and other solutions	42.97	3.836	86.00	0.1723
	5	42.82±0.1	10	42.63	99.0	14	42.69	97.86	Poor 5t below 99 km*	41.93	0.138	96.48	0.1882
	6	42.9 ±0.1	18	43.00	101.5				Poor fit below 78 km*	41.90	0.055	102.27	0.1942
	8	42.44±0.1	22	42.44	98.8				Poor 5t below 106 km*	41.11	0.078	99.25	0.2266
	9	43.52±0.1	22	43.41	93.75	18	43.41	94.75	Poor 5t below 96 km	42.17	0.172	94.40	0.2324
	10	41.68±0.1	18	42.03	94.8				Fits this value only	40.96	0.120	92.78	0.2365
	11	41.90±0.1	18	42.21	101.9	14	43.14	102.8	Fits both solutions equally	42.21	0.035	102.85	0.2468
	12	42.24±0.05	14	42.45	105.0	18	42.55	104.2	Lies between these values	41.53	0.027	105.78	0.2409
	13	41.16±0.05	14	41.34	103.25	18	41.36	102.1	Fits ξ=18 better	40.41	0.039	104.83	0.2311
	14	42.20±0.1	18	42.12	109.85	22	42.16	109.2	Poor fit below 112 km	40.94	0.011	111.88	0.2279
Mean value		†42.42								41.62	0.385	100.4	

*Values plotted (figs. 14 to 16).
†Values obtained from tables 3 and 4.

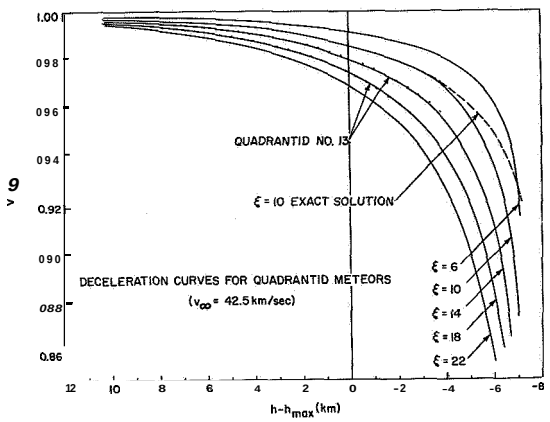

FIGURE 11.—Variation of velocity observed for Quadrantid 13 superimposed on theoretical curves for different values of ablation energy ξ. It can be seen that this event was of insufficient duration to define ξ precisely.

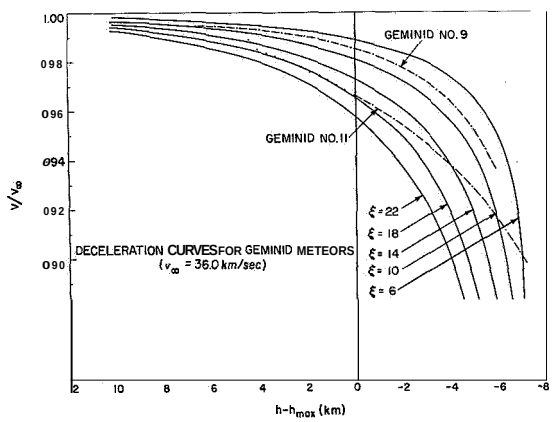

FIGURE 12.—Variation of velocity for Geminids 9 and 11. In the case of 9 it is believed that $\xi = 8$ represents the only likely solution. Geminid 11 departs by an amount too large to be attributed to the use of the approximate solution for the velocity.

illustrated in figure 11 for $\xi = 10$, and seems sufficient to explain why Quadrantids **6 (fig.** 13) and 14 do not fit the theoretical curve. However, in the other four cases (Geminid **11,** Quadrantids **5, 8,** and 9), the departure of theory from experiment is too marked to be explained by the use of the approximate theory, and one is tempted to conclude that an air cap had formed around the meteor. When this happens, the drag coefficient is decreased and consequently ξ (equal to $\gamma\ell/\Lambda$) is also reduced. Thus, a meteor that begins by following a particular curve **for** ξ (e.g., Geminid **11** follows $\xi = 18$) will

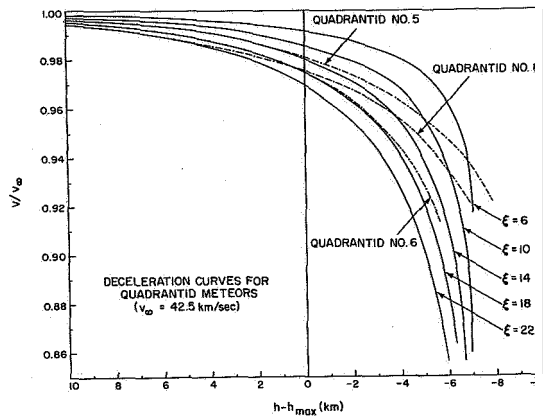

FIGURE 13.—Variation of velocity for Quadrantids 5, 6, and 8. Event 6 departs from the theoretical curve by an amount that can be attributed to the fact that approximate solutions (see fig. 11) were used. Both events 5 and 8 depart from theoretical curves in a manner too large to be attributed to this cause.

gradually depart from this line toward curves of lower values of ξ. We note from table **6** at what height cap formation seems to begin from the height at which agreement between theory and observation becomes poor. In one case (Quadrantid **6)** this is **78** km, but in the remaining cases it is **96** km **or** higher and throws some doubt on an explanation in terms of cap formation.

A mean for all the values of ξ listed in table **6** is **15.4** km^2/sec^2, which is in remarkable agreement with the value employed by Verniani **(1962) (16** km^2/sec^2) in his reduction of photographic data published by Whipple (1954). The spread of values is large and suggests that individual meteors may have values widely different from this average value. There is no clear-cut difference between the Geminids and Quadrantids in table **6,** and we cannot comment on the conclusion reached by Jacchia (1958) that ξ increases with velocity.

RADIUS.—A more sensitive test of whether the meteor is behaving according to the theory for a single particle with free molecular flow is achieved by computing the equivalent radius and comparing its behavior with that expected. From equation (17) we have

$$r\delta = \frac{3}{2} v\rho \sec \chi \left(\frac{dv}{dh}\right)^{-1}, \qquad (19)$$

in which v, ρ, $\sec \chi$, and dv/dh are known functions of height for each meteor. It follows that $r\delta$ may be computed as a function of height, and if the assumption is made that the meteor density δ does not change with height, the behavior of r with height is obtained.

We obtained values of $r\delta$ for each of the velocity values (at 0.05-sec intervals) listed in the tables (Evans and Brockelman, 1964). First, the values of dv/dh required in equation (19) were obtained from the difference between adjacent values of velocity and height in the tables. A better approach might have been to perform a least-mean-squares fit, but our method gave values sufficiently accurate for the present purpose. Next, we found the atmospheric density ρ (from the U.S. Standard Atmosphere, 1962) by making a table of density and scale height at 2-km intervals above 70 km. By interpolation using the appropriate scale height, we obtained the density at any given height. The remaining term ($\sec \chi$) was obtained from the range R (computed at the time the height h was computed), together with the value of the antenna elevation angle α from

$$\cos \chi = \frac{R + R_E \sin \alpha}{(R_E^2 + R^2 + 2RR_E \sin \alpha)^{1/2}}, \quad (20)$$

in which R_E is the radius of the earth.

We now form a table in which the corresponding values of v, dv/dh, h, $\sec \chi$, and ρ are known. Hence, $r\delta$ can be computed from equation (19). These values are tabulated in the published tables (Evans and Brockelman, 1964).

It is to be expected that if the meteor atoms are ablated singly the density δ would remain constant. The variation of $r\delta$ with density should then follow the curve given in figure 2. A check has been made to see whether this is so. By taking the value of h_∞ given in table 6 for each point in the tables, we computed the ratio ρ/ρ_{max}. The corresponding values of r/r_∞ were plotted against these values of ρ/ρ_{max}. The initial radius of the meteor r_∞ is not known. Hence, use was made of the fact that $r_{max} = 2r_\infty/3$, and the values of r/r_∞ were simply forced to pass through the value 2/3 at the point $\rho/\rho_{max} = 1$. The results of these operations are given in figure 14a–h for some of the meteors; the approximate theoretical variation

$$r = r_\infty \left(1 - \frac{\rho}{3\rho_{max}}\right) \quad (21)$$

is also shown.

Upon inspecting these results we find that in some cases (Quadrantids 10, 11, 12, and 13) (fig. 14e–h) there is fair agreement between theory and experiment. However, in many cases (Geminids 2, 4, and 11, and Quadrantids 1, 5, 8, and 9) there is violent disagreement. Three of these meteors (Quadrantids 5, 8, and 9) are illustrated in figure 14a, c, d. These cases were recognized in the previous section as being events in which the velocity behavior was anomalous; however, the plots of r/r_∞ provide a more sensitive test of anomalous behavior. We note that in six cases (Geminids 4 and 13, and Quadrantids 1, 5, 8, and 9), where the departure of theory from observations seems to exist from the very commencement of the event, the mean height at which these events were first observed is 104 km. It seems impossible to attribute these discrepancies to cap formation since this could hardly occur at such a great height. We note that the anomalous cases are all those in which the duration was large ($\sim$2 sec), and hence they are also the cases where an error in the assumed zenith angle will introduce the largest error in the difference between the beginning and the end heights. This could, in the worst case, be $\sim$6 km, which would be sufficient to account for the difference between theory and experiment. Those meteors for which the zenith angle is larger than assumed will descend less rapidly than expected and will appear to have decelerated less than they should. On the other hand, those meteors descending more rapidly than assumed may simply be found to match a theoretical curve for a value of ξ lower than the true value.

One meteor (Geminid 6) suffered a very rapid deceleration, which can only be attributed to fragmentation. In effect, the cross section σ increased as the meteor descended. Most other cases exhibited a decrease of r with increasing atmospheric density ρ, which is less than that predicted by theory, but this is probably due to errors in the height scale. Only in one case (Quadrantid 6) does it seem reasonable to

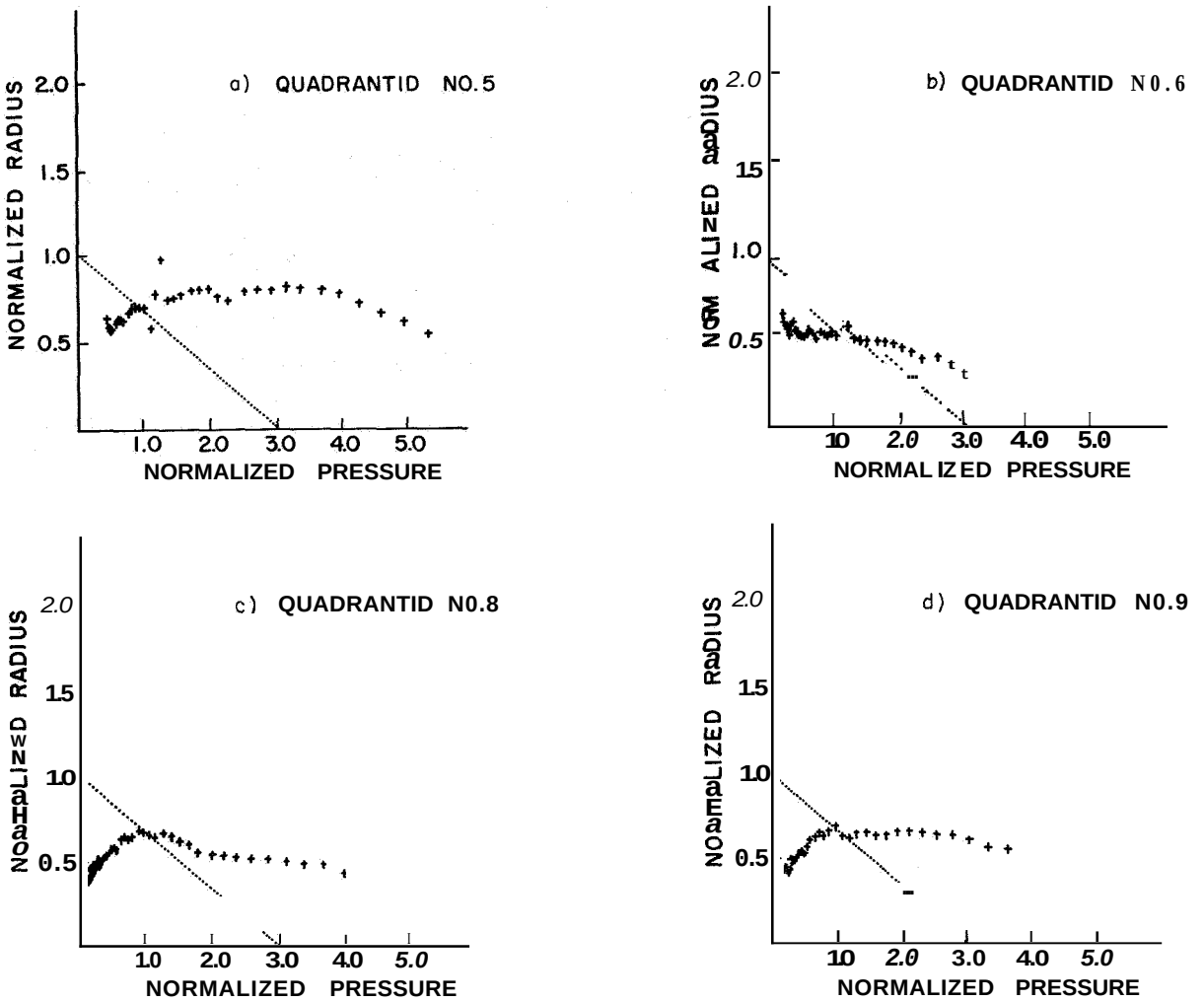

FIGURE 14*a-d*.—Observed and predicted variation of meteor radius plotted as a function of atmospheric pressure: *a*, Quadrantid 5; *b*, Quadrantid 6; *c*, Quadrantid 8; and *d*, Quadrantid 9.

attribute the anomalous behavior to the gradual formation of an air cap as the meteor descended.

Meteor masses

Despite the differences between theory and experiment, the mean values of $r\delta$ do have some significance. They are plotted as a function of height in figure 15 and are listed for each meteor in table 6. It can be seen (fig. 15) that the values are spread in height approximately along the curve representing the variation of the air density. This is an effect that can in part be explained by the large uncertainty in the true height of the meteor (± 7 km). This alone would distribute the values of $r\delta$ over one order of magnitude. We can arrive at crude estimates of the average mass and radius by assuming a value 6 for the density. The mean values of $r\delta$ (table 6) are biased by two very large values (Geminid 6, which appears to have fragmented and been given an erroneous value, and Quadrantid 4, which is so large that it is not included in fig. 15). If we eliminate these and Quadrantid 14, which is particularly low, the mean value of $r\delta$ is ~ 0.08 g/cm^2. There seems to be no pronounced difference between the values for the Geminids and the Quadrantids, although such a difference has been found by Verniani (1964). If we assume $\delta \sim 1$ g/cm^3, in agreement with the density deduced by Verniani (1964) for photographic Geminid meteors, then the average radius is —0.08 cm,

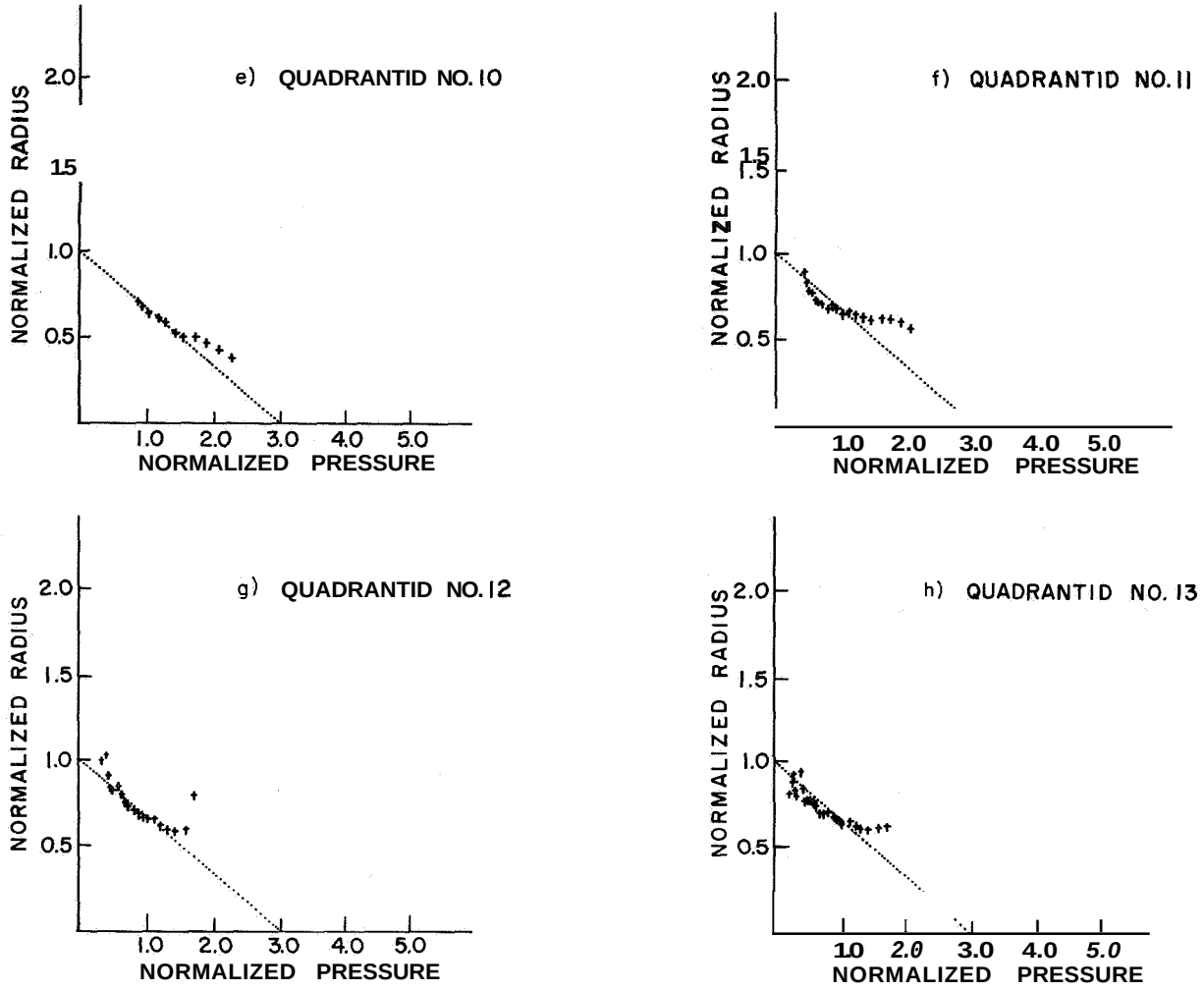

FIGURE 14*e–h*.—Observed and predicted variation of meteor radius plotted as a function of atmospheric pressure: e, Quadrantid 10; *f*, Quadrantid 11; g, Quadrantid 12; and *h*, Quadrantid 13.

and with considerably more uncertainty the average mass is $\sim 10^{-2}$ to 10^{-3} g.

Most estimates of the mass of zero visual magnitude meteors lie between 1 and 10^{-1} g (McKinley, 1961). The observed value for the mean mass of the meteors observed in this work (10^{-2} and 10^{-3} g) therefore implies that the meteors are approximately of *+5* visual magnitude. This estimate seems reasonable in view of the fact that the limiting magnitude of sporadic meteors seen traversing the beam at right angles was estimated to be +8 (paper 1). We should expect the shower meteors observed here to be brighter because the trail cross section must be reduced when viewed from the end; in any event, the showers contain many more bright members than does the sporadic background (paper 1).

Conclusions

No previous reports of meteors observed traveling directly toward the radar have been published. It is most unfortunate that the observations of meteor deceleration reported here could not be used to yield accurate mass values. The principal requirement for detecting meteors approaching directly toward the radar is that the elevation of the radiant be low. Evidently, simultaneous photographic observations would require a number of wide-angle cameras at considerable distances from the radar in an area beneath the intersection of the

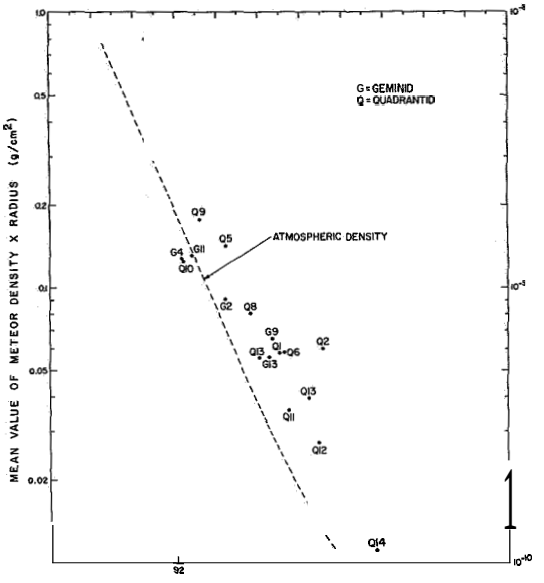

References

EVANS, J. V.

1965. Radio-echo studies of meteors at 68-centimeter wavelength. Journ. Geophys. Res., vol. **70,** pp. 5395–5416.

EVANS, J. V., and BROCKELMAN, R. A.

1964. Radio echo studies of meteors at **68** cm wavelength, Part **11:** Shower meteors. Tech. Rep. **341, Lincoln** Lab., Lexington, Mass.

HAWKINS, G. S., and SOUTHWORTH, R. B.

1958. The statistics of meteors in the earth's atmosphere. Smithsonian Contr. **Astro**phys., vol. **2,** no. **11,** pp. **349–364.**

JACCHIA, L. G.

1955. The physical theory of meteors, VIII: Fragmentation as a cause of the faint-meteor anomaly. Astrophys. Journ., vol. **121,** pp. **521–527.**

1958. On two parameters used in the physical theory of meteors. Smithsonian Contr. Astrophys., vol. **2,** no. **9,** pp. **181–187.**

MCKINLEY, D. W. R.

1961. Meteor Science and Engineering. McGraw-Hill Book Co., New York, **309** pp.

ÖPIK, E. J.

1958. Physics of Meteor Flight in the Atmosphere. Interscience Publ., New York, **174** pp.

U.S. STANDARD ATMOSPHERE

1962. U.S. Standard Atmosphere **1962.** Prepared under NASA, USAF, and USWB, Washington, D.C., **278** pp.

VERNIANI, F.

1961. On meteor ablation in the atmosphere Nuovo Cimento, vol. **19,** pp. **415–442.**

1962. On the density of meteoroids, I: The density of bright photographic meteors. Nuovo Cimento, vol. **26,** pp. **209–230.**

1964. On the density of meteoroids, **11:** The density of faint photographic meteors. Nuovo Cimento, vol. **33,** pp. **1173–1184.**

WHIPPLE, F. L.

1943. Meteors and the earth's upper atmosphere. Rev. Mod. Phys., vol. **15,** pp. **246–264.**

1954. Photographic meteor orbits **and** their distribution in space. Astron. Journ., vol. **59,** pp. **201–217.**

WHIPPLE, F. L., and HAWKINS, G. S.

1959. Meteors. *In* Handbuch der Physik, vol. **52,** ed. by S. Flugge, Springer-Verlag, Berlin, pp. **519–564.**

WHIPPLE, F. L., and JACCEIA, L. G.

1957. Reduction methods for photographic meteor trails. Smithsonian Contr. Astrophys., vol. **1,** no. **2,** pp. **183–206.**

Abstract

By means of a narrow-beam high-power radar operating at 68 cm it has been possible to detect meteors traveling radially toward the radar. In these observations the antenna is directed at the radiant point of an intense meteor shower and the receiver tuned to the expected doppler-shifted signal. Because the actual doppler shift can be measured with precision, both the velocity and deceleration of the approaching meteor can be determined. The behavior of the velocity is compared with the theory for a solid particle entering the earth's atmosphere at heights where no air cap is formed. Anomalous behavior was observed in several cases, but the height at which this appears to begin is too great to be accounted for by cap formation. We conclude that errors in the computed height of the meteor may be responsible for the anomalous cases. A mean value for the effective ablation energy of 15.4 km^2/sec^2 was obtained, but individual meteors showed wide departures from this value. The mean mass of the meteors is estimated to be in the range 10^{-2} to 10^{-3} g, corresponding to a visual magnitude of +5.

Radar Meteor Echoes

P. M. MILLMAN [1]

Since 1947 radio observations of meteors, accompanied by group visual observations, have been carried out near Ottawa, Ontario, Canada. In particular, since October 1957, a patrol meteor radar has been operated continuously at the Springhill Meteor Observatory (45°2 N, 75°5 W), while visual observations have been conducted sporadically at Springhill and have been collected from numerous outside observing groups in various parts of the USA and Canada. The data collected since 1957 now consist of visual observations of some 150,000 meteors and over 10,000,000 tabulated meteor echoes.

The statistical reduction of this material is progressing steadily, and detailed results are appearing in a series of papers (Millman and McIntosh, 1966). I wish here to deal briefly with certain aspects of the analysis of meteor rates and the problems of the comparison between radar rates and visual rates. The discussion is more in the nature of a current progress report rather than a statement of final results and conclusions, and I will welcome helpful comments on the points raised. It is my feeling that often a series of observational data are accepted without sufficient attention being paid to the significance of the figures involved and the possible errors that may lie hidden in the statistics.

To keep the subject in the observational field rather than in the theoretical, the standard reference frame will be taken as the visual absolute meteor magnitude M, i.e., the visual magnitude of a meteor at 100-km height in the zenith. It will be convenient fist to consider what is involved in deriving a visual hourly rate.

[1] National Research Council, Ottawa, Canada.

Visual meteor rates

In Canada we have always stressed the visual group count as approaching closer to the complete picture of what is seen from one station. Counts are normally reduced to a standard team of six observers, although the actual observations at Springhill generally involve a team of eight observers and one recorder. Factors that can seriously affect the counts are clouds, haze, moon, aurora, and artificial illumination. Most analyses are carried out only with Weather I observations, defined as those made when all the above disturbing factors are virtually absent.

The ratio of the numbers of meteors seen, counted down to two successive magnitude limits, is defined as r. This ratio generally can be assumed roughly constant over a short magnitude range, but caution must be used in extending this assumption to a long range of magnitude. From a study of the Ottawa visual records, and assuming that r exhibits no sudden discontinuities, Millman and Burland (Millman, 1957) concluded that a team of six visual observers recorded the following percentages of the meteors actually visible.

apparent magnitude	0	1	2	3	4	5
percentage recorded	100	60	30	10	2	½

Group visual programs carried out in Weather I conditions result in a mean visual apparent magnitude in the range between two and three. Hence, much the greater portion of the meteors contributing to the visual hourly rates are from magnitude classes where 70 to 90 percent are never recorded. The situation

is probably even worse for most single-observer data. When one adds the problems of subjective variations in magnitude scale, and unknown personal equation factors, it is not surprising that visual hourly rate data can be misleading if not reduced carefully.

It is of interest to note the elevation distribution of the meteors recorded by group counts. For the Ottawa team, where all eight observers are in standard observing positions, this distribution is surprisingly constant for any given set of weather conditions. Three examples of the percentages of meteors observed at Springhill in various elevation ranges are given in table 1. The observations made on December 13/14, 1958, are representative of exceptional transparency and maximum darkness of the sky background. These conditions resulted in over 1000 meteors being recorded in a watch of just over 8 hours. It is evident that the better the weather, the greater the percentage of meteors recorded at low elevations.

If we take into account the area of the sky contained in each elevation range of table 1, we can find the relative density of meteors per unit sky area. These values are listed in table 2, where the relative densities are found by dividing the figures of table 1 by the percentage of sky area in each elevation zone.

The determination of r from visual records is discouraging. At the bright end of the scale one is hampered by inhomogeneity and the small numbers of observations available; at the faint end one is faced with the problem of deciding how to allow for the large percentage of meteors not observed. In addition to these problems, the effective magnitude scale adopted by the visual observers may vary considerably from one observing group to the next and between the bright and the faint magnitude ranges. Figure 1 is reproduced from a paper presented by Millman and Burland (1956) at the New York Meeting of the American Astronomical Society in 1956. Here, an attempt was made to bring together the evidence from several independent methods of estimating r. Later, these authors published additional material from the Ottawa program (Millman and Burland, 1961). In spite of the collection of a large amount of new data during the IGY, little improvement has yet been made in the consistency of the results.

We can summarize the situation by saying that visual programs generally give r in the range 2.5 to 3.5, and that the adoption of $r=3.0$ for an overall average is probably as good a guess as any. This corresponds fairly well with Öpik's results from the Arizona Expedition (Öpik, 1958). There is no doubt that the determination of r from any given set of observations is quite sensitive to a number of conditions. For example, some of the best visual observations from Springhill were analyzed by determining r from meteors observed at various elevation ranges. It was found that r varied from roughly 3.5 for meteors seen near the zenith to as low as 2.3 for meteors around 20° above the horizon. It can be

Elevation (degrees)	0	10	20	30	40	50	60	70	80	90
December 13/14, 1958	1	8	21	24	21	13	7	4	1	
1957–1961 Weather I	1	7	16	21	21	17	11	5	1	
1957–1961 Weather II	1	4	12	19	21	20	15	7	1	

Elevation (degrees)	0	10	20	30	40	50	60	70	80	90
December 13/14, 1958	0.1	0.5	1.3	1.7	1.7	1.3	1.0	0.9	0.7	
1957–1961 Weather I	0.1	0.4	1.0	1.5	1.7	1.7	1.5	1.1	0.7	
1957–1961 Weather II	0.1	0.2	0.8	1.3	1.7	2.0	2.0	1.6	0.7	

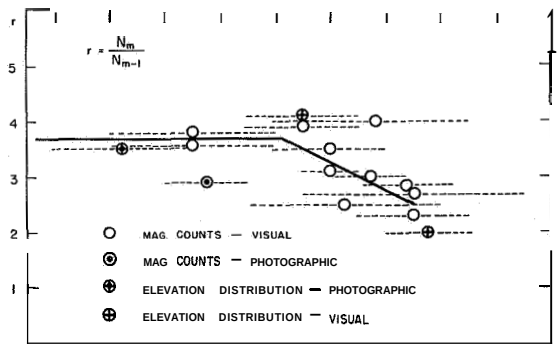

FIGURE 1.—Representative values of r, the ratio in numbers of meteors counted down to successive whole magnitude limits, plotted against the corresponding absolute visual magnitude range for the data used in each case. Taken from an unpublished paper presented by Millman and Burland (1956) at a meeting of the American Atsronomical Society, December 1956.

shown that, on the basis of normal meteor heights and atmospheric extinction factors, there should be no great variation in the r for apparent magnitudes at different elevation ranges, provided the r for absolute magnitudes is reasonably constant. The above observational result emphasizes once again the difficulty of deriving good r values from visual programs.

Radar meteor rates

The Springhill patrol radar (33 Mc/sec, 20 kw peak power) records meteor echoes on 35-mm film with a continuous range-time presentation. Film readers then transfer these echo data manually to IBM cards (Millman and McIntosh, 1963). The antenna system is omnidirectional, recording fairly uniformly down to 15° to 20° above the horizon. Reduction factors have been developed to allow for the subjective errors of the film readers and for the effects of interference, particularly serious in 1957–1958. The smallest echoes recorded correspond to underdense trails and are aspect sensitive. This will cause uncertainty in the cutoff at the lower limit and will vary with the integrated pattern of the meteor paths in the atmosphere. Echoes with appreciable duration correspond to overdense trails and will be little subject to aspect sensitivity, as was early shown by McKinley and Millman (1949) and further confirmed in more recent data (Millman, 1962).

The Springhill data are read in five duration classes: all echoes, duration ≥ 1 sec, duration ≥ 2 sec, duration ≥ 4 sec, and duration ≥ 8 sec. Mean hourly rates for each day of the year have been determined for each of these five classes for the 5-year period 1958–1962. Tables for all echoes and for ≥ 8-sec echoes were published by Millman and McIntosh (1964), and data for the other classes appear in a paper by Millman and McIntosh (1966).

If we concentrate on the echoes ≥ 1 sec in duration, we are dealing in the main with overdense trails. Here the standard equation for echo duration T is

$$T \propto \frac{\lambda^2 q}{D},$$

where λ is the wavelength, D is the upper-air diffusion coefficient, and q is the number of electrons per meter of path length. If we assume λ and D constant for the patrol program, we have $T = K_1 q$, where K_1 is a constant. If the visual magnitude is related to q by an expression of the form $M = A + B \log q$, and if N is the number of echoes with duration $\geq T$, it can be shown that

$$\log N = K_2 - K_3 \log r \log T,$$

where $K_3 \log r$ is the slope between $\log N$ and $\log T$, designated by S. If q is proportional to the intensity I, K_3 will be 2.5. It is convenient to write $S = Y(2.5 \log r)$. Where the parameter Y will indicate the nature of the relation between q and I, if $Y = 1$, then $q \propto I$.

The slope S for seventy-three 5-day periods during the year is plotted in figure 2, taken from Millman and McIntosh (1966). It will be noted that S varies considerably throughout the year, reaching minima at the time of the major annual meteor showers. One of the unexpected features of this plot is a fairly regular variation of S between the shower periods. This is particularly marked during the first quarter of the year. The nonshower meteors also exhibit a difference in S between the first part of the year and the last 6 or 7 months of the year.

The values of S range from 1.1 down to an extreme low of 0.2 for the Perseid meteors on the date of the maximum of this shower. If

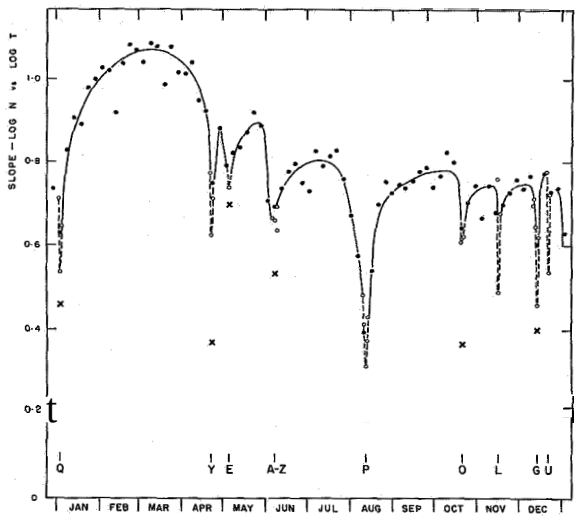

FIGURE 2.—The annual variation of the slope S of log N vs log T, plotted in black dots for seventy-three 5-day intervals from the records of the Ottawa meteor patrol radar. The open circles refer to singleday values for all meteors, and the crosses to shower meteors only for the day of shower maximum. [Taken from Millman and McIntosh (1966).]

$Y=1$, the range of S means a range of r from 2.7 to 1.2. This is an impossibly low range, particularly for the lower values, which correspond to most of the shower meteors. It is obvious that Y must be considerably less than 1 in many cases, perhaps as low as **0.3 or 0.2.**

We are in the process of comparing the visual rates from the IGY period with the radar rates, using the diurnal variation of the radar rates so that the comparison is made for the same hours of local mean time. Only the top category of visual records has been reduced so far. The radar rates for $\geq$1-sec echoes average 85 percent of the visual rates for six observers. This would indicate that the radar rates for 2 1-sec echoes correspond to a complete recording of meteors down to about +1.5 visual apparent magnitude. There is a difference in the radar/visual ratio during the December–March period as compared with the July–November period. In the first case the ratio is well over 1, while in the second it is only 0.75.

It must be remembered that the nature of the cutoff at the faint limit of the records will be different for the visual and for the radar programs. This is now being investigated. Unfortunately, with r values near 3, small differences in the nature of the cutoff will make major differences in the hourly rates. No comparison has yet been made between the probable distribution in elevation of the patrol radar meteor echoes and the data in table 1. For meteors observed visually at Ottawa, however, there is a tendency for those observed high in the sky to have a greater probability of an associated echo on the high-power meteor radar. The average probability of a visual meteor having a radar echo drops from about 65 percent for elevations greater than 60° to about 45 percent for elevations under 15°. This type of relation will not necessarily hold true for the faintest echoes recorded on the radar meteor patrol, as most of these correspond to meteors that have not been detected visually.

Acknowledgment

A portion of the data reduction for this paper was carried out under Duke University Contract No. DA-31-124-ARO-D-59.

References

McKINLEY, D. W. R., and MILLMAN, P. M.
1949. A phenomenological theory of radar echoes from meteors. Proc. Inst. Radio Eng., vol. 37, pp. 364–375.

MILLMAN, P. M.
1957. The relative numbers of bright and faint meteors. Journ. Roy. Astron. Soc. Canada, vol. 51, pp. 113–115.
1962. The meteor radar echo: an observational survey. Astron. Journ., vol. 67, pp. 235–240.

MILLMAN, P. M., and BURLAND, M. S.
1956. The magnitude distribution of visual meteors. Presented at 96th Amer. Astron. Soc. meeting, New York, December.
1961. Meteor magnitude distributions. Astron. Journ., vol. 66, pp. 291–292.

MILLMAN, P. M., and McINTOSH, B. A.
1963. A preliminary report on radar meteor counts. *In* Proceedings of the Symposium on the Astronomy and Physics of Meteors. Smithsonian Contr. Astrophys., vol. 7, pp. 45–51.
1964. Meteor radar statistics, I. Canadian Journ. Phys., vol. 42, pp. 1730–1742.
1966. Meteor radar statistics. II. Canadian Journ. Phys., vol. 44, pp. 1593–1602.

ÖPIK, E. J.
1958. Statistical results from the Arizona Expedition for the study of meteors. Contr. Armagh Obs., no. 26, pp. 1–82.

Abstract

The problems of comparing visual meteor rates with the echo rates recorded by meteor radar equipment are discussed. The uncertainty in the determinations of the magnitude distribution for visual meteors is noted. For most of the visual magnitude range the ratio between numbers in successive whole magnitude groups may be taken as approximately three. Recent studies of the data from the Ottawa radar meteor patrol show marked variations throughout the year in the ratio between the numbers of short- and long-duration echoes. Comparison with the visual data suggests that the ionization in a meteor trail is not proportional to the visual luminosity, and that this relation may vary considerably for different groups of meteors. Preliminary results indicate that visual rates for six observers average 15 to 20 percent higher than the patrol rate for meteor echoes with durations greater than or equal to 1 sec.

Structure of the Major Northern-Hemisphere Meteor Streams

L. M. G. Poole [1]

1. Introduction

Of the meteor streams that produce regular annual showers observable in the Northern Hemisphere, the Quadrantids (which occur in early January), the Perseids (mid-August), and the Geminids (mid-December) are among the most important. These are all characterized by a reliably high level of activity and are separated in date of occurrence from other periods of significant shower activity. Since these showers all occur during hours of darkness, they lend themselves to observation by both visual and radar techniques. The only other regular northern showers of comparable intensity are those due to the daytime streams, Arietids, and ζ Perseids. These both occur early in June and can be observed only by radar, so that unless special radiant-determining equipment is used it is difficult to distinguish between the activity of the two showers (see Evans, **1960).**

Radio observations on various meteor showers have been carried out at Sheffield since **1962,** with the emphasis on the accurately controlled recording of echo-amplitude information, in order to achieve reliable determinations of the absolute incident flux and magnitude distribution of the shower meteors. These quantities are related, respectively, to the spatial density and mass distribution of a stream's population in the vicinity of the earth, so that a study of their variation with solar longitude (in the cases where the shower activity persists for a sufficient length of time) enables us to deduce the structure of the stream at its intersection with the earth's orbit. Hence, further inferences can be made concerning the formation and history of the stream.

Kaiser **(1960)** has given, in a practical form, the theory relating absolute incident flux of shower meteors to the observed radio-echo rate and equipment parameters. The application of this theory to the present series of experiments is described in some detail by Kaiser, Poole, and Webster **(1966).** It may briefly be summarized as follows.

The absolute radio magnitude of a meteor is defined as

$$M_r = 35 - 2.5 \log_{10} (\alpha_z), \qquad (1)$$

where α_z, cm^{-1} is the zenithal electron line density (produced by a vertically incident meteor) and is given by $\alpha_z = \alpha_m \sec \chi$, where α_m cm^{-1} is the maximum line density of a meteor whose zenith angle is χ. The magnitude distribution can thus be described in terms of the exponent s in the relation

$$\Theta(\alpha_z) = c/\alpha_z^{s-1}, \qquad (2)$$

where $\Theta(\alpha_z)$ is the incident flux producing zenithal line densities greater than α_z, and c is a constant. The form of equation **(2)** has been established empirically, and is found to give an adequate representation of the meteor magnitude distribution over a reasonably wide magnitude range.

"Decay-type" echoes occur when the electron line density α at the reflection point is $\ll 2 \times 10^{12}$ cm^{-1}, and in this case the maximum returned echo power is given by

$$P_R = \frac{(2.5 \times 10^{-28}) P_T G^2 \lambda^3 \alpha^2}{R^3}, \qquad (3)$$

[1] Department of Physics, The University, Sheffield, England; now with Department of Physics, Rhodes University, Grahamstown, South Africa.

when the quantities are in units of gaussian cgs. Here, P_T is the transmitted power, G is the power gain of the antenna in the direction of the reflection point, which is at slant range R from the observing station, and λ is the radio wavelength used. If $\alpha \gg 2\times10^{12}$ cm^{-1}, the echo becomes of the "persistent" type with $P_R \propto \alpha^{1/4}$. The transition between the two echo types occurs at $M_r \sim +4$ (see eq. (1)).

At any instant the reflection points on trains associated with a particular shower can to a good approximation be assumed to lie along a line, the "echo line," drawn through a surface at the mean height of meteoric ionization, which for radio meteors is usually taken to be about 100 km. If the equipment sensitivity is such that echoes are predominantly of the decay type, the rate of echoes obtained from an echo line associated with a particular shower with echo power greater than P_R is given by

$$N_P = Hf(\chi_0, s)\Theta(\alpha_{p_0}) \int \rho^{s-1} d\ell, \qquad (4)$$

where H is the atmospheric scale height, $f(\chi_0, s)$ is a function given by Kaiser (1960, fig. 8), $\rho = \alpha_{p_0}/\alpha_p$, where α_{p_0} is the minimum value of α_p, which is the value of α at any point along the echo line required to give an echo power P_R, and $d\ell$ is an element of the echo line. The parameter ρ thus accounts for the variation of equipment sensitivity along the echo line. The direction of maximum aerial sensitivity is that for which $\rho = 1$, and does not necessarily intersect the echo line at a given instant. Provided N_P is determined over an interval of time during which the quantities of $f(\chi_0, s)$ and $\int \rho^{s-1} d\ell$ do not change appreciably, we see from equations (2) and (4) that $\log N_P$ should be a linear function of $\log(\alpha_{p_0})$ such that

$$-\frac{d(\log N_P)}{d(\log \alpha_{p_0})} = s - 1. \qquad (5)$$

The left-hand side of equation (5) is an experimentally determinable quantity (see section 2), and the value of s thus obtained can be substituted back into equation (4) to allow explicit evaluation of Θ as a function of α_{p_0} (or, using eq. (1), of M_r). Figure 1 shows contours of equal ρ projected onto a surface at a height

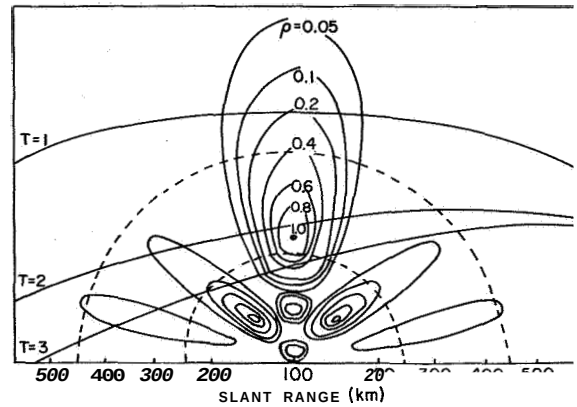

FIGURE 1.—Meteor sensitivity contours at a height of 100 km for the 17 Mc/sec rhombic aerial. The positions of the echo line at various times, T (hours), before transit of the Perseid radiant (Dec. = 53°) are shown for the case when the aerial is directed westward. The broken curves represent the range limits 250 to 450 km.

of 100 km for the 17 Mc/sec equipment described in section 2. Superimposed upon these contours is shown the position of the echo line at various times relative to the transit of the Perseid radiant, For given shower radiant coordinates and known aerial geometry, the movement of the echo line with time can be used to predict the time variation in the range distribution of echoes associated with a particular shower (the "range-time motion"). Equation (4) can be used to predict the expected variation of shower echo rate within any given range limits (the "rate curve") by evaluating the quantity $\int \rho^{s-1} d\ell$ over the intercept of the echo line between the chosen range limits (represented in fig. 1 by dotted curves).

2. Equipment

The equipment used in the present investigation is located at the Edgemont research station (53'26' N, 1'53' W) near Sheffield, England. Most of the data have been obtained with a noncoherent pulsed radar system operating at a frequency near 17 Mc/sec with a mean pulse power $\approx$ 7 kilowatts, pulse length 100 μsec, and repetition frequency 50 sec^{-1}. The rhombic antenna system, used for transmission and reception, produced a beam of width $\approx 20°$ (to half-power points) directed due west at an elevation of 17". The beam was capable of being directed due east should the occasion demand (see section 3.C). The overall effective power gain of this antenna over an isotropic

radiator was 21.3. The receiver output was recorded on magnetic tape, which had a dynamic range of more than 40 db, and the system was calibrated with sets of standard pulses graduated in increments of 6 db from an equivalent signal source replacing the aerial. The recorded meteor echoes were subsequently displayed on a large-screen oscilloscope with a free-running time base adjusted so that echoes appeared as amplitude-time profiles. A photograph of two such profiles is shown in plate 1. The echoes were selected between range limits chosen so as to minimize the contribution of sporadic meteors to the total observed rates, and the left-hand side of equation (5) was evaluated by counting the rate of decay-type echoes with amplitudes above various levels on the screen defined by the calibration pulses.

The minimum value of α_{p0} observable under average noise conditions is determined by the equipment parameters (equation (3)). For the 17 Mc/sec equipment, this value corresponded to $M_r=+8.3$. When meteors brighter than $M_r\sim+6$ are counted, the proportion of persistent-type echoes observed begins to become appreciable, and equation (4) is no longer valid. The magnitude range over which the rate of decay-type echoes could reliably be determined was thus $+8.3>M_r\gtrsim+6$ for this equipment.

The tape-recording system was supplemented by a camera, which photographed an intensity-modulated range display on a film moving continuously in a direction normal to that of the trace sweep, so that the distribution of echoes in range and time was automatically plotted on the film (range-time photograph). Examples taken during the activity of the Quadrantid shower are shown in plates 2 a and b. It should be noted that the range-time motion associated with a particular shower will usually appear distinct from the mean-range distribution of the sporadic background only if the value of s for the shower meteors is substantially less than for the sporadic meteors (for which $s=2.16\pm0.04$; Baldwin and Eaiser, 1965).

In addition to the 17 Mc/sec equipment another radar with a similar tape-recording and calibration system, and used with a rotating dipole antenna, was operated at a frequency near 30 Mc/sec. The faintest observable meteor on this equipment had $M_r=+7.0$.

3. Results

The shower-radiant coordinates given in this section have been provided by Evans (1960): R.A.=right ascension, Dec.=declination, $\odot$= solar longitude. Where more detailed descriptions of the various experiments are to be published, the appropriate references are given.

A. PERSEIDS.—(Kaiser, Poole, and Webster, 1966)

$$\text{R.A.}=(48.5\pm0.3)^\circ+(1.21\pm0.2)\,(\odot-138)^\circ,$$
$$\text{Dec.}=(52.9\pm0.2)^\circ+(0.13\pm0.2)\,(\odot-138)^\circ.$$

The main series of observations on this stream was carried out in 1962 between August 1 ($\odot=128\overset{\circ}{.}2$) and August 21 ($\odot=147\overset{\circ}{.}6$) with the 17 Mc/sec equipment. Certain aspects of these results were checked by a more Kited set of observations carried out in 1963.

The expected rate curve for Perseid meteors occurring within the range limits 250 to 450 km (fig. 1), determined as outlined in section 1 for August 13 (when Perseid activity was at a maximum in 1962), is shown in figure 2, together with the observed rate curves for the same date in 1962 and 1963. The experimental peak in activity is significantly wider than the theoretical one, and this has been attributed to an overall diffuseness in the Perseid radiant. A comparison of the expected range-time motion with that observed on August 13, 1962 (not reproduced here; see Eaiser, Poole, and Webster, 1966), indicates a fairly sharp radiant, and it was consequently assumed that meteors associated with the Perseid shower emanate from a complex radiant comprisiig a discrete central component surrounded by a more diffuse "halo." This is in broad agreement with the result of Hawkins and Almond (1952).

The activity of the radiant as a whole was assessed by determining the hourly rates of meteors brighter than $M_r=+8.3$, $+7.5$, and $+6.8$ over a half-hour period centered at 04.05 UT, and that of the diffuse component by determining the corresponding rates over a similar period centered at 05.15 UT (see fig. 2). To allow for the contribution of sporadic meteors to the observed rates, the hourly rates over the corresponding half-hour intervals on

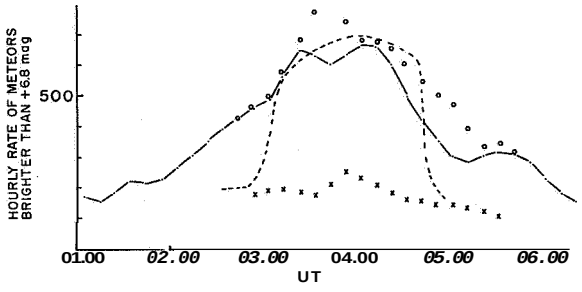

FIGURE 2.—Hourly echo rate vs time for different dates:

—	—		August 13,1963
0	0	0	August 13,1962
X	X	X	August 1,1962
----------			Theoretical rate curve (on an arbitrary scale) for a point radiant, R.A.=49.°5, Dec.=53°, assuming $s=1.6$.

dates between August 1 and August 5 (inclusive) were averaged and subtracted from the observed rates. This could not be done for dates following Perseid activity since a study of range-time photographs indicated that the enhanced rate persisting until August 21 (the latest date on which records were obtained in 1962) was due to shower meteors, and this was again apparent in 1963. The shower rates thus obtained for the Perseid radiant as a whole and for the diffuse component are shown in figures 3 a and b, respectively, as functions of solar longitude. It was found that over a more limited range of solar longitude, the contribution of the discrete radiant to the total Perseid rate could be estimated with sufficient accuracy by subtracting the rates in figure 3b from the corresponding ones in figure 3a, to give figure 3c.

The value of the exponents was determined as a function of $\odot$ for the curves in figures 3a–c from equations (1) to (5). The results are shown in figures 4a, b. The valued Θ obtained from equation (4) for the discrete radiant on August 13, 1962, is shown in figure 5 as a function of M_r.

The most striking feature of these results is the rapid decrease of s with $\odot$ for the discrete radiant in figure 4c, which suggests that the distribution of meteoroid masses changes as the earth moves through the stream. The low value of s at $\odot=139°.9$ in figure 4c supports previous suggestions (e.g., Hawkins and

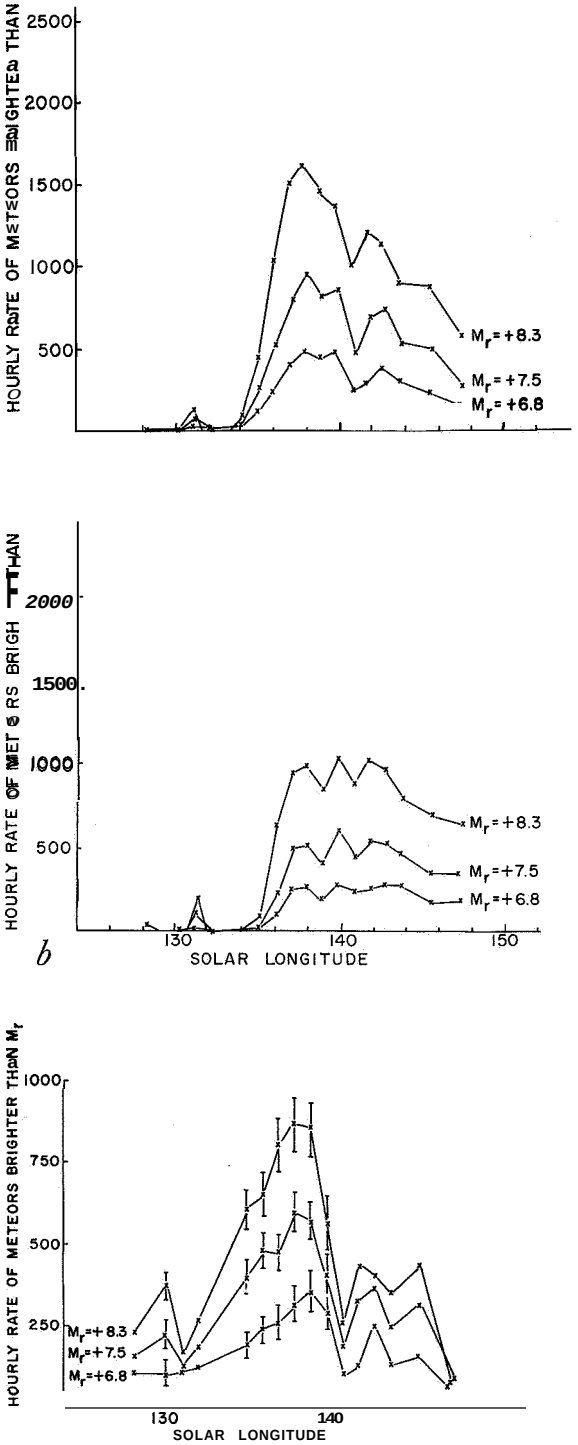

FIGURE 3.—Mean hourly echo rates for meteors associated with: *a*, the Perseid radiant as a whole vs solar longitude (1962); *b*, the diffuse component of the Perseid radiant vs solar longitude (1962); c, the discrete component of the Perseid radiant vs solar longitude (1962).

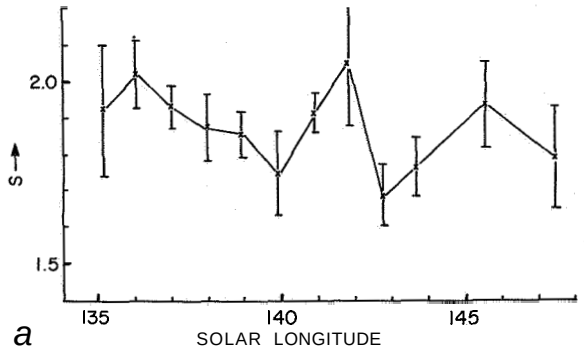

a

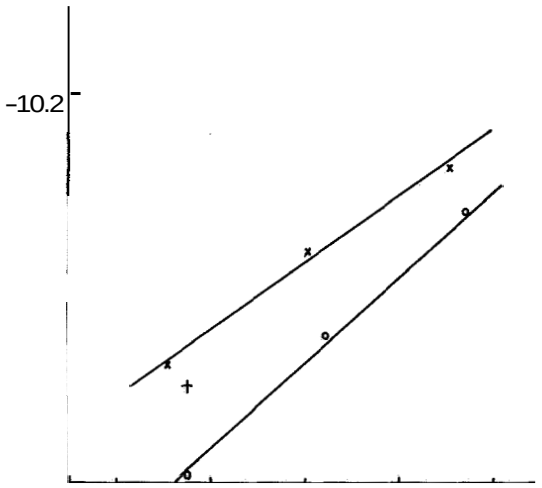

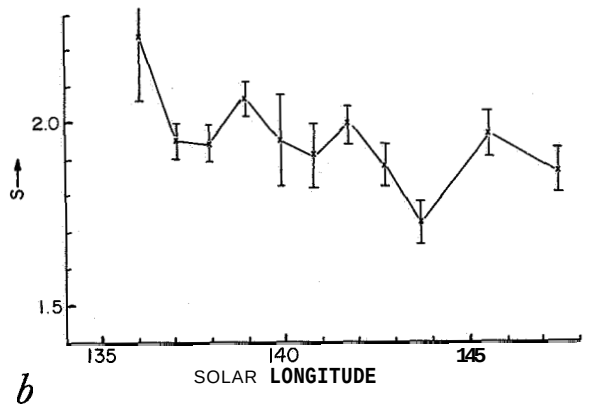

b

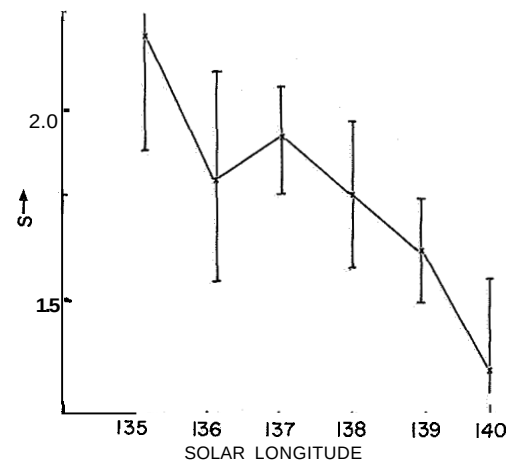

FIGURE 4.—Variation of the exponent s with solar longitude (1962) for: *a*, the Perseid radiant as a whole; b, the diffuse component of the Perseid radiant; *c*, the discrete component of the Perseid radiant.

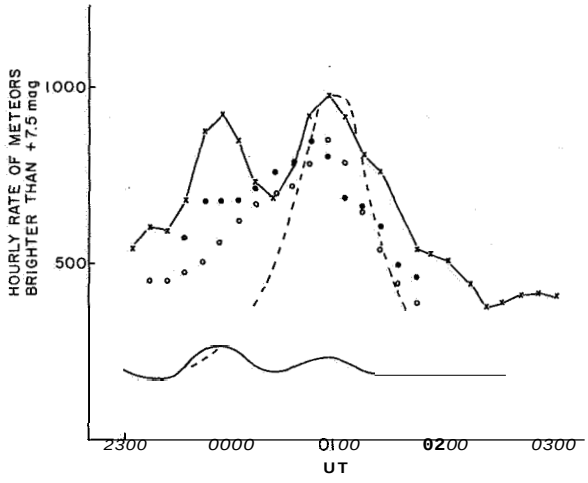

FIGURE 6.—Hourly echo rates vs time for different dates:
X——X——X December 13, 1962
0 0 0 December 13, 1963
——— Mean of rates on November 26 and December 22,1962
..... Theoretical rate curve (on an arbitrary scale) for a point radiant, R.A.=112°.6, Dec.=33°.3, assuming $s=1.6$

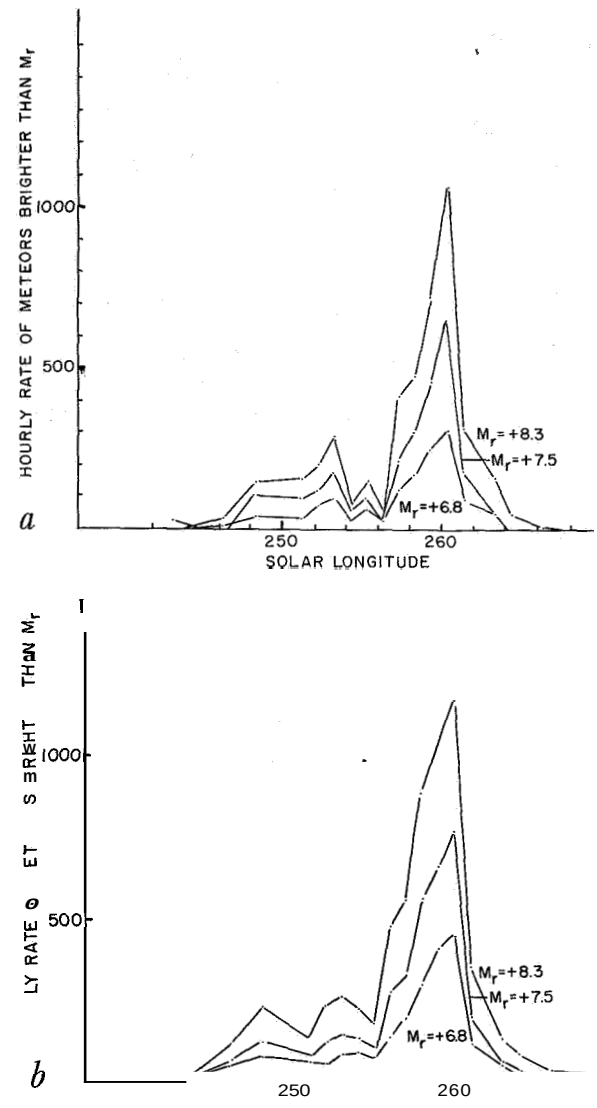

and has been tentatively ascribed to the activity of a secondary radiant (the "early radiant") with a similar declination to that of the main radiant, but with R.A. ~15° smaller. On the range-time photograph for December 13 (Webster, Kaiser, and Poole, 1966), the activity of such a radiant can be detected, but it is less noticeable than that of the main radiant. Observations during different years correspond as closely as possible in solar longitude.

The hourly rates associated with the early and main radiants in 1962 were determined for each day of observation over 20-min intervals centered at 23.55 UT and 00.55 UT, respectively, and appear in figures 7a, b as functions of $\odot$. In this case the sporadic contribution was determined on November 26 and December 22. The plots of s vs $\odot$ for the two radiants are shown in figures 8a, b. As for the Perseids, a gradient in s is apparent for the main Geminid radiant, while the early radiant appears to be associated with a more complex structure with a minimum for s at $\odot=256°.3$. It will be noticed that on December 13 ($\odot=260°.5$), s is significantly higher for the early radiant than for the main one, and this could explain the comparatively poor experimental range-time plot obtained for the former radiant (see section 2). We have obtained Θ for the maximum activity of the main radiant in 1962 (December 13), as shown in figure 5.

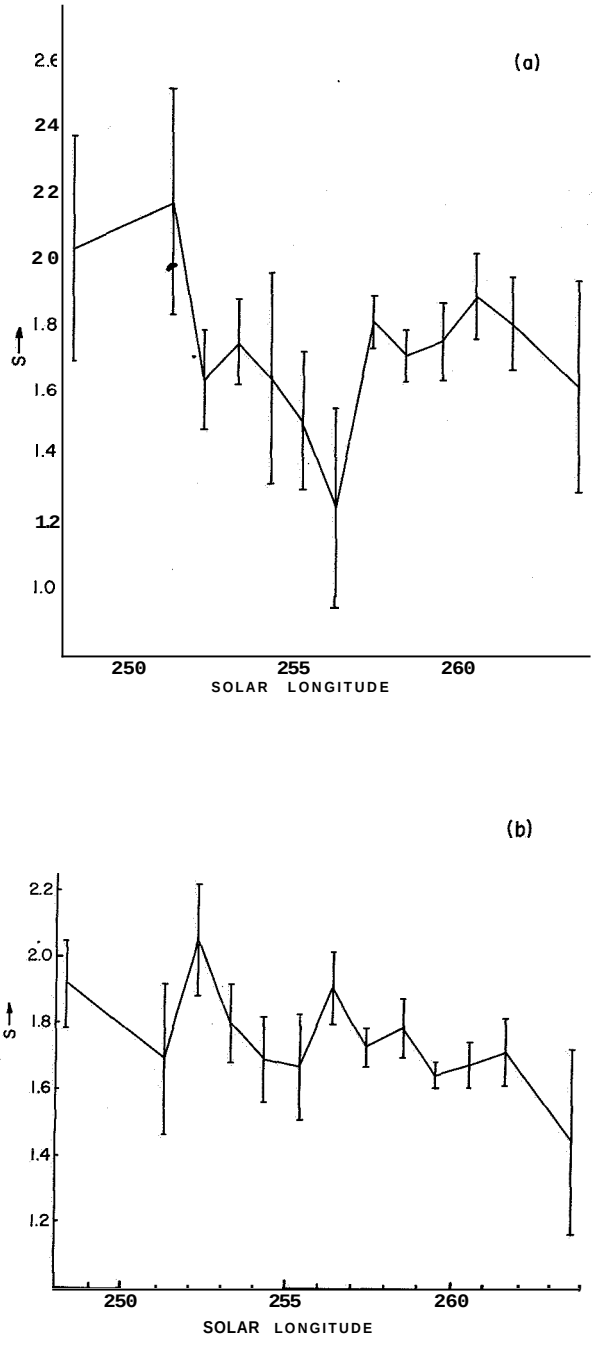

FIGURE 8.—Variation of the exponent *s* with solar longitude (1962) for: *a*, the early Geminid radiant; *b*, the main Geminid radiant.

The fact that the early peak has not thus far reappeared since 1962 has led to the surmise that it might be connected with the periodic Sextanid stream, which has an orbit similar to that of the Geminids (Nilsson, 1964). The Sextanids appear in September every 4 or 5 years, so that if the "early Geminids" exhibit a similar periodicity we might expect their return in 1966 or 1967.

C. QUADRANTIDS.—(Poole, Webster, and Kaiser in preparation)

$$\left.\begin{array}{l}\text{R.A.}=233°\pm2\\ \text{Dec.}=50°.5\pm0.3\end{array}\right\}\ \text{at}\ \odot=283°.$$

This shower does not endure over a sufficient range of solar longitude to permit a study of structure as described in sections 3.A and 3.B. The main activity extends over $<1°$ in $\odot$, and Bullough (1954) has reported an intense subcenter that extends over a mere $0.°1$ in $\odot$. Observations of Quadrantid activity have been considerably hampered at Sheffield by the severe weather conditions prevalent at the time of year. In January 1963 attempts to make recordings completely failed, and in 1964 only limited success was achieved. Every effort was made to ensure satisfactory results in 1965, especially since the 17 Mc/sec aerial geometry was favorably disposed to observe Bullough's (1954) subcenter during this encounter. On this occasion, however, the sporadic control days before the date of maximum activity were lost.

The expected and observed range-time plots for January 4, 1964, are shown in plate 2a. The well-defined experimental plot is indicative of a narrow shower radiant and low *s* value, and on January 3, 1965, an estimate of the radiant coordinates was made by switching the antenna so that it was directed eastward after transit in order to obtain the "mirror image" range-time photograph shown in plate 2b (the interference evident after the switchover is from European stations). This facilitated the more exact determination of the time of transit, and hence of R.A.; declination was estimated by comparing the theoretical range-time envelopes for various declinations with the experimental plots. The radiant found was R.A.$=231°\pm0.1$, Dec.$=+50°\pm2$ for $\odot=282°.65$. This agrees well with Evans' mean radiant, although the latter appears to be more diffuse.

The theoretical rate curve derived for the above radiant predicts a peak in activity at 06.55 UT, and figure 9 (comprising 2 years'

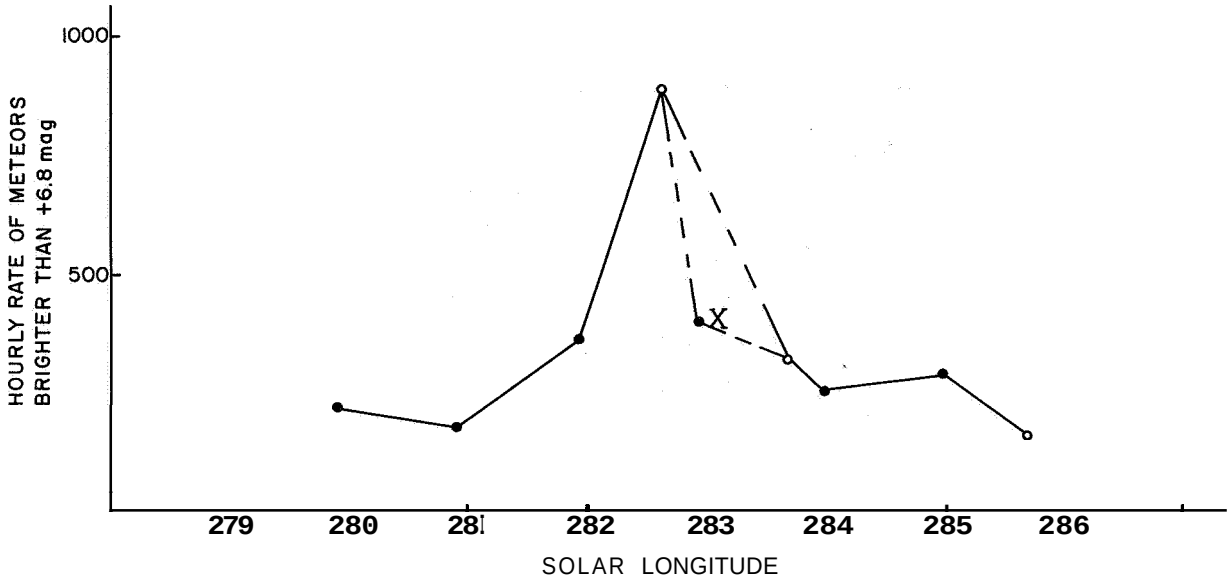

FIGURE 9.—Mean hourly echo rates determined over a half-hour period centered at 06.55 UT vs solar longitude. Full circles: results obtained in 1964; open circles: results obtained in 1965. The accuracy of the point marked X is in doubt.

results) shows the variation with $\odot$ of total hourly rate of meteors brighter than $M_r = +6.8$ determined over a half-hour interval centered at this time. The high rate at $\odot = 282°.7$ was obtained on January 3, 1965, and the corresponding value of Θ for $M_r = +6.8$ is shown in figure 5. The rate of persistent echoes during this encounter was too high to allow a meaningful determination of the echo rate for fainter meteors, and this has rendered the determination of s for this shower difficult. The best estimate from the available data is $s = 1.55 \pm 0.2$. The point marked $\times$ in figure 9 was obtained on January 4, 1964, when heavy icing of the antenna occurred, and its accuracy is consequently in doubt.

D. ARIETIDS.—(J. Jones, unpublished)

$$\text{R.A.} = (45.1 \pm 0.2)° + (0.69 \pm 0.11)(\odot - 78.3)°,$$
$$\text{Dec.} = (23.8 \pm 0.5)° + (0.43 \pm 0.25)(\odot - 78.3)°.$$

For these observations the 30 Mc/sec rotating dipole equipment was used in an experiment designed to examine the effect of changing zenith angle (χ) on shower meteor rates. The observations were conducted between June 1 and June 20, 1964. Every effort was made, through suitable adjustment of aerial azimuth and of the range gate, to avoid observing echoes associated with the ζ-Perseid stream (R.A. $\approx 59°$, Dec. $\approx 22°$), but for moderate values of χ contamination by the latter stream appears to have been unavoidable. The observed daily rates for the (contaminated) Arietid meteors determined over successive 24-hour intervals centered on the time of radiant transit (thus encompassing a range of values of χ) are shown in figure 10 against solar longitude, and the corresponding values of s in figure 11. These agree well with the mean value of 2.14 ± 0.02, obtained by Brooks (1963) at Sheffield, for a mixture of Arietid and ζ-Perseid meteors observed between June 3–8 (inclusive), 1959.

E. ORIONIDS, LEONIDS, AND LYRIDS.—The Orionid shower occurs over a few days in October with a maximum around October 21. This shower has produced a noticeable range-time plot on a continuous slow-film recording being conducted at Sheffield, but the overall activity has not been investigated in detail.

Tape recordings were taken with the 17 Mc/sec equipment on November 16–18, 1964, to investigate the activity of the Leonid stream, since the period 1964 to 1966 coincides roughly with the 33-year cycle characteristic of this shower. However, no significant activity associated with the shower could be detected. Further observations were planned for 1965.

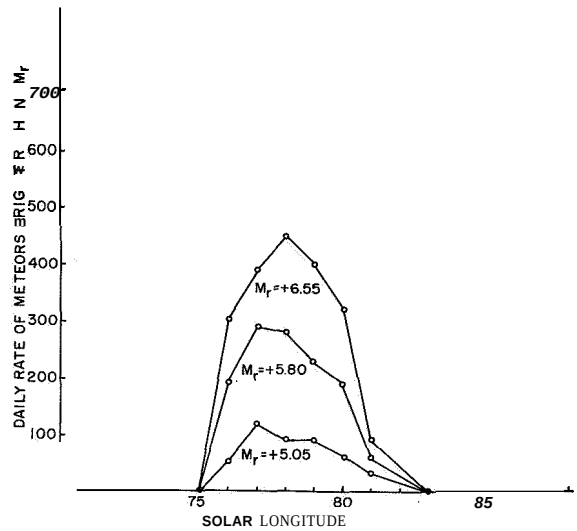

FIGURE 10.—Daily echo rates for meteors associated with the Arietid stream vs solar longitude (1964).

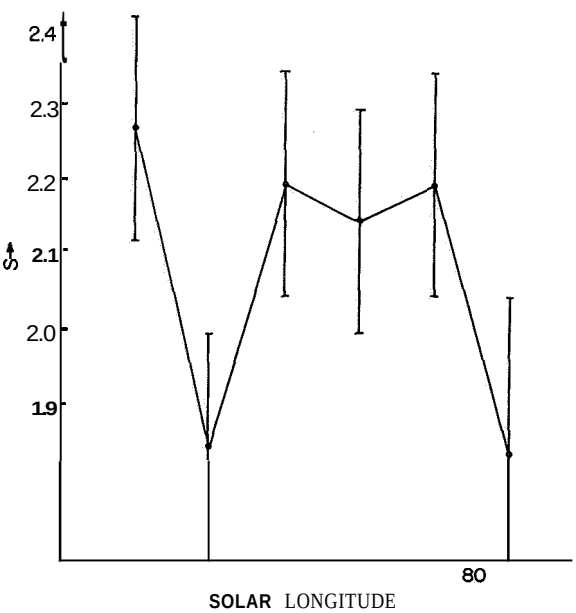

FIGURE 11.—Variation of the exepnont s with solar longitude (1964) for meteors associated with the Arietid stream.

Observations have **also** been carried out on the Lyrid shower during April **1964** with the **30** Mc/sec equipment, but again no significant shower activity was detected.

4. Conclusion

The present results, where they cover aspects already examined by other workers, are in general agreement with the previous work. Points of difference worth noting are: **(1)** activity associated with the Perseid stream persists until a later date than is suggested by other results (and appears to be associated with the diffuse component of the radiant); **(2)** a double radiant associated with the Geminid stream has not previously been detected by radar methods, although complexities in this radiant have been found from visual observations (King, **1926);** and **(3)** the Quadrantid radiant is apparently well defined according to the present evidence, whereas Evans **(1960)** finds a comparatively large radiant diameter.

For many of the various radiants studied significant variations in s with $\odot$ are revealed. Of the various processes acting throughout the lifetime of a stream that might produce changes and gradients in the distribution **of** masses among members of the streams, three appear to be of prime importance: **(1)** the Poynting-Robertson effect, discussed by Wyatt and Whipple **(1950);** (2) the drag induced by the solar wind; and **(3)** the sputtering of meteoroids by the solar wind (Kresák, **1960).** The effect of these mechanisms is difficult to assess quantitatively, but each acts within the orbital plane of the stream; any resulting gradients will thus be detected by the earthbound observer only if the inclination of the stream to the ecliptic is sufficiently low. Processes **(1)** and (2) will preferentially shorten the major axes of orbits of the smaller particles in the stream so that in time an increase of s among meteors with shorter orbits may be expected; on the other hand, **(3)** tends to decrease s, preferentially among the shorter orbit meteors. The trend in s with $\odot$ observed will thus depend on which of these mechanisms is predominant and on the direction of the earth's motion through the stream.

Of the streams under consideration here the Geminids and Arietids have the lowest inclinations ($\lesssim 20°$). **As** the earth traverses the Geminid stream, it intersects orbits **of** increasing major axis, and the value of s (for the main radiant, fig. 8b) is found to decrease. In the case of the Arietids the situation is reversed, and we would expect the trend in s to be opposite to that for the Geminids. No such trend is immediately apparent in figure **11** (if

anything, s again tends to fall), The orbit of the Perseid stream is steeply inclined to the ecliptic, and the rapid variation of s in figure 4c for the discrete radiant is again unexpected. These results thus do not generally support an evolutionary theory of stream structure (at least in terms of the above selective processes), and imply that the observed gradients are more probably dependent on the mode of a stream's formation than on its subsequent history. Southworth **(1963)** has shown that the present width of the Perseid stream can be explained in terms of an explosion of the parent comet some 1000 years ago, and it is thought that most streams are likewise formed by the disintegration of cometary-type bodies, although this is probably a gradual process in many cases. The velocities imparted to meteoroids leaving the parent body might well be size dependent, and this could in principle explain the existence of cores and discontinuities within streams. The structure of a stream would thus depend on such factors as the nature of the comet, the distribution of particle sizes within the nucleus, and the mode of disintegration.

It is well known that the values of s for shower meteors are generally lower than those for the meteors comprising the sporadic background, and this is confirmed by the present results (with the exception of the Arietid shower). This low value of s has again been ascribed (Wyatt and Whipple, **1950;** Kresák, **1960)** to the processes discussed above, which will selectively remove smaller particles from the streams. The time scales involved are, however, still uncertain, and it is doubtful whether any streams are sufficiently long lived for the effect of these processes to become apparent (Kresák, **1960).** It is conceivable that the increased value of s for sporadic meteors is due to fragmentation through mutual collisions of meteoroids over a period of time long compared to the average age of a meteor stream. This might also account for their relative lack of abundance (to which attention has also been drawn by Kresák, **1960)** in the solar system.

Acknowledgments

The author is indebted to his colleagues, Drs. T. **R.** Kaiser, **A. R.** Webster, and J. Jones, on whose work he has drawn in the preparation of this communication. The work has been supported by the Scientific Research Council.

References

BALDWIN, J. P., and KAISER, T. R.
1965. Radio observations of sporadic meteors at 17 Mc/s. Monthly Notices Roy. Astron. Soc., vol. **129,** pp. **85–102.**

BROOKS, D.
1963. Radar echoes from the aurora and meteors and their association with other phenomena. Ph.D. Thesis, Sheffield Univ., Sheffield, England.

BULLOUGH, K.
1954. Radio echo observations of the day- and night-time meteor streams **1951** October to **1953** December. Jodrell Bank Ann., vol. 1, pp. **68–97.**

EVANS, G. C.
1960. Radio echo observations of meteor activity between **1954** December and **1958** December. Jodrell Bank Ann., vol. **1,** pp. **280–337.**

HAWKINS, G. S., and ALMOND, M.
1952. Radio echo observations of the major night-time meteor streams. Monthly Notices Roy. Astron. Soc., vol. **112,** pp. **219–233.**

KAISER, T. R.
1960. The determination of the incident flux of radio meteors. Monthly Notices Roy. Astron. Soc., vol. **121,** pp. **284–298.**

KAISER, T. R.; POOLE, L. M. G.; and WEBSTER, A. R.
1966 Radio-echo observations of the major night-time meteor streams, **I:** Perseids. Monthly Notices Roy. Astron. Soc., vol. **132,** pp. **225–237.**

KING, A.
1926. An emphemeris of the Geminid radiant-point. Monthly Notices Roy. Astron. Soc., vol. **86,** pp. **638–641.**

KRESÁK, Ľ.
1960. The effect of solar corpuscular emission on the magnitude distribution of meteors. Bull. Astron. Inst. Czechoslovakia, vol. **11,** pp. **1–9.**

NILSSON, C. S.
1964. Short communications. The Sextanid meteor stream. Australian Journ. Phys., vol. **17,** pp. **158–160.**

SOUTHWORTH, R. B.
1963. Dynamical evolution of the Perseids and Orionids. *In* Proceedings of the Symposium on the Astronomy and Physics of Meteors. Smithsonian Contr. Astrophys., vol. 7, pp. **299–303.**

WEBSTER, A. R., KAISER, T. R., and POOLE, L. M. G.
1966. Radio-echo observations of the major night-time meteor streams, 11: Geminids. Monthly Notices Roy. Astron. Soc., vol. **133,** pp. **309–319.**

WYATT, S. P., Jr., and WHIPPLE, F. L.
1950. The Poynting-Robertson effect on meteor orbits. Astrophys. Journ., vol. **111,** pp. 134–141.

Abstract

Systematic radar observations on the major northern meteor streams have been carried out at Sheffield since **1962** in order to study the variation of the total incident flux and magnitude distribution exponent (s) of shower meteors with solar longitude ($\odot$). Significant gradients in s with $\odot$ have been found for the Perseid, Geminid, and Arietid showers, which are not generally easy to explain in terms of known selective processes acting during the lifetime of the streams. Information has also been obtained concerning the radiant structure of some of the showers. The Perseid radiant is found to consist of a discrete center of activity surrounded by a more diffuse "halo." The main Geminid radiant was accompanied in **1962** by a less active radiant that transited an hour earlier than the main one, but which has not since reappeared, and is possibly connected with the periodic Sextanid stream. In **1965** the Quadrantid stream provided a higher meteor rate than any other stream observed, but the high level of activity was maintained over a range of $\odot$ of less than 1°, and appears to be associated with a well-defined radiant.

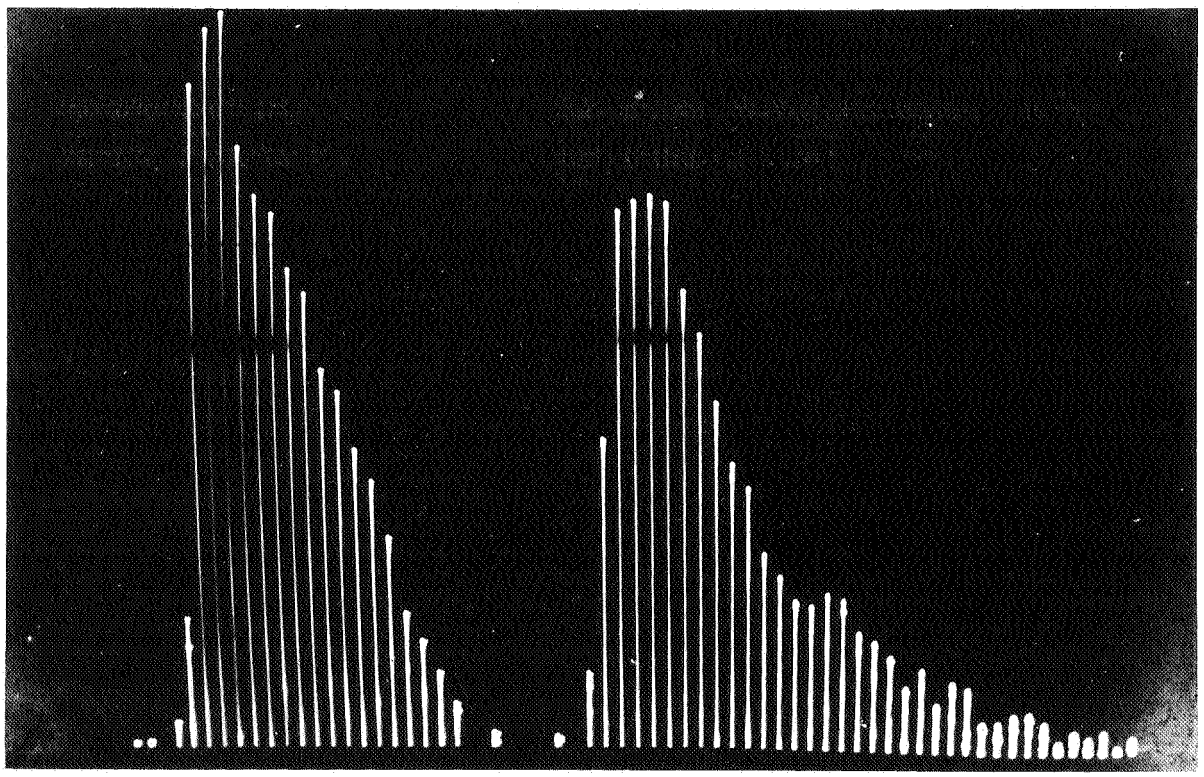

PLATE 1
Photograph of two decay-type echoes as displayed on the large-screen oscilloscope.

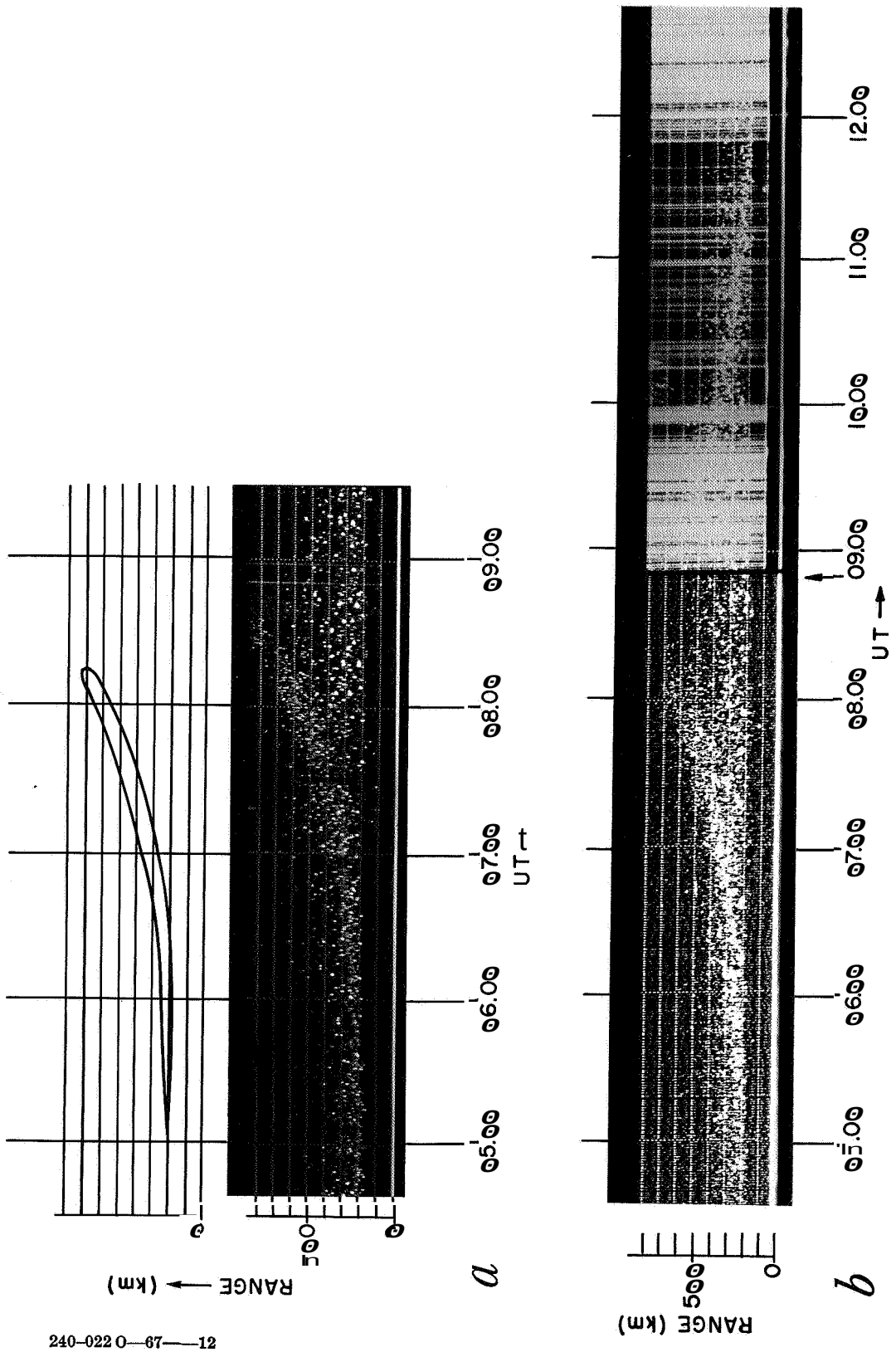

PLATE 2

Range-time photographs: *a*, January 4, 1964. For comparison the theoretical range-time envelope is shown for the point radiant, R.A.=233°, Dec.=50.°5, and for echoes received from the segment of the echo time where $\rho > 0.1$. Aerial is directed westward. *b*, January 3, 1965. Aerial is directed westward before the time marked by the arrow, and eastward afterward. (Meteor echoes appear as white dots.)

240-022 O—67——12

Luminosity Function of Sporadic Meteors and Extrapolation of Influx Rate to Micrometeorite Region

B.-A. LINDBLAD[1]

The statistics of meteor magnitudes form the basis for the derivation of the distribution of meteor masses. To determine the mass influx rate of meteors we must study the characteristics of the luminosity function of meteors. Experimental investigations suggest that the luminosity function is of the form

$$F(m)=F(0)\times r^{m}, \qquad (1)$$

where $F(m)$ is the number of meteors equal to or brighter than a given magnitude m. The parameter r, which is assumed to be constant over a fairly wide range of magnitudes, determines the increase in meteor numbers as we go to fainter meteors. Taking logarithms to the base 10 and differentiating equation (1), we get

$$\frac{d \log F(m)}{dm}=\log r. \qquad (2)$$

If the ratio of increase r is independent of magnitude, the logarithms of the accumulated meteor numbers lie on a straight line of slope $\log r$. It follows that the ratio r may be determined directly from an experimental plot of $\log F(m)$ against m, provided a sufficiently large meteor sample is available.

A number of experimental investigations of the luminosity function of meteors have been published. The vast majority of these studies are based on naked-eye observations. It is difficult to assess the significance of many of these studies since information about the area of sky searched for meteors, the sky conditions, the date and length of the observational periods, etc., is missing. In addition, the investigators usually analyze the luminosity function of apparent magnitudes, which may differ considerably from that of the absolute magnitudes. It is hence not surprising that there is considerable divergence in the experimental determinations of the ratio of increase r. For sporadic or nonshower meteors, published values of r vary between 2.3 and 4.0. Shower meteors tend to show some individual peculiarities, but values of r generally lie in the range 3.0 to 4.0. For complete references as well as a general discussion of the visual investigations see, for example, the monographs by McEinley (1961), Millman and McKinley (1963), and Hawkins (1964).

[1] Lund Observatory, Sweden.

Previous investigations

In the following, reference will be given only to a few representative investigations that were based on carefully supervised group observations or where the circumstances of the observations were otherwise carefully controlled.

One of the first large-scale attempts to study meteor phenomena was the Arizona expedition. As part of this project, Watson (1937) analyzed a small number of naked-eye and telescopic magnitudes collected by Öpik and Boothroyd. Independent, naked-eye data published by Hoffmeister (1931) were also analyzed. The study gave $r=4.0$ for naked-eye meteors. In a later summarizing discussion of all the available Arizona data, Öpik (1958) found an average value of $r=3.3$. This ratio he found to be constant over the apparent magnitude range $+1$ to $+5$ mag.

The most extensive investigations in recent years of the luminosity function of naked-eye meteors have been carried out by Millman and collaborators. In an analysis of Canadian meteor observations, Millman and Burland **(1956)** deduced from a study of the apparent magnitudes that $r=3.7$ for a mixture of shower and nonshower meteors. This ratio is constant over the absolute magnitude range -6 to $+1$ mag. For fainter meteors the authors suggest that the ratio decreases, possibly reaching a value as low as 2.5 for meteors of absolute magnitude $+5$ mag. It is noted, however, that there is considerable uncertainty involved in determining the ratio for faint meteors, since it is very dependent on the corrections made for objects missed by the observers.

A detailed investigation of photographic meteor magnitudes has been published by Hawkins and Upton **(1958).** This study differs from the previous ones in that it analyzes the luminosity function of absolute magnitudes. The authors studied the magnitudes of randomly selected meteors photographed with Super-Schmidt cameras, and found a constant ratio $r=3.4$ over the photographic absolute magnitude interval from -2.5 to $+3.4$ mag. No tendency was found for r to decrease as fainter meteors were studied.

The conversion of photographic meteor magnitudes to visual magnitudes (or vice versa) presents certain scale problems that are not yet completely solved, and that may influence the magnitude statistics. Hawkins and Upton in their discussion corrected for a variable color index and found that the gradient of the luminosity function of sporadic meteors on the visual magnitude scale was not entirely constant over the magnitude range studied; however, this effect was not very pronounced in their study, and they apparently accepted $r=3.4$ as the best estimate of the ratio of increase on the visual magnitude scale as well.

Several attempts have been made to deduce the luminosity function of meteors from telescopic observations. If the observing instrument is directed to high elevations, the inclusion of telescopic meteors considerably extends the magnitude range of a study; however, the telescopic data are as a rule quantitatively small and the telescopic magnitudes are extremely difficult to evaluate on the naked-eye magnitude scale. Further large magnitude-dependent corrections for the effective field of view of the instrument must be applied to the observed frequencies of magnitudes.

Watson **(1939)** made a study of the luminosity function of meteors in the telescopic magnitude range $+4.5$ to $+9.5$ mag. The difficulties involved in a telescopic study are well illustrated by Watson's paper. The original apparent telescopic magnitudes were first corrected to the naked-eye scale by means of a nonlinear relation between apparent telescopic magnitude and true magnitude. After a correction of the observed frequencies for variation of effective telescopic field with meteor magnitude, Watson concluded that the ratio of increase was $r=2.7$. Very similar results have been obtained by other investigators such as Williams **(1939)** and Kresáková and Kresák **(1955).**

A model distribution of meteor magnitudes was published in tabular form by Watson **(1941).** This model distribution, which is based on an assumed ratio of increase $r=2.5$ over the magnitude range -3 to $+10$ mag, has been used extensively in the literature. The observational basis for this table is not stated, but presumably it is based on Watson's **1939** paper. It can be shown that a ratio $r=2.5$ produces the mathematically convenient result that there is constant mass per magnitude interval in the meteor population. This result, sometimes referred to as Watson's law of constant mass, has formed the basis of a number of theoretical discussions about meteors and interplanetary dust.

Present investigation

The purpose of the present investigation is to obtain the luminosity function of meteors from a study of the absolute magnitudes of naked-eye meteors. The data were collected in the years **1953** to **1964** as part of a more general study of meteors, which is being carried out by the Lund and Onsala Observatories in Sweden by both radar and visual techniques. Details of the radar equipment and of the general program are given elsewhere (Lindblad, **1963).**

OBSERVATIONAL PROCEDURE.—The same basic observational procedure has been followed ever

since the inauguration of these studies in 1953. Visual recording is made by a standard team of three observers. The observers estimate meteor magnitudes and also plot the meteors on star charts. Meteor brightness is estimated to the nearest half-magnitude by direct comparison with standard magnitudes within the field of observation. The probable error of a magnitude estimate is 0.3 mag.

The detailed arrangement of our visual program differs in certain respects from that of other workers. In radar-visual studies the total field of the observers is determined by the obvious condition that adequate sky coverage must be obtained over the beamed sky area of the meteor radar. Since we are using a moderately directive antenna, the observed sky area is limited to a field of approximate radius 40". This field in turn is subdivided into three standard regions, which are assigned to the individual observers. These regions, each of approximate radius 25°, are kept fixed with respect to the horizon. Two adjacent fields are centered at an elevation of 40° to 50°, and the thiid field corresponds to the adjacent zone in zenith.

A meteor is always entered in the records as having been seen by only one observer. The responsibility of recording and plotting a meteor trail normally rests on the observer in whose field the meteor appears. If the circumstances of observation are unfavorable, which may be the case if the meteor rate is high, the responsibility may by mutual agreement be transferred to another member of the team.

The position of a meteor in the observer's field of view is of importance for the following discussion. For future reference we therefore note that a meteor recorded within the observer's regular field will have an angular distance from the fixation point of the observer of less than 25°, and a meteor recorded in the field of another observer will have a value larger than 25°.

OBSERVATIONAL DATA.—The observational material used comprised 4000 meteors recorded during the month of August in the years 1953 to 1964. Of these meteors, 2865 belonged to the Perseid shower, 238 to the δ-Aquarid shower; 859 were sporadic meteors, and 38 were identified members of various other showers.

REDUCTION OF MAGNITUDE DATA.—The recorded apparent magnitudes were reduced to a zenithal or absolute value by adding a correction $Am = 10 - 5 \log d$, where d is the distance in kilometers to the meteor. The zenithal correction was computed to 0.1 mag. Visual absolute magnitudes of the present paper are therefore nominally given to 0.1 mag.

Computation of Am demands a knowledge of the distance to the meteor. For about one-third of the meteors recorded by us a direct radar range determination of d was available and Am was computed directly from the above formula. To obtain Am for the remaining objects we prepared nomograms that directly on a curved earth basis gave Am as a function of elevation angle and mean meteor height. The mean height adopted in our investigation was 95 km for sporadic and δ-Aquarid meteors and 100 km for Perseid meteors.

As a check upon the consistency of the reduction procedure, a random sample of meteors with radar data was chosen and the absolute magnitude was computed by both procedures. The standard deviation of the difference between absolute magnitudes computed from range data and from elevation data turned out to be 0.2 mag. This error was thus the additional magnitude error appearing in the no-radar data group when we reduced the apparent magnitudes to absolute magnitudes using elevation information only. It should be noted that if one neglects the zenith correction Am one introduces a far larger error—in exceptional cases it may amount to several magnitudes. A study of the luminosity function of meteors should therefore always be based on absolute magnitudes computed for each single meteor in the investigation. The sole reason these studies in the past were based on apparent magnitudes is that no range or elevation information had been recorded.

For each meteor in our study, the absolute magnitude, the code number of the observer, and the position in the sky were collected on a punched card together with other relevant information. Luminosity functions of absolute magnitudes were then studied for various groupings of the data.

Luminosity function of absolute magnitudes

In figure 1 the log accumulated numbers of absolute magnitudes are plotted for every tenth of a magnitude for the total meteor sample. In figures 2, 3, and 4 cumulative curves are drawn for nonshower, Perseid, and δ-Aquarid meteors, respectively. Inspection of the cumulative curves shows that the slope of log $F(m)$ against m in each case may be represented by a straight line over a fairly wide magnitude range. From the slope of this line we deduce the values of r listed in table 1.

COMPLETENESS OF SURVEY.—For magnitudes fainter than approximately +2 mag the nonshower and δ-Aquarid curves become nonlinear. It is unlikely that this is a real effect; more probably the departure from linearity at +2 mag represents a decrease in efficiency of the eye, which is associated with the apparent speed of the meteors. Support for this conclusion, may be found if the departure values of all three samples as listed in the fourth column of table 1 are compared with the estimated mean angular velocities. The departure points given in table 1 thus indicate the faintest absolute magnitude at which the particular survey is complete.

RATIO OF INCREASE r.—Inspection of table 1 shows that the two showers studied by us exhibit significantly higher values of r than the sporadic meteor background. In particular, the high r value obtained for the δ-Aquarid shower is interesting, since it indicates that this shower is very rich in faint meteors and thus of recent origin.

For the purpose of the present paper interest is focused mainly on the ratio r for sporadic meteors. From the straight line slope we deduce that $r=3.2$. This result applies to an absolute magnitude range −3 to +2 mag and to an analysis in which no corrections for losses or for observational errors have been applied.

The observed cumulative curve of absolute magnitudes is distorted by two main factors: (1) the selectivity depending upon magnitude leading to a progressive loss of meteors as the study is carried to fainter objects, and (2) the accidental errors of individual magnitude estimates. Both these factors operate to lower the observed slope, and thus also the experimental value of r. In careful meteor studies based on counts by trained observers the distortive effect of the accidental magnitude errors is of minor importance, and the progressive loss of meteors with decreasing luminosity is the main distortive factor. This factor may be ascribed to a dependence of the diameter of the field of vision upon the brightness of a meteor.

VARIATION OF r WITH SIZE OF OBSERVED FIELD.—We investigated how the experimental ratio r varied with the radius of the field of vision of an observer. This study was facilitated by the observational procedure used in the present program, which implies that the same three carefully delineated regions of sky are observed each year. Although in consecutive years different individuals may be responsible for any one region, the center of the field is consistently well defined. It is thus possible to compute for each meteor the angular distance to the appropriate center of field or fixation point. From this information cumulative curves of absolute magnitudes can be studied for selected intervals of angular distance.

The data were first split into 3 angular zones or rings with the limits 0°–19°, 20°–39°, and 40°–59°. Figure 5 depicts the value of log r for

TABLE 1.—*Ratio of increase* r

	Slope of line ($\log^{10} r$)	Ratio of increase (r)	Completeness of survey (magnitudes)	Linear velocity (km/sec)	Angular velocity (deg/sec)
Sporadics	0.51	3.2	2.0	40	15
δ Aquarids	0.68	4.8	2.0	40	16
Perseids	0.56	3.6	0.0	60	20
All meteors	0.56	3.6	—	—	—

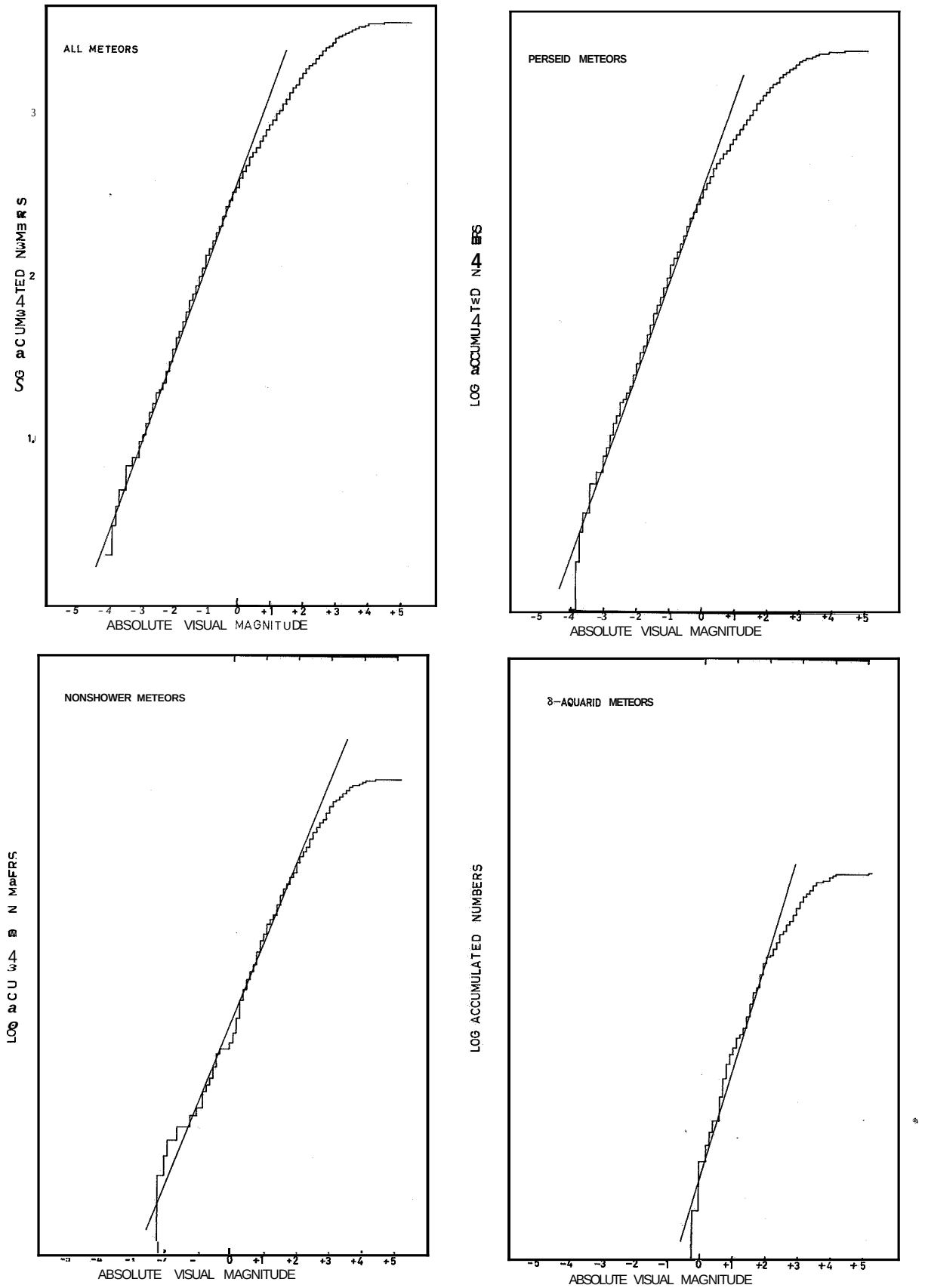

FIGURES 1–4.—Log accumulated numbers versus absolute visual magnitude.

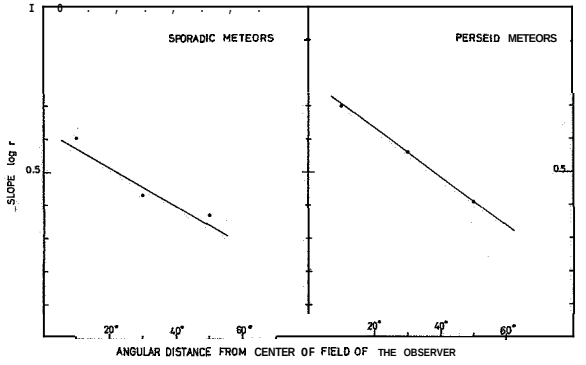

FIGURE 5.—Slope log r as determined for three separate angular zones.

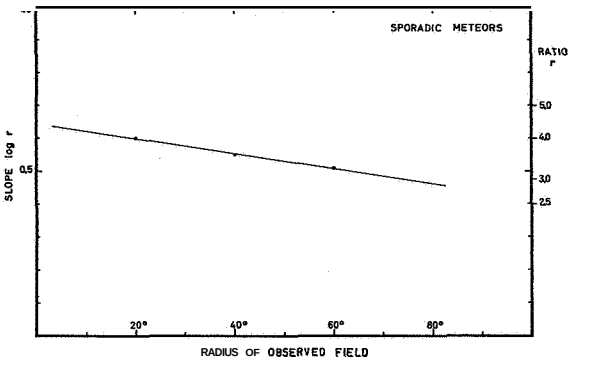

FIGURE 6.—Variation of log r with size of observed field.

these zones as deduced from plots of log $F(m)$ against m. It is convenient to treat the sporadic and Perseid data separately. This division corresponds roughly to a classification into a low-velocity and a high-velocity group. Both diagrams exhibit the same general trend, the value of log r rapidly decreasing when only meteors in the outer rings are studied. Extrapolation of the sporadic meteor data to zero angular distance gives log $r=0.63$. Incidentally, the same value of log r is obtained if the study is restricted only to meteors appearing within the limits 0°–19°, i.e., to meteors appearing within 20° of the fixation point of the observer. It is thus concluded that the true ratio of increase for nonshower meteors is *4.3*.

The datum points in figure 5 that refer to the Perseid shower should probably be treated with some caution, since shower meteors are not uniformly distributed over the sky. Figure 5 suggests that the variation of r with angular distance is more pronounced for objects of high angular velocity. This result indicates that the observers have difficulty in ascertaining whether fast luminous streaks seen in the outskirts of their fields are real phenomena or not.

The dependence of the ratio r on the radius of the total field of vision is shown in figure *6*. The datum points refer to sporadic meteors only and correspond to radii 20°, 40°, and 60°, respectively. The decrease in the ratio r, as the observer extends his field, is very clearly brought out.

The datum points of figures 5 and 6 are deduced from a group count in which the recording procedure is arranged to minimize the loss of meteors. Hence, there is reason to believe that the general trend shown in the diagrams will be more pronounced in studies of data collected by a single observer. In the case of a single observer the ratio r may also be strongly dependent on individual peculiarities in the magnitude scale of the observer. It therefore does not appear unreasonable that these two factors alone may explain the discrepancy found between the results of various investigators, thus causing an experimental spread over the range 2.5 to 4.0 in determinations of r.

Mean influx rate of sporadic meteors

A mean value of the influx rate of sporadic meteors may be determined from our data if the collecting area of the atmospheric layer at a height of 95 km is computed. It is a good approximation to assume that the collecting area was an ellipse with the major axis located between zenith distances $-50°$ and $+65°$. A value of 33,000 km^2 is then computed and adopted as the total collecting area of the team.

The relation between influx rate, luminosity function, and time-area product may be written

$$\log N=\log F(m)-\log A\times t, \qquad (3)$$

where N is the accumulated influx rate, $F(m)$ the luminosity function, A the collecting area, and t the observing time. Let m be the faintest absolute magnitude at which the survey is complete. The total number of sporadic meteors recorded down to the magnitude of completeness of the survey is, in our data, 255. The total observing time is 212 hours and the

time-area product is 7×10^{6} hrs km^{2}. Inserting numerical values in equation (3) we find that the mean influx rate of meteors of +2.0 absolute magnitude or brighter is 1.0×10^{-14} meteors m^{-2} sec^{-1} (2π sterad)$^{-1}$. If we adopt the slope log $r=0.51$, as deduced from our total sporadic sample, we find the influx of sporadic meteors of zero visual magnitude or brighter to be 1.0×10^{-15} meteors m^{-2} sec^{-1} (2π sterad)$^{-1}$.

The above influx rate is deduced from nighttime observations made during the month of August at a northern latitude ($\phi=57°.4$). It should therefore be corrected for diurnal, seasonal, and latitude effects. From a study of radar rates, Hawkins (1956) has predicted the diurnal and seasonal variations in meteor influx rate to be expected at various latitudes. Inspection of his tabular data indicates that the mean rate over the hours of darkness agrees to within 5 percent with the mean rate over a 24-hour period. Further, it is found that latitude effects are negligible. The conversion of our August rate to a mean yearly rate introduces a correction factor of approximately 0.6. Hence we conclude that the influx rate of sporadic meteors of zero magnitude or brighter averaged over the entire year is 0.6×10^{-15} meteors m^{-2} sec^{-1} (2π sterad)$^{-1}$.

It is interesting to compare our mean influx rate with that obtained by Hawkins and Upton (1958) for photographic meteors. Their influx rate of 1.26×10^{-14} meteors m^{-2} sec^{-1} at zero photographic magnitude corresponds to 2.5×10^{-15} meteors m^{-2} sec^{-1} at zero visual magnitude, if a meteor color index of -1.3 mag is assumed. Our influx rate is, therefore, lower than that of Hawkins and Upton by a factor of four.

EXTRAPOLATION TO MICROMETEORITE REGION.—For comparison with results obtained by other meteor-counting techniques it is tempting to extrapolate the log accumulated numbers curve of naked-eye meteors to the micrometeorite region. On the basis of the above influx rate and the observed (uncorrected) slope of the luminosity function, an extrapolation through the 30th magnitude produces the linear relationship marked log $r=0.51$ in figure 7. A similar extrapolation based on the corrected slope produces the relationship marked log $r=0.63$. In order to obtain conformity with similar diagrams published elsewhere, the results are shown in figure 7 on a mass scale. This scale is based on the assumption that meteor velocities are independent of magnitude and that log mass is proportional to log luminosity. A mass of 1 g has been adopted for a zero-magnitude sporadic meteor.

The line marked log $r=0.40$ is an extrapolation of the tabular data given by Watson (1941). The photographic data of Hawkins and Upton are not plotted in figure 7, but they would not deviate much from our curve marked log $r=0.51$. The same conclusion applies to the data of Millman and Burland (1956) if the extrapolation is based on the r value obtained for the magnitude range over which their study is complete ($m<+1$ mag).

Inspection of figure 7 shows that extrapolated micrometeorite fluxes based on precise studies of visual or photographic meteors are several orders of magnitude higher than the values obtained from Watson's model. Either this large discrepancy may be due to some systematic error in the telescopic magnitude estimates on which the Watson model is based, or one must postulate a change in the ratio r somewhere below the limiting magnitude of the visual and photographic studies.

Extrapolations of naked-eye or telescopic data may be in error for several reasons. The observational data determining the slope of the luminosity function in the naked-eye meteor region had a range of error that is considerably magnified in the extension into the micrometeorite region. The range of uncertainty involved is well illustrated by our two experimental relationships shown in figure 7. Further, the adopted mass-magnitude relation may be in error. Additional, but less important, errors are associated with the assumed collection area of the visual observers on which the influx rate of visual meteors is based.

COMPARISON WITH SPACE-PROBE RESULTS.—Direct studies of micrometeorite particles in the upper atmosphere and in interplanetary space are possible by means of rocket and satellite-borne instruments. Statistically, the most significant data to date have been obtained with piezoelectric microphone detectors. A number of micrometeorite influx rates as determined by these sensors have been pub-

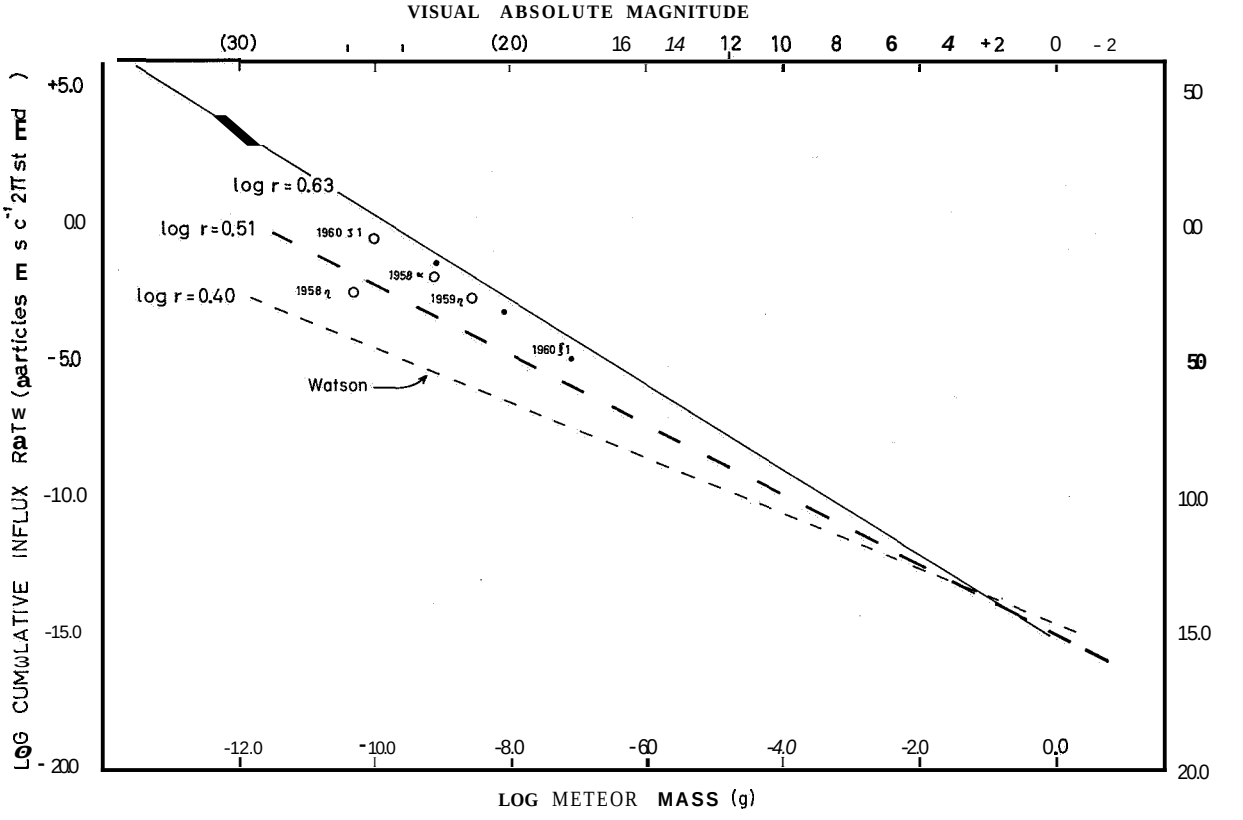

FIGURE 7.—Log cumulative influx rate versus log mass.
– – – –Flux based on Watson's meteor model.
— — — —Extrapolated flux based on visual observations by Lindblad; all meteors.
————Extrapolated flux based on visual observations by Lindblad; meteors within 20° of the center of field of observation.

lished. In figure 7 we inserted datum points from investigations by LaGow and Alexander (1960), Dubin (1960), Soberman and Della Lucca (1963), and McCracken and Alexander (1963). In this compilation the threshold masses are standardized to an assumed velocity of 30 km/sec. With the exception of 1960 ζ1, the datum points represent influx rates uncorrected for earth shielding.

Inspection of figure 7 indicates that the space-probe impact counts are several orders of magnitude higher than the influx values deduced by extrapolation of Watson's meteor model. Agreement between the space-probe measurements and our extrapolated meteor counts based on an observed ratio of increase $r=3.6$ (curve marked log $r=0.51$), however, is satisfactory. The agreement between our data and the space-probe results is further improved if we base the extrapolation on the corrected experimental ratio $r=4.3$ (curve marked log $r=0.63$). Superficially at least, the micrometeorite impact data thus support the conclusions of the present paper, indicating that the slope of the luminosity function of meteors is considerably steeper than the slope assumed in the Watson model.

Distribution law of meteor masses

The relation between magnitude and mass may be written $m=m_0-2.5 \log \mathcal{M}$, where $\mathcal{M}$ is meteor mass and m_0 is a constant assumed independent of m and $\mathcal{M}$. Inserting into equation (1) we get

$$F(\mathcal{M})=\text{constant}\times r^{-2.5 \log \mathcal{M}},$$

where $F(\mathcal{M})=F(m)$ is the number of meteors of mass equal to or greater than $\mathcal{M}$. Applying an elementary law of logarithms, we obtain the cumulative mass law

$$F(\mathcal{M})=F(1)\times\mathcal{M}^{-2.5 \log r}, \qquad (4)$$

where $F(1)$ is the number of meteors of mass equal to or greater than unit mass, and r is the ratio of increase per unit magnitude interval.

The distribution law of meteor masses may thus be inferred from studies of the luminosity function of meteors, since the exponent in the mass law is directly determined by the slope log r. Experimental values of log r lie in the range 0.4 to 0.7, and these studies thus suggest an exponent in the cumulative mass law in the range −1.0 to −1.8. Inserting experimental values as obtained in the present study, we find that the exponent in the mass law is −1.28 or −1.58, depending on whether or not the data are weighted as a function of the angular distance of the meteor from the center of field of the observer.

Acknowledgments

The author is indebted to the directors of the Lund Observatory and the Onsala Observatory, Professors C. Schalén and O. Rydbeck, respectively, for their constant interest in the work. Among those who assisted at various times in the reduction of the data, the author would like to express his thanks particularly to Miss I. Olsson.

Financial support for the investigation was received from the Swedish Natural Science Research Council.

References

DUBIN, M.
1960. IGY micrometeorite measurements. *In* Space Research, ed. by H. Kallmann-Bijl, pp. 1042–1058, North-Holland Publ. Co., Amsterdam.

HAWKINS, G. S.
1956. Variation in the occurrence rate of meteors. Astron. Journ., vol. 61, pp. 386–391.
1964. Meteors, Comets and Meteorites. McGraw-Hill Book Co., New York, 134 pp.

HAWKINS, G. S., and UPTON, E. K. L.
1958. The influx rate of meteors in the earth's atmosphere. Astrophys. Journ., vol. 128, pp. 727–735.

HOFFMEISTER, C.
1931. Zur Theorie der Variation der Sternschnuppenhäufigkeit. Veroff. Universitätssternwarte Berlin-Babelsberg, vol. 9, no. 1.

KRESÁKOVÁ, M., and KRESÁK, Ľ.
1955. On the activity of telescopic meteors and some related problems. Contr. Astron. Obs. Skalnaté Pleso, vol. 1, pp. 40–77.

LAGOW, H. E., and ALEXANDER, W. M.
1960. Recent direct measurements of cosmic dust in the vicinity of the earth using satellites. *In* Space Research, ed. by H. Kallmann-Bijl, pp. 1033–1041, North-Holland Publ. Co., Amsterdam.

LINDBLAD, B.-A.
1963. The relation between visual magnitudes of meteors and the durations of radar echoes. *In* Proceedings of the Symposium on the Astronomy and Physics of Meteors. Smithsonian Contr. Astrophys., vol. 7, pp. 27–39.

MCCRACKEN, C. W., and ALEXANDER, W. M.
1963. The distribution of small interplanetary dust particles in the vicinity of earth. *In* Proceedings of the Symposium on the Astronomy and Physics of Meteors. Smithsonian Contr. Astrophys., vol. 7, pp. 71–83.

MCKINLEY, D. W. R.
1961. Meteor Science and Engineering. McGraw-Hill Book Co., New York, 309 pp.

MILLMAN, P. M., and BURLAND, A. S.
1956. The magnitude distribution of visual meteors. (See Millman, Journ. Roy. Astron. Soc. Canada, vol. 51, pp. 113–115, 1957.) Presented at 96th Amer. Astron. Soc. Meeting, New York, December.

MILLMAN, P. M., and MCKINLEY, D. W. R.
1963. Meteors. *In* The Solar System, vol. IV, ed. by B. M. Middlehurst and G. P. Kuiper, Univ. of Chicago Press, Chicago, pp. 674–773.

ÖPIK, E. J.
1958. Statistical results from the Arizona Expedition for the study of meteors. Contr. Armagh Obs., no. 26, pp. 1–82.

SOBERMAN, R. K., and DELLA LUCCA, L.
1963. Micrometeorite measurements from Midas II (Satellite 1960 ζ1). *In* Proceedings of the Symposium on the Astronomy and Physics of Meteors. Smithsonian Contr. Astrophys., vol. 7, pp. 85–88.

WATSON, F. G.
1937. Distribution of meteoric masses in interstellar space. Ann. Astron. Obs. Harvard, vol. 105, pp. 623–632.
1939. A study of telescopic meteors. Proc. Amer. Phil. Soc., vol. 81, no. 4, pp. 493–504.
1941. Between the Planets. Blakiston Press, Philadelphia, Pa.
WILLIAMS, J. O.
1939. Relative frequencies of meteor magnitudes. Astron. Journ., vol. 48, pp. 100–103.

Abstract

Data for visual meteors, observed under carefully controlled conditions, are used to determine the luminosity function and mean influx rate of sporadic meteors. The log cumulative distribution curve of absolute meteor magnitudes is studied. It is deduced that the observed number of sporadic meteors increases by a factor of 3.6 per absolute visual magnitude. The mean influx rate of sporadic meteors brighter than or equal to zero absolute magnitude is 0.6×10^{-15} meteors m^{-2} sec^{-1} $(2\pi$ sterad$)^{-1}$.

Analysis of the visual data shows that the observed ratio of increase r systematically varies with the size of the field of an individual observer. A correction for this effect indicates that the true number of sporadic meteors increases by a factor of 4.3 per absolute visual magnitude.

The resulting slope for log cumulative flux versus log mass is -1.28 or -1.58, depending on whether or not the data are weighted as a function of the angular distance of the meteor from the center of field of the observer.

Conversion of the observed meteor counts to a mass influx rate and linear extrapolation of the influx data to the micrometeorite region on the basis of the observed r values produce influx rates in good agreement with recent influx data from satellites and space probes.

Duration Distribution of Radio Echoes Obtained from Underdense Shower Meteor Trains

L. M. G. POOLE [1]

Radio echo theory predicts that the amplitude of an echo obtained from an underdense meteor train (with electron line density $\alpha \ll 10^{-12}$ cm^{-1}) at time t is given by

$$A_t = A_0 \exp(-t/\tau), \quad (1)$$

where A_0 is the peak amplitude at time $t=0$. The decay constant τ is given by (Herlofson, **1948)**

$$\tau = \lambda^2/16\pi^2 D, \quad (2)$$

where λ is the wavelength and D the ambipolar diffusion coefficient in the meteor train. Various theoretical expressions for D (Kaiser, **1953;** Weiss, **1955)** predict that for an isothermal atmosphere D is inversely proportional to the atmospheric density ρ, which at a height h is given by

$$\rho = \rho_0 \exp\left(\frac{h_0 - h}{H}\right), \quad (3)$$

where ρ_0 is the density at height h_0 and H the atmospheric scale height. The distribution in $\ln\tau$ (duration distribution) for a sample of such meteor echoes should thus give a direct measure of their distribution in height.

Duration distributions have been obtained (Poole and Kaiser, in preparation) for underdense echoes recorded on a **17** Mc/sec radar during the activity of the Perseid, Geminid, and Quadrantid meteor showers, and compared with the theoretical height distributions of Eaiser **(1954).** In every case the r.m.s. deviation of the measured distributions was considerably smaller than expected. Basically two interpretations can be placed on this: **(1)** the distribution in $\ln\tau$ does not reflect the true height distribution, or **(2)** the actual height distribution is not as predicted by Eaiser **(1954).**

Let us consider these possibilities separately.

1. Even assuming that equations **(1)** to **(3)** are valid, there are several reasons why D might not be inversely proportional to ρ, and the duration distribution in this case will not correspond to the height distribution. There are certain high-altitude selection effects (Greenhow, **1963)** that could result in the formation of an apparent echo "ceiling," and it can be shown that the geomagnetic field is, in principle, capable of affecting diffusion (Eaiser, **1953).** In either case, the observed value of D is likely to increase less rapidly with height than expected, but provided the variation remains essentially exponential we can define an apparent scale height $H' > H$. If this inequality exists for the present results, the geomagnetic field is most probably responsible since the effect of the ceiling is not thought to be important here owing to the comparatively low frequency used (see Greenhow, **1963).**

2. If meteoric ionization is not correctly described by the classical evaporation theory (Herlofson, 1948), deviations from Kaiser's theory **(1954)** may be expected. This theory has been adapted by Weiss **(1960)** to allow for variations in effective train length, and by Poole and Kaiser (in preparation) to allow for variations of the exponent n in the relation

$$\rho_1 \propto \alpha_1^n, \quad (4a)$$

[1] Department of Physics, The University, Sheffield, England; now with Department of Physics, Rhodes University, Grahamstown, South Africa.

where α_1 is the maximum electron line density of a meteor and occurs at the height where $\rho=\rho_1$. The classical theory predicts $n=\frac{1}{3}$. When dealing with duration results we are more fundamentally concerned With the analogous relation

$$D_1 \propto \alpha_1^{-n'}, \tag{4b}$$

where D_1 is the value of D at the height where $\alpha=\alpha_1$, and n' is given by

$$n'=nH/H'. \tag{4c}$$

We can measure n' directly by comparison of the mean $\ln\tau$ for meteors occurring within different ranges of magnitude, and for the present data values obtained range between —0.3 and —0.4.

It has been shown (Jones and Kaiser, 1966) through consideration of the effect of the thermal capacity of particles capable of producing radio meteors that the onset of ablation can be sufficiently delayed to cause significant foreshortening of the train and consequent enhancement of maximum line density. If we use reasonable values for the boiling point, specific heat, and latent heat (of vaporization) of stony meteor material, the air density at the height of ablation commencement (ρ_0) is found to be $\rho_0\approx 0.3\rho_1$ for meteors in the size range under consideration. With this result, and if we assume initially that $H'=H$ and $n=n'=0.33$, the expected r.m.s. deviation of the duration distribution is calculated from the equations of Weiss (1960), and the agreement with observation is fairly good. However, external evidence (e.g., Greenhow and Hall, 1960a) indicates that H' could be greater than H by a factor of as much as 1.4, and from equation (4c) we see that the upper limit of n is thus —0.5. The expected r.m.s. deviation calculated, if we assume $H'=1.4H$ and $n=0.5$, also agrees well with observation, and other values of the ratio H'/H in the range $1\lesssim H'/H\lesssim 1.4$, and of n in the range $0.33\lesssim n\lesssim 0.5$, can likewise be shown to be consistent with the present results. It seems reasonable to conclude that the quantities H'/H and n lie within these limits.

Other height (Evans, 1954) and duration (Greenhow and Hall, 1960b) distribution results tend to support this conclusion if train lengths are as predicted by Jones and Eaiser (1966); the results in Evans (1954) imply that $n\approx 0.5$, and the results in Greenhow and Hall (1960b) indicate that $H'/H>1$ for all values of n between 0.33 and 0.5.

The conclusions to be drawn from the present evidence can thus be summarized: (1) meteor trains are considerably shorter than predicted by the classical evaporation theory; (2) the geomagnetic field appears to have a noticeable height-dependent effect on diffusion in meteor trains; and (3) the exponent $n\gtrsim\frac{1}{3}$ (Weiss, 1960, suggests $n\lesssim\frac{1}{3}$).

References

EVANS, S.

1954. Scale heights and pressures in the upper atmosphere from radio-echo observations of meteors. Monthly Notices Roy. Astron. Soc., vol. 114, pp. 63–73.

GREENROW, J. S.

1963. Limitations of radar techniques for the study of meteors. In Proceedings of the Symposium on the Astronomy and Physics of Meteors. Smithsonian Contr. Astrophys., vol. 7, pp. 5–17.

GREENHOW, J. S., and HALL, J. E.

1960a. Diurnal variations of density and scale height in the upper atmosphere. Journ. Atmos. Terr. Phys., vol. 18, pp. 203–214.

1960b. The importance of initial train radius on the apparent height and number distributions of meteor echoes. Monthly Notices Roy. Astron. Soc., vol. 121, pp. 183–196.

HERLOFSON, N.

1948. The theory of meteor ionization. Phys. Soc., Rep. Prog. Phys., vol. 11, pp. 444-454.

JONES, J., and KAISER, T. R.

1966. The effects of thermal radiation, conduction and meteoroid heat capacity on meteoric ablation. Monthly Notices Roy. Astron. Soc., vol. 133, pp. 411–420.

KAISER, T. R.

1953. Radio echo studies of meteor ionization. Adv. Phys., Phil. Mag. Suppl., vol. 2, pp. 495–544.

1954. Theory of the meteor height distribution obtained from radio echo observations, I: Shower meteors. Monthly Notices Roy. Astron. Soc., vol. 114, pp. 39–51.

WEISS, A. A.

1955. Diffusion coefficients from the rate of decay of meteor trails. Australian Journ. Phys., vol. 8, pp. 279–288.

1960. Meteor height distribution and the fragmentation hypothesis. Australian Journ. Phys., vol. 13, pp. 532–549.

Radar Studies of Meteors

B. L. KASHCHEYEV and V. N. LEBEDINETS[1]

Introduction

Radar studies of meteors, together with photographic observations and direct rocket- and satellite-borne measurements, are at present the main sources of information on meteoritic matter in the vicinity of the earth's orbit as well as on the physical processes associated with meteors in the upper atmosphere.

Compared with the photographic method, the radar method has a number of advantages: the possibility of carrying out 24-hour measurements in any weather, high sensitivity of apparatus, which permits the study of very weak meteors, etc. A basic shortcoming of this method is the somewhat lower accuracy of the measurements. It is impossible to interpret correctly the results of any observations without first solving the main problems of the physical theory of meteors. Because of the specific character of radio observations, the physical theory of radio meteors is more complicated than that of optical meteors.

In this paper we shall present results of radar measurements of meteors carried out at the Eharkov Polytechnical Institute according to the IGY program, and also of theoretical studies on the physical theory of meteors. Particular attention was paid to the analysis of the data on radiants and velocities of individual meteors.

Apparatus and methods of measurements

In our complex studies of meteors and their associations we included radar measurements of velocities and radiant coordinates of individual meteors. Velocities were determined by the pulse-diffraction method (Ellyett and Davies, 1948). The coordinates of the radiant were determined by using three stations for the reception of radio waves scattered by a meteor trail in the process of formation (Gill and Davies, 1956).

A description of the radar station (RS) used for the measurements has been published (Eashcheyev et al., 1960). The basic RS parameters are: wavelength $\lambda=8$ m, peak power $P_t=75$ kw, pulse frequency $F=500$/sec, pulse duration $\tau=10$ μsec, gain coefficients of transmitting antennas and receiving antennas $G_t=G_r=16$, threshold sensitivity of the receiver $\epsilon=2\times10^{-14}$ watts.

One of the receivers was located near the transmitter at the main receiving point. Two outside receiving points were located at distances $d_1=4.3$ km northeast and $d_2=7.1$ km northwest from the principal point. The angle between the base lines is 85°. For each meteor the following were measured: time of the occurrence T, velocity V, and time displacements t_1 and t_2 between the corresponding extremes of diffraction patterns of signals received in three points. If the lengths of the base lines are much less than the distance R to the point of specular reflection on the trail, the angles θ_1 and θ_2 between the base lines and the trail may be deduced from

$$\cos\theta_1=\frac{2vt_1}{d_1},\quad \cos\theta_2=\frac{2vt_2}{d_2}. \tag{1}$$

If the trail orientation in space and the meteor velocity are known, it is possible to calculate the orbit of the meteor body. Coordinates of the corrected radiant and orbital elements were calculated according to a somewhat modified

[1] Kharkov Polytechnical Institute, USSR.

Kleiber scheme (1891) adjusted to the "Ural" electronic computer. Four quantities, T, v, t_1, and t_2, were assumed as incoming data. The remaining values, which are usually taken from the astronomical almanac, were expressed as analytical time functions. The calculations were carried out in the following order: A, z=horizontal coordinates of visible radiants; a, δ=equatorial coordinates of corrected radiants; v_0, v_g=extra-atmospheric and geocentric velocities; A, β=ecliptic coordinates of corrected radiants; A', β'=ecliptic coordinates of true radiants; v_h=heliocentric velocity; E, E'= elongation of corrected and true radiants of apex; a, e, q, i, Ω, ω=orbital elements.

Measurement errors

The accuracy of the measurements was determined from an analysis of different sources of errors and also from the inner consistency of the results of measurements for known meteor showers.

From December 9 to 14, 1959, velocities and radiants of 298 meteors of Geminid showers were obtained (Kashcheyev, Lebedinets, and Lagutin, 1961). The distribution of deviations of individual values of velocity and radiant coordinates from the average values appeared to be close to the gaussian. The root-mean-square errors are $\Delta v_0 = \pm 2.0$ km/sec, $\Delta\alpha = 2\overset{\circ}{.}7$, and $\Delta\delta = \pm 2\overset{\circ}{.}4$.

The main sources of errors when measuring the velocity are inaccurate consideration of the atmospheric deceleration, the effect of diffusion and atmospheric turbulent winds, the effect of resonance during the reflection of radio waves from the train, and inaccuracy of pulse counting in the Fresnel zones. For meteors with velocities of 20 to 50 km/sec, the root-mean-square error in the determination of extra-atmospheric velocity of an individual meteor is $\Delta v_0 \approx \pm 2.0$ km/sec. In the case of very slow meteors, the errors of velocity measurements increase owing to the inaccurate consideration of deceleration and the effect of turbulent winds. When $v_0 > 50$ km/sec, the errors increase because of the diffusion effect and an inexact consideration of deceleration. When $v_0 < 20$ km/sec and $v_0 > 50$ km/sec, the root-mean-square error of one measurement of velocity is $\Delta v_0 \approx \pm 3$ km/sec.

From (1) we shall obtain

$$\Delta\theta = \pm \cot\theta \left[\left(\frac{\Delta v_0}{v_0}\right)^2 + \left(\frac{\Delta t}{t}\right)^2\right]^{1/2}. \qquad (2)$$

Errors in velocity determinations and in measurements of time delays contribute nearly equally to errors in the determination of radiant coordinates. Errors in time delays are due mainly to turbulent winds in the atmosphere (Lebedinets, Lagutin, and Lysenko, 1960). The role played by the other factors (resonance effect, inaccuracy of pulse counting, diffusion effect) is relatively small. For meteors with velocities $v_o > 30$ km/sec, the root-mean-square errors in the determination of radiant declination and right ascension are $\Delta\delta \approx \pm 2\overset{\circ}{.}5$ and $\Delta\alpha \approx 2\overset{\circ}{.}5 \sec\delta$. With $v_o < 30$ km/sec, the errors increase as the velocity decreases, and at $v_o < 20$ km/sec they may reach $\pm 5°$.

Results of measurements

During an annual cycle of measurements from November 1959 to December 1960, the necessary data were obtained for the calculation of velocities and radiants of several tens of thousands of meteors brighter than +7 mag. The best records were selected from these observational data and the orbits of 12,500 meteor bodies were obtained.

Radio-technical measurements of individual radiants and velocities of meteors were made by Davies and Gill (1960) at Jodrell Bank and by Nilsson (1964) at Adelaide. According to measurements carried out from May 1954 to April 1955, Davies and Gill obtained 2474 orbits for meteors ranging from +5 to +7 mag, the catalog of which was not published. From the results of measurements in 1961, Nilsson obtained 2200 orbits for meteors brighter than +6 mag. The catalog of orbits was not published, and the results of researches on sporadic meteor orbits were not reported.

The orbits of small meteor bodies derived at Jodrell Bank (Davies and Gill, 1960) and at Kharkov (Eashcheyev and Lebedinets, 1961) differ essentially from the orbits of larger bodies generating photographic meteors (Whipple, 1954; McCrosky and Posen, 1961; Babadzhanov and Kramer, 1963). These discrepancies may

be caused both by a real difference in the orbits along which the particles of different size are moving and by selective differences between radar and photographic methods with respect to velocity and radiant coordinates. While reducing the obtained observational material, we paid particular attention to these selection effects.

Detectability of radio meteors

The selectivity of radio observations of meteors was considered by Lebedinets **(1963).** To transfer from a measured to a real orbit distribution we must take into account the following factors: **(1)** a geometrical factor, $1/P_1$, which characterizes a relative detection probability **of** meteors with different radiant declinations, determined by the geometry of radio-wave reflection from meteor trails and by the sensitivity diagram of the antennas; **(2)** a physical factor, $1/P_2$, which characterizes a relative detectability of meteors with different velocities and zenith distances of radiants, defined by a dependence **of** the ionization coefficient β, evaporation height h, and distribution of linear electron density **a** along the trail on v_0, z, and on the initial mass of the meteor body M_0, and also by a dependence of an initial radius of ionized trail r_0 on v_0 and h; and **(3)** an astronomical factor, $1/P_3$, which characterizes the dependence of the probability **of** an encounter with the earth on the parameters of the particle orbit.

The astronomical factor affects to the same extent the results of ground observations, irrespective of the method used. The value P_3 was calculated by Öpik **(1951):**

$$P_3 \approx \frac{v_g \sin i}{v_0^2}\left[2-\frac{1}{a}-a(1-e^2)\right]^{1/2}. \qquad (3)$$

δ	−20"	0"	+20°	+40°	+60°	+80°
$\sim/P_1$	0.3	0.6	0.9	1.6	2.5	3.4

the values of $P_1(\delta, v_0)$ for RS as used in Kharkov, the antennas being oriented eastward for meteors with $v_0=40$ km/sec.

The maximum value for power of a signal scattered by the meteor train with $\alpha<10^{12}$ electron/cm is

$$P_r=\frac{P_t G_t G_r \lambda^3 \alpha^2}{32\pi^2 R^3}\left(\frac{e^2}{mc^2}\right)^2 \varphi^2(\Delta) e^{-2(2\pi r_0/\lambda)^2} \qquad (4)$$

where

$$\varphi(\Delta)=\frac{1-e^{-\sqrt{2}\Delta}}{\sqrt{2}\Delta}, \qquad \Delta=\frac{8\pi^2 D\sqrt{R}}{v\lambda^{3/2}}, \qquad (5)$$

e and m are charge and mass of the electron, respectively, e is the light velocity, and D is the coefficient of ambipolar diffusion.

The value and dependence on the velocity of the ionization coefficient, determining the scale of radio-meteor masses, have been considered (Kashcheyev and Lebedinets, **1961;** Öpik, **1958).** The most thorough measurements of the coefficient of ambipolar diffusion were carried out by Kashcheyev **(1963).**

We discussed **(1963)** the theory of an initial expansion of ionized meteor trails. We deduced that r_0 is proportional to v_0 and inversely proportional to the atmospheric density. Measurements of r_0 by parallel radar observations of meteors on two wavelengths were carried out at Jodrell Bank (Greenhow and Hall, 1960), Kharkov (Kashcheyev and Lebedinets, **1961,** 1963), and Kiev (Bairachenko, **1963).** From our **1963** paper it is evident that the results of measurements are in satisfactory agreement with theory. At the height **of 95** km with $v_0=40$ km/sec, $r_0\simeq 1$ m.

The effective sensitivity of RS is characterized by a minimum value of the effective linear electron density, α_{ef}^{min}, **of** meteor trails, which may be determined in the direction of maximum radiation. When due account is taken of some random position of the point of specular reflection on the trail, the probability of the detection of the trail formed by the meteor body with the given M_0, v_0, and z is proportional to the length **of** the trail path $l(M_0, v_0, z, A, \alpha_{ef}^{min})$, where $\alpha_{ef}>\alpha_{ef}^{min}$. **Here,** $\alpha_{ef}=\alpha\varphi(\Delta)e^{-(2\pi r_0/\lambda)^2}$.

Relative detectability of meteors with different v_0 and z is

$$\frac{1}{P_2(v_0, z, \lambda, \alpha_{ef}^{min})} = \int_0^\infty \ell(M_0, v_0, z, \lambda, \alpha_{ef}^{min}) n(M_0) dM_0. \quad (6)$$

Here $n(M_0)$ is the differential distribution of meteor bodies by masses, which are usually given in the form

$$n(M_0) = \frac{c}{M_0^s}. \quad (7)$$

Generally speaking, c and s coefficients may be somewhat different for different intervals of meteor-body masses.

To calculate the physical factor we must know the height of maximum evaporation of meteor bodies with different masses, velocities, and zenith distances of radiants, and distributions of ionization along the meteor trails.

Greenhow **(1963)** used the simplest physical theory of meteors (Herlofson, **1948)** to calculate the height of maximum evaporation h_m for meteor bodies of any mass. He obtained $h_m = 128$ km for meteors of brightness **+15** mag with $v_0 = 40$ km/sec. At this height the initial radius of the trail is so large that the observations of such meteors are for the most part possible only with $\lambda > 30$ m no matter how great the RS power. Hence Greenhow concluded that radar studies of very weak meteors are impossible.

Lebedinets **(1963, 1964)** deduced more precise formulas for h_m and also gave the luminous intensity and ionization curves with different masses and velocities of meteor bodies. With $v_0 = 40$ km/sec for meteors of brightness +15 and **+20** mag, the heights of maximum evaporation are practically the same and equal to **102** km. With sufficiently high RS power, observations of such meteors are quite possible at $\lambda \geq 12$ m.

The physical factor was calculated with different values of the parameters z, λ, s, and α_{ef}^{min}. Table **2** gives the values of P_2 calculated with $\cos z = \frac{2}{3}$, **X=8** m, $s = 2$, and $\alpha_{ef}^{min} = 2 \times 10^{10}$ electron/cm.

Ascribing the statistical weight $P_1 P_2$ to every meteor, we correct the results of continuous

v_0 km/sec	15	20	30	40	50	60	70
$1/P_2$	0.06	0.40	1.10	1.00	0.68	0.36	0.20

Hence our selection of orbits of meteor streams and associations was divided into stages.

All meteors for every month were divided into overlapping groups according to their velocities: 10–20, 15–25, . . ., 60–70, 65–75 km/sec. Meteor radiants of each of the groups were roughly reduced to the middle of the observational intervals and were marked on individual charts. The meteor velocity was written down next to the appropriate radiant. Since the measurements were carried out for 5 to 10 days during each month, the inaccuracy of reducing the radiants to the middle of the interval did not lead to an appreciable scattering of stream radiants, if there were any in the given group. Meteor associations were marked on the charts.

A mean velocity $\bar{v}$ was roughly determined for each of these associations. Meteor radiants, with velocities from $\bar{v}-2.5\Delta v$ to $\bar{v}+2.5\Delta v$, were then marked on a corresponding part of the chart several tens of degrees on α and 6 in size. In the process of such repeated markings on the charts, some of the associations recorded earlier stood out more clearly against the background of sporadic meteors. Some of the associations, on the contrary, practically coincided with the background of sporadic meteors. Such groups of radiants were ignored in the following investigation.

Preliminary mean orbital elements $\bar{e}$, $\bar{q}$, $\bar{i}$, $\bar{\omega}$, and their theoretical deviations from the mean Ae, Ap, Ai, and $\Delta\omega$, corresponding to mean measurement errors Av, Ad, $\Delta\delta$, were calculated for each association. A further selection was carried out by consideration of orbital elements e, p, i, and w. A meteor was referred to a given association if the following conditions were satisfied:

$$|e-\bar{e}|<2\Delta e;\ |i-\bar{i}|<2\Delta\bar{i},$$
$$|q-\bar{q}|<2\Delta q;\ |\omega-\bar{\omega}|<2\Delta\omega. \qquad (8)$$

When the mean orbital elements were obtained, a search for meteors belonging to the given association observed in the adjacent months was carried out.

By applying the method described above to the obtained catalog of orbits, we found that 3529 orbits can be related to 194 meteor streams and associations. In table 3 we included streams and associations for which we obtained $N\geq 15$ orbits, as well as a number of known streams whose orbits are known from radar and photographic observations. The following data are given for each association: the number, day, and month of the beginning and the end of observations, the number of orbits obtained, mean radiant coordinates, velocity, and orbital elements. The names of the streams, whose orbits were obtained earlier by photographic or radar measurements, are given in the last column.

The highest number of orbits was obtained for Geminid (401) and Arietid (380) streams. A large number of orbits was also obtained for certain known streams: Southern δ Aquarids (151), Southern Taurids (73), Orionids (61), ζ Perseids (60), η Aquarids (51), and Northern δ Aquarids (50). A total of 1227 meteors belong to these 8 streams.

For 104 streams and associations the number of measured orbits is $N\geq 10$. Most of them are apparently real streams where meteor bodies have a common origin. Some of them may be random groups of bodies with similar orbits.

Ninty-three meteors are referred to 21 small streams and associations with $N\leq 5$. A considerable number of such small groups may be random. Among them, however, Lyrids and σ Leonids are known. The orbits of some of the others are similar to orbits of associations discovered by other observers.

For the Perseids, the most active stream in photographic and visual observations, 10 orbits in all were obtained. During our measurements of meteor activity, Perseids were practically indistinguishable against the background of sporadic meteors. The small number of recorded radio meteors in a stream cannot be explained by poor detectability by radio observations of fast meteors, since a great number of radio meteors is observed in streams having still higher velocities, e.g., Orionids and η Aquarids. Evidently in the Perseids stream there are comparatively few small meteor bodies.

A comparison with other results

From the results of basic radar and photographic measurements, several authors obtained more than 150 meteor streams and associations. The orbits of 24 of them are close to the orbits of streams and associations obtained from our catalog. Tables 4 to 16 give for several streams

TABLE 3.—*Catalog of meteor streams and associations*

No.	Days of observations	N	α	δ	v_0 km/sec	a	e	q	i	Ω	ω	Name of stream
1	14.3–15.3	5	172°	+3°	23	1.95	0.67	0.64	0°.1	175°	83"	σ Leonids
2	14.3–23.3	9	188	+1	30	1.94	0.82	0.36	6	356	297	Virginids
3	15.4–26.5	86	356	+8	37	1.27	0.92	0.10	27	32	28	
4	15.4–25.4	34	7	+3	31	1.32	0.32	0.22	0.5	30	45	
5	15.4–22.4	16	343	+20	40	1.42	0.85	0.21	61	29	44	
6	15.4–25.4	16	12	+10	29	1.55	0.78	0.34	6	30	59	
7	15.4–26.4	18	288	+10	58	1.92	0.50	0.95	120	28	211	
8	15.4–25.4	16	18	+4	27	1.66	0.77	0.39	3	210	246	
9	3.5–24.5	30	291	+29	34	0.89	0.27	0.65	67	48	309	
10	4.5–27.5	16	41	+23	27	1.94	0.77	0.44	6	54	74	
11	4.5–27.5	43	33	+9	31	1.68	0.84	0.27	5	232	233	
12	4.5–19.6	60	52	+23	30	1.61	0.80	0.31	6	71	57	ζ Perseids
13	4.5–27.5	17	17	+19	39	1.64	0.93	0.11	30	52	32	
14	4.5–20.6	380	43	+23	39	1.66	0.94	0.10	19	77	30	Arietids
15	4.5–27.5	16	293	+22	33	0.78	0.47	0.41	68	55	327	
16	4.5–27.5	17	276	+13	33	0.96	0.64	0.35	56	55	312	
17	5.5–27.5	51	338	+0.5	64	3.34	0.84	0.54	161	47	90	η Aquarids
18	6.5–27.5	18	20	+21	33	1.09	0.86	0.15	23	57	34	
19	6.6–20.6	33	44	+12	39	1.34	0.95	0.06	20	258	202	
20	6.6–10.6	15	53	+7	37	1.84	0.90	0.18	26	257	223	
21	4.7–30.7	17	6	+27	60	1.59	0.45	0.88	138	116	234	
22	4.7–29.7	23	98	+16	40	5.18	0.97	0.18	16	297	228	
23	4.7–28.7	41	13	+66	42	1.72	0.49	0.87	77	115	126	
24	6.7–31.7	17	330	+2	35	0.93	0.90	0.09	41	115	336	
25	6.7–29.7	23	20	+75	42	3.65	0.76	0.87	71	116	133	
26	6.7–14.8	50	337	−5	42	2.16	0.97	0.06	18	128	334	Northern ι Aquarids
27	4.7–13.8	13	328	−18	33	2.12	0.88	0.26	8	307	126	
28	4.7–13.8	13	321	−8	35	1.92	0.89	0.20	12	120	313	Southern ι Aquarids
29	15.7–12.8	34	340	−8	39	1.38	0.96	0.05	1.4	126	339	
30	14.7–14.8	151	341	−16	41	2.04	0.96	0.08	28	307	151	Southern δ Aquarids
31	14.7–28.7	23	0	+56	41	1.09	0.18	0.90	83	114	107	
32	16.7–13.8	32	340	−26	42	4.31	0.96	0.17	45	303	114	
33	3.8–14.8	18	53	+33	60	1.45	0.54	0.67	152	132	92	
34	3.8–14.8	10	41	+57	60	11.0	0.91	0.95	113	136	151	Perseids
35	4.8–14.8	15	38	+37	61	1.52	0.35	0.98	141	137	173	
36	21.9–28.9	83	42	+20	43	2.98	0.98	0.07	16	198	332	
37	20.9–22.10	73	27	+9	31	2.07	0.84	0.33	2.2	15	118	Southern Taurids
38	21.9–27.9	16	86	+9	63	1.52	0.40	0.91	152	2	47	
39	21.9–27.9	21	162	+16	45	48.0	1.00	0.11	26	0	39	
40	10.10–21.10	21	108	+15	66	1.90	0.51	0.94	166	23	3	
41	10.10–27.10	13	104	+25	69	3.58	0.75	0.88	175	203	223	ε Geminids
42	10.10–22.10	20	81	+29	58	1.69	0.84	0.27	163	201	307	
43	10.10–22.10	17	88	+12	58	1.48	0.74	0.38	152	23	119	
44	10.10–21.10	18	40	+15	33	1.74	0.86	0.24	1.2	22	131	Southern Arietids
45	10.10–21.10	15	34	+20	38	4.05	0.95	0.22	112	201	307	
46	10.10–22.10	28	44	+14	42	4.46	0.98	0.11	7	22	145	
47	10.10–21.10	24	52	+15	42	1.74	0.97	0.05	17	21	158	
48	11.10–27.10	61	93	+16	66	4.76	0.83	0.57	164	25	86	Orionids
49	11.10–22.10	18	141	+23	59	1.36	0.71	0.39	161	203	62	
50	11.10–23.10	13	34	+18	30	2.19	0.84	0.36	6	205	295	Northern Taurids
51	9.12–14.12	401	111	+33	36	1.31	0.89	0.14	24	260	326	Geminids

TABLE 4.—Radiant and orbit of Geminids

Source	N	α	δ	v_0	1/a	e	q	i	n	w
Authors	401	11104	+32°6	36.0	0.76	0.89	0.14	23°7	25906	32508
Whipple (1954)	13	112.7	+32.4	36.4	0.73	0.90	0.14	23.9	261.2	324.4
McCrosky and Posen (1961)	72	111.3	+32.5	36.3	0.71	0.90	0.14	23.1	260.2	324.2
Jacchia and Whipple (1961)	20	111.4	+32.5	36.2	0.74	0.90	0.14	23.3	260.2	324.3
Southworth and Hawkins (1963)	16	112.6	+32.3	36.3	0.73	0.90	0.14	23.3	261.4	324.1
Babadzhanov and Kramer (1963)	12	111.2	+32.4	36.9	0.76	0.90	0.13	24.8	258.7	326.2
Nilsson (1964)	22	109.4	+30.4	34.2	0.79	0.88	0.15	17.4	259.8	325.1

Mean daily motion of the radiant according to our measurements: $\Delta\alpha = 0°.83$ and $\Delta\delta = -0°.28$.

TABLE 5.—Radiant and orbit of Arietids

Source	N	α	δ	v_0	1/a	e	q	i	Ω	w
mean	380	4303	+22°9	38.6	0.60	0.94	0.10	1807	7606	2909
Authors{June 17–20	18	52.1	+25.1	39.8	0.60	0.96	0.08	22.8	87.4	25.4
Davies and Gill (1960)	6	50.0	+26.0	41.0	0.75	0.97	0.04	46.0	89.0	19.0
Nilsson (1964){(1)	8	46.1	+26.1	39.6	0.67	0.96	0.06	33.4	84.8	23.0
Nilsson (1964){(2)	7	46.6	+25.0	43.6	0.44	0.98	0.04	38.9	84.6	20.3
Lovell (1954){1950 observations	—	43.8	+21.9	37.7	0.67	0.94	0.10	18.0	77.0	29.0
Lovell (1954){1951 observations	—	43.4	+23.9	38.7	0.62	0.94	0.09	21.0	76.8	29.0

Mean daily motion of the radiant: $\Delta\alpha = +0°.7$ and $\Delta\delta = +0°.1$.

TABLE 6.—*Radiant* and orbit of Northern3 Aquarids

Source	N	α	6	v_0	1/a	e	q	i	Ω	w
Authors	50	33678	—479	41.8	0.46	0.97	0.06	1800	12707	33808
McCrosky and Posen (1961)	2	346.0	0.0	42.2	0.38	0.98	0.08	14.0	142.0	332.5
Southworth and Hawkins (1963)	3	346.7	+2.6	39.8	0.41	0.95	0.12	21.2	143.2	324.4
Ceplecha et al. (1964)	1	345.4	+0.8	40.9	0.30	0.96	0.12	18.3	142.4	323.4

Mean daily motion of the radiant according to our measurements: $\Delta\alpha = +0°.9$ and $\Delta\delta = +0°.3$.

TABLE 7.—Radiant and orbit of Southern δ Aquarids

Source	N	α	δ	v_0	1/a	e	q	i	Ω	w
Authors	151	34102	−16°4	41.2	0.49	0.96	0.08	2804	30677	15101
Katasev (1964)	1	339.5	−15.2	44.3	0.18	0.99	0.07	240	308.5	150.6
McCrosky and Posen (1961)	17	341.6	−14.6	42.4	0.35	0.97	0.08	25.0	309.2	151.1
Jacchia and Whipple (1961)	11	341.3	−14.4	42.2	0.36	0.97	0.08	22.7	309.2	151.1
Southworth and Hawkins (1963)	3	338.6	−16.7	42.6	0.40	0.97	0.07	28.9	304 6	153.5
Babadzhanov and Kramer (1963)	8	341.6	−15.9	40.8	0.37	0.96	0.11	23.7	311.0	145.4
Ceplecha et al. (1964)	1	350.7	−13.8	40.1	0.32	0.96	0.14	22.8	322.5	139.4
Gill and Davies (1960)	35	339.0	−19.0	43.0	0.44	0.96	0.09	30.0	304.0	150.0
Nilsson (1964)	48	339.4	−17.3	41.2	0.43	0.97	0.07	32.5	305.8	152.4

Mean daily motion of the radiant according to our measurements: $\Delta\alpha = 0°.85$ and $\Delta\delta = +0°.35$.

TABLE 8.—*Radiant* and *orbit of* Southern Taurids

Source	N	α	δ	v_0	1/a	e	q	i	Ω	ω
Authors	73	27°.2	+8°.6	30.9	0.48	0.84	0.33	202	14°.6	11802
Whipple (1954)	8	52.8	+13.9	30.1	0.43	0.84	0.38	5.5	43.3	111.2
McCrosky and Posen (1961)	17	42.6	+10.7	28.8	0.53	0.80	0.37	5.3	31.2	114.6
Jacchia and Whipple (1961)	13	37.5	+9.6	29.8	0.55	0.81	0.34	5.1	24.5	117.8
Southworth and Hawkins (1963)	11	28.0	4-7.5	30.4	0.56	0.82	0.32	5.0	13.7	122.7
Babadahanov and Kramer (1963)	8	24.2	+6.2	31.5	0.54	0.83	0.33	3.4	9.5	118.9
Ceplecha et al. (1964)	1	28.2	4-7.0	33.3	0.45	0.88	0.26	6.4	11.9	125.2
Nilsson (1964)	17	59.0	+16.6	25.8	0.48	0.76	0.50	4.2	56.1	99.0

TABLE 9.—Radiant and *orbit of Orionids*

Source	N	α	δ	v_0	1/a	e	q	i	Ω	ω
Authors	61	9301	+1600	65.9	0.21	0.88	0.57	16402	2504	8601
Whipple (1954)	2	95.4	+15.5	66.3	0.16	0.92	0.54	162.9	29.3	87.8
McCrosky and Posen (1961)	48	94.9	+15.4	68.2	0.02	1.01	0.58	162.8	30.9	80.3
Jacchia and Whipple (1961)	5	95.2	+16.0	67.6	0.06	0.96	0.57	164.4	28.6	82.3
Southworth and Hawkins (1963)	12	95.6	+16.2	67.6	0.05	0.97	0.57	164.9	29.2	82.8
Babadahanov and Kramer (1963)	5	95.9	+20.2	70.7	0.25	1.16	0.63	161.6	28.7	72.5
Ceplecha et al. (1964)	4	90.0	+15.4	69.4	0.05	1.03	0.66	164.0	21.2	70.6
Nilsson (1964)	8	96.7	+14.4	65.3	0.16	0.92	0.50	160.3	32.3	90.9

TABLE 10.—Radiant and orbit *of ζ* Perseids

Source	N	a	δ	v_0	1/a	e	q	i	Ω	ω
Authors	60	5105	+22°.9	29.8	0.62	0.80	0.31	5°.7	7006	57°.0
Nilsson (1964)	27	50.7	+21.5	29.9	0.59	0.82	0.31	4.8	70.5	56.3

TABLE 11.—Radiant and orbit of Southern Arietids

Source	N	α	δ	v_0	1/a	e	q	i	Ω	ω
Authors	18	3906	+14°.7	32.7	0.57	0.86	0.24	102	2205	13007
McCrosky and Posen (1961)	13	38.8	+10.5	30.0	0.57	0.83	0.30	5.8	24.2	122.5
Nilsson (1964)	30	448	+12.4	30.2	0.50	0.83	0.34	5.9	33.0	118.3

TABLE 12.—*Radiant* and *orbit of* Southern ι Aquarids

Source	N	α	δ	v_0	1/a	e	q	i	Ω	ω
Authors	13	32708	−1708	33.4	0.47	0.88	0.26	706	30606	12509
McCrosky and Posen (1961)	10	330.9	−12.9	35.7	0.36	0.92	0.22	4.2	310.3	129.6
Jacchia and Whipple (1961)	6	322.4	−14.8	34.4	0.40	0.90	0.25	3.6	303.3	126.3
Southworth and Hawkins (1963)	4	323.8	−14.6	35.5	0.50	0.88	0.23	1.2	301.1	133.5

TABLE 13.—*Radiant* and *orbit* of *Northern ι Aquarids*

Source	N	α	δ	v_0	1/a	e	q	i	Ω	ω
Authors	13	32007	−802	34.8	0.52	0.89	0.20	1200	11906	31304
McCrosky and Posen (1961)	2	332.5	−5.5	33.2	0.49	0.88	0.25	7.5	134.5	308.0
Jacchia and Whipple (1961)	2	332.6	−4.2	35.9	0.52	0.91	0.17	15.9	129.4	318.8
Southworth and Hawkins (1963)	1	323.8	−6.8	38.5	0.29	0.95	0.18	15.0	124.1	312.8
Nilsson (1964)	3	326.2	−12.3	31.5	0.64	0.85	0.23	6.9	125.3	312.5

TABLE 14.—*Radiant* and *orbit* of *Perseids*

Source	N	α	δ	v_0	1/a	e	q	i	Ω	ω
Authors	10	41°0	+56°6	59.9	0.09	0.91	0.95	113°1	13605	15009
Whipple (1954)	12	45.2	+56.9	60.7	0.05	0.91	0.95	114.2	138.5	152.9
Katasev (1964)	25	46.1	+57.8	60.3	0.12	0.88	0.96	113.0	138.7	150.0
McCrosky and Posen (1961)	44	45.6	+58.8	60.2	0.02	0.98	0.94	112.3	138.5	151.1
Jacchia and Whipple (1961)	10	46.1	+57.8	60.2	0.05	0.95	0.95	112.8	138.5	150.5
Southworth and Hawkins (1963)	9	45.2	+57.1	60.6	0.04	0.96	0.95	113.8	138.0	150.9
Babadzhanov and Kramer (1963)	94	45.1	+57.6	61.1	0.04	1.04	0.95	112.5	137.8	150.5
Ceplecha et al. (1964)	15	44.2	+57.8	61.2	0.01	0.99	0.96	112.7	137.5	151.9

Source	N	α	δ	v_0	1/a	e	q	i	Ω	ω
Authors	13	3305	+18°2	30.5	0.46	0.84	0.36	505	20504	294°6
Whipple (1954)	7	46.0	+20.9	30.6	0.42	0.85	0.36	3.8	218.1	293.1
McCrosky and Posen (1961)	15	53.8	+21.6	30.9	0.43	0.85	0.35	2.9	224.6	294.6
Katasev (1964)	1	54.2	+20.0	30.7	0.45	0.83	0.39	0.8	226.9	290.3
Jacchia and Whipple (1961)	6	53.2	+21.1	31.2	0.42	0.86	0.34	2.6	223.6	295.3
Southworth and Hawkins (1963)	8	47.9	+20.5	31.9	0.48	0.85	0.31	3.8	216.1	300.9
Babadzhanov and Kramer (1963)	1	62.8	+23.2	29.2	0.48	0.81	0.39	2.2	234.8	290.6

source	N	o r	δ	v_0	1/a	e	q	i	Ω	ω
Authors	9	18802	+1°2	30.5	0.51	0.82	0.36	5°7	35505	29609
Whipple (1954)	4	182.3	+4.4	31.6	0.25	0.90	0.42	5.5	353.5	284.0
McCrosky and Posen (1961)	5	179.4	[illegible]	28.7	0.46	0.80	0.44	0.8	351.4	285.4
Jacchia and Whipple (1961)	3	175.6	+0.1	29.4	0.37	0.83	0.45	1.7	170.0	101.9
Nilsson (1964)	3	188.5	−3.8	34.3	0.42	0.89	0.26	2.9	354.5	304.3

the number of observations, radiants, velocities, and orbital elements according to the measurements of the various authors.

We showed (1961) that, for the period of visibility of the Geminids, a systematic variation of the velocity of the meteor stream as well as of the eccentricity and semimajor axis of the orbit occurs. Taking into account the differences in the mean solar longitudes of different observers, our measurements agree

well with photographic observations. The radiant and orbit of Geminids, obtained by Nilsson, differ somewhat from the results of the other authors. This is explained by Nilsson (1964) to be the result of relatively large errors in his measurements due to a low position of the stream radiant above the horizon in Adelaide.

The Arietids radiant is close to the sun; hence the stream orbit is determined only from radio observations. Nilsson detects two stream branches with very close radiants but with different velocities. Since the measurements of Davies and Gill (1960) and also those of Nilsson refer to the end of the period of stream visibility (June 15 to 21), table 5 gives separately the results of our measurements from June 17 to 20. Since measurements of individual Arietids orbits are few in number, table 5 also gives, for purposes of comparison, the results of statistical measurements by the Clegg method, carried out at Jodrell Bank in 1950 and 1951 (Lovell, 1954).

The radiant and the orbit of Arietids (table 5) obtained by us are in good agreement with the results of statistical measurements. Radiant location obtained by Davies and Gill differs from ours by 3°; the velocity differs by 1 km/sec, which is evidently caused by the small number of orbits determined by Davies and Gill, and by the comparatively low accuracy of measurements of individual radiants and meteor velocities by the radar method. Nilsson overestimates the accuracy of his measurements. With such a low number of measurements (Nilsson, 1964) two simultaneously active streams, whose radiants are separated by 1° and whose velocities differ by 4 km/sec, can hardly be distinguished.

The obtained radiant and orbit of the Northern δ Aquarids (table 6) agree satisfactorily with the results of quite scanty photographic measurements.

Within the limits of scatter of the results obtained by different authors, the radiant and orbit of the Southern δ Aquarids (table 7) obtained by us are in satisfactory agreement with data of photographic and radar measurements.

For the Southern Taurids a good agreement of our results with the data of photographic measurements is observed (table 8). The difference of orbits obtained by Ceplecha et al. (1964) and by Nilsson from the results of the other authors is evidently due to the fact that their measurements refer to the very beginning and the end of the stream visibility, respectively. The great scatter of data obtained by different authors is associated apparently with the diffusivity of the stream whose visibility period exceeds 2 months.

Except for Badadzhanov and Eramer, all the other authors obtained very close positions of the radiant of the Orionids (table 9). In spite of a large number of measurements, the mean velocity of the stream obtained by different authors from photographic observations varies within the rather wide limits of 66.3 to 70.7 km/sec. Correspondingly, the scatter of mean α and e values is also great. The values of v_0, a, and e for individual meteors in each of the catalogs change within wide limits. This scatter greatly exceeds measurement errors and can be explained by a complex stream structure associated with great disturbances of the parent of the Orionids stream—Comet Halley.

Our results for the daytime stream of the ζ Perseids are practically identical with those of Nilsson (table 10). For the Southern Arietids, the results obtained by different authors are in satisfactory agreement (table 11).

In spite of the scantiness of photographic and radar measurements, the results of different authors for the streams of both Southern and Northern ι Aquarids agree satisfactorily (tables 12 and 13).

Though some of the photographic catalogs include a large number of orbits of Perseids, quite a large scatter of mean radiant positions and orbital elements is observed, which apparently exceeds the errors due to the photographic method of measurements. The scatter is very great for individual meteors in each of the catalogs. This indicates a higher diffusivity of the stream. Our results, within the limits of measurement accuracy, agree with the data of photographic observations (table 14).

The results of all the measurements for the Northern Taurids are in good agreement (table 15). Within the limits of real precision of the

measurements for the Viginids the results of the different authors are in good agreement (table 16).

Connection of meteor streams with comets

To carry out a comparison with our measurements we shall make use of the catalog (Kramer, 1953) of 280 comet radiants, computed for comets whose orbits approach the earth's orbit by a distance of not more than **0.3** a.u.

Out of 194 meteor streams and associations observed by us, 14 have orbits similar to those of 11 comets from Kramer's catalog. Table 17 presents for each of them: (1) mean radiant coordinates, velocity, and orbital elements obtained by us; **(2)** comet radiant coordinates, velocity, and comet orbital elements; and **(3)** solar longitude $\lambda\odot$ at the moment of the earth's encounter with the comet orbit for which radiant and velocity are calculated.

Table 18 gives the orbits of Comets Giacobini-Zinner, Biela, and 1866 I, and of their associated meteor streams, Draconids, Andromedids, and Leonids, which were not observed by us. The orbits of streams are taken from photographic measurements.

The data given in Tables 8, 9, 14, 15, 17, and 18 show good agreement of orbital ele-

TABLE 17.—*Data for* streams and associated comets

Stream/comet	α	δ	v_∞	e	q	i	ω	Ω	$\lambda\odot$
Aquarids	338°	0°	64	0.84	**0.54**	161°	90°	47°	
Orionids	93	+16	66	0.88	0.57	164	86	25	
Comet Halley (1835 III)	337	0	—	0.97	0.59	162	111	55	43°
	94	+19	67						
Taurids	64	+15	31	0.85	0.34	7	243	258	
Southern Taurids	27	+9	31	0.84	0.33	2	118	15	
Northern Taurids	34	+18	30	0.84	0.36	6	295	205	
Comet Encke (1937 VI)	85	+13	32	0.85	0.33	12	185	205	98
	56	+8	32						221
Lyrids	272	+31	48	0.84	0.92	82	216	28	
Comet 1961 I	270	+34	48	0.98	0.92	80	213	30	
Perseids	41	+57	60	0.91	0.95	113	151	136	
Comet 1861 III	44	+57	61	0.96	0.95	114	153	137	139
Association 45	34	+20	38	0.95	0.22	12	307	201	
Comet 1948 IV	45	+28	41	1	0.21	23	317	203	
Association 66	338	—9	66	0.85	0.65	179	104	46	
Comet 1698	338	—8	68	1	0.73	169	151	66	40
Association 108	57	+49	59	0.77	0.70	123	108	134	
Comet 1764	51	+45	60	1	0.56	127	105	120	123
Association 124	41	+9	67	0.59	0.98	168	22	314	
Comet 1946	26	+4	71	1	1.02	170	22	301	121
Association 182	124	+29	68	0.60	0.98	164	164	205	
Comet 1366	149	+31	70	0.90	0.98	150	165	227	227
Association 193	163	+30	64	0.81	0.81	138	249	249	
Comet 1798 II	158	+34	66	1	0.78	138	215	250	249
Association 195	190	+75	34	0.66	0.89	52	224	270	
Comet Tootle (1926 IV)	210	+76	36	0.82	1.02	55	207	270	270

TABLE 18.—Data for streams and associated comets *(not* observed at *Kharkov)*

Stream/comet	α	δ	v_0	e	q	i	ω	Ω
Draconids[1]	271°	+47°	20	0.70	1.00	25'	177°	196°
Draconids[2]	271	4-47	20	0.70	1.00	25	177	196
Comet Giacobini-Zinner 1926 VI	264	+54	—	0.72	0.99	31	172	
Andromedids[1]	26	+32	21	0.71	0.74	9	247	225
Andromedids[2]	19	+5	22	0.70	0.70	0.4	74	26
Comet Biela 1852 III	24	+43	—	0.76	0.86	13	246	223
Leonids[3]	153	+22	72	0.93	0.99	163	174	233
Leonids[1]	152	+23	72	0.92	0.98	162	171	233
Comet 1866 I	150	+23	—	0.91	0.98	163	171	231

[1] Jacchia and Whipple (1961).
[2] Southworth and Hawkins (1963).
[3] Whipple (1954).

ments of comets and of their associated meteor streams only in 4 instances: Comet 1862 III and Perseids, Comet Giacobini-Zinner and Draconids, Comet 1866 I and Leonids, and Comet 1861 I and Lyrids. In all the other cases the orbits of comets and of meteor streams differ noticeably.

These results are quite natural if we consider the magnitude of the encounter between comet orbits and the earth. The earth passes close to the orbits of the four enumerated comets. The minimum distances between them are 0.009, 0.003, 0.007, and 0.002 a.u., respectively. For other comets, these distances are much larger. If the comet's orbit passes at a large distance from the earth's orbit, the orbit of the related stream, to be observed at the earth, should differ noticeably from the comet's orbit. Since a relation between a number of streams (Andromedids, Northern and Southern Taurids, etc.) and comets that do not suffer very close encounters with the earth's orbit has been quite reliably established, there are indeed differences between the orbits of comets and the streams generated by them.

These differences may be explained by two reasons:

1. The present orbit of a comet due to planetary perturbations may differ appreciably from the orbit along which the comet moved during the generation of the stream. A partial disruption of the comet nucleus, which caused a stream to be generated, may also lead to a change of the orbit.

2. Immediately after formation of the stream it begins to be disrupted by differential planetary perturbations, deceleration of meteor bodies due to the Poynting-Robertson effect, resistance of interplanetary media, etc. From the very beginning the stream may have a complicated structure if the nucleus disruption occurs during several returns of the comet in different orbits. All these factors lead to a considerable broadening of streams. The width of known meteor streams, such as Perseids, Taurids, etc., near the earth's orbit is measured by many tens of millions of kilometers. The earth meets only a small part of such an extensive stream of meteor bodies. In connection with this the orbit of the stream obtained by observation of meteors from the earth may differ essentially from the mean orbit along which the parent comet of the stream moved during the process of its formation.

Distribution of orbits of meteor bodies

Figures 1 to 4 give the distribution of orbital elements of small meteor bodies obtained by the various authors: (a) measured distribution; (b) distribution corrected for selectivity of radio observations (for geometrical and physical factors); (c) distribution corrected for geometrical, physical, and astronomical factors. For a comparison, figures 5 to 8 give the distribution of orbital elements of larger meteor bodies (McCrosky and Posen, 1961) generating meteors brighter than approximately +3 mag: (a) measured distribution; (b) distribution of

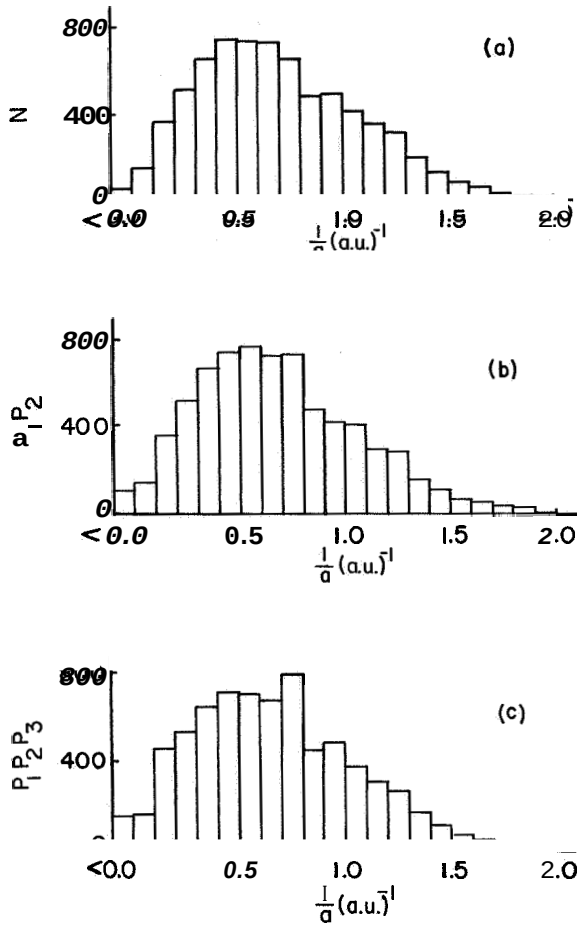

FIGURE 1.—Distribution of orbits of small meteor bodies in reciprocal semimajor axis.

orbital elements corrected for the dependence of luminosity coefficient on the velocity and for the astronomical factors. Figure 9 gives the distribution obtained by Whipple (1954) of semimajor axes of orbits of large meteor bodies, generating meteors brighter than approximately 0 mag.

Let us consider the distribution of each of the orbital elements separately.

SEMIMAJOR AXIS.—Consideration of the selectivity of the radar method of measurements and also of the astronomical factor does not affect practically the obtained orbit distribution in $1/a$. Large meteor bodies generating meteors brighter than 0 mag usually have a values of the order of 5 a.u. A large number of orbits are nearly parabolic. Smaller particles generating meteors of brightness 0 to +3 mag usually have orbits with $a \approx 3$ a.u. The nearly parabolic orbits occur more rarely than in the case of meteors brighter than 0 mag. About 6 percent of orbits have $a < 1$ a.u., and for several $a < 0.56$ a.u.

In the case of still smaller meteor bodies generating meteors of brightness +5 to +7 mag, the maximum of distribution is displaced

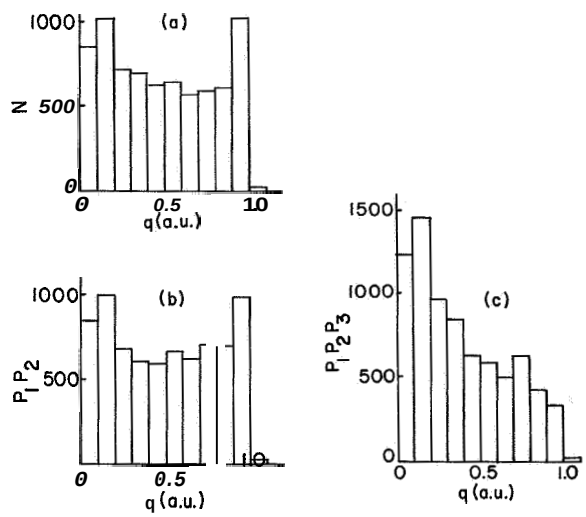

FIGURE 3.—Distribution of orbits of small meteor bodies in perihelion distance.

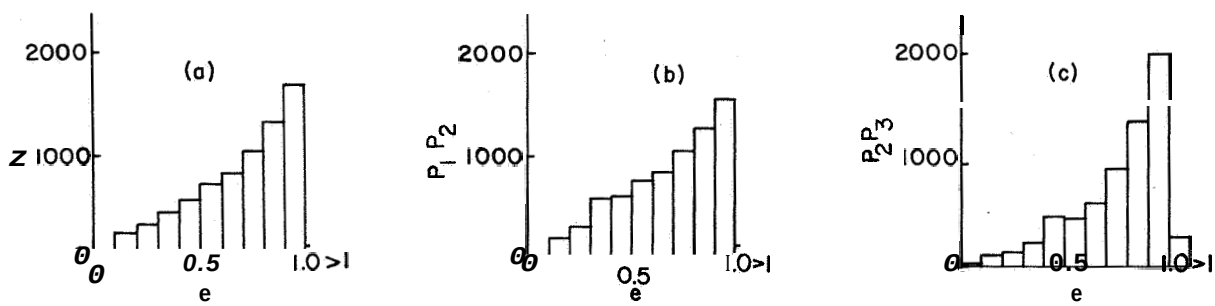

FIGURE 2.—Distribution of orbits of small meteor bodies in eccentricity.

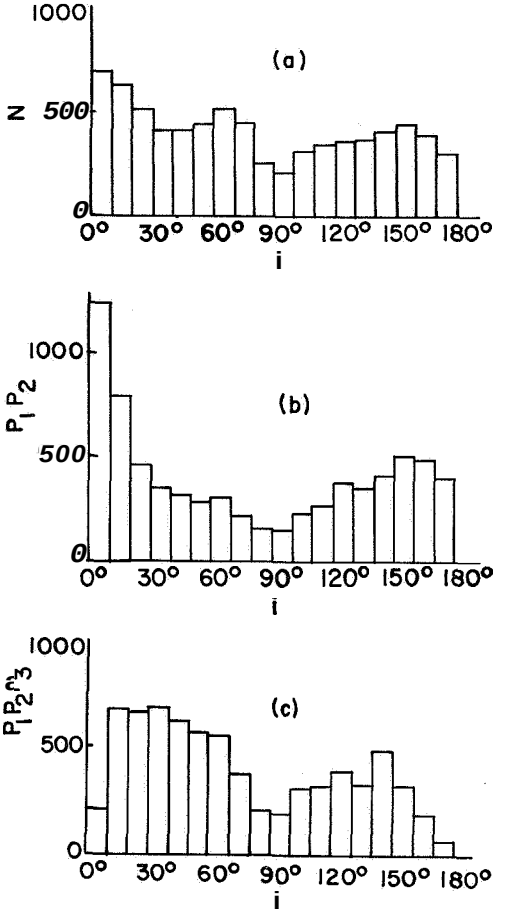

FIGURE 4.—Distribution of orbits of small meteor bodies in inclination.

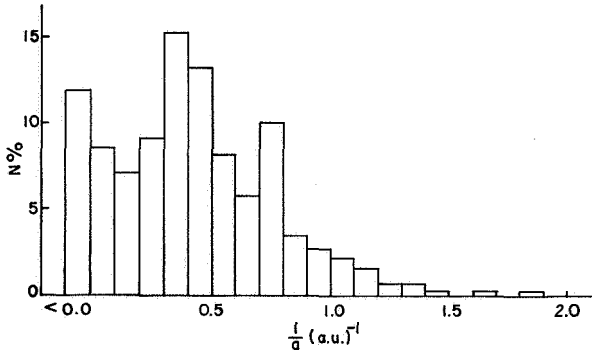

FIGURE 5.—Distribution of orbits of large meteor bodies in reciprocal semimajor axis.

to the region of still lower values, $a \approx 2$ a.u. About 20 percent of orbits have $a < 1$ a.u., and several tens of orbits, $a < 0.56$ a.u. The number of nearly parabolic orbits is considerably less than in the case of photographic meteors.

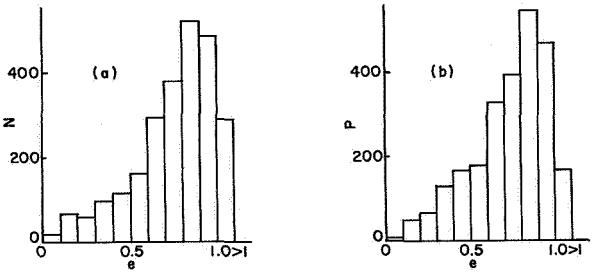

FIGURE 6.—Distribution of orbits of large meteor bodies in eccentricity.

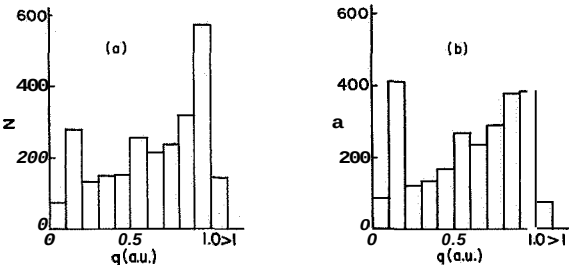

FIGURE 7.—Distribution of orbits of large meteor bodies in perihelion distance.

Thus, with the decrease of mass of meteor bodies there is a systematic decrease of the average sizes of the orbits along which they move.

ECCENTRICITY.—Radar and photographic measurements give a nearly similar distribution of eccentricities of meteor orbits. With a variation of e from 0 to 1, a monotonic increase of the distribution function is observed. Correcting for the selectivity of observations and the astronomical factor leads to still higher increases of the number of orbits with eccentricities of 0.9 to 1.0.

PERIHELION DISTANCE.—The astronomical factor produces the highest effect on the measured distribution of meteor orbits in q and i. From radio observations we obtain a nearly even distribution of orbits in q within the interval of $0.2 < q < 0.9$ a.u., and two maxima occurring at $0.05 < q < 0.2$ and $0.9 < q < 1.0$ a.u. After consideration of selectivity of measurements and of astronomical factor the second maximum disappears. The distribution function increases almost monotonically with the decrease of q from 1.0 to 0.05 a.u.

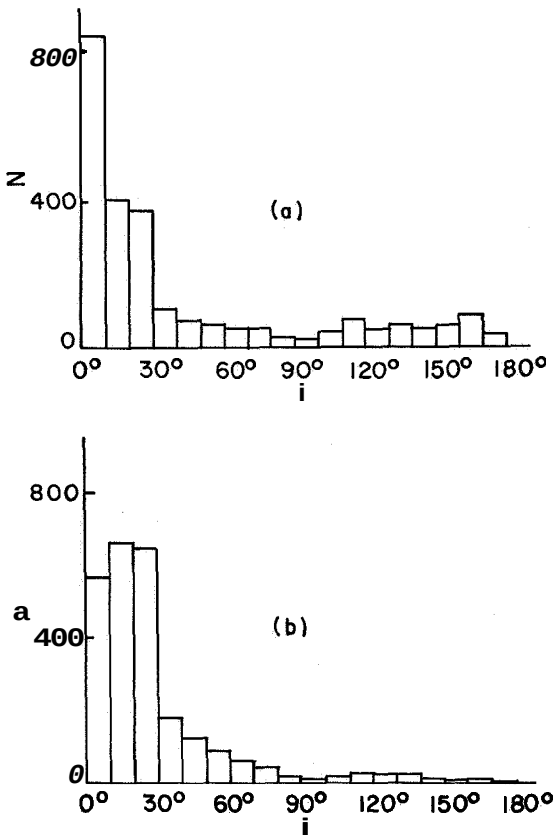

FIGURE 8.—Distribution of orbits of large meteor bodies in inclination.

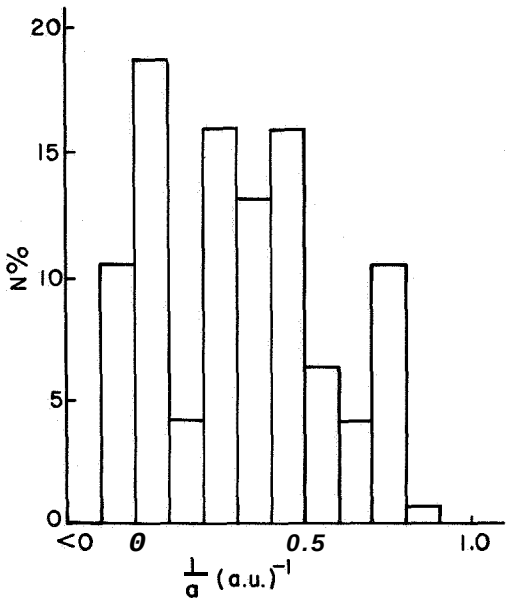

FIGURE 9.—Distribution of orbits of large meteor bodies (approx. 0 mag) in reciprocal semimajor axis (Whipple, 1954).

. The distribution of perihelion distances of orbits of larger meteor bodies appears to be essentially different. With a decrease of q from 1 to 0, a nearly monotonic decrease of distribution function occurs. The sharp maximum at $0.1<q<0.15$ a.u. is caused by meteors of the Geminids stream. The mean perihelion distance of orbits of small meteor bodies generating meteors of brightness $+5$ to $+7$ mag appears to be almost twice as small as for larger particles generating meteors of brightness 0 to $+3$ mag.

ORBIT INCLINATION.—Radar measurements give an almost even distribution of meteor orbits in i. A certain increase of the number of orbits takes place with $i<30°$, and a decrease within the interval of $80°<i<105°$. With the consideration of selectivity of radio observations the number of orbits increases with small inclinations to the ecliptic plane. After consideration of the astronomical factor the number of orbits with $i<15°$ sharply decreases. There are two wide maxima at $15°<i<65°$ and $120°<i<160°$. The minimum at $i\approx 90°$ remains nearly the same as with directly measured distribution.

In the case of photographic meteors the orbits with small inclinations $i<30°$ prevail. The values of $5°<i<25°$ occur most often. The minimum of distribution function occurs at $i\approx 90°$, and a certain increase with $110°<i<150°$.

In the case of large meteor bodies the distribution in i is different for orbits with small and large eccentricities. With $e>0.8$, distribution in i is almost even within the interval of $30°<i<180°$. A comparatively small increase of orbit concentration within the region of small inclinations is observed. With $e<0.7$ nearly all the orbits have small inclinations $i<30°$. Such an increase of concentration to the ecliptic plane with the decrease of eccentricity is especially typical of the orbits of the largest meteor bodies, generating meteors brighter than 0 mag. Out of 144 orbits given by Whipple (1954), only 1 is in the region of $30°<i<150°$ and $e<0.7$. Meteors brighter than $+3$ mag have less than 10 percent of such orbits, At the same time about 30 percent of radio meteors have orbits of the same type. After consideration of the selectivity of radio observations and astronomical factor, a con-

centration of orbits with $e<0.7$ is found within the interval of inclinations of $30°<i<80°$ and $110°<i<165°$.

A comparison of orbits obtained by photographic and radar measurements permits us to deduce a number of generalizations on the nature of movement in the solar system of meteor bodies of different size. From photographic observations of several hundred meteors brighter than 0 mag, two basic types of orbits of large meteor bodies can be distinguished: **(1)** Orbits similar to those of long-period comets; for these, high values of a, as well as arbitrary inclinations to the ecliptic plane, are typical. **(2)** Orbits similar to those of short-period comets; these are characterized by their comparatively small sizes ($a \lesssim 5$ a.u.) and small inclinations to the ecliptic plane. A small number of meteor bodies had an asteroidal-type orbit (low values of e and i).

When 2500 orbits of smaller meteor bodies generating meteors brighter than +3 mag were obtained, a much greater variety of orbits was discovered. There were orbits with $a<1$ a.u., nearly circular orbits, and also a small number of orbits with low eccentricities and great inclinations; however, the vast majority of the orbits belonged to the above-mentioned types **(1)** and **(2).**

Basic radar measurements carried out at Jodrell Bank and at Kharkov revealed a third basic type **(3)** of orbits characteristic of meteors weaker than about +5 mag. Orbits of type **(3)** have small eccentricities ($e<0.7$) and large inclinations ($30°<i<165°$). About 30 percent of orbits obtained by radio observations belong to this type.

An analysis of 12,500 orbits, obtained by us, shows that the majority of small meteor bodies moves along the orbits of a fourth type (4), which by their shape and inclination to the ecliptic plane are close to the orbits of short-period comets, but differ from them by having considerably less perihelion distances and still smaller sizes ($a \lesssim 3$ a.u.). From photographic observations such orbits were obtained for several meteor streams (Geminids, δ Aquarids, etc.), the parent comets of which were not discovered. In the case of small meteor bodies orbits of type **(4)** are characteristic for a great number of meteor streams and for sporadic meteors.

The discovery of the two new types **(3)** and **(4)** of orbits of small meteor bodies is very important for the study of the origin and evolution of meteor matter. Two groups of comet orbits are connected with each other since the perturbations of Jupiter can transfer the comets from orbits of type **(1)** to type **(2).** Orbits of types **(2)** and **(4)** hardly ever occur among the known greater bodies of the solar system and are not derivatives of orbits of type **(2)** or asteroid orbits.

As Davies and Gill **(1960)** showed, the discovery of the basic type **(3)** of orbits indicates that a considerable part of small meteor bodies is formed on the orbits of large sizes. Under the influence of the Poynting-Robertson effect the sizes of their orbits gradually decrease as the mass of meteor body decreases. During a certain interval of time the orbit appears to be close to that of Jupiter, and the meteor body may suffer close encounters with Jupiter. For large bodies this interval is longer and the probability is great that the body will be affected by Jupiter and thrown into the orbit of type **(2)** or thrown out of the solar system. Öpik **(1951)** has shown that with small orbit inclination to the ecliptic plane, the "Jupiter barrier" may be overcome only by very small meteor bodies, generating meteors weaker than about +9 mag. With large inclinations, the "Jupiter barrier" may be overcome by some larger particles.

The discovery of a great number of meteors with orbits of type **(4)** shows that in the solar system a great number of short-period comets with orbits of such a type must appear. Due to their closeness to the sun in perihelion, the lifetime of comets in orbits of type **(4)** is very short; it is evidently much shorter than the lifetime of meteor streams generated by such comets.

References

BABADZHANOV, P. B., and KRAMER, E. N.
1963. Methods and some results of the photographic researches of meteors. Ionosphere and Meteors, Sec. V of IGY Program, no. 12, Publ. House Acad. Sci. USSR, Moscow.

BAIRACHENKO, I. V.
1963. Physics of interaction of radio waves with meteor trails. IGY Reports, Univ. of Kiev, Kiev.

CEPLECHA, Z.; JEŽKOVA, M.; NOVÁK, M.; RAJCHL, J.; SEHNAL, L.; and DAVIES, J. G.
1964. Ondfejov double-station meteors during the IGY and IGC. Bull. Astron. Inst. Czechoslovakia, vol. 15, pp. 144–155.

DAVIES, J. G., and GILL, J. C.
1960. Radio echo measurements of the orbits of faint sporadic meteors. Monthly Notices Roy. Astron. Soc., vol. 121, pp. 437–462.

ELLYETT, C. D., and DAVIES, J. G.
1948. Velocity of meteors measured by diffraction of radio waves from tails during formation. Nature, vol. 161, pp. 596–597.

GILL, J. C., and DAVIES, J. G.
1956. A radio echo method of meteor orbit determination. Monthly Notices Roy. Astron. Soc., vol. 116, pp. 105–113.

GREENHOW, J. S.
1963. Limitations of radar techniques for the study of meteors. In Proceedings of the Symposium on the Astronomy and Physics of Meteors. Smithsonian Contr. Astrophys., vol. 7, pp. 5–17.

GREENHOW, J. S., and HALL, J. E.
1960. The importance of initial trail radius on the apparent height and number distributions of meteor echoes. Monthly Notices Roy. Astron. Soc., vol. 121, pp. 183–196.

HERLOFSON, N.
1948. The theory of meteor ionization. Phys. Soc., Rep. Prog. Phys., vol. 11, pp. 444–454.

JACCHIA, L. G., and WHIPPLE, F. L.
1961. Precision orbits of 413 photographic meteors. Smithsonian Contr. Astrophys., vol. 4, no. 4, pp. 97–129.

KASHCHEYEV, B. L.
1963. On studies of properties of the upper atmosphere by radar observations of meteors. "Meteory," no. 2, Kharkov Univ., Kharkov.

KASHCHEYEV, B. L.; DUDNIK, B. S.; LAGUTIN, M. F.; and LYSENKO, I. A.
1960. Instrumentation for radar observations of meteors. "Meteory," no. 1, Kharkov Univ., Kharkov.

KASHCHEYEV, B. L., and LEBEDINETS, V. N.
1961. Radar studies of meteor phenomena. Izd. Akad. Nauk SSSR.
1963. The initial radius of ionized meteor trails. *In* Proceedings of the Symposium on the Astronomy and Physics of Meteors. Smithsonian Contr. Astrophys., vol. 7, pp. 19–22.

KASHCHEYEV, B. L.; LEBEDINETS, V. N.; and LAGUTIN, M. F.
1961. Radar determination of the orbits of individual meteors. Astron. Journ. USSR, vol. 38, pp. 681–691.

KATASEV, L. A.
1964. Photographic Methods in Meteor Astronomy. Trans. from Russian by Israel Program for Scientific Translations, Jerusalem, 114 pp.

KLEIBER, I. A.
1891. Determination of Orbits of Meteor Streams. St. Petersburg, 330 pp.

KRAMER, E. N.
1953. Cometary radiants and the association of meteor streams with comets. Izv. Astron. Obs. Odessa, vol. 3, pp. 163–247.

LEBEDINETS, V. N.
1963. Density of meteoric matter in the vicinity of the earth's orbit, from radar observations of meteors. Astron. Journ. USSR, vol. 40, pp. 719–732.
1964. On the mechanism of formation of a region of higher atomic density with atoms of meteoric origin at 100–110 km. *In* Space Research IV, ed. by P. Muller, North-Holland Publ. Co., Amsterdam, pp. 553–560.

LEBIDINETS, V. N.; LAGUTIN, M. F.; and LYSENKO, I. A.
1960. The effect of atmosphere turbulent wind on measurements of radiants and meteor velocities. "Meteory," no. 1, Kharkov Univ., Kharkov.

LOVELL, A. C. B.
1954. Meteor Astronomy. Clarendon Press, Oxford, 463 pp.

MCCROSKY, R. E., and POSEN, A.
1961. Orbital elements of photographic meteors. Smithsonian Contr. Astrophys., vol. 4, no. 2, pp. 15–84.

NILSSON, C. S.
1964. A southern hemisphere radio survey of meteor streams. Australian Journ. Phys., vol. 17, pp. 205–256.

ÖPIK, E. J.
1951. Collision probabilities with the planets and the distribution of interplanetary matter. Proc. Roy. Irish Acad., vol. 54, Ser. A, pp. 165–199.
1958. Physics of Meteor Flight in the Atmosphere, Interscience Publ., New York, 174 pp.

SOUTHWORTH, R. B., and HAWKINS, G. S.
1963. Statistics of meteor streams. In Proceedings of the Symposium on the Astronomy and Physics of Meteors. Smithsonian Contr. Astrophys., vol. 7, pp. 261–285.

WHIPPLE, F. L.
1954. Photographic meteor orbits and their distribution in space. Astron. Journ., vol. 59, pp. 201–217.

Further Data Concerning the 1963 Anomalous Increase in Radar Meteor Rates

B. A. McIntosh [1]

An increase in radar meteor rates during the middle months of 1963 was observed in the Northern Hemisphere (McIntosh and Millman, 1964) and in the Southern Hemisphere (Ellyett and Eeay, 1964). The worldwide nature of the event, the extended period of time over which it occurred, and the fact that the rates were proportionally higher throughout the day make an explanation difficult.

Figure 1 shows the monthly mean diurnal variations for May and June 1963 compared with those of the average of 5 years (1958 through 1962). The bars indicate the standard deviation of a *single* year in the 5-year average. The excess counts in 1963 exceed the standard deviation by a factor that averages 7 times in May and 4 times in June.

Ellyett and Eeay (1964) reject an extraterrestrial or an atmospheric cause and tend to favor a man-made agency. In considering atmospheric effects, one thinks immediately of the "height ceiling," which is presumed to restrict stringently the fraction of incoming particles that can be observed by radar. Since short-duration echoes from underdense trails are more severely affected by the height ceiling than long-duration echoes, a raising of the height ceiling would explain the observation that the increase in rates was restricted to short-duration echoes.

Although the Ottawa radar provides no height information, an increase in average height should appear as an increase in average range. From a preliminary examination of the range data it may be said that there appears to be a tendency for the average range of the echoes to be higher during the middle months of 1963, as illustrated in figure 2. Each point represents an average of 7 hours of the monthly mean day, and the standard deviations are those of the average of the 7-hour values. It should be emphasized that the differences in

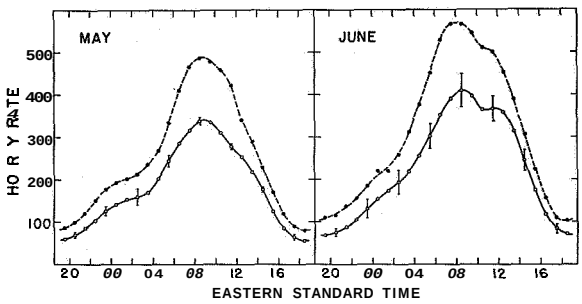

FIGURE 1.—Comparison of 1963 radar meteor counts (dashed curve) with 5-year average rates (solid curve) for 2 typical months during the anomalous period. Vertical bars indicate the standard deviation of a single value in the 5-year average.

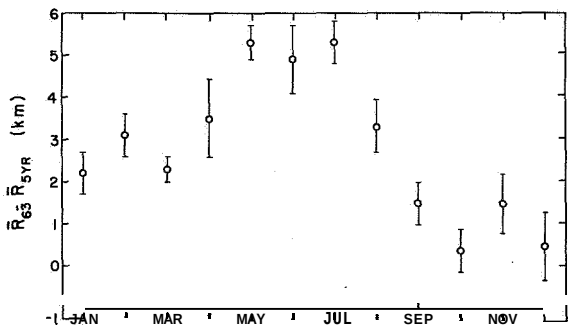

FIGURE 2.—Difference between monthly mean average range of meteor echoes for 1963 and for combined 5-year data (1958 through 1962). Vertical bars indicate standard deviation in the average of 7 hours in the monthly mean day.

[1] National Research Council, Ottawa, Canada.

average range are of the order of 3 km in 160 km, and that the statistical significance of the values in figure 2 has not yet been determined quantitatively. We do not have figures for the dispersion in the 5-year mean values of average range.

The results of Greenhow and Hall (1960) indicate that, of the total population of meteors, the fraction n that can be observed with a radar of wavelength λ is approximately

$$n_\lambda \propto \lambda^{2.3}.$$

The attenuation of reflected power, which gives rise to the height-ceiling effect, is

$$\exp\,[-8\pi^2(r_0/\lambda)^2],$$

where r_0 is the initial radius of the ionized meteor trail. If we take

$$r_0 \propto \rho^{-1},$$

where ρ is the atmospheric density at the height in question, then the effect of atmospheric density on the fraction of meteors that can be observed goes approximately as ρ^2.

It must be noted, however, that if there is a uniform increase in atmospheric density down to meteor heights (such as occurs at the minimum of the sunspot cycle), there would be no increase in the number of meteor echoes since the entire meteor population rises in height and the relative position of the height ceiling remains the same. Only an unusual increase in atmospheric density in a localized height region could contribute to an increase in rates.

Acknowledgment

A portion of the data reduction for this paper was carried out under Duke University Contract No. DA-31-124-AROD-59.

References

ELLYETT, C. D., and KEAY, C. S. L.
1964. Meteors: an unexpected increase in 1963. Science, vol. 146, p. 1458.

GREENHOW, J. S., and HALL, J. E.
1960. The importance of initial trail radius on the apparent height and number distributions of meteor echoes. Monthly Notices Roy. Astron. Soc., vol. 121, pp. 183–196.

MCINTOSH, B. A., and MILLMAN, P. M.
1964. Radar meteor counts: anomalous increase during 1963. Science, vol. 146, p. 1457.

Zodiacal Light as an Indicator of the Nature of the Interplanetary Matter—Past, Present, and Prospective Results

J. L. WEINBERG

Introduction

Considerable use has been made of zodiacal light observations over the past two decades in an attempt to infer something of the characteristics of gas and dust in the interplanetary space. The degree of success has been only slightly more discouraging than that of attempts to rationalize widely discordant zodiacal light observations.

A number of models of the interplanetary matter have been constructed on the basis of families of solutions to the integral equations describing the brightness and polarization of the zodiacal light (e.g., Whipple and Gossner, **1949;** Behr and Siedentopf, **1953;** Siedentopf, **Behr,** and Elsasser, **1953).** In most of the models the degree of polarization was used only to estimate the number density of free electrons that contributed to the observed brightness of the zodiacal light. The fact that the observed polarization is considerably less than that expected for a component of free electrons was erroneously explained on the grounds that the dust component is probably unpolarized and therefore dilutes the polarization field **of** the electron component. On the basis of this method one could obtain an electron density of the order of 10^3 cm^{-3} at the earth's distance. The situation remained much the same for a number of years, with principal effort being given to redetermining, by various techniques, the number density of free electrons at 1 a.u.

Hawaii Institute of Geophysics, Haleakala Observatory, Kula, Hawaii.

Subsequent laboratory polarization measurements (Kloverstrom and Rense, **1952;** Richter, **1962a;** Borngen and Richter, **1962;** Richter, Oberender, and Wallis, **1956)** and theoretical studies (van de Hulst, **1955)** suggested that dust particles could probably account for at least part of the polarization of the zodiacal light, since the degree of polarization was found to be quite large for some size distributions and classes of particles.

Recent developments in instrumental techniques for both laboratory and field studies, coupled with new methods of observing the zodiacal light and the use of large computers in problems associated with scattering theory, have led to a new picture of the gas and dust in the solar system, namely, relatively few electrons **(—10** cm^{-3} at 1 a.u.) and metallic particles and large numbers of small dielectric particles.

Comparison of theory and observations

The experimentally determined scattering phase functions of Richter are in fairly good agreement with Giese's **(1961)** calculations of theoretical (Mie) scattering phase functions for mixtures of spherical particles of diameter of the order of 1 μ (Borngen and Richter, **1962);** and as a follow-up to Giese's work, Giese and Siedentopf **(1962)** calculated the brightness (I_1+I_2) and polarization (p) to be expected from 4 different groups **of** models of the interplanetary matter in the plane of the ecliptic. The size-distribution law was chosen to be of the form $n(\alpha)=n(\alpha_0)(\alpha/\alpha_0)^{-k}$, where α is the size parameter (circumference/wavelength), α_0

corresponds to the smallest particles present, and k is a constant. The resultant distributions were compared with the observations of Elsasser (1958) and Blackwell and Ingham (1961a) (see fig. 1).

The first group of models consisted of six single-component models of spherical particles and free electrons. The metallic, dielectric, and free-electron models of this group are shown in figure 2. The maximum polarizations for the dielectric component models (see figs. 2a, 2b) are associated with the Nebelbogeneffektc: (haze bow) in the brightness and are followed by a sharp decrease to negative polarizations at large elongations (angular distance from the sun). Note, also, the negative polarizations at small elongations. The other two single-component models consisted of a hypothetical isotropically reflecting material giving no polarization and a hypothetical metal giving a low brightness. Although our observational results from Haleakala (see figs. 4, 5, and 6 and Weinberg, 1964c) differ from those used by Giese and Siedentopf, we support their conclusion that none of these single-component models can quantitatively produce the observed brightness and polarization of the zodiacal light.

The second and third groups consisted of mixtures of dielectric particles and electrons, and of mixtures of dielectric and metallic particles and electrons, respectively. All three models in each group had the same spatial density distribution law for electrons and electron densities of about 1000 and 300 cm^{-3} at 1 a.u. for the second and third groups, respectively. The composite distributions of brightness and polarization are very similar for the models in each of these groups, and we therefore show only one representative model for each group (models I and II of fig. 3). Apart from the strong evidence (e.g., Blackwell and Ingham, 1961b; Gringauz et al., 1961; Bridge et al., 1962; Beggs et al., 1964) against the existence of an electron component of density 10^3 cm^{-3} at 1 a.u., model I predicts a degree of polarization considerably larger than that which we observe. We do not observe the large degree of polarization predicted by model II in the region $40° \leq \epsilon \leq 60°$ (from the inclusion of metallic dust particles), and the magnitude of the brightness distribution is too small for all elongations. We therefore conclude that models I and II do not satisfactorily represent our observations.

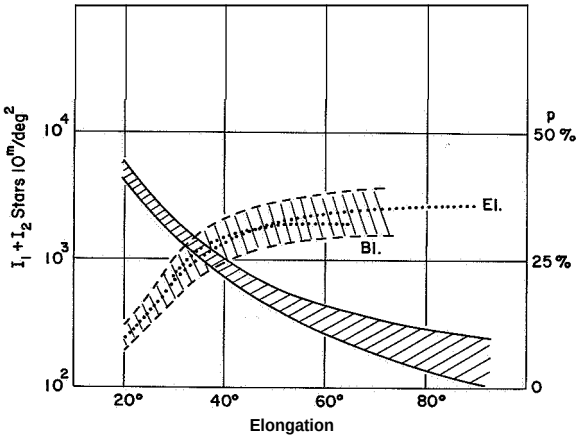

FIGURE 1.—Giese and Siedentopf (1962) observational model for the brightness (in 10th-mag stars/deg^2 in S_{10} (vis) units) and polarization of the zodiacal light (Giese, 1962, fig. 7). El.= Elsasser (1958), Bl.= Blackwell and Ingham (1961a).

The fourth group (one model) consisted of a mixture of an isotropically reflecting dielectric and a hypothetical metal. This model is the result of a variation of parameters to reproduce as closely as possible the observational model of figure 1. Our results (especially at large elongations) rule out any serious consideration of this model.

The "Venus Flytrap" observations of Hemenway and Soberman (1962) led Giese (1962) to suggest another group of models that involves the presence of large numbers of small particles and no electrons. Model III (see fig. 3) is an example of one of these models. The degree of polarization for this model is very similar to that of model I (i.e., too large), and the magnitude of the brightness distribution is unquestionably too small, but it demonstrates again that electrons are not required to produce a significant degree of polarization.

Giese (1962) justifiably concluded that none of their single-component models quantitatively approximate their limited (in elongation) observational model. The lower polarization of our observational model, however, makes it unnecessary to postulate the existence of large numbers of electrons or metallic particles, and we find that one of Giese's single-component models agrees reasonably well with the magni-

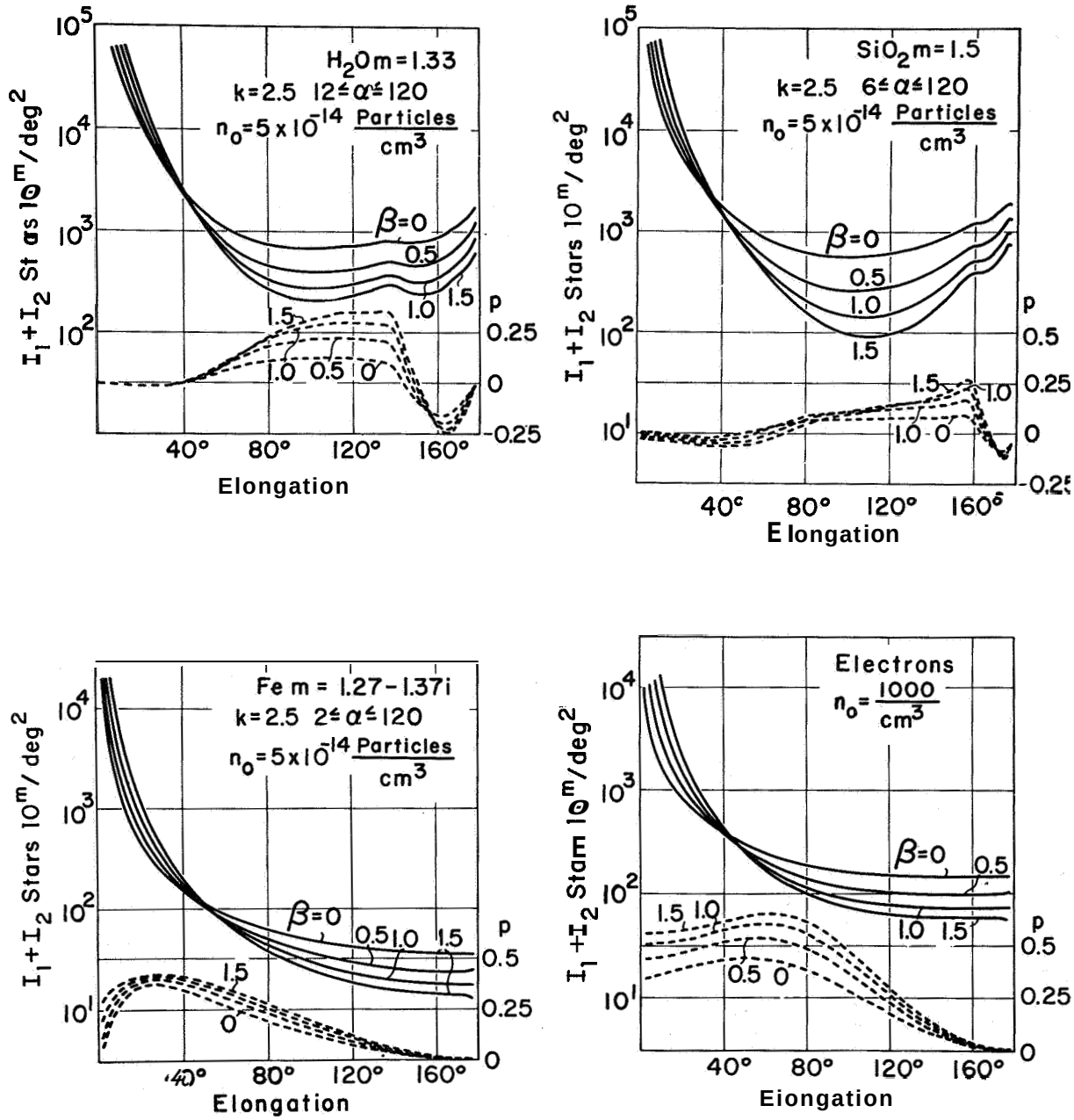

FIGURE 2.—Surface brightness (upper curves) and degree of polarization for single-component models of the interplanetary matter (Giese and Siedentopf, 1962; Giese, 1962, figs. 9a, b, c, e). Here n_o is the number density of particles at 1 a.u., m the refractive index, α the size parameter, β the power dependence on the distance from the sun ($\sim r^{-\beta}$), and k the slope of the distribution of particle sizes.

tude and distribution of our results. This model, which is compared with our observations in figure 4, is characterized by a very steep particle-size distribution and contains a large number ($n_o = 1.5 \times 10^{-11}$ particles cm^{-3}) of small, Rayleigh-like dielectric particles. The size parameter for this model extends from 1 to 26, which corresponds to a range of particle diameters of 0.17 μ to 4.4 μ for 5300 A radiation. The lack of a large haze bow in the zodiacal light radiation indicates that large spherical particles do not play a dominant role. A small

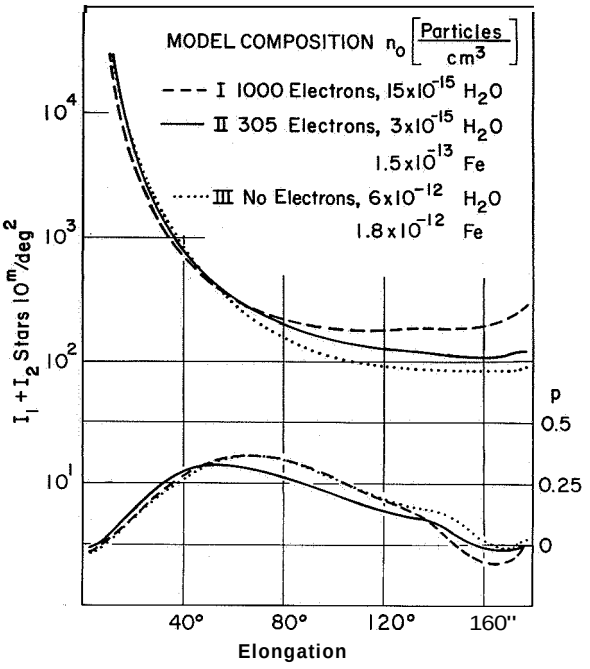

FIGURE 3.—Surface brightness and degree of polarization for multiple-component models of the interplanetary matter (Giese, 1962, fig. 10).

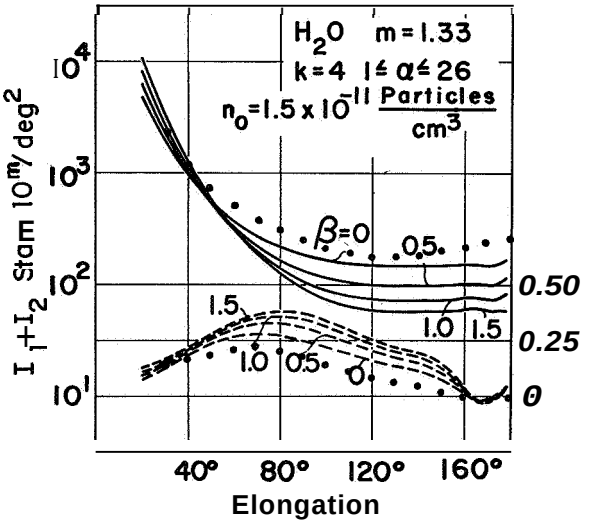

FIGURE 4.—Surface brightness and degree of polarization for a model composed of a large number of small dielectric particles (Giese, 1962, fig. 9d). The dots correspond to the observations of Weinberg (1964c).

haze bow is associated with the small-particle model (see fig. 4), but it could easily escape detection. This comparison suggests that small dielectric particles can account for the major fraction of both the brightness and the polarization of the zodiacal light that we observe. A more definitive test for the presence of small particles would be the demonstration that there exists a wavelength dependence of the polarized component.

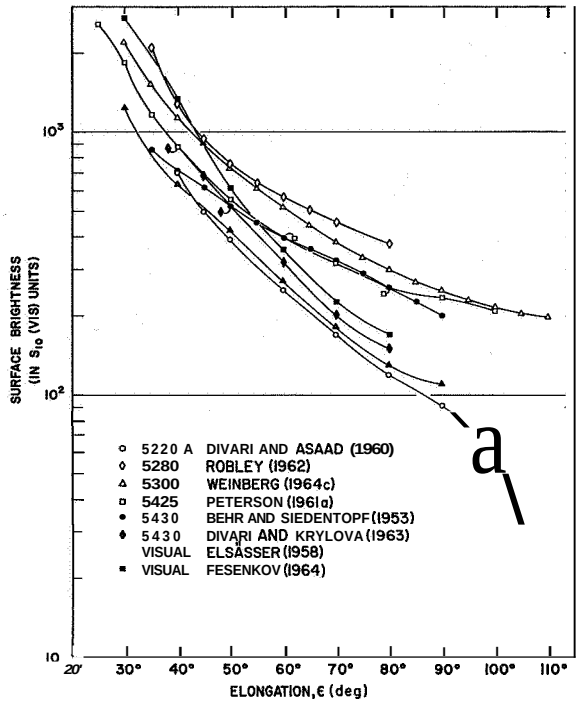

FIGURE 5.—Representative post-1950 results for the surface brightness of the zodiacal light in the plane of the ecliptic.

From this comparison of theory and observation we see the following: (1) only dielectric-component models produce a gegenschein effect (see also Walter, 1958); (2) only dielectric-component models produce an irregular decrease of polarization such as we observe at large elongations; (3) for those models discussed here only dielectric- or electron-component models (or combinations of these) give a maximum polarization at $\epsilon \approx 70°$ such as we observe; (4) metallic-component models cannot alone account for the observed brightness and polarization; and (5) to include more than some tens [2] of electrons cm^{-3} at 1 a.u., we must postulate the existence of a hypothetical nonpolarizing dust component.

The theoretical results are based on spherical particles because we do not yet have enough

[2] A closer estimate cannot yet be made since electrons and very small particles are nearly equivalent in their polarization properties.

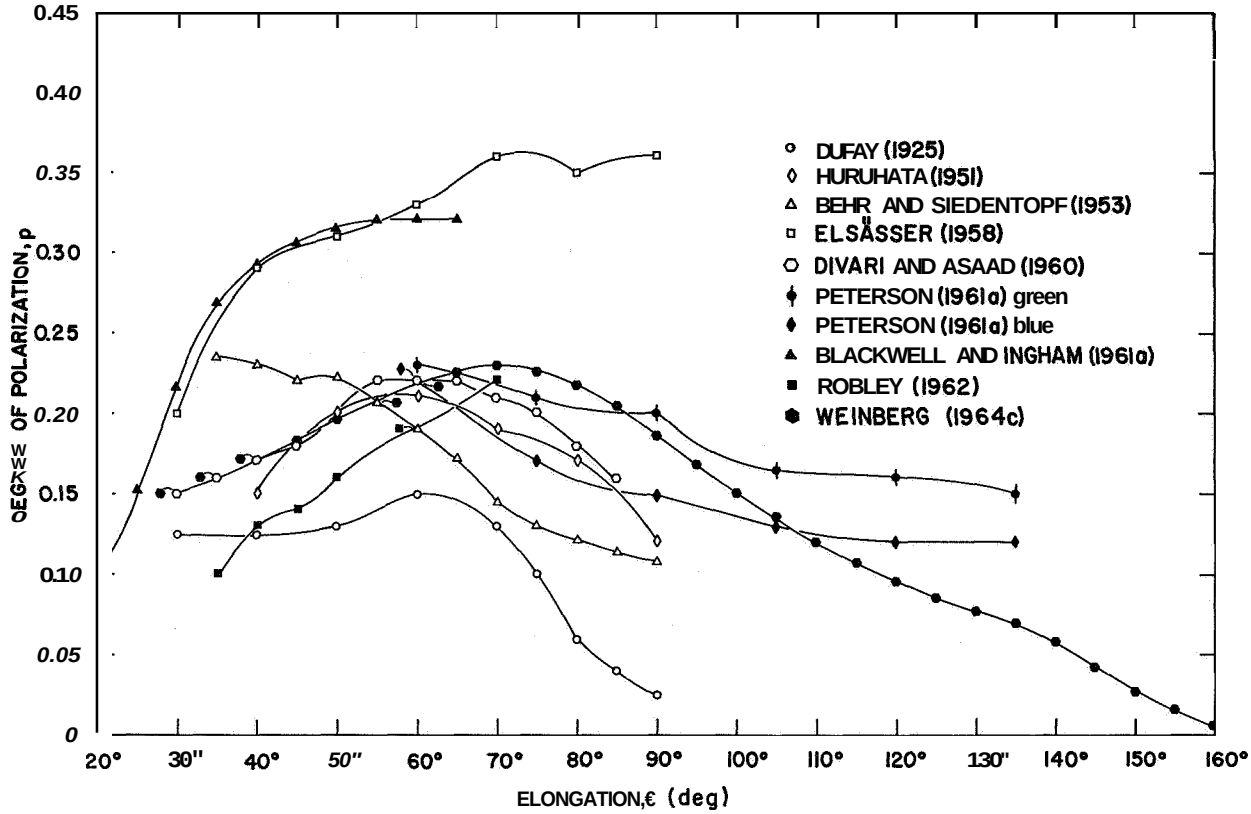

FIGURE 6.—The degree of polarization of the zodiacal light in the plane of the ecliptic.

information on the scattering properties of mixtures of differently shaped particles. While there appears to be some evidence (Donn and Powell, 1963) that irregular particles, in general, are somewhat larger than the so-called equivalent spheres for indices of refraction greater than or equal to those of the spherical particles, such inferences regarding the kind of particle (i.e., dielectric versus metallic) will probably be unaffected. In an attempt to assess whether one is justified in applying the Mie theory for crushed nonspherical aggregates, Little, O'Mara, and Aller (1964) performed calculations (as per Giese and Siedentopf, 1962) using Richter's particle-size distributions in the Mie theory. Their findings concur with our results on the importance of dielectric particles to the observed zodiacal light.

Choice of an observational model

Clearly, the aforementioned method of analysis depends most critically on the reliability of the observations. A meaningful comparison of theoretical scattering calculations with zodiacal light observations can be accomplished only if observational uncertainties are recognized. These uncertainties, which are reflected in the widely divergent results of zodiacal light observers, arise primarily from (1) the lack of a rigorous method for separating the individual components of the night-sky radiation field, (2) the lack of a satisfactory formulation for the effects of tropospheric scattering, (3) difficulties associated with the absolute calibration of low light-level extended sources, and (4) limited observational coverage in time and over the sky. To illustrate the divergence of zodiacal light results and the resultant difficulty in specifying the nature of the interplanetary matter, we have collected all known zodiacal light results as of 1964 (Weinberg, 1964a).

In figure 5 representative post-1950 results for the surface brightness of the zodiacal light are plotted as a function of elongation in the plane of the ecliptic. To indicate more clearly the extent of the divergence of results, we have chosen results only in the visible spectral region

and only in the more easily observed bright portions. If results are included for other wavelengths and for regions far from the sun, the disagreement becomes worse. There are no observations of the zodiacal light in the ultraviolet or infrared. Of particular interest in figure 5 are (1) the generally lower results of the Russian observers and of Elsasser (1958), and (2) the sharp decrease of brightness at large elongations found by Divari and Asaad (1960). If we forced our brightness determinations to agree with the results of Divari and Asaad, we would find that the degree of polarization approaches unity in some parts of the sky. This is untenable. Furthermore, contrary to the findings of the Russian observers, we now have conclusive evidence (Weinberg, 1965) that the zodiacal light does indeed extend to high ecliptic latitudes. There is some evidence (Roach and Smith, 1964) of a calibration error in the work of Elsasser.

In figure 6 we have plotted all known distributions of polarization in the plane of the ecliptic. Of particular interest are the large polarizations found by Blackwell and Ingham (1961a) and by Elsasser (1958). Unpublished results by Ney (1964) indicate general agreement with our polarization results from Haleakala (Weinberg, 1964c). Since inferencesfrom the aforementioned scattering calculations are very sensitive to the magnitude and distribution of the polarization, the nature of these polarization discrepancies is particularly important.

In an attempt to rationalize these differences, we have made polarization measurements by various techniques using different sources of laboratory and field calibrations, and the common difficulty is always that of the separation of the zodiacal light from the total radiation field. The importance of wavelength discrimination (i.e., avoiding the principal airglow emission lines) is magnified by our recent finding at Haleakala that there are nonzodiacal light sources of polarization (both astronomical and atmospheric) in the night-sky radiation. In particular, we have found small polarizations (several percent and less) associated with the 5577-A and 6300-A airglow lines. It does not concern us here (nor does it concern the instrument) whether the polarization arises from the process of line formation or from atmospheric scattering (or from both). The salient fact is that although the degree of polarization is small, these lines are ',bright," and a significant amount of polarized light will be measured by instruments whose bandpasses admit (and this includes many instruments) these airglow line radiations.

In view of this result, of the inherent difficulty in measuring low light levels, and of the number of factors involved in each set of measurements (instrument bandpass, time, place and duration of observation, measurement and analysis technique, calibration, etc.), it is perhaps remarkable that the disagreement is as small as it is.

Recent results

ZODIACAL LIGHT AT LARGE ELONGATIONS.—A year ago (Weinberg, 1964b), I reported that while we had found in our observations through 1962 some cases of negative polarization at large distances from the sun in the plane of the ecliptic, the low polarization in this region made it extremely difficult to obtain accurate quantitative results. Its importance for interpretation of the nature of the zodiacal material led us to modify our observing techniques and to conduct a concentrated study of this region in an effort to obtain accurate observational results.

Measurements were made on top of Haleakala during 17 nights between October 1963 and October 1964 with the instrument (Weinberg, 1964c) fixed in the zenith? The detailed results are still being analyzed, but we are able to present preliminary results on the observed brightness (B_{obs}), the orientation of the plane of polarization (χ_z) for the E vector, and the degree of polarization (P_{tot}) for one night's study (October 4–5, 1964) as observed at the base of the atmosphere (fig. 7). Of particular interest are the fluctuations of χ_z and the nature of the distribution of P_{tot}. The enhancement starting at approximately 0510 is associated with astronomical dawn.

There are two principal sources of the variation of χ_z: statistical fluctuation noise associated

3 Contrary to recent remarks in the literature, accurate measurements of the Stokes' parameters of the zodiacal light at large elongations can be made from the ground if these regions are observed far from the Milky Way when they are at or near the zenith where the airglow is faint(er) and extinction and scattering are much reduced.

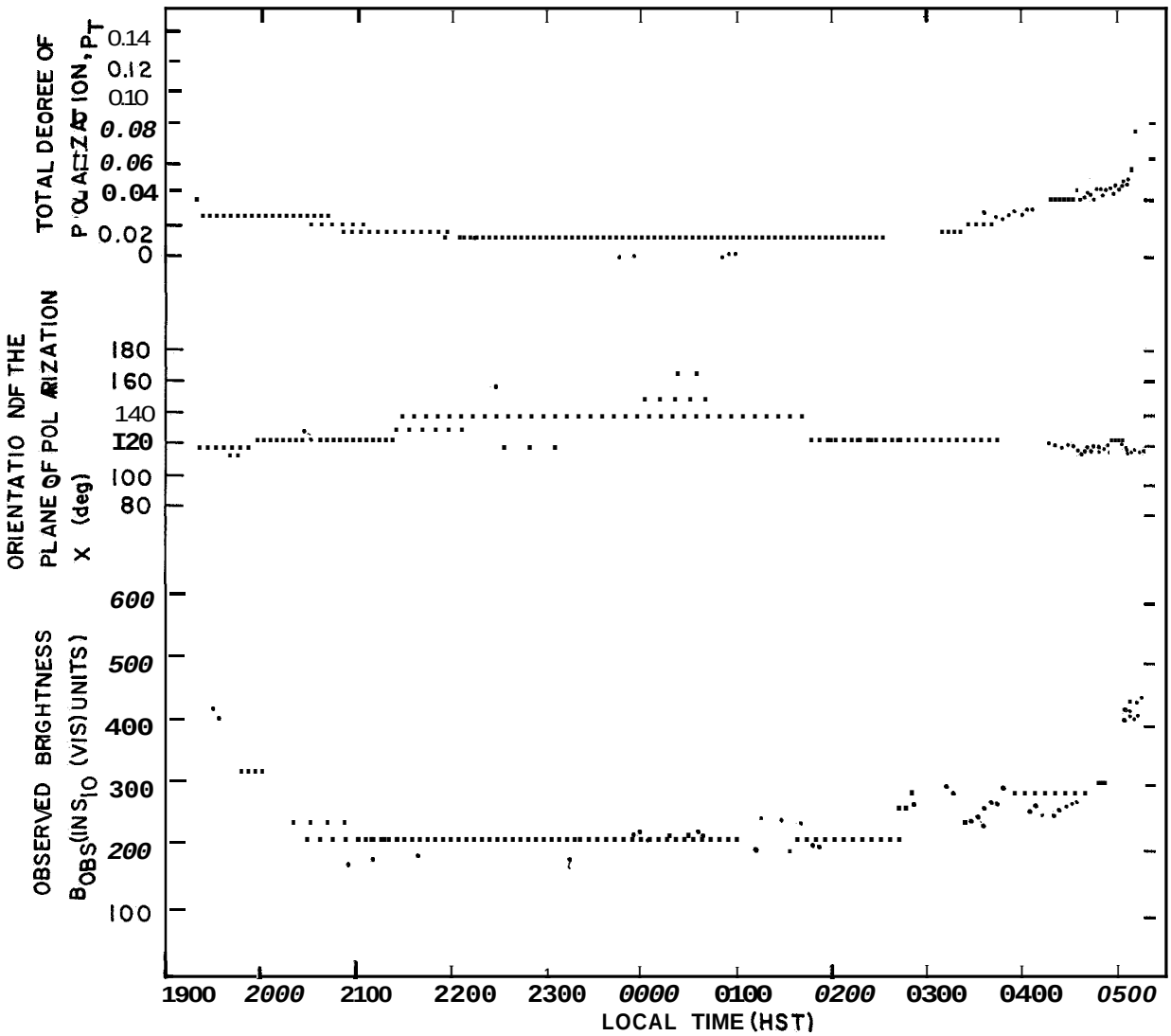

FIGURE 7.—Brightness and polarization parameters as measured at the zenith October 4–5, 1964.

with uncertainties resulting from the nearness to zero polarization where χ_z is not defined (note, especially, the region between 2230 and 0200); and as yet unexplained structure near the plane of the ecliptic (as seen in the zenith at approximately **0300).** In the interval 2230 to **0200** HST the ecliptic latitude and elongation (β, e) vary from 26°,150° to 6°,148°. At 0330 the coordinates are *0"*,128°.

The small and slowly varying degree of polarization is characteristic of this region of the **sky,** and, while we (and R. D. Wolstencroft, 1965, private communication) have again found some cases of negative polarization, it was always of small magnitude. These results and the fact that it is difficult to determine the polarization at large elongations provide further evidence that relatively few large dielectric particles contribute to the observed zodiacal light.

ZODIACAL LIGHT AT HIGH ECLIPTIC LATITUDES.— Preliminary results and some description of the difficulties associated with both the measurement and analysis of the night-sky radiation at high ecliptic latitudes have been given by Beggs et al. (1964), Weinberg (1964c), Divari, Krylova, and **Moroz** (1964), and Smith, Roach,

and Owen **(1965).** As we would expect, the divergence of results increases rapidly as we move toward high ecliptic latitudes.

Contrary to the results of most Russian observers, there is now considerable evidence for an appreciable polarization in regions far from the ecliptic. Recent broad-band studies of the zodiacal light at high latitudes by Beggs et al. **(1964)** are in agreement with our findings on the measured polarization of the night-sky, but in disagreement with the inferred polarization of the zodiacal light in these regions.

In a recent result (Weinberg, 1965) we have shown that the principal component of the polarization far from the ecliptic is associated with the zodiacal light. This is not at all an obvious conclusion, since, as previously mentioned, we have found nonzodiacal light sources of polarization in the night-sky radiation. One of these components, which is associated with the starlight at low galactic latitudes, manifests itself as a rotation of the plane of polarization as we scan through these regions. R. **D.** Wolstencroft **(1965,** private communication) reports that he has recently found similar results at low galactic latitudes. This component of polarization in conjunction with the distribution of starlight at low galactic latitudes (Weinberg, in preparation) offers some hope of separating the starlight into its components: integrated starlight and galactic light.

Smith, Roach, and Owen **(1965)** have recently given an isophotal map of the brightness of the zodiacal light over the sky. Their results are discussed by one of the authors (Roach, see pp. 225–226), and we only remark here that we (Wolstencroft and I) do not confirm some of the details in the map—in particular, the so-called photometric perturbation at 65° from the sun at high ecliptic latitudes.

Conclusion

Investigations of the zodiacal light have dealt primarily with the brightness and polarization averaged over the period during which observations were obtained. There has not been a detailed analysis of fluctuations in the zodiacal light radiation field. This is due, in part, to the lack of accurate polarimetric observations until recent years, and, of more importance, to the lack of a method for separating diurnal variations of the airglow from zodiacal light fluctuations. Simultaneous, long-term studies of the zodiacal light and of the principal airglow radiations are now being carried out at the Haleakala Observatory in an attempt to analyze fluctuations in the night-sky radiation.

The apparent concentration of dust about the earth (de Jager, **1955;** Beard, **1959;** Singer, **1961;** Whipple, **1961;** Hibbs, **1961;** and others) is based on a comparison of zodiacal light results and direct measurements. It is interesting to note that if submicron dielectric particles exist in the quantity predicted by Giese's **(1963)** model (fig. **4),** the geocentric concentration for these particles may be only a factor of **10.**

As we have shown, it is meaningless to use an average of zodiacal light observations for comparison with results of theoretical and laboratory studies of the scattering by microscopic particles. Recent findings on some of the reasons for the wide divergence in zodiacal light results should soon lead to better agreement on results in the ecliptic and at high ecliptic latitudes, and to preliminary results on the wavelength dependence of the polarized component. The night-sky radiation field is dominated by terrestrial radiations (atomic and molecular) to the extent that observations have been made of the zodiacal light only in a small number of narrow wavelength intervals in the visible part of the spectrum. This fact, in conjunction with the wide divergence in existing observations and the lack of ultraviolet and infrared observations, necessarily precludes our finding the wavelength dependence on the basis of existing observations.

We do not share the current widespread belief that observations from a satellite will reduce to insignificance those difficulties associated with ground-based observations of the zodiacal light. There are, however, a number of observations that can be accomplished only from a satellite, e.g., ultraviolet and infrared studies, and observations close to the sun using an external system, not the earth, to occult the solar disk. The first satellite observations of the zodiacal light are now being processed at

the University of Minnesota by Ney and his associates.

Further information on the small, solid particles in the solar system should be forthcoming from studies of doppler shifts of Fraunhofer absorption lines in the spectrum of zodiacd light (Ring et al., 1964), of thermal radiation by interplanetary dust (Peterson, 1961b, 1963a, 1964; Harwit, 1964; and others), and, we hope, of further scattering calculations as a function of wavelength for spherical and irregular particles.

Acknowledgment

This research was supported by the National Aeronautics and Space Administration under grant NsG–676.

References

BEARD, D. B.
1959. Interplanetary dust distribution. Astrophys. Journ., vol. 129, pp. 496–506.

BEGGS, D. W.; BLACKWELL, D. E.; DEWHIRST, D. W.; and WOLSTENCROFT, R. D.
1964. Further observations of the zodiacal light from a high altitude station and investigation of the interplanetary plasma. Monthly Notices Roy. Astron. Soc., vol. 128, pp. 419430.

BEHR, A., and SIEDENTOPF, H.
1953. Untersuchungen uber Zodiakallicht und Gegenschein nach lichtelektrischen Messungen auf dem Jungfraujoeh. Zeits. f. Astrophys., vol. 32, pp. 19–50.

BLACKWELL, D. E., and INGHAM, M. F.
1961a. Observations of the zodiacal light from a very high altitude station, I: The average zodiacal light. Monthly Notices Roy. Astron. Soc., vol. 122, pp. 113–127.
1961b. Observations of the zodiacal light from a very high altitude station, 11: Electron densities in interplanetary space. Monthly Notices Roy. Astron. Soc., vol. 122, pp. 129–141.

BÖRNGEN, F., and RICHTER, N.
1962. Experimentelle Untersuchungen zur Beleuchtung interplaneterer Materie, II Teil. Streuung und Polarisation elektromagnetischer Wellen an Wolken feiner Partikel unregelmassiger Gestalt. Veroff. Sternw. Sonneberg, vol. 5, pp. 195–224.

BRIDGE, H. S.; DILWORTH, C.; LAZARUS, A. J.; LYON, E. F.; ROSSI, B.; and SCHERB, F.
1962. Direct observations of the interplanetary plasma. Journ. Phys. Soc. Japan, vol. 17, Suppl. A–II, pp. 553'-560.

DE JAGER, C.
1955. The capture of zodiacal dust by the earth. Mem. Soc. Roy. Sci. Liège, vol. 15, pp. 174–182.

DIVARI, N. B., and ASAAD, A. S.
1960. On the emission of the green line of the night sky in zodiacal light. Sov. Astron.—AJ, vol. 3, pp. 320–325.

DIVARI, N. B., and KRYLOVA, S. N.
1963. Photoelectric observations of zodiacal light from a high-altitude observatory. Sov. Astron.—AJ, vol. 7, pp. 391–398.

DIVARI, N. B.; KRYLOVA, S. N.; and MOROZ, V. I.
1964. Polarization measurements of the zodiacal light. Geomagnetism and Aeronomy, vol. 5, pp. 684–687.

DONN, B., and POWELL, R. S.
1963. Angular scattering from irregularly shaped particles with application to astronomy. In ICES Electromagnetic Scattering, ed. by M. Kerker, Macmillan Co., New York, pp. 151–158.

DUFAY, J.
1925. La polarisation de la lumière zodiacale. Comp. Rend., vol. 181, 2er Semestre, pp. 399401.

ELSÄSSER, H.
1958. Neue Helligkeits- und Polarisationsmessungen am Zodiakallicht und ihre Interpretation. Die Sterne, vol. 34, pp. 166–169.

FESENKOV, V. G.
1964. Isophotes of zodiacal light from observations made in Egypt during the autumn of 1957. Sov. Astron.—AJ, vol. 7, pp. 829–834.

GIESE, R. H.
1961. Streuung elektromagnetischer Wellen an absorbierenden und dielektrischen kugelformigen Einzelteilchen und an Gemischen solcher Teilchen. Zeits. f. Astrophys., vol. 51, pp. 119–147.
1962. Light scattering by small particles and models of interplanetary matter derived from the zodiacal light. Space Sci. Rev., vol. 1, pp. 589–611.

GIESE, R. H., and SIEDENTOPF, H.
1962. Optische Eigenschaften von Modellen der interplanetaren Materie. Zeits. f. Astrophys., vol. 54, pp. 200–216.

GRINGAUZ, K. I.; KURT, V. G.; MOROZ, V. I.; and SHKLOVSKII, I. S.
1961. Results of observations of charged particles observed out to R=100,000 km, with the aid of charged-particle traps on Soviet space rockets. Sov. Astron.—AJ, vol. 4, pp. 680–695.

HARWIT, M.
1964. Infrared appearance of different zodiacal cloud models. Mem. Soc. Roy. Sci. Libge, vol. 9, pp. 506–519.

HEMENWAY, C. L., and SOBERMAN, R. K.
1962. Studies of micrometeorites obtained from a recoverable sounding rocket. Astron. Journ., vol. **67,** pp. **256–266.**

HIBBS, A. R.
1961. The distribution of micrometeorites near the earth. Journ. Geophys. Res., vol. **66,** pp. **371–377.**

HURUHATA, M.
1951. Photoelectric study of the zodiacal light. Publ. Astron. Soc. Japan, vol. **2,** pp. **156–171.**

KLOVERSTROM, F. A., and RENSE, W. A.
1952. Reflection from meteoric surfaces. Astrophys. Journ., vol. **115,** pp. **495–500.**

LITTLE, S.; O'MARA, B. J.; and ALLER, L. H.
1964. Light scattering by small particles in the zodiacal light (abstract). Astron. Journ., vol. **69,** p. **550.**

NEY, E. P.
1964. Recent balloon observations of the zodiacal light. Trans. IAU, vol. XII B, p. **244.**

PETERSON, A. W.
1961a. Three-colorphotometery of the zodiacallight. Astrophys. Journ., vol. **133,** pp. **668–674.**
1961b. General Dynamics Report, ERR–FW–102.
1963. Thermal radiation from interplanetary dust. Astrophys. Journ., vol. **138,** pp. **1218–1230.**
1964. Thermal radiation from interplanetary dust. 11. Distribution of the dust. Ann. New York Acad. Sci., vol. **119,** pp. **72–81.**

RICHTER, N.
1962a. Experimentelle Untersuchungen zur Beleuchtung interplanetarer Materie. I Teil. Photometrische Untersuchungen an Stein- und Eisenmeteoriten. Veroff. Sternw. Sonneberg, vol. **5,** pp. **157–193.**
1962b. The photometric properties of interplanetary matter. Quart. Journ. Roy. Astron. Soc., vol. **3,** pp. **179–186.**

RICHTER, N.; OBERENDER, W.; and WALLIS, D.
1956. Experimentelle Untersuchungen zur Beleuchtung staubformiger Wolken. I Teil. Grobe partikel. Veroff. Sternw. Sonneberg, vol. **2,** pp. **369–389.**

RING, J.; CLARKE, D.; JAMES, J. F.; DAEHLER, M.; and MACK, J. E.
1964. Profile of the $H\beta$ line in the spectrum of zodiacal light. Nature, vol. **202,** pp. **167–168.**

ROACH, F. E.
1967. The brightness of the zodiacal light at the ecliptic pole. Smithsonian Contr. Astrophys., vol. **11,** pp. **225–226.**

ROACH, F. E., and SMITH, L. L.
1964. Absolute photometry of the night sky—the zenith intensity of Haleakala (latitude N **20.7°**) and at Fritz Peak (latitude N **39.9°**). NBS Tech. Note No. **214,** June.

ROBLEY, R.
1962. Photométrie des lumières zodiacale et antisolaire. Ann. Géophys., vol. **18,** pp. **341–350.**

SIEDENTOPF, H.; BEHR, A.; and ELSÄSSER, H.
1953. Photoelectric observations of the zodiacal light. Nature, vol. **171,** pp. **1066–1067.**

SINGER, S. F.
1961. Dust shell around the earth (abstract). Journ. Geophys. Res., vol. **66,** pp. **2560–2561.**

SMITH, L.; ROACH, F.; and OWEN, R.
1965. The absolute photometry of the zodiacal light. Planet. Space Sci., vol. **13,** pp. **207–217.**

VAN DE HULST, H. C.
1955. On the polarization of the zodiacal light. Mem. Soc. Roy. Sci. Liège, vol. **15,** pp. **89–95.**

WALTER, H.
1958. Theoretische Deutung des Gegenscheins durch Lichtstreuung an sphärischen Partikeln. Zeits. f. Astrophys., vol. **46,** pp. **9–16.**

WEINBERG, J. L.
1964a. Summary report on zodiacal light. Hawaii Inst. Geophys. Rep. **HIG–64–11,** July.
1964b. A summary report on the current status of zodiacal light research. Trans. IAU, vol. XIIB, p. **244.**
1964c. The zodiacal light at **5300 Å.** Ann. d'Astrophys., vol. **27,** pp. **718–738.**
1965. Zodiacal light at the celestial pole. Planet. Space Sci., vol. **13,** pp. **1311–1312.**

WHIPPLE, F. L.
1961. The particulate contents of space. *In* Medical and Biological Aspects of the Energies of Space, ed. by P. Campbell, Columbia Univ. Press, New York, pp. **49–79.**

WHIPPLE, F. L., and GOSSNER, J. L.
1949. An upper limit to the electron density near the earth's orbit. Astrophys. Journ., vol. **109,** pp. **380–390.**

Abstract

A brief summary is given of the current status of zodiacal light research with emphasis on the interpretation in terms of small solid particles in the solar system. Recent observations are presented which provide further evidence for the existence of large numbers of small dielectric particles as the principal constituents responsible for the observed zodiacal light.

Conditions of Encounter between Dust and the Planets

C. W. McCRACKEN [1]

Introduction

Dust-particle sensors on spacecraft for direct measurements of the speeds and directions of motion of small dust particles with masses $m \geq 10^{-12}$ g have been developed during the past few years. These sensors were designed for the study of interplanetary dust particles for which the force of solar radiation is not negligible in comparison with the force of solar gravity. The range of sensitivity of the sensors extends into the region of particle size where dust particles can be blown out of the solar system by sunlight.

The effects of solar-radiation pressure must therefore be included when the measured speeds and radiants of small dust particles are used in computing the orbits. Evaluation of these effects requires an investigation of the conditions of encounter between a planet and interplanetary dust particles for which radiation pressure modifies the heliocentric orbital speeds. These conditions also have an important bearing on the problem of the enhanced flux of small dust particles measured in the vicinity of the earth and possibly existing also near the other planets.

Earth's dust belt

The flux of small dust particles measured in the vicinity of the earth from rockets and satellites is higher than would be expected if radiation pressure were neglected and the orbits of small interplanetary dust particles were assumed to be similar to those of larger, meteor-producing meteoroids. This enhancement of the flux of small dust particles has been called a dust blanket by Beard (1959), a dust belt by Whipple (1961), and a dust shell by Singer (1961). Prom existing data we are unable to distinguish the various models envisioned by these and other investigators. A knowledge of the geocentric trajectories is critical in discussions of the nature and origin of the earth's dust belt. Referring to the phenomenon as an enhancement of the flux of small dust particles in the vicinity of the earth carries few implications about the currently unknown geocentric trajectories of the dust particles and, more importantly, permits close contact with the available observational data.

The rate at which information can be obtained with a satellite-borne dust-particle sensor is increased by the enhancement of the flux of small dust particles near the earth. At the same time, the complicated geocentric trajectories responsible for this phenomenon make the experimental determination of the orbits of the small dust particles more difficult than for meteoroids.

The geocentric enhancement of the flux of small dust particles is shown in figure 1, which is a cumulative flux distribution expressed in terms of the particle mass. The numerical data in figure 1 are given in table 1. The data selected are considered to be representative of the available data, although figure 1 is a corrected version of a rather outdated figure that was presented in an earlier paper (McCracken and Dubin, 1964).

The geocentric enhancement of the flux of small dust particles is revealed by plotting in figure 1 the cumulative flux distributions for two different regions of space. The data from studies of the zodiacal light, meteors, and the

[1] Goddard Space Flight Center, National Aeronautics and Space Administration, Greenbelt, Md.

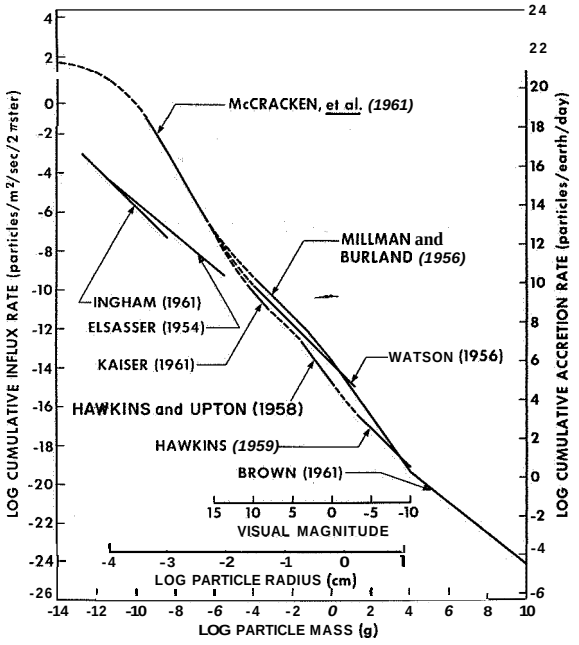

FIGURE 1.—Cumulative flux distribution compiled from the data in table 1 to show the enhancement of the flux of small dust particles in the vicinity of the earth.

frequency of meteorite falls are used to represent the flux of dust particles and meteoroids at the earth's distance from the sun but in regions removed from the earth. The direct measurements made in the vicinity of the earth are used to represent the flux near the earth. The flux of meteoroids is essentially the same for both regions of space, since the known distributions of orbits and the high speeds of encounter (20 to 40 km/sec, on the average, as determined by radar and photographic studies of meteors) preclude any appreciable geocentric enhancement of the flux of meteoroids. The flux of 10^{-8} particles/m²/sec/2π ster for meteoroids with masses $m \sim 1.3 \times 10^{-6}$ g, observed by Elford, Hawkins, and Southworth **(1964)** by means of radar, indicates that no measurable geocentric enhancement of the flux occurs for the faint radar meteors.

Comparison of the flux in interplanetary space with the higher flux measured in the vicinity of the earth leads to the conclusion that a geocentric enhancement of the flux of small dust particles exists. The degree of this enhancement and the particle mass at which the flux begins to increase both depend on which of the various size distributions derived from studies of the zodiacal light and solar F corona is used to represent the flux of small dust particles in interplanetary space. The size distribution derived by Ingham **(1961)** and shown in figure 1 represents the best fit to the distribution of surface brightness of the zodiacal light that was observed by Ingham and Blackwell. This size distribution, if extended to smaller sizes of dust particles, is in good agreement with the size distribution of small dielectric spheres (water ice) used by Giese **(1962)** in calculating models for the zodiacal light. The photoelectric observations of the surface brightness and polarization of the zodiacal light reported by Weinberg **(1964)** are fitted more closely by the size distribution given by Giese than by any of the other size distributions that have been suggested. The size distribution given by Elsasser **(1954)** has subsequently been altered and was included in figure 1 only to indicate the desirability of a smooth transition between the cumulative flux distribution for the zodiacal dust particles and the one for the radar meteors.

The geocentric enhancement of the flux of small dust particles, as shown in figure 1, begins to appear at a particle mass between 10^{-6} and 10^{-7} g and reaches a maximum ($\sim 10^4$ enhancement) for dust particles with masses in the neighborhood of $m \sim 10^{-11}$ g. This suggests that some nongravitational force, such as that of solar-radiation pressure, may play an important role in this phenomenon. If so, similar enhancements of flux can be expected to exist in the vicinity of other planets. Investigation of this possibility again requires that radiation pressure be included in the conditions of encounter between small interplanetary dust particles and the planets.

The following sections are devoted to an approximate treatment of the conditions of encounter between the planets and small interplanetary dust particles. Solar-radiation pressure is included in the treatment, but other

TABLE 1.—*Selected observational data on the mass distribution of interplanetary dust particles*

Type of observation	Source	Equation of distribution*	Range of validity
Meteor observations	Watson (1956)	$\log N(M_v) = 5.88 + 0.4M_v$	$-3 \leq M_v \leq 10$
	Millman and Burland (1956) [in McKinley (1961, p. 110)]	$\log N(M_v) = 6.3 + 0.4M_v$	$3 \leq M_v \leq 10$
		$\log N(M_v) = 6.0 + 0.50M_v$	$0 \leq M_v \leq 3$
		$\log N(M_v) = 6.0 + 0.57M_v$	$-10 \leq M_v \leq 0$
	Hawkins and Upton (1958)	$\log N(M_v) = 4.93 + 0.538M_v$	$0 \leq M_v \leq 4.1$
	Hawkins (1959)	$\log N(M_v) = 4.52 + 0.4M_v$	$-10 \leq M_v \leq -3$
	Kaiser (1961)	$\log N(M_r) = 4.86 + 0.468M_r$	$8 \lesssim M_r \lesssim 10.8$
Meteorite collections	Brown (1960, 1961)	$\log N(m) = 3.5 - 0.8 \log m$	$10^4 \lesssim m \lesssim 10^{11}$ g
Zodiacal light studies	Elsässer (1954)	$\log I(s) = -14.32 - 2.5 \log s$	$2\mu \leq s \leq 0.2$ cm
	Ingham (1961)	$\log I(s) = -16.38 - 3.0 \log s$	$0.4\mu \leq s$
Direct measurements	McCracken, Alexander, and Dubin (1961)	$\log I(m) = -17.30 - 1.70 \log m$	$10^{-10} \lesssim m \lesssim 10^{-6}$ g

*$N(\ )$=cumulative accretion rate in particles/earth/day, $I(\ )$=cumulative flux in particles/m²/sec/2π ster, M_v=visual magnitude, M_r=radar magnitude, $M_r = M_v$, m=particle mass in g, s=particle radius in cm.

nongravitationad forces such as corpuscular drag, coulomb drag, and Lorentz forces are neglected in this first-order approximation. Any force that effectively reduces the central gravitational force exerted by the sun can produce effects on the motion of a small dust particle similar to the effect of radiation pressure.

Equations of motion and Poynting-Robertson effect

The equations used here provide a convenient means for introducing parameters needkd in the discussion. The scalar equations of motion given by Robertson **(1937)** or by Wyatt and Whipple **(1950)** form a convenient starting point.

Expressed in polar coordinates (r, θ), the equations for the heliocentric motion of a dust particle of mass m moving in the combined gravitational and radiation fields of the sun of mass $M_\odot \gg m$ are

$$\frac{d^2r}{dt^2} - r\left(\frac{d\theta}{dt}\right)^2 = -\frac{\mu_{eff}}{r^2} - \frac{2\alpha}{r^2}\frac{dr}{dt}, \quad \text{(radial)}$$

and

$$\frac{1}{r}\frac{d}{dt}\left(r^2\frac{d\theta}{dt}\right) = -\frac{\alpha}{r}\frac{d\theta}{dt}, \quad \text{(angular)}$$

where

$$\mu_{eff} = \mu - \alpha c, \ \mu = GM_\odot, \text{ and } \alpha = \frac{3L_\odot}{16\pi c^2}\frac{Q_{pr}}{\delta s},$$

G is the constant of gravity, $L_\odot$ is the luminosity of the sun, c is the speed of light, δ is the mass density of the dust particle, and s is the particle radius (all measured in cgs units). The parameter Q_{pr} is the radiation-pressure efficiency factor defined by

$$C_{pr} = Q_{pr}\pi s^2,$$

where C_{pr} is the cross-sectional area of the dust particle effective in intercepting sunlight to produce radiation pressure on the dust particle.

The magnitude of the force of radiation is $F_r = u(r)C_{pr}$, where $u(r)$ is the energy density of sunlight at a heliocentric distance r. The magnitude of the force of gravity is

$$F_g = \frac{\mu m}{r^2}.$$

A dimensionless parameter β, defined as

$$\beta = \frac{F_r}{F_g} = \frac{3L_\odot}{16\pi c\mu}\frac{Q_{pr}}{\delta s},$$

will be used extensively throughout the following discussions. The parameter β is simply the magnitude of the force of radiation measured in units of the force of gravity. Both the flux of sunlight and the force of solar gravity vary inversely as the square of the distance from the

sun; hence, the parameter β is independent of the heliocentric distance. Other nongravitational forces could be introduced at this point by using an additional parameter β' that would not (in general) be independent of the heliocentric distance. By substituting the appropriate numerical values for the various constants, we obtain

$$\beta=5.78\times10^{-5}\,\frac{1}{\delta s}\,\frac{g}{cm^2}.$$

The equations of motion may also be written in terms of the dimensionless parameter β as

$$\frac{d^2r}{dt^2}-r\left(\frac{d\theta}{dt}\right)^2=-\frac{\mu}{r^2}+\frac{\mu\beta}{r^2}\left(1-\frac{1}{c}\frac{dr}{dt}\right)-\frac{\mu\beta}{r^2}\frac{1}{c}\frac{dr}{dt},$$

and

$$\frac{1}{r}\frac{d}{dt}\left(r^2\frac{d\theta}{dt}\right)=-\frac{\mu\beta}{r^2}\frac{r}{c}\frac{d\theta}{dt},$$

since β and α are related by the expression

$$\beta=\frac{\alpha c}{\mu}.$$

Radiation pressure produces several effects on the motion of a small dust particle. A dust particle moving in a heliocentric orbit receives sunlight from a source that is moving relative to the dust particle, so the incident sunlight undergoes aberration through a small angle

$$\phi\sim\frac{r}{c}\frac{d\theta}{dt},$$

which can be neglected in a first approximation. The component of motion of the dust particle along the position vector of the dust particle causes sunlight of frequency ν to be shifted through the doppler effect to a new frequency ν' given by

$$\nu'=\nu\left(1-\frac{1}{c}\frac{dr}{dt}\right).$$

The radial motion of the dust particle and the shift in frequency of the incident sunlight produce a corresponding change in the energy density of the intercepted radiation and, hence, in the radiation pressure exerted on the dust particle. The terms

$$\frac{\mu\beta}{r^2}\frac{1}{c}\frac{dr}{dt}\text{ and }\frac{\mu\beta}{r^2}\frac{r}{c}\frac{d\theta}{dt}$$

represent the radial and tangential components, respectively, of the acceleration produced by this drag force. The equations of motion given previously are correct to the first order in the ratio of the speed of the dust particle to the speed of light. The problem was first formulated correctly by Robertson (1937), who used a relativistic treatment in order to derive the generalized equations of motion. The action of sunlight, which effectively reduces the central gravitational force of attraction by the sun and gives rise to the nonconservative drag force, is called the Poynting-Robertson effect.

The energy and angular momentum no longer constitute constants of motion because of the presence of the nonconservative drag force introduced by radiation pressure. Integration of the angular equation of motion yields

$$h=r^2\frac{d\theta}{dt}=h_0-\frac{\mu\beta\theta}{c},$$

where h is the angular momentum (per unit mass) of the dust particle and h_0 is the value of h at some epoch, $t=t_0$. As time t (or θ) increases, the angular momentum decreases. Since the dust particle loses angular momentum and energy of motion, it spirals toward the sun. The dynamical evolution of the orbits of meteoroids under the Poynting-Robertson effect has been considered by Wyatt and Whipple *(1950)* for elliptic orbits as well as for the circular orbits considered by Robertson *(1937).*

By dropping the small terms in

$$\frac{1}{c}\frac{dr}{dt}\text{ and }\frac{r}{c}\frac{d\theta}{dt}$$

from the equations of motion, we obtain

$$\frac{d^2r}{dt^2}-r\left(\frac{d\theta}{dt}\right)^2\doteq-\frac{\mu}{r^2}(1-\beta)$$

and

$$\frac{1}{r}\frac{d}{dt}\left(r^2\frac{d\theta}{dt}\right)\doteq0.$$

The radial equation of motion now displays only the action of solar-radiation pressure in effectively reducing the central force of gravity. A value $\beta>1$ makes the right-hand side of this equation positive and causes the central force to become one of repulsion. A dust particle for which $\beta>1$ will be blown out of the solar system by radiation pressure, while one for which $\beta=1$ will not be subject to any acceleration by the sun.

Integration of these approximate equations of motion yields the orbital speed v of the dust particle as

$$v^2=\mu(1-\beta)\left(\frac{2}{r}-\frac{1}{a}\right),$$

where a is the semimajor axis of the orbit of the dust particle. Comparison with the analogous equation

$$v^2=\mu\left(\frac{2}{r}-\frac{1}{a}\right)$$

for a dust particle sufficiently large so that $\beta\doteq 0$ shows that radiation pressure reduces the orbital speed of a small dust particle below that for the purely gravitational case. A small dust particle moving in a planet-like orbit moves more slowly than the planet and therefore has a nonzero speed relative to the planet. This effect was noted by Poynting in **1912,** soon after the existence of radiation pressure had been experimentally verified.

An assumption commonly used in simplified treatments of this type is that a dust particle is perfectly absorbing and absorbs sunlight over an area equal to the geometric cross-sectional area **of** the particle. Values of β computed under this assumption ($Q_{pr}=1$) are shown graphically in figure **2** for various values of the mass density 6 and particle radius s. As was noted previously, a value $\beta>1$ means that the dust particle will be blown out of the solar system by radiation pressure. The values $\beta=1$ occur in figure **2** for particle radii $s\sim 1\ \mu$, which are comparable to the wavelength of sunlight **(—0.55** μ). The assumption that classical optics could be used to compute β fails. The radiation-pressure efficiency factor Q_{pr} (and hence β) is one of the parameters that can be computed through use of the Mie theory of light scattering by spherical particles of

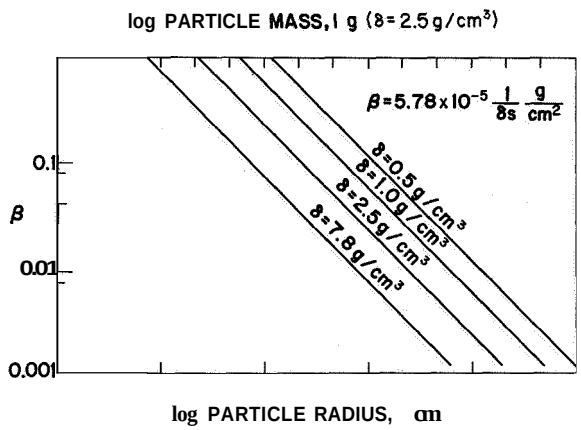

FIGURE 2.—Dependence of the ratio (β) of the force of radiation to the force of gravity on the size and mass density of a dust particle.

arbitrary size and known index **of** refraction. It is unlikely that interplanetary dust particles are isotropic homogeneous spheres, but at present we have no alternative in computing the values of β but to assume a composition for which the index of refraction is known and to use the Mie theory far computing Q_{pr}.

Further treatment of the rather complicated relations among particle mass or size, mass density, composition, structure, shape, and the parameter β is beyond the scope of this work. An extensive treatment of the Mie theory can be found in van de Hulst **(1957).** The important points in the present discussion can be adequately illustrated if we take $Q_{pr}=1$ and use figure **2** to relate β to the physical parameters of the dust particles. A scale of particle mass computed for a mass density **of** $\delta=2.5$ g/cm³ has been added along the top border in figure **2** for this purpose.

The direct measurements apply for dust particles with masses $m\lesssim 10^{-7}$ g. figure **2** shows that such dust particles have values of $\beta\gtrsim 0.1$ for any of the values of mass density 6 that are represented. A value $\beta=0.01$ might be considered to be negligible in comparison with unity, but such a value applies only **for** the upper end of the range **of** particle mass encompassed by the direct measurements. The majority of the direct measurements apply for dust particles with masses between about 10^{-11} and 10^{-8} g. A dust particle with a mass $m=$

10^{-11} g and a mass density $\delta=2.5$ g/cm^3 has a radius of about 1 μ and, from figure 2, a value of $\beta \doteq 0.23$, which is hardly negligible compared to unity.

The dependence of the speed at encounter (entry of the dust particle into the sphere of influence of a planet) on the value of β as the mass of the dust particle is varied from $m \sim 10^{-7}$ g down to any limits ($\beta=1$) set by radiation pressure must be emphasized. The treatment is approximate because of the simplifying assumptions made in relating β to the particle mass or the particle size. It is also approximate to the extent that we follow the heliocentric motion of a dust particle by using the two-body equations of motion presented earlier with radiation pressure included. As the dust particle enters the planet's sphere of influence, gravitational control is transferred to the planet, and the motion of the dust particle in the region of the planet is treated as a two-body problem. The small tangential drag force produced by radiation pressure can be neglected during an encounter but should be included in the motion of a dust particle between encounters.

The orbital speed of a dust particle at encounter is given by

$$v^2=\mu(1-\beta)\left(2-\frac{1}{A}\right),$$

in which the semimajor axis a of the heliocentric orbit of the dust particle is measured in units of the semimajor axis a_0 of the planet's orbit (assumed to be circular), and

$$A=\frac{a}{a_0}.$$

The notation used here is that employed by Öpik (1951). The relative speed can then be found by vector addition of the velocity of the dust particle and the velocity of the planet. Alternatively, and much more simply, the problem can be formulated as a Jacobi three-body problem with radiation pressure included. The speed U of the dust particle at encounter (measured relative to the planet and expressed in units of the circular speed v_c of the planet) is given by

$$U^2=\left(\frac{v}{v_c}\right)^2=1-2(1-\beta)^{1/2}[A(1-e^2)]^{1/2}\cos i + (1-\beta)\left(2-\frac{1}{A}\right),$$

where e is the eccentricity of the heliocentric orbit of the dust particle, and i is the inclination of the heliocentric orbit of the dust particle measured relative to the plane of the planet's orbit. If we set $i=0°$ and replace A by Q, where

$$Q=A(1-e),\ q=a(1-e),\ \text{and}\ Q=\frac{q}{a_0},$$

we obtain

$$U^2=1-2(1-\beta)^{1/2}[Q(1+e)]^{1/2} + (1-\beta)\left(2-\frac{1-e}{Q}\right).$$

This expression reduces to the quadratic equation

$$U^2=1-2(1-\beta)^{1/2}(1+e)^{1/2}+(1-\beta)(1+e)$$

for encounter at the perihelion passage ($Q=1$) of the dust particle, and has the root

$$U=1-(1-\beta)^{1/2}(1+e)^{1/2}.$$

Now, $U=0$ for $\beta=\beta_0$, where β_0 and e are related by the expression

$$\beta_0=1-\frac{1}{1+e}.$$

The ranges of β_0 and e for which $U=0$ can occur, when radiation pressure is included, are

$0 \leq \beta_0 < 0.5,\ 0 \leq e < 1,$ (elliptic orbits)

$\beta_0=0.5,\ e=1,$ (parabolic orbits)

$0.5 < \beta_0 < 1,\ e > 1.$ (hyperbolic orbits)

Circular heliocentric orbits ($e=0$) give $U=0$ only for $\beta=0$, which applies to dust particles considerably larger than those studied through the direct-measurement technique. Figure 3 shows U (or v/v_c) as a function of β for circular orbits and for several values of the inclination.

The ordinate on the right will be explained and used later. It should be noted that small dust particles with $\beta \gtrsim 0.01$ and planet-like orbits do not have particularly low speeds of encounter (even for zero inclination) when the effect of radiation pressure on the orbital speed of a dust particle is included.

Figure 4 gives U (or v/v_c) as a function of β for two values of eccentricity e arbitrarily chosen such that β_0 falls in the range of particle size ($\beta \gtrsim 0.01$) encompassed by the direct measurements. Figures 3 and 4 show that very low speeds of encounter between planets and small dust particles can occur for dust particles with noncircular heliocentric orbits of fairly low inclination. Further calculations show that the singular solutions illustrated in figure 4 are but two of an entire class of orbits for which small dust particles can have low speeds at encounter. Figure 5 shows the (A^{-1}, e) domain in which the clear areas contain values of A and e for which planetary encounters are possible. Representative values of β_0 are noted along the line for perihelion intercepts. The class of singular solutions that gives $U=0$ for $i=0°$ forms a line singularity. An eccentricity $e \gtrsim 0.01$ is required for β_0 to fall in the range ($\beta \geq 0.01$, $m \lesssim 10^{-7}$ g) encompassed by the direct measurements. The entire class of orbits for which $i \lesssim 5°$ and $e \gtrsim 0.01$ provides small dust particles that have low speeds at encounter near the perihelion passage of a dust particle. The action of radiation pressure in reducing the perihelion distance of a dust particle through the

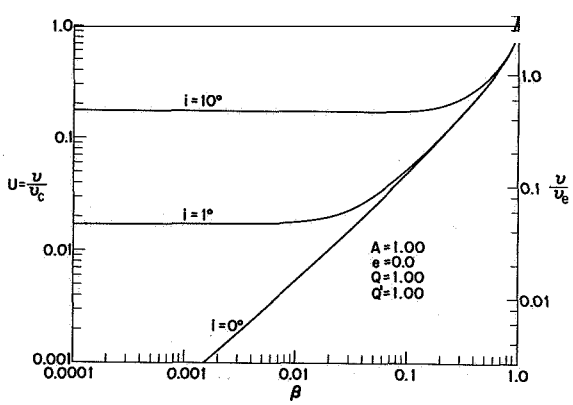

FIGURE 3.—Dependence on particle size (or β) of the speed at encounter for dust particles and a planet when both are moving in circular heliocentric orbits.

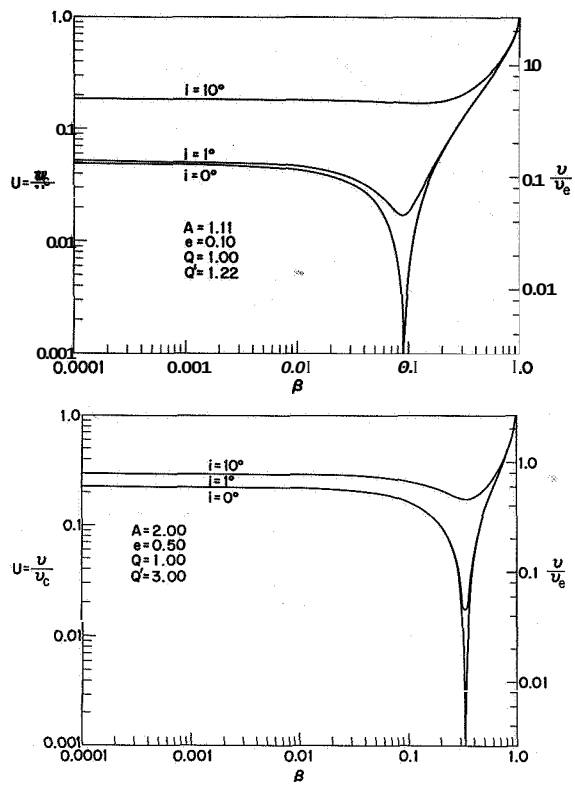

FIGURE 4a,b.—Two examples of the dependence on particle size (or β) of the speed at encounter for a planet moving in a circular orbit and dust particles moving in elliptic heliocentric orbits.

Poynting-Robertson effect further serves to move orbits of low inclination continuously into position for the low-speed encounters to occur. The line singularity appearing at $Q=1$ in the (A^{-1}, e) domain for $i=0°$ presents no problem regarding an "infinite" enhancement of the flux in the vicinity of a planet, because the number of dust particles with such orbits is finite. The orbits of primary interest in the problem of the enhanced flux near a planet are those in the neighborhood of the line $Q=1$ in the (A^{-1}, e) domain for $i=0°$ and having $0.1 \lesssim e < 1$.

The component of U normal to the plane of the planetary orbit is given by

$$U_z = \pm (1-\beta)^{1/2}[A(1-e^2)]^{1/2} \sin i;$$

hence, as i increases from 0° a nonvanishing component is added to U fairly rapidly through the dependence of U_z on sin i. The factor $(1-\beta)^{1/2}$ broadens the range of i over which

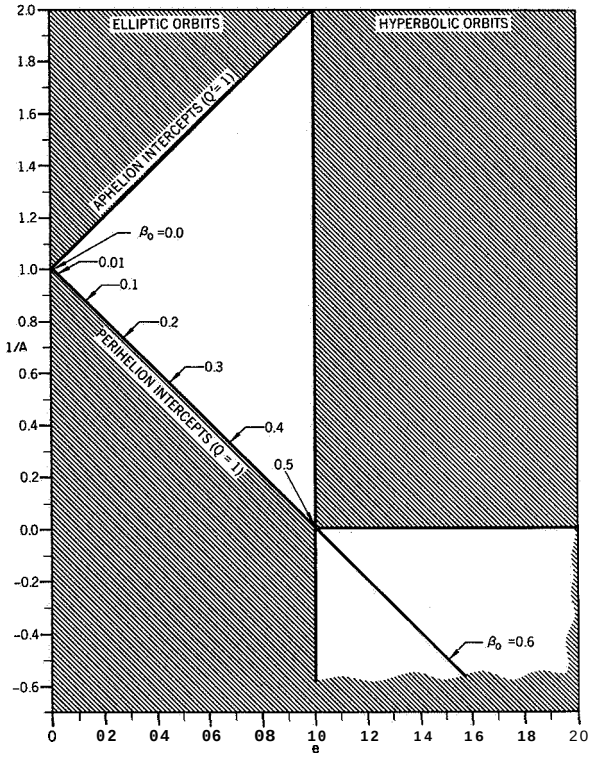

FIGURE 5.—The (A^{-1}, e) domain showing the orbits for which planetary encounters are possible and the line singularity next to which are clustered the orbits that yield very low speeds of encounter for small dust particles in orbits of low inclination.

a given small value of U_z can be obtained. The component of U along the heliocentric position vector of a dust particle is

$$U_z = \pm(1-\beta)^{1/2}\left[\left(2-\frac{1}{A}\right)-A(1-e^2)\right]^{1/2}.$$

A nonvanishing component is added to U fairly rapidly as Q is reduced below 1. Again, the factor $(1-\beta)^{1/2}$ reduces the magnitude of the nonvanishing component. Evaluation of the degree of enhancement of the flux of small dust particles that will occur near a planet therefore requires an integration over the orbital elements a, e, and i as well as over a size distribution or a distribution of the values of β for the dust particles encountered by the planet. I have not yet succeeded in performing this integration.

The action of radiation pressure in reducing the orbital speed of a small dust particle also affects the apparent radiant of the dust particle. If the size of a dust particle is varied so that the value of β crosses a singularity of the type shown for $i=0°$ in figure 4, the radiant of the dust particle is shifted by 180°. Dust particles having orbits with $e>0$, $i \doteq 0°$, and $\beta<\beta_0$ appear to overtake the planet, while those in similar orbits but having $\beta>\beta_0$ appear to be overtaken by the planet. If a planet encounters a cloud of dust particles all with similar orbits of low inclination and a distribution of values of β encompassing the value of β_0 appropriate for the eccentricity of the orbits, the dust particles can appear to enter the planet's sphere of influence from all directions. Such a cloud of dust particles would, of course, be in the process of dispersing because of the differential effects of radiation pressure on the heliocentric orbits of the dust particles.

The effects of radiation pressure on the conditions of encounter described in the preceding paragraphs apply also to the small dust particles detected by a dust-particle sensor mounted on an interplanetary probe such as Mariner 4. The effects of radiation pressure on the speeds and radiants of the dust particles detected by such an instrument need to be investigated in greater detail.

The effect of radiation pressure on the accretion process has some implications (the importance of which has not yet been investigated) regarding the formation of planetesimals in a rotating circumstellar nebula out of which a star forms. As a newly formed star becomes luminous and clears away the gas in the nebula, the small dust particles that are not blown away by radiation pressure assume Keplerian orbits about the star. The accretion process may then change because of the differential effects of radiation pressure on the planetesimals and the smaller dust particles being accreted by the planetesimals. The solar system is in a stage somewhat analogous to the latter. The nebular gas is gone, so the planets are now accreting small dust particles that have their heliocentric motion modified by radiation pressure and the radial flow of the solar wind.

Gravitational enhancement of the flux of interplanetary dust particles

The geocentric enhancement of the flux of small dust particles has been the subject of considerable discussion both before and after its exist-

ence was recognized in the results obtained with dust-particle sensors flown on rockets and satellites. Whipple **(1961)** suggested that the dust particles were the product of meteoroidal impacts on the moon. The majority of the remaining proposed explanations for the existence of the enhanced flux basically depend on the gravitational concentration of interplanetary dust particles streaming at low speed into the vicinity of the earth. No attempt is made here to review the numerous variations on this theme, because the effects of radiation pressure on the conditions of encounter have been neglected.

The gravitational enhancement of the flux of interplanetary dust particles entering the vicinity of the earth has been treated through the use of Liouville's theorem by Singer **(1956, 1961)** and by Shelton, Stern, and Hale **(1964).** The three-body problem (consisting of the sun, the earth, and **a** dust particle) was treated as a succession of two-body approximations. Singer **(1961)** assumed that the velocities of the dust particles were isotropic at infinity (entry into the earth's gravitational field).

The degree of enhancement of the flux depends on the average speed at which dust particles enter the vicinity of a planet. The requirements on the speed of encounter can be illustrated by a very brief treatment using Liouville's theorem and following closely the expositions given by Singer **(1961)** and by Shelton, Stern, and Male **(1964).** The general treatment applies for any planet, with the degree of enhancement of the flux depending rather sensitively on the distributions of a, i, and β for the dust particles encountered by the planet.

The densities at two points $(\mathbf{r}_g, \mathbf{v}_g)$ and $(\mathbf{r}'_g, \mathbf{v}'_g)$ on a dynamic trajectory in a six-dimensional phase space composed of the geocentric position and velocity vectors $\mathbf{r}_g$ and v, are related through Liouville's theorem by

$$n(\mathbf{r}_g, \mathbf{v}_g) = n(\mathbf{r}'_g, \mathbf{v}'_g)$$

if no particles are lost. The density of dust particles in real space at a geocentric distance r_g is obtained by integrating $n(\mathbf{r}_g, \mathbf{v}_g)$ over velority space, giving

$$\rho(r_g) = \int_{\mathbf{v}_g} n(\mathbf{r}_g, \mathbf{v}_g) d\mathbf{v}_g.$$

The scalar flux of dust particles at **a** geocentric distance r_g is

$$\Phi(r_g) = \rho(r_g) v_g(r_g),$$

where r'_g v'_g β, and Φ_∞ are taken to apply when the particles enter the earth's gravitational field. This leads to the density enhancement

$$\frac{\rho(r_g)}{\rho_\infty} = f\left[1 + \frac{v_g^2(r_g)}{v_\infty^2}\right]^{1/2},$$

and the flux enhancement

$$\frac{\Phi(r_g)}{\Phi_\infty} = f\left[1 + \frac{v_g^2(r_g)}{v_\infty^2}\right],$$

at a geocentric distance r_g. The factor f allows for those dust particles that are absent from the receding flux because they collided with the earth. The algebraic expression for the factor f is given by Shelton, Stern, and Hale **(1964).** The numerical values of f range between **0.5** and 1. The speed at infinity v_∞ corresponds to the speed at encounter V used earlier in the discussion of the conditions of encounter.

The conservation of energy of geocentric motion yields

$$v_g^2(r_g) = v_\infty^2 + v_e^2(r_g),$$

where

$$v_e(r_g) = \left(\frac{2\mu_\oplus}{r_g}\right)^{1/2}$$

is the speed of escape from the earth at a distance r_g. At the altitudes of the near-earth satellites ($r_g \sim 7000$ km), the speed of escape is

$$v_e \sim 10 \text{ km/sec}.$$

For speeds at encounter

$$v_\infty << v_e \sim 10 \text{ km/sec},$$

we have

$$v_g^2(r_g) \sim v_e^2(r_g),$$

so that the density and flux enhancements reduce to

$$\frac{\rho(r_g)}{\rho_\infty} \sim f \frac{v_e(r_g)}{v_\infty}$$

and

$$\frac{\Phi(r_g)}{\Phi_\infty} \sim f \frac{v_e^2(r_g)}{v_\infty^2}.$$

An enhancement of the flux by a factor $\sim 10^4$ therefore requires $v_\infty \sim 0.1$ km/sec. The concept of the sphere of influence inherent in the simplified treatment using Liouville's theorem causes trouble, for 0.1 km/sec is not small compared to the speed of escape at the distance of the boundary of the sphere of influence for the earth. A realistic treatment of the problem therefore requires numerical integration of the three-body equations of motion with radiation pressure included.

The orbits for which very low speeds at encounter are possible for dust particles of various sizes were discussed earlier and are represented in figures 3, 4, and 5. The speed at encounter v measured in units of the speed of escape v_e at the altitudes of the near-earth satellites is given as the ordinate on the right in figures 3 and 4.

Singer (1961) assumed that relatively large dust particles ($s \sim 200\ \mu$) have almost circular heliocentric orbits of very low inclination ($e \doteq 0$, $i \doteq 0°$) in order to justify taking $v_\infty = 1$ km/sec, which leads to a flux enhancement $\sim 10^2$. A subclass of these orbits was investigated by Dole (1962), who numerically integrated the geocentric trajectories of dust particles with initial circular heliocentric orbits of zero inclination ($e = 0$, $i = 0°$). Southworth (1963) has criticized the two-dimensional model used by Dole and argued that the fraction of zodiacal dust particles with such heliocentric orbits must be quite small.

A dust particle of radius $s \sim 200\ \mu$ and mass density 1 g/cm³ has a value of $\beta \sim 2.4 \times 10^{-3}$, which justifies the neglect of radiation pressure by Singer (1961). But the same dust particle has a mass $m \sim 3.3 \times 10^{-5}$ g, which removes it from the region of particle mass covered by the direct measurements and places it in the region of radar meteors. The available direct measurements apply for dust particles with masses $m \lesssim 10^{-7}$ g, with the maximum enhancement of the flux occurring for dust particles with masses in the neighborhood of $m \sim 10^{-11}$ g. A dust particle of mass $m = 10^{-11}$ g and mass density $\delta = 2.5$ g/cm³ has a radius $s \doteq 1\ \mu$. The value of β is about 0.23, according to figure 2. The speed of encounter for such a dust particle with an earth-like orbit is about 3.6 km/sec. If we take this as an average speed we obtain a flux enhancement of only 8, which is very much less than the factor $\sim 10^4$ given by the direct measurements.

The shortcomings of the treatments by Singer (1961) and Dole (1962) are shared by numerous other proposed explanations for the geocentric enhancement of the flux of small dust particles in which radiation pressure was neglected. The work of Dole was mentioned here because such numerical integrations should be extended to a three-dimensional model and to the case in which radiation pressure is not neglected. The formulation of the problem of the gravitational enhancement of flux in terms of Liouville's theorem as given by Singer (1961) is useful, provided two important changes are made, namely, (1) radiation pressure should be included so that the discussion can be directed to the range of particle size for which the measured geocentric enhancement of the flux occurs, and (2) the assumption that the small dust particles that produce the zodiacal light have predominantly circular heliocentric orbits of very low inclination should be avoided. The assumption that small dust particles with orbits of fairly low inclination contribute most to the enhancement of the flux near a planet cannot be avoided, but the restriction on the range of the inclination can be relaxed slightly because of the presence of the term $(1-\beta)^{1/2}$ in the expression for U_z. The low-speed encounters occur only for noncircular orbits of fairly low inclination when dust particles of the sizes involved in the measured enhancement of the flux are considered.

The remaining unsolved problem consists of integrating over the unknown distribution of orbits and the rather poorly determined size distribution for the small interplanetary dust particles in an attempt to ascertain whether appreciable planetocentric enhancements of the flux can occur directly. The boundary conditions that must be met by any distributions of orbits and size distributions assumed for use in such an integration include the observed distribution of surface brightness and polarization of the zodiacal light over the celestial sphere.

Summary

The conditions of encounter between planets and small interplanetary dust particles have

been investigated in an approximate manner. Solar-radiation pressure has been included in the conditions of encounter, and the dependence of the speed at encounter on the size of a dust particle has been emphasized.

The low speeds of encounter, which occur near perihelion passage, encompass an entire class of noncircular heliocentric orbits of fairly low inclination when dust particles of the *sizes* studied with the use of spacecraft are considered. This class of orbits provides dust particles that can encounter the planets at the very low speeds necessary for a gravitational enhancement of the flux to occur. Evaluation of the effectiveness of this class of orbits in directly producing the enhanced flux of small dust particles measured in the vicinity of the earth is made difficult by the present lack of knowledge about the orbits of small dust particles both in the vicinity of the earth and in interplanetary space. The source of the small dust particles and the mechanism for the enhancement of the flux measured in the vicinity of the earth with the use of spacecraft are not yet satisfactorily explained.

References

BEARD, D. B.
1959. Interplanetary dust distribution. Astrophys. Journ., vol. **129,** pp. **496–506.**

BROWN, H.
1960. The density and mass distribution of meteoritic bodies in the neighborhood of the earth's orbit. Journ. Geophys. Res., vol. **65,** pp. **1679–1683.**
1961. The density and mass distribution of meteoritic bodies in the neighborhood of the earth's orbit: Addendum. Journ. Geophys. Res., vol. **66,** pp. **1316–1317.**

DOLE, S. H.
1962. The gravitational concentration of particles in space near the earth. Planet. Space Sci., vol. **9,** pp. **541–553.**

ELFORD, W. G.; HAWKINS, G. S.; and SOUTHWORTH, R. B.
1964. The distribution of sporadic meteor radiants. Harvard Radio Meteor Project Res. Rep., no. **11,** December.

ELSÄSSER, H,
1954. Die raumliche Verteilung der Zodiakallichtmaterie. Zeits. f. Astrophys., vol. **33,** pp. **274–285.**

GIESE, R. H.
1962. Light scattering by small particles and models of interplanetary matter derived from the zodiacal light. Space Sci. Rev., vol. **1,** pp. **589–611.**

HAWKINS, G. S.
1959. The relation between asteroids, fireballs and meteorites. Astron. Journ., vol. **64,** pp. **450–454.**

HAWKINS, G. S., and UPTON, E. K. L.
1958. The **influx** rate of meteors in the earth's atmosphere. Astrophys. Journ., vol. **128,** pp. **727–735.**

INGHAM, M. F.
1961. Observations of the zodiacal light from a very high altitude station, IV: The nature and distribution of the interplanetary dust. Monthly Notices Roy. Astron. Soc., vol. **122,** pp. **157–176.**

KAISER, T. R.
1961. The determination of the incident flux of radio-meteors, **11:** Sporadic meteors. Monthly Notices Roy. Astron. Soc., vol. **123,** pp. **265–271.**

MCCRACKEN, C. W.; ALEXANDER, W. M.; and DUBIN, M.
1961. Direct measurement of interplanetary dust particles in the vicinity of the earth. Nature, vol. **192,** pp. **441–442.**

MCCRACKEN, C. W., and DUBIN, M.
1964. Dust bombardment on the lunar surface. *In* The Lunar Surface Layer, Materials and Characteristics, ed. by J. W. Salisbury and P. E. Glaser, Academic Press, New York, pp. **179–214.**

MCKINLEY, D. W. R.
1961. Meteor Science and Engineering. McGraw-Hill Book Co., Inc., New York, **309** pp.

ÖPIK, E. J.
1951. Collision probabilities with the planets and the distribution of interplanetary matter. Proc. Roy. Irish Acad., vol. **54,** pp. **165–199.**

ROBERTSON, H. P.
1937. Dynamical effects of radiation in the solar system. Monthly Notices Roy. Astron. Soc., vol. **97,** pp. **423–438.**

SHELTON, R. D.; STERN, H. E.; and HALE, D. P.
1964. Some aspects of the distribution of meteoric flux about an attractive center. *In* Space Research IV, ed. by P. Muller, North-Holland Publ. Co., Amsterdam, pp. **875–907.**

SINGER, S. F.
1956. Measurements of interplanetary dust. *In* Scientific Uses of Earth Satellites, ed. by J. A. van Allen, Univ. of Michigan Press, Ann Arbor, pp. **301–316.**
1961. Interplanetary dust near the earth. Nature, vol. **192,** pp. **321–323.**

SOUTHWORTH, R. B.
1963. On S. H. Dole's paper "The gravitational concentration of particles in space near the earth." Planet. Space Sci., vol. **11,** pp. **499–503.**

VAN DE HULST, H. D.
1957. Light Scattering by Small Particles. John Wiley and Sons, Inc., New York, **470** pp.
WATSON, F. G.
1956. Between the Planets. Rev. ed., Harvard Univ. Press, Cambridge, Mass., **188** pp.
WEINBERG, J. L.
1964. The zodiacal light at **5300 Å.** Ann. d'Astrophys., vol. **27,** pp. **718–738.**
WHIPPLE, F. L.
1961. The dust cloud about the earth. Nature, vol. **189,** pp. **127–128.**
WYATT, S. P., Jr., and WHIPPLE, F. L.
1950. The Poynting-Robertson effect on meteor orbits. Astrophys. Journ., vol. **111,** pp. **134–141.**

Abstract

The conditions of encounter between interplanetary dust particles and the planets are investigated for the range of particle size where the force of solar radiation is not negligible in comparison with the force of solar gravity. The action of solar-radiation pressure in reducing the heliocentric orbital speed of a small dust particle makes possible very low planetocentric speeds at encounter for an entire class of heliocentric orbits of nonzero eccentricity and fairly low inclination. The speed at encounter and the apparent radiant depend on the size of the dust particle for a given heliocentric orbit throughout the range of particle size investigated by means of dust-particle sensors mounted on spacecraft.

3

The Brightness of the Zodiacal Light at the Ecliptic Pole [1]

F. E. ROACH [2]

The brightness of the zodiacal light at the pole of the ecliptic is pertinent to an understanding of the nature of the zodiacal cloud. A trivial polar brightness resulting from low integrated scattered sunlight from particles normal to the plane of the ecliptic would imply that, the zodiacal cloud is highly concentrated toward the ecliptic plane in agreement with the historical conception based on visual observations. The fact that many observers have been able to distinguish the zodiacal band over the full sweep from its bright region some 25° from the sun to the gegenschein opposite the sun shows that the ecliptic concentration is a general property of the phenomenon. However, the visual observations should not be trusted as a guide in the matter of the polar brightness, which must be based on a careful resolution of the observed brightness near the ecliptic pole into the three major competing components: airglow, integrated starlight, and zodiacal light.

This review is based on a recent study by Smith, Roach, and Owen (1965). The principal results of the study are given in their tables 4 and 5, from which two plots are here given (figs. 1 and 2).

Two general statements can be made:

1. For an elongation of 90° the brightness in the ecliptic is equivalent to 250 10th-magnitude visual stars per deg ^{2} (S_{10} (vis)); the brightness at the pole is 110 S_{10} (vis); the ratio of brightness is thus 250/110=2.3.

2. The ratio of brightnesses goes to a maximum value of 4.9 at an elongation of about 35°.

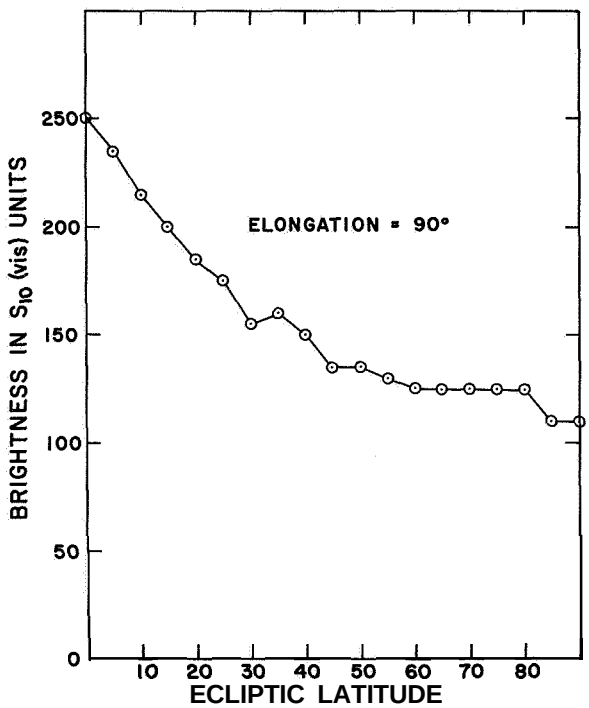

FIGURE 1.—Brightness of the zodiacal light as a function of ecliptic latitude for an elongation of 90°.

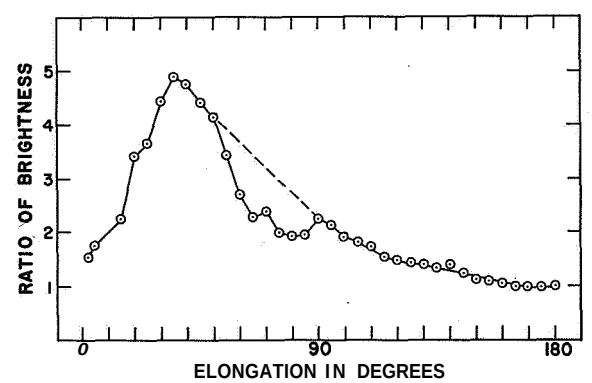

FIGURE 2.—Ratio of brightness in the plane of the ecliptic to that in a plane perpendicular to the ecliptic as a function of elongation.

[1] Résumé of paper presented at the Symposium.

[2] Institute for Telecommunication Sciences and Aeronomy, Environmental Science Services Administration, Boulder, Colo.; formerly at Central Radio Propagation Laboratory, National Bureau of Standards Boulder, Colorado.

The indication is that the ecliptic concentration of the zodiacal light (and therefore the zodiacal cloud) is significant but smaller than generally thought. In particular, it is noted that figure 1 calls for 2.3 times as much light looking tangentially along the earth's orbit as at right angles. This does not imply exactly 2.3 times as many scattering particles in the line of sight, since the scattering angle will vary as a function of the individual particle's distance. The distribution of particles with distance in the two directions will differ and affect the integrated brightness observed photometrically.

References

SMITH, L. L.; ROACH, F. E.; and OWEN, R. W.
1965. The absolute photometry of the zodical light. Planet. Space Sci., vol. 13, pp. 207–217.

Interplanetary Dust-Particle Flux Measurements between 1.0 and 1.56 a.u. from Mariner 4 Cosmic-Dust Experiment

W. M. ALEXANDER: O. E. BERG,[2] C. W. MCCRACKEN,[2] L. SECRETAN,[2] and J. L. BOHN[3]

Abstract

A cosmic-dust detector on the Mariner 4 spacecraft has measured the flux and mass distribution of dust particles in interplanetary space between 1.0 and 1.56 a.u. During the 228-day interval starting a few hours after launch (00^h00^mUT, November 29, 1964) and ending with Mars encounter (01^h00^mUT, July 15, 1965), 215 particles were detected by the experiment sensor. The threshold sensitivity of the detector transducer was $(6\pm0.7)\times10^{-5}$ dyne sec. The salient features of the measurement are:

1. Between 1.0 and 1.25 a. u., a mean flux of 7.3×10^{-5} particles/m^2 sec/πster was determined for particles of mass 6×10^{-11}g (assuming a mean impact velocity of 10 km/sec). From 1.25 to 1.36 a.u., the mean flux was 2.1×10^{-4} particles/m^2 sec/πster, and the flux continued to increase, reaching a peak between 1.36 and 1.43 a.u. where the mean value was 3.3×10^{-4} particles/m^2 sec/πster. The interval from 1.43 to 1.49 a.u. showed a mean flux of 2.2×10^{-4} particles/m^2 sec/πster; the last interval, which ended at Mars encounter, 1.49 to 1.56 a.u., revealed a flux of 1.8×10^{-4} particles/m^2 sec/πster.

2. The cumulative flux-mass distributions near the orbits of the earth and Mars were proportional to $m^{-1/2}$, while the distribution between 1.25 and 1.36 a.u. appears to be proportional to $m^{-0.9}$. These values indicate a variation between the distributions of dust particles ($10^{-11}g \leq m \leq 10^{-9}g$) (a) in the vicinity of the orbits of large planetary bodies, and (b) in deep space.

3. No statistically significant evidence of any well-defined dust-particle streams has been revealed from the measurement.

4. The flux indicated by the Mariner 2 cosmic-dust experiment is in good agreement with the Mariner 4 measurement between 1.0 and 1.26 a.u.

5. There was no measurable enhancement of the flux in the vicinity of Mars (closest approach to Mars was about 3 Mars radii).

The data from the Mariner 4 cosmic-dust experiment have been obtained from "quick look" telemetry records, and, therefore, the measurement results presented above are preliminary. However, the gross variations in the flux and mass distributions, which indicate perturbations by the two large planetary bodies, earth and Mars, are not expected to change significantly.

[1] Temple University, Philadelphia, Pa.; formerly at Goddard Space Flight Center, National Aeronautics and Space Administration, Greenbelt, Md.

[2] Goddard Space Flight Center, National Aeronautics and Space Administration, Greenbelt, Md.,

[3] Temple University, Philadelphia, Pa.

A New Solar-Terrestrial Effect

C. HOFFMEISTER [1]

The neutral point of atmospheric polarization, named after Arago, can be observed in the sky opposite the sun before and after sunset and sunrise above the antisolar point. The variable distance of the neutral point from the antisolar point has been extensively investigated as an indicator of atmospheric turbidity. During my three temporary visits in South Africa (1937–38, 1952–53, and 1959), 2½ years in all, I measured the Arago point not only for meteorological purposes but also in order to ascertain how it is affected by upper-atmospheric conditions. This required reaching the highest possible negative values of the solar elevation. Surprisingly, I noticed that the strong increase of the Arago distance in the evening, after $h_\odot \sim -2°$, does not continue up to the time of invisibility due to the darkening of the sky, but attains a maximum at about $h_\odot = -7°.8$, after which the distance decreases again by several degrees until the end of the observation. Most previous observations were discontinued at about $h_\odot = -7°.15$; only those made by Neuberger show an indication of this effect.

Early in 1965 I compared my 1959 measurements with those previously obtained and noticed large differences in the mean maximal Arago distances far exceeding the scatter of the individual values. I found that these variations were clearly related to solar activity. Values of 30° and 31° were associated with the period of maximum solar activity, and values of 23° and 24° with minimum solar activity. Of all the series of observations made in the past I could find only a few that could confirm this phenomenon; many had to be rejected because of too large scatter. The most reliable observations, however, such as those of Dorno, Menze, and Neuberger, confirmed this relation to solar activity. I repeated my observations in the spring of 1965 at the Sonneberg Observatory and obtained a value that further substantiates this dependency on solar activity.

I examined my 1959 observations, made at the Boyden Observatory near Bloemfontein, to see whether there is a connection with the actual rapid changes in solar activity; only a very slight interrelation, if any, was found. This is significant in the explanation that I propose below.

The theory of the Arago neutral point depends on the fact that in the sunlit atmosphere the plane of polarization passes through the sun and the zenith, while in the region of indirect illumination, i.e., the earth's shadow, the plane is at right angles to the vertical through the sun. Arago uses the concept of "positive" and "negative" polarization, the interaction of which causes a line of neutral light. The rise in the neutral point is explained as an effect of direct sunlight fading, and the decrease that occurs after the maximum distance might be understood if we assume that, at $h_\odot = -8°$, the lower regions of the atmosphere are practically dark, while at higher altitudes, near 80 to 100 km, there is a source of reflected light strong enough to produce a relative increase of the "positive" polarization.

We may ask: What polarizes the scattered sunlight in the region above 80 km? There are several possible contributing factors: atmospheric molecules and atoms, free electrons of the ionosphere and possibly of the Van Allen belts, dust particles in the layer near 100 km

[1] Deutsche Akademie der Wissenschaften zu Berlin, Sternwarte Sonneberg in Thüringen, East Germany.

and those suspended in higher layers of the atmosphere or gravitating in outer space near the earth. It is difficult to estimate the extent to which each of the above factors contributes, but there are indications that dust plays a considerable, if not decisive, part. At the International Astronomical Union meeting in Hamburg in 1964, F. Link stated that at $h_\odot = -10°$ the light from the zenith is 10 to 100 times stronger than if only atmospheric particles were involved. He attributes this effect to the dust layer at 100 km, but from my measurements it is most probable that dust at higher layers is also involved.

Our next question is: What kind of polarization is responsible for the greater Arago distances at times of maximum solar activity? The immediate cause must be a decrease of the ('positive" or an increase of the "negative" polarization. This means that the phenomenon cannot be explained as due to changes in air density, in which case the opposite effect would be expected. In addition, the air density is so strongly affected by solar events that a much greater scatter of the measured values would occur. But there is another phenomenon that, according to my investigations, behaves in a similar fashion, i.e., shows practically no correlation with the instantaneous solar activity, but exhibits a well-established correlation with the 11-year and probably also with the 80-year period. This phenomenon is the enhanced airglow. I explain the phenomenon as caused by the interaction of interplanetary dust particles and the atoms and molecules of the atmosphere, which results in an increased release of stored solar energy. The maxima coincide with the minima of solar activity. This explanation is supported by an interrelation between the annual variations of solar activity and the short-period meteor streams, especially the ecliptical streams. In this case the long-period variation is caused by the change of radiative pressure, which at the times of strong solar activity acts like a weakening of the sun's gravitational field, thus increasing the semimajor axes of the orbits of the dust particles and changing them into ellipses of long periods, or even into hyperbolic orbits. Dust particles will follow their orbits through perihelion, but afterward will move to large distances and not return, if ever, for a long time. The effect is a decrease in the density of dust near the earth. This explanation holds good for the rather slow reaction of the observable secondary phenomena and for the absence of an immediate effect. The decrease in dust density explains both the weakness of the increased airglow and the decrease of "positive" polarization, which results in large values of Arago point distances.

From this explanation and from the fact that the minimum of solar activity did not occur prior to late 1964, the 1965 value appears to be a little too high when compared with the 1952 and 1953 values. An interesting interpretation of this is that, as a result of the extremely high maxima of solar activity in 1947 and 1957, a continuous decrease in the airglow phenomena is observed, and the low density of the dust also weakens the "positive" polarization. We might, therefore, expect a very high mean maximum of Arago distances in 1968.

The results set out in this paper follow my earlier works on enhanced airglow, noctilucent clouds, and interplanetary dust, published in 1951 and 1960.

References

HOFFMEISTER, C.

1951. Spezifische Leuchtvorgänge im Bereich der mittleren Ionosphare. Ergebnisse der exakten Naturwissenschaften, vol. 24, pp. 1–53:

1960. Interplanetare Materie und verstärktes Nachthimmelleuchten. Zeits. f. Astrophys., vol. 49, pp. 233–242.

Rocket and Satellite Studies of Meteoric Dust

T. N. NAZAROVA [1]

For some time now meteoric particles have been studied by optical and radar techniques, as well as by the collection and analysis of meteoric bodies that have fallen onto the earth. These investigations have contributed to a thorough study of meteoric matter.

From observations of meteoric bodies at the moment of their encounter with the earth, the vector velocity, mass, density, composition, and spatial density of particles with mass $m \geq 10^{-4}$ g have been determined. From an analysis of these data we can obtain information of meteoric matter in interplanetary space.

As far as particles with smaller mass are concerned, until recently it has been possible from photometric observations of the zodiacal light and solar F corona to obtain only integral characteristics of particles and their spatial density in interplanetary space. Extrapolation of data characteristic of particles with mass $m > 10^{-4}$ g to particles of smaller mass is not always accurate—in particular, the type of change in spatial density with decrease in mass.

With the advent of rockets and artificial earth satellites it became possible to record individual particles with mass of up to about 10^{-13} g in the neighborhood of the earth and in interplanetary space.

When a meteoric particle moving with a velocity of $> \sim 5$ km/sec (with respect to the satellite) strikes the surface of the detector (mounted on the satellite), the particle bursts and the momentum of the ejected material in the explosion impact is considerably greater than the momentum of the particle itself. Measurement of this "reactive" momentum will not yield the momentum of the particle, but a function of its mass and velocity.

The theoretical calculation performed by Stanyukovich **(1960)** has shown that for high velocities the recorded momentum I is proportional to the particle energy E. This relation $I-E$ is not universally accepted. Lavrent'ev **(1959)** assumes $I \sim mv^{1.6}$, where m and v are the mass and velocity of the particle, respectively. In our reduction of experimental data we assumed $I-E$.

To record a reactive momentum Izakovich and Roy **(1958)** used a ballistic piezoelectric detector with separate mass and elastic elements. Deflection of the elastic elements caused a deformation of the piezo elements and the latter produced an electric potential. Absolute calibration of the detector can be achieved by observing the height to which a small ball of known mass rebounds after falling from a known height. In fact, for the actual values of the "collision" times obtained in the case of the impact of the ball, the detector operates as a ballistic device in the same way as it does during meteoric impact.

When meteoric particles strike the detector, a voltage output in the form of transient damped oscillations develops in the piezo elements; these voltages enter the amplifier-transformer, provide sesonance amplification of the signals, their distribution into ranges according to amplitude, the memorizing of the number of impacts on the trigger elements, and the yield of the remembered information to the telemetry device from each element of the memory system. Thus the piezoelectric detectors of different design that we used made it possible to record both the number of impacts

[1] Institute of Geochemistry and Analytical Chemistry of the USSR Academy of Sciences, Moscow.

of particles per unit area per unit time and some function of the particle mass and velocity that is apparently close to its energy.

An estimate of the mass of the recorded particle depends, of course, on the velocity assumed. When we reduced the results of our first measurements we assumed the particle velocity to be 40 km/sec. Whipple's conclusion (1961a) that the speed of encounter of the meteor particles and the satellite is about 15 km/sec appears to us to be well founded. Hence, for the first experiments recalculations were made, and from 1961 onward we assumed the speed to be 15 km/sec.

Table 1 summarizes the results of investigations of meteoric particles from Soviet rockets and satellites (Nazarova, 1962; Nazarova, Bektabegov, and Komissarov, 1963). For all the experiments the table gives the area of the working surface S (the effective surface area is listed for the geophysical rockets), the operating time t of the instrument, the impact rate, and the height ranges. In the geophysical rocket experiments the equipment was tested in the process. The impact rates of the meteoric particles recorded in these experiments contain an uncertainty (of the order of about three).

Table 1 does not include unprocessed observational results from the satellite Elektron 4 and the space probe Zond 2. These results contain data of sporadic meteoric matter and meteoric bodies of some streams. According to preliminary data they do not contradict the results given in this paper.

The increased density of meteoric particles near the earth observed with the USA rockets, in the experiments known to us, at altitudes of 100 to 150 km, was recorded in the USSR during our experiments conducted at heights of 100 to 300 km.

Recent studies of the brightness of the atmosphere at heights of 120 to 450 km by means of instruments carried by rockets (Mikirov, 1965) made it possible to estimate the density of scattering matter at those heights. According to Mikirov, at a height of 450 to 500 km the aerosol matter has a density of 10^{-20} g/cm^3. This estimate is the lowest limit. Thus the density of the dust particles is greater, by not less than an order of magnitude, at a height of 500 km than in interplanetary space.

Independent confirmation of the presence of a high density of dust particles in the neighborhood of the earth is given by observations of the twilight glow (Divari, 1957, 1964). From photometric observations of twilight glow, Divari has determined the dust concentration at a height of 100 km to be 2×10^{-4} cm^{-3}, which exceeds by 6 to 7 orders of magnitude the concentration obtained experimentally from rockets and satellites. Divari explains this discrepancy by the presence in this region of fine dust not recorded by means of rockets and satellites, but which scatters solar radiation. This concentration of fine dust responsible for twilight scattering of solar radiation decreases with increasing height much more rapidly than does the concentration of larger particles recorded by the satellites (Divari, 1964). This fact may be regarded as a proof that the height range from 100 to at least 300 km is the region where fine dust particles are formed as a result of fragmentation of the circumterrestrial cloud, or the region of their accumulation.

Several hypotheses have been advanced to explain the presence of a dust cloud around the earth. According to Moroz (1962) there is a special class of interplanetary particles that are relatively unstable and possibly consist of ice. He suggests that these particles separate into fragments at heights of a few hundred kilometers above the earth and cause an increase in the dust concentration in the earth's vicinity; however, it seems that none of the hypotheses so far advanced to explain the enhanced density of meteoric particles near the earth can be finally accepted.

Investigations of meteoric matter from rockets and satellites have shown that its spatial density decreases with increase of distance from the earth.

For particles with mass 10^{-8} g at heights 100 to 300 km, the number of impacts N is 3×10^{-2} to 7×10^{-1} m^{-2} sec^{-1}. At heights 400 to 2000 km, $N=10^{-3}$ m^{-2} sec^{-1}. At distances of tens and hundreds of thousands of kilometers from the earth, according to measurements obtained from Lunik 2 and Lunik 3, $N=9\times10^{-4}$ to 10^{-3} m^{-2} sec^{-1}. During the time interval of 3.6×10^4 sec, no impacts were recorded from Lunik 1. Measurements obtained from Explorer 6 and Pioneer 1 give $N=5\times10^{-6}$ to

TABLE 1.—Rocket and satellite meteoric dust data

Satellite or rocket	Date	Area S (m^2)	Time t (sec)	Area×time (m^2 sec)	Altitude range h (km)	Mass of recorded particle m (g)	Influx rate (m^{-2} sec^{-1})
Geophysical rocket	May 24, 1957	4	134	536	100—200	10^{-8}	0.06
Geophysical rocket	Aug. 25, 1957	4	148	592	100—210	10^{-8}	0.05
Geophysical rocket	Feb. 22, 1958	4	85	340	126—297	10^{-8}	0.75
Sputnik 3	May 15, 1958	0.34	1.8×10^{4}	6×10^{3}	400—1880	$6\times10^{-8}-2\times10^{-7}$	7
	May 16–17, 1958				400—700		5×10^{-4}
	May 18–25, 1958				400–700		$<10^{-4}$
First Cosmic rocket	Jan. 2, 1959	0.2	3.6×10^{4}	7.2×10^{3}	2000—360,000	$2\times10^{-8}-10^{-7}$	$<2\times10^{-3}$
						$10^{-7}-10^{-6}$	$<5\times10^{-4}$
						$>10^{-6}$	$<10^{-4}$
Second Cosmic rocket	Sept. 12, 1959	0.2	1.1×10^{4}	2.2×10^{5}	2000—360,000	$10^{-8}-4\times10^{-8}$	$<5\times10^{-5}$
						$4\times10^{-8}-4\times10^{-7}$	$<5\times10^{-5}$
						$>10^{-7}$	9×10^{-5}
Automatic interplanetary station (third Cosmic rocket)	Oct. 4–18, 1959	0.1	2.3×10^{5}	2.3×10^{4}	102,000—470,000	$7\times10^{-9}-2\times10^{-8}$	4×10^{-4}
						$2\times10^{-8}-6\times10^{-8}$	2×10^{-3}
						$>6\times10^{-8}$	4×10^{-4}
Interplanetary station Mars 1	Nov. 1, 1962	1.5	6×10^{3}	9×10^{3}	$6.6\times10^{3}-42\times10^{3}$	$>10^{-7}$	7×10^{-3}
	Nov. 31, 1962–Jan. 30, 1963	1.5	1.5×10^{4}	2.3×10^{4}	$23\times10^{6}-45\times10^{4}$	$>10^{-7}$	5×10^{-3}
Satellite Elektron 2	Jan. 30–31, 1964	0.03	5.4×10^{4}	1.6×10^{3}	7130—400	1.3×10^{-9}	1.1×10^{-1}
						$4.4\times10^{-9}-1.3\times10^{-9}$	10^{-1}
						$10^{-8}-4.4\times10^{-9}$	6×10^{-3}
						$3.3\times10^{-8}-10^{-8}$	4×10^{-3}
						$>3.3\times10^{-8}$	10^{-3}
	Feb. 11–13, 1964	0.03				$6.5\times10^{-8}-2\times10^{-8}$	2.4×10^{-3}
	Feb. 23–25, 1964	0.03				$6.5\times10^{-8}-2\times10^{-8}$	5.8×10^{-3}
	Feb. 29, 1964	0.03				$6.5\times10^{-8}-2\times10^{-8}$	10^{-3}
	Mar. 5, 1964	0.03				$6.5\times10^{-8}-2\times10^{-8}$	1.5×10^{-3}

4×10^{-5}. The large scatter of the data obtained possibly indicates fluctuations of the density of meteor matter in interplanetary space. Extreme estimates of matter in the zodiacal cloud obtained by a photoelectric method give $N=10^{-5}$ to 10^{-4} m^{-2} sec^{-1}.

As pointed out by Whipple (1961b), there is a strong $N(h)$ dependence. However, the change in N with increase of distance from the earth up to heights of about 10^4 km is difficult to explain by one type of $N(h)$ dependence. In the height range 100 to 200 km, N falls more steeply than in the range from 2000 km and above.

An average cumulative mass distribution curve of the influx rates of sporadic meteoric

particles with mass 10^{-7} to 10^{-11} g plotted by Alexander et al. (1963) (fig. 1) shows good consistency of the experimental data,[2] although, as mentioned earlier in this paper, Soviet and United States workers made different assumptions. The former assumed $I \sim A(mv^2/2)$, while the latter assumed $I \sim mv$. Apparently the differences in the numerical values of the coefficient and in the velocity values assumed for calculations compensate each other, and the results agree within the accuracy of the measurements.

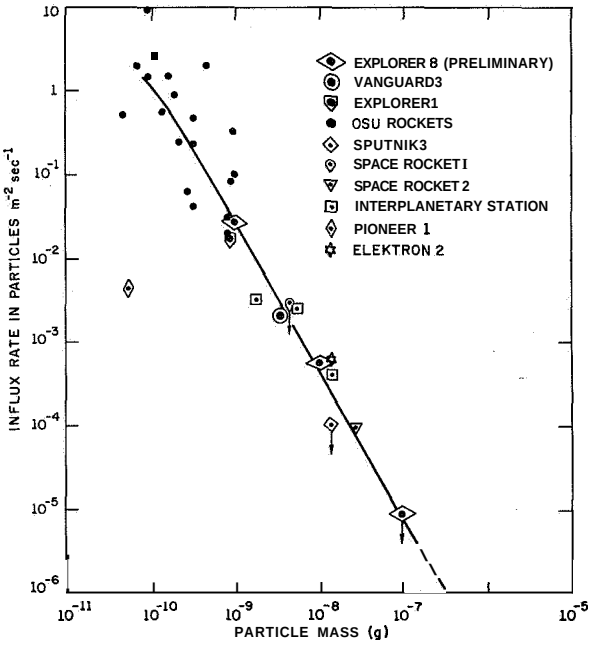

FIGURE 1.—Average cumulative mass distribution curve for the vicinity of the earth (Alexander et al., 1962, fig. 2).

The data based on recording meteoric particles that penetrated the screens of satellites Explorer 16 (D'Auitolo, 1964) and Ariel 2 (Jennison and McDonnell, 1966) for the mass range of about 5×10^{-8} to 10^{-11} g do not lie on the curve of figure 1. This confirms the suggestion made by Whipple (1963), on the basis of observing meteors from the earth, of the presence of meteoric bodies with densities of about 0.5 g/cm³.

Measurements taken from rockets and satellites have demonstrated that the density of meteoric particles is subjected to spatial and time fluctuations. Apart from the streams, individual collections of meteoric particles were observed to have unequal spatial density of particles in them. The linear dimensions of these aggregations varied within wide limits reaching millions of kilometers.

There exist, evidently, very rarefied formations that are difficult to detect because of their small spatial density.

Aggregations of micrometeoric particles unobserved on the earth and not belonging to the known meteor streams have been discovered by means of satellites. From Elektron 2 (Nazarova and Rybakov, 1966), for the exposure time of approximately 479 hours from January 30 to March 10, three aggregations of meteoric particles were recorded. The aggregations were observed during the time period from 14 to 49 hours (the distance between them by time was 147–177 hours) when not a single impact was recorded.

The linear dimensions of these aggregations reached 3 to 5×10^6 km. The first of them, recorded on January 30–31, 1964, was sufficiently dense to enable us to determine the direction of its motion.

During approximately 15 hours, 185 impacts were recorded. The distribution of the impacts over the orbit enabled us to separate a part of it for which out of 185 impacts only 3 impacts took place (fig. 2). Such a distribution of impacts is possible when the earth passes the aggregation of meteoric particles (similar to crossing the stream). In this case, for an appropriate angle between the satellite orbit plane and the aggregation vector velocity, a greater or smaller portion of the satellite orbits turns out to be shielded by the earth.

A geometric consideration of the problem has shown that in the above case this angle is $\sim 36°$, and the angle between the direction of the aggregation vector and the earth's velocity vector is $\sim 42°$.

If we assume that the aggregation had the velocity of 42 km/sec, which is the maximum for the distance of the earth from the sun, the average relative velocity of the encounter of meteroric particles with the sensors was ~ 61 km. In this case the average impact rate was 1.1×10^{-1} m^{-2} sec^{-1}. To estimate the mass of recorded particles, we used, as in our previous

[2] This graph shows, in addition, results pertaining to the satellite Elektron 2.

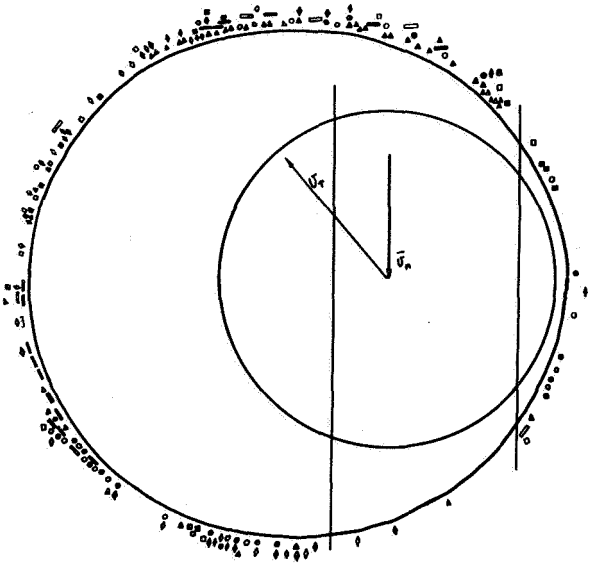

FIGURE 2.—Concentration of meteoric particles recorded by the satellite Elektron 2, January 30-31, 1964.

papers, the relation $I \sim mv^2/2$, and assumed that $v = 61$ km/sec.

As is evident from table 2, the distribution of particles by mass for this aggregation cannot be characterized by one law. In the formula $F(M) \sim 1/M^n$, $n > 2$ for m_1 and m_2, $n < 2$ for m_2 and m_3, and $n < 2$ for m_3 and m_4.

Mass of particles (g)	Number of particles
$4.4\times10^{-9} \geq m_1 \geq 1.3\times10^{-9}$	166
$1\times10^{-8} \geq m_2 \geq 4.4\times10^{-9}$	10
$3.3\times10^{-8} \geq m_3 \geq 1\times10^{-8}$	7
$m_4 \geq 3.3\times10^{-8}$	2

During the time up to March 10, 1964, while the equipment was functioning, two more aggregations of meteoric particles were observed on February 11–13 and on February 23–25. Since only a small number of impacts were recorded (in one case 10, and in another, 24), we were unable to determine the direction of motion of these aggregations; when we estimated the mass of the particles we assumed the velocity to be 15 km/sec, which is the value we usually take for sporadic meteoric particles. The number of recorded impacts of particles with mass 6.5×10^{-8} g $\geq m \geq 2\times10^{-8}$g in these cases was $N_2 = 2.4\times10^{-3}$ and $N_3 = 5.8\times10^{-3}$ m^{-2} sec^{-1}.

From February 29 to March 10, 4 impacts of meteoric particles were recorded, among them 2 during approximately 22 hours from February 29 to March 1, and 2 on March 5 during approximately 14 hours.

It should be noted that the average impact rate for particles with mass $6.5\times10^{-8} \geq m \geq 2\times10^{-8}$g from February 3 to March 10 during a period of ~460 hours was 7.5×10^{-4} m^{-2} sec^{-1}, which fits well on the curve plotted by Alexander et al. (1963) (fig. 1).

Aggregations of micrometeoric particles that do not coincide with the known streams were observed earlier. Near the earth, on May 15, 1958, Sputnik 3 recorded an aggregation of particles with mass 2×10^{-7}g $\geq m \geq 6\times10^{-8}$g (with $v = 15$ km/sec); N rose from 4 to 11 impacts m^{-2} sec^{-1}, i.e., approximately by 3.5 orders of magnitude higher than was observed during subsequent days. The mass of particles in this aggregation may have been 5×10^{-10}g with an assumed velocity of 70 km/sec.

The interplanetary probe Mars 1 permitted us to investigate meteoric matter beyond the earth's orbit at large distances from the sun. On the day of launching, September 1, 1962, both the earth and Mars 1 crossed the Taurids. At a distance 6600 to 42,000 km from the earth during 100 minutes of the flight, 60 impacts of meteoric particles with mass $\geq 10^{-7}$ g were recorded. The average impact rate was 7×10^{-3} m^{-2} sec^{-1}. Since for sporadic meteoric bodies the number of impacts of the particles of mass $\geq 10^{-7}$ g is approximately 10^{-5} m^{-2} sec^{-1}, we may infer that all the recorded particles belonged to the stream (Taurids).

The spatial density of the meteoric bodies in the stream was extremely uneven (fig. 3). The particles moved in space in individual condensations, observed at distances of 4000 to 45,000 km from each other. The measured spatial density of the meteoric bodies averaged over the time during which the impacts were recorded (2 min) varied within the limits $(5.4$ to $0.35)\times10^{-6}$ m^{-3}, i.e., one meteoric body in a cube of side 60 to 140 m.

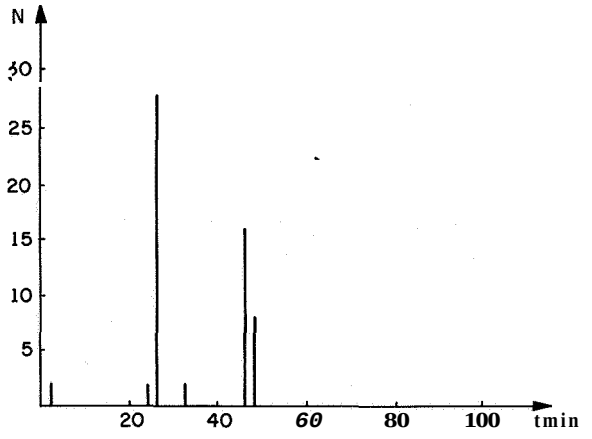

FIGURE 3.—Observation of the Taurid stream. Data from the 100-min period of November 1, 1962.

In the second half of November and December, at a distance of up to 23×10^6 km from the earth, during a total observation time of approximately 7.5 hours, no impact was recorded. Hence, we may infer that the data on the number of sporadic meteoric bodies with mass $\geq10^{-7}$ g obtained for the vicinity of the earth's orbit (according to observations at a distance of thousands of kilometers from the earth) apparently remain correct for distances from the sun, i.e., for $m\geq10^{-7}$ g, $\overline{N}\leq10^{-5}$ m^{-2} sec^{-1}.

From December 31, 1962, to January 30, 1963, at a distance 23 to 45×10^6 km from the earth, Mars 1 again recorded an increased density of meteoric matter in interplanetary space. This aggregation could not be identified with any known meteor stream. During the total recording time of — 4 hours, 104 impacts were recorded, the average impact rate being 4.5×10^{-3} m^{-2} sec^{-1}.

The spatial density of meteoric bodies in this formation was uneven, as in the Taurid stream. The densities of some of the condensations varied within the limits 1.7×10^{-6} to 6.7×10^{-4} m^{-3} and the distances from 8000 to 190,000 km.

After January 30, 1963, the instrumentation for recording meteoric particles ceased to function. Therefore, it is not known how long Mars 1 continued to move in the region of enhanced spatial density. Using Explorer 1, American investigators (Dubin, 1960) also observed a "stream of sporadic meteors" that was not recorded on the earth.

According to preliminary reports (1965), the spacecraft Mariner 4 recorded on some portion of its trajectory an enhanced density of meteoric particles belonging perhaps to a condensation similar to the one recorded by Mars 1.

Apparently meteoric matter is mostly associated in space into more or less dense formations with linear dimensions varying within wide limits.

In interplanetary space there are many meteoric streams and aggregations unknown on the earth, and so far it is impossible to predict them.

Regular observations from artificial earth satellites will enable us to reveal those streams encountered by the earth during its motion along the orbit and those &accessible to observations from its surface.

Further investigations of different regions of interplanetary space by means of space vehicles will increase our knowledge of the solid components of interplanetary matter, extend the number of the known meteoric streams, and perhaps in the future enable us to predict the probability of meteor particle encounter with spaceships.

References

ALEXANDER, W. M.; MCCRACKEN, C. W.; SECRETAN, L.; and BERG, O. E.
1963. Review of direct measurements of interplanetary dust from satellites and probes. *In* Space Research III, ed. by W. Priester, North-Holland Publ. Co., Amsterdam, pp. 891–917.

D'AIUTOLO, C. T.
1964. Satellite measurements of the meteoroid environment. Ann. New York Acad. Sci., vol. 118, pp. 82–97.

DIVARI, N. B.
1957. Über die Polarisation des Dämmerungshimmellichts im Zenit. Doklady Acad. Sci., USSR, vol. 112, pp. 217–220.
1964. The dust concentration in the upper layers of the earth's atmosphere. Geomagnetism and Aeronomy, USSR Acad. Sci., vol. 4, no. 5, pp. 886–892.

DUBIN, M.
1960. Meteoritic dust measured from Explorer I. Planet. Space Sci., vol. 2, pp. 121–129.

IZAKOVICH, M. A., and ROI, N. A.
1958. An accoustical method for the measurement of the mechanical parameters of meteorites. Artificial Earth Satellites, USSR Acad. Sci., vol. 2, pp. 105–107.

JENNISON, R. C., and MCDONNELL, J. A. M.
1966. Interpretation of the interplanetary dust measurements in the Ariel II Satellite. In Space Research VI, ed. by R. L. Smith-Rose, Macmillan Co., New York, pp. 937–944.

LAVRENT'EV, M. A.
1959. The problem of piercing at cosmic velocities. Artificial Earth Satellites, USSR Acad. Sci., no. 3, pp. 85–91.

MIKIROV, A. E.
1965. Investigations of atmospheric brightness at heights of 120–450 km. Cosmic Studies, USSR Acad. Sci., vol. 3, no. 2, pp. 201–210.

MOROZ, V. I.
1962. On the "dust envelope" of the earth. Artificial Earth Satellites, USSR Acad. Sci., no. 12, pp. 166–174.

NAZAROVA, T. N.
1962. Rocket and satellite studies of meteor dust. Artificial Earth Satellites, USSR Acad. Sci., no. 12, pp. 154–158.

NAZAROVA, T. N.; BEKTABEGOV, A. K.; and KOMISSAROV, O. D.
1963. Preliminary results of a study of meteoric matter along the trajectory of the interplanetary stationary "Mars 1." Cosmic Studies, USSR Acad. Sci., vol. 1, no. 1, pp. 137–139.

NAZAROVA, T. N., and RYBAKOV, A. K.
1966. Meteoric dust measured by the satellite Elektron II. In Space Research VI, ed. by R. L. Smith-Rose, Macmillan Co., New York, pp. 946–951.

STANYUKOVICH, K. P.
1960. Elements of the theory of the impact of solid bodies with high (cosmic) velocities. Artificial Earth Satellites, USSR Acad. Sci., no. 4, pp. 292–333.

WHIPPLE, F. L.
1961a. The particulate contents of space. In Medical and Biological Aspects of the Energies of Space, ed. by P. Campbell, Columbia Univ. Press, New York, pp. 49–79.

1961b. The dust cloud about the earth. Nature, vol. 189, pp. 127–128.

1963. On meteoroids and penetration. Journ. Geophys. Res., vol. 68, pp. 4929–4939.

Recent NASA Meteoroid Penetration Results from Satellites

C. T. D'AIUTOLO,[1] W. H. KINARD,[2] and R. J. NAUMANN

Introduction

One of the principal parameters to be considered in the design of space vehicles is the possibility of damage resulting from impacts with extraterrestrial debris. Depending upon their kinetic energy, the impingement of high-velocity particles on spacecraft structures may result in surface erosion, puncture, or catastrophic rupture of sensitive spacecraft structures.

The problem of the spacecraft designer is to provide protection for vital parts of the spacecraft and for the occupants, if any. He must be able to estimate the likelihood of damage, in flight, of structures of various configurations and materials.

Early knowledge of the hazard resulting from the meteoroid environment was based on information obtained from two broad fields of inquiry—astronomy, the foremost source of information, and laboratory hypervelocity impact studies. Combined information from these two sources was used to estimate the magnitude and character of the meteoroid hazard to spacecraft.

Two early estimates of the meteoroid-penetration frequency, based on data from these sources, are shown in figure 1. The estimated number of penetrations/m²/day is plotted as a function of thickness for the penetration of aluminum sheets. The upper curve combines an early estimate by Whipple (1958) of the meteoroid flux with the penetration criteria determined experimentally by Charters and Summers at the Ames Research Center, reported by Summers (1959), and represents a

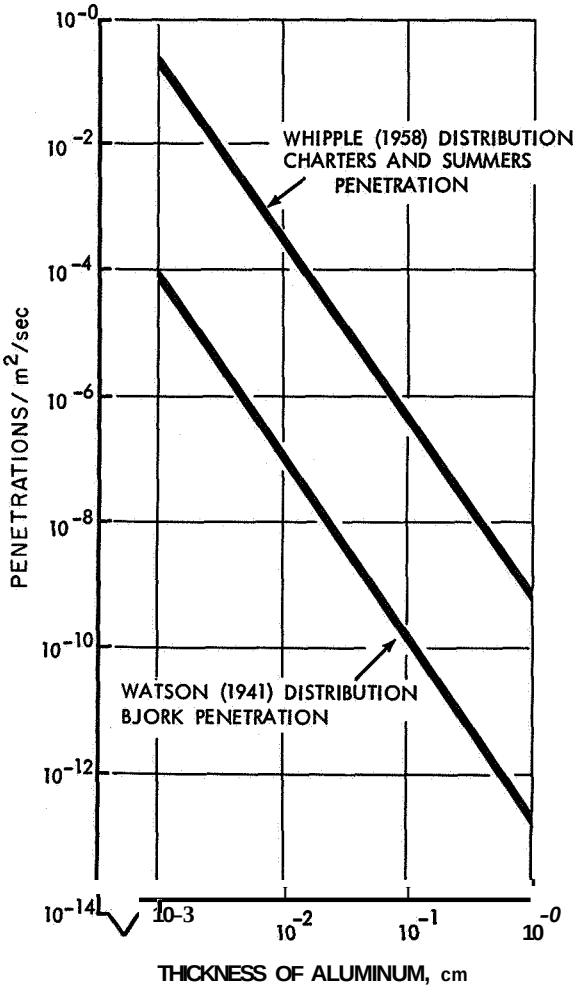

FIGURE 1.—Estimated meteoroid penetration frequency.

[1] National Aeronautics and Space Administration Headquarters, Washington, D.C.

[2] Langley Research Center, National Aeronautics and Space Administration, Hampton, Va.

[3] Marshall Space Flight Center, National Aeronautics and Space Administration, Huntsville, Ala.

pessimistic limit for the hazard. The lower curve combining Watson's (1956) estimate of the meteoroid flux with the theoretical penetration criteria derived by Bjork (1961) represents an optimistic limit for the hazard. For a given material thickness, an uncertainty of over three orders of magnitude existed in the estimated penetration frequency. The following example illustrates what such an uncertainty means in the design of space vehicles. In design studies for one particular spacecraft we found, from the upper curve of figure 1, that for adequate meteoroid protection an additional weight of about 12,500 pounds would be required. This weight would entail a severe performance penalty. Use of the lower curve resulted in no additional weight for meteoroid protection. The dilemma of the designer is readily apparent.

In order to narrow the uncertainties that have existed in predicting the probabilities of meteoroid penetrations in spacecraft structures, the Office of Advanced Research and Technology of the National Aeronautics and Space Administration has formulated a comprehensive program of investigation, which includes flight experiments to measure meteoroid penetrations over a range of material thicknesses in the near-earth environment.

This paper will summarize the results to date from two series of spacecraft in this program. First, we shall present the results from the Explorer 16 and Explorer 23 satellites, each of which exposed to the meteoroid environment a total area of about 2.0 m^2 of very thin materials and used pressurized cells as the prime experiment. Next, we shall describe preliminary results from the large satellites, Pegasus 1 and 2, each of which exposed more than **200** m^2 of material thicknesses up to 0.040 cm and used electrical capacitor-type detectors that discharge when penetrated. Finally, we shall make a comparison of the preliminary results from these satellite penetration measurements with the latest estimates based on observations of meteors.

Spacecraft and experiments

EXPLORER 16

Spacecraft.—Two Explorer-series micrometeoroid satellites have been launched to date with the primary objective of obtaining meteoroid penetration rates in relatively thin target materials. The first of these two satellites, designated Explorer 16 (1962 Beta Chi 1), was launched December 16, 1962, from the NASA Wallops Station onboard a Scout launch vehicle. It was placed in an earth orbit having an apogee of 1180 km, a perigee of 750 km, and an inclination to the earth's equator of 52°. The weight of the spacecraft, including the spent last-stage rocket motor, which remained as part of the orbiting satellite, was 233 pounds (106 kg).

Explorer 16 continued to transmit useful data for approximately 7½ months, failing on July 22, 1963. Several NASA Technical Memorandums (Hastings, 1963a, b, c, 1964) describing this satellite and the data obtained have been published. The data have also been presented at various symposia (D'Aiutolo, 1964a, b).

Figure 2 is a schematic of the Explorer 16 spacecraft, cylindrical in shape, 58.5 cm in

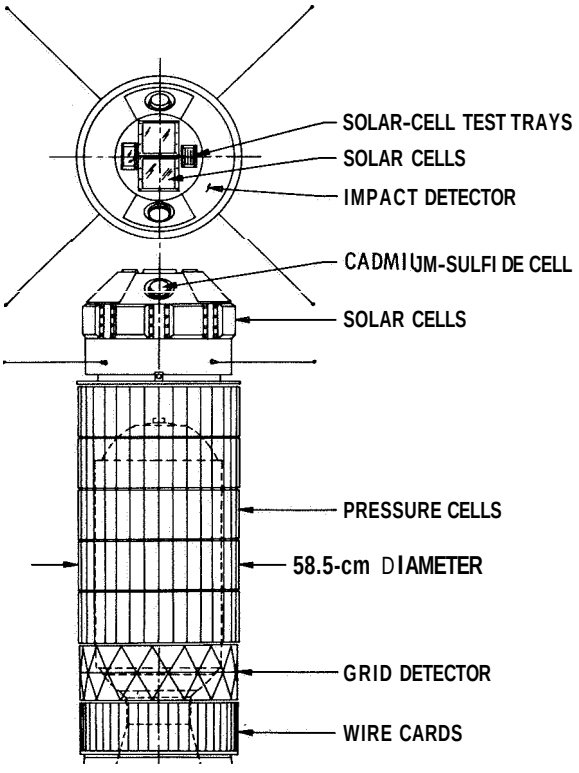

FIGURE 2.—Explorer 16 (1962 Beta Chi 1) satellite.

diameter, and 193 cm long. The primary penetration detectors onboard consisted of pressurized cells mounted around the periphery of the last-stage rocket motor.

Other penetration-type detectors placed on the spacecraft were stainless steel-covered grid detectors mounted in a ring just aft of the pressure cells, copper wire card detectors mounted in a ring just aft of the steel-covered grid detectors, and two cadmium-sulfide cell detectors mounted on the spacecraft nose section. Sounding-board-type impact detectors were also mounted on the spacecraft nose section.

Experiments.—Figure 3 is a drawing of the pressurized-cell penetration detector. The cell consisted of a thin exposed surface in which penetrations were detected, a base plate, a pressure-sensitive capsule, and a microswitch. Each cell, approximately 5.0 cm in diameter and 18.8 cm long, was filled with helium. When the cell was punctured the gas leaked out and the resulting pressure loss actuated the switch, which signaled the telemeter of the penetration. Each cell can detect only one penetration. Beryllium copper was selected as the cell material because of previous experience in fabricating pressure diaphragms.

At the time Explorer 16 was launched, no direct measurements of meteoroid penetration rates existed, and, as shown previously, estimates of expected rates varied by orders of magnitude. To ensure that some useful penetration data would be obtained, the number of cells of each thickness was varied inversely as the cell skin thickness. The exact cell and thickness distributions were as follows: 100 0.0025-cm cells for a total exposed area of 1.0 m^2, forty 0.0051-cm cells for a total exposed area of **0.4** m^2, and twenty 0.0127-cm cells for a total exposed area of **0.20** m^2.

The stainless steel-covered grid detector (Davison and Winslow, 1964) is shown in figure 4. These detectors were made in triangular segments with each side about 11.6 cm long. The stainless steel covers were 0.0025, 0.0076, and 0.0152 cm thick. They were bonded to 12.7-μ mylar, which had a thin continuous grid circuit. A break in this continuous grid indicated when the stainless steel cover plate was penetrated. The area distribution for these detectors was as follows: 0.14 m^2 of 0.0025-cm, 0.19 m^2 of 0.0076-cm, and 0.023 m^2 of 0.0152-cm thick materials.

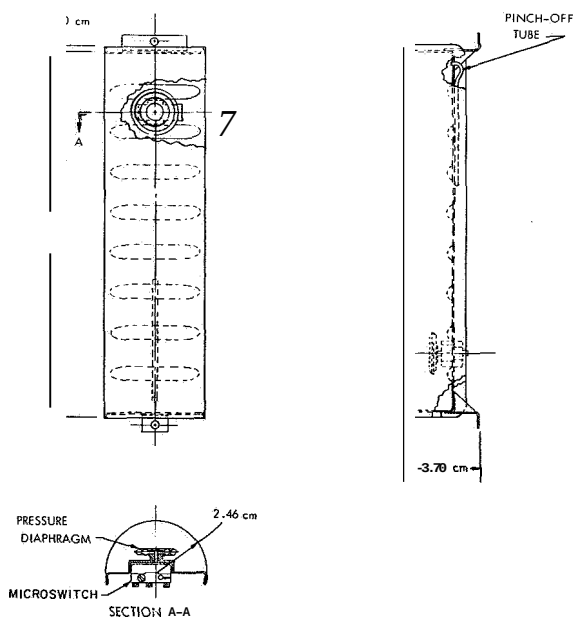

FIGURE 3.—Pressurized cell detector.

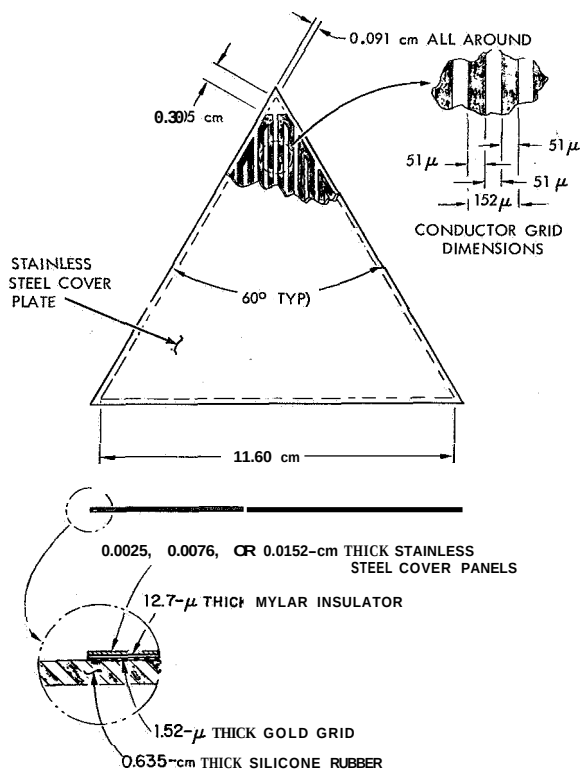

FIGURE 4.—Stainless steel-covered grid detector.

EXPLORER 23

Spacecraft.—The primary mission of the second Explorer meteoroid satellite, Explorer 23 (1964 74A), was to define more accurately the penetration flux in the 0.0051-cm material and obtain additional data on the 0.0025-cm material, thus establishing at a higher confidence level the slope of the penetration flux curve in the region of 0.0025-cm and 0.0051-cm thick materials. This spacecraft was launched on November 6, 1964, from the NASA Wallops Station on board a Scout launch vehicle. It was placed in an earth orbit having an apogee of 979 km, a perigee of 464 km, and an inclination to the earth's equator of 52°. The weight of the spacecraft, including the spent last-stage rocket motor, which remained as part of the orbiting satellite, was 296 pounds (135 kg).

A schematic of Explorer 23 is shown in figure 5. It is basically very similar to Explorer 16. The primary penetration detectors were of the pressurized-cell type flown on Explorer 16; however, the Explorer 23 detectors were made of stainless steel rather than beryllium copper. Since fabrication techniques had advanced so far as to permit the use of stainless steel, this material was selected because it is a more typical spacecraft structural material.

Explorer 23 had 70 cells of 0.0025-cm stainless steel for a total area of 0.69 m^2, and 140 cells of 0,0051-cm stainless steel for a total area of 1.38 m^2. The area thickness distribution mas selected to provide approximately the same number of events in the 0.0025-cm and 0.0051-cm cells based on the penetration-rate data obtained by Explorer 16.

Explorer 23 also had on board two capacitor-type penetration detectors with a combined total area of 0.073 m^2.

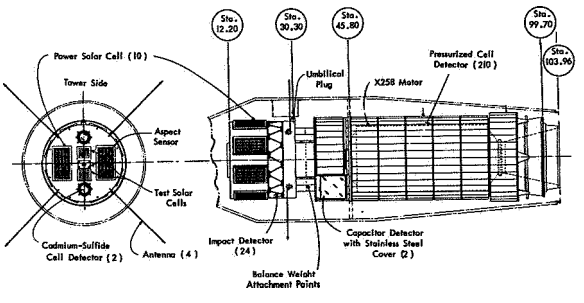

FIGURE 5.—Schematic of Explorer 23 (1964 74A).

Experiments.—The primary penetration detectors (pressurized cells) are described above.

Figures 6a and b show the details of the capacitor-type detectors on board. Each detector was approximately 16.8 cm×21.1 cm. The outer target material was 0.002-cm stainless steel. A dielectric consisting of a bilaminate of 4-μ mylar was bonded together and to the stainless steel, with the thickness of each adhesive bond approximately 0.76 μ. Approximately 0.3 μ of copper was deposited on the rear surface of the dielectric to serve as the rear capacitor electrode.

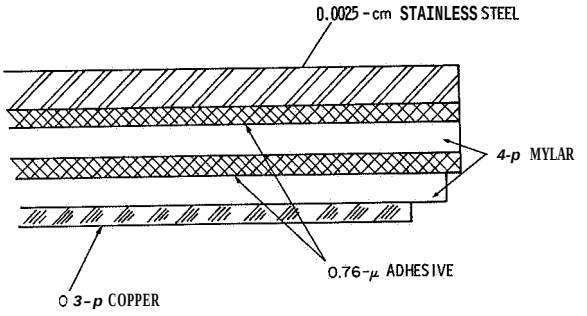

FIGURE 6a.—Typical cross section of Explorer 23 capacitor detector.

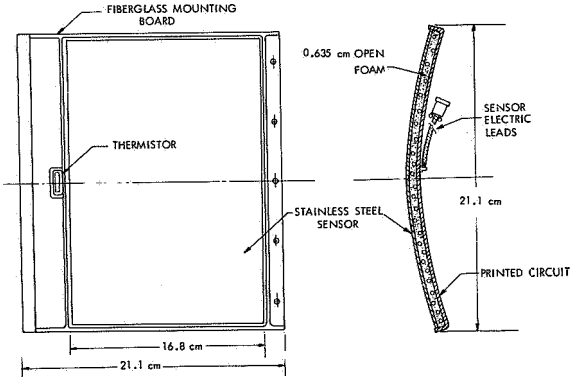

FIGURE 6b.—Explorer 23 capacitor penetration detector.

The capacitors were charged to approximately 14 volts. The operation of the detector depended on ionization being created by the energy dissipated by a penetrating meteoroid. This ionization, which is very short-lived, provided a conducting path through which the capacitor was partially discharged. The discharging of the capacitor thus provided the signal of the penetration event. Since the

shorting mechanism is temporary, the detector can recharge and be used repeatedly for detecting meteoroid penetrations.

PEGASUS 1 AND 2

Spacecraf.—The primary mission of the Pegasus spacecraft was the measurement of meteoroid penetration rates in materials up to 0.040 cm in thickness. The first spacecraft, Pegasus 1 (1965 09A), was launched on February 16, 1965, from Cape Kennedy on board the SA–9, Saturn 1 launch vehicle. It was placed in an earth orbit having an apogee of 740 km, a perigee of 495 km, and an inclination to the earth's equator of 32°. The second spacecraft, Pegasus 2 (1965 39A), was launched from Cape Kennedy on May 25, 1965, on board the SA–8, Saturn 1 launch vehicle, and was placed in an almost identical orbit: apogee, 745 km; perigee, 510 km; and inclination, 32°. A third spacecraft, Pegasus 3 (1965 60A), was launched on July 30, 1965, from Cape Kennedy on board the SA–10, Saturn 1 launch vehicle, and placed into a near-circular earth orbit: apogee, 541 km; perigee, 520 km; and inclination, 29°. Since at the time of this writing Pegasus 3 has been in orbit only a few weeks, the results obtained from it will not be reported here, but will be published later when more data are available.

Each spacecraft was identical in configuration. Plate 1 is an artist's concept of the Pegasus spacecraft in orbit. During launch the spacecraft was folded and when inserted into orbit was extended in an accordion-like manner. To provide a lifetime of at least one year, the spacecraft remained attached to the spent second stage of the launch vehicle. In the fully extended condition, the spacecraft has a span of about 29.2 m. Exclusive of the attached spent second stage, the weight is about 3200 pounds (1455 kg).

Experiments.—The penetration detectors on board consist of parallel plate capacitors. The erectile winglike structure of the Pegasus spacecraft supports 208 such detectors, each of which measures 50 cm × 100 cm, attached to both sides of the wings. As shown in figure 7, the parallel plate capacitor penetration detectors are formed by backing target sheets with a 12-μ mylar trilaminate, which in turn is backed by a vapor-deposited copper layer. The capacitors were bonded to each side of a 2.54-cm foam core, which acts as a structural support as well as a barrier to prevent the meteoroid and debris resulting from the penetration of one capacitor from impinging on the opposite capacitor. An Alodine coating was placed on the target sheets for thermal control. Thicknesses of the target sheets are: 40 μ–1100–0 aluminum, 200 μ–2024 T–3 aluminum, and 400 μ–2024 T–3 aluminum. The winglike structure provides 194.5 m^2 of instrumented area, of which 171 m^2 is allocated to the 400-μ thickness, 16 m^2 to the 200-μ thickness, and 7.5 m^2 to the 40-μ thickness.

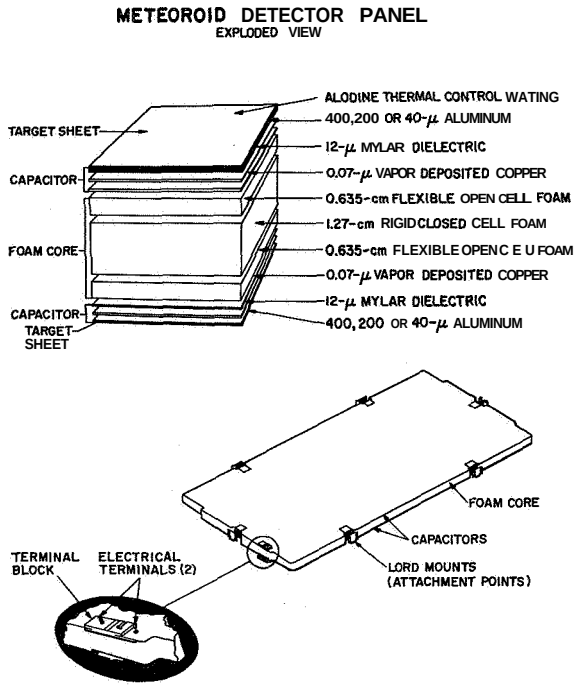

FIGURE 7.—Pegasus capacitor detector.

The 400-μ area is subdivided into 48 identifiable logic groups, each containing 5 to 8 individual detector sheets; the 200-μ area has 6 logic groups, each containing 3 to 8 individual detectors; the 40-μ area has 8 logic groups, each with 2 detectors. Figure 8 shows the location of the various panel logic groups; the number without a letter represents the 400-μ thickness, the letter B the 200-μ thickness, and the letter C the 40-μ thickness.

A penetration through the detector target sheet and mylar dielectric momentarily shorts the capacitor detector, which is normally

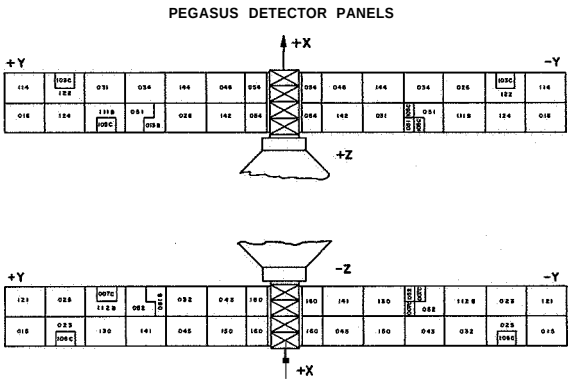

FIGURE 8.—Pegasus wing-panel schematic showing location of various logic groups.

maintained at a 40-volt potential by a network of current-recharge amplifiers (GRA). The energy stored in the capacitor is dumped into the shorted area, which burns away the copper-vapor deposit and clears the detector in approximately 1 sec. The initial voltage drop across the capacitor starts an integrator in the hit detector, which integrates the voltage variation across the detector panel for 250 μsec. If the integrated voltage-time product is greater than a certain predetermined value, a hit word is written in the memory and a cumulative counter is incremented.

The recharge of the panel is accomplished by three CRA's, which are selected by a diode-resistor logic matrix in a unique pattern for each logic group. This pattern is also written into the hit word.

In laboratory testing of the detectors, it was found that the discharge voltage produced by a high-velocity particle ranged from fractions of a volt to full discharge. No direct correlation between discharge level and any projectile property could be found, although there was some indication that the signal levels increased somewhat at higher velocities. The voltage-time product required to record a hit word was selected so that a typical discharge of 4 volts would be registered on Pegasus 2 and 3, 3 volts on the 40-μ panels on Pegasus 1, and 5 volts on the remainder of the Pegasus 1 panels. Laboratory tests indicated that these settings would accept 80 to 90 percent of the signals resulting from meteoroid penetrations.

Rate of meteoroid penetrations

EXPLORER 16

Accumulative Penetrations.—Explorer 16 has provided the first signiscant data on the penetrating capability of meteoroids in thin structural materials. Figure 9 shows the accumulated punctures as a function of time for the 0.0025-cm and 0.0051-cm beryllium-copper pressurized cells as well as for the 0.0025-cm and 0.0076-cm stainless steel-covered grid detectors. The data presented extend from December 16, 1962 (launch), through July 22, 1963, at which time the spacecraft ceased to transmit data. During the 7½ months in orbit, forty-four 0.0025-cm and eleven 0.0051-cm beryllium-copper penetrations were recorded. Six 0.0025-cm and one 0.0076-cm stainless steel penetrations were also recorded in this time period. As discussed by Secretan (see pp. 307–315), several penetrations of the cadmium-sulfide cell were recorded. Although not reported, two penetrations were recorded in copper wire card detectors. No penetrations were recorded in the 0.0127-cm beryllium-copper pressurized cells or in the 0.0152-cm stainless steel wire grid.

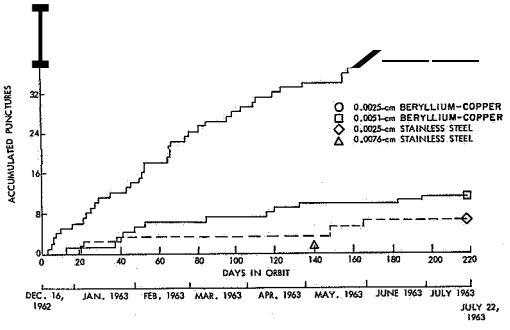

FIGURE 9.—Explorer 16 history of accumulated penetrations.

Penetration Rates.—The penetration data obtained from the pressure cells and the stainless steel-covered grid detectors are shown in figure 10; the thickness of the detector target is plotted against the puncture rate.

Some preliminary impact tests performed at Langley Research Center and at Ames have indicated that equal thicknesses of the stainless steel and of the beryllium copper used have approximately the same resistance to penetration.

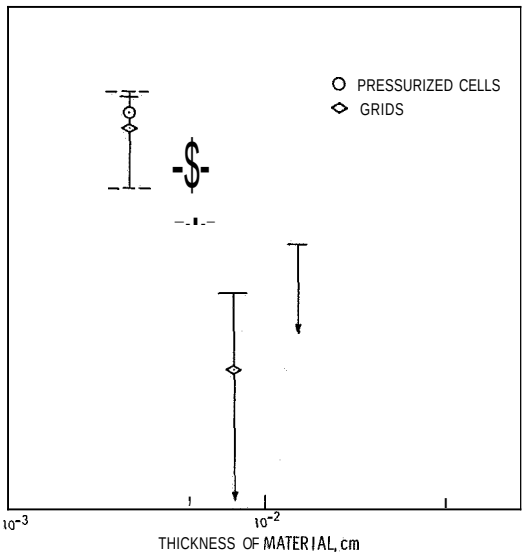

FIGURE 10.—Explorer 16 penetration rates.

It can be seen that a flux of 3.86×10^{-6} punctures/m²/sec was observed in the 0.0025-cm pressure cells. This flux is based on the 44 penetration events. The flux measured in the 0.0051-cm cells was 1.99×10^{-6} punctures/m²/sec based on the 11 events. No penetration was observed in the 0.0127-cm cells, and the point shown in figure 10 represents an upper limit of the flux.

. Because of their small exposed area, the stainless steel-covered detectors received only a small number of penetrations. The six 0.0025-cm penetrations gave a flux rate of 1.329×10^{-6} punctures/m²/sec, while the one 0.0076-cm penetration gave a flux rate of 8.68×10^{-7} punctures/m²/sec.

In summary, Explorer 16 established with a reasonable level of confidence the penetration flux in 0.0025-cm beryllium copper and, to a reduced confidence level, the flux in 0.0051-cm beryllium copper. The stainless steel data seem to agree with the beryllium results.

EXPLORER 23

Accumulative Penetrations.—Figure 11 illustrates the accumulated punctures as a function of time for the 0.0025-cm and 0.0051-cm stainless steel pressurized cells. The data presented extend from November 6, 1964 (launch), through July 22, 1965. During this period, forty-three 0.0025-cm and fifty-four 0.0051-cm

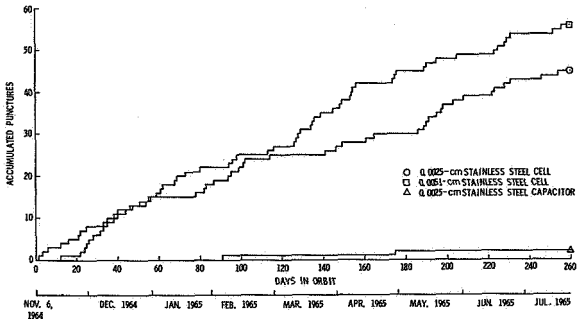

FIGURE 11.—Explorer 23 history of accumulative penetrations.

pressurized cells were penetrated. Two penetrations were also recorded in the capacitor detectors during the same period.

Penetration Rates.—The penetration data obtained by Explorer 23 prior to July 22,1965, are presented in figure 12, which is a plot of the penetration rate on the ordinate and the material thickness on the abscissa. The penetration rates for the 0.0025-cm and 0.0051-cm materials were 3.74×10^{-6} and 1.87×10^{-6} penetrations/m²/sec, respectively.

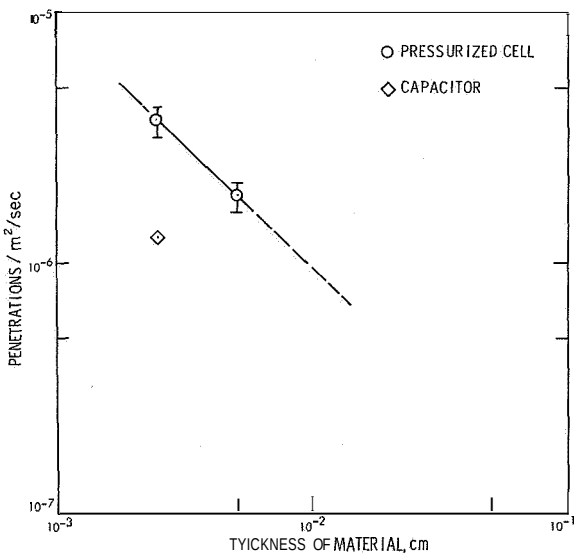

FIGURE 12.—Explorer 23 penetration rates.

As of July 22, 1965, the capacitor detectors had been penetrated only twice, and, as a result, calculated penetration rates for these detectors have little statistical significance. The calculated rate for the capacitors does seem to be in reasonable agreement with the 1-mil pressure cells. The fact that the capacitor-detector rate

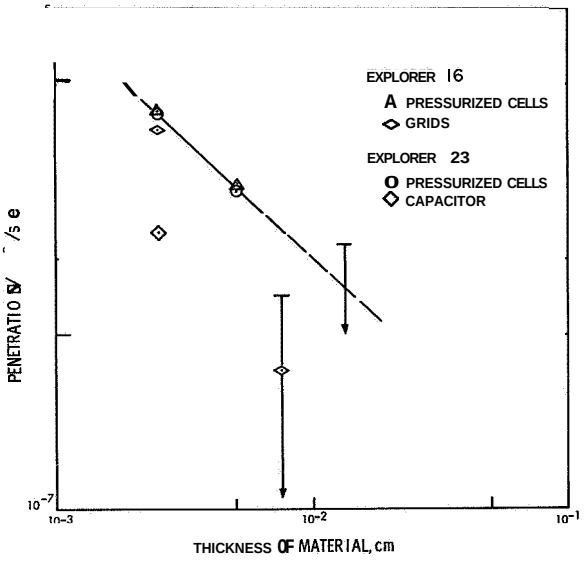

FIGURE 13.—Comparison of Explorer 16 and Explorer 23 penetration rates.

is low, compared to the pressure-cell rate, could result from either or both of two factors: the first, as already mentioned, is the small data sample of only two events; the second, which would cause the capacitor-detector rates to be lower than the cell rates, results from a difference in the threshold detection for each detector. The pressure-cell detectors will indicate as a penetration any impact that penetrates into the material to a sufficient depth to allow small cracks to develop between the crater bottom and the rear of the plate. The actual penetration depth in these cases may be only ⅔ the thickness of the plate. The capacitor detectors, on the other hand, require a complete penetration of the target and the dielectric forming the capacitor before an impact is detected; consequently, even though both types of detectors have 0.0025-cm plates, the capacitor will require a little larger particle under the same impact velocities to detect a penetration.

Figure 13 compares the results of Explorer 16 and Explorer 23. It can be seen that the data from the beryllium-copper pressure cells of Explorer 16 fall almost on top of the data obtained by the stainless steel cells of Explorer 23. This fact supports the finding from ground tests, which indicated that both the stainless steel and beryllium-copper material used have about the same resistance to penetrations. There is also good agreement in the data obtained from the 0.0025-cm pressurized cells and the 0.0025-cm stainless steel grid detector. The 0.0076-cm stainless steel grid data and the 0.0127-cm beryllium-copper-cell data have little significance, since only one penetration was recorded in the grid detector and no penetration was recorded in the beryllium-copper-cell detector.

With the large total data sample obtained by both satellites, the rates at the 0.0025-cm and 0.0051-cm materials based on the pressure-cell measurements are established with very good confidence, as evidenced by the confidence limits shown on the data points.

PEGASUS 1 AND 2

Minor instrumentation difficulties in Pegasus 1 prevented panel identification and recharge times from being recorded for the 200-μ and 400-μ panels. Also, it was found that these panels had a tendency to become intermittent; that is, a single panel may suddenly generate many hit words in the space of a few orbits. It is believed that such a condition is caused by debris or ragged edges around a meteoroid perforation that produce point physical shorting. The energy stored in the capacitor would burn away such a short, but thermal expansion and contraction could cause the process to repeat many times. Laboratory tests to investigate this phenomenon will be conducted in the near future.

Pegasus 1 received four hit indications on the 400-μ panels in the first 11 days. However, several panels became intermittent at that time, and the lack of panel identity precluded separating valid hits from the intermittent events after that time. Based on four events in 1925 m^2 day, the penetration frequency is 0.0021/m^2 day.

For Pegasus 1, a very high fraction of the penetrations on the 200-μ panels resulted in shorts, and since there were only six logic groups, the 200-μ area very quickly became lost. There were nine hit indications in 248 m^2 day exposure, which resulted in a penetration frequency of 0.036/m^2 day. Again it should be pointed out that the 200-μ and 400-μ hit words did not contain panel identity or recharge time unless a short resulted. Therefore, some of the tests for validity could not be made.

The 40-μ panels gave panel identification about **70** percent of the time for Pegasus 1 and are still functioning extremely well. A total of **104** penetrations have been recorded in **858** m^2 day for **a** flux of 0.121/m^2 day. A time history of the cumulative events is shown in figure **14.**

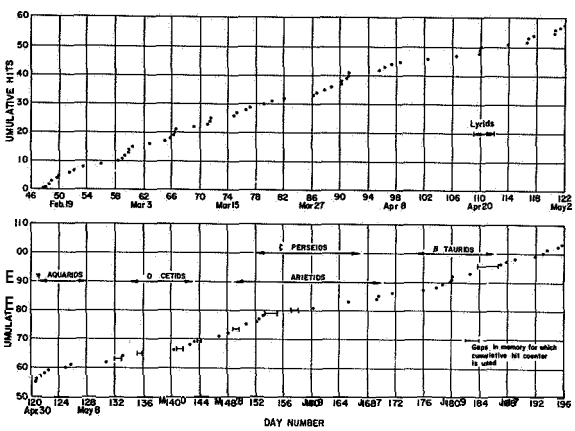

FIGURE 14.—Time history of accumulated penetrations for 40-μ panels on Pegasus 1.

The number of penetrations, area-time exposure, and puncture frequency observed by Pegasus 1 and 2 (as **of** July 20, **1965)** are summarized in table 1. Note that the few punctures observed in the 200-μ and 400-μ Pegasus 1 'detectors are in reasonably good agreement with Pegasus 2 results. The total 40-μ events give a somewhat higher puncture rate **for** Pegasus 2 than for Pegasus 1.

TABLE *1.—Pegasus 1 and 2 penetration rates*

	Number of penetrations	Area-time (m^2 day)	Frequency of penetrations (number/m^2 sec)
Pegasus 1			
400 μ	**4**	**1925**	2.4×10^{-8}
200 μ	**9**	**248**	4.2×10^{-7}
40 μ	**104**	**858**	1.4×10^{-6}
Pegasus 2			
400 μ	**30**	**8457**	4.0×10^{-8}
200 μ	**14**	**734**	2.0×10^{-7}
40 μ (total)	**61**	**357**	2.0×10^{-6}
40 μ (showerpeak	**12**	**26**	5.3×10^{-6}
40 μ (sporadic)	**40**	**299**	1.5×10^{-6}

One possible explanation may be seen by comparing the time history of the 40-μ cumulative counts on Pegasus **2** ***(fig.*** **15)** with figure **14.** There appears to be a significant increase in counts during the period June **6** to June 12. It is interesting to note that this period corresponds with times of known meteor-shower activity, i.e., the Arietids and the ζ Perseids. If the shower events are subtracted from the Pegasus 2 counts, a sporadic background that is very close to the Pegasus 1 data is obtained. Of course, a reasonable explanation must be found for the nonobservation of the showers by Pegasus 1.

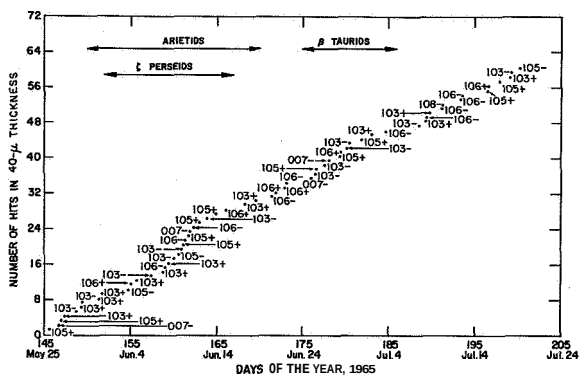

FIGURE 15.—Time history of accumulated penetrations for 40-μ panels on Pegasus **2.**

One plausible explanation may be found in the difference of the rotational behavior of the two satellites. Angular momentum in the form of rotation about the x axis was imparted to both spacecraft when the residual propellants were vented. Since the x axis is **a** principal axis of least moment of inertia, such a rotational state is quasistable far a semirigid body. Pegasus 1 underwent a transition to the minimum rotational energy state (i.e., rotation about the z axis, which is the axis of maximum moment of inertia) in **15** days. This rotation stabilized the sensor plane in space. Gravity gradient torque causes a precession of the rotational axis, which provides a relatively slow sranning **of** the celestial sphere.

The result **of** this motion may be seen in terms of the angle the sun makes nith the sensor plane shown in figure **16.** Preliminary analysis indicates that the normal to the sensor plane made angles **of** 50° tind 65° with the radiants

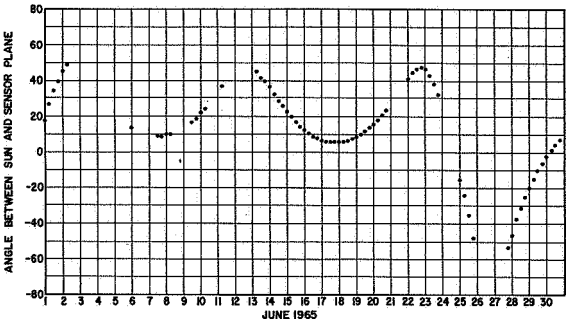

FIGURE 16.—Angle sun makes with Pegasus 1 sensor plane as a function of time.

of the Arietids and ζ Perseids, respectively, during the times of peak activity. Since the area presented to the shower direction is reduced by the cosine of the angle of incidence, and since the penetrtiting ability of an impacting meteoroid falls roughly as the $ power of the cosine of the angle of incidence, it is understandable that these showers may be missed by Pegasus 1. Of course, the deviation that was attributed to shower events in Pegasus 2 data is small and may very well be nothing more than a coincidental statistical fluctuation.

Pegasus 2, for reasons that are not yet completely clear, retained its rotation about the X axis. This rotational configuration, together with the lower angular momentum imparted to it, results in a more rapid precession of the rotational axis as is evident in figure 17, which shows the angle between the sun and the rotational axis. The motion is such that the entire celestial sphere is swept with the sensor axis in a period of a single day. Therefore, the observation of showers having a population of detectable particles sufficiently above the sporadic background is virtually assured.

The time histories of the 200-μ and 400-μ cumulative counts are shown in figures 18 and

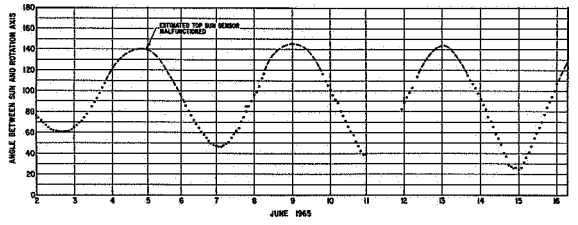

FIGURE 17.—Angle sun makes with Pegasus 2 rotational axis as a function of time.

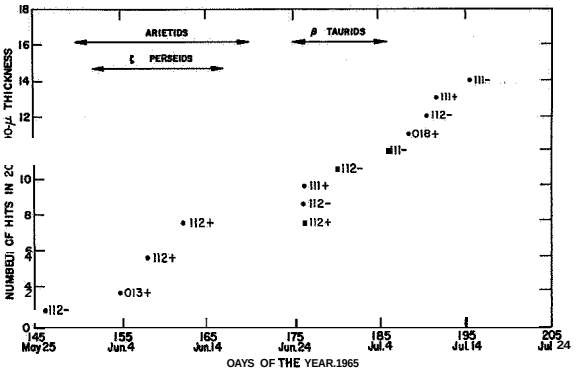

FIGURE 18.—Time history of accumulated penetrations for 200-μ panels on Pegasus 2.

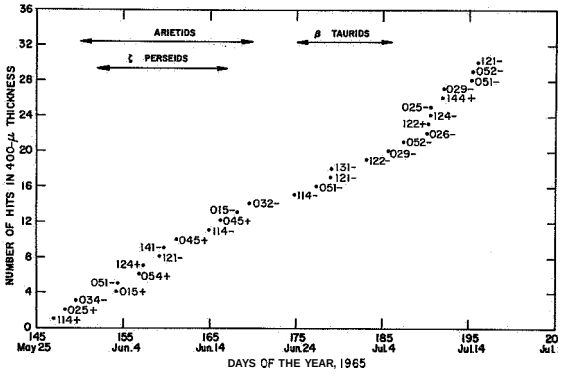

FIGURE 19.—Time history of accumulated penetrations for 400-μ panels on Pegasus 2.

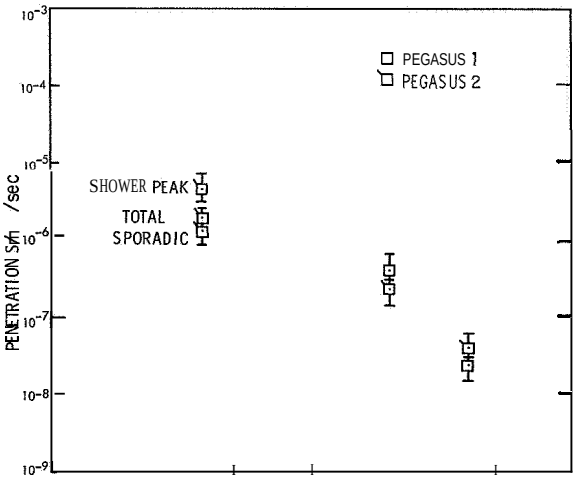

FIGURE 20.—Pegasus 1 and 2 penetration rates.

19. The sampling rates for these thicknesses are too low to see any shower effects.

The penetration rates in the various thicknesses for Pegasus **1** and **2** are shown in relation to one another in figure **20.** The error bars indicate 95 percent confidence limits.

Comparison of meteoroid penetration rates

In figure **21** the direct near-earth meteoroid penetration measurements obtained from Explorer **16** and Explorer **23,** as well as from Pegasus 1 and 2, are compared with a current estimate (Whipple, **1963)** of the expectation of frequency of meteoroid penetrations. The number of penetrations/m^2 day is plotted as a function of thickness for the penetration of aluminum sheets. The 0.0025-cm and 0.0051-cm Explorer **16** beryllium-copper-cell data, as well as the 0.0025-cm and 0.0051-cm Explorer **23** stainless steel-cell data, are plotted at equivalent thicknesses of aluminum based on laboratory impact tests wherein it was determined that the resistance to penetration of the beryllium copper and stainless steel is about twice that for aluminum. The bars on the satellite data indicate the statistical uncertainty in the direct measurements. With a **95** percent confidence, the actual value lies between the bars shown. There is reasonably good agreement between measurements obtained from the several spacecraft in spite of the fact that a number of refinements, as pointed out previously, have not yet been applied to the data. For the thinner materials, the rate of decrease of the frequency of penetration with thickness is seen to be considerably less than that previously estimated. **Also,** for the thin materials, there are approximately two orders of magnitude difference between the measured and the estimated penetration rates. On the other hand, the penetration frequency and the rate of change in thick materials are in better agreement with the estimates.

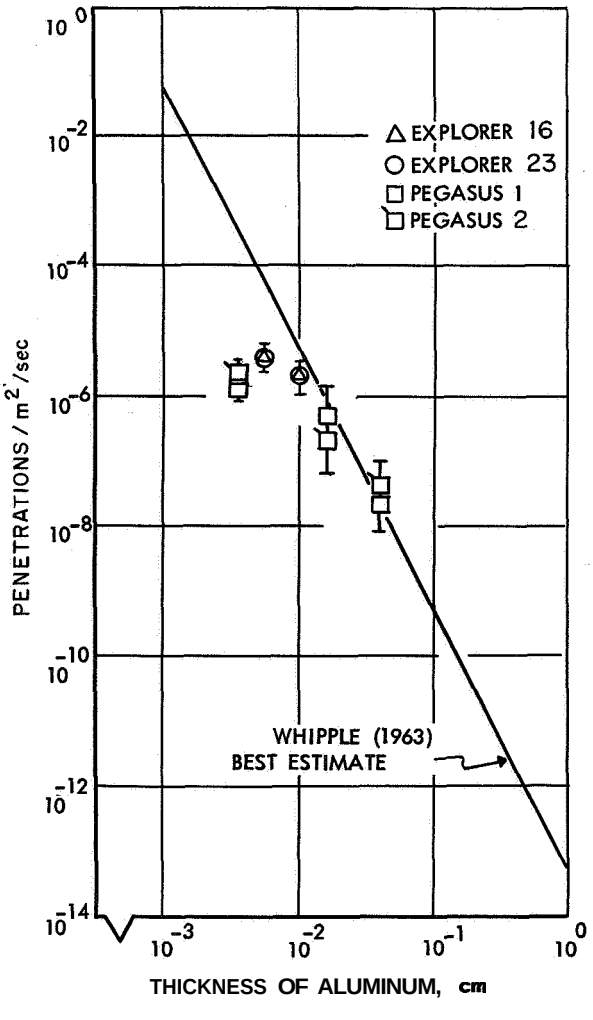

FIGURE 21.—Comparison of meteoroid penetration rates.

Concluding remarks

The direct meteoroid-penetration measurements by spacecraft have significantly narrowed the uncertainty in predicting the penetration frequency in materials approaching actual spacecraft skin thicknesses. Although the data obtained are extremely useful to spacecraft designers, measurements of penetration rates in thicker materials, which will correlate with ground-based observations, must be determined before a complete appraisal of the near-earth meteoroid hazard to space flight can be ascertained.

References

BJORK, B. L.
1961. Meteoroids vs. space vehicles. Amer. Rocket Soc. Journ., vol. 21, pp. 803–807.

D'AIUTOLO, C. T.
1964a. Review of meteoroid environment based on results from Explorer XIII and Explorer XVI Satellites. *In* Space Research IV, ed by P. Muller, North-Holland Publ. Co., Amsterdam, pp. 858–874.
1964b. Satellite measurements of the meteoroid environment. Ann. New York Acad Sci., vol. 119, pp. 82–97.

DAVISON, E. H., and WINSLOW, P. C., Jr.
1964. Micrometeoroid satellite (Explorer XVI) stainless steel penetration rate experiment. NASA Tech. Note D–2445, August.

HASTINGS, E. C., compiler
1963a. The Explorer XVI micrometeoroid satellite: Description and preliminary results for the period December 16, 1962 through January 13, 1963. NASA Tech. Memo. X–810, February.
1963b. The Explorer XVI micrometeoroid satellite, Supplement I: Preliminary results for the period January 14, 1963 through March 2, 1963. NASA Tech. Memo. X–824, April.
1963c. The Explorer XVI micrometeoroid satellite, supplement II: Preliminary results for the period March 3, 1963 through May 26, 1963. NASA Tech. Memo. X–899, September.
1964. The Explorer XVI micrometeoroid satellite, Supplement 111: Preliminary results for the period May 27, 1963 through July 22, 1963. NASA Tech. Memo. X–949, March.

SECRETAN, L.
1967. Measurements of interplanetary dust-particle flux from Explorer XVI CdS and wire grid dust-particle detectors. Smithsonian Contr. Astrophys., vol 11, pp. 307–315.

SUMMERS, J. L.
1959. Investigation of high-speed impact: Regions of impact and impact at oblique angles. NASA Tech. Note D–94, October.

WATSON, F. G.
1956. Between the Planets. Harvard Univ. Press, Cambridge, Mass., 188 pp.

WHIPPLE, F. L.
1958. The meteoritic risk to space vehicles. *In* Vistas in Astronautics, vol. 1, ed. by M. Alperin and M. Stern, Pergamon Press, London, pp. 115–124.
1963. On meteoroids and penetration. Jourii. Geophys. Res., vol. 68, pp. 4929–4939.

Abstract

The need for direct measurements in the space environment to determine meteoroid penetration rates for application to spacecraft design is discussed. Recent penetration measurements by the Explorer 16 and the Explorer 23 satellites and the Pegasus series of satellites are presented. The primary experiment on the Explorer satellites utilized thin-wall pressurized cells. These cells, covering an aggregate area of about 2 m^2 on each spacecraft, gave indication of meteoroid puncture by loss of internal gas pressure. Each of the large-winged Pegasus satellites measured meteoroid penetrations over a surface area of more than 200 m^2 by means of electrical capacitor-type detectors that discharge when penetrated. The large detector area on these spacecraft permitted the use of target materials up to 0.040 cm in thickness. The penetration statistics obtained to date from the satellites are presented and compared with estimates of expected penetration rates.

The satellite measurements appear to have reduced significantly the uncertainty in predicting the penetration frequency in materials approaching actual spacecraft-skin thicknesses. Further measurements are required, however, before an accurate mass-frequency distribution of penetrating meteoroids can be established.

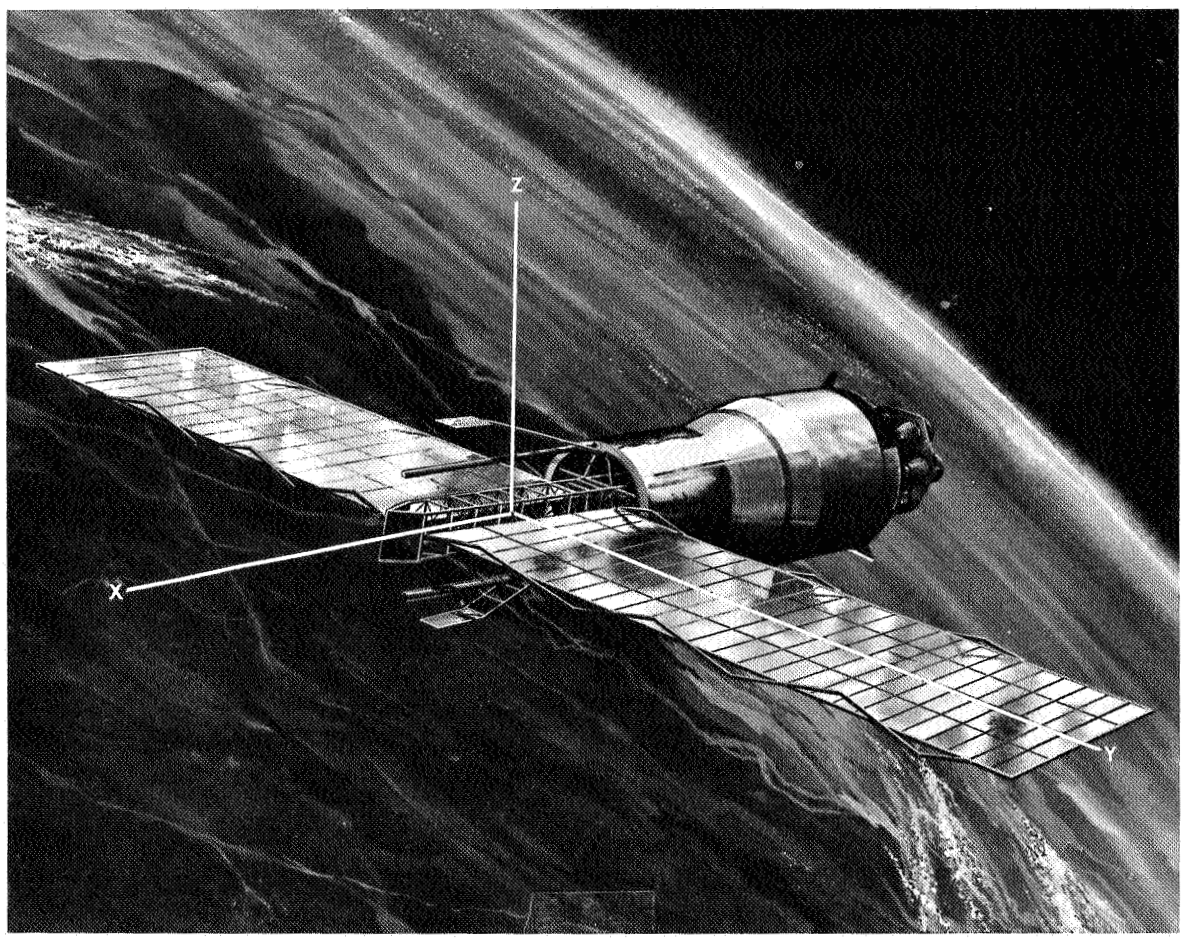

Pegasus satellite configuration with body-fixed coordinate axes indicated.

Some Penetration and Charge-Detection Techniques

R. C. JENNISON [1]

Between **1960** and **1964** the Space Research Group at the Nuffield Radio Astronomy Laboratories of the University of Manchester developed a number of techniques for the investigation of the dust particles in space. The first of the techniques to be flown were rocket-borne penetration detectors mounted on Skylark rockets launched at Woomera, Australia. The first series of launchings were not successful as a result of failures of the rockets, but the technique is of interest and has not been described in previous publications.

The Skylark rocket was fitted with **a** split nose cone, which could be separated and discarded at a height of about **60** km. Within the nose cone four roller blinds of aluminum foil about 1 m long and 10 cm wide were erected so as to be exposed to the space environment. The foils were supported by a pulley system, which was locked while the rocket was in the upper part of its trajectory but which could release the blinds so that they were withdrawn onto the rollers in armored cassettes when the vehicle descended to a height of **60** km. The cassettes were then sealed by the simple process of feeding an electrical current into a small resistor, which heated a loop of nylon thread and released a spring-controlled lid that locked into place over each cassette.

In the first rocket shots the roller blinds were double, spaced apart by about 1 cm over the whole of their length in the erected position but retracting together onto the same rollers when withdrawn into the cassettes. The reason for this arrangement was that it was hoped that if a particle penetrated the outer foil the second foil could also be examined for a coincident hole or signs of debris from the first impact; this would provide information on the impacting of the particles, help in the analysis of true punctures, and possibly provide information for the development of future techniques. Unfortunately, these early experiments were mounted on an ill-fated series of rockets that came to grief for a variety of reasons.

Similar equipment was later successfully launched, but on this occasion it was designed to study the impacts in aluminum foil bonded to mylar and no secondary foils were incorporated. In this experiment *six* holes were found in the foils when they were recovered and removed from the sealed cassettes. These holes were extensively analyzed and examined with high-powered microscopes. None of them was of the type that had been anticipated from hypervelocity impacts, for the holes were of various shapes, ragged and elongated, and it could not definitely be established that they were formed through the impact of the dust particles in space. Nevertheless, the holes were not there on the foils before launching and identical control foils, which were subject to similar treatment at Woomera but were not flown in the rocket, did not show any holes. It appeared that the holes in the flight foils must have been formed during the flight but might have resulted from fatigue of the aluminum. The foils were exposed in space for less than **10** min, so that if the holes were true dust-particle punctures the impact rate would be very high, commensurate with that claimed for the Venus Flytrap experiment. The research group had to be disbanded and it was not possible to follow up this result with a further series **of** rocket

[1] The Electronics Laboratories, The University of Kent, Canterbury, England: formerly at the Physical Laboratories, The University, Manchester, England.

shots, though it was highly desirable to sample the penetration rate, if it were real, at a number of heights in the atmosphere, as there was a possibility that the rocket penetrated a dust layer at about 80 km. A continuously moving roller blind would form the basis of a simple future experiment.

Ariel 2 experiments

An experiment to determine the distribution of particle sizes that could puncture thin aluminum foils was incorporated in the Ariel 2 satellite, which was launched on March 27, 1964. This experiment incorporated four sensor units, two of which were designated Instaneous-Read-Out Detectors (IRODs) and two were called Delayed-Read-Out Detectors (DRODs). All four units were arranged around the equator of the satellite and utilized the light from the sun, combined with the spin of the satellite, to scan the holes in the foil. The satellite had an initial spin rate of 5.5 rpm falling to 0 after 6 months. The apogee and perigee were 1358 and 289 km, respectively; the inclination of the orbit was 5107.

Instantaneous-Read-Out Detectors

These detectors were wedge-shaped, with the apex of the wedge parallel to the axis of the satellite and the base of the wedge mating to the cylindrical outer surface of the satellite. The base carried an aperture or slot 10¾ by 2 inches and the aluminum foil was wound very slowly from a full spool at one end to a take-up spool at the other end, behind the aperture. The foil width was approximately 4 inches, the extra 2 inches being taken up in light-tight, slotted guides at the edges of the aperture, and the wind-on occurred in discrete movements of about 1/16 inch every other time the satellite passed into the earth's shadow. A 7-inch strip of silicon solar cells approximately 1/16 inch wide was mounted in the apex of the detector parallel to the satellite spin axis. In contact with this strip, on the sensitive side nearest the aluminum foil, a molded epoxy resin cylindrical lens ½ inch in diameter served to enlarge the apparent width of the solar cells and reduce the resolving power of the system without appreciably reducing the electrical sensitivity. The triangular end covers of the wedge-shaped detectors were of aluminum alloy sheet, polished on the inner side to serve as mirrors so that the image of a hole in the foil could scan across the cylindrical lens and silicon cells when the sun was inclined at angles of up to 35° to the plane normal to the spin axis of the satellite.

The 10¾ by 2-inch aperture in the base of each detector had two struts on the inner surface between the foil and the cylindrical lens. These struts were 1 inch wide and were inset approximately 1/32 inch behind the foil. From the inside of the detector the struts appeared to divide the foil into three equal sections. They served to strengthen the detector while suppressing readout of the micrometeorite holes during the readout of calibration holes, which were mounted in line with the struts about 1 inch from the two mirror surfaces. The foils installed in the two detectors were 12-μ and 15-μ aluminum, respectively.

Both detectors used a Ledex solenoid-type actuator to wind on the foil in discrete steps of approximately 1/16 inch at a time. The Ledex had an angular movement of 25°, which was limited by a ratchet mechanism to about 15°, thus imparting the requisite motion to the take-up spool, which was ½-inch diameter before the foil was taken up. The gradually increasing effective diameter of the take-up spool resulted in an increase in the rate of wind-on, but this was not significant during the lifetime of the satellite.

The output of each silicon solar cell strip was amplified and then telemetered at a rate of 26 samples per second. Repeated scans of one foil could be combined later when analyzing the data to obtain a higher resolution. The detectors were scanned throughout alternate orbits, their outputs being switched in turn to the telemetry orbit by orbit.

Delayed-Read-Out Detectors

These units were designed to detect finer micrometeorite particles but could also record impacts by larger particles. They were much less sensitive to satellite spin than the Instantaneous-Read-Out Detectors but incurred an appreciable delay between the formation of the holes and the telemetering of the information concerning them.

The detectors employed an exposed area of aluminum foil bonded to mylar, which was wound on in discrete movements of approximately 1/16 inch across a rectangular aperture. The film in this case was wound on in a direction parallel to a spin axis so that holes in the main part of the foil were brought over strips of silicon cells by the wind-on action. Thus, resolution was achieved primarily by the wind-on action, while the problem of diffraction from the smallest holes was removed. Two flaps on either side of the aperture restricted the illumination onto the foil so that the sun swept across the strip of foil in front of the silicon strip and would, if there were a large flux of small penetrating particles, give rise to a triangular pulse lasting for 90° of the rotation of the satellite and having a height dependent upon the integrated flux of the smallest particles capable of penetrating the metal surface. Larger particles would cause rectangular pulses whose phases in relation to the calibration holes would determine their position across the width of the strip. Thus, larger holes could be resolved by the system in both the longitudinal and lateral directions.

The foils used in the DROD sensors were 5- and 9-μ thick. The foils in their virgin state were not free from pinholes, and for this reason two strips of silicon cells were employed in each detector, one on each end of the aperture, so that the foil was examined immediately before and after exposure to micrometeorites.

Calibration of the system was automatically performed by pinholes at the base of a slot immediately to one side of the detectors. These pinholes covered a section of the silicon cells and produced pulses immediately before the sun illuminated the foil.

The width of the strip of solar cells was 2.5 times the wind-on stepping distance, i.e., approximately 0.2 inch.

The outputs of the detectors were amplified and telemetered, each output being sampled three times a second. The beforeexposure outputs of two detectors were transmitted concurrently on separate telemetry channels for one orbit, and the after-exposure outputs were transmitted for the next orbit, and so on. A full account of the equipment has been published elsewhere (Jennison et al., 1965).

Performance in orbit

All four sensor units operated satisfactorily from the time of injection into orbit until the present. The spin rate of the vehicle fell to zero after 6 months and, although occasional readouts are still obtained, the analysis of data is confined to the first half year, and in particular to those periods when the attitude of the satellite was such that the sun was within $\pm 35°$ of the normal to the spin axis. The calibration holes of all the units gave clear and easily recognized signals, while a sequence of holes, preformed with a laser in the actual foils, also gave clear signals, which moved on in the correct manner relative to the calibration holes as the foils were transported across the sensors. Computer processing of the data will enable a very much higher sensitivity to be obtained than that apparent in figure 1, which was recorded directly from two successive spins of the telemetered data.

The analysis of the DROD data is not yet complete, but that for the IRODs covers most of the 6-month period. No holes have been detected that can be attributed to micrometeorites. A single hole appeared after 2 months exactly at the point where the foil enters the exposed aperture, and it was transported across the aperture during the succeeding days. This hole was almost certainly a defect in the virgin foil that had either escaped observation on the preflight examination, or from which the small blob of black paint, applied to such defects, had become detached. Nevertheless, there is a slight possibility that this hole could have been formed by a micrometeorite that impacted at the extreme end of the exposed surface.

Upper limits for the penetration rates of the foils are shown in figure 2, with the abscissa marked in microns. The IROD limits shown

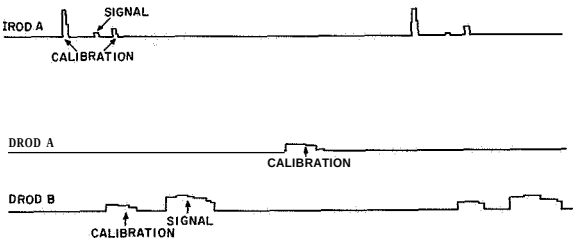

FIGURE 1.—Telemetry output.

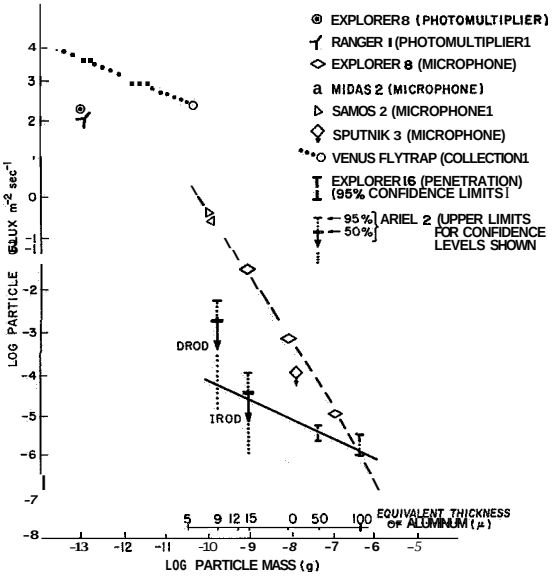

FIGURE 2.—Cumulative flux of particles.

are those for 15-μ aluminum, and the DROD limits correspond to the incomplete analysis of the 9-μ foil. The thick bars across the vertical arrows indicate 50 percent confidence limits, and the dotted vertical extensions give the limits for 95 percent confidence.

The most definitive result of the experiment concerns the hazard from the micrometeorite particles in space. The penetrating power of the smaller particles appears to be such that the lifetime for the survival of thin surfaces is many orders of magnitude greater than that anticipated when the experiment was designed. Not only is the penetrating power of the average particle very low but less than one in a thousand of those detected by microphones within the range of sensitivity of the Ariel 2 detectors could have a mass commensurate with a solid particle of iron or stone. The results indicate that the density of the particles is probably very small and the radiation pressure limit for the particle size is probably considerably higher than most earlier estimates.

Charge-detection techniques

A technique was developed some years ago that has considerable possibilities for determining a number of parameters associated with the dust particles. Unfortunately, although a rocket payload was prepared, the closing down of the group's activities in space research resulted in the premature abandonment of the project.

The technique detects the dust particle by virtue of any electrostatic charge it may have. The charge q_m is related to the potential of the surface of the micrometeorite V_m by the micrometeorite self-capacity, which in electrostatic units equals the radius of the particle r_m: $q_m = r_m \cdot V_m$.

In an ionized medium the currents formed by the processes of emission and capture of ions are both proportional to the area of surface considered, and thus the potential of particles in space remains largely independent of the particle dimensions. It is the potential, and not the charge, that remains the common parameter of bodies in space of differing dimensions but of similar surface properties.

The ion-capture current is a function of the potential of the micrometeorite; if the micrometeorite is negatively charged up to a voltage of, say, V volts, it will repel all electrons up to an energy of eV electron volts. If it is positively charged it will attract electrons, constituting an effective area of capture very much greater than its physical area. Estimates of the micrometeorite potential differ by a small factor and are dependent on environmental conditions that have not been fully established. The processes affecting the variation of micrometeorite potential in differing environmental conditions are, however, reasonably well understood quantitatively. In the Van Allen belts, capture of the flux of energetic electrons causes a negative micrometeorite potential. In the F2 regions, where there is a high concentration of thermal energy electrons, the potential may again assume a negative value, but of lower magnitude.

If the dust particle is illuminated by the sun, a certain fraction of the absorbed photons will create photoelectrons over a wide range of energies. The photoelectrons of low energy may return to the micrometeorite under the influence of its potential if this is positive, but those of energy greater than the micrometeorite potential will escape completely from the micrometeorite, the effect of which is to cause the equilibrium potential to become less negative.

This photoelectric current is insufficient to cause the potential of the dust particle to

become positive in the Van Allen and F2 regions, but may do so at greater distances from the earth where the concentration of electrons is less than a value of the order of $100/cm^3$. As the potential increases beyond a value of +6 V, corresponding to the energy of the Lyman emission, there is a reduction of one order of magnitude in the photoelectric current.

These considerations render it unlikely that at. all distances from the earth the environmental conditions will be so well balanced as to maintain a micrometeorite potential of lower than several volts. A potential of 5 V on a spherical dust particle of radius 1 μ corresponds to a charge of 3×10^3 electrons. The charged particle may be detected in a passive system in which it is allowed to pass through a hollow cylindrical detector that is suitably screened from various sources of interference. The induced signal is independent of the satellite potential; it is probable that the satellite and micrometeorite will be at similar potentials, but even if the two potentials are identical the micrometeorite charge will still be detected.

If the micrometeorite radius is $r\mu$, the potential is V_m volts, and the total input capacity of the detecting system is C_d picofarads, then the signal voltage is given by

$$V_s=\frac{111\cdot r_m\cdot V_m}{C_d}$$

It has been shown (Jennison and McDonnell, 1964) that this voltage may be clearly detected against the background noise in a transistor amplifier using a high-impedance field-effect transistor in the input stage.

A single detector in the form of a hollow cylinder will provide a pulse from which the micrometeorite charge may be obtained. A second detecting cylinder makes it possible to determine the time separation of the two pulses and thus to derive the micrometeorite velocity. The particle is not affected in passing through the cylinders, and the two detectors may be followed by a microphone sensor that is sensitive to a function closely related to the micrometeorite momentum. By combining this measurement with the measurement of velocity from the two detecting elements, the velocity and mass of each micrometeorite may be obtained. The complete system is sensitive to particles in a relatively small solid angle and may be used to determine the radiants of the detected particles, but the price paid for this is a considerable reduction of the flux of detectable particles.

The original technique was capable, in principle, of detecting micrometeorites greater than 3-μ diameter (3×10^{-12} g for a density of 0.3 g/cm^3), and even more sensitive if potentials of greater than 5 V exist on micrometeorites in space. Greater sensitivity may be obtained by the use of improved components.

References

JENNISON, R. C., and MCDONNELL, J. A. M.
1964. A technique for the detection and determination of the velocity, mass, radiant, charge and flux of micrometeorite particles in space. Planet. Space Sci., vol. 12, pp. 627–635.

JENNISON, R. C.; MCDONNELL, J. A. M.; RODGER, I.; and SMITH, M.
1965. Proo. Inst. Electronics, vol. 8, no. 1.

Direct Measurements of the Mass Distribution and Time Variations in the Flux of Small Dust Particles

C. W. McCracken,[1] W. M. Alexander,[2] and M. Dubin [3]

Introduction

Dust-particle sensors mounted on rockets, satellites, and space probes have been used extensively during the past decade for studying small dust particles outside the atmosphere of the earth. The sensitivities of the sensors ranged from about 10^{-6} to 10^{-13} g, and most of the data were obtained in the range of dust-particle mass 10^{-8} to 10^{-11} g. These studies yielded information concerning (1) the flux of small dust particles, both in the vicinity of the earth and in interplanetary space, (2) the mass distribution for dust particles in the vicinity of the earth, and (3) the time variations in the flux near the earth. Most of the data relating to the mass distribution and the time variations in the flux were obtained with the microphone type of dust-particle sensor flown on near-earth satellites.

A summary and analysis of the available direct measurements of small dust particles were given earlier (Alexander et al., 1963). The direct measurements obtained by various investigators with several types of dust-particle sensors were found to be in good agreement with the mass distribution that was measured with the microphone system on Explorer 8. An obvious lack of statistically valid data, which could be used for investigating a possible decrease in the flux of small dust particles with increasing geocentric distance, was noted. The somewhat lower flux measured with the microphone system on Pioneer 1 was considered to be indicative of a radial decrease in the flux, but the data sample was limited (17 impacts at geocentric distances ranging between 2 and 19 earth radii). If we allow for a possible decrease in the mean relative speed of the particles with increasing geocentric distance, the flux measured with Pioneer 1 comes within the range of the time variations in the flux measured with the microphone system on Vanguard 3. An indirect (but quite sound) argument for the existence of a geocentric enhancement of the flux of small dust particles was provided by Whipple, who pointed out that the flux measured in the vicinity of the earth was several powers of 10 higher than the flux expected in interplanetary space on the basis of studies of the zodiacal light and solar F corona.

Additional data on the flux of small particles near the earth were obtained with a set of penetration-type dust-particle sensors flown on Explorer 16 (D'Auitolo, 1964). These data indicated that the penetrating flux was 10 to 100 times lower than had been expected on the basis of the flux measured with microphone systems. This discrepancy, if real, might be interpreted in terms of a low penetrating power for particles of the sizes measured by the two different types of sensors. It could occur if dust particles with radii between about 10 and 100 μ have irregular shapes and a fluffy or dendroidal structure and are therefore less effectivein penetrating a target than is a dense particle of comparable mass. Another possible explanation is that a size-dependent parameter

[1] Goddard Space Flight Center, National Aeronautics and Space Administration, Greenbelt, Md.
[2] Temple University, Philadelphia, Pa.; formerly at Goddard Space Flight Center, National Aeronautics and Space Administration, Greenbelt, Md.
[3] National Aeronautics and Space Administration, Headquarters, Washington, D.C.

is present in the hypervelocity cratering formulas used in calculating the sensitivity for penetration-type sensors. These penetration criteria axe, for the most part, based on laboratory studies of craters formed by larger particles than those registered in space by penetration-type dust-particle sensors. The apparent discrepancy that has arisen between the results obtained with the microphone systems and the penetration-type sensors requires further investigation.

This paper was to have been a review of the data obtained with the microphone type of dust-particle sensor. With the exception of the new data from the microphone systems on Mars 1, Elektron 2, Mariner 4, and OGO–1 being presented at this symposium, only the data from Mariner 2 are to be added to the information summarized in the earlier review. We shall discuss anew some aspects of the older data obtained with microphone systems and of the bearing of these data on the problems of the mass distribution and time variations in the flux of small dust particles. In addition, we shall include the latest available readout of the data obtained with the microphone systems on Vanguard 3 and Mariner 2.

Neither the Soviet nor the U.S. investigators have succeeded in obtaining statistically valid measures of the flux in cislunar space that could be used in establishing the radial dependence of the geocentric enhancement of the flux of small dust particles. The data included in this review clearly limit our discussions to the immediate vicinity of the earth.

Time variations

The first evidence for large time variations in the flux of small dust particles was obtained with the microphone system flown on Explorer 1 (Dubin, 1960a). The impacts of 145 dust particles were registered on a real-time telemetry basis during a 12-day interval following launch on February 1, 1958. An interval of enhanced flux occurred approximately 38 hours after launch and persisted for about 15 hours. This interval accounted for 67 of the 145 recorded impacts; thus, 46 percent of the impacts occurred during only 6 percent of the time for which telemetered data were received.

The maximum number of impacts recorded during any one pass over a telemetry station was 12. These 12 impacts occurred during an interval of 261 sec beginning at 0141 UT, February 3. The corresponding impact rate (2.8 impacts/min) was the highest recorded during the interval of enhanced flux and was higher by a factor of 25 than the average impact rate (0.11 impacts/min) for the entire 12-day interval.

Although the sample time and the number of impacts recorded for any one given telemetry pass are small, the interval of enhanced flux actually can be traced for a 23-hour interval between the two passes beginning at 1512 UT, February 2, and 1405 UT, February 3. The systematic dependence of the impact rate on the position of the satellite during this interval is shown in figure 1. The apparent shielding of the satellite during the early morning passes and the dependence of impact rate on position suggest that the swarm of dust particles in this sporadic shower may have overtaken the earth in the manner that would occur if the dust particles had noncircular heliocentric orbits of fairly low inclination.

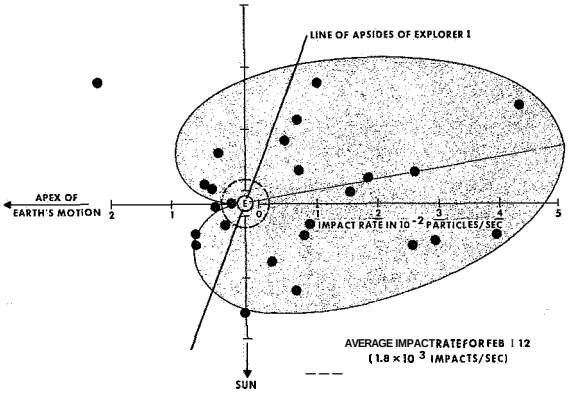

FIGURE 1.—Dependence of impact rate on the position of Explorer 1 during the dust-particle shower on February 2 and 3, 1958.

Nazarova (1960) reported that the microphone system on Sputnik 3 recorded a flux of 4 to 11 particles/m²/sec on May 15, 1958, which was the day of launch. The flux subsequently decreased by a factor of 10^4 to a level of 5×10^{-4} particles/m²/sec for May 16 to 17. The flux during the remainder of the sampling interval (May 18 to 26) was less than 10^{-4} particles/m²/

sec. The exact number of impacts recorded by Sputnik 3 is not available to us.

A microphone system on Vanguard 3, launched on September 18, 1959, recorded the impacts of 6307 dust particles during 80 days of continuous operation. The experiment included a cumulative counter, which was read out during passes over telemetry stations (Alexander and LaGow, 1960). The known time history for the cumulative counter defines both the number of real-time impacts recorded during each telemetry pass and the total number of impacts recorded between successive telemetry passes.

Of the numerous experiments performed by us, only two are known to have been subject to interference problems. The data from OSO–1 obtained with a combination microphone and photomultiplier type of dust-particle sensor (like the one flown successfully on Ranger 1) have never been presented, because interference appeared during the flight. The other system for which interference occurred was the microphone system on Vanguard 3. Interrogation of the magnetometer sometimes caused the cumulative counter in this microphone system to advance by one or more counts.

Almost complete recovery of the data from the microphone system on Vanguard 3 was accomplished by Messrs. C. M. Stout and R. D. Carper, whose painstaking and time-consuming work is gratefully acknowledged. Corrections were applied for the false counts observed to be caused by interrogations of the magnetometer, leaving 6307 indicated impacts of dust particles. There were some interrogations of the magnetometer that could not be monitored because of loss of signal, poor signal-to-noise ratio, lack of telemetry coverage, etc. Some of the unmonitored interrogations, like many of the monitored interrogations, are known to have caused no false counts because the settings of the cumulative counter were identical before and after the interrogations.

An estimated 5 percent of the 6307 indicated impacts may have been caused by the unmonitored interrogations. It may therefore be said, with reasonable confidence, that the microphone system on Vanguard 3 registered the impacts of approximately 6000 dust particles during the 80 days of continuous operation extending from 0735 UT, September 18, to 2321 UT, December 6, 1959. Impact rates and fluxes for intervals of less than 80 days are, for lack of complete restoration of the data, computed on the basis of the 6307 impacts listed in the processed data, which had been corrected for the false counts caused by monitored interrogations of the magnetometer. The data presented here are based on the best available processed data from Vanguard 3 and, as such, supersede the data presented in earlier papers (Alexander and LaGow, 1960; Alexander, McCracken, and LaGow, 1961). A more detailed discussion of the time variations is therefore possible.

The recovered data from Vanguard 3 established the time dependence of the flux of dust particles during the mid-November 1959 dust-particle event (Alexander, McCracken, and LaGow, 1961), which was the most spectacular dust-particle shower observed through the use of satellites. During the 3-day interval extending from 0122 UT, November 16, to 0054 UT, November 19, 2436 of the 6307 impacts occurred. This interval constitutes only 3.8 percent of the sampling time but accounts for ~40 percent of the recorded impacts. The impact rates during this interval are shown in figure 2. The data for November 16, 17, and 18 are shown on an expanded time scale and have been filtered to the extent that sampling intervals of less than 30 min are combined with

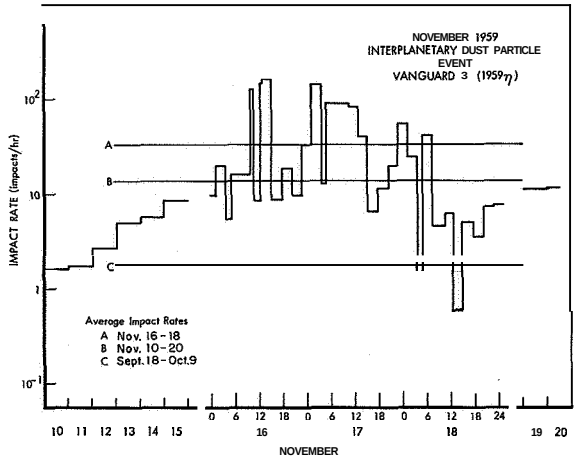

FIGURE 2.—Time variations in the impact rate during the dust-particle shower observed with Vanguard 3 in mid-November 1959.

adjacent intervals. The daily average impact rates are shown for the remainder of the rather arbitrarily chosen 10-day interval extending from November 10 through November 20.

The highest impact rate occurred during a real-time pass at 0336 UT, November 17, when 190 ± 5 impacts were recorded in 7^m19^s. This interval does not appear in figure 2 because of filtering, but the impact rate (1560 impacts/hour) lies outside the range of the logarithmic ordinate that is used. The highest impact rate shown in figure 2 is based on 363 impacts recorded in 2^h3^m on November 16, while the next highest is based on 351 impacts recorded in 2^h30^m on November 17. At the opposite extreme is an interval of 2^h18^m on November 18 during which no impacts were recorded, although the impact rate on this day was 249 impacts/day or about 10 impacts/hour.

The number of impacts recorded on each day during the 80 days of operation of the microphone system on Vanguard 3 is shown in figure 3. Day-to-day variations in the daily count are considerably larger than the variations expected on the basis of the counted numbers of impacts. The lowest count was 8 impacts on October 22, and the highest was 1354 impacts on November 17. The daily counts do not apply for sampling intervals of exactly 24-hour duration, since the sampling intervals were set by the location of the telemetry stations. The daily counts are therefore converted to daily impact rates, which are presented in figure 4.

Figure 4 also shows the 80-day mean and the 10-day means of the daily rates. Error flags denoting one standard deviation of the daily impact rates from the 80-day mean and each

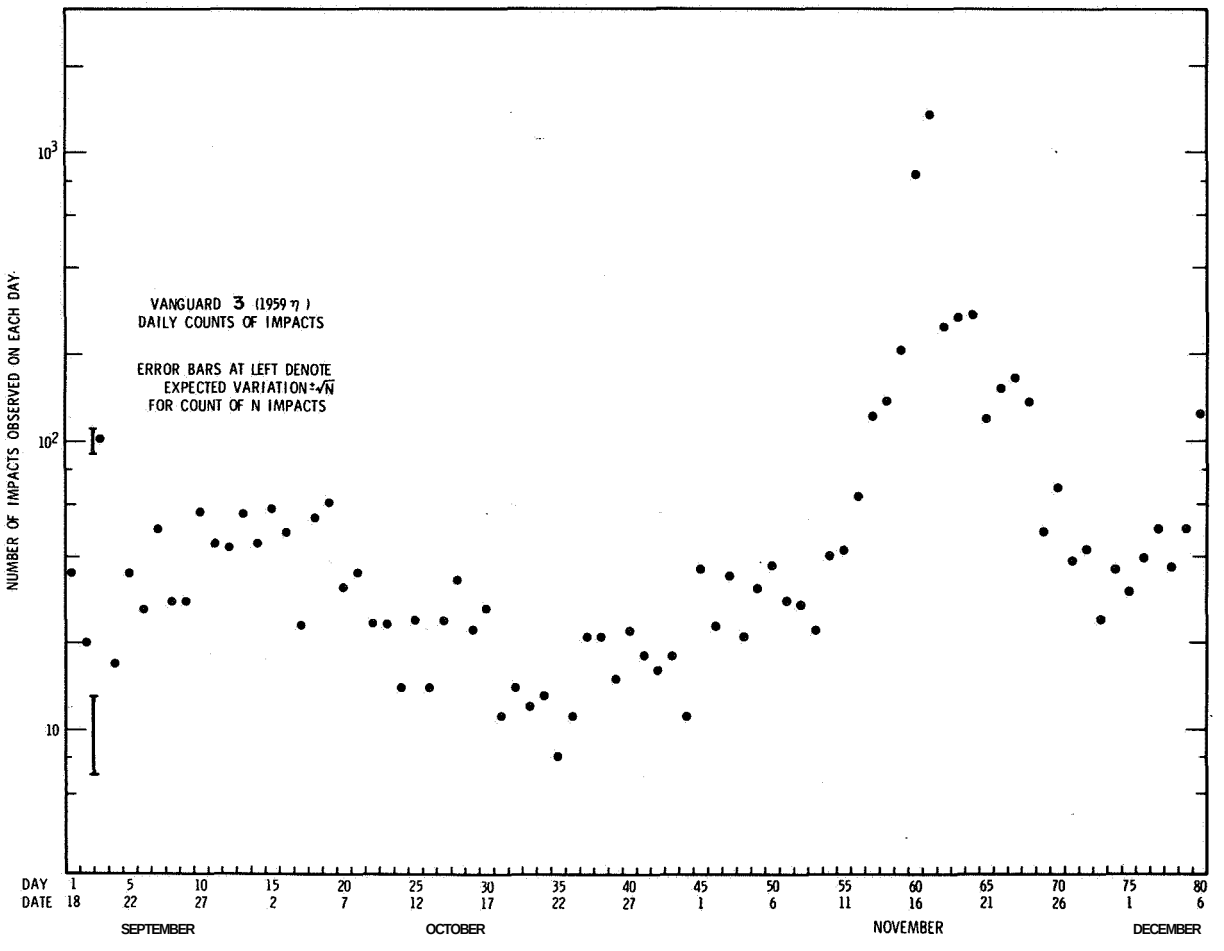

FIGURE 3.—Daily counts of dust particles recorded with the microphone system on Vanguard 3.

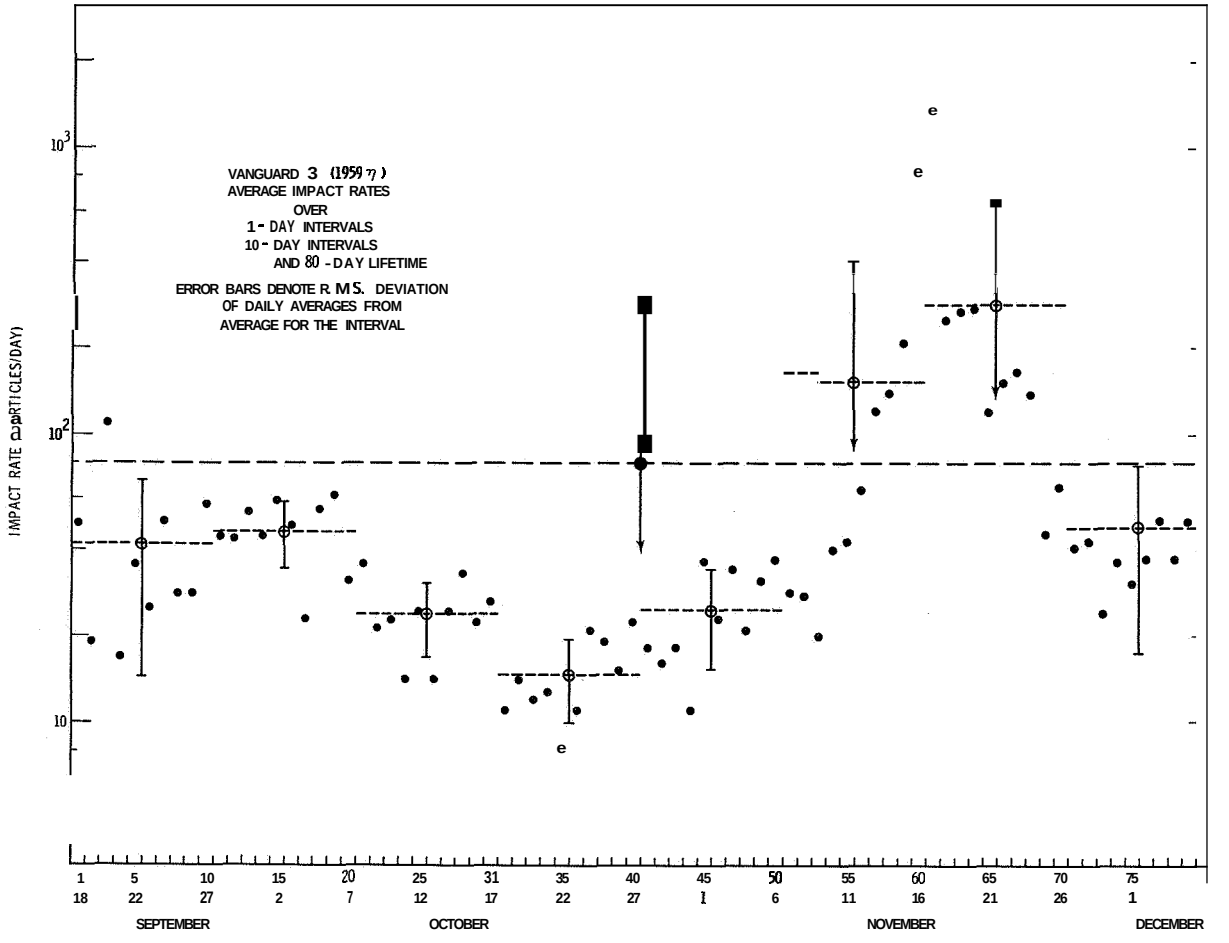

FIGURE 4.—Daily impact rates and means over various intervals for the dust particles recorded by Vanguard 3.

of the 10-day means are included. The standard deviation from the 80-day mean is larger than the 80-day mean of the daily impact rates, so the lower end of the error flag cannot be shown on the logarithmic ordinate used in figure 4. Similarly, the standard deviations for two of the 10-day intervals are larger than the 10-day means of the daily impact rate. In figure 4 numerous cases are apparent where the daily impact rate easily changes by a factor of 2 from one day to the next.

The logarithmic ordinate and linear abscissa used in figure 4 are reminiscent of the decay curves used in determining the half-life of a radioactive element. The half-life for the mid-November 1959 dust-particle shower can be read directly from figure 4 and is about 2 days. The rapid decay rate for the flux does not at all suggest that the dust particles were trapped into closed geocentric orbits with long lifetimes.

It has been suggested that the mid-November 1959 dust-particle shower might have been associated with the Leonid meteor stream (Alexander, McCracken, and LaGow, 1961). Leonid meteors show high speeds (-70 km/sec) because the meteoroids meet the earth almost head on. Neither gravitational concentration nor the action of radiation pressure is effective for such high speeds in increasing the accretion cross section of the earth above the geometric cross section. Any geocentric enhancement of the flux of small dust particles associated with the Leonid stream must have proceeded from the level of the flux in the stream rather than from the higher level of the average flux near the earth. Such an association seems to be very doubtful when the incremental mass

influx (which emphasizes the amount of material rather than the number of dust particles) is considered.

During the 80 days of operation, there were 112 cases where Vanguard 3 completed one or more orbits (a period of 130 min) without registering the impact of a single dust particle. The longest interval showing zero impacts was 15^h15^m in duration (7 orbits) and occurred on October 20. The durations of the intervals generally appear to exceed those expected statistically for random variations in the impact rate. The complete interval distribution cannot be established, because the intervals between individual impacts are not known. The existence of the long intervals (1 to 7 orbits) that showed no impacts provides considerable assurance to the experimenters that the microphone system on Vanguard 3 was not subject to environmental interference (thermal, electrical, and energetic-particle radiation) beyond the previously discussed interference from the magnetometer.

Only 417 of the 6307 impacts registered by Vanguard 3 were recorded while real-time telemetry was being received. Of these, 190 ± 5 impacts occurred in 439 sec during the previously mentioned pass at 0336 UT on November 17, 27 ± 5 occurred in 492 sec during a pass at 2026 UT on November 16, and 31 occurred during a pass at 0414 UT on December 6. The remaining 169 impacts were distributed throughout the remainder of the 80 days to yield an average of 2 impacts/day. This low rate precludes determining the dependence of the flux on the position of the satellite from the impacts recorded during telemetry passes. Attempts to use the numbers of impacts recorded between successive telemetry passes in lieu of real-time impacts for investigating the dependence of the flux on position of the satellite, altitude of the satellite, phase of the moon, etc., have also failed to yield any results of statistical significance because of the effect of the terrestrial distribution of telemetry stations on the sampling intervals. Further investigations will have to wait until more definitive data can be obtained.

The microphone system on Explorer 8 included a cumulative counter that was read out in the same manner as for Vanguard 3. All impacts registered by the microphone system on Explorer 8 were stored in the cumulative counter, but alternate impacts were included in the telemetered data. Recovery of the data from Explorer 8 to the extent accomplished for Vanguard 3 is not feasible. Although the data obtained on Explorer 8 were insufficient for studying time variations in the flux, it was possible to determine the total number of impacts recorded for each of the three levels of sensitivity during the 40 days of continuous operation. No evidence for the occurrence of intervals of enhanced flux like those observed with Explorer 1 and Vanguard 3 appears in the data from the microphone system on Explorer 8.

Mass distribution

Establishing a mass distribution for the small dust particles studied through the use of spacecraft involves measuring the flux as a function of some observable parameter for the dust particles. Microphone systems employing piezoelectric crystals respond very accurately to the momentum for spherical glass beads dropped at normal incidence and low speeds during laboratory calibrations of the systems. If we assume that microphone systems respond also to the momentum for dust particles impacting at high speeds, we can express the measured flux as a function of the particle momentum. The transformation from momentum to mass is then accomplished by assuming an average speed for the dust particles registered by a microphone system. The small uncertainties introduced by these assumptions will be discussed after a brief review of the available data.

The spacecraft, which carried microphone systems, and the number of dust particles recorded by each are listed in table 1. Other numerical data pertinent to the various systems (except for Mariner 2) were given in the earlier summary (Alexander et al., 1963). The microphone system on Mariner 2 recorded the impacts of two dust particles between the orbits of the earth and Venus. Telemetry was available for approximately 75 days out of the 90-day flight. The area of the sensor was 350 cm^2, and the sensitivity of the system was 7.4×10^{-4} dyne sec (Alexander, 1962). The

omnidirectional flux computed on the basis of the two impacts is 2.1×10^{-5} particles/m²/sec. The power for the instrument was applied when the spacecraft was approximately two lunar distances from the earth, so the flux indicated by Mariner 2 applies strictly to interplanetary space. The small number of impacts was roughly what was expected on the basis of studies of the solar F corona. Technological limitations and the time schedule simply prevented the building of a more sensitive instrument at the time the design for the system was set.

Table 1 shows that more than 10,000 impacts of dust particles have been recorded with microphone systems. (The data given by Nazarova (1963) can be used to calculate that a few hundred dust-particle impacts were recorded by Sputnik 3 and the three Soviet Geophysical Rockets.) The impacts registered by the microphone systems on Mars 1 and Elektron 2 (Nazarova, see pp. 231–237) and those on Mariner 4 and OGO–1 (Alexander et al., see p. 227) will bring the total to more than 11,000 dust particles. Since almost 10,000 impacts were recorded on Explorer 8 and Vanguard 3, we depend very heavily on these results of continuous operation (—3700 impacts during 40 days and —6000 impacts during 80 days, respectively).

The data obtained with microphone systems are shown in figure 5 as a cumulative flux distribution expressed in terms of the particle mass. This figure (which is figure 2 in Alexander et al. (1963) with the data from the photomultiplier type of dust-particle sensors deleted and the data from Mariner 2 added) should be revised after further information has been obtained regarding (1) the geocentric trajectories of the small dust particles, (2) the average speed for small dust particles at various geocentric distances, and (3) the response of microphone systems for dust particles having speeds of at least 15 km/sec. The revisions have a tendency to counteract one another, and when the necessary information becomes available, corrections will probably leave the cumulative mass distribution shown in figure 5 relatively unchanged. Hence revision of figure 5 through the use of assumed values for the correction factors hardly seems worth while at the present time. A discussion of the magnitudes of the corrections, as they are currently

TABLE 1.—*The numbers of dust-particle impacts recorded on microphone systems mounted on various vehicles*

Vehicle	Number of dust particles
Explorer 8	3726
Vanguard 3	—6000
Explorer 1	145
Pioneer 1	17
Ranger 1	64
Midas 2	67
Samos 2	157
SLV–I	10
OSU Rockets	287
Sputnik 3	(?)
Lunik 1	<16
Lunik 2	7
Interplanetary Station	2
Soviet Geophysical Rockets	(?)
Manner 2	2
Total	—10,500

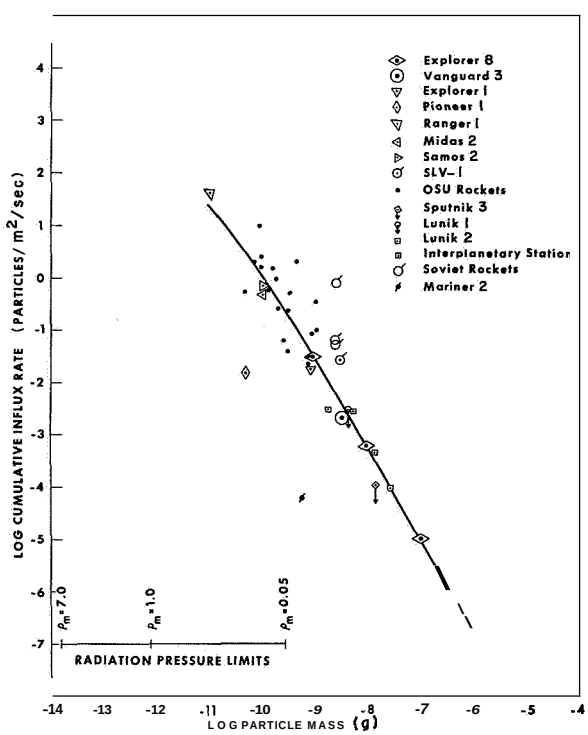

FIGURE 5.—Cumulative flux distribution showing the data obtained with microphone systems.

known, should serve equally well until experimentally determined values for the corrections become available for use in a realistic revision of the cumulative mass distribution.

The corrections applied for shielding of a sensor by the earth and for the effective solid angle of a sensor depend on the distribution of orbits for the dust particles. The present lack of knowledge concerning the geocentric trajectories of small dust particles leaves the omnidirectional flux uncertain by a factor of about 2, which is much smaller than the time variations in the observed flux. The ordinate used in figure 5 refers to the omnidirectional flux (reduced to 4π ster). A flux expressed in units of 2π ster is physically more meaningful because of both the general lack of omnidirectionality for dust-particle sensors and the presence of shielding by the earth for sensors mounted on rockets and near-earth satellites. Revision of figure 5 would therefore be accompanied by a change from omnidirectional flux to a flux expressed in units of 2π ster.

In the original version of figure 5 we assumed that the average speed of dust particles detected by an omnidirectional microphone on a near-earth satellite was 30 km/sec. We assigned different values for an average speed for the various spacecraft because some of the sensors did not scan the whole celestial sphere. The existence of the geocentric enhancement of the flux of small dust particles now requires the assumed average speed to be reduced from 30 km/sec to about 15 km/sec, which changes the mass sensitivity of the microphone systems only by a factor of 2. Reduction of the assumed average speed used in converting from momentum sensitivity to mass sensitivity for the microphone systems will shift the results shown in figure 5 toward slightly larger values of particle mass by factors ranging from about 1.5 to 4, depending on the particular set of data. This small correction and the correction that may be required if the average speed varies appreciably with geocentric distance are better left until information, about the geocentric trajectories of the dust particles can be obtained so that the revision will be more realistic and more accurate than one based on assumed values for the average speed.

The magnitude of the small correction required by the reduction of the assumed average speed depends on the assumption that microphone systems respond to the momentum of an impacting dust particle. Öpik's (1958) theory of hypervelocity impact predicts that the impulse delivered to a target will be about three times the momentum of the projectile. The effective coefficient of restitution for high-speed impacts would therefore be about 2, provided the microphone systems respond *to* the impulse delivered by an impacting dust particle. The effective coefficient was purposely set equal to zero in stating the sensitivities for several of the microphone systems, pending a determination of the correct value. The sensitivities given for other microphone systems were based on the assumption that the effective coefficient of restitution is unity, while the effective coefficients of restitution that apply for the Soviet results are unknown to us. Despite attempts to handle all the data shown in figure 5 in a consistent manner, inconsistencies have unfortunately appeared through the use of different values for the effective coefficient of restitution. Use of an effective coefficient of 2, as predicted by Öpik (1958), rather than the values of zero and unity that were used, serves to shift the results shown in figure 5 toward smaller values of particle mass by factors as large as 2. The required corrections for the most part cancel one another.

The assumption that microphone systems respond to the momentum of a high-speed particle has been the subject of considerable controversy. There is a lack of hypervelocity particle accelerators that could be used for realistically calibrating microphone systems (like those on the spacecraft listed in table 1) with particles having accurately known masses and speeds. The Soviet investigators have assumed, on the basis of the hypervelocity cratering theory of Stanyukovich, that their microphone systems respond to the kinetic energy of a dust particle impacting at high speed. The U.S. investigators have assumed that their microphone systems respond to the momentum of an impacting dust particle. This assumption is supported by the hypervelocity

cratering theory of Öpik. Despite the different assumptions, the results reported by the two groups are in fair agreement concerning the flux of dust particles of any given mass.

There are some experimental data that support the assumption that microphone systems respond to the momentum of a dust particle impacting at high speed. Calibrations performed at the Stanford Research Institute showed that systems using crystal microphones constructed by Professor J. L. Bohn of Temple University responded (within a factor of 2) to the particle momentum for steel spheres accelerated by shaped charges to speeds as high as 4 km/sec (Dubin, 1960b). The microphones used in the systems on Explorer 1, Pioneer 1, and the U.S. rockets were all constructed by Professor Bohn.

A converted 2-Mev van de Graff machine is now being used routinely in calibrating microphone systems with iron carbonyl particles having speeds that range up to 3 km/sec. These calibrations show that microphone systems somewhat more sensitive than those with which the data in figure 5 were obtained respond (within a factor of 2) to the momentum of a high-speed particle. Preliminary results for particles having speeds as high as 8 km/sec indicate that the effective coefficient of restitution is appreciably larger than unity.

We assume that the microphone systems represented in figure 5 responded to the momenta of impacting dust particles. The cumulative flux distribution shown is uncertain by the small factors previously discussed in connection with the revision known to be required for figure 5. The results could shift considerably in particle mass if the effective coefficient of restitution should prove to be markedly greater than unity. It is unlikely that any such shift would alter the slope of the distribution curve. A small change in slope could conceivably occur if the average speed is a function of the particle mass, but such an effect surely must be negligible for the range of particle mass encompassed by the direct measurements shown in figure 5. The presence of a size-dependent parameter in the hypervelocity cratering process might also cause a small change in the slope of the distribution. The suspected (or demonstrated) presence of such a size-dependent parameter would require further evaluation of the apparent discrepancy between the results obtained with the microphone type and the penetration type of dust-particle sensor.

It is evident from figure 5 that there are two basic ways in which to establish the mass distribution of small dust particles. The first involves the use of a microphone system having several levels of sensitivity that encompass a range of several powers of 10 in the particle mass. The second involves the use of a system with a single level of sensitivity or one with two or more levels of sensitivity that are limited in effectiveness by either close spacing or a limited data sample. The latter approach requires accumulated data from several flights of systems with different sensitivities; it is also necessary to assume that the flux remains fairly constant from one flight to the next. This assumption has been in question since the first flight of a microphone system on a satellite (Explorer 1), which gave evidence for large time variations in the flux.

The first approach is exemplified by the microphone system flown on Explorer 8, and the second by all the other microphone systems flown on rockets and near-earth satellites. The validity of both methods is well illustrated in figure 5, which shows the good agreement among the various data obtained in the vicinity of the earth. Due allowance should be made for the fact that Pioneer 1, Luniks 1 and 2, the Interplanetary Station, and SLV–1 operated at somewhat greater geocentric distances where the flux is undoubtedly intermediate between that near the earth and that in interplanetary space where Mariner 2 operated. The small number of impacts recorded at geocentric distances greater than about 2 earth radii currently limits a discussion of the mass distribution to the immediate vicinity of the earth.

The cumulative flux distribution shown in figure 5 is combined in figure 6 with other data on the flux of meteoroids and small dust particles. (The numerical data used in figure 6 are given in McCracken, see pp. 213-224.) The distribution curves refer to the average flux and do not show the effects of meteor showers and dust-particle showers. The flux of meteoroids is essentially the same near the earth as

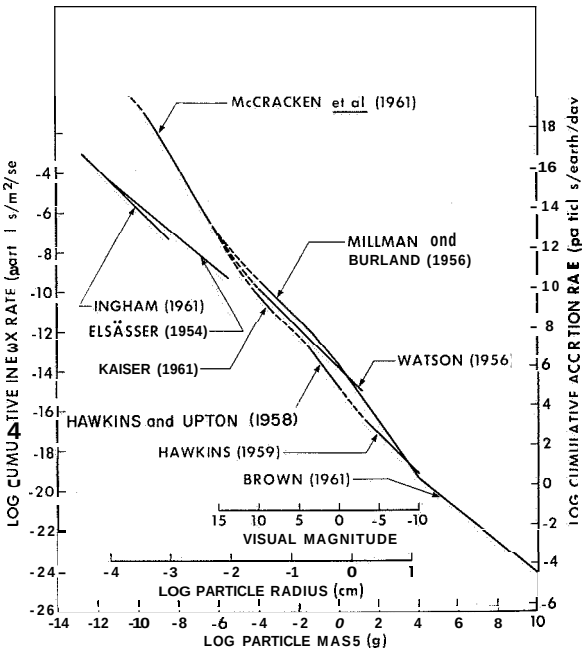

FIGURE 6.—Cumulative flux distribution based on data from various sources and showing the enhanced flux of small dust particles ($m<10^{-6}$ g) in the vicinity of the earth.

in interplanetary space near the orbit of the earth, but the flux of small dust particles having masses $m<10^{-6}$ g shows a geocentric enhancement of the flux. This enhancement appears as the difference between the flux measured in the vicinity of the earth and the flux inferred from studies of the zodiacal light for interplanetary space. The degree of enhancement of the flux depends on the particle mass and appears to reach a maximum of about 10^4 for a particle mass $m\sim10^{-11}$ g. The interpolation between the flux distribution measured with microphone systems and that for radar meteors has reeently been verified by the results of Elford, Hawkins, and Southworth (1964), who used radar to obtain a flux of 10^{-8} particles/m²/sec/2π ster for meteoroids having masses $m\sim1.3\times10^{-6}$ g.

Several points regarding the validity of the direct measurements obtained with the microphone type of sensor deserve special comment. The open literature contains statements that these data are highly uncertain and that the flux measured with satellites decreases during the first day or so following launch. The known uncertainties in the calibration of the systems were discussed in the preceding paragraphs. The alleged uncertainty possibly refers to the large decrease in the flux measured with Sputnik 3 on the day of launch. This decrease represents a large variation in the flux rather than an uncertainty, if the data are to be accepted. Such large variations in the flux are not representative of the data obtained with the remaining microphone systems. Large time variations in the flux were recorded by the microphone systems on Explorer 1 and Vanguard 3, but these showers of dust particles occurred after these satellites had completed a considerable number of orbits. The system on Explorer 1 indicated eight impacts while the satellite was being injected into orbit, but there is nothing peculiar about the numbers of impacts recorded after injection was completed. These 8 impacts were questionable and were subtracted from the 153 nonredundant indicated impacts in order to obtain the 145 impacts reported for Explorer 1. The first available readout of the cumulative counter for the system on Vanguard 3 was obtained about 2 hours (almost 1 orbit) after launch. The detailed time history of the cumulative counter during the first day of operation shows no cause for alarm. The impact rate on the day after launch was lower than on the day of launch, but the impact rate on the second day after launch was higher than on either of the two preceding days (see fig. 4). Likewise, the time history of the cumulative counter for the microphone system on Explorer 8 shows no systematic trend in the impact rate following launch that would arouse suspicion concerning the validity of the data. The microphone system on Pioneer 1 did show an impact, rate that decreased with time during the outbound portion of the trajectory. A probe that was meant to go to the moon should show such a decrease in the impact rate if the geocentric enhancement of the flux exists and the flux decreases with increasing geocentric distance. The data from Explorer 6 have not been published because instrumental difficulties occurred after the satellite was launched. The microphone system on Vanguard 3 was definitely subject to interference from interrogations of the magne-

tometer, but the effects of this interference have been largely removed from the latest data presented earlier in this paper. The data presented by us as valid are not characterized by a flux that decreases systematically following launch.

There is an acute need for data from composite dust-particle sensors for which a sequence of events absolutely unique to the impact of a dust particle is required before the system will register an impact. The data from the combination of microphone and photomultiplier flown on the short-lived Ranger 1 represent limited success in this direction. Further progress toward obtaining data that unquestionably apply for impacting dust particles has been realized with the development of the composite dust-particle sensor being flown on the Orbiting Geophysical Observatories. The data obtained with the microphone type of dust-particle sensor have been most essential in the development of the more complex sensors that are now being flown in order to obtain additional information about the speeds, directions of motion, momenta, and kinetic energies of small dust particles.

Summary

The microphone type of dust-particle sensors flown on rockets, satellites, and interplanetary probes has given information concerning the average flux and time variations in the flux for dust particles with masses between about 10^{-7} and 10^{-11} g. The flux is known as a function of particle mass for the vicinity of the earth, so the cumulative mass distribution for this region of space has been fairly well established. The cumulative flux distribution, if slightly extended toward larger dust particles, is in very good agreement with the flux of radar meteors.

The flux of small dust particles observed in the vicinity of the earth sometimes undergoes large systematic variations with time. On one occasion, the flux rose by a factor of 170 above the average value. The measured flux also shows variations by a factor of 10 within intervals of a few hours' duration. None of the intervals of enhanced flux can be positively associated with the known meteoroid streams.

Further investigation of the small-particle content of meteoroid streams and of the mechanism by which the flux of small particles is enhanced near the earth will have to await definitive data regarding the orbits of these particles.

References

ALEXANDER, W. M.
1962. The mission of Mariner 11: Preliminary observations: Cosmic dust. Science, vol. **138,** pp. 1098–1099.

ALEXANDER, W. M.; BERG, O. E.; MCCRACKEN, C. W.; SECRETAN, L.; and BOHN, J. L.
1967. Interplanetary dust particle flux measurements between **1.0** and **1.56** a.u. from Mariner IV cosmic dust experiment. Smithsonian Contr. Astrophys., vol. **11,** p. **227.**

ALEXANDER, W. M., and LAGOW, H. E.
1960. Recent direct measurements of cosmic dust in the vicinity of the earth using satellites. *In* Space Research, ed. by H. Kallmann-Bijl, North-Holland Publ. Co., Amsterdam, pp. **1033–1041.**

ALEXANDER, W. M.; MCCRACKEN, C. W.; and LAGOW, H. E.
1961. Interplanetary dust particles of micron-size probably associated with the Leonid meteoroid stream. Journ. Geophys. Res., vol. **66,** pp. **3970–3973.**

ALEXANDER, W. M.; MCCRACKEN, C. W.; SECRETAN, L.; and BERG, O. E.
1963. Review of direct measurements of interplanetary dust from satellites and probes. *In* Space Research III, ed. by W. Priester, North-Holland Publ. Co., Amsterdam, pp. **891–917.**

BROWN, H.
1960. The density and mass distribution of meteoritic bodies in the neighborhood of the earth's orbit. Journ. Geophys. Res., vol. **65,** pp. **1679–1683.**
1961. The density and mass distribution of meteoritic bodies in the neighborhood of the earth's orbit: Addendum. Journ. Geophys. Res., vol. **66,** pp. **1316–1317.**

D'AUITOLO, C. T.
1964. Review of meteoroid environment based on results from Explorer XIII and Explorer XVI satellites. *In* Space Research IV, ed. by P. Muller, North-Holland Publ. Co., Amsterdam, pp. 858–874.

DUBIN, M.
1960a. Meteoritic dust measured from Explorer I. Planet. Space Sci., vol. **2,** pp. **121–129.**
1960b. IGY micrometeorite measurements. *In* Space Research, ed. by H. Kallmann-Bijl, North-Holland Publ. Co., Amsterdam, pp. **1042–1058.**

ELFORD, W. G.; HAWKINS, G. S.; and SOUTHWORTH, R. B.
1964. The distribution of sporadic meteor radiants. Harvard Radio Meteor Project Res. Rep., no. **11,** December.

ELSÄSSER, H.
1954. Die raumliche Verteilung der zodiakallicht-materie. Zeits. f. Astrophys., vol. **33,** pp. **274–285.**

HAWKINS, G. S.
1959. The relation between asteroids, fireballs, and meteorites. Astrophys. Journ., vol. **64,** pp. **450–454.**

HAWKINS, G. S., and UPTON, E. K. L.
1958. The influx rate of meteors in the earth's atmosphere. Astrophys. Journ., vol. **128,** pp. **727–735.**

INGHAM, M. F.
1961. Observations of the zodiacal light from a very high altitude station, IV: The nature and distribution of the interplanetary dust. Monthly Notices Roy. Astron. Soc., vol. **122,** pp. **157–175.**

KAISER, T. R.
1961. The determination of the incident flux of radio-meteors, II: Sporadic meteors. Monthly Notices Roy. Astron. Soc., vol. **123,** pp. **265–271.**

MCCRACKEN, C. W.
1967. Conditions of encounter between dust and the planets. Smithsonian Contr. Astrophys., vol. **11,** pp. **213–224.**

MCCRACKEN, C. W.; ALEXANDER, W. M.; and DUBIN, M.
1961. Direct measurements of interplanetary dust particles in the vicinity of earth. Nature, vol. **192,** pp. **441–443.**

MILLMAN, P. M., and BURLAND, M. S.
1956. The magnitude distribution of visual meteors. Presented at 96th Amer. Astron. Soc. Meeting, New York, December. (See Millman, Journ. Roy. Astron. Soc., Canada, vol. **51,** pp. **113–115, 1957.)**

NAZAROVA, T. N.
1960. The results of studies of meteoric dust by means of Sputnik III and space rockets. *In* Space Research, ed., by H. Kallmann-Bijl, North-Holland Publ. Co., Amsterdam, pp. **1059–1062.**
1963. Rocket and satellite studies of meteoric dust. *In* Proceedings of the Symposium on the Astronomy and Physics of Meteors. Smithsonian Contr. Astrophys., vol. **7,** pp. **105–108.**
1967. Rocket and satellite studies of meteoric dust. Smithsonian Contr. Astrophys., vol. **11,** pp. **231–237.**

ÖPIK, E. J.
1958. Meteor impact on solid surface. Irish Astron. Journ., vol. **5, PP. 14–33.**

WATSON, F. G.
1956. Between the Planets. Harvard Univ. Press, Cambridge, Mass., **188** pp.

WHIPPLE, F. L.
1961. The dust cloud about the earth. Nature, vol. **189,** pp. **127–128.**

Abstract

Information concerning the mass distribution and the time variations in the flux of small dust particles has been obtained with dust-particle sensors flown outside the atmosphere of the earth. The relevant data have been obtained primarily with the microphone type of dust-particle sensor flown on near-earth satellites. These measurements are in good agreement with the mass distribution measured with the microphone system on Explorer **8.** The measured flux of dust particles often shows temporal variations of a factor of **10** within intervals of several hours, as well as larger, systematic enhancements of flux or sporadic showers which persist for intervals ranging from several hours to a few days.

Physical Parameters of Cosmic Dust Obtained from Rocket Collections

O. E. BERG [1] and L. SECRETAN

An Aerobee rocket specifically instrumented to measure and record various parameters of the earth's cosmic dust environment was launched at 0700 MST on December 17, **1964,** at the White Sands Missile Range. The principal experiment aboard the rocket was designed to register and recover physical evidence of impacts by extraterrestrial particles.

Development

One of the major problems in the evaluation of the meteoroid environment hazard is the absence of definitive measurements and data regarding the character and effects of the hypervelocity microparticle impact as they apply to true meteoric bodies at meteoric velocities.

The state of the art of laboratory microparticle accelerators is limited to low meteoric velocities and to solid, high-density, essentially spherical microparticles. There is little or no justification for assuming that the physical characteristics of cosmic dust are generally similar to those of the hypervelocity laboratory particles. Donn **(1964)** has recently published the results of a study of the various sources of cosmic dust, which indicate that the particle geometries range from high-density spherules to fluffy particles or whiskery aggregates.

Several attempts made in the past to collect physical evidence of micrometeoric impacts, such as craters, have failed, partially or totally, because of technological difficulties readily recognized by investigators engaged in micro-analytical techniques. The major technological difficulties can be expressed as follows:

1. The size of the hypervelocity microparticle impact crater is near the limits of resolution of the finest optical microscopes.

2. Even the finest optically polished surfaces contain inherent surface defects having dimensions and characteristics similar to those of the craters sought for study. Two striking examples of such "craters" are shown in plate 1. Both "craters" appeared on the surface of an aluminized lucite block, which had been optically polished and coated with an opaque layer of aluminum in preparation for an exposure to micrometeoritic impacts. The experiment was abandoned when numerous crater-like irregularities of a similar nature were discovered in the preflight surfaces.

In view of the existence of these surface defects, it is obvious that the finest prepared surfaces available remain inadequate, per se, as a medium for the registration of meteoric impacts. One stringent criterion must be observed for the surface medium: that every square micron of that surface be scanned before and after cosmic-dust exposure with a precision that will categorically single out cosmic-dust impacts from inherent surface defects.

It is believed that this criterion has been fulfilled by instruments and techniques that were developed for and are described in this experiment.

The exposure substrate selected for this experiment was in the form of a glass cylinder **11.4** cm in diameter and **10.2** cm long, with a total impact area of **0.037** m^2. The exterior

[1] Goddard Space Flight Center, National Aeronautics and Space Administration, Greenbelt, Md.

surface of each cylinder was optically polished and coated with an opaque layer of evaporated metal 2500 A in thickness. The entire surface of each cylinder was photometrically mapped for preflight pinholes or similar surface transparencies in a precision photometric scanner shown schematically in figure 1.

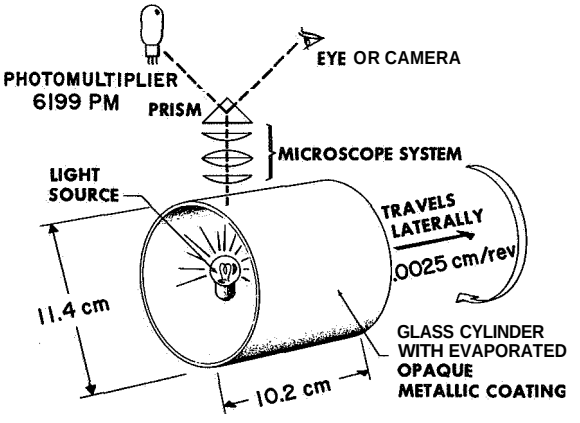

FIGURE 1.—Precision photometric scanner.

The exposure cylinder is rotated in the scanner at 2 sec/rev. The evaporated metal layer normally presents an opaque barrier between the light source and the photomultiplier. If, during the scanning procedure, a pinhole in the opaque layer appears in the light-source photomultiplier axis, it will transmit an amount of light relatively proportional to its area. The momentary light transmission is detected by a 6199 photomultiplier, amplified, and recorded on Sanborn tape. Recorded simultaneously with the light pulse and on the same tape is the precise position of the pinhole in the cylinder to an accuracy of ±0.005 cm laterally and ±2°.0 circumferentially.

A slit in the optical system of the microscope limits its lateral field of view to approximately 0.008 cm of the surface. Thus, any particular pinhole will record its relative amplitude and its position for each of several consecutive revolutions of the cylinder, since the field of view of the microscope (0.008 cm) is greater than the cylinder's lateral travel per revolution (0.0025 cm).

Plate 2 shows a section of Sanborn tape that has recorded the registration of a typical pinhole during a scan. Each of the spacings between the five positive pulses represents one revolution of the cylinder in the scanner. This particular registration is that of a pinhole approximately 1 μ in diameter.

The resolution capability of the experiment to detect perforations produced in thin coatings by high-density, hypervelocity dust particles has been determined with the GSFC Dust Particle Accelerator. Impacts by carbonyl iron spheres having masses ranging from 10^{-10} to 10^{-12} g and velocities from 2 to 8 km/sec exhibited perforations in the opaque layer sometimes only a fraction of a micron in diameter but readily detectable in the scanning system.

Unfortunately, we cannot determine from this calibration a practical detection capability for cosmic-dust-particle impacts because: 1) (as stated earlier, the physical characteristics of cosmic dust may vary widely from those of the iron spheres used in the laboratory; and 2) accordingly, the crater and penetration characteristics of low-density particles are not well known. In a recent theoretical study, Bjork (1962) concluded that for craters produced by impacts between unlike materials (target and projectile) we might expect substantial deviations from the generally accepted crater characteristics. He concluded further that the crater characteristics do deviate from an idealized pattern as a function of particle velocity and may vary widely as a function of particle geometry.

All flight cylinders were photometrically scanned twice previous to installation in their individually sealed flight containers. A timer in the payload was used to extend the three cylinders at 73 sec and retract them at 410 sec, providing an exposure of 337 sec. These times correspond to rocket altitudes of 73.6 km and 92.7 km and to rocket velocities of 1.6 km/sec and 1.4 km/sec, respectively.

After recovery of the payload, each cylinder was removed and scanned again. A comparison of the postflight record with the preflight record revealed the location and relative magnitude of new perforations. Only new perforations were considered and accepted for further analysis.

A total number of 14 "probable impacts" was discovered on the surface of the three exposed cylinders. "Probable impacts" refer to all new

pinholes or transparent areas that were definitely not present in the preflight scanning records.

The "control cylinder," prepared and flown under the same conditions as the three exposed cylinders but not extended to the cosmic-dust environment, showed no new pinholes nor transparent areas.

It is customary and sometimes advantageous to separate collections into groups or classes and proceed to discuss each group or class separately. The impacts discussed in this paper, however, are not readily divided into groups, but tend to show gradual transitions over a wide range of densities, velocities, sizes, and shapes. For this reason, only 6 of the 14 impacts will be illustrated and discussed as representative samples of the collection.

Plate 3 shows the largest of the impact areas recovered. The shallow, large-area character of this crater suggests an irregularly shaped, low-density, hypervelocity projectile. The refracting areas in the bottom of the crater denote physical damage to the substrate—the glass—possibly inflicted by smaller inclusions of higher density in the impacting particle.

Another representative impact area, shown in plate 4, was produced by a projectile, probably similar to the previous one but possibly more filamentary and having a lower velocity. The streaks emanating from only one side of the crater suggest a low-angle impact favoring nonsymmetrical ejecta.

One of the more significant features generally observed in the 14 impacts is the relatively shallow crater. This impact, as an example, shows a large area affected by the impact, while only the relatively small areas at either end of the crater show penetration through the very thin layer.

The next impact shown in plate 5 exhibits an interesting extrorse effect, which is evident in several other impacts in the collection. The dark-shaded parallel streaks emanating from the impact proper are most assuredly associated with the plastic surface deformation imparted by the impact. Similar extrorse effects are commonly observed in impacts produced by the Goddard Dust Particle Accelerator. We believe this is the first time this type of surface deformation due to microparticle impacts has been visually detected. Its appearance is inconsistent with normal shock-wave effects, which exhibit essentially symmetrical, concentric patterns annexed to the impact proper. That this effect is truly plastic deformation is substantiated by the hypervelocity impact shown in plate 6. This impact crater, recorded by J. F. Friichtenicht of the Space Technology Labs, was produced upon a solid aluminum block by a 1-μ iron sphere accelerated to a few km/sec in an Electrostatic Dust Particle Accelerator. The magnification is indicated in the lower left corner by the two marks separated by 1μ. The plastic surface deformation as revealed by distortions of the surface polishing marks extends from the center of the impact outward to several crater diameters, and is markedly asymmetrical. This extrorse effect is at present the subject of a separate study, the results of which will be published later.

The next two impact areas are most informative when considered together, since they are remarkably similar in appearance although created by two completely dissimilar means on similar targets. One of the two impacts shown in plate 7a was produced in the laboratory by a 1-μ iron sphere having a velocity of a few km/sec. Notice the total asymmetry of the impact proper as well as the plastic deformation. The other impact shown in plate 7b was created by a cosmic-dust particle. The general similarities of the impacts and their associated effects lead us to believe that both impacts were produced by similar projectiles, i.e., high density and high speed.

Two of the 14 impacts recovered were of the type shown in plate 8. Although the interesting feature of this impact is the deposit of material on the surface, its impact had produced a detectable perforation in the opaque film, by which it was registered as a postlaunch event. These two impacts will be further studied by an electron microprobe and microchemical analysis.

It is interesting, but not particularly practicable, to compare the cosmic-dust influx rates as indicated by this experiment with established influx rates as measured by a variety of real-time sensors in rockets, probes, and satellites. The impracticability of such a comparison is a consequence of the conditions of exposure

under which this experiment was performed. During the early phase of the exposure, the surfaces were traversing an atmosphere laden with extraterrestrial dust particles that are decelerated and "slowly settling to earth." At that time the rocket velocity relative to "stationary" particles was sufficient to inflict detectable perforations in the opaque film, at least for solid, high-density particles. Hence, any concentration of cosmic dust in the 80- to **90-km** layer (Fiocco and Smullin, **1963;** Fiocco and Colombo, **1964)** should have contributed appreciably to the integrated impact rate measured in this flight.

The data composing the general cumulative meteoric influx curve reported by Alexander et al. **(1962)** and shown in figure **2** for comparison were obtained, in general, from impacts by cosmic dust essentially outside the earth's atmosphere and with an assumed average velocity of **25** km/sec.

The exposure area of **0.11** m^2 (for three cylinders), corrected for earth shielding **(50** percent) and rocket shielding **(30** percent), yields a correction factor of **65** percent or an effective exposure area of **0.033** m^2, and an area-time factor of **11.1** m^2 sec. The impact rate then becomes **14111.1** m^2 sec or **1.2** impacts/m^2/sec, which is plotted as a point on the ordinate with the absicssa variation representing the present existing uncertainties in computing particle masses from studies of hypervelocity craters.

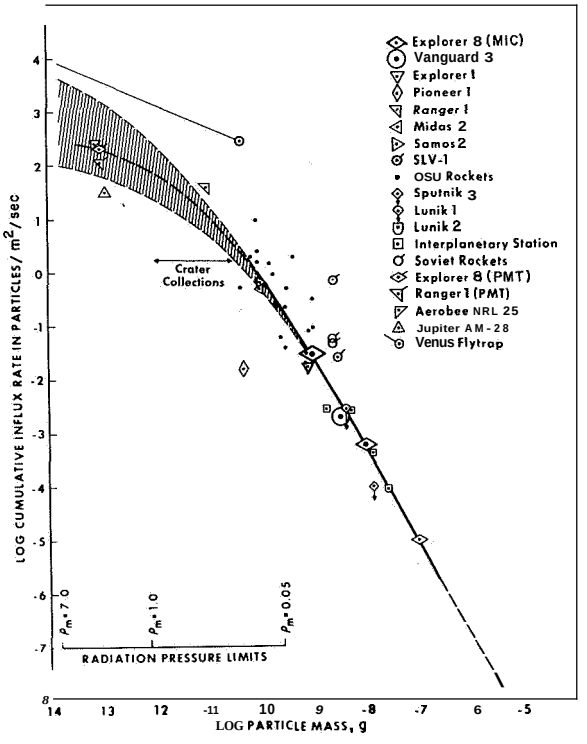

FIGURE 2.—Average cumulative mass distribution curve.

The relatively low influx rates exhibited by the new measurement on the well-established plot are somewhat surprising inasmuch as the impact detectability of the latter experiment has been shown to be sensitive to craters produced by 10^{-12} g iron carbonyl particles having a speed of only a few km/sec.

There are two possible explanations for the low influx rates: **(1)** the real-time sensors are capable of and have been recording impacts by particles that by virtue of their fragile, low-density structure are not capable of penetrating the opaque metallic layer; and **(2)** the penetration characteristics of low-density projectiles are not well known. Accordingly, there may be for this system a detectability cutoff for low-density particles that may differ by a factor of **10** or more from that of solid particles.

The following conclusions are based on the results of this experiment: **(1)** cosmic dust encompasses a wide range of particle densities and shapes as well as sizes and velocities; **(2)** penetration parameters for low-density, hypervelocity microparticles may vary widely from accepted values derived from dissimilar laboratory-produced particles; and **(3)** as indicated by this experiment, the large area of the impact proper, coupled with the evidence of plastic surface deformation, strongly suggests that surface damage rather than penetration presents the greater hazard to space material.

References

ALEXANDER, W. M.; MCCRACKEN, C. W.; SECRETAN, L.; and BERG, O. E.
1962. Review of direct measurements of interplanetary dust from satellite and probes. *In* Space Research III, ed. W. Priester, North-Holland Publ. Co., Amsterdam, pp. 891–917.

BJORK, R. L.
1963. Review of physical processes in hypervelocity impacts and penetration. Sixth Hypervelocity Symp., vol. 2, pp. 1–58.

DONN, B.
1964. The origin and nature of solid particles in space. Ann. New York Acad. Sci., vol. 119, pp. 5–16.
FIOCCO, G., and COLOMBO, G.
1964. Optical radar results and meteoric fragmentation. Journ. Geophys. Res., vol. 69, pp. 1795–1803.
FIOCCO, G., and SMULLIN, L. D.
1963. Detection of scattering layers in the upper atmosphere (60–140 km) by optical radar. Nature, vol. 199, pp. 1275–1276.

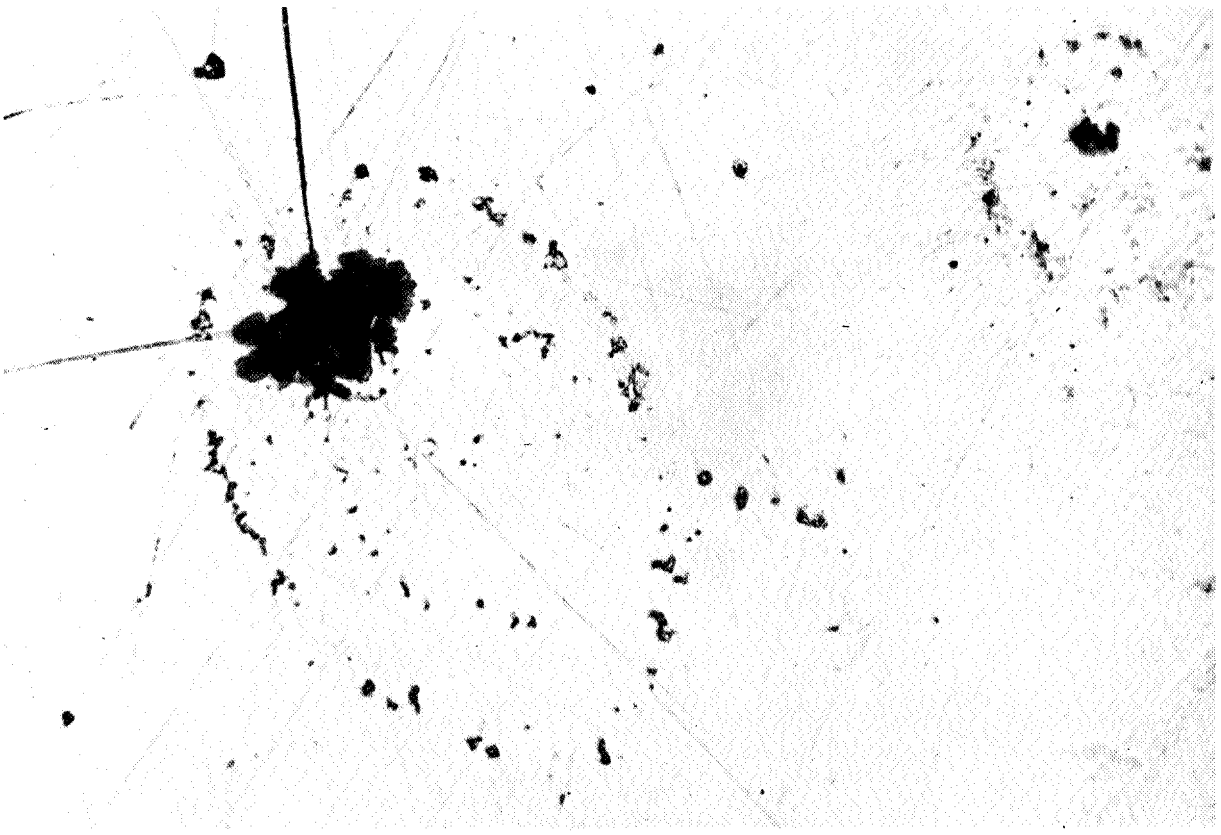

PLATE 1

Inherent surface defects (500×).

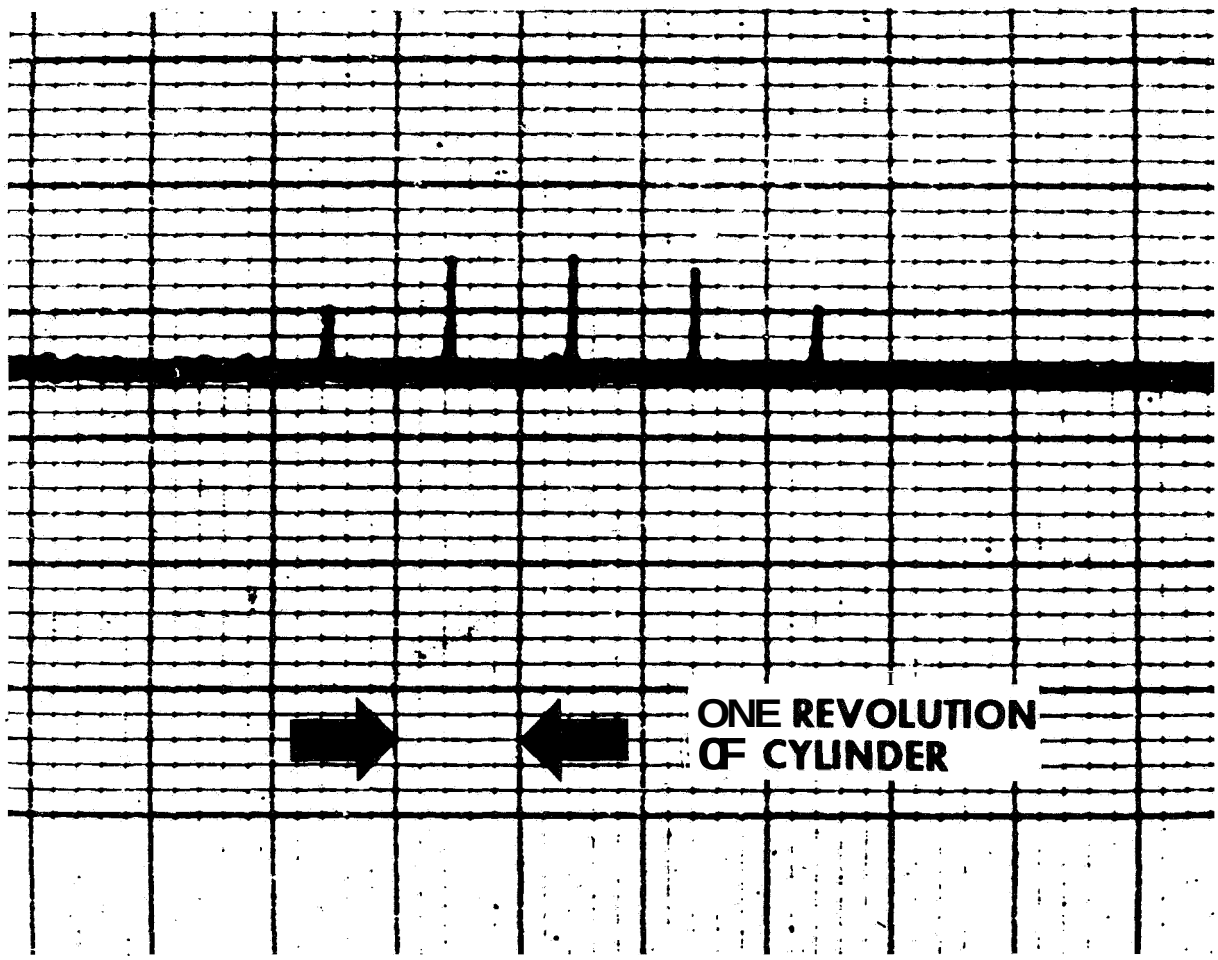

PLATE 2

A typical photometric scan recording.

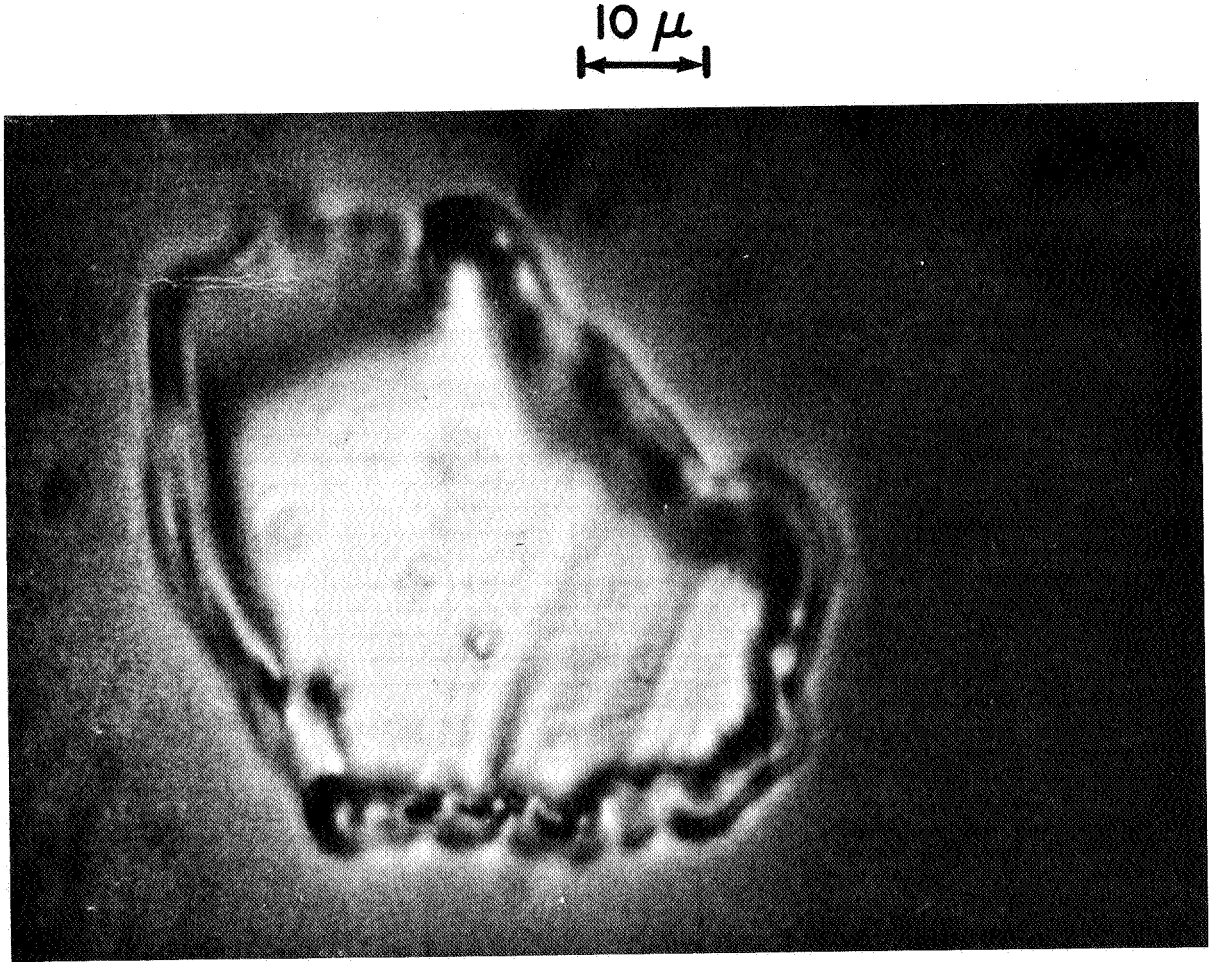

PLATE 3

Cosmic-dust-particle impact crater.

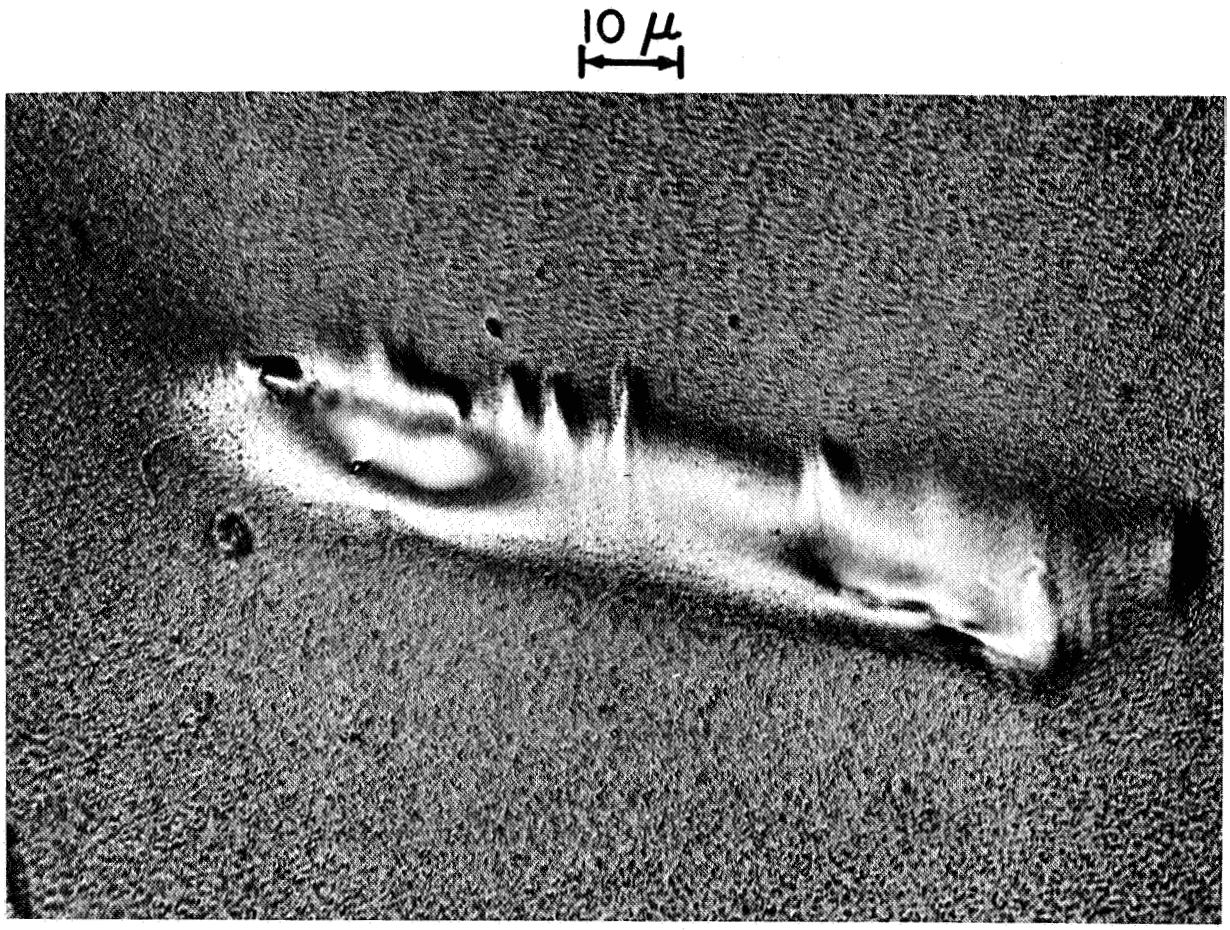

PLATE 4

Cosmic-dust-particle impact crater.

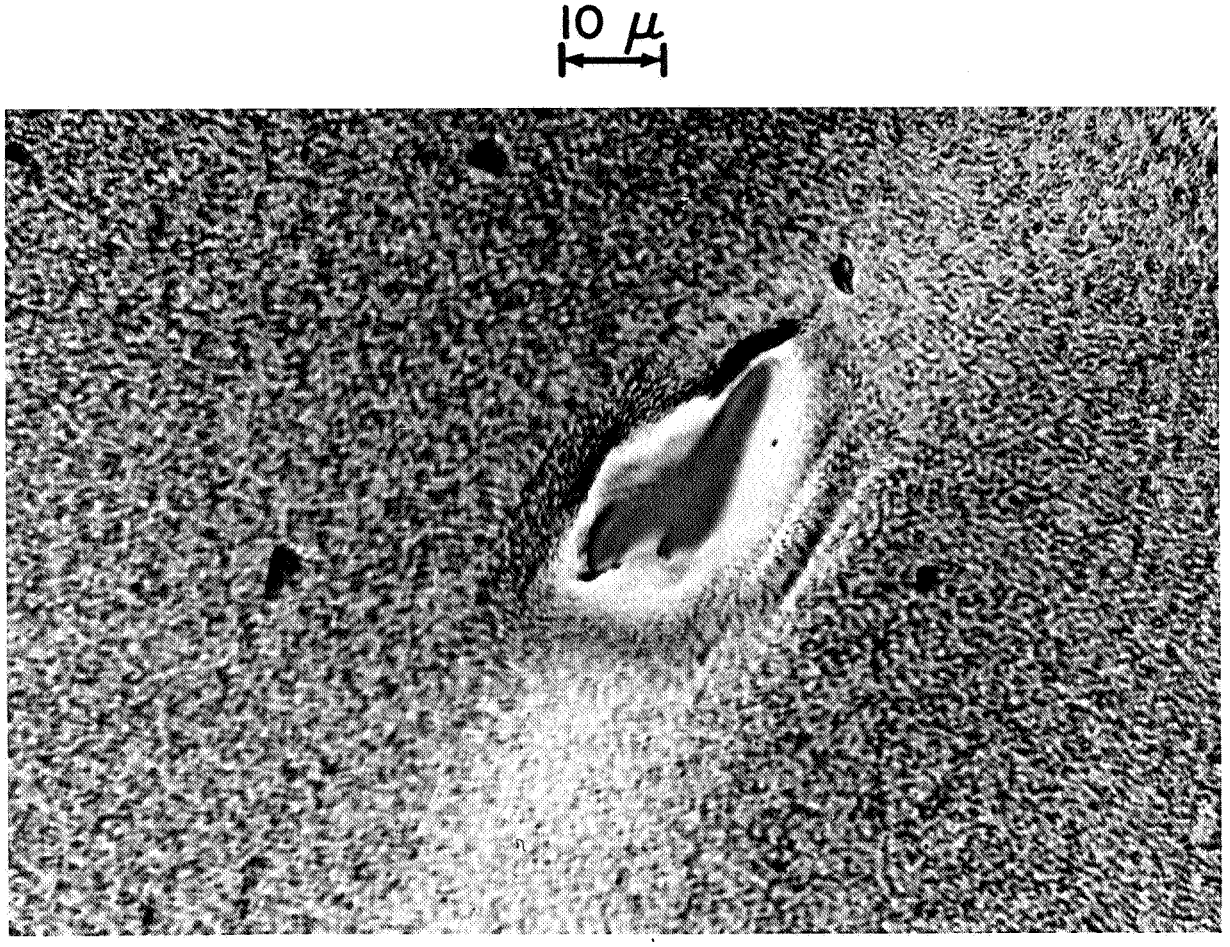

PLATE 5

Cosmic-dust-particle impact area showing plastic surface deformation.

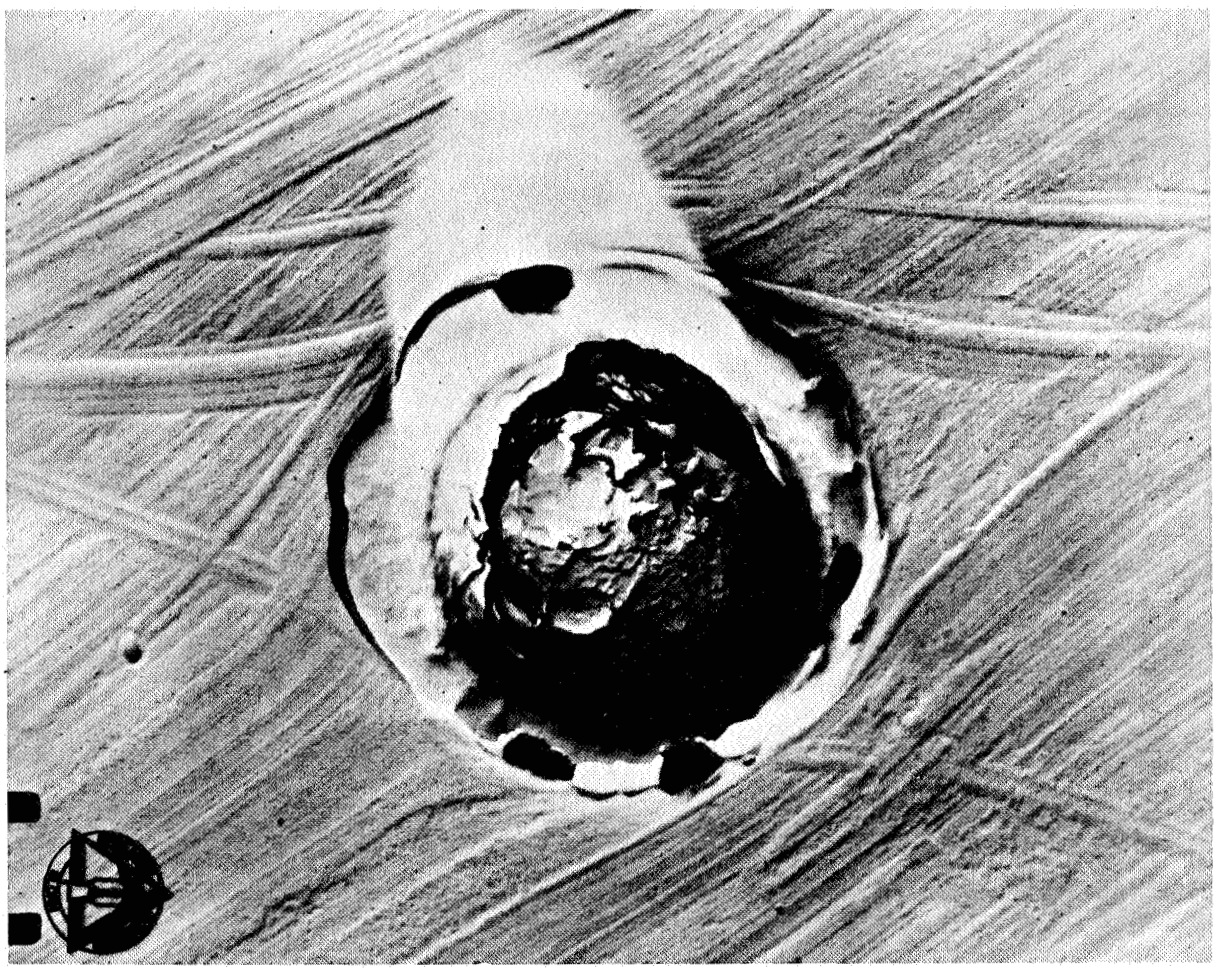

PLATE 6

Simulated micrometeoritic impact crater showing plastic surface deformation.

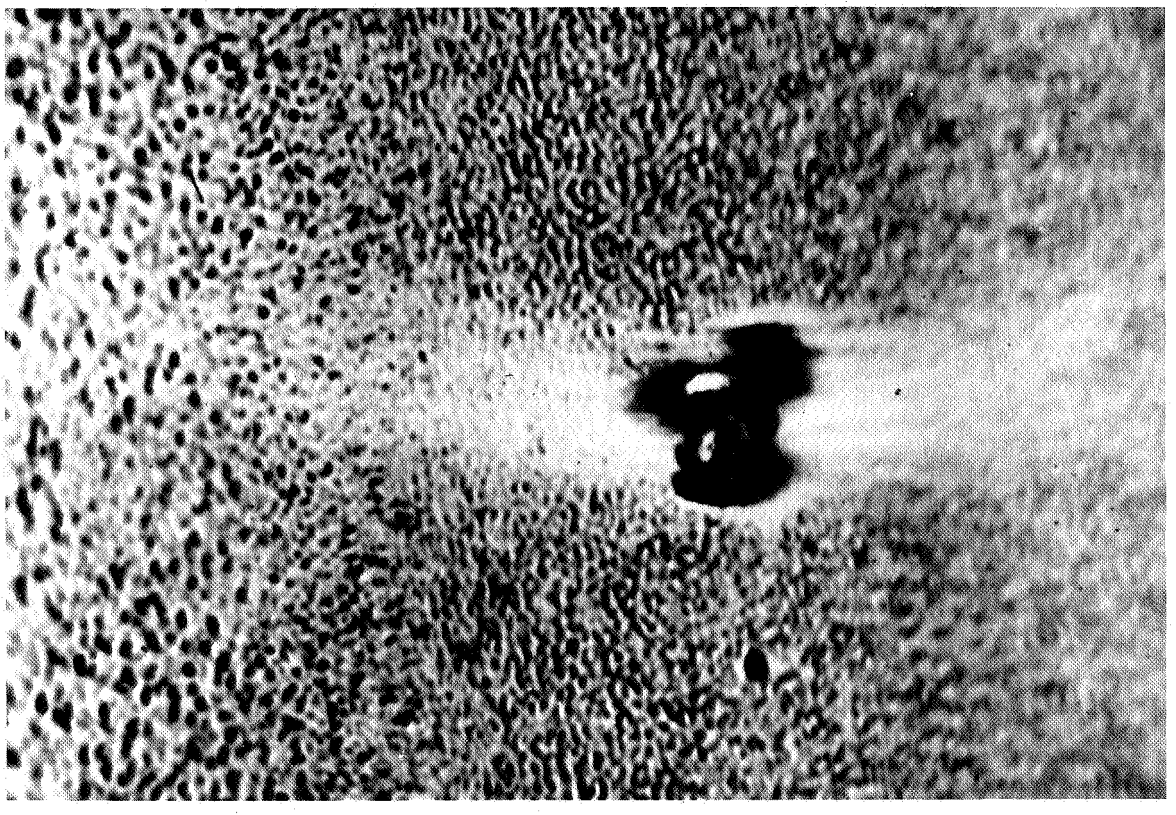

PLATE 7A

Simulated micrometeoritic impact crater.

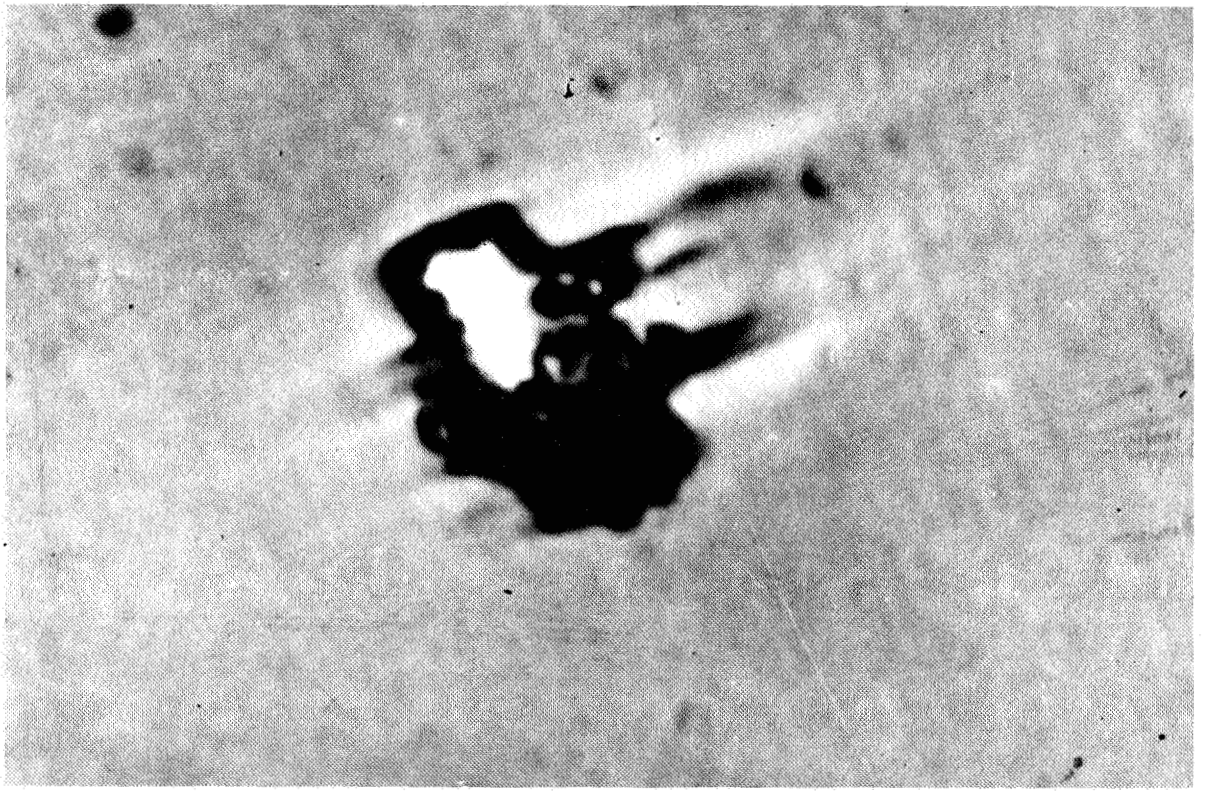

PLATE 7B

Cosmic-dust impact crater.

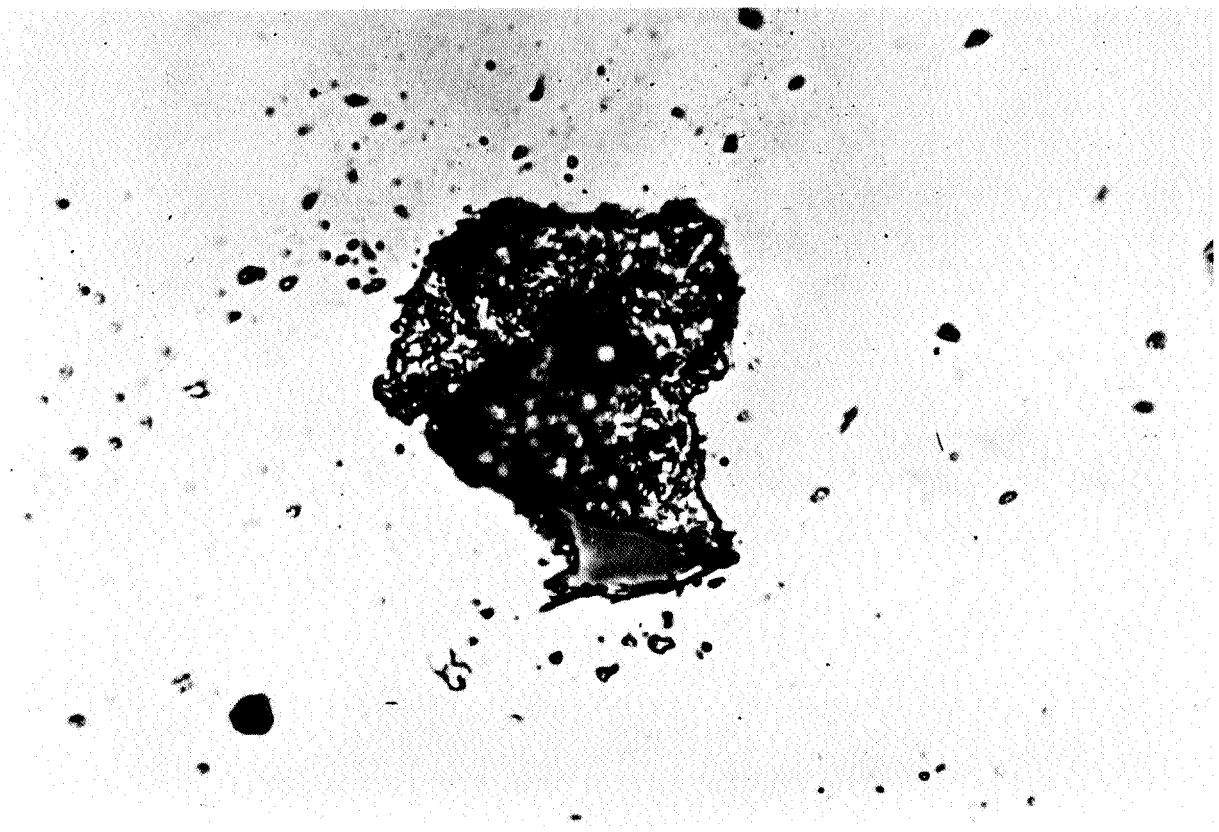

PLATE 8

Cosmic-dust impact area containing debris.

Electron Diffraction Control Studies of Venus Flytrap Particles

N. N. GREENMAN and C. B. GILPIN[1]

Introduction

The first successful collection of particles from high altitudes for direct study was provided by the Venus Flytrap rocket launched on June 6, 1961, at White Sands Proving Grounds, New Mexico. The nose cone carried particle collectors of the impact variety mounted on extendible and retractable leaves. Collection was made between altitudes of 88 and 168 km for about 4 min, the entire flight lasting about 8 min. The project was carried out by R. K. Soberman and his group at the Meteor Physics Branch of the Air Force Cambridge Research Laboratories (AFCRL), Bedford, Mass., and they very kindly provided us with samples for study.

One of the findings reported by Soberman et al. (1963) in their initial studies was that the possible extraterrestrial particles generally showed no selected area diffraction patterns in the electron microscope, a circumstance they suggested may be due to crystalline damage by cosmic radiation. Our first studies, which confirmed this observation, were based on this feature and were an attempt to determine whether the apparent lack of crystallinity was in fact due to radiation damage. The reason for this approach was that terrestrial sources of contaminants in micrometeorite collections are either crystalline or amorphous, not radiation-damaged. Extraterrestrial particles, on the other hand, could suffer such damage to the crystalline lattice, according to Ryan's (1964) calculations. Moreover, that damage could survive in small particles that fall through the atmosphere too slowly to undergo appreciable frictional heating. Therefore, radiation damage, if demonstrated to exist, would be a valuable criterion for distinguishing extraterrestrial from terrestrial particles.

[1] Space Sciences Department and Astropower Laboratory, Douglas Missile and Space Systems Division, Santa Monica, Calif.

Venus Flytrap studies

Because radiation damage is known to anneal out at temperatures well below the melting point, the Venus Flytrap particles were heated in stages of increasingly higher temperature and examined in the electron microscope after each stage for evidence of newly produced crystallinity. The substrates, as a result of their poor heat resistance, suffered enough destruction during the tests to make it almost impossible to follow the same particle through every heating stage. For this reason a statistical approach was used in which as many particles as possible were examined after each stage.

The results of heating to 250° C, 400° C, and 500° C were that in general the percentage of particles showing evidence of crystallinity increased with increasing temperature. The diffraction spots were small in number and included both symmetrical pairs or groups and single, unpaired spots (pl. 1*a*, b). Only the symmetrical spots, however, were considered evidence of crystallinity because of the possibility that individual spots might be due to spurious effects, such as film defects, rather than to diffraction by the particle. Statistical analysis indicated that the crystallinity was probably produced by the heating, although the differences in percentages were not great enough to be certain on this point. The *d* spacings of the diffraction spots were found to

correspond rather well with those of olivine and enstatite, the major minerals of the most abundant meteorite type, thus indicating that annealing of radiation damage could have occurred. On the other hand, similar correspondence was found with other materials, such as mica and aluminum oxides and hydroxides, that could be contaminants or reaction products formed in the course of the heating tests. The results of these first tests, described in detail by Greenman (1964), were thus suggestive but inconclusive.

Two factors were chiefly responsible for the failure to achieve conclusive results. The first was the inadequate heat resistance of the available substrates, which not only limited the maximum temperature of the test but also made it impossible to follow a particular particle through every heating stage so as to be certain that changes had or had not occurred. The second was the scarcity of information on the electron diffraction characteristics of silicate particles, both normal and radiation-damaged, in the same size range as the Venus Flytrap particles—about 0.1 to 1 μ.

To overcome the first of these difficulties, we have developed a heat-resistant substrate of good collection efficiency, which is now being flown on a second series of Venus Flytrap flights. To overcome the second, we have begun control studies of submicron particles of olivine, $(Mg,Fe)_2SiO_4$, and enstatite, $(Mg,Fe)SiO_3$. These are the two most common minerals of the stony meteorites, the most abundant type of meteorite, and may therefore well represent the micrometeorites. One of the objectives of the control studies is to determine the type and quality of the electron diffraction patterns and how the patterns are affected by size, shape, crystallographic orientation, substrate thickness, radiation damage and annealing, and other variables. Another objective is to determine from irradiation and annealing tests of the olivine and enstatite whether likely micrometeorite minerals can be damaged by space radiation to the extent that they appear amorphous by electron diffraction and, if so, whether annealing well below the melting point can restore the crystallinity. The purpose of this paper is to describe some of the first results of these control studies with olivine and enstatite.

Control studies

Samples of olivine and enstatite were pulverized by placing them in a hardened steel tube with hardened steel balls and vibrating the tube in a Crescent Wiggly Bug apparatus for 4 hours. Tests had shown that such treatment produced particles of these minerals from about 0.08 to 10μ in size. To prepare the samples for viewing in the electron microscope, we shook the powder and, after allowing a short period of time for the coarsest particles to settle, inserted a freshly prepared carbon substrate into the residual cloud of fine material. No shadowing was used with this series of observations. A tilting stage that allowed the particle to be tilted up to 15° in any direction from the axis of the electron beam was used to obtain for each particle the orientation that produced the most diffraction spots and the best symmetry of the spot pattern.

Olivine particles and their diffraction patterns are shown in plates 1*c* to 2b. The smallest particle of plate 1*c*, about 0.5 μ in its longest dimension, yielded the pattern shown in plate 1*d*, the best pattern observed. The main rectangular and diagonal dimensions give **d** spacings of 4.82, 3.82, and 3.07 A, which agree rather well with the X-ray measurements of this same material of 5.09, 3.86, and 2.98 A and with the ASTM card file values for olivine. These correspond to the (020), (021), and (002) planes, respectively, and indicate the particle is oriented with (200) normal to the beam.

The pattern shown in plate 2*a* for the 0.9-μ particle in plate 1*c* has many spots but poor symmetry. The one **d** spacing that can be measured with fair accuracy agrees reasonably well with that for the (002) plane of olivine.

The olivine particle of plate 2*b* yielded no diffraction pattern, even though it is of about the same size as the one of plate 1*c* that gave the best pattern, and even though the lighter areas around its edge indicate some transmission of the electron beam.

Plates 2*c* to 3*c* show enstatite particles and their diffraction patterns. Plates 2d and 3b show that even a particle as large as 4 μ can give a diffraction pattern if thin edges are present. In this case it is a ring rather than a

spot pattern. Also the pattern is not complete, probably because those parts of the beam diffracted toward the central thick portion of the particle are not transmitted. Spacings of 2.31 and 1.64 A are obtained from the rings.

The spot pattern of plate 3a is from the 0.4-μ particle of plate 2c. The spots give d spacings of 3.62 and 2.18 A. All four spacings in plates 2d and 3a agree reasonably well with those from X-ray measurements of this same material, or with the ASTM card file values for enstatite.

The two enstatite particles of plate 3c gave no diffraction patterns although, like the olivine particle of plate 2b, lighter areas indicative of electron-beam transmission are present around the edges.

From the above observations and from observations on other olivine and enstatite particles, it can be concluded that crystalline silicate particles at least as large as 4 μ and ranging down to about 0.1 or 0.2 μ, though opaque to the electron beam, can yield diffraction patterns from thin, partially transparent edges. There is some limiting size, in the neighborhood of 0.1 to 0.2 μ, for which the particle is still opaque to the electron beam but is too small for thin edges to be present or to be effective; such particles generally give no diffraction pattern. Particles smaller than this limiting size are thin enough to be transparent to the electron beam and again can give diffraction patterns. In the larger particles, in which the diffraction is from thin edges, the part of the beam that is diffracted into rather than away from the particle is not transmitted, so that incomplete or asymmetrical patterns may result (plate 2c). Possibly some of the unpaired spots that appeared in the heat-annealing tests with the Venus Flytrap particles may have been due to this effect. If so, perhaps a higher degree of crystallinity or a larger percentage of particles with new crystallinity was produced than was originally supposed.

The conditions under which diffraction patterns can be obtained are as follows. First, the substrate must be thin. Second, observation and photographic recording must be made rapidly before the buildup of contamination due to electron-beam decomposition of vacuum-system hydrocarbons. The diffraction pattern is much more sensitive to contamination buildup than the particle image, and in a number of cases the former was seen to disappear while being observed whereas the latter showed no change. Third, a tilting stage should be used to allow the most favorable crystallographic orientation to be selected. Because of the very short wavelength of the electron beam, only crystallographic planes that are nearly parallel to the beam can produce observable diffraction spots. Therefore, a detectable pattern appears only in some, not all, orientations. The particles shown in plates 2b and 3c may have failed to yield diffraction patterns because of unfavorable orientation within the 15° range of the tilting stage, although it is also possible that excessive contamination built up during the observation before a favorable orientation was found.

Application to Venus Flytrap studies

In applying these results to our Venus Flytrap studies, we can easily meet the first two of the above conditions. The substrates being flown on the present series of Venus Flytrap flights have been carefully prepared to be of optimum thickness for this type of study. Also, the problem of contamination can be solved by suitable instrument modification, such as better cold traps on the vacuum system of the electron microscope, and by rapid observing and photographing of the diffraction patterns. However, the problem involved in the third condition, that of unfavorable orientation, may prove troublesome. Unfavorably oriented Venus Flytrap particles, even though crystalline and with visibly thin edges, will appear amorphous before and after the heat-annealing tests, assuming, of course, that the particles do not change position during the heating runs. The same can be said of any unfavorably oriented particles that are radiation damaged. On the other hand, in the absence of a severe biasing factor, a significant proportion of the particles can be expected to have favorable orientation within the range of the tilting stage; with these a pattern will be found after heating where none was present before if annealing of radiation damage occurs. Therefore, by examining a large number of particles, we should

be able to establish whether or not radiation damage is characteristic of those that are extraterrestrial. Additional study is being devoted to methods of obtaining diffraction patterns in all cases in which the particles are crystalline.

Acknowledgment

We would like to thank Mr. Don Paul for his valuable assistance with the electron microscopy.

References

GREENMAN, N. N.
1964. Heat annealing experiments performed upon "Venus Flytrap" particles. Ann. New York Acad. Sci., vol. 119, pp. 298–317.

RYAN, J. A.
1964. Corpuscular radiation produced crystalline damage at the lunar surface. *In* The Lunar Surface Layer, ed. by J. W. Salisbury and P. E. Glaser, Academic Press, N.Y., pp. 265–312.

SOBERMAN, R. K.; HEMENWAY, C. L.; RYAN, T. G.; CHREST, S. A.; FRISSORA, J.; FULLAM, E. F.; BALSAMO, J. J.; COLE, J.; HALLGREN, D.; YEDINAK, P.; GOODMAN, A.; and HOFF, G.
1963. Micrometeorite collection from a recoverable sounding rocket, parts I and II. *In* Proceedings of the Symposium on the Astronomy and Physics of Meteors. Smithsonian Contr. Astrophys., vol. 7, pp. 89–98.

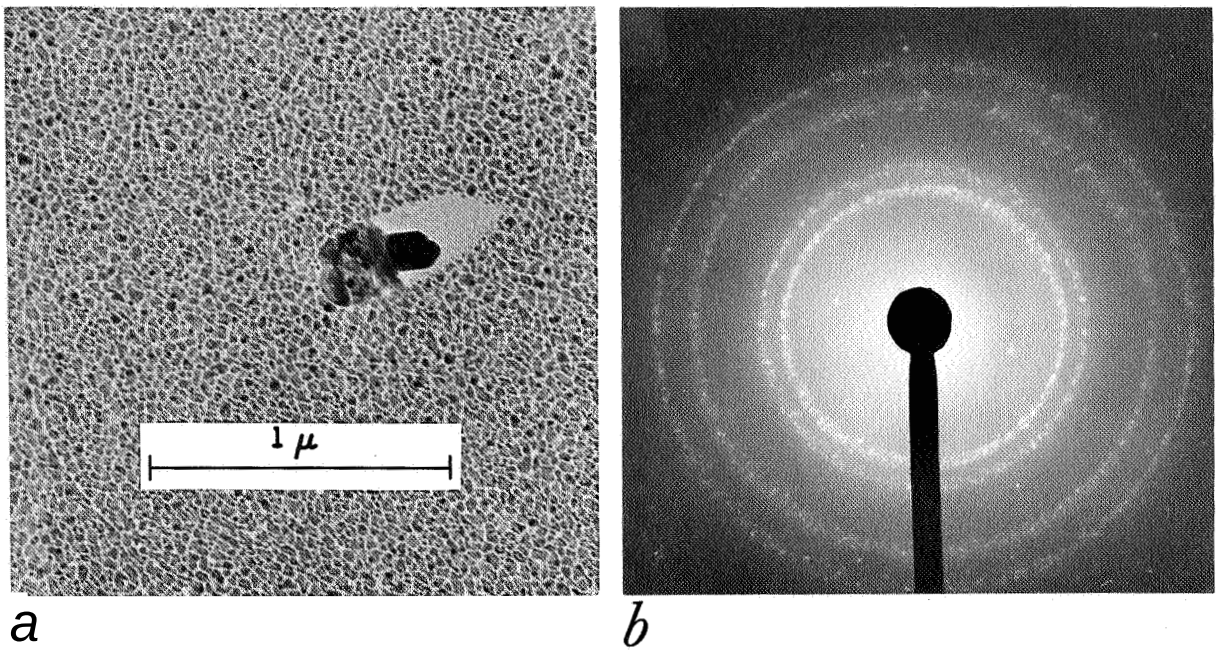

PLATE 1

a, Venus Flytrap particle, heated to 400° C for 1 hour. Grainy material is the aluminum shadow coat that forms part of the substrate. *b,* Selected area diffraction pattern of figure *a.* The ring pattern is due to the aluminum and is the only pattern generally appearing in the unheated particles. The two symmetrical spots inside the innermost ring are supposedly due to crystallinity produced by the heating. The *d* spacing is **3.62 A.** *c,* Olivine particles. *d,* Selected area diffraction pattern of smallest (0.5 μ) particle of figure *c.* The diffuse rings are due to the carbon substrate. The prominent *d* spacings are **4.82, 3.82,** and **3.07 A,** corresponding to the **(020), (021),** and **(002)** planes.

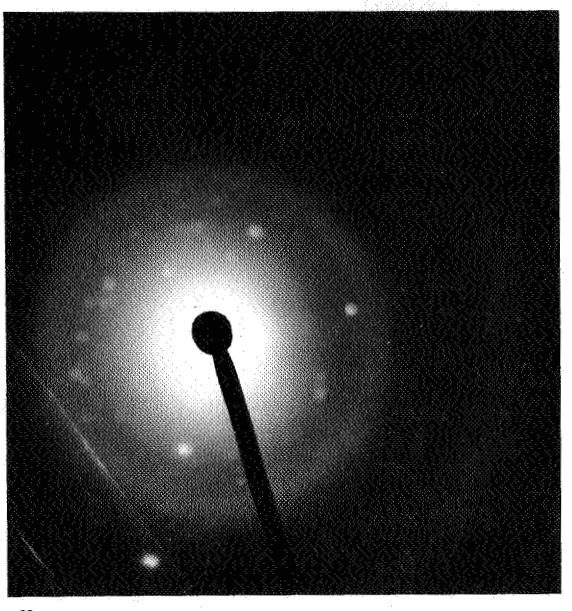

a

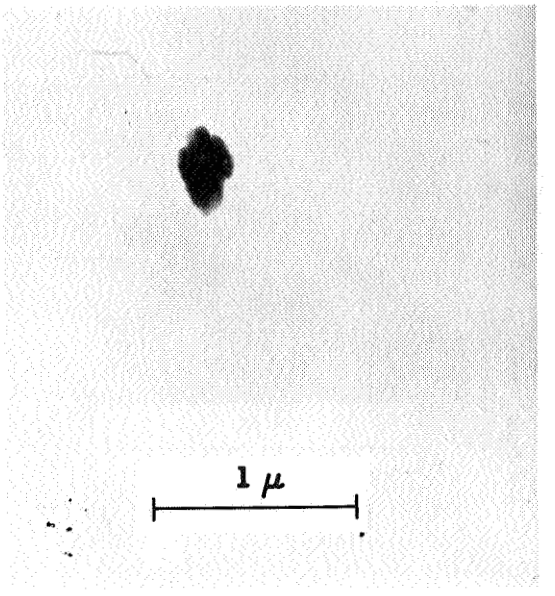

b

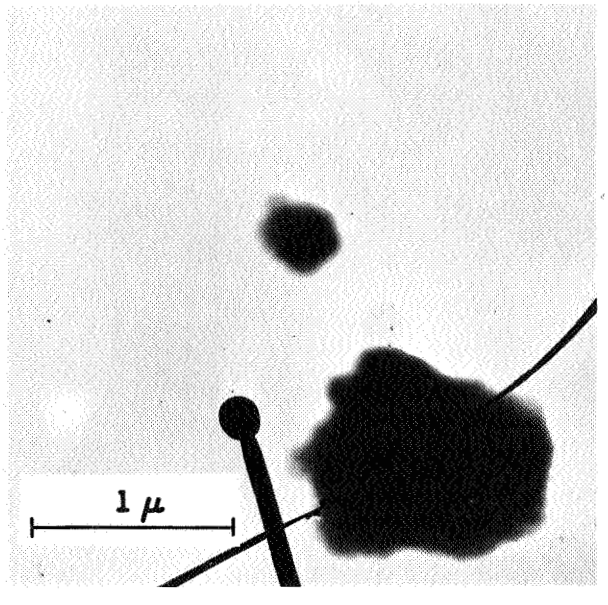

c

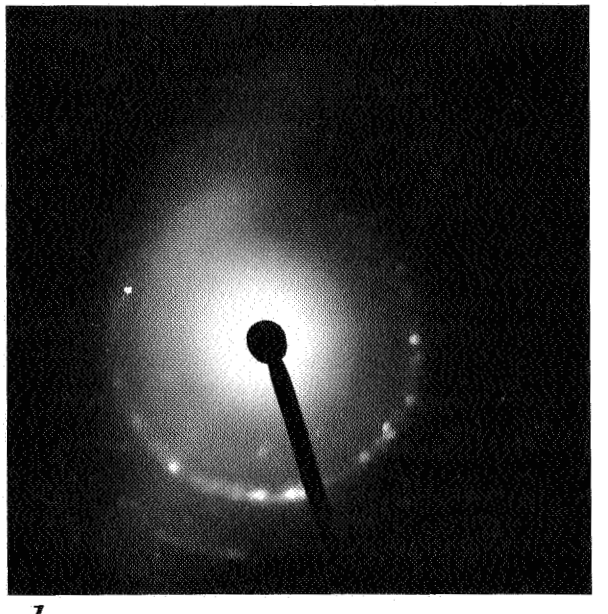

d

PLATE 2

a, Selected area diffraction pattern of second largest particle (0.9 μ) of figure 1*c*. Most prominent d spacing is **3.12 A.** *b*, Olivine particle. *d*, Selected area diffraction pattern of figure 3*c*. The d spacings are **2.31** and 1.64 **A.** *c*, Enstatite particles.

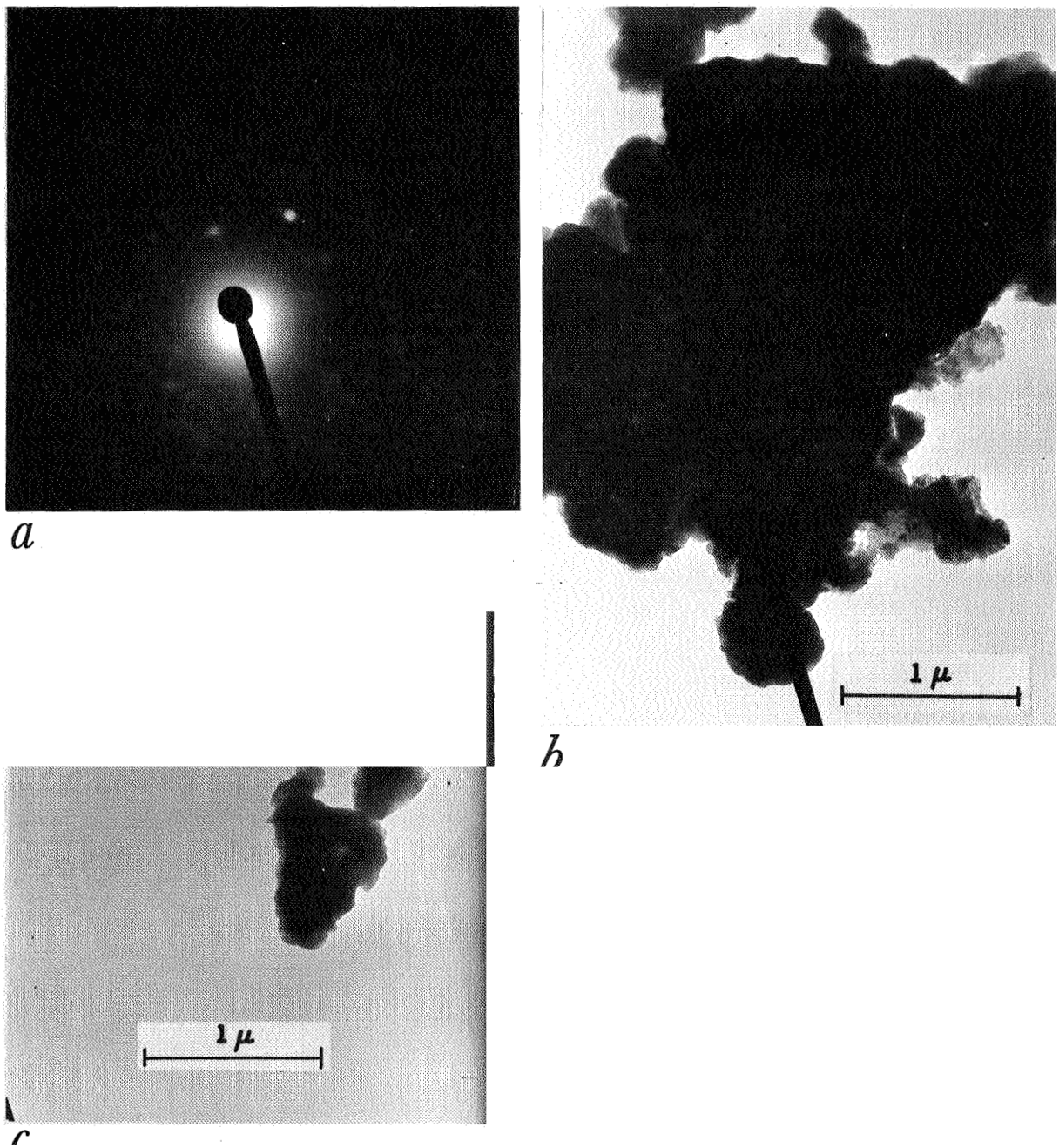

PLATE 3

a, Selected area diffraction pattern of smaller particle (0.4 μ) of figure 2*c*. The *d* spacings are 3.62 and 2.18 A. *b*, *c*, Enstatite particles.

Aerosol Samples Obtained from 9- to 12-km Altitude

C. E. MELTON [1]

Introduction

Aerosol samples have been obtained at monthly intervals in the altitude range from approximately 9 to 12 km over the southern California area. This air-borne monitoring program has been conducted in an effort to investigate the spatial density of the dust and determine the particle types and size distributions as functions of altitude and time. Particular attention has been directed toward detecting increases in specific types of particles that may be associated with meteor-shower activity. Such an approach has been undertaken in view of results obtained by previous investigators, namely, Parkin, Hunter, and Brownlow (1962) and Parkin and Hunter (1962), who have noted metallic flakes, some with amorphous attachments, in collections obtained shortly after peak meteor-shower periods, and Crozier (1962), who has noted possible shower-related increases in the deposition rate of black metallic spherules.

To date, aerosols from a total of 14 collection flights have been examined visually. The experimental procedures used in the collection program and the results and conclusions are discussed in the following sections.

Collectors

Ram-jet-type collectors are used in the aerosol collection program. These are identical with those used in the Extraterrestrial Dust Project of the Smithsonian Astrophysical Observatory, and have been described previously (Melton, 1964). The assembled collectors, prepared for high-altitude chamber test, and the struts used to mount the collectors on the aircraft are shown in plate 1. The wiring is attached to the rear of the collectors for altitude chamber test only. In actual collection, a solenoid-activated valve is opened, air is admitted through the 6-mm forward opening, passed into an expansion chamber, and filtered by a commercial cellulose-type filter. When the valve is closed, the air flow is diverted before reaching the collection chamber.

The collectors are mounted on the nose of the DC–8 and protrude about 25 cm from the plane's surface so that they are well into ambient air. Two collectors were flown on all flights: one was used for the aerosol collections, while the other served as a control and was not opened during flight.

Assembly procedure

In order to minimize contamination problems, the collectors used are cleaned and assembled under clean-room conditions. The exposed collection filters as well as the blank controls are also handled under clean-room conditions. The detailed procedure has been described previously (Melton, 1964). After exposure, the filters are mounted as illustrated in figure 1, and then subjected to optical examination.

Laboratory observational procedure

Filters were examined under direct lighting with magnifications up to 500×. Attention was directed toward the central exposed area of the filter, encompassing 269 mm². Particles > 4 μ were mapped and counted. Colored and transparent particles were mapped but not included in the count, since work by previous investigators (Hodge, 1961; Hodge and Wright, 1962; Fireman and Kistner, 1961)

[1] Space Sciences Department, Douglas Missile and Space Systems Division, Santa Monies, California.

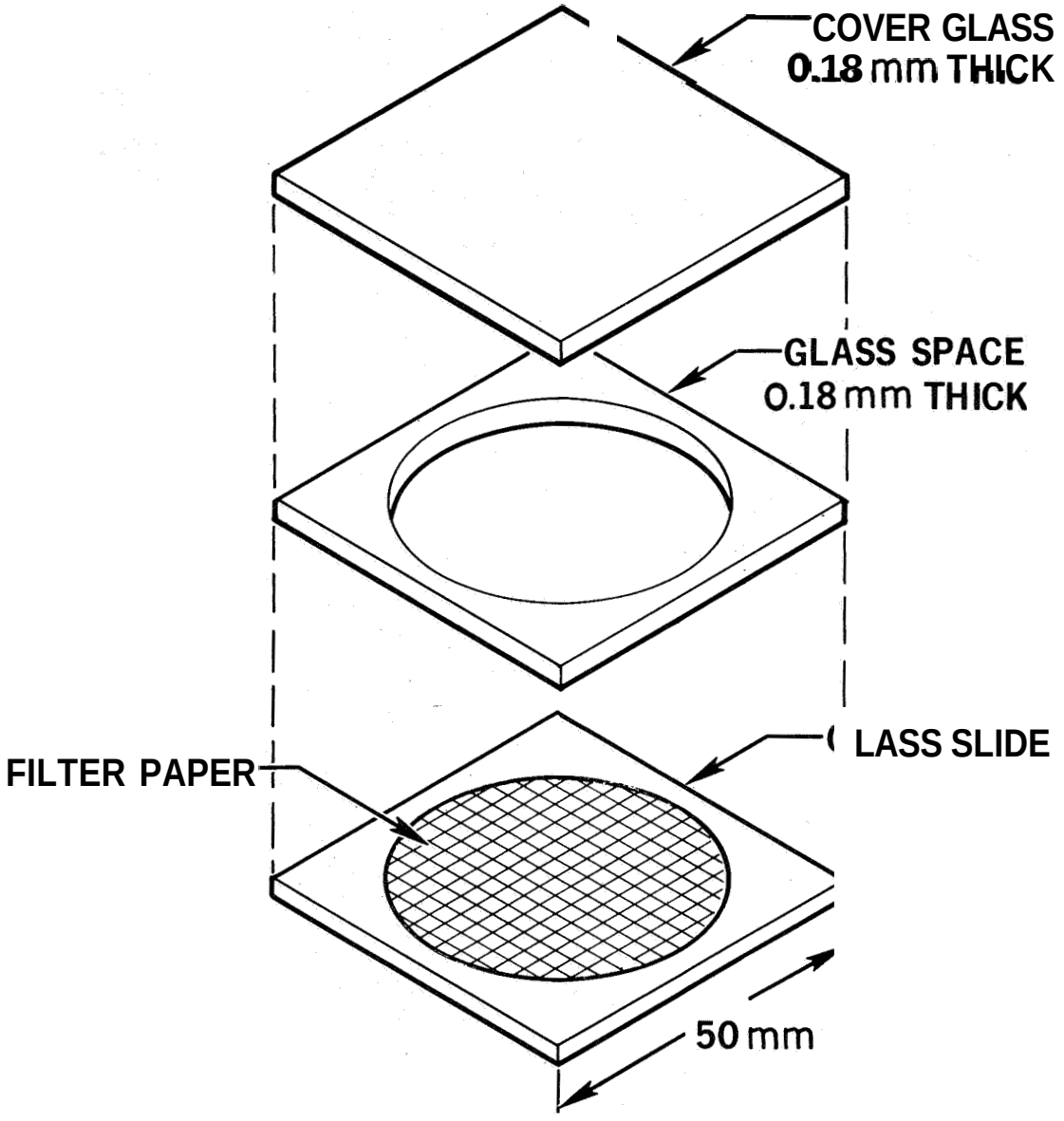

FIGURE 1.—Mounting assembly for optical examination of aerosols.

has indicated that these types are probably of terrestrial origin. Obvious collector fragments were also excluded.

Results and discussion

The fight data and results obtained from 14 collections are summarized in table 1. The particles counted on all filters were grouped into two general categories, spherules and opaque irregular types.

The total opaque particle density varied widely and showed no dependence on altitude, within the 9- to 12-kmrange. Also, no relationship could be established between particle spatial density and geographical location, i.e., number density of particles collected over inland areas varied as greatly as that observed in collections made from 50 to 100 km off the West Coast. Spatial densities of all opaque particles collected with sizes $\geq 4\ \mu$ ranged from about 20 to 200 particles/m^3. These results are typical of those obtained by other investigators (Hodge and Wright, 1962) for this altitude range.

TABLE 1.—*Summary of flight data* and *results*

Flight	Date	Altitude (km)	Volume sampled (m^3)	Total opaque particle density ($\geq 4\ \mu$) per m^3	Highly irregular number ($\geq 4\ \mu$)	Glassy spherule number ($\geq 4\ \mu$)		Opaque spherule density ($\geq 4\ \mu$) per m^3
						Test	Control	
1	July 19,1963	12.0-12.2	7.16	143	1	0	0	6.95
2*	July 20,1963	11.9–12.2	9.03	—	0	1	0	3.12
3	Aug. 18,1963	10.7–11.3	30.0	39	2	0	2	2.56
4	Aug. 19,1963	10.3–10.9	6.94	117	2	0	1	5.76
5	Sept. 17,1963	10.6–10.9	22.5	17	1	0	0	1.33
6	Oct. 8,1963	10.9–11.7	22.8	22	0	0	0	0.88
7	Oct. 9, 1963	9.4	11.5	47	1	1	0	1.75
8	Oct. 22, 1963	10.9–11.2	17.1	32	1	1	0	2.34
9	Feb. 8,1964	10.6–11.4	18.2	48	0	1	0	3.88
10	May 12,1964	11.0	11.1	180	1	0	1	5.45
11	June 19,1964	10.6–12.0	40.2	58	1	4	1	4.46
12	Aug. 5,1964	11.2–11.3	13.2	110	2	0	0	3.03
13	Aug. 10,1964	10.8–11.1	16.0	45	3	0	0	1.88
14	Nov. 17,1964	9.9–11.0	11.3	81	1	1	0	2.73

'Control filter torn.

Irregular particles

Although irregular particles are expected to predominate in the total extraterrestrial dust influx, little conclusive work has been done on them owing to the formidable contamination and discrimination problems involved. In the present program an attempt has been made to surmount these problems by looking for time variations in the spatial density of irregular particles correlated with meteor-shower activity. It was reported in a previous paper (Melton, 1964) that certain irregular fluffy-type particles were detected on filters exposed shortly after the Perseid meteor shower (August 1963). Similar particles were collected on flights during the 1964 Perseid shower (see table 1). However, as can be noted from table 1, a few such particles have also been found on several of the other flights.

A total of 16 of these highly irregular particles has been observed; none has been evident on the control filters. All the irregular particles have been collected during months in which there is considerable shower activity (see table 1). The single fight during the shower-free period, February–April, revealed no particles of this type. While this quiet period is long enough to ensure that even shower-related particles with slow fall times should not be present in any significant numbers, additional flights will have to be performed during the shower-free periods to provide more conclusive evidence that these irregular particles are indeed shower-associated. Several of the irregular particles are currently being prepared for electron-microprobe analyses, and data concerning the nature of these particles should be available shortly.

Spherules

The second group of particles, the spherules, are very conspicuous and are easily classified. Two distinct groups of spherules have been noted: transparent, sometimes colored, glassy types and opaque types.

The glassy spherules are of interest because of current theories concerning their possible origin as material that has been ejected from the lunar surface through meteoroid shower impacts. The present study provides no support for this theory, since there is no correlation of the number of glassy spherules collected with shower activity or with the relative position of the moon. Furthermore, since many of these spherules appeared on control filters, there is no evidence to indicate that any spherules collected were of extraterrestrial origin.

Among the smooth, opaque, perfect spherules, those that are black and metallic-appearing have been selected for detailed study, since they are the types often considered by other investigators as being meteoric in origin. Smooth, gray spherules as well as rough-appearing or slightly irregular spherules have been rejected from the present study. Particular attention has been directed toward determining any flux increase in black spherules that might be related to shower activity. The results for the spherule counts are given in table 1. It can be seen that the ratio of the number of spherules to the total particles remains approximately the same; that is, from 3 to 8 percent of the total, with the largest percentage of spherules collected on the February 1964 flight (during the quiet period). These data give no indication of marked variation with shower activity.

From the observed total number of metallic spherules in each 1-μ interval, a size distribution over the range 4 to 8 μ was obtained by least squares. The equation for the size distribution may be given as

$$n(\ell)=\frac{5.43\times10^4}{\ell^{3.63}}, \qquad (1)$$

where $n(\ell)$ is the number of spherules per micron of diameter ℓ (microns), corrected for a collector efficiency of 10 percent (F. W. Wright, 1963, private communication). The differential distribution (1) can be used to compute a cumulative flux distribution for comparison with results from other investigations. Since equation (1) is presumably reliable only to about 10 μ, the differential size distribution was extended to 50 μ by a function representing an inverse 4.6-power law, fitted to equation (1) at $\ell=10$ μ. The inverse 4.6-power represents a convenient exponent for the approximate differential size distribution obtained from Crozier's (1962) data for spherules in the size range 10 to 50 μ. The contribution from spherules of diameter >50 μ was neglected. A fall velocity based on Stokes' law has been assumed for spherule sizes to 50 μ.

The results of the present study as plotted in figure 2 are apparently in good general agreement with the other results shown. For the most part, the differences among these results can probably be accounted for by differences in experimental conditions, uncertainties in the efficiencies of collectors, and locations at which collections were made.

The differential size distribution given by equation (1) has been used to obtain an estimate of the mass accretion rate by the earth, in the size range 4 to 10 μ. That is,

$$M=\int_4^{10}\frac{5.43\times10^4}{\ell^{3.63}}\,\frac{v}{V}\,\frac{\pi}{6}\rho\ell^3 d\ell, \qquad (2)$$

where $v=A\ell^2$, fall velocity from Stokes' law, $V=$ total air volume, and $\frac{\pi}{6}\rho\ell^3=$ mass of spherule of diameter ℓ. The total volume measured was 237 m^3. The constant in the expression for the fall velocity has been evaluated with $v=10^{-2}$ m/sec for a spherule of diameter 10 μ. The density ρ was taken as 5 g/cm^3.

The mass influx obtained is 8.4×10^4 metric tons over the surface of the earth per year in the size range 4 to 10 μ. This is compared in table 2 with results from other investigators.

The mass influx derived above is apparently consistent with results obtained by others in the given size range. Extrapolation of the present differential size distribution, given by equation (1), beyond 10 μ seems to be incorrect, as noted previously. Such extrapolation leads to a spherule mass influx upon the earth of approximately 4.2×10^6 metric tons/year, which is much too high when compared with observation (Crozier, 1962; Schmidt, 1963). This result provides additional evidence that the decrease in the number of spherules with increasing size is indeed much greater for spherules whose diameters exceed 10 μ than for those in the interval studied here.

Summary and conclusions

Results from the 14 flights analyzed so far can be summarized as follows: The spatial density of all opaque particles collected (≥ 4 μ) at an altitude of 9 to 12 km varied widely, ranging from about 20 to 200 particles/m^3. These particle spatial densities show no dependence on altitude. Some highly irregular particles have been found but have not as yet been definitely related to shower activity. The results give no evidence that extraterrestrial glassy spherules were collected. There is no indication of an

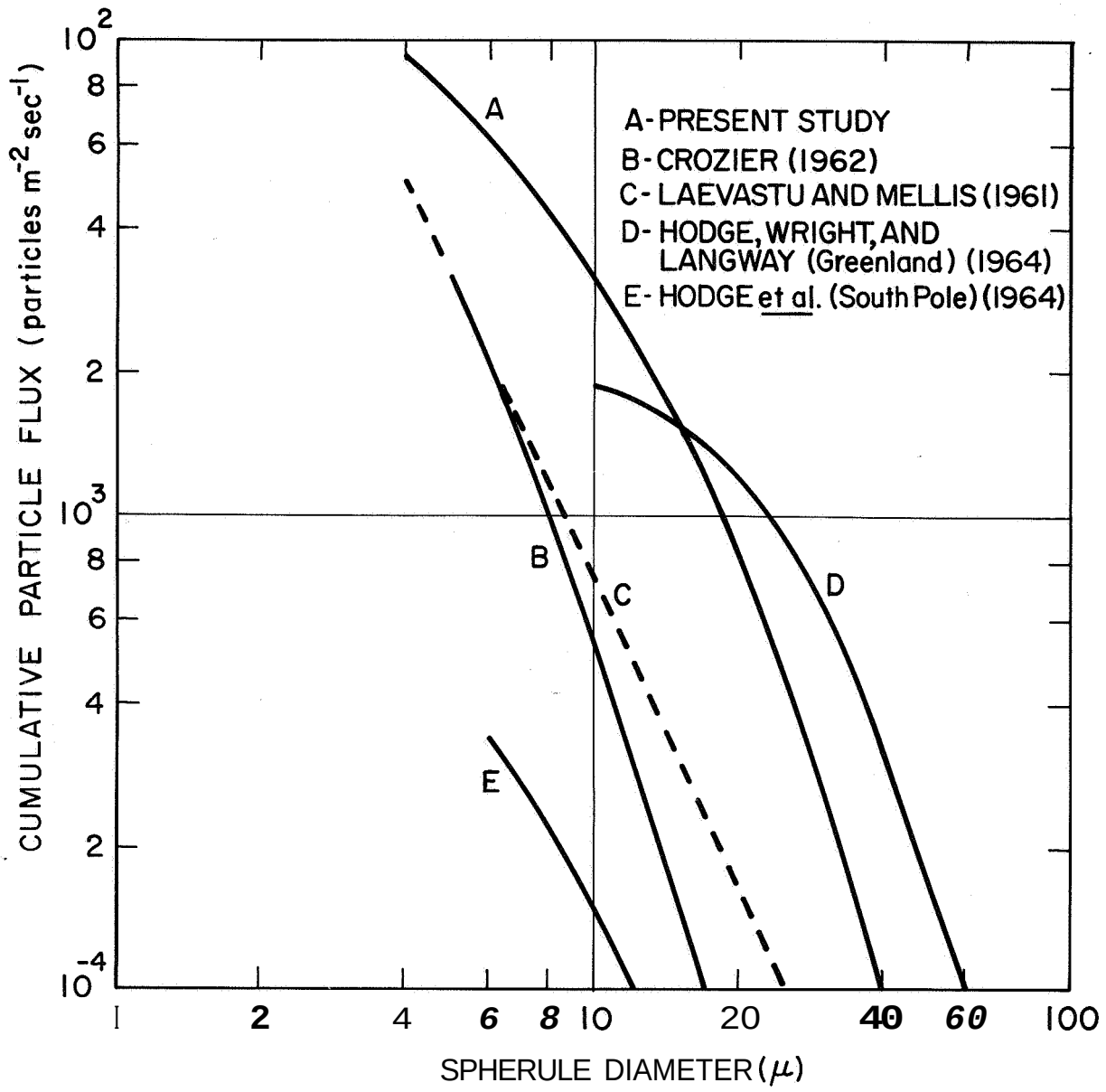

FIGURE 2.—Cumulative flux distribution for spherules,

increase in the spatial density of metallic spherules associated with meteor showers. The differential size distribution for the collected metallic spherules follows approximately an inverse fourth-power law. This distribution leads to values of the cumulative flux of particles and of the total earth accretion rate in the observed size range that are consistent with results of other investigators.

Acknowledgments

I wish to thank Drs. F. W. Wright, Smithsonian Astrophysical Observatory, and P. W. Hodge, University of California, Berkeley, **for** permitting me to use one of their collectors in this program. I am also greatly indebted **to** Dr. J. A. Ryan and Mr. M. B. Baker, Douglas Missile and Space Systems Division, Santa Monica, for many valuable discussions and comments. The

TABLE 2.—*Estimated* annual deposit of metallic spherules *over* the earth

Particle size range (μ)	Source for particles	Accretion rate (metric tons/year)	Reference
30–250	Pacific sediments	2.4×10^3 to 5×10^3	Pettersson and Fredriksson (1958)
10–170	Antarctic snow	1.2×10^5 (average)	Schmidt (1963)
5–160	Greenland snow	9.1×10^5	Langway (1963)
5–60 (>15	Air	1.6×10^5 (5×10^4)	Crozier (1962)
3–30	Air	3×10^4 to 3×10^5	Fireman and Kistner (1961)
3–15	Air	5×10^5	Hodge and Wildt (1958)
>3	Air	2×10^5	Wright and Hodge (1962)
>5	Greenland ice	2×10^5	Wright, Hodge, and Langway (1963)
4–10	Air	8.4×10^4	Present study

cooperation of the Douglas Flight Test Group, Long Beach, in the aircraft flights, and the assistance of Mr. R. H. Edwards in the collection program are greatly appreciated.

References

CROZIER, W. D.
1962. Five years of continuous collection of black magnetic spherules from the atmosphere. Journ. Geophys. Res., vol. 67, pp. 2543–2548.

FIREMAN, E. L., and KISTNER, G. A.
1961. The nature of dust collected at high altitudes. Geochim. et Cosmochim. Acta, vol. 24, pp. 10–22.

HODGE, P. W.
1961. Sampling dust from the stratosphere. Smithsonian Contr. Astrophys., vol. 5, no. 10, pp. 146–152.

HODGE, P. W., and WILDT, R.
1958. A search for airborne particles of meteoric origin. Geochim. et Cosmochim. Acta, vol. 14, pp. 126–133.

HODGE, P. W., and WRIGHT, F. W.
1962. The space density of atmospheric dust in the altitude range 50,000 to 90,000 feet. Smithsonian Contr. Astrophys., vol. 5, no. 14, pp. 231–238.

HODGE, P. W.; WRIGHT, F. W.; and LANGWAY, C. C., Jr.
1964. Studies of particles for extraterrestrial origin, 3: Analyses of dust particles from polar ice deposita. Journ. Geophys. Res., vol. 69, pp. 2919–2931.

LAEVASTU, T., and MELLIS, O.
1961. Size and mass distribution of cosmic dust. Journ. Geophys. Res., vol. 66, pp. 2507–2508.

LANGWAY, C. C., Jr.
1963. Sampling for extraterrestrial dust on the Greenland ice sheet. Int'l. Assoc. Sci. Hydrology, publ. no. 61, pp. 181–198.

MELTON, C. E.
1964. Atmospheric aerosol collections near 40,000 feet with a DC–8. Ann. New York Acad. Sci., vol. 119, pp. 116–125.

PARKIN, D. W., and HUNTER, W.
1962. Meteorites and cosmic dust. In Advances in Astronomy and Astrophysics, ed. by Z. Kopal, Academic Press, New York, pp. 105–163.

PARKIN, D. W.; HUNTER, W.; and BROWNLOW, A. E.
1962. Metallic cosmic dust with amorphous attachmenta. Nature, vol. 193, pp. 639–642.

PETTERSSON, H., and FREDRIKSSON, E.
1958. Magnetic spherules in deep sea deposits. Pacific Sci., vol. 12, pp. 71–81.

SCHMIDT, R. A.
1963. Microscopic extraterrestrial particles from the Antarctic Peninsula Traverse. Univ. Wisconsin Geophys. and Polar Res. Ctr. Rep. no. 63-3.

WRIGHT, F. W., and HODGE, P. W.
1962. Space density of dust in the stratosphere. Nature, vol. 195, p. 269.

WRIGHT, F. W.; HODOE, P. W.; and LANGWAY, C. C., Jr.
1963. Studies of particles for extraterrestrial origin, 1. Chemical analyses of 118 particles. Journ. Geophys. Res., vol. 68, pp. 5575–5587.

Abstract

Aerosol samples have been obtained at monthly intervals in the altitude range from 9 to 12 km over the southern California area. The spatial density of all opaque particles collected ($\geq 4\ \mu$) varied widely, ranging from about 20 to 200 particles/m³, and showed no dependence on altitude. Certain highly irregular particles have been found, but have not as yet been definitely related to meteor-shower activity. No increase in the spatial density of metallic spherules was determined to be associated with meteor showers. The differential size distribution for the collected metallic spherules follows approximately an inverse fourth-power law. This distribution leads to a mass influx of 8.4×10^4 metric tons per year upon the earth.

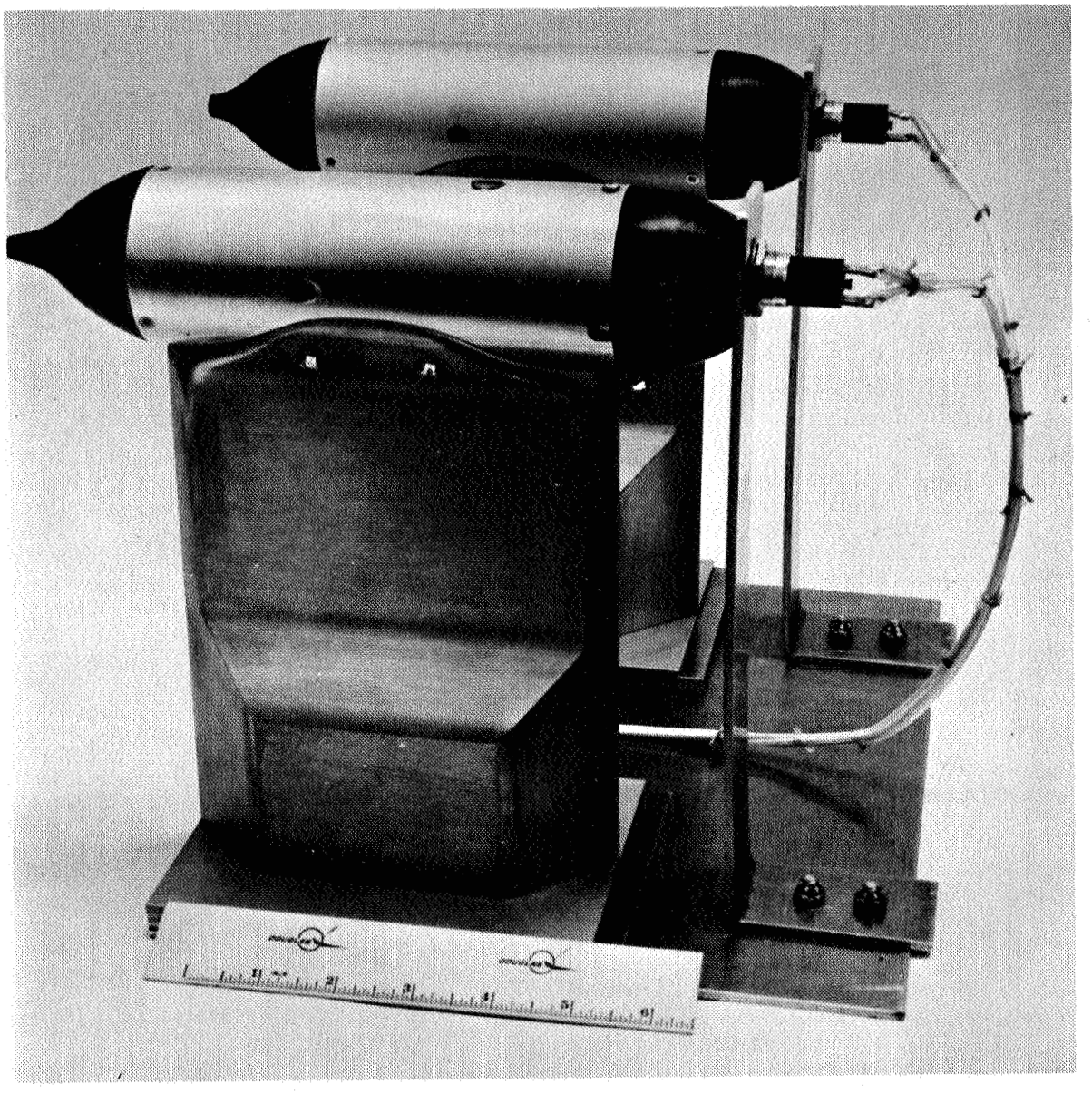

PLATE 1

Aerosol collectors mounted for high-altitude chamber test.

Measured Velocities of Interplanetary Dust Particles from OGO–1

C. S. NILSSON [1] and W. M. ALEXANDER [2]

An Interplanetary Dust Particle Experiment was flown on the OGO–1 satellite launched September 5, 1964. The primary purpose of the experiment was to measure the speeds and directions of arrival of dust particles within 120,000 km of the earth's surface, and thus determine the orbits of these particles. If sufficient orbits had been measured, the nature of the apparent dust cloud around the earth (Whipple, 1961) could have been determined. Troubles were encountered with both the spacecraft and the experiment, however, and only three probable dust-particle impacts were recorded. The probable orbits of these particles are described in this paper in greater detail than in an earlier report (Nilsson et al., 1965).

The detector array consists of four tubular detectors aligned along the three body axes of the spacecraft. One detector looks radially away from earth ($-Z$ direction), and the other three look in a plane normal to the Z direction. Each detector accepts particles with an apparent radiant not more than 6° removed from the detector axis (see fig. 1). An impacting micrometeoroid first encounters the front thin film sensor, which comprises two thin films and a grid. The plasma generated by the passage of the particle through these films starts a 2 mc/sec clock, which is stopped when the particle impacts on the rear sensor 10 cm down the tube. Thus, the time of flight over 10 cm is measured, and the particle velocity following the penetration of the front sensors is determined. The deceleration suffered by a 10^{-10} g iron particle passing through the front sensor at speeds around 3 km/sec has been experimentally determined to be about 10 percent.

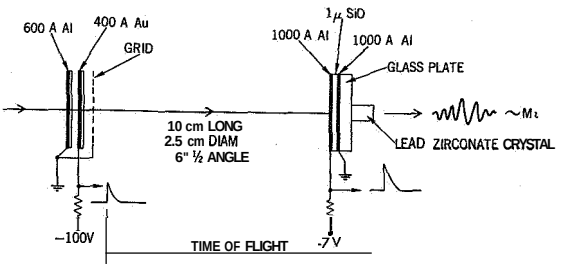

FIGURE 1.—The OGO–1 micrometeoroid sensor, which determines particle mass and velocity.

The rear sensor performs two main functions: First, there is a thin film capacitor deposited on a glass plate. This capacitor momentarily shorts when a particle impacts and the resultant signal stops the time-of-flight clock. Second, a lead zirconate transducer bonded to the back of each glass plate provides a measure of the momentum of each impacting particle. With the velocity known, the particle mass can be determined. It was found from the impact of small iron particles accelerated to 3 to 5 km/sec that the transducer system would respond to momenta exceeding 3×10^{-5} dyne-sec.

Thus, each tubular detector can provide a measure of the velocity, direction of arrival, and mass of an impacting dust particle.

Three particle impacts were recorded on one tube during the first 10 days of operation. Spacecraft trouble was such that the experiment was turned on for only 56 hours of this time,

[1] Smithsonian Astrophysical Observatory, Cambridge, Mass.; formerly at Goddard Space Flight Center, National Aeronautics and Space Administration, Greenbelt, Md.

[2] Temple University, Philadelphia, Pa.; formerly at Goddard Space Flight Center, National Aeronautics and Space Administration, Greenbelt, Md.

and data were recorded for only 4 of these 56 hours. It can be seen from figure 2 that a total of 17 hours of data was received during these 10 days, but 13 hours of this corresponded to times during which the experiment was turned off. We cannot tell from the data alone whether the experiment was turned on or not; only from the records of the power commands transmitted to the spacecraft do we know the periods for which power was applied to the experiment. This fact is of .importance in our assessing the reality of the impact data, as will be shown below. Unfortunately, the rear sensor capacitors can suffer a permanent short when subjected to particle impact with the power off the experiment. There was no provision for clearing such a short on this particular experiment, and we believe that three of the four capacitors were dead before experiment data were received. The experiment was again turned off for a short period after the third impact had been recorded, and although a great quantity of data has been received since, no more impacts have been noted. This suggests that the fourth sensor was shorted by impact when the experiment was turned off on the 10th day after launch.

In view of the paucity of data (the impacts total only 10 bits of information with no redundancy), we had to look rather closely into the statistical reality of the data, considering both experiment noise and telemetry noise. There is no history of the former in our experience with the instrument flown. The unit is well shielded electrically, and also a time-of-flight measurement requires two independent events to occur within a very restricted time interval. There were no spacecraft commands sent at the time of the three events, nor did the neighboring telemetry words show any signs of radio-frequency interference. We have considered the possibility of telemetry noise indicating false impacts, and treated the first weeks of data in considerable detail. The probabilities of events occurring by chance in 43 hours' data are given in the left-hand column of figure 2. Thus, we can see that there is less than 1×10^{-3} probability that all three events recorded to day 270 were due to chance telemetry noise. This strongly suggests that at least some of the data are real, and that the cessation of events after day 259 was due to the failure of the last sensor. This being the case, we can strengthen the probabilities of the events being real. The experiment was turned on only during 4 of the 17 hours for which we received data from launch through day 259. *All* three apparent impacts were extracted from the data without knowledge of whether the experiment was on or off. Subsequently, we found that all three events occurred during the 4 hours that the experiment was turned on. This fact is not only heartening, but can be used to improve the probability figures concerning the reality of the data. The right-hand column includes this information. There is only a 0.1 chance that any one impact is false, and less than 3×10^{-3} probability that two of the three events are false. These figures could be further improved by our decreasing the data interval from day 270 to day 260, and also by our using the fact that all three hits were recorded on the one sensor.

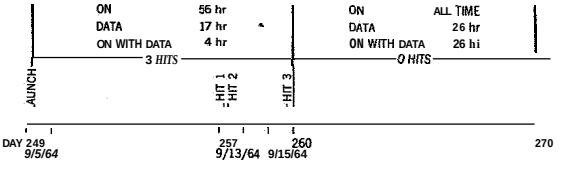

STATISTICAL REALITY OF DATA

	TELEMETRY NOISE TO DAY 270	TOTAL PROBABILITY
3 FALSE	$1.0\ 10^{-3}$	$1.8\ 10^{-5}$
≥ 2 FALSE	$1.7\ 10^{-2}$	$2.9\ 10^{-3}$
≥ 1 FALSE	$1.8\ 10^{-1}$	$1.1\ 10^{-1}$
ALL REAL	$8.2\ 10^{-1}$	$8.9\ 10^{-1}$

FIGURE 2.—Details of operation of the micrometeoroid experiment on OGO–1. The lower table indicates the likelihood of the three impacts being false.

The details of the three impacts are shown in table 1. The first two were recorded within 27 min of each other at altitudes in excess of several earth radii, and the observed velocities were in the range 30 to 50 km/sec. These velocities preclude any possibility that the particles were in closed orbits around the earth. The third impact indicates a low-velocity particle that impacted at a much lower altitude and may have had a mass an order of magnitude greater than the masses of the first two. No

TABLE 1.—*Impact parameters of particles observed by the cosmic-dust experiment on OGO-1*

	Time of impact UT *1964*	Altitude (km)	Observed velocity (km/sec)	Geocentric velocity (km/sec)	Mass (g)
Hit *1*	$257^d03^h45^m$	*22,490*	$40<v_0<50$	$40<v_g<70$	$<7\times10^{-12}$
Hit *2*	$257^d04^h12^m$	*28,740*	$33<v_0<40$	$30<v_g<60$	$<1\times10^{-11}$
Hit 3	$259^d18^h35^m$	*2,960*	$e\ 7<v_0<4.8$	$8<v_g<15$	$<7\times10^{-11}$

minimum values for the particle masses are given, as in each case there was no recorded output from the transducer, presumably because the impact momenta were below the threshold of the experiment.

The uncertainty in 'the observed velocity arises partly from the necessity to digitize the time of flight for telemetry and partly from the uncertainty in the actual deceleration through the front sensor. The maximum deceleration allowed in computing the possible geocentric velocities was 30 percent. The attitude of the spacecraft at the times of the three impacts was unfortunately not known, so that the range of geocentric velocities possible for each impact was broadened even further to the values given in table 1. Even with the true geocentric velocities being subject to such wide limits and with only the spin axis of the spacecraft known, it has been possible to deduce something about the probable orbits of these three particles before impact.

The probable orbital elements of each particle have been computed in the following manner. The total acceptance angle of each tubular sensor is about 12°, so we have divided the spin revolution into 36 intervals of 10° each and then computed the orbit of each particle for 36 directions of arrival. In addition, we have considered four possibilities for the time-of-flight digitizing error and four values of deceleration through the front thin films. Thus, there are 16 possibilities for the true velocity and 36 possibilities for the direction of arrival of the particle. This totals 576 possibilities. By computing the orbital parameters for each of the 576 cases and summing them, one can obtain a probability distribution for each orbital element. We have done this for each of the three particles.

Consider hit 3 first. The particle could have been in either a closed geocentric orbit or an orbit of low eccentricity around the sun. There is little we can learn about the geocentric orbit, owing to the large uncertainty in the velocity vector, so we shall consider only the heliocentric possibilities. Figure 3 shows the probability distribution for the reciprocal semimajor axis. The orbit must have been similar in size to that of the earth. From figure 4 we can see that the orbital eccentricity must have been small, probably less than 0.3. Finally, from figure 5, we see that the inclination to the

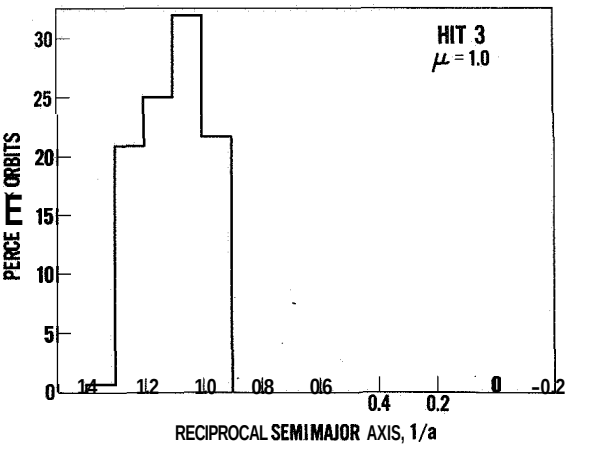

FIGURE 3.—The probability distribution for the semimajor axis of the orbit of particle 3.

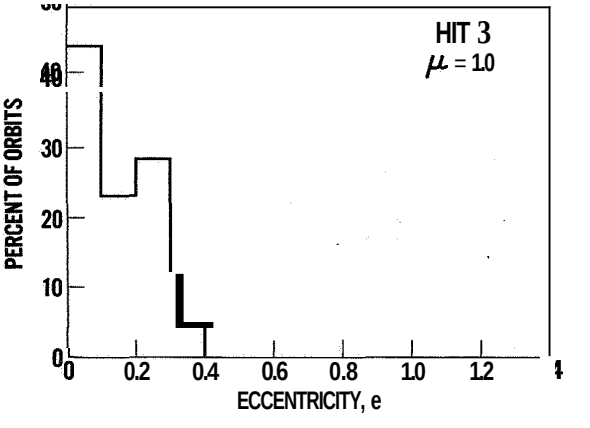

FIGURE 4.—The probability distribution for the eccentricity of the orbit of particle 3.

plane of the ecliptic must also have been small. Thus, if this particle was in a heliocentric orbit at the time of impact, the orbit must have been direct, of small inclination and low eccentricity, and of a size similar to that of the earth's orbit; the particle would have stood a good chance of being captured by the earth.

In figure 6 we see the probable geocentric velocity of the first particle. The velocity relative to the earth could have been anywhere from 40 to 70 km/sec, with a most probable value around 50 km/sec. We cannot learn much about the size of the orbit, but the eccentricity shows a meaningful distribution, as can be seen in figure 7. All the cases for which the computed eccentricity is greater than 1.4 have been excluded from the distributions. This value corresponds to a very markedly hyperbolic orbit around the sun, and any particle in such an orbit would quickly leave the solar system. Thus, we are not likely to meet many of these particles. The particle probably had a high eccentricity. Two histograms are shown for different values of the effective gravitational constant μ. Radiation pressure is quite significant for particles of this size and, like gravity, radiation pressure decreases as the square of the distance from the sun. Thus, we can allow for radiation pressure by reducing the effectivegravitational constant. We have used 0.75, an arbitrary value for μ, to assess the importance of this phenomenon. In this case, it slightly increases the probability of a high value of eccentricity.

Figure 8 shows a distribution of inclination to the ecliptic plane for hit 1, which is quite revealing. The orbit was possibly retrograde, or at least of high inclination. The particle could not have been traveling in a direct orbit near the ecliptic plane. Davies and Gill (1960), Hawkins (1962), and Nilsson (1964) have detected radio meteors in high-inclination orbits, but generally these are orbits of low

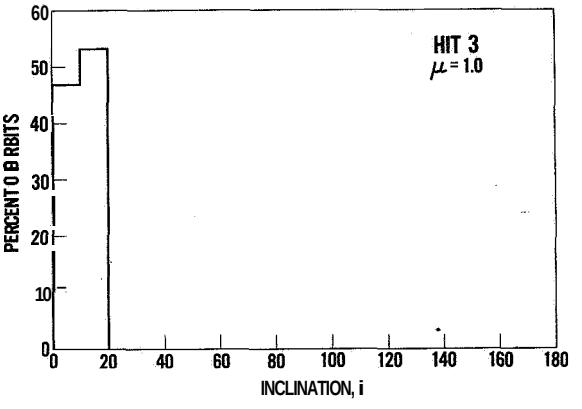

FIGURE 5.—The probability distribution for the inclination of the orbit of particle 3.

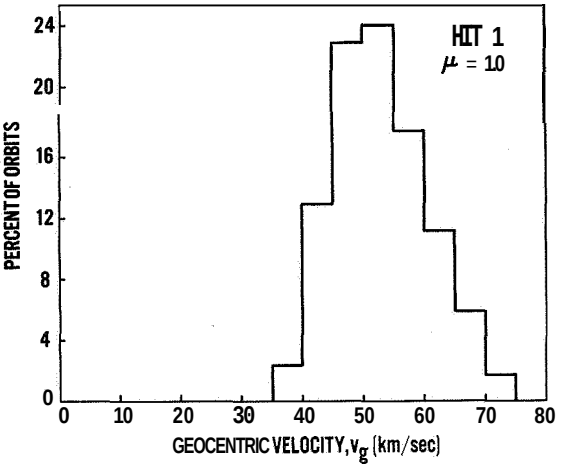

FIGURE 6.—The probability distribution for the geocentric velocity of particle 1.

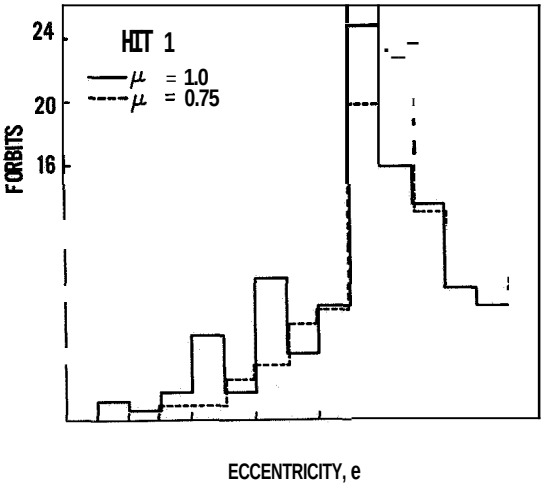

FIGURE 7.—The probability distributions for the eccentricity of the orbit of particle 1. The distribution μ=0.75 corresponds to a value of effective gravitational constant reduced by radiation pressure.

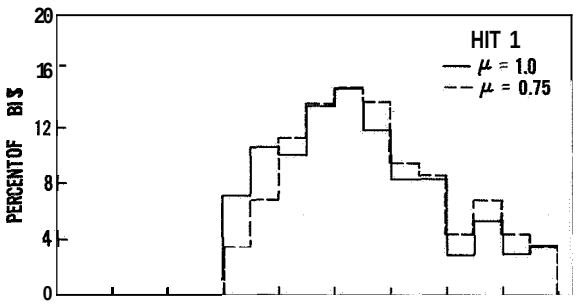

FIGURE 8.—The probability distributions for the inclination of the orbit of particle 1.

eccentricity, say $e<0.5$. Hit 2 has similar orbital parameters to those of hit 1, so here we have two particles in high-inclination orbits of high eccentricity. For masses less than 10^{-11} g we would not expect the particles to remain in these orbits for periods much greater than 10^3 or 10^4 years, so probably they were of relatively recent origin, perhaps from a long-period comet. The direction of the spin axis of the spacecraft precludes any possibility that the two high-speed particles came from the moon. They must have been in heliocentric orbits.

Finally, it should be noted, without too much emphasis, that the flux based on these three impacts in 4 hours is in excellent agreement with the microphone data recorded by previous near-earth satellites (Alexander et al., 1963).

Acknowledgment

One of the authors (C. S. N.) has been supported in this work by a NAS–NASA Research Associateship.

References

ALEXANDER, W. M.; MCCRACKEN, C. W.; SECRETAN, L.; and BERG, O. E.
1963. A review of direct measurements of interplanetary dust from satellites and probes. *In* Space Research 111, ed. by W. Priester, North-Holland Publ. Co., Amsterdam, pp. 891-917.

DAVIES, J. G., and GILL, J. C.
1960. Radio echo measurements of the orbits of faint sporadic meteors. Monthly Notices Roy. Astron. Soc., vol. 212, pp. 437-462.

HAWKINS, G. S.
1962. Radar determination of meteor orbits. Astron Journ.,. vol. 67, pp. 241-244.

NILSSON, C. S.
1964. A Southern Hemisphere radio survey of meteor streams. Australian Journ. Phys., vol. 17, pp. 205-256.

NILSSON, C. S.; ALEXANDER, W. M.; MCCRACKEN, C. W.; BERG, O. E.; and SECRETAN, L.
1965. Measured velocities of interplanetary dust particles. Nature, vol. 208, pp. 673-674.

WHIPPLE, F. L.
1961. The dust cloud about the earth. Nature, vol. 189, pp. 127-128.

3

Measurements of Interplanetary Dust-Particle Flux from Explorer 16 CdS and Wire Grid Dust-Particle Detectors

L. SECRETAN [1]

Introduction

Explorer **16** (plate **1)** was designed essentially to assess the micrometeoroid hazard to thin sheet metal exposed in space. Two other experiments were added in the form of wire grids and a mylar-covered CdS photoconductor. The purpose of this paper is to describe these two experiments and to analyze the data derived from them.

Explorer **16** was the third satellite in a series of three Scout **S55** launches. The first launch failed, and the second partially failed without providing data. The latter launch was aloft long enough to show a defect in the design of the CdS detector. This was corrected and the detector operated normally in Explorer **16,** and will be described presently. Explorer **16** was launched on December **16, 1962.** It had a twin telemetry system **A** and B. System **A** operated normally until May **29, 1963,** and **B** operated until July **25, 1963. A** report on all the experiments for the first **28** of **221** days of satellite operation is given by Hastings **(1963).** The description of the wire grid and of the CdS experiments follows, but no attempt is made to compare these with the other experiments aboard the satellite.

Description of the two sensors

CDS CELLS.—The design of the Explorer **16** CdS sensors was derived from the original design used successfully on Vanguard **3** (1959η) (LaGow, Secretan, and Giuliani, **1958)** and on Explorer **7** (1959 ι1) (LaGow and Secretan, **1963).** Figure **1** shows a cross section of the cell with the mylar stretched across the face of the cell. The vent holes, shown in plate **2,** are designed to provide large air passages, but do not permit the sunlight to reach the sensitive cell.

The mylar film covering the cells was coated on both sides with aluminum in order to provide absolute opacity and to ensure that any light input would be caused by perforation and not by surface erosion or flaking. There is one cell for each telemetry system **A** and B. The effective area of each cell is 2×10^{-3} m^2. The mylar film of cell **A** was left completely opaque, while the film of cell B was perforated with a nominal 0.002-inch hole for in-flight calibration purposes. When the satellite was in orbit, the initial resistance of cell B dropped to a value near **40** K ohms, which showed that the system started operating as expected with a solar aspect angle of 30° from the normal. During the lifetime of the experiment, this aspect angle was **30" or** less.

COPPER WIRE GRIDS.—The wire-wound cards are shown in figure **2,** and their dimensions are given in table **1.** Hastings **(1963)** has described the wire-grid experiment in detail.

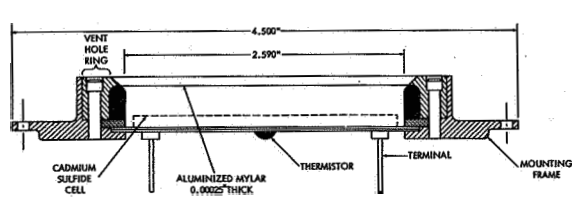

FIGURE 1.—The CdS cell.

[1] Goddard Space Flight Center, National Aeronautics and Space Administration, Greenbelt, Md.

TABLE 1.—*Wire* thicknesses and the areas of the wire cards

Diameter of wire		Number of sensors	Areal sensor (ft^2)	Total area	
(inch)	(μ)			(ft^2)	(m^2)
0.002	50	14	0.0474	0.664	6.1×10^{-2}
0.003	75	32	0.0948	1.517	14.1×10^{-2}

Total projected area $=20.2\times10^{-2}$ $m^2=0.2$ m^2

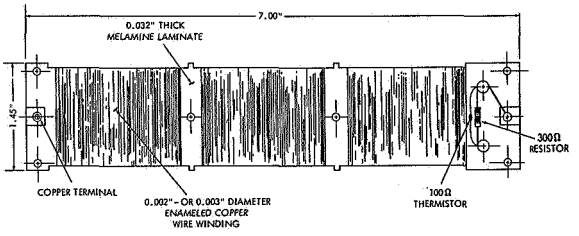

FIGURE 2.—The copper-wire card detector.

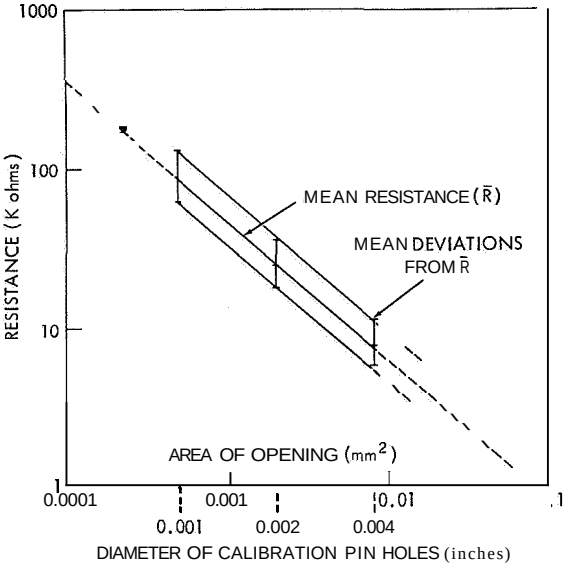

FIGURE 3.—Calibration of Explorer 16 CdS cells.

Calibration of detectors

CDS PHOTOCONDUCTORS.—About a dozen CdS cells were tested and calibrated to find two that had nearly the same sensitivity to light inputs. The calibration established the change of resistance of each cell for a given light input through calibrated pinholes. The cells with the most uniform light sensitivity across their entire surfaces mere selected. The calibration curve applicable for the two cells in orbit is shown in figure 3. The abscissa shows the area of the pinhole in square millimeters; the calibration pinholes used were 0.001, 0.002, and 0.004 inch (or 25, 50, 100 μ) in diameter. The ordinate shows the resistance of the cells in E ohms. The line drawn through the mean values, obtained when the cell was rotated for 5 min in a xenon arc beam, has been used to evaluate the telemetered resistance data. Preliminary tests were made to establish the correlation between the light intensity of the xenon arc and that of the sun. The scatter in the data for figure 3 represents the variation in sensitivity over the complete area of the cell established by the positioning of single pinholes during the calibration. The cumulative characteristics of the detector were established during laboratory calibrations. Since in flight the detector measures the cumulative area of many necessarily random perforations, the resistance value for a large number of holes approaches the mean value shown in figure 3. The relationship between the perforated hole diameter in ¼-mil mylar and particle size has been established in the laboratory by Friichtenicht (1961) and independently by the author. For iron particles, $\rho=7.8$ g/cm^3, the hole size is 1 to 1.5 times larger than the penetrating particle.

The CdS cells were calibrated with respect to temperature, and a linear relationship between resistance and temperature was determined for the expected operating thermal range.

Wire grid thermo-electric compensation

The copper-wire grids were temperature-compensated for resistance changes, which were not to exceed 3 percent between —20° C and 60° C. Figure 4 shows the circuit of the 21 TE5 compensating thermistor and associated wire grids. The resulting resistance curves are shown for 0.003- and 0.002-inch wires, compared with a curve for uncompensated wire.

Results of CdS cell and wire-grid experiments

The processed data from the two experiments were received in the following forms: (1)

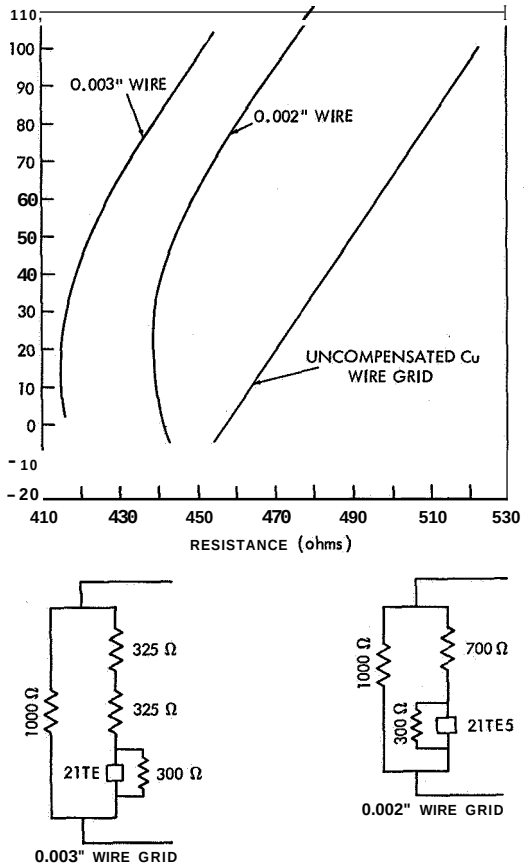

FIGURE 4.—Thermo-electric compensation of copper-wire grids.

resistances of cells A and B (ohms), (2) temperature of cells A and B (°C), (3) information indicating continuity or breakage of a wire on one or more cards, and (4) length of interrogation, date, and station.

The resistance data were normalized to the launch temperature of the cells (35° C) by means of the empirical linear relationship between temperature and resistance: $R_t = R_{35} + K(t - T_{35})$, where $K = 660$ ohms and t is the cell temperature in °C.

The thermal relationship remained valid for cell B until December 31, 1962. After this date the temperature correlation changed and it became impossible to establish a relationship between resistance and hole size. For cell A the case was more favorable, and the data could be followed to February 5, 1963, when, as a result of successive perforations, the minimum recordable resistance was obtained.

The changes of aspect to the sun have been considered. The geometry of the orbiting vehicle is such that after 55 days the sensor aspect is the same as at launch time. The data are interpreted in terms of total cumulative perforated areas. Intermediate changes tabulated are affected by an aspect uncertainty factor of 2.

A simplified diagram of the compensated CdS data is shown in figure 5. Cell A remained dark at about 300 E ohms until 2 days after launch. The first indication of light penetration was on December 18, 1962, when the cell showed a decrease in resistance. The first marked event happened on December 23, 1962. The cell was still showing darkness in twilight December 23, 1962, at 11:40, but showed an 0.002-inch hole during the next pass at 12:30. Further penetration measurements of cells

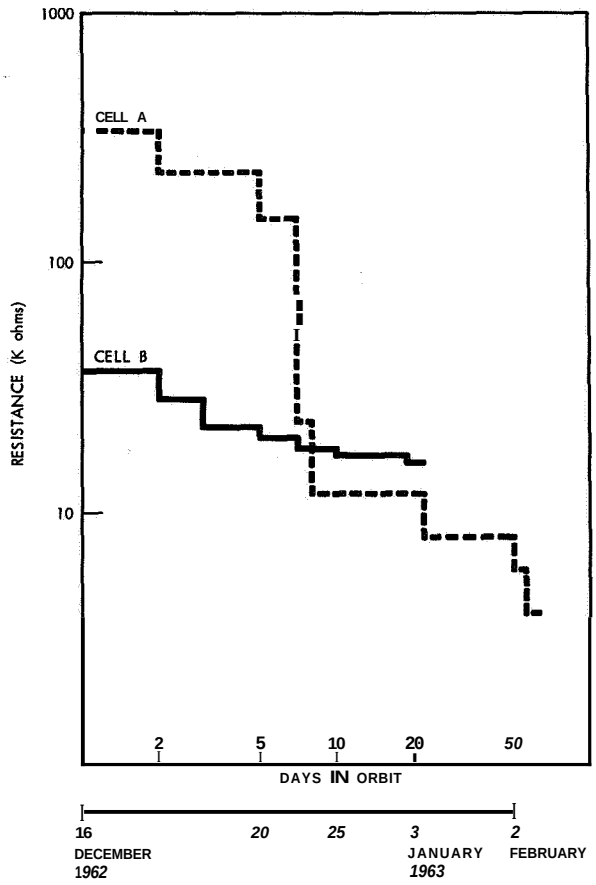

FIGURE 5.—Drop of resistance of cells A and B with time io orbit.

A and B occurred, as may be seen from tables 2 and 3.

The wire grids were monitored for the lifetime of the satellite. Two breaks occurred, one of the 3-mil and one of the 2-mil wire.

Owing to the satellite's rotation with respect to the sun, the resistance of the cell is lowest when the sun's rays are normal to the mylar film. For this reason the lowest resistance readings have been considered exclusively as data points in evaluating the size of the perforations. Dates of those readings and the estimated additional cumulative perforated areas are tabulated in chronological order in tables 2 and 3. It must be emphasized that the data in these tables do not represent discrete events, but cumulative status readouts when the satellite was in a suitable position both as to orbit and aspect to the sun.

TABLE 2.—*Cell A data compensated to 35° C for a 55-day period*

Date	Cumulative days	Hole area (mm²)	
		Total area	Additional perforated area
December 16		0	0
December 18	2	0.00015	0.00015
December 21	5	0.00024	0.00009
December 23	7	0.0020	0.00178
December 24	8	0.011	0.009
January 7	22	0.023	0.012
February 4	50	0.033	0.010
February 9	55	0.080	0.047

Date	Cumulative days	Hole area (mm²)	
		Total area	Additional perforated area
December 16–17		0.0012	0
December 18	2	0.0016	0.0004
December 19	3	0.0020	0.0004
December 21	5	0.0022	0.0002
December 23	7	0.0025	0.0003
December 26	10	0.0065	0.0040
January 4	19	0.0080	0.0015
Total additional area=0.0068			

Data analysis

Tables 2 and 3 are interpreted in the following manner: The CdS cell detectors measured the cumulative perforated area caused by in-flight impacts on the mylar by dust particles. As previously stated, the accuracy of the measurements increases with the number of perforations. Therefore, the method of analysis applied in this paper is as follows:

1. From hypervelocity microparticle-impact experiments performed in the laboratory, it is found that the threshold mass of the perforating particles is approximately 10^{-10} g for the denser and 10^{-9} g for the less dense particles. The diameter of the hole in mylar is 1 to 1.5 times the diameter of the perforating particle, allowance being made for the range of specific gravity of the impacting particles.

2. It is considered that the total perforated area is caused by particles of masses near the threshold limit of the detector.

3. A model for the cumulative flux distribution of dust particles in the vicinity of the earth is assumed in order to compute an expected rate of perforation.

4. Finally, the expected cumulative area of perforations is compared with the data.

5. Due to uncertainties in aspect and thermal corrections, the expected accuracy of the cumulative perforated areas is limited to a factor of 2.

The computations were carried out for: (1) a cumulative flux mass distribution model $\log I = -17.0 - 1.7 \log M$ (eq. 1 of Alexander et al., 1963); (2) three different mass threshold sensitivities, 10^{-10}, 10^{-9}, 10^{-8} g mass; and (3) three different possible densities of particles, $\rho_1 = 1$ g/cm³ (ice), $\rho_2 = 4$ g/cm³ (stone), and $\rho_3 = 8$ g/cm³ (iron).

The expected cumulative perforated areas as a function of time for masses 10^{-10}, 10^{-9}, and 10^{-8} g and densites of 1, 4, and 8 g/cm³ have been computed from the above-mentioned equation 1 (tables 4, 5, 6, and 7).

The data from cell A showed a cumulative perforated area of 0.08 mm² for the 55-day

TABLE 4.—Area of *one* hole *in mylar*

	Mass=1X10^{-10} g			Mass=1×10^{-9} g			Mass=1×10^{-8} g		
	Density of particle g/cm^3			Density of particle g/cm^3			Density of particle g/cm^3		
	$\rho=1$	$\rho=4$	$\rho=8$	$\rho=1$	p=4	$\rho=8$	$\rho=1$	$\rho=4$	$\rho=8$
Diameter of particle (μ)	5.8	3.6	2.9	12.4	7.9	6.2	26.9	16.9	13.7
Diameter of hole (mm)	0.0087	0.0054	0.0044	0.0189	0.0119	0.0095	0.0404	0.0254	0.0206
Area of hole (mm^2)	5.9×10^{-5}	2.3×10^{-5}	1.5×10^{-5}	2.8×10^{-4}	1.1×10^{-4}	7.1×10^{-5}	12.8×10^{-4}	5.1×10^{-4}	3.3×10^{-4}

log $M=-10$ $I=1X10^0=1$ impacts/m^2 sec	log $M=-9$ $I=1X10^{-1.7}$ impacts/m^2 sec	log $M=-8$ $I=1\times10^{-3.4}$ impacts/m^2 sec
10^{-10}		
	10^{-10}	
		10^{-10}

A discussion follows on the possibility of erosion of the front coating of the mylar film.

Discussion of results

In the course of the discussion at this symposium on the results of the CdS experiment, it was pointed out by Professor Whipple that the drop of resistance of the CdS cells may have been due to the transparency of the coating of the mylar film, or to pinholes, in case the total front area had been eroded.

The experiments on Vanguard 3 and on Explorer 7 have proved conclusively that the front film did not erode completely; the cells remained "dark."

Regarding the transparency of the back film, the following experiment has been performed with a spare film fabricated at the same time (and by the same people) as the flight films.

1. The front film was completely etched away.

2. The film was placed on a CdS cell of the same type as the flight unit.

3. A strong light spot 1 cm in diameter was focused on the cell. A reading was obtained.

4. The same arrangement was repeated, replacing the film with a clear pinhole 0.0025 cm in diameter. The same reading was obtained as with the 1-cm cleared-up film. The ratio of areas was roughly 2×10^5. The flux required to erode an equivalent area would be 5 orders of magnitude greater and the particle

TABLE 6.—*Impacts per day*

Mass (g)	Particle influx	Sensor area (m^2)	Area X time (AT)	Impacts per day
10^{-10}	1×10^{0} or 1	2×10^{-3}	1.73×10^{2} m^2 sec	1.73×10^{2}
10^{-9}	$1\times10^{-1.7}$	2×10^{-3}	1.73×10^{2} m^2 sec	3.45
10^{-8}	$1\times10^{-3.4}$	2×10^{-3}	1.73×10^{2} m^2 sec	6.91×10^{-2}

Particle mass (g)	Specific (g/cm^3)	Expected cumulative perforated areas (mm^2)	
		20 days, cell B	55 days, cell A
1×10^{-10}	1	5.2×10^{-2}	1.43×10^{-1}
	4	2.0×10^{-2}	5.5×10^{-2}
	8	1.2×10^{-2}	3.6×10^{-2}
1×10^{-9}	1	4.8×10^{-3}	1.32×10^{-2}
	4	1.9×10^{-3}	5.2×10^{-3}
	8	1.2×10^{-3}	3.4×10^{-3}
1×10^{-8}	1	4.4×10^{-4}	1.21×10^{-3}
	4	1.7×10^{-4}	4.8×10^{-4}
	8	1.1×10^{-4}	3.1×10^{-4}

mass would be of the order of 10^{-14} g. The size of these particles would be in the range of 1000 A. Because of radiation-pressure effects it is improbable that these particles exist in the vicinity of the earth.

Appendix A: Micrometeoroid impacts on wire grids

From equation (1) below, we can compute the number of impacts N for the wire-wound sensors. First let the particle with a diameter 60 μ and a density of 1 g/cm^3 be the mass ($M=10^{-7}$ g) that would break the copper wires used; then

$$\log I = -17.0 - 1.7 \log M \qquad (1)$$

$$= -5,$$

$$I = 1\times10^{-5} \text{ impacts/m}^2 \text{ sec.}$$

Since

$$AT = 62\times10^{4} \text{ m}^2 \text{ sec},$$

$$N = ATI = 62\times10^{4}\times10^{-5}$$

$$= 6.2 \text{ impacts.}$$

This value compares favorably with the experimental results, which show two broken wires. In considering the impacts upon the wire-wound grids, we see that the wires will not always be hit head on (i.e., the particles may graze the wire or merely penetrate the insulation surrounding each of the wires).

If the above calculation is performed for particles with $M=10^{-6}$ g, then $N=0.1$ impact. Therefore, since the actual number of impacts must be greater than those recorded (i.e., all the micrometeoroids will not hit the wires head on), the particles detected by the wire grids are of the order of 10^{-7} g or larger.

References

ALEXANDER, W. M.; MCCRACKEN, C. W.; SECRETAN, L.; and BERG, O. E.
1963. Review of direct measurements of interplanetary dust from satellites and probes. In Space Research III, ed. by W. Priester, North-Holland Publ. Co., Amsterdam, pp. 891–917.

FRIICHTENICHT, J. F.
1961. Study of crater physics. Space Technology Labs., Ramo Wooldridge Inc., Report no. 3, July 18.

HASTINGS, E. C., Jr., Compiler
1963. The Explorer XVI micrometeoroid satellite: Description and preliminary results for the period December 16, 1962, through January 13,1963. NASA Tech. Memo. X–810, February.

LAGOW, H. E., and SECRETAN, L.
1963. Results of micrometeorite penetration experiment on the Explorer VII satellite (1959 Iota). NASA Tech. Note D–1722, April.

LAGOW, H. E.; SECRETAN, L.; and GIULIANI, J.
1958. Experiments for satellite environmental measurements. In International Geophysical Year, vol. 6, parts 1–4, Pergamon Press, New York, pp. 319–321,

Abstract

The CdS dust-particle detectors on Explorer 16 provide a means of determining the flux of dust particles in the vicinity of the earth by measuring the area of the perforations due to impacts of dust particles $\geq 10^{-10}$ g through a ¼-mil aluminized mylar film.

One of the CdS detectors measured a total area of 0.08 mm^2 perforated by dust particles for a period of 55 days. (The other measured an area of 0.068 mm^2 in 19 days.) The perforated area is proportional to the cumulative flux of all impacting particles $\geq 10^{-10}$ g.

The flux measured by the detectors is compared with several models provided by other satellite and various ground-based observations. When the flux model derived from the direct satellite measurements is wed, where $\log I = -17.0 - 1.7 \log M$, it is found that approximately 10^3 impacts would occur. The area opened up by these impacts is in excellent agreement with the results of the CdS detector experiment. Flux models derived from ground-based observations predict too few impacts for the mass range of particles considered here.

The wire grid experiment would detect particles of 10^{-7} g and larger. Two wires were broken. This is in good agreement with the dust-particle flux model derived from direct satellite measurements.

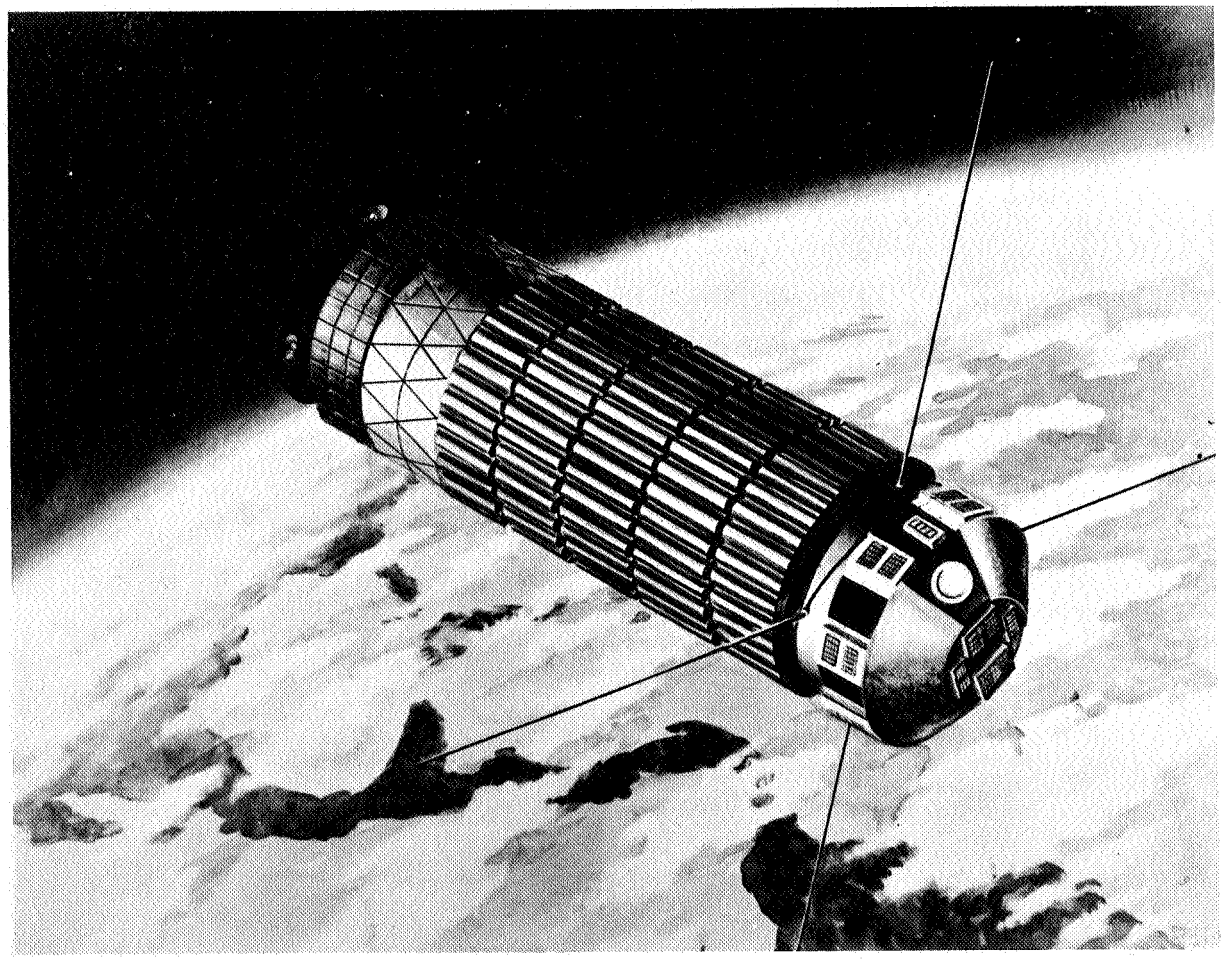

PLATE 1

Explorer 16.

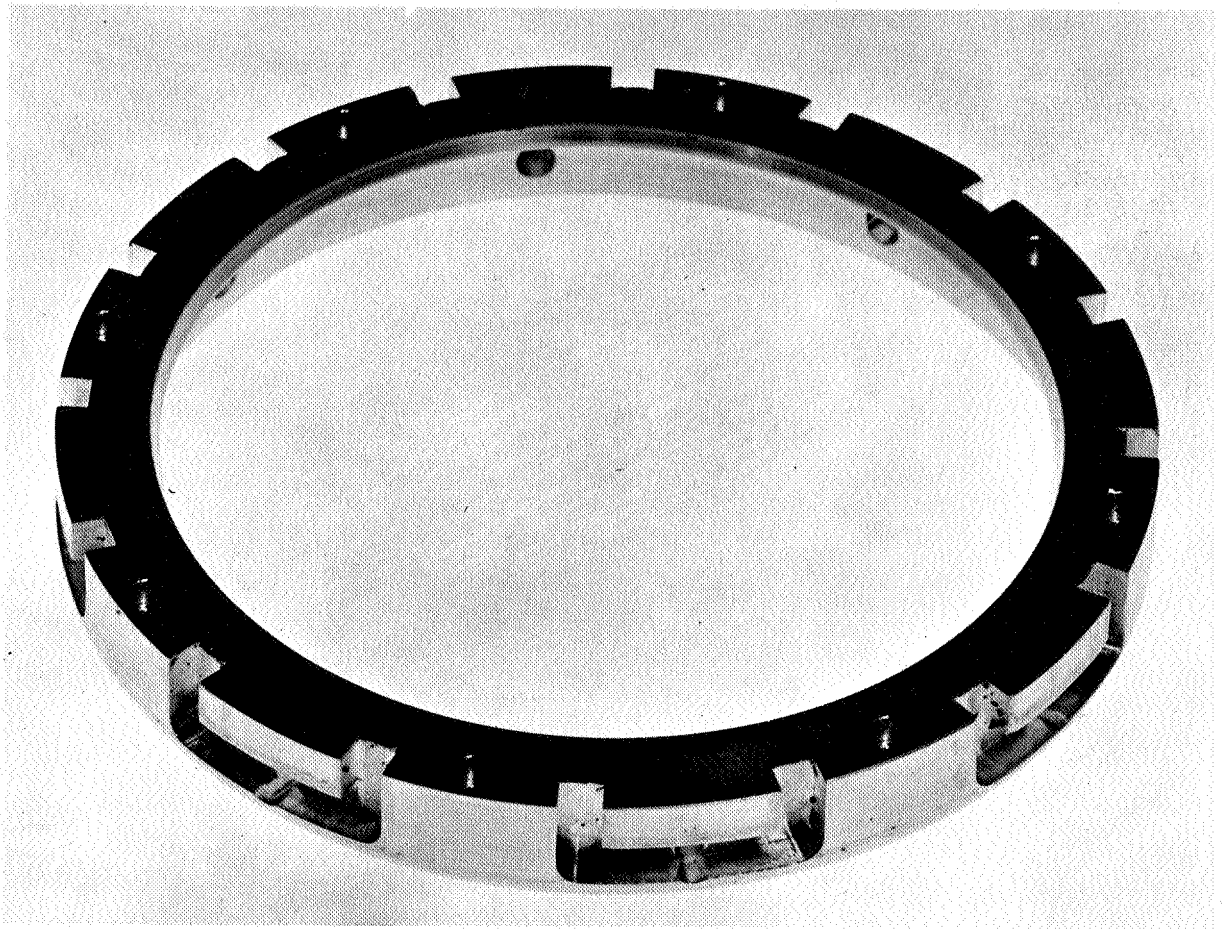

PLATE 2

Ring showing the vent holes for the CdS cell.

Dust Dynamics in the Magnetosphere and Interplanetary Space[1]

S. F. SINGER[2]

Introduction

Evidence regarding the size distribution and other properties of interplanetary dust comes from different types of observations, such as optical observations of the zodiacal light, impacts of dust particles on satellite detectors, and collection of dust in the ionosphere and stratosphere.

Unfortunately, the evidence is conflicting. The greatest amount of analysis has gone into the interpretation of zodiacal-light data. The earliest analyses, and those made until very recently, have tended to favor a rather flat distribution, $f(a)da \sim a^{-2.8}da$, with the radius a of the order of 20 to 50 μ.

More recently, work by Ingham, Giese, and Weinberg (for the review, see Weinberg, 1964) has tended to stress another interpretation that gives a much steeper spectrum, with an exponent of 4 or even greater, extending to particles of submicron size. According to R. H. Giese (private communication, 1965), there still exists a basic uncertainty between these two rather different possibilities.[3]

Dynamic effects of minor forces

We will assume that particles of very small size are present and that, therefore, the effects of **minor** (nongravitational) forces cannot be neglected. Just what constitutes a small particle depends on the particular application. In general, since the **minor** force produces a perturbation on the major (gravitational) force, the product of perturbation and time is significant. The longer the time scale over which forces are considered to act, the larger is the size of the particle that we find interesting to consider; i.e., in the Poynting-Robertson effect, we may consider particles of size 100 μ or more, while for a discussion of the effects of Lorentz forces, the particles would be of submicron size.

The influence of these minor forces then leads to some very surprising effects. So far none of these effects has been observed, nor have they been particularly looked for. Therefore, many of the phenomena I shall describe must await experimental verification. We shall see how the observations agree with the predictions.

Since I shall discuss many new effects, it is necessary first to deal with the minor forces and then to list their effects.

One minor force is *radiation **pressure*** due to the solar radiation. The larger the area-to-mass ratio of the particle, the more important radiation pressure becomes. Table 1 gives typical values for the radiation pressure, and compares it to the gravitational forces. It can be seen how the importance of radiation pressure increases as the size of the particle decreases. For submicron particles the com-

[1] Adapted from a paper entitled "Dust and Needles in the Magnetosphere," delivered at the American Geophysical Union Annual Meeting, Washington, D.C., April 19, 1963.

[2] University of Miami, Coral Gables, Fla.

[3] One novel method of investigating this point has been suggested by Bandermann and Singer (1965). It consists of measuring the neutral hydrogen produced when the ionized solar wind recombines on the surface of interplanetary dust particles. Under certain assumptions regarding the dust-particle size distribution, sufficient neutral hydrogen is produced to be easily detectable through the scattering of Lyman-α photons. On the other hand, an absence of an appreciable Lyman-α contribution coming from the plane of the ecliptic would indicate that the number of particles present is insufficient to release hydrogen. Extreme assumptions, both on the high and low sides, for dust-particle distributions give hydrogen release rates of 1.8×10^{-7}/cm^3 down to 1.6×10^{-11}/cm^3 at 1 a.u., with a neutral hydrogen lifetime of 2.5×10^6 sec. Concentrations of hydrogen can be obtained, from barely detectable to those that give more than an optical depth.

TABLE 1.—*Ratio of solar-radiation pressure to solar gravitational force (independent of distance to sun)*

Particle radius (μ)	Particle material		
	Iron (density 7.8)	Dielectric (density 3.3)	
		Large refractive index m	m=1.5
100	0.002	0.0015	0.0005
10	0.02	0.014	(0.004)*
1	0.25	0.13	(0.08)*
0.3	1.0	0.8	0.5
0.1	1.8	1.8	0.39
0.005	2.0	1.4	0.085
small	≈1.1	small	small

*Uncertain because of unknown diffraction effects in this critical size range.

position plays an important role: metallic particles smaller than 0.3 μ are blown out of the solar system, while nearly transparent dielectric particles can survive down to any size.

A second important minor force is the ***Coulomb drag*** or electric charge drag. I have considered its effects first on dust particles (Singer, 1956), and, more recently, on the West Ford needles (Singer, 1961b), which I consider as artificial dust particles. The Coulomb drag arises because bodies in space acquire an electric charge due to the presence of the plasma and of solar ultraviolet radiation. I have discussed the charging process before and state here only that close to the earth the charge is negative, while in interplanetary space it becomes positive. A minimum is reached somewhere between, probably at about 1 earth radius, but the uncertainties here are very large.

The Lorentz force has been considered earlier (Singer, 1956), and again more recently by Parker (1964).

I shall now review four topics in which the effects of these minor forces enter in an important way: (1) the question of the dust shell around the earth; (2) the possibility of a morning-to-evening difference between incident interplanetary dust; (3) the question of dust particles in captured orbits, trapped in the gravitational field; and (4) the question of the sweepout of dust from interplanetary space.

DUST SHELL AROUND THE EARTH.—A theory published in 1961 (Singer, 1961a) predicts the existence of a dust ***shell*** around the earth (fig. 1). Specifically, we should look for the existence of a maximum in the dust-particle flux at an altitude of about 2000 to 3000 km above sea level.[4] In other words, there should be a decrease below this altitude. Unfortunately, the observations are difficult and are complicated by the fact that the motion of the

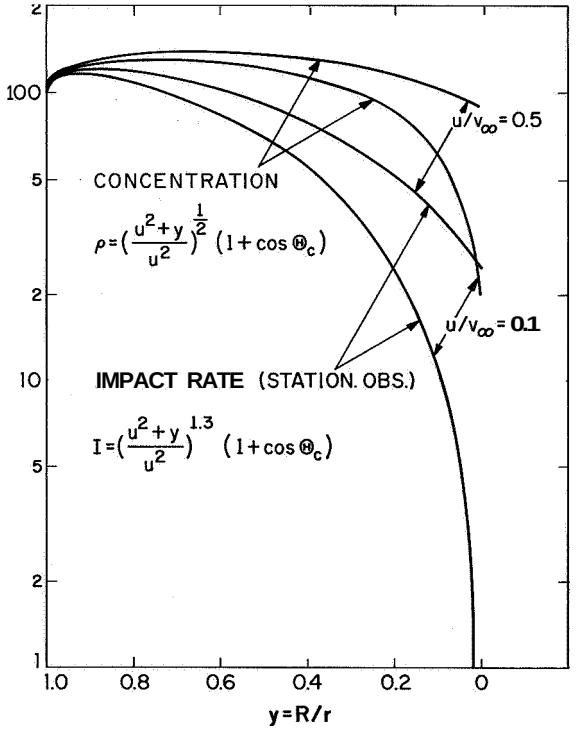

FIGURE 1.—The concentration (particles/cm³) and the impact rate (impacts/cm²/sec) are both shown as a function of distance from the earth's center. The distance unit y is inversely proportional to distance r, and is expressed in earth radii R. Thus, $y=1.0$ corresponds to the earth's surface (or just above the atmosphere), while $y=0$ corresponds to infinity. It can be seen that the theory gives only a modest increase in concentration as one approaches the earth, with a maximum before one reaches the earth's atmosphere. Note that the impact rate, however, depends on the particle-size distribution chosen and can increase by 2 orders of magnitude or more when the geocentric velocity is small.

[4] These results have been confirmed by work of Colombo, Lautman, and Shapiro (1965) and by Hale and Wright (1964), but not by others.

detector itself influences the measurement. Note particularly that while the dust flux increases by a factor of 10^2 or 10^3 between interplanetary space and the earth, the dust concentration increases only by a factor of 2 to 5.

It should be noted that the main component of interplanetary dust consists of particles that are so large that the minor forces do not affect the distribution around the earth, particularly since the major contribution to the flux comes from particles in hyperbolic orbits that simply go past the earth or may hit the earth, but do not remain in the earth's vicinity for a long time.

MORNING-EVENING ASYMMETRY.—The effects of radiation pressure from the sun acting on small dust particles in interplanetary space lead to a very peculiar phenomenon. The particles orbit around the sun at a smaller velocity than that of the earth. Hence, the earth catches up with them and overtakes them. In essence, therefore, the earth runs into particles on the morning side at 6 a.m. However, the proper analysis of the problem shows that the measured flux will be greater on the evening side and not on the morning side. The effect is shown in figure 2. It can be seen how the magnitude of the effect increases as the particle size diminishes. In fact, this method could be used to measure the size distribution of the incoming dust particles in a completely objective manner by measuring the morning-to-evening asymmetry in the flux (Singer, 1963).

There will also be a seasonal asymmetry observed in the dust flux that should be independent of the dust particles' size. This seasonal asymmetry is caused by the fact that the earth has a slightly eccentric orbit, while the orbit of dust particles in interplanetary space should be nearly circular. It would be interesting to look for this effect. In the winter we should have more dust particles on the evening side, and in the summer we should observe more dust particles on the morning side.

DUST PARTICLES IN TRAPPED ORBITS.—One of the most intriguing questions that have been considered for many years is whether dust particles exist around the earth in satellite orbits. The observations of large dust-particle fluxes

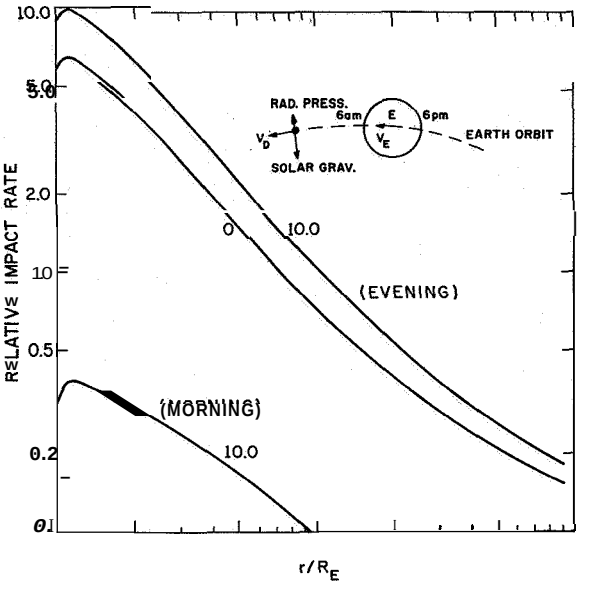

FIGURE 2.—The impact rate of dust particles on a stationary impact detector as a function of distance from the earth's center. The existence of a maximum above the earth's surface is clearly shown. The curve marked 0 applies to particles of large dimension unaffected by radiation pressure. The curves marked "evening" and "morning" correspond to the impact rates observed on the evening and morning sides of the earth for particles having a directed geocentric velocity ($V_E - V_D$) of 10 km/sec; this rather extreme value corresponds to a particle of submicron size that is sufficiently affected by radiation pressure so that its orbital velocity V_D around the sun is 19.8 km/sec; $V_E = 29.8$ km/sec.

near the earth, seen in satellites and space probes, have led various people to suggest that there must be many trapped dust particles. This is not necessarily the case. I am persuaded that the evidence so far does not require trapped dust particles for their explanation; the theory explained above, namely, gravitational concentration of particles coming from infinity, is adequate. However, there must be some particles in trapped orbits and the question is: "How important are they?"

I have looked into this subject from time to time for several years, but much patience is required. It is not sufficient to inject particles into trapped orbits. We must also make sure that their lifetime is long. It is the product of injection rate and lifetime that gives a large, steady-state concentration. I have looked into capture of small dust particles into trapped orbits through the effect of the Coulomb drag. I

find that this is possible only if the particles are extremely small or if they have highly unusual shapes, for example, if they are needle shaped. A paper given in December 1960 (Singer, 1962) investigates where the particles could spend a long time and, therefore, be quasitrapped: at an altitude of about 4000 miles, where their potential might be a minimum. On the whole, however, this particular investigation was not too promising.

I have now attempted another approach—to study the injection of particles by the moon. The mechanism has been suggested by Whipple (1961): it consists of meteoroids hitting the lunar surface and splashing out material. I have tried to see how much material is splashed out and how much of it can be trapped. I find that in order to be trapped, the splashed-out particles must have a velocity greater than 2.38 km/sec to escape the moon's gravitational field, and less than 2.78 km/sec not to escape the earth's gravitational field. The number of particles in this narrow velocity interval is small. In addition, most of them are again swept up (in ~380 years), since on subsequent orbits they will intersect with the moon (fig. 3). A smaller number will experience enough drag (Coulomb drag) to shrink sufficiently within the moon's orbit so that they will miss the moon. Naturally, only small particles can be affected this way. Fairly rough estimates show that the lifetime cannot exceed, in any case, 10^4 years and that the equilibrium density will be small. The uncertainties in the calculation are such that we can exclude only the possibility of increasing the flux by a large factor or by orders of magnitude, but cannot exclude, say, a factor of 2.5

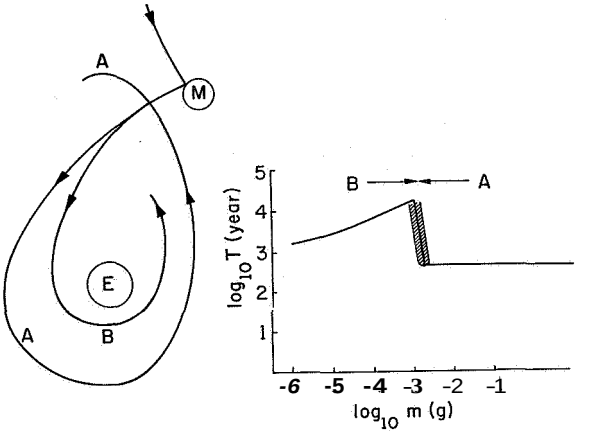

FIGURE 3.—Schematic diagram indicating the ejection of particles from the lunar surface by a meteorite incident on the lunar surface. Particle A is large and subject only to gravitational fields. Particle B is small and assumed to be affected by Coulomb drag. The diagram shows the approximate lifetime of ejected particles as a function of their mass. Particles greater than 10^{-3} g are eventually swept up by the moon or ejected from the earth-moon system. Particles smaller than 10^{-3} g shrink in orbit and are absorbed by the earth.

DUST PARTICLES IN INTERPLANETARY SPACE.—In interplanetary space, dust particles are affected by a solar gravitational field, by solar-radiation pressure (and the resulting Poynting-Robertson effect), and finally by the Coulomb drag caused by the interaction between the electrically charged particle and the interplanetary plasma. The radiation pressure is given by the following expression:

$$F_{RP}=1.5\times10^{-4}a^2\left(\frac{r}{R}\right)^{-2}.$$

The Poynting-Robertson (PR) effect produces a tangential "drag" force which causes the particles to spiral in toward the sun. Its magnitude is given by

$$F_{PR}=\frac{\text{energy/sec}}{c}\cdot\frac{v}{c}=F_{RP}\cdot\frac{v}{c}$$

$$=1.5\times10^{-8}a^2\left(\frac{r}{R}\right)^{-5/2},$$

and the rate of spiraling-in is given by

$$\dot{r}_{PR}=-\left(\frac{3.6}{a}\right)\left(\frac{r}{R}\right)^{-1}\frac{\text{km}}{\text{year}}$$

$$=-\left(\frac{2.4\times10^{-8}}{a}\right)\left(\frac{r}{R}\right)^{-1}\frac{\text{a.u.}}{\text{year}},$$

where a is the particle radius, r the distance from the sun, R the earth-sun distance, v the particle velocity, and c the velocity of light.

[5] A similar problem has been considered by Colombo, Lautman, and Shapiro (1965), but with an important difference: instead of Coulomb drag, they consider radiation-pressure perturbations. coincidentally, however, their final conclusion regarding the existence of particles in trapped orbits is similar to ours.

It is seen that it is the tangential forces that really determine the fate of the particle, its lifetime in the solar system.

Finally, we evaluate the (tangential) Coulomb force F_C for a particle in a near-circular orbit having an electric potential of 30 volts (taken as an upper limit). We consider two extreme cases: (1) a cold nonrotating plasma, density $n=10/\text{cm}^3$; (2) a plasma corotating with the sun's angular velocity, $n=10/\text{cm}^3$.

(1) Nonrotating plasma

$$10^{-8}a^2\left(\frac{r}{R}\right)^{-5/2}$$

$$\dot{r}_C \text{ (km/year)} \qquad -\left(\frac{2.4}{a}\right)\left(\frac{r}{R}\right)^{-1}$$

(2) Co-rotating plasma

$$F_C \qquad 2.5\times10^{-10}a^2\left(\frac{r}{R}\right)^{-4}$$

$$\dot{r}_C \text{ (km/year)} \qquad +\left(\frac{0.5}{a}\right)\left(\frac{r}{R}\right)^{-5/2}$$

Thus the Coulomb drag, case (1), enhances the PR effect and causes the particle to spiral in faster; for example, a 10-μ particle would have a lifetime of only about 10^4 years.

On the contrary, a corotating interplanetary plasma decreases the PR effect, at a rate that becomes greater as the particle approaches the sun. We can form the ratio

$$\frac{F_{C(\text{rot})}}{F_{PR}}=1.67\times10^{-2}\left(\frac{r}{R}\right)^{-3/2}$$

It becomes unity at a value $r/R=0.07$, well within the orbit of Mercury.

It can be seen that the Coulomb drag introduces interesting cosmological consequences for the interplanetary dust.

Unfortunately, no final statement can as yet be made; e.g., the effects of the Lorentz force are surely important; dynamic effects due to the (moving) solar wind and moving magnetic fields need to be considered.

It is clear, however, that the traditional view, which considered only the Poynting-Robertson effect, will not be adequate to deal with the problem.

Acknowledgment

I wish to thank Mr. Lothar W. Bandermann for his assistance in the calculations. The work was supported under NASA Grant NGR-10-007-011.

References

BANDERMANN, L., and SINGER, S. F.
1965. Neutral hydrogen in interplanetary gas (abstract). Trans. Amer. Geophys. Union, vol. 46, p. 133.

COLOMBO, G.; LAUTMAN, D. A.; and SHAPIRO, I. I.
1965. Dynamics of small particles in the solar system (abstract). Trans. Amer. Geophys. Union, vol. 46, p. 428.

HALE, D. P., and WRIGHT, J. J.
1964. Meteoric flux and density fields about an infinitesimal attractive center generated by a stream monoenergetic and monodirectional at infinity. Journ. Geophys. Res., vol. 69, pp. 3709–3717.

PARKER, E. N.
1964. The perturbation of interplanetary dust grains by the solar wind. Astrophys. Journ., vol. 139, pp. 951–958.

SINGER, S. F.
1956. Measurements of interplanetary dust. *In* Scientific Uses of Earth Satellites, ed. by J. A. van Allen, Univ. of Michigan Press, Ann Arbor, pp. 301–316.
1961a. Interplanetary dust near the earth. Nature, vol. 192, pp. 321–323.
1961b. Interaction of West Ford needles with the earth's magnetosphere and their lifetime. Nature, vol. 192, p. 1061.
1962. Distribution of dust in cislunar space. *In* Lunar Explorations and Spacecraft Systems, ed. by R. Fleisig, Plenum Press, New York.
1963. Dust and needles in the magnetosphere (abstract). Trans. Amer. Geophys. Union, vol. 44, p. 29.

WEINBERG, J. L.
1964. The zodiacal light at 5300 Å. Ann. d'Astrophys., vol. 27, pp. 718–738.

WHIPPLE, F. L.
1961. The dust cloud about the earth. Nature, vol. 189, pp. 127–128.

Abstract

The major forces acting on dust particles near the earth or in interplanetary space are produced by gravitational fields. For very small bodies of micron or submicron size, however, we must take into account minor forces, such as radiation pressure, Coulomb drag, and the Lorentz force. These minor forces can produce significant effects on dust particles near the earth, e.g., an evening-morning asymmetry in dust impacts. They also affect the distribution and lifetime of dust in interplanetary space.

Extraterrestrial Dust Concentrations in the Upper Atmosphere

R. K. SOBERMAN [1]

Introduction

Particle sampling of the northern latitude mesopause has produced new data regarding the phenomenon of noctilucent clouds (Hemenway, Soberman, and Witt, **1964;** Soberman and Hemenway, **1965).** These data have, however, not explained the reasons for the formation of these clouds. The present paper presents a highly idealized mechanism that attempts to explain the results of the sampling experiments and other observations. Since we will utilize the results from the "Kronogård 62" program, it is useful to present a brief description of how the data were obtained. A complete description of the experimental apparatus is given in Soberman et al. **(1964).**

The particle collectors were carried by the two-stage Nike-Cajun solid propellant rockets, which burned out before reaching an altitude of **15** km but continued to ascend to a peak altitude of **110** km. The sampling began at the altitude of **75** km and was terminated at **98** km while the vehicle was still ascending. The collection surfaces were mounted perpendicular to the axis of the rocket (plates **1** and **2).** The efficiency of the nose cone design was greater than **95** percent for particles with a diameter larger than **0.01** μ. Of the four types of collection surfaces used, only the aluminum-shadowed nitrocellulose will be considered here. The others were intended primarily for the study of the individual noctilucent cloud particles. We shall be concerned here with comparative numbers of particles. The nitrocellulose surfaces were approximately **200** A thick and were coated with a thin film of aluminum deposited by vacuum evaporation. Extreme cleanliness precautions were observed throughout all phases of the experiment to minimize contamination from terrestrial particles collecting on the surface during the preparation, handling, and analysis procedures. A number of techniques were used to identify such contaminant particles. These included aluminum shadowing and the use of a portion of the collection surface as a control by shielding this area from particles collected during the flight. These control techniques have been described in detail elsewhere (Hemenway and Soberman, **1962;** Hemenway et al., **1964).**

The Kronogård launch site in northern Sweden, which was used for the **E-62** experiments, was located at latitude **66°** N and longitude **19°** E. Two collections were successfully recovered during the program. The first was obtained at a time when no noctilucent clouds were visible to a system of airborne and ground observers distributed over several hundred kilometers about the launch area. The last previous cloud sighting had been **13** days earlier, and the next did not occur until **4** days afterward. The vehicle, termed Nattpip **1,** was launched on August **7, 1962,** at **0147** hours local time **(0047** UT). The second successful collection was obtained in the presence of a noctilucent cloud display that was seen and photographed by the ground observer network. The Nattpip **2** was launched on August **11, 1962,** at **0240** hours local time **(0140** UT). From the limited data available, the two flights appear to have been similar in all respects, with the possible exception of the coning. The Nattpip **1** remained within 6°

[1] Air Force Cambridge Research Laboratories, Bedford, Mass.; now at General Electric Co., Valley Forge, Pa.

of the vertical throughout the sampling portion of the flight, whereas the Nattpip 2 may have had a coning angle as large as 30° or more.

The collection surfaces were examined by electron microscopy in several laboratories in the U.S. and Sweden. Plate 3 indicates the type of micrographs obtained. Particle-size distributions for the two flights are presented in figure 1. There was some variation in these results, as was pointed out by Hemenway et al. (1964). To eliminate one source of the variation, both the curves of figure 1 were obtained by one microscopist utilizing the same model instrument. The data have been previously presented (Hemenway et al., 1964; Soberman and Hemenway, 1965). The data of figure 1 have been normalized for diameter intervals of 10^{-2} μ. The curves were fitted by eye.

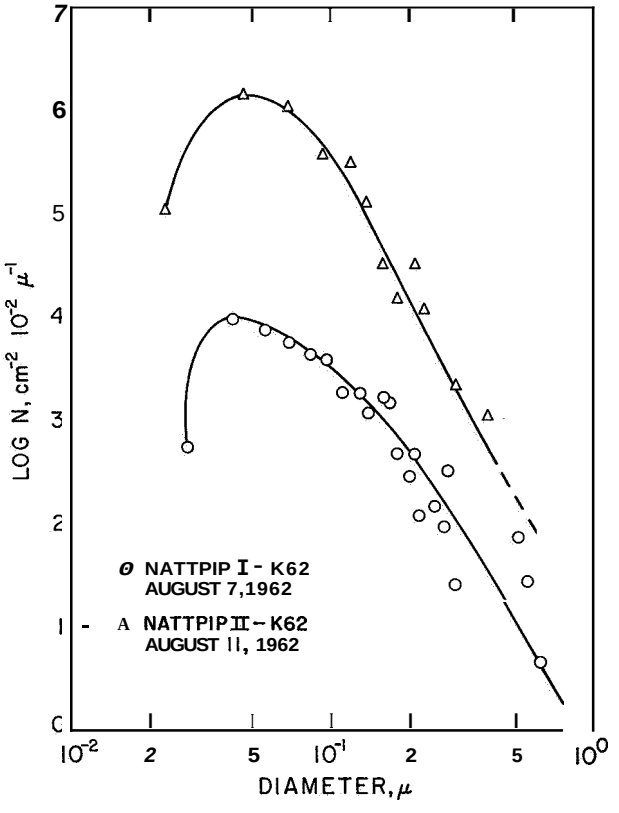

FIGURE 1.—Particle concentrations per unit area from the noctilucent cloud (upper curve) and noncloud (lower curve) samplings of 1962. These curves are normalized for particle diameter intervals of 10^{-2} μ.

Discussion

Since it was concluded from the measurements that the noctilucent cloud particles or the nonvolatile nuclei of the ice-coated cloud particles were extraterrestrial in origin (Hemenway, Soberman, and Witt, 1964), then the first obvious explanation of the clouds is simple enhancement of the influx of meteoric dust. Although we cannot rule out this hypothesis, several items seem to argue against it. For one, it might be expected that the same enhancement would be seen for all particle sizes. This does not appear to be the case. We might also ask why the clouds are not seen at lower altitudes, lower latitudes, or at other times of the year when enhanced meteoric activity exists. Further, this hypothesis offers no explanation for the ice coatings that were associated with some of the particles in the cloud.

A class of hypotheses sometimes invoked to explain the clouds is the concentration or focusing of meteoric particles due to electromagnetic fields in space or in the upper atmosphere. The difficulty with this argument is the small charge-to-mass ratio that such particles could support. A reasonable estimate of the maximum field at the surface of a particle in a good vacuum is about 10^8 volts/m. If we use this value, the maximum charge-to-mass ratio for a spherical particle is

$$\frac{q}{m}=\frac{5.3\times10^{-3}}{\rho_p\delta}\ \text{coul/kg}, \qquad (1)$$

where the particle density ρ_p is expressed in kg/m^3 and the diameter δ is in meters. For a particle with a specific gravity of 3 and a diameter of 0.04 μ, the ratio is 44 coul/kg. This is a factor of about 2×10^6 smaller than the charge-to-mass ratio for a proton at rest. As an example, it would require a field of 0.2 volt/m merely to counteract the acceleration of the near-earth gravity field. As can be seen from equation (1), the situation is worse for larger diameter particles.

Another possible mechanism that could produce noctilucent clouds is a vertical wind or updraft. The simplest form of this updraft hypothesis is a vertical wind at the mesopause of sufficient strength to counter the terminal

fall velocity of the particles. If we take the noncloud results of figure 1 (the lower curve) to be due to the "normal" meteoric influx (with no vertical winds) and calculate the flux in the manner of Soberman and Hemenway (1965), we arrive at a flux of $3\times10^{-2}\,\mathrm{cm^{-2}\,sec^{-1}}\,(10^{-2}\,\mu)^{-1}$ for spherical particles of 0.04-μ diameter and a specific gravity of 3. For this flux to produce the concentration of the same size particles observed in the cloud measurement (upper curve, fig. 1) would require an updraft with a speed of about 5 cm/sec acting for 3×10^{7} sec or about 1 year. Clearly this time requirement is unrealistic.

From the foregoing, we are led to the conclusion that the particles that form noctilucent clouds must come from below the mesopause. That is not to say that these particles are of terrestrial origin, but that they must be "stored" at lower altitudes and then be lifted to the altitude at which the clouds are observed.

To compute the conditions necessary to produce the measured concentration, we first, look at the "normal" condition again. A small measure of confidence in assuming the 1962 noncloud sampling as a norm is gained when we compare this measurement with a similar measurement made in June of 1961 at White Sands, New Mexico. These two measurements yielded calculated particle fluxes that agreed within a factor of 3 (Soberman and Hemenway, 1965). Thus, from the lower curve of figure 1 we compute the normal (no vertical wind) concentration of meteoric dust particles in the upper atmosphere. This is done from the relation

$$\eta(\delta, Z)=\phi(\delta)/V_p(\delta, Z), \qquad (2)$$

where $\eta(\delta, Z)$ is the number of particles per unit volume (a function of diameter and altitude), $\phi(\delta)$ is the flux, and $V_p(\delta, Z)$ is the terminal velocity of the particles. The values of the lower curve in figure 1 are taken to be equal to

$$N_0(\delta)=\int_{Z_0}^{Z_1}\eta(\delta, Z)dZ=\phi(\delta)\int_{Z_0}^{Z_1}dZ/V_p(\delta, Z), \qquad (3)$$

where Z_0 and Z_1 are the altitudes at which the sampling was begun and terminated (i.e., 75 and 98 km, respectively). The terminal velocities were calculated from the relation (Kennard, 1938)

$$V_p=\pi mg/\alpha\bar{c}\sigma\rho_a, \qquad (4)$$

where m is the particle mass, g the acceleration of gravity, $\bar{c}$ the ambient mean atmospheric molecular speed, σ the particle cross section, ρ_a the ambient atmospheric density, and α an empirical constant that can be taken as (1.4) $4\pi/3$. We again assume spherical particles with a specific gravity of 3 and use the tables of the U.S. Standard Atmosphere (1962), for atmospheric values. Curves for several particle diameters are shown in figure 2.

To determine what sort of updraft would be necessary to lift these. particles back to the mesopause, we wrote a one-dimensional computer program that adds a vertical upward velocity to the fall velocity of the particles. The distribution for a given diameter is originally divided into 1-km intervals and then moved upward. As the number of particles in a grouping moves upward, the velocity varies in accordance with

$$V_t(\delta, z)=V_w(Z)-V_p(\delta, Z), \qquad (5)$$

where $V_w(Z)$ is the imposed wind velocity, which can also be vaned with altitude. Implicit in the model is the assumption that the atmospheric properties at each altitude are not disturbed by the process. The program is terminated when the particle concentration at any altitude reaches a predetermined value, or when the "updraft" has been operating for a predetermined time.

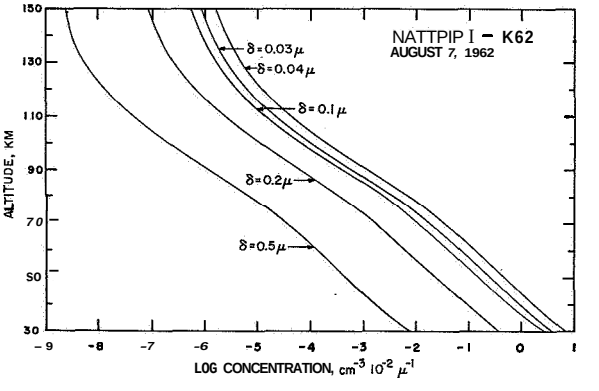

FIGURE 2.—Normal (no vertical wind) distribution of meteoric dust in the upper atmosphere.

Two wind models were used. The first, for simplicity, was a constant velocity model independent of altitude. The first step was to apply the model to particles 0.04 μ in diameter. When the concentration in the 75- to 98-km region reached 1.05×10^6 cm^{-2} (the value read from the upper curve of fig. 1), the time was read out. The same wind velocity was then allowed to operate for that length of time on the other particle sizes. The resultant concentrations in the 75- to 98-km range were then read out. The results for wind speeds of 0.50 and 0.25 m/sec are shown in figure 3. The times involved were 6.8×10^4 and 1.4×10^5 sec, respectively (or about ¾ and 1½ days). In figure 3 we have replotted the size distribution of noctilucent cloud particles (upper curve, fig. 1). To this we have added the points obtained by simply normalizing the lower or noncloud curve at the 0.04-μ diameter point and the computed concentrations. Notice that the smaller wind velocity appears to give the better fit for the larger diameter particles. This wind model predicts that each size will concentrate at the altitude where the net velocity is zero. It is to be noted that the two largest diameter points of the 0.25 m/sec wind model fall below the noctilucent cloud curve. This is because peak concentration altitudes for these larger particles occur just below 75 km, where the sampling began. Winds faster than 0.50 m/sec or slower than 0.25 m/sec give poorer fits. It was not deemed worthwhile to seek the optimum wind velocity.

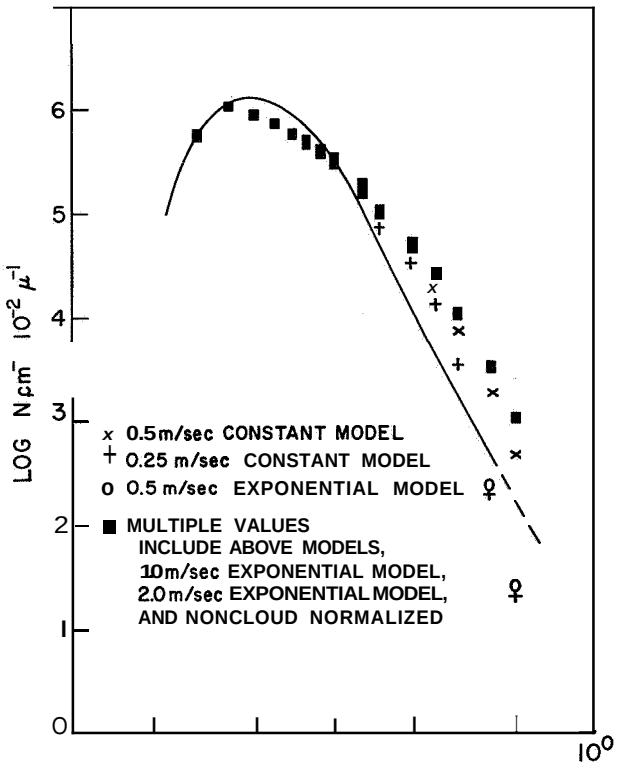

FIGURE 3.—Calculated noctilucent cloud particle concentrations. The solid curve was obtained experimentally.

C. Rooth (private communication) pointed out that the constant-velocity model was unrealistic in that it violated the conservation of mass for a continuous updraft. To conform to the conservation laws and yet keep the program reasonably simple, we imposed a wind velocity that vaned inversely with the atmospheric density (i.e., $\rho_a V_w = \text{const}$). The magnitude of this "exponential" updraft was specified at the 80-km level and set equal to zero above that height. The results for the 2.0, 1.0, and 0.5 m/sec wind models are also shown in figure 3. We see that, to a first approximation, the higher velocity models yield the same results as normalizing the noncloud curve. The 0.5 m/sec model also follows these same points with the exception of the two largest diameters, where the wind velocity can no longer suspend the particles in the sampling regime. The times necessary to build these distributions are 6.4×10^5, 1.3×10^6, and 2.6×10^6 sec, or approximately 1 week, 2 weeks, and 1 month for the 2.0, 1.0, and 0.5 m/sec cases, respectively. Faster and slower models gave poorer fits. Again, it was not deemed worthwhile to seek the optimum velocity profile.

Conclusions

While none of the models fit the experimental results with any great precision, it must be remembered that they are extremely naive and are intended only to serve as guideposts for a more sophisticated approach. The major uncertainties are in the available experimental data, the use of the standard atmosphere, and in the use of a model that holds densities and temperatures constant while major mass motions are taking place. Nonetheless, the conclusions and predictions that result from these

simple models are of interest. It is important, therefore, to clarify the hypothesis being put forth. It should be clear that we do not propose that the vertical winds or updrafts are necessarily in operation at the place where the noctilucent clouds are being observed. Rather, it is far more likely that these persistent updrafts are the result of the continuous solar heating of the ozone below the mesosphere during the Arctic summer.

In the present models the smaller particles come from altitudes as low as 42 km. It is far more likely that the particles are raised from above the 50-km temperature inversion. This inversion would also serve as a barrier against the mixing of extraterrestrial and terrestrial particles. The low altitudes from which the particles are drawn in these computations probably result from the use of the standard-atmosphere tables. The supplemental seasonal and latitude atmospheres (Cole and Kantor, 1963), reliable at these altitudes only to 60°, show increased densities (fig. 4) and an increased lapse rate (fig. 5) during the summer months, which would increase the altitudes above which the particles need be raised. The suggested updraft could be part of a large-scale cellular convective pattern, as suggested by C. Rooth (private communication), in which the noctilucent clouds are seen as particles in horizontal transit following the atmospheric flow from the region of updraft to the region of downdraft (in the earth's shadow). In so moving, they would cross the twilight where observation is possible. Due to the Coriolis effect, they would be seen moving from northeast to southwest. The ice coatings on the particles would result from the water vapor, raised with the particles, which proceeds to condense on the particles at the extremely low temperatures of the arctic summer mesopause. For this reason, the additional mass of the ice coatings on the particles was not considered in the above computations of the updraft mechanism. Since the lifting would occur in the region of 24-hour daylight, this would explain why the increased concentration is not observed at lower altitudes during the course of the buildup. It would further explain why noctilucent clouds

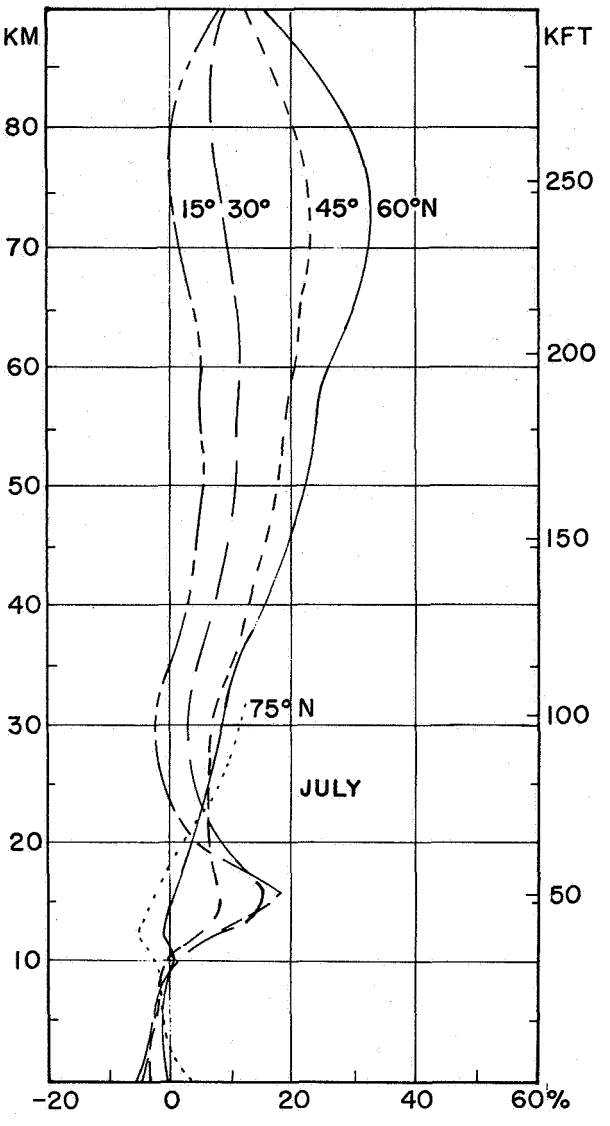

FIGURE 4.—Density departures from the standard atmosphere as a function of latitude (after Cole and Kantor, 1963).

are phenomena of the summer months at high latitudes and why the clouds are seen at higher latitudes later in the season (Hemenway, Soberman, and Witt, 1964). The long times required for the lower updraft velocities would also explain why the cloud displays are seen with greater frequency during July and August.

One major point that the updraft mechanism does not explain is the 'sporadic nature of noctilucent cloud displays. It is believed that, although the proposed updraft mechanism is necessary for the occurrence of noctilucent

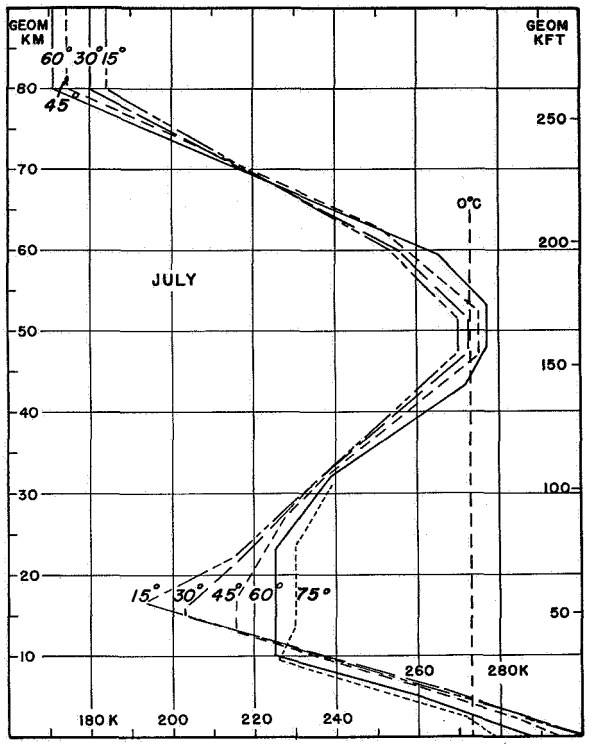

FIGURE 5.—Temperature variation as a function of height and latitude (after Cole and Kantor, 1963).

clouds, it is not sufficient. An enhanced influx of meteoric material into the updraft would explain not only why the clouds occur sporadically but also why the clouds can be seen to appear and then disappear within a 24-hour period, while meteoric showers are usually not that sharply defined in time. Such a combined mechanism would also explain why some experienced noctilucent cloud observers will claim (privately) that the probability of having a display on certain dates is higher than for the rest of the season.

In the discussion of the sampling experiments (Hemenway, Soberman, and Witt, 1964) it was pointed out that the ratio of cloud to noncloud particles collected is likely to be 10^3 or greater. The enhancement expected from meteoric showers is probably not much more than one order of magnitude, and the present proposed mechanism cannot raise the concentration much over the two orders of magnitude indicated. It is therefore probable that only the combined effects of meteoric showers and the raising of particles from below can produce the needed particle concentrations.

In conclusion, the present hypothesis predicts that noctilucent clouds should be observed at high southern latitudes during the latter summer months at periods of high meteoric activity. The direction of motion in the Southern Hemisphere should be southeast to northwest.

Acknowledgments

The author wishes to thank Dr. Claes Rooth of the Woods Hole Oceanographic Institute for a stimulating discussion during which he made a number of helpful suggestions. Thanks are also due to Mr. Neil Grossbard, of General Computing Services Inc., who programmed the problem and put it through the computer. Mr. Grossbard's services were made available under contract AF19(628)5005 to the Data Analysis Branch of the Air Force Cambridge Research Laboratories. For their help in the preparation of the paper, the author is indebted to Mrs. Pauline Sullivan and Messrs. Christopher Brayton and Ralph Carnevale of the Advanced Metals Research Corporation.

References

COLE, A. E., and KANTOR, A. J.
1963. Air Force interim supplemental atmospheres to 90 kilometers. Air Force Surveys in Geophysics, no. 153, AFCRL–63–936.

HEMENWAY, C. L.; FULLAM, E. F.; SKRIVANEK, R. A.; SOBERMAN, R. K.; and WITT, G.
1964. Electron microscope studies of noctilucent cloud particles. Tellus, vol. 16, pp. 96–102.

HEMENWAY, C. L., and SOBERMAN, R. K.
1962. Studies of micrometeorites obtained from a recoverable sounding rocket. Astron. Journ., vol. 67, pp. 256–266.

HEMENWAY, C. L.; SOBERMAN, R. K.; and WITT, G.
1964. Sampling of noctilucent cloud particles. Tellus, vol. 16, pp. 84–88.

KENNARD, E. H.
1938. Kinetic Theory of Gases. McGraw-Hill Book Co., New York, 438 pp.

SOBERMAN, R. K.; CHREST, S. A.; MANNING, J. J.; REY, L.; RYAN, T. G.; SKRIVANEK, R. A.; and WILHELM, N.
1964. Techniques for rocket sampling of noctilucent cloud particles. Tellus, vol. 16, pp. 89–95.

SOBERMAN, R. K., and HEMENWAY, C. L.
1965. Meteoric dust in the upper atmosphere. Journ. Geophys. Res., vol. 70, pp. 4943–4949.

U.S. STANQARD ATMOSPHERE
1962. U.S. Standard Atmosphere **1962.** Prepared under NASA, USAF, and USWB, Washington, D.C., 278 pp.

Abstract

A theory for the mechanism of formation of noctilucent clouds is presented. It is suggested that the clouds are composed of extraterrestrial particulate matter, coated with ice, which is following a major mesospheric convection motion across the arctic twilight. Computer calculations based upon the results of particulate-sampling experiments show that mean updrafts of less than 1 m/sec could produce the particulate concentrations measured in the noctilucent clouds. It is proposed that the required persistent updraft results from the continuous solar heating of the ozone layer during the arctic summer. This updraft serves to "reraise" particles that have settled through the mesopause. These, combined with the enhanced influx of particles during a meteoric shower, produce a cloud of particles that follows the convective cell across the twilight to a downdraft on the dark side of the earth. The convective motion also serves to raise water vapor that condenses on the particles in the arctic mesopause. The theory explains a number of the peculiarities of noctilucent clouds, such as the times of appearance and the direction of motion, and yields predictions for future experiments.

240-022 O—67——22

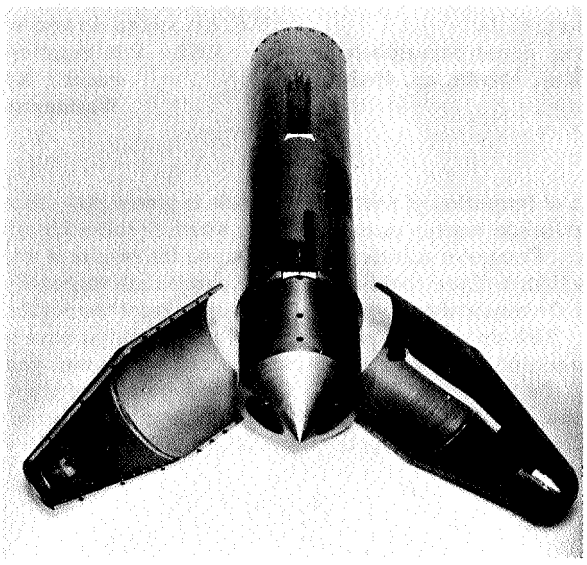

PLATE 1

Forward section of Nike-Cajun sampling payload with the spring-ejected outer nose tip. Sampling ports are shown open.

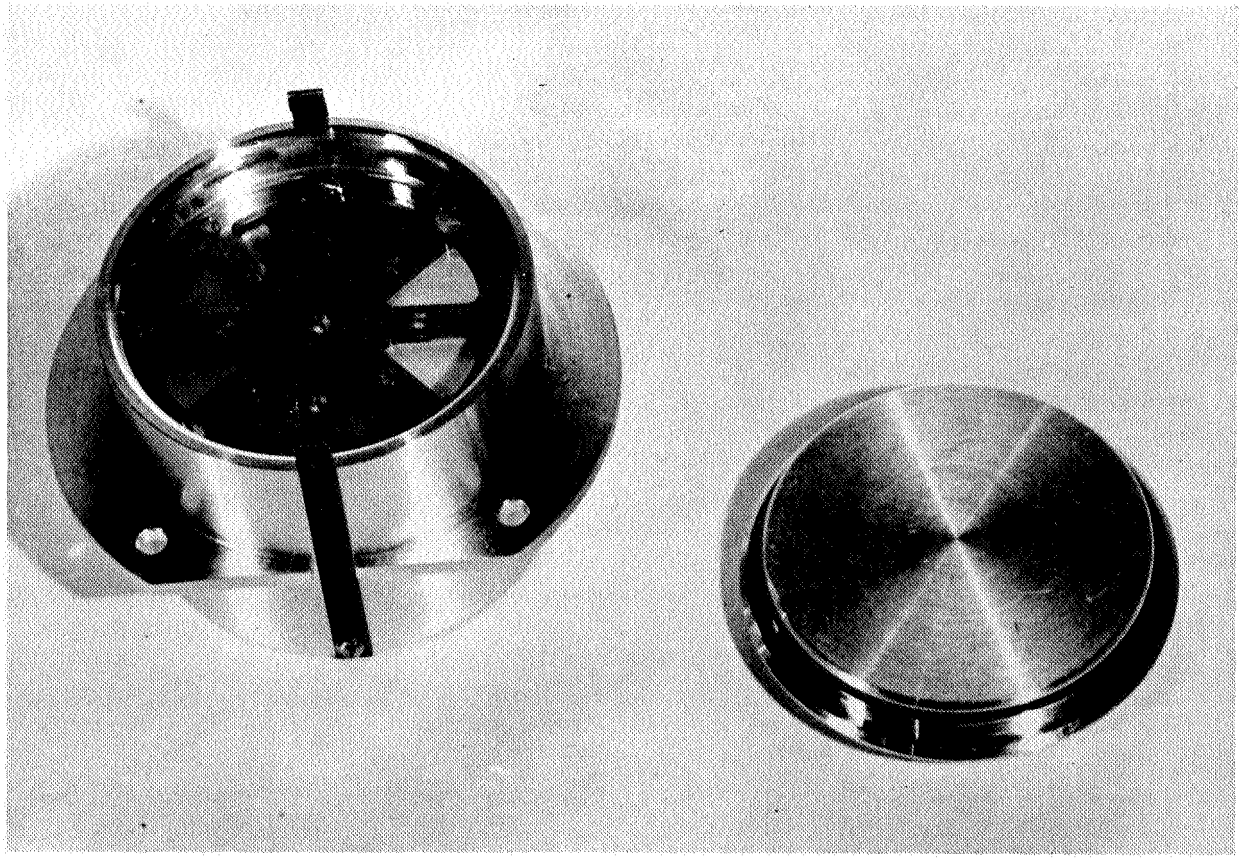

PLATE 2

One of the two sampling cans with cover. One can is located below each sampling port of nose cone.

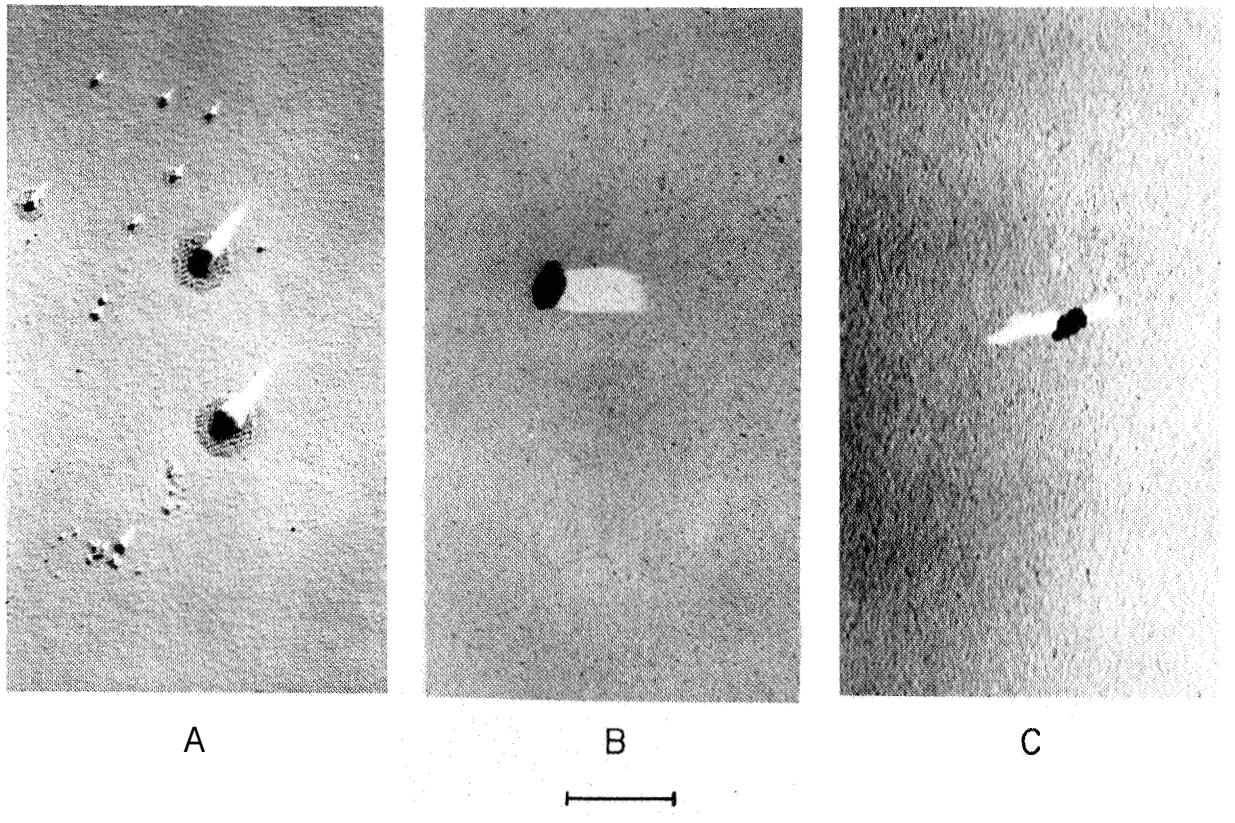

PLATE 3

Electron micrographs from the Kronogård-62 sampling experiments: (a) typical field from noctilucent cloud collection, (b) typical particle from noncloud collection, (c) typical contaminant. Scale equals 1 μ.

Photographs of Particles from an Aerobee Rocket at 130- to 204-km Altitude

R. Tousey,[1] M. J. Koomen,[1] R. E. McCullough,[1] and R. T. Seal[1]

Introduction

A white-light coronagraph, flown in an Aerobee-150 rocket from the White Sands Missile Range on June 28, 1963, was successful in photographing the sun's white-light corona from 3.5 to 10 solar radii (R_s), something not previously accomplished without the aid of a total solar eclipse. The luminance of the white-light corona was found to be approximately twice that recorded by experiments conducted during total eclipses (e.g., Blackwell, 1955). This doubled luminance was interpreted as evidence for dust within a few earth radii, which was illuminated by full sunlight in the rocket experiment, but was within the umbra or penumbra during an eclipse (Koomen et al., 1964; Tousey, 1965). A similar result has been found with the U.S. Naval Research Laboratory (NRL) photoelectric coronagraph on the second orbiting solar observatory *(OSO-2)* launched by the National Aeronautics and Space Administration (NASA). The coronal photographs were covered with artifacts of various types that resulted in much obscuration of the coronal features. Many were tracks of small particles, slowly crossing the field of view; some were close, and others far from the rocket. The altitudes at which the photographs were made ranged from 131 km to 204 km.

The instrument was a small Lyot coronagraph, with objective lens of focal length 30 cm and diameter 25 mm. An external occulter prevented direct sunlight from falling on the objective lens; sunlight diffracted from the occulter's edge was directed away from the lens by use of the saw-toothed occulter design of Purcell and Koomen (1962a,b). The residual stray-light background level was about 10 percent of the coronal luminance for quiet solar conditions over the entire field of the instrument. The coronagraph was kept pointed at the sun with an accuracy of better than ± 1 arcmin, but there was no control of rotation around the solar vector. A slow rotation of the focal plane was produced by the precession of the rocket, its rate varying during the precession cycle from 0 to a maximum value of $\approx \pm 0.8$ deg/sec. At the margin of the field, $R = 10R_s$, this was equivalent to about 2 arcmin in yaw or pitch per sec.

The coronagraph proved to be an excellent camera for photographing tiny particles in space; however, a requirement for photographing them is that they cross the field of view with a rather small angular velocity, that is, that they be moving at very nearly the same velocity as the rocket, or else be far away and very bright. This ruled out detecting small particles in geocentric orbits.

The reason that the coronagraph was able to photograph small particles is that they shone so brightly by scattered sunlight, because of the Mie effect. From the inner to the outer edge of the field the scattering angles ranged from 1° to 2°.5. The theory of Mie shows that the forward-scattered intensity within this range of angles is enhanced over the intensity at other angles by a very large factor; for 1-μ diameter dielectric spheres of refractive index 1.33, the factor is $\approx 10^3$, and for 10-μ spheres, $\approx 10^5$.

[1] E. O. Hulburt Center for Space Research (sponsored jointly by the Office of Naval Research and National Science Foundation), U.S. Naval Research Laboratory, Washington, D.C.

In the 23 exposures made during flight, reproduced in plate 1, many particle trails were photographed. Some of these were close by, as evidenced by their unsharp, and often very broad trails; others were far away, since their tracks were in perfect focus.

The question is, did these objects come from the rocket, or were they a small sample of natural objects in space? One would suppose at first that they must have come from the rocket, since then they would have almost exactly its velocity, the condition required to photograph their trails. There is, however, another possibility that is difficult to rule out. Although meteorites at these altitudes would in general be moving much too fast to be photographed, there should be a few particles of natural origin having velocities very close to that of the rocket.

Particle tracks were recorded by Newkirk and Bohlin (1965; private communication) with their similar but larger balloon-borne coronagraph, flown on September 10, 1960. These particles, however, were shown to have originated from some Styrofoam insulation, because on a flight in 1965, when this material was not used, almost no trails were present. Moreover, these particles must have been very large, since the balloon reached only 30-km altitude. Here the sky luminance is still sufficient to produce a background that would swamp the trails of faint particles.

Explanation of pictures

The photographs in plate 1 contain various features that must be explained for the particle tracks to be interpreted. The separate exposures are arranged in sequence, but each picture is oriented with solar north at the top and east to the left. The external occulter and the arm supporting it cast a conspicuous shadow. This was very diffuse, because the instrument was focused for infinity and the occulter was only 20 inches from the objective lens. The occulter therefore gave rise to a strong vignetting action. This can be seen from the last picture in plate 1, which is an exposure made with a uniform field in the laboratory. By chance the vignetting function and the radial brightness function of the corona just about neutralized each other; therefore, the background exposure, produced by the corona, was approximately uniform in density over the entire field. The individual exposures ranged from 1.1 to 55.8 sec, causing their densities to differ widely. In the reproduction they were printed to appear as nearly alike as possible.

Of the various artifacts present, an array of permanent bright spots is conspicuous on each exposure. These spots were fixed in position from exposure to exposure, and are explained as having been caused by particles loosened from the interior of the instrument and deposited on a lens surface during launch. There is a bright patch at the right edge of the occulter shadow, which gradually becomes less intense, until it is nearly absent in the last exposure. This was caused by a slight mispointing of the biaxial pointing control, which allowed a little of the light diffracted from the edge of the occulter to reach the objective lens. Also present are faint scratches on the film, produced during transport; these are the very sharp, parallel straight lines that are visible in the shortest exposures. The great lune in exposures 3 and 4 is a double exposure, caused by failure to transport the film far enough to separate the frames completely.

The amount of rotation caused by the rocket precession is shown for each exposure by the arrow at the left edge of the frame. Absence of the arrow indicates negligible rotation. Also shown is the mean position of the center of the shadow of the occulter support; this position rotates gradually in correspondence with the precession cycle of the rocket, as do the permanent specks on the optical surfaces.

Particle tracks

The tracks of more than 2 dozen fairly well-established particles are indicated in plate 1 by the letters a to z. They vary from extremely sharp tracks, such as x, to great blobs of light like f produced by a particle within a foot or so of the lens. A preliminary analysis of some of these tracks has been attempted.

The distance of each particle was established from the track width, with the assumption that the particle was small enough to be considered as a point source. The calculated relation between track width and particle distance, confirmed by laboratory measurements, is shown in

figure 1. The optical system was quite well corrected, and the image of a true point source at infinity, as registered on Eastman Eodak Spectroscopic 1–D, the emulsion employed, measured a minimum of 0.02-mm diameter for a low-density exposure. Because of the vignetting, out-of-focus images of points were actually crescent-like; for close particles this produced trails with a sharp inner edge like the unlabeled streak in exposure 15. One difficulty in estimating distances from trail widths comes from the dependence of apparent width on the difference between the density of the trail and the density of the background, an effect produced by the nonuniform distribution of intensity across the out-of-focus image. Another, of course, lies in the assumption of a point source.

The angular velocity of particles crossing the field was established directly from the exposure time and the length of the trail, when both ends of the trail could be located. Another method employed undulations in the tracks, which were caused by hunting of the pointing control. These are extremely prominent in tracks x and w. Plate 2 shows a portion of x greatly enlarged. Comparison of the undulation wavelength, exposure time, and trail length led to the determination of the undulation frequency as 1 cps. This was approximately the hunting frequency of the pointing control in both elevation and azimuth. The double amplitude of trail x was 30 to 35 μ, which corresponds to a tracking jitter of ± 10 arcsec; this was excellent stability for the biaxial pointing control system, which was the first of a new type designed and constructed by a group at the University of Colorado under the direction of F. Wilshusen. Still another method of establishing the speed, when a trail ended on one exposure and began on the next, was from the gap produced by the film transport time, which was about 0.2 sec.

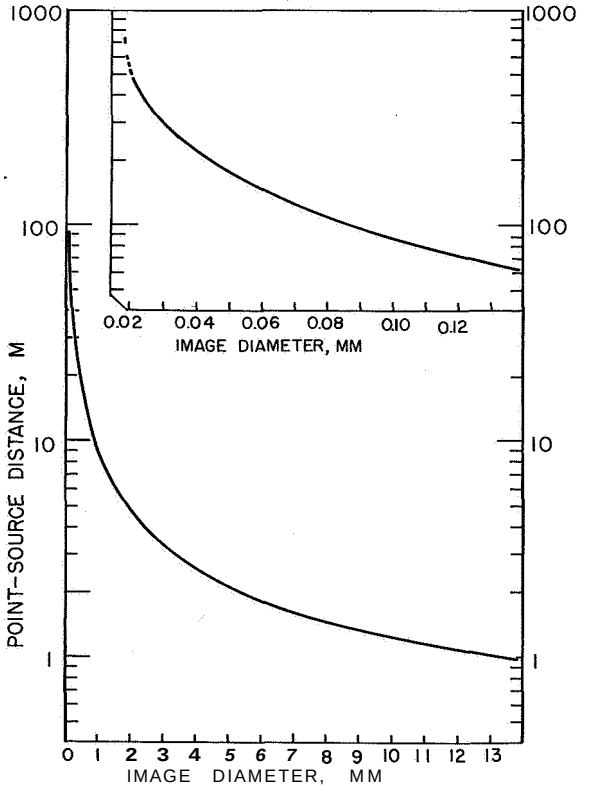

FIGURE 1.—Effect of point-source distance on image diameter in photographic coronagraph NE 3.129.

A conspicuous characteristic of each trail is that there is very little change in density from the beginning to the end, even though the particle was changing distance rapidly. There is a simple explanation for this. For a given particle, the flux per unit area on the film, and hence the density, is given by

$$D=f\left(E\frac{1}{\dot{\theta}}\frac{1}{w}\right),$$

where E is the illumination produced at the objective by the particle at distance d, $\dot{\theta}$ is the angular speed of motion of the image, and w is the width of the trail. While E varies as $1/d^2$, the "inverse square law," $\dot{\theta}$ varies as $1/d$, and w does likewise provided d is large compared to the focal length of the lens. Therefore, the track density is independent of the distance, for a particle of a given velocity, until the distance becomes so great that the track width is limited by the resolution of the film and optical system. Vignetting makes no difference because it simply changes the size of the out-of-focus image and consequent track width but does not change the flux per unit area.

All of the trails are curved to a greater or lesser extent. In order to interpret the curve

it is necessary first to correct for rotation of the image plane during the exposure. This has been done in plate 3, which shows a composite pieced together from exposures 19 to 23 and a diagram giving corrected paths for particles x, y, and w.

In table 1 a summary is presented of the principal characteristics of the trails, to the extent that the analysis has been carried out. The velocity values refer to the component in the plane normal to the solar vector; they are relative to the rocket and are based on the estimated distances and the measured angular velocity. The rocket velocity components were approximately 90 m/sec north, 23 m/sec east, and a vertical component ranging from 1.2 km/sec up at exposure 1, to 0 at peak, to 0.8 km/sec down at the end of exposure 23.

TABLE 1.—*Preliminary analysis of particle trails; NE 3.129, June 28, 1963*

Particle	Apparent speed (m/sec)	Distance (m)	
		Initial	Final
a	0.1	4	20
b		very close	
c		16	21
d	0.35	9	50
e		4	3
f		very close	
g	0.1	9	9
h	0.2	20	70
i	0.2	1	70
j	1.0	200	200
k		4	5
k'		100	100
l		15	15
l'		15	15
l''		22	22
m	0.2	8	15
m'	0.52	200	200
n	0.16	200	200
o	0.45	26	26
o'	0.2	15	15
p	0.1	15	22
p'	0.35	100	100
	0.2	35	55
r	0.2	100	44
s	0.2	100	44
t	0.7	30	90
u	0.1	13	21
v	0.03	1	9
w	0.24	50	50
x	0.1	100	200
y	0.5	100	100
z	0.2	15	27
1	>1.55	>500	>500
2	>0.20	>200	>200
3	0.11	30	30

It is obvious that the relative velocities of all the particles with respect to the rocket, ranging as they do from 0.1 to 1.5 m/sec, are very low compared to the actual rocket velocity, even at peak. This appears to be *prima facie* evidence that they originate from the rocket. There is, however, the alternative explanation that some, at least, are particles of natural origin. That they should all have almost exactly the same velocity as the rocket is simply a result of the selective action of the photographic coronagraph. For faint particles, only those that move across the field with low angular velocity will be able to expose a trail, especially when the background is dense, as it is in the long exposures. If there is a large number density of small particles within the altitude range covered by the rocket, there should be a few within the velocity range that can be photographed.

This selective action applies principally to the velocity component in the plane perpendicular to the solar vector, and is quite stringent. At peak, for example, it acts to select particles having a north velocity component of between 91 and 89 m/sec and a vertical velocity of 0 ± 1 m/sec. At exposure 22, the vertical velocity must remain within 1 m/sec of the rapidly increasing free-fall velocity, which is near 700 m/sec, and the same north velocity component restriction still holds. For the velocity component along the solar vector, however, the selection effect is less stringent.

An estimate of particle size was made, based on the assumptions that the particles are spherical, have an index of 1.33, and are nonmetallic. This was done by means of the Mie theory, as presented by Penndorf (1962), for $\lambda = 5000$ A and a scattering angle close to 0°. It was also necessary to calibrate the coronagraph in order to obtain approximate values of stellar magnitude for the various particles producing the trails. Laboratory calibrations made with point sources of light indicated that 3d-magnitude stars were easily recorded in 2 sec, and 4th-magnitude stars were photographable in 1 sec

when they did not move in the field. An unexpected check was obtained in flight from the 3d-magnitude star μ Geminorum, which happened to lie 1°44′ from the sun, well within the field of view. This was present in most of the pictures; it was a well-exposed point of diameter 0.02 mm in the 1-sec exposures, and was drawn out into a short arc in longer exposures where the rocket precession rotated the instrument. Plate 4 shows two exposures where the star trail is easily seen. The motion of the star also confirmed the analysis of the rocket precession as derived from the magnetometer and the pointing control elevation angle.

The conclusion reached from the observed trails and the Mie theory was that the particles photographed must have been in the range 10-μ diameter and larger. Particles smaller than 10 μ would have been too faint to photograph. Among the smallest and faintest is **J,** in plate 1, at a distance of at least 200 m. Even farther is particle 1 of plate **5,** whose trail width, **0.02** mm, indicates a distance of **500** m or more. According to the Mie theory the luminous intensity increases with the fourth power of the diameter, approximately, for particles near 10-μ diameter. This means that only a small increase in diameter is required to account for the brighter trails. It appears that 20 or 30 μ may be the upper diameter limit of particles photographed. These particle sizes fall within the dimension limits of particles collected by Hemenway, Soberman, and collaborators, from balloons and rockets following meteor showers. One may question the assumptions involved in applying the Mie theory, but because the magnitude change with size is so very rapid, the shape and optical constants should not be of too great importance in connection with the luminosity of the particle.

With regard to the possibility of a natural origin for these particles, it is useful to consider some details of the trails. In the first place, the particles seem to appear in puffs. Particles are few or absent in the first 4 exposures, then become prominent in the following exposures, including the 9th, and are absent again in exposures 11 and 12. Particles are again evident in exposures 14 through 19, but have subsided markedly in exposures 20 through 23. Although this sort of behavior might perhaps be expected of an outgassing rocket, it may also be characteristic of meteor showers.

For exposures earlier than 13, all trails were downward, indicating an ascending cloud of particles through which the rocket was ascending at a slightly greater velocity. Before peak, however, particles are present that were traveling upward faster than the rocket (exposures 14 to 16). From about exposure 20 on, the particles appear to be traveling up as the rocket falls and are a cloud not falling quite so fast as the rocket. In the north and south direction the particles for the most part show a small velocity component relative to the rocket toward the south.

At first sight these small relative velocity effects may seem to be caused by atmospheric drag; however, at these altitudes the mean free path is very long. For example, at 204 km it is 220 m, and at 130 km it is 14 m. Under these conditions the drag should be quite small, even for 10-p particles. Moreover, one would certainly expect the drag effect to be altitude dependent, but there is no correlation between particle velocity relative to the rocket and altitude.

It is not at all easy to explain the behavior of particles x, y, and w by changes of speed produced by drag. Particle x is particularly puzzling. Its trail can be followed in each exposure, from 19 through 23, and is shown as a composite in plate **3.** Its path is also shown replotted with the correction made for rotation of the instrument during exposure. This particle was far away, as evidenced by its sharp trail. It entered the field on the descent at 202 km, 2 km below peak, when the rocket velocity downward was about **70** m/sec, and stayed in the field for a full minute, until the rocket reached 174 km, where its velocity was 650 m/sec. First it fell faster than the rocket, but after 30 sec the rocket overtook it, and 30 sec later it left the field. In the north-to-south direction it entered with almost no relative velocity, for a time seemed to gain on the rocket, but left the field traveling south relative to the rocket. Critical inspection of the sharpness of the trail suggests that it was moving eastward faster than the rocket, since the trail is sharpest at the end of exposure **23.**

Its distance, on entrance, was 100 m, and after 30 sec was 200 m.

Particle w entered late in exposure 19, and appears faint because of the dense background of the 56-sec exposure. After correction it makes an angle of 26° with the zenith. The trail of particle y is closely parallel to that of particle w, though it entered earlier and left later. It is difficult to reconcile these two trails with possible atmospheric drag effects. If the south component of each is ascribed to drag associated with the north rocket velocity, 90 m/sec, there would have to be a drag effect on the vertical component as well. But the constant character of the north component and the increasing vertical velocity would combine with the increasing drag at lower altitudes to cause these two trails to be strongly curved; since they probably are not of the same size they would not be expected to remain parallel.

Exposure 15 of plate 1 contains the largest collection of particles and is shown enlarged in plate 5. The rocket was near the top of its trajectory during this exposure and was approaching zero vertical velocity. This exposure shows many particles with relative horizontal motions in a direction opposite to the horizontal travel of the rocket. However, there are also particles with vertical motions that are now in the same direction as the rocket motion, that is, they are overtaking the rocket. In the direction toward the sun, two are approaching and others are receding. This situation cannot be explained by drag. In particular, consider particles 1, 2, m', and n (plate 5), with distances >500, >200, 200, and 200 m, respectively; no two paths are parallel, and their directions range through more than 90°. Yet in this exposure these four particles lie within 2°.5 of each other. Without resorting to a collision process of some sort, it would be impossible to eject from the rocket four particles and have them reach this small, distant region with velocities so far from parallel.

Amongst the particles that were very close to the coronagraph, there are many that show strongly curved paths. These may be caused by electrostatic effects. Another factor comes from the precession of the rocket, since the rocket nose, swinging around in a cone, would impart nonlinear transverse velocities to the coronagraph under certain conditions. However, strongly curved paths do not require that these particles originate from the rocket, since natural particles could equally well be strongly charged and be deflected when passing close by the rocket.

It is difficult to arrive at a really clear-cut conclusion without making a calculation of the number density of photographable particles, based on known and estimated distributions at these altitudes. The best proof that they are natural particles is that many are far from the rocket and their behavior is not easy to explain on the basis of an origin from the rocket.

It is of interest that the date of the rocket flight, June 28, 1963, lies in the month when meteor counts are at a maximum, and is in the period of the Corvid, β-Taurid, and Draconid showers, and only a few days after the Arietid shower. Moreover, from May through November in the year 1963, according to McIntosh and Millman (1964) and Ellyett and Keay (1964), there was an unexpected increase in the meteor count, especially for small particles. Perhaps meteors entering more or less parallel to the earth's surface produce, in the breakup process, enough fragments moving upward and reaching the 200-km level with relatively low velocities to account for the photographed trails.

Acknowledgment

This work was supported in part by the National Aeronautics and Space Administration.

References

BLACKWELL, D. E.
1955. A study of the outer corona from a high altitude aircraft at the eclipse of 1954 June 30. I. Observational data. Monthly Notices Roy. Astron. Soc., vol. 115, pp. 629–649.

ELLYETT, C. D., and KEAY, C. S. L.
1964. Meteors: An unexpected increase in 1963. Science, vol. 146, p. 1458.

KOOMEN, M. J.; PURCELL, J. D.; SEAL, R. T., Jr.; and TOUSEY, R.
1964. Solar corona photographed from a rocket (abstract). Journ. Opt. Soc. Amer., vol. 54, p. 1409.

MCINTOSH, B. A., and MILLMAN, P. M.
1964. Radar meteor counts: Anomalous increase during 1963. Science, vol. 146, p. 1457.

NEWKIRK, G., Jr., and BOHLIN, J. D.
1965. Coronascope 11. Observation of the white light corona from a stratospheric balloon. Ann. d'Astrophys., vol. 28, pp. 234–238.

PENNDORF, R.
1962. Angular Mie scattering. Journ. Opt. Soc. Amer., vol. 52, pp. 402408.

PURCELL, J. D., and KOOMEN, M. J.
1962a. Coronagraph with improved scattered-light properties. Journ. Opt. Soc. Amer., vol. 52, pp. 596–597.
1962b. A coronagraph improvement. Sky and Telescope, vol. 24, p. 197.

TOUSEY, R.
1965. Observations of the white-light corona by rocket. Ann. d'Astrophvs., vol. 28, pp. 600–604.

Abstract

Photographs were obtained of the solar corona from 1° to 205 from the sun's center, at altitudes from 131 km to 204 km, by means of an externally occulted Lyot coronagraph flown in an Aerobee-150 rocket on June 28, 1963. They show many tracks produced by particles, shining brightly by sunlight scattered forward at a small angle. Analysis of the trails indicates that the particle diameters were 10 to 30 μ. Distances from the rocket ranged from 1 to 500 feet or more. The velocities relative to the rocket were 0.1 to 1.5 m/sec. This is not surprising, because particles with greater relative velocities would not have been detected photographically. It is difficult to explain the behavior of the distant particles on the assumption that they came from the rocket. It is proposed that some are natural particles, of meteoritic origin.

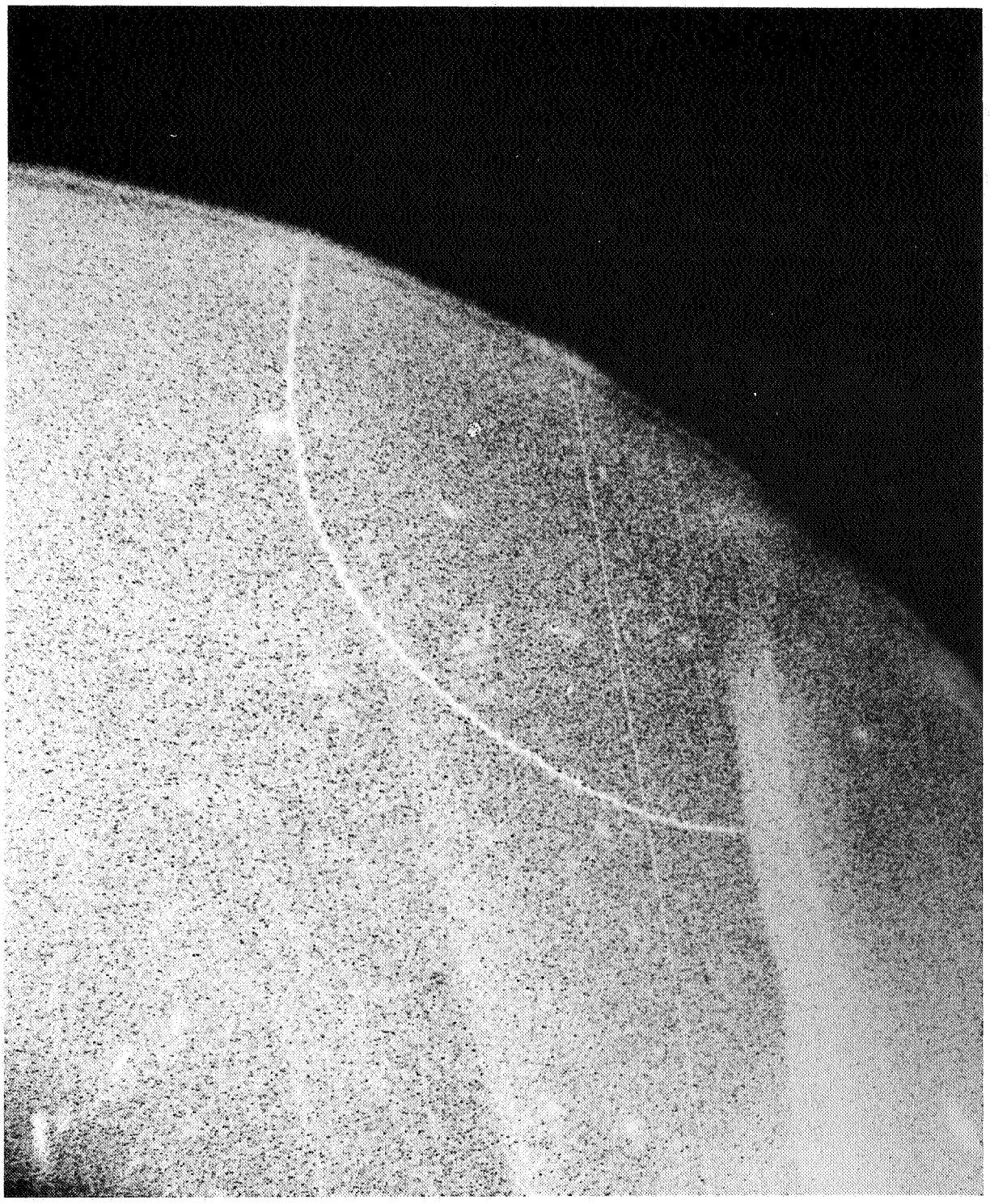

PLATE 1

Photographs taken with rocket coronagraph on June 28, 1963.

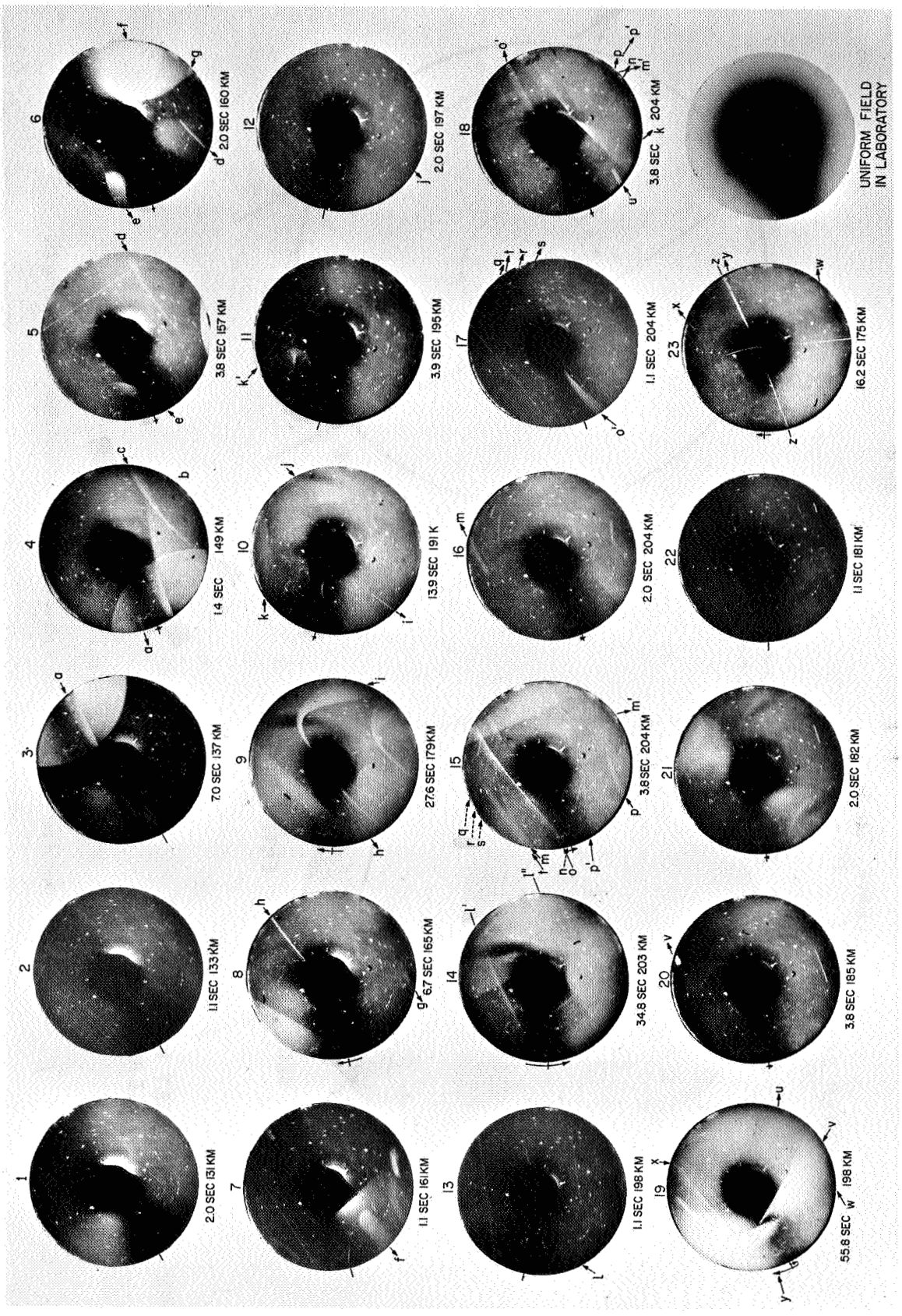

PLATE 2

Enlargement f particle track no. x, exposure 19.

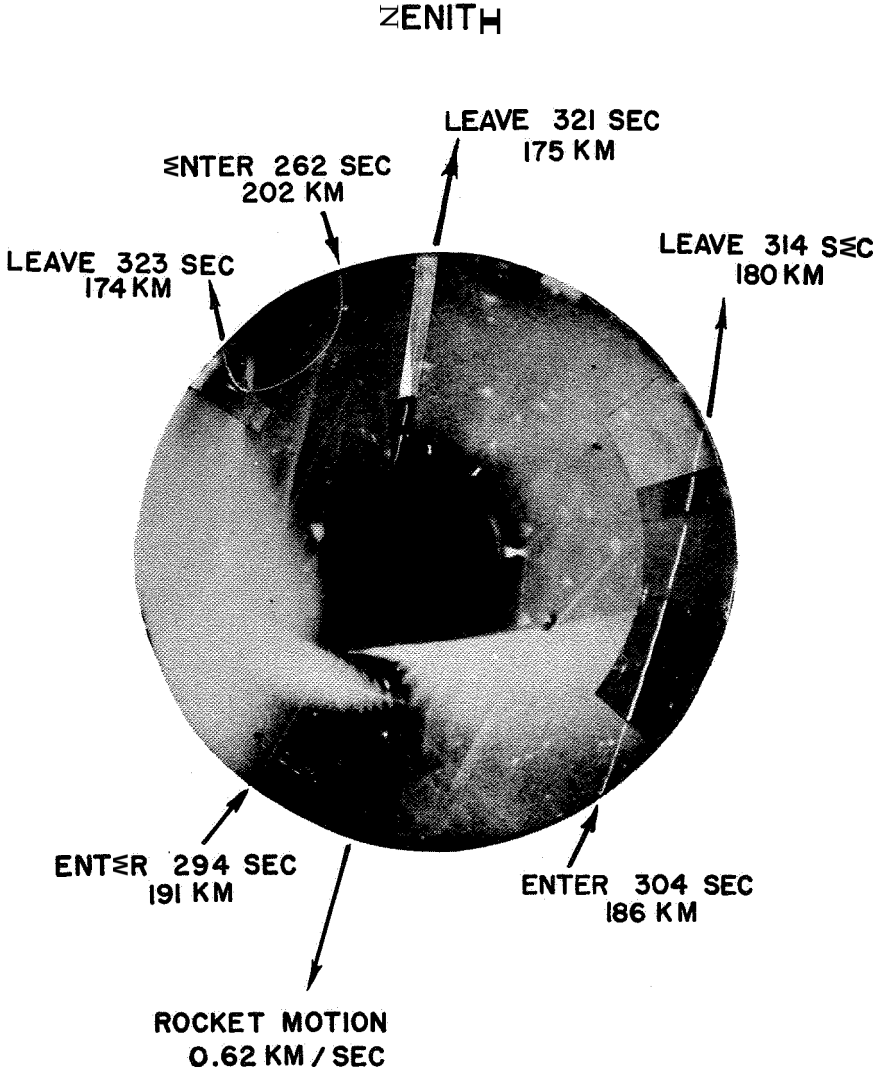

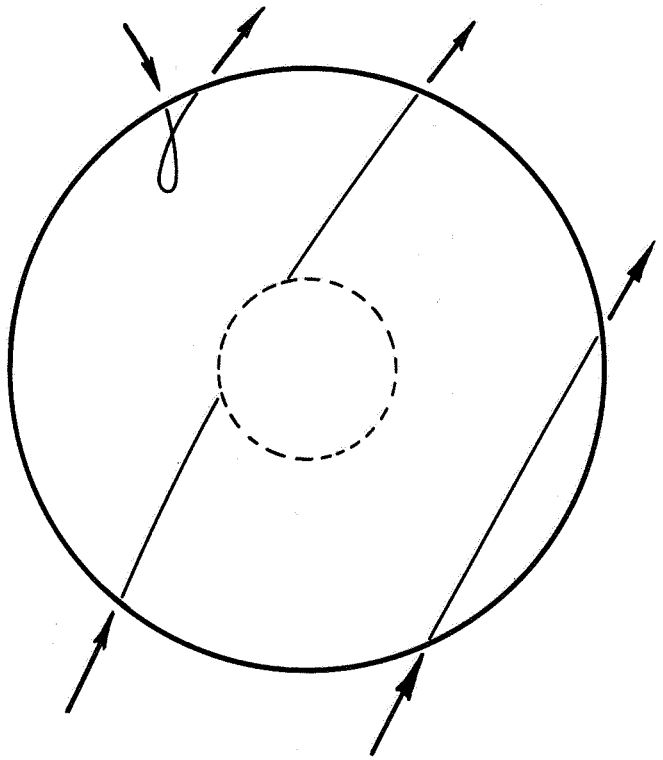

PLATE 3

Composite photograph of the tracks x, y, and w corrected for rotation of focal plane; exposures 19 to 23.

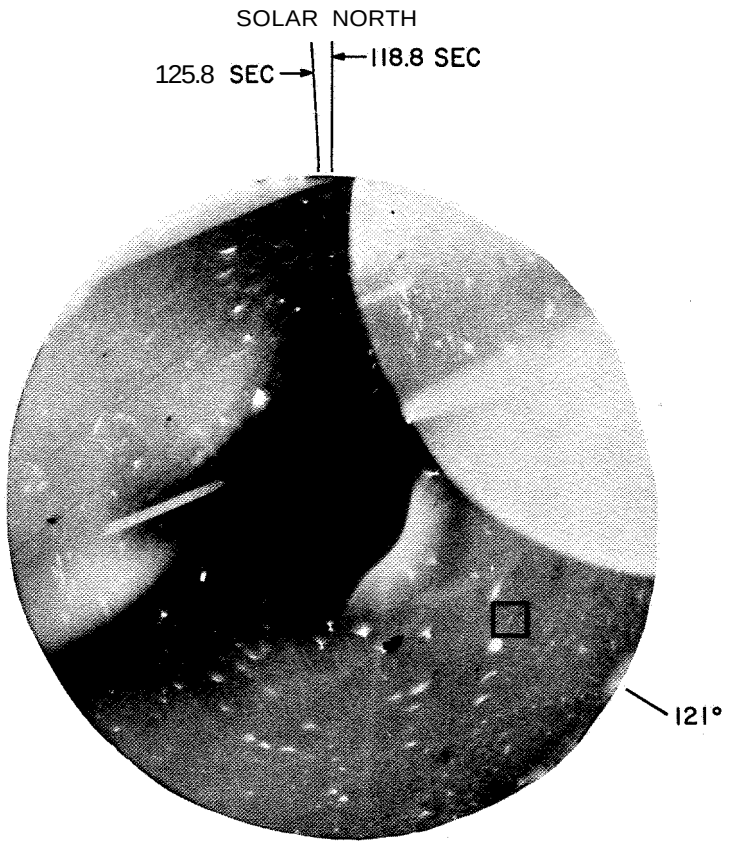

FRAME #3, 7.0 SEC, 137 KM

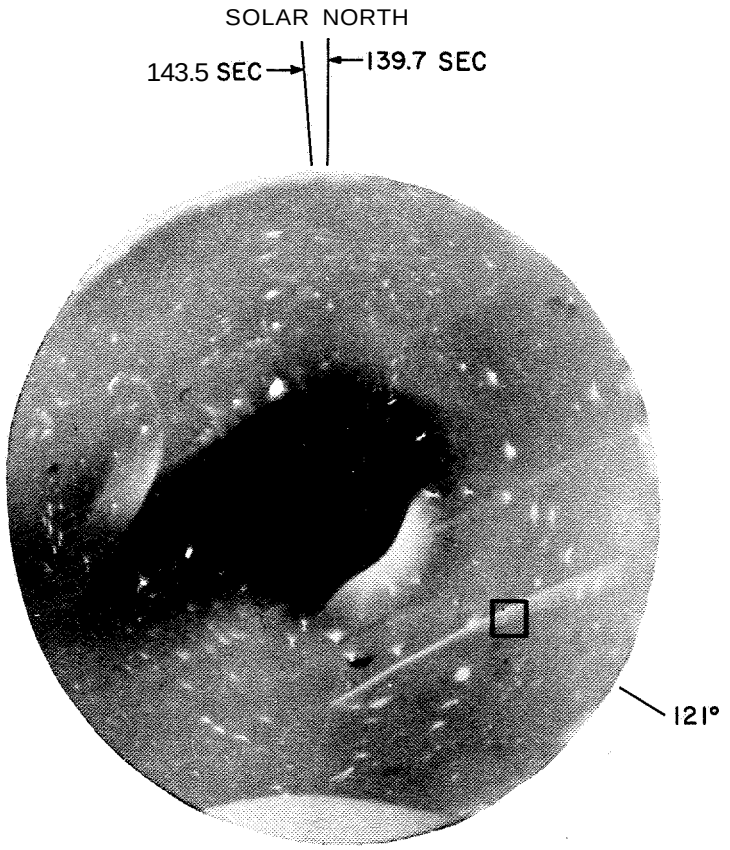

FRAME #5, 3.8 SEC, 160 KM

μ GEMINORUM, **Mag** 2.86

AEROBEE NE 3.129 (CORONAGRAPH) **JUNE** 28,1963

PLATE 4

Exposures 3 and 5, showing image of μ Geminorum, mag +2.86, Aerobee NE 3.129 (coronagraph), June 28, 1963.

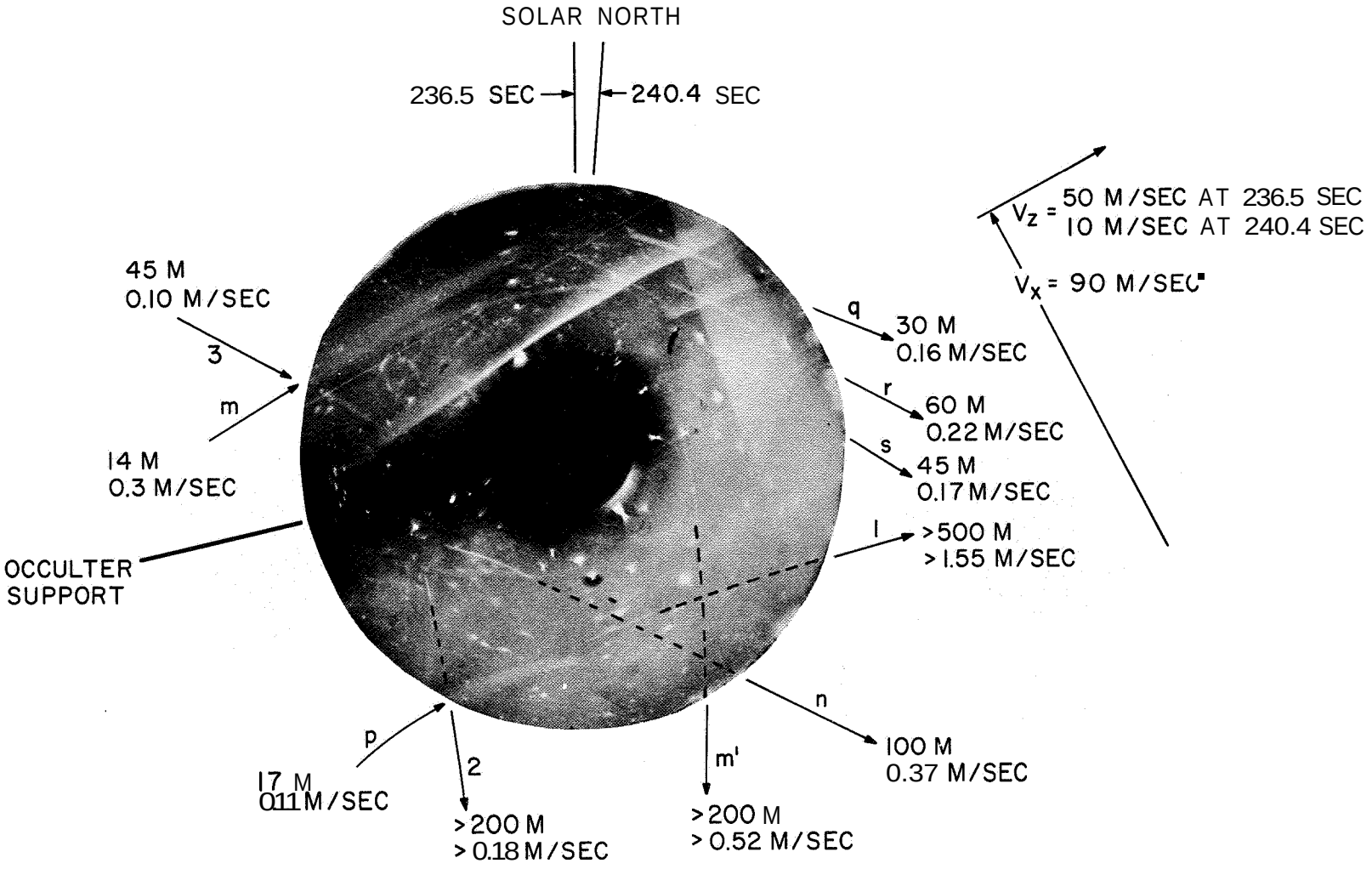

PLATE 5

Exposure 15, near peak of rocket trajectory, at 3.8 sec, 204.2 to 204.3 km, Aerobee NE 3.129 (coronagraph), June 28, 1963.

Vertical Distribution of Dust in the Stratosphere

J. M. ROSEN [1] and E. P. NEY [1]

Introduction

The estimation of meteoriticdust influx from particle samples collected in the atmosphere and on the earth has been plagued by the problem of identifying terrestrial contamination. Because of the similarity between the meteoritic and terrestrial dust, physical and chemical methods of distinguishing the two components are very difficult, if not impossible (Wright and Hodge, **1964;** Merrihue, **1964).** Testing for the presence of cosmogenic nuclides in dust samples would seem to offer a possible solution to the problem, but the contrary results of researchers leave this method still in question (Merrihue, **1964;** Schaeffer, Megrue, and Thompson, **1964).**

Measurements of the vertical distribution of dust, on the other hand, can distinguish the particle source by the spatial distribution of particles in the atmosphere. This method affords a relatively simple way of obtaining the total meteoric-dust influx.

Instrumentation

A balloon-borne photoelectric particle counter was used of the type invented by Gucker and collaborators at Armour Research Foundation (Gucker and O'Konski, **1949).** It is a relatively simple instrument capable of counting and sizing particles down to 0.25-μ diameter. A diagram of the instrument is shown in figures **1** and **2.** It is basically a dark-field microscope in which an individual dust particle in the sampled air scatters light into a photomultiplier. A complete description of the instrument can be found elsewhere (Gucker and O'Konski, **1949;** Rosen, **1964).**

[1] School of Physics and Astronomy, University of Minnesota, Minneapolis, Minn.

240-022 0-67 —23

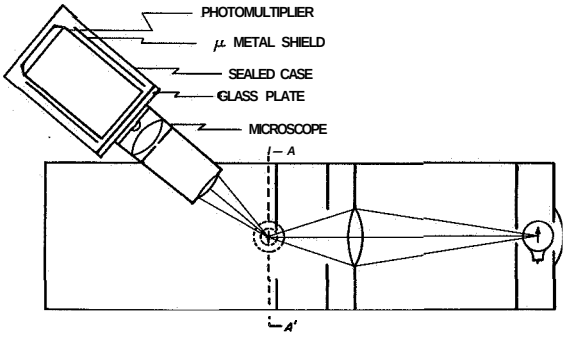

FIGURE 1.—Optical system of the photoelectric counter.

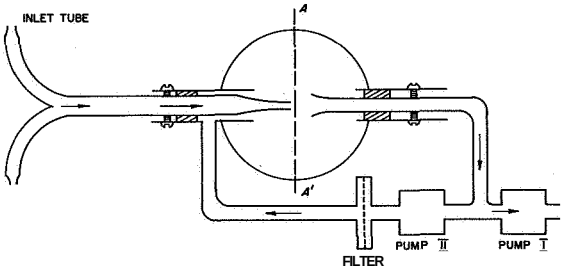

FIGURE 2.—Air-flow system of the photoelectricparticle counter.

Results

Representative data from four balloon flights are shown in figures **3** through **6.** With the exception of Flight **747,** the data indicate that the dust concentration above 100 mb is proportional to the pressure (that is, the dust exhibits a constant mixing ratio). A different graph was used to plot the data of Flight **747** so as to show clearly that it is composed of discontinuous segments along which the mixing ratio is constant.

Discussion

The problem of dust falling through a diffusing atmosphere has been given rigorous mathe-

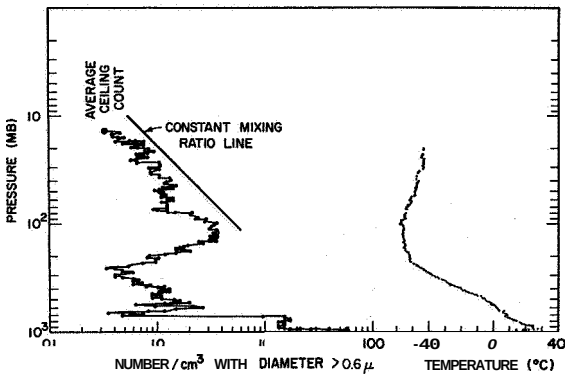

FIGURE 3.—Dust concentration on ascent of Flight 667, August 20, 1963.

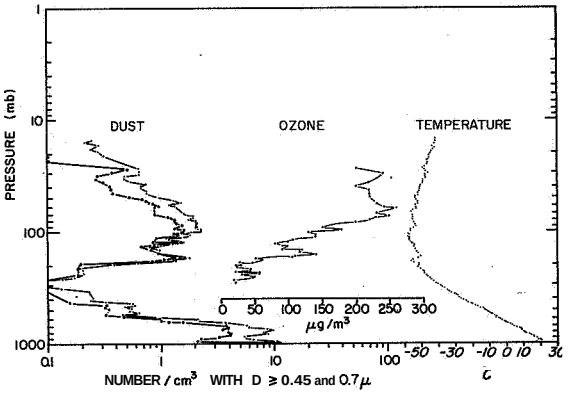

FIGURE 4.—Dust concentration on ascent of Flight 719 and ozone concentration on descent of Flight 720, August 18, 1964.

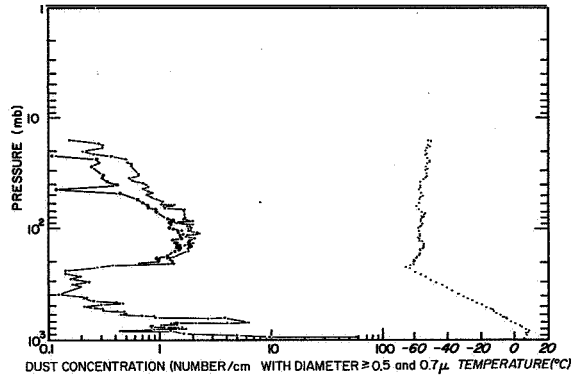

FIGURE 5.—Dust concentration on ascent of Flight 729, August 28,1964.

matical treatment by a number of authors (Lettau, 1951; Junge, Chagnon, and Manson, 1961). The important results of such a treatment, however, can be obtained by a simple physical argument.

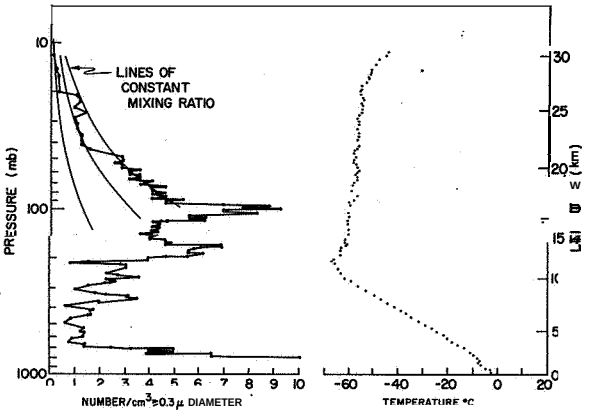

FIGURE 6.—Dust concentration on ascent of Flight 747, April 28, 1965.

The vertical distribution of dust from a constant source above a quiescent atmosphere is governed only by the gravitational fall velocity of the particles. Since the fall velocity in the stratosphere is inversely proportional to the pressure, it follows that the dust concentration must be proportional to the pressure. Now taking into account the motion of the atmosphere, the effect of turbulence is to mix the atmosphere in such a way as to keep the ratio of dust particles to air molecules a constant, that is, to preserve the constant mixing ratio and not destroy it.

The vertical distribution of dust from a constant source at 100 mb would be considerably different. In this case, there is a direct competition between atmospheric turbulence trying to establish a constant mixing ratio and the settling of dust trying to destroy it. From what is known about the magnitude of diffusion in the stratosphere, the mixing ratio would drop sharply above a 100-mb dust source (Junge, Chagnon, and Manson, 1961).

In summary, the behavior of the mixing ratio of dust in the stratosphere is a criterion for the source of dust: if the mixing ratio is constant in a given region, then the source is above that region. If, on the other hand, the mixing ratio drops sharply in the given region, then the source is below that region.

Conclusions

There can be little doubt that the source of the stratospheric dust observed on theballoon flights

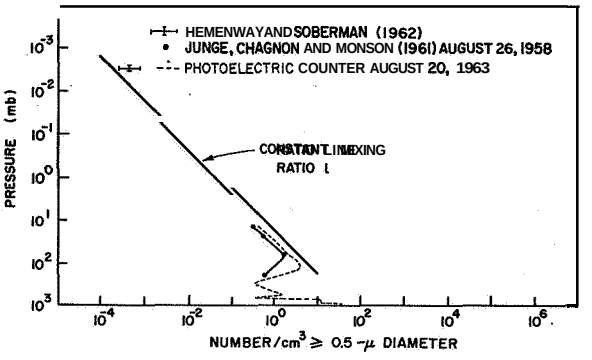

FIGURE 7.—A comparison of dust concentration measured in the stratosphere with that measured at high altitude in the Venus Flytrap experiment. The line of constant mixing ratio connecting the high-altitude dust concentration with the low-altitude dust concentration suggests that most of the dust is of meteoritic origin.

was above 27 km. Flight 747 suggests why the mixing ratio is not always constant even though the dust may be of meteoritic origin. If the influx over the earth's surface is not uniform, then horizontal mixing in the stratosphere should produce layers in which the mixing ratio would be constant; at the boundaries of these layers, however, the mixing ratio would be discontinuous. This argument would seem to explain the data of Flight 747.

The evidence that the stratospheric dust is of meteoritic origin is given in figure 7. Only the results of experiments involving the direct sampling of dust particles in the size range 0.5 to 2 μ are shown (Junge, Chagnon, and Manson, 1961; Hemenway and Soberman, 1962). Since all the data fall nearly on the same line of constant mixing ratio, it seems likely that the stratospheric dust is mostly extraterrestrial in origin.

The particle flux observed with the photoelectric particle counter is about 4×10^{-2} cm^{-2} sec^{-1} for diameters between 0.5 and 2 μ. This implies a mass flux of about 4×10^{6} meteoric tons per year over the earth.

Acknowledgment

This research was supported under Contract No. Nonr-710(22).

GUCKER, F. T., Jr., and O'KONSKI, C. T.
1949. Electronic methods of counting aerosol particles. Chem. Rev., vol. 44. pp. 373–388.

HEMENWAY, C. L., and SOBERMAN, R. K.
1962. Studies of micrometeorites obtained from are coverable sounding rocket. Astron. Journ., vol. 67, pp. 256–266.

JUNGE, C. E.; CHAGNON, C. W.; and MANSON, J. E.
1961. Stratospheric aerosols. Journ. Meteorol., vol. 18, pp. 81–108.

LETTAU, H.
1951. Diffusion in the upper atmosphere. *In* Compendium of Meteorology, Amer. Meteor. Soc., Boston, pp. 320–333.

MERRIEUE, C. M.
1964. Rare gas evidence for cosmic dust in modern Pacific red clay. Ann. New York Acad. Sci., vol. 119, pp. 351–367.

ROSEN, J. M.
1964. The vertical distribution of dust to 30 kilometers. Journ. Geophys. Res., vol. 69, pp. 4673–4676.

SCHAEFFER, O. A.; MEGRUE, G.; and THOMPSON, S. O.
1964. Experiments to test the presence of cosmogenic nuclides in ocean sediments. Ann. New York Acad. Sci., vol. 119, pp. 347–350.

WRIGHT, F. W., and HODGE, P. W.
1964. Compositional studies of extraterrestrial particles. AM. New York Acad. Sci., vol. 119, pp. 287–297.

Meteoric Dust in the Stratosphere Determined by Optical Scattering Techniques

G. NEWKIRK, JR.[1]

Introduction

Light-scattering measurements have long been used to estimate the size distribution and concentration of meteoric material in the zodiacal light. Only more recently have similar techniques been employed to determine the meteoric content of the atmosphere, where the concentration of cosmic particles is magnified many orders of magnitude over the interplanetary value. Of course, many of the meteoroids are destroyed or modified upon entering the atmospheric trap, and the existence of contaminating aerosols adds a new dimension to the problem of determining the influx rate of material. Moreover, the months or years of residence time of meteors and meteoric debris in the atmosphere below 100 km imply that any such observation of influx rate represents average conditions over a similar period.

Although the light scattered from a collection of aerosols (meteoric as well as other particles) contains sufficient information to fix the size distribution and concentration of the particles, several limitations in the technique occur. For mathematical simplicity it is usually necessary to assume the particles to be spherical—a condition that the work of Hemenway and Soberman **(1962)** has shown to be questionable for many meteoric particles. Also the refractive index of the particles may be only approximately known. Frequently, measures of the angular distribution of scattered light cannot be made over a sufficient range of angles to allow the size distribution of the aerosol to be determined unambiguously. In the forward scattering lobe (for scattering angles ϕ less than 20° to 30°) the gradient of scattered intensity with increasing scattering angle becomes steeper with increasing α. Thus, small-angle scattering measures can, in principle, lead to a good estimate of the size distribution of particles. Radiation scattered at large angles, however, contains no such unambiguous signature of the particle size, and the size distribution can be fixed within only very broad limits. In fact, only the most precise large-angle scattering measures can distinguish between a change in the particle concentration and a change in particle size. This latter limitation does not apply, of course, to determinations of the scattering from individual particles.

It must also be remembered that scattering measurements are intrinsically effective for only those particles whose radii are of the order of the wavelength of the radiation. Scattering at optical wavelengths thus allows the size distribution of the particles to be determined only over the range $0.1\ \mu \leq r \leq 3\ \mu$.

One unique advantage possessed by light-scattering measurements of atmospheric aerosols is that a large sample of particles is examined at once. For example, a photometer looking upward from the stratosphere receives radiation from the particles in about 10^7 m^3 for every square degree of viewing angle.

As part of a program to investigate the feasibility of observations of the corona out to 5 solar radii, the High Altitude Observatory has flown an externally occulted coronagraph up to heights of 25 km to measure the angular

[1] High Altitude Observatory, Boulder, Colo.

and wavelength distributions of the daylight sky. The instrument and the details of the observations and their interpretation in terms of the scattering of sunliiht by aerosols have been described elsewhere (Newkirk and Eddy, **1962, 1963, 1964).** The basic data consisted **of** sky radiances at scattering angles from 1°.67 to 57°.8 measured at altitudes of from **6** to **25 km** at **4400** A.

An example of the variation of sky radiance with height at one scattering angle appears in figure **1.** The observations are compared with what would be expected if the sky radiances were measured in a pure, molecular atmosphere with three different models of the radiation originating from below. Both the observations and the calculated values, taken from Coulson, Dave, and Sekera (1960), include the effects **of** the variation of the solar zenith distance during flight. Attention is called to the sharp approach of the observed sky radiance toward the calculated values above an altitude of 20 km.

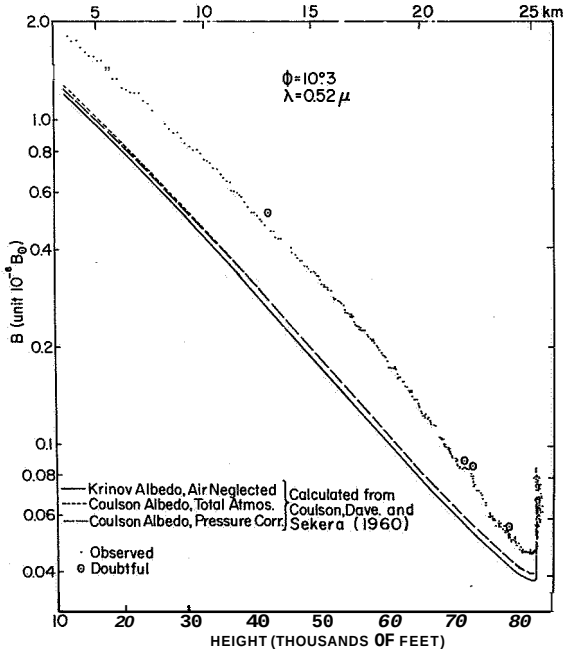

FIGURE 1.—Photoelectric observations of the sky radiance at a scattering angle of 10°.3 at λ=0.52 μ. The "hook" at 82,000 feet was produced by the variation of solar zenith distance during the floating period of 2 hours. The observations are compared with three models of the radiation from a pure molecular sky.

Interpretation

In order to interpret observations such as those shown in terms of the size distribution of aerosol above the balloon at any moment, we must solve the equation governing the transfer of radiation through a turbid atmosphere. To this end, Sekera **(1956)** and Deirmendjian **(1957, 1959)** have demonstrated the convenience of dividing the equation of transfer into two simultaneous equations—one describing the intensity due to scattering by the molecules, and the other describing the intensity due to scattering by the aerosols. The first, governing the intensity in the pure molecular or Rayleigh atmosphere, has been solved by Chandrasekhar **(1950)** and tabulated by Coulson, Dave, and Sekera **(1960).** By considering that, insofar as the overall transfer of radiation is concerned, the Mie scattering in the upper atmosphere represents a small perturbation on the solution of the Rayleigh problem, we can use their tabulated solution. Subtraction of the radiance of the pure molecular sky from that observed then yields the residual sky, which is attributed to scattering **by** the larger particles. By assuming that the irradiation **of** Mie particles by the rest of the atmosphere and by the ground is negligible and that $\mu \approx \mu_\odot$, we can write an approximate equation

$$\mu \frac{B_{M^j}}{B_\odot} = \omega_\odot \frac{\lambda^2}{8\pi^2} \int_{r_1}^{r_3} N(r, h) i^j(\alpha, \phi) dr, \qquad (1)$$

where

$\mu = \cos Z$,

Z = zenith distance **of** the point in the **sky**,

B_{M^j} = radiance of the sky at height h, in the j^{th} polarization component, due to the scattering by large particles,

$B_\odot$ = mean radiance of the solar disk observed at the height ***h***,

$\omega_\odot$ = solid angle subtended by the sun,

h = height in the atmosphere,

$i^j(\alpha, \phi)$ = Mie scattering intensity function in the j^{th} polarization component for a spherical drop of size parameter α, of refractive index m, scattering through an angle ϕ (see van

de Hulst (1957) for a complete definition),

ϕ = scattering angle counted from the direction of forward scattering,

$\alpha = 2\pi r/\lambda$ = size parameter of the droplet,

$N(r, h)$ = particle concentration in a column above height h with radii between r and $r+dr$.

The unit of N is cm^{-2} per micron dr. The usual convention is that $j=1$ refers to radiation with electric vector vibrating perpendicular to the scattering plane, while $j=2$ refers to radiation with electric vector normal to this plane. Calculation shows that the errors committed by using the simplified equation in the stratosphere are of the order of 15 percent. Since most of the published Mie scattering coefficients are for $m=1.33$, we have made our interpretation in terms of the scattering by spherical water drops. All particles are considered to have their radii between the limits r_1 and r_3.

The size distribution of the scattering aerosols is taken to have the form

$$N = N_0 \left(\frac{r}{r_2}\right)^{-\delta}, \qquad (2)$$

where

$$\delta = 0, \quad \frac{r}{r_2} \leq 1,$$

$$\delta = \delta, \quad \frac{r}{r_2} > 1.$$

Junge, Chagnon, and Manson (1961) have found by direct sampling, and Volz (1954), Newkirk (1956), Deirmendjian (1957, 1959), and Volz and Bullrich (1961) have inferred from optical measurements that such a form adequately describes the size distribution of atmospheric aerosols.

Comparison between calculated and observed angular distributions of the residual skylight (fig. 2) sets the parameter δ of the size distribution at $\delta \sim 3.5$ in the stratosphere. As is shown in figure 3*a* these optical data yield concentrations and size distributions that are quite consistent with those obtained by direct sampling.

By differentiation of the size distributions with respect to height, one can determine the variation of particle concentration with altitude (fig. 3*b*). Quite clearly, our observations confirm the conclusion of Junge and his collaborators that an aerosol layer at a height of approximately 20 km exists. The form of such a layer suggests that the majority of particles in it are of terrestrial origin and that the maximum is due either to the concentration of particles by advection or by in situ formation.

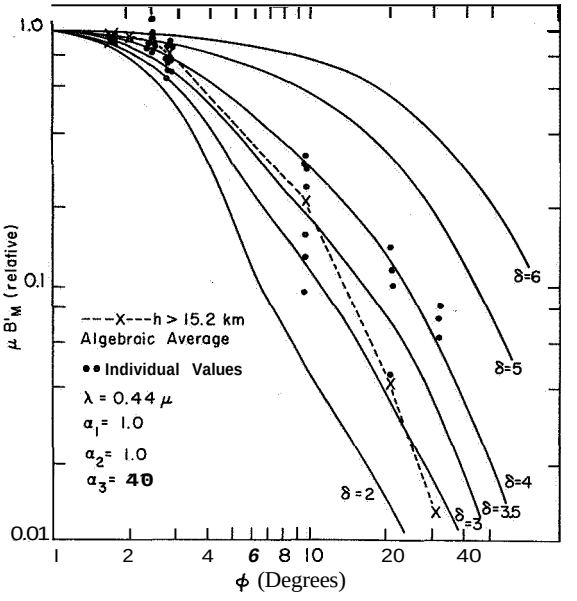

FIGURE 2.—The observed angular distribution of residual sky radiance at heights above 15.2 km (dots and dashed line) is compared with theoretical angular distributions (solid curves) differing only in the parameter 6. Individual values ≤ 0 for $\phi = 20°.7$ and $\phi = 31°.4$ are not shown on the diagram. The particles are assumed to be spheres of refractive index 1.33. The observations are normalized at $\phi = 2°$.

Meteoric influx rates

The sharp drop of particle concentration with height above the maximum of the aerosol layer can be further interpreted under the assumption that a steady state prevails and only two mechanisms—diffusion and sedimentation—govern the flow of particles. Junge, Chagnon, and Manson (1961) write the vertical flux of particles γ_s as

$$\gamma_s = -n_s w_s - n \frac{dv_s}{dz} D, \qquad (3)$$

where

n_s = concentration of particles of radius r,

w_s = fall speed of the particles of radius r,

n = concentration of air molecules (number per cm^3),

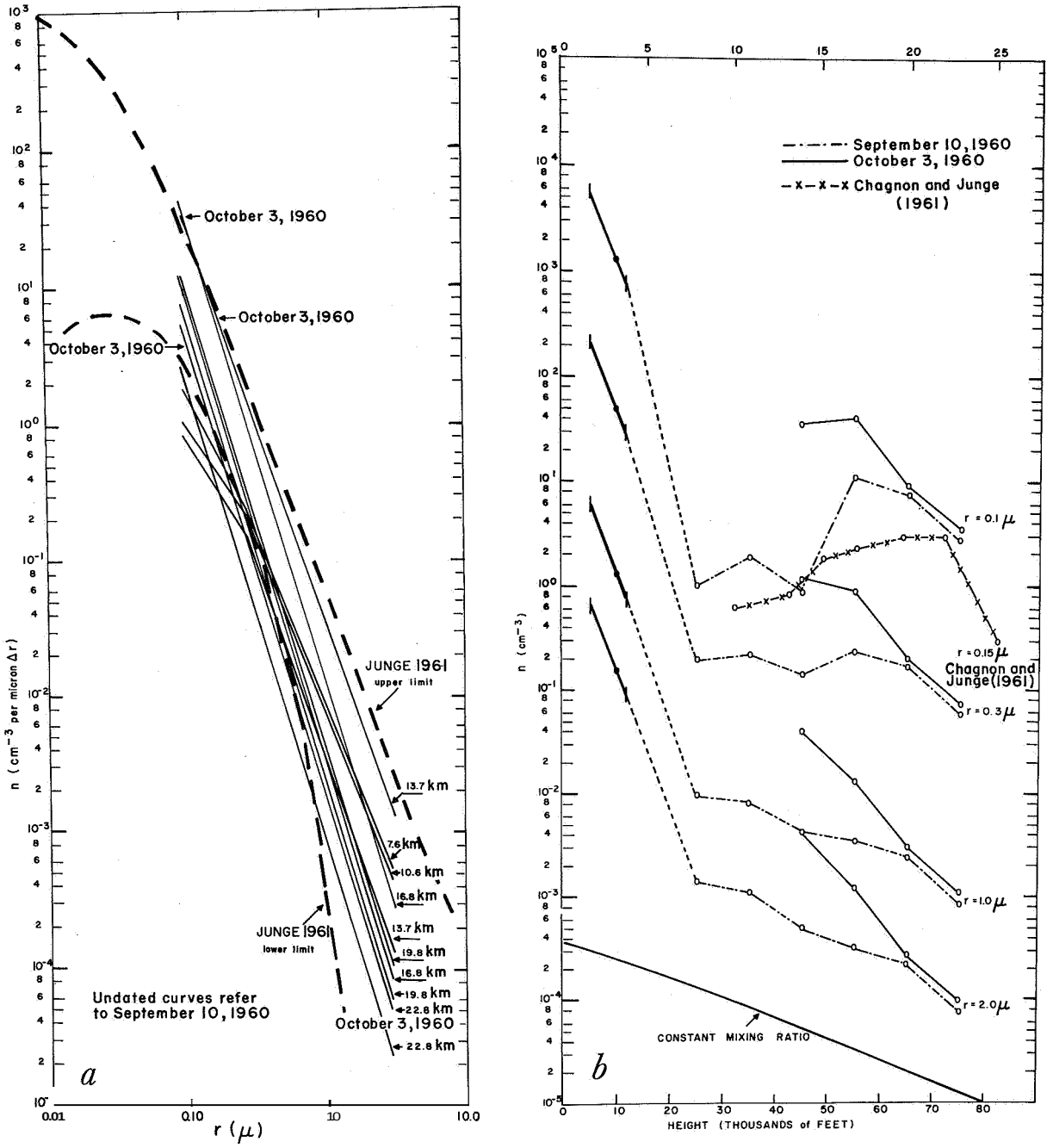

FIGURE 3.—*a*, The inferred particle size distributions of aerosols in the atmosphere at the heights indicated. The upper and lower limits of the particle concentrations determined by direct sampling also appear. *b*, Change of the concentration of particles of radius r with altitude. The concentrations above 7.6-km altitude from this investigation are to be compared with the distribution obtained for $r=0.15\ \mu$ by direct sampling. The heavy lines at approximately 3 km show the concentrations and scale height ($H=1$ km) inferred in an earlier investigation (Newkirk, 1956). Particles distributed with a constant mixing ratio with air would display a decrease in concentration with altitude parallel to the bottom curve.

ν_s = concentration of particles relative to the concentration of air molecules,
D = diffusion parameter.

The fall speed is that given by the Stokes-Cunningham relation (Davies, **1945**), while the diffusion parameter contains the effects **of** both eddy and molecular diffusion. Within the layers of the atmosphere of concern in our problem, eddy diffusion is dominant (Lettau, **1951**). The solution of equation **(3)** in an atmosphere of scale height H yields

$$n_s = n_{s0} e^{-z/H - \int_0^z (w/D)\,dz'} - \frac{\gamma}{w}\left\{1 - e^{-\int_0^z (w/D)\,dz'}\right\}, \quad (4)$$

where the concentration is n_{s0} at $z=0$. By interpreting the observed drop in particle concentration with height above the maximum

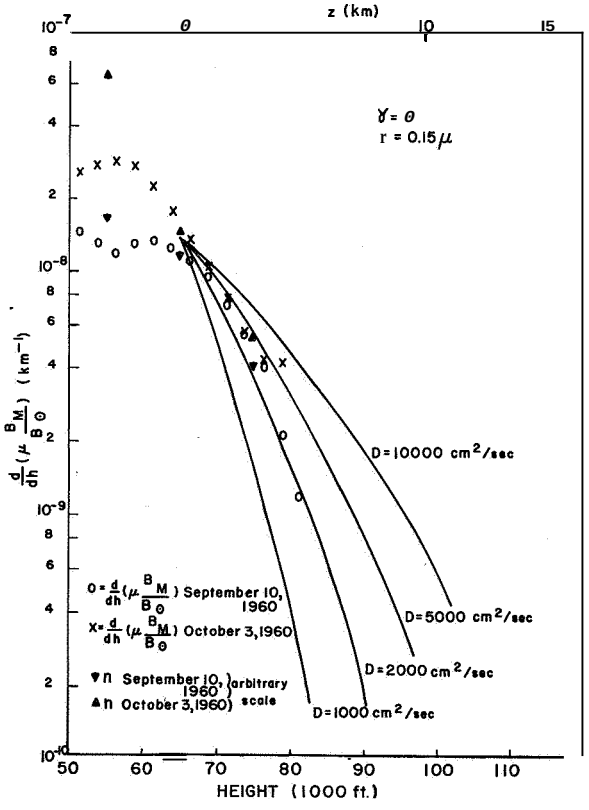

FIGURE 4.—The decrease of relative particle concentration above the "source level" at 20 km as observed and as calculated for various values of the vertical diffusion coefficient D. The calculated curves and observed concentrations are fitted to the photoelectrically measured gradients, which are proportional to concentration, at $h=20$ km.

of the aerosol layer at **20** km (fig. **4**) as due to the mechanism of sedimentation-diffusion, we can determine that the diffusion constant **D** from **20** to **25 km** lies in the range **2000** cm²/sec **<D<** **10,000** cm²/sec with the best fit **for** $D \approx 5000$ cm²/sec. This value is in rough agreement with the $D \approx 10^3$ estimated by Lettau **(1951)** for temperate latitudes from models **of** the representative zonal circulation and the lapse rate.

The additional assumption, however, that D is constant above **25** km allows the calculation of the total concentration in the cm² column overhead of particles with radius r that have been carried aloft by diffusion. (In fact, the usual profile of temperature vs height above **25** km would lead to the expectation that D should decrease slightly with height.) This calculation yields column concentrations for **0.3** $\mu < r < 3\ \mu$ that are below those required by the scattering observations. In other words, the air above **25** km contains more particles in this size range than can be explained by diffusion from below. The origin of the excess particles is to be found in the sedimentation of meteoric material downward. Thus, **for a** particular value of D, the observations lead to a value of the meteoric influx y. In figure 5 appears a comparison between the meteoric influx for **0.3** $\mu < r < 3\ \mu$ derived in this manner and as determined by various rocket and satellite experiments. Except for Watson's **1941** (see Watson, **1956**) flux estimate and that from the "Venus Flytrap" rocket, the results appear in good agreement.

The departure of the "Venus Flytrap" observations from the other data may be explained by the encounter of the "Flytrap" with an abnormally high, transient shower **of** meteors or by the sampling of particles orbiting close to the earth. If the high fluxes inferred from the "Flytrap" actually had been precipitating continuously into the atmosphere, the sharp drop of particle concentration above **20** km would not be present and the concentration of meteoric particles at $h \sim 20$ km would exceed the observed concentration **of** all particles.

The influx rates shown in figure **5** allow the calculation of the total mass influx of meteoric material into the earth's atmosphere. By ap-

proximating the number flux of particles as

$$-\gamma = 10^{-1} r^{-2.5}, \quad 0.1\ \mu < r < 3\ \mu, \quad \text{(HAO curve)}$$

$$-\gamma = 20\, r^{-6}, \quad 3\ \mu < r < 10\ \mu, \quad \text{(satellite curve)}$$

$$-\gamma = r^{-4.5} \quad 10\ \mu < r < 10^{4}\ \mu, \quad \text{(visual and radar meteors curve)}$$

we determine a mass flux of 2×10^{-15} g sec^{-1} or 10^{3} metric tons per day or 3×10^{5} metric tons per year over the surface of the earth. This rate of deposition is smaller than the 10^{4} metric tons per day estimated by Dubin and McCracken (1962) and others (Dubin, 1960; LaGow and Alexander, 1960; Whipple, 1961a) from the extrapolation of the satellite observations to the radiation pressure limit (under the assumption that rocket and satellite sample particles are actually precipitating into the atmosphere). We interpret our smaller daily influx rate as evidence that above 100 km a significant fraction of the particles in the size range $0.3\ \mu < r < 3\ \mu$ are in geocentric, quasi-closed orbits. This hypothesis is strengthened by the agreement of our estimates with the rate of approximately 10^{5} metric tons per year for meteoric dust settling through the air or deposited on the ground (Crozier, 1960; Laevastu and Mellis, 1961; Pettersson, 1960; Crozier, 1961; Thiel and Schmidt, 1961; Crozier, 1962; Wright and Hodge, 1962). An alternate explanation is that the majority of meteoric particles are too fragile to survive passage through the atmosphere.

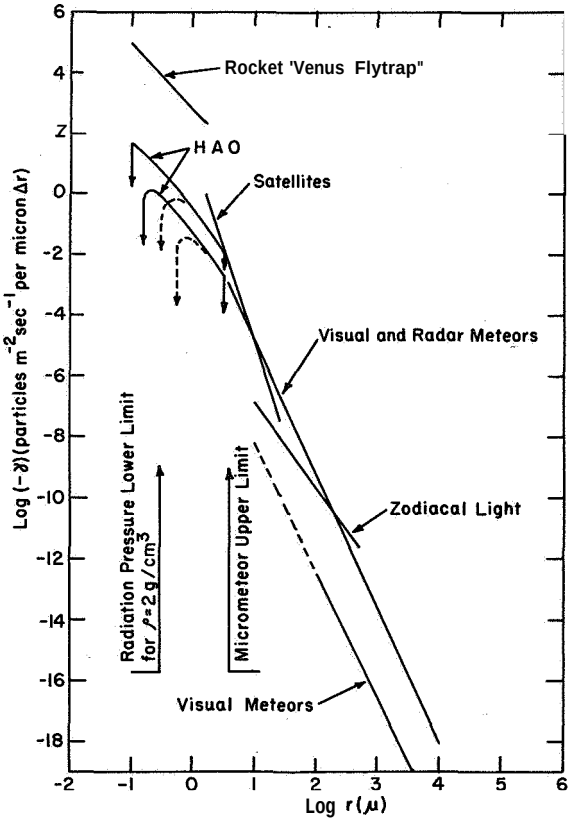

FIGURE 5.—Comparison of the meteoric influx rates inferred in this paper (labeled HAO) with the fluxes determined from the rocket "Venus Flytrap" (Hemenway and Soberman, 1962), from satellites (Alexander et al., 1963), from visual and radar meteors (Whipple, 1961a), from zodiacal light (van de Hulst, 1947), and from visual meteors (Watson, 1956). The higher HAO curves refer to the results of September 10, 1960; the lower curves, to October 3, 1960. For $D=2000$ cm² sec^{-1} the solid HAO curves apply, while for $D=10{,}000$ cm² sec^{-1} the dashed curves apply. The lower size limit of particles to remain in the solar system against radiation pressure and the upper size limit of particles to survive passage through the atmosphere (Whipple, 1950, 1951) are indicated.

Meteoric fluxes in the atmosphere of 4×10^{6} tons per year and 2×10^{7} tons per year recently estimated by Rosen (1964) and Fiocco and Colombo (1964) require special comment. Rosen's determination is apparently based on the misconception that all aerosols at an altitude of 20 km in the size range $0.5\ \mu \leq r \leq 2\ \mu$ are of meteoric origin. As is shown in the next section, only 1 to 10 percent of the stratospheric aerosols are meteoric. The discrepancy with the optical radar estimates may well be resolved by the suggestion of Fiocco and Colombo that the particles at 120 km are meteoric fragmentation products of radii $r \sim 0.1\ \mu$, which naturally escape detection in our measurements. Although their interpretation has been criticized (Deirmendjian, 1965), it should be remarked that the sedimentation of particles in the concentrations inferred for 120 km (about 10^{-5} cm^{-3}) down to 20 km would not be in excess of the Aitken nuclei counts at the lower altitude (Junge, Chagnon, and Manson, 1961). The

overwhelming proportion of Aitken nuclei in the stratosphere, however, are believed to be of terrestrial origin.

Concentration of meteoric particles in the stratosphere

The relative concentration of meteoric particles in the stratosphere is of interest in the analysis of dust-sampling studies as well as to the meteorologist. Bowen's (1953) hypothesis that meteoric activity influences world rainfall presupposes that either a substantial fraction of the particles in the lower stratosphere are of meteoric origin or that meteoric debris is outstandingly effective as a nucleating agent. Although we do not intend to discuss the second alternative, the fluxes inferred from our measurements show that meteoric dust represents a small fraction of the particulate matter below 20 km (see table 1). Above 25 km meteoric debris appears to constitute a major part of the aerosols with radii larger than 0.3 μ.

TABLE 1.—*Relative concentration of meteoric debris (ordinary numbers refer to measurements of September 10, 1960; those in parentheses, to October 3, 1960)*

$r(\mu)$	$n_{meteoric}/n_{observed}$ Local concentration		$N_{meteoric}/N_{observed}$ Column concentration ($h>25$ km)
	$h=20$ km	$h=25$ km	
0.1	0	0	0
0.3	0.10 (0)	0.42	0.76
0.5	0.12 (0.01)	0.53	0.95
1.0	0.13 (0.02)	0.55	0.99
2.0	0.13 (0.04)	0.55	1.00

Temporal variations of meteoric influx

Although showers of visual and radar meteors are frequently spectacular, temporal variations in the meteoric content of the stratosphere and lower atmosphere appear to have eluded consistent detection. Bigg (1956), from measurements of the twilight, and Zacharov (1952), from determination of the transparency of the atmosphere, claim to have identified an increase in the dust content of the atmosphere associated with the Perseid shower; however, the precise twilight photometry of Volz and Goody (1962) shows only a broad maximum of stratospheric turbidity in the winter months. Similarly, measurements of the radiance of the zenith sky at 28 km from May through September 1962 (before the Bali volcanic eruption) by Newkirk and Bohlin (unpublished) fail to show any clear influence of the Perseid shower. Apparently, the storage of debris for many months or years in the atmosphere effectively smooths out the variations of meteoric influx present at the top of the atmosphere.

Concentration of interplanetary material

For particles that are not destroyed in their passage through the atmosphere, the interplanetary concentration n_{IP} is related to the influx rate by

$$-\gamma = n_{IP} v, \tag{5}$$

where v is the geocentric speed with which particles leave the interplanetary medium and impinge upon the upper atmosphere. The interplanetary concentrations obtained with $v=30$ km sec^{-1} from the HAO data and from the measurement of meteor impacts on rockets and satellites are compared with the concentrations inferred from the photometry of the zodiacal light in figure 6. A detailed critique of the interpretation of the zodiacal light is not necessary. Although quite some divergence appears in the concentrations of interplanetary particles from the various zodiacal light models, two facts seem outstanding. First, for $r>10$ μ the meteor concentrations exceed the zodiacal light concentrations by about a factor of 10. Second, for smaller radii our concentrations exceed those from the zodiacal light by a factor of about 1000. (For the extrapolated satellite curve the excess would be still larger.) We thus conclude that a geocentric condensation of interplanetary dust, such as suggested by de Jager (1955), Beard (1959), Hibbs (1961), Singer (1961), and Whipple (1961a, 1961b), does indeed exist. The magnitude of this condensation (approximately 10^3 for the smaller particles) is in agreement with the theoretical

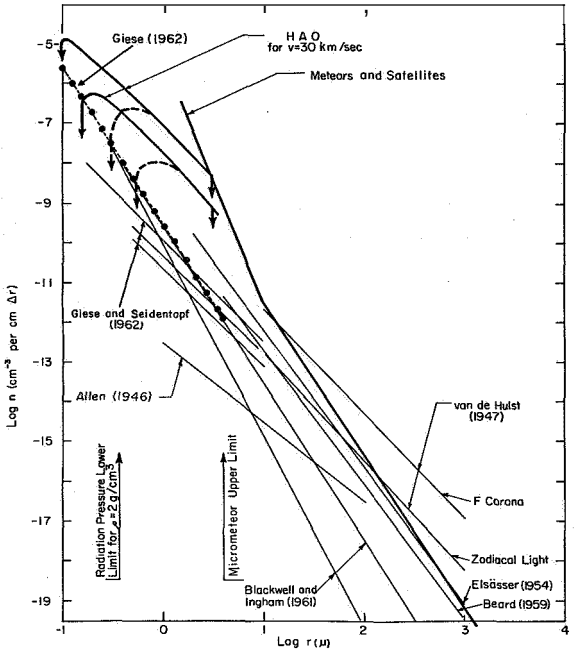

FIGURE 6.—Comparison of the concentration of interplanetary dust particles as inferred in this paper (labeled HAO) with the concentrations determined from satellites (Alexander et al., **1963)** and visual and radar meteors (Whipple, 1961a) as well as with the various determinations from the photometry of the zodiacal light. The fact that the zodiacal light concentrations are approximately a factor of 1000 lower than those determined by our analysis is taken as evidence for a local gravitational condensation of the interplanetary dust in the neighborhood of the earth. Note that the model inferred by Allen **(1946)** refers only to the concentration required if all the particles are of a given radius between **1** and 100 μ rather than a true size distribution.

calculations. The fact that the observed geocentric condensation is much smaller for larger particles ($r > 10\ \mu$) suggests that the Poynting-Robertson effect has not sufficiently reduced the eccentricities and major axes of the orbits of these larger meteoroids for effective capture by the earth. The Poynting-Robertson theory predicts that smaller particles in the solar system will take circular orbits more rapidly and hence will be more effectively captured by the earth.

Acknowledgments

This discussion has been largely based upon the joint work of John A. Eddy and myself with support by the Office of Naval Research under contract Nonr 393(05).

References

ALEXANDER, W. M.; MCCRACKEN, C. W.; SECRETAN, L.; and BERG, O. E.
1963. Review of direct measurements of interplanetary dust from satellites and probes. *In* Space Research III, ed. by W. Priester, North-Holland Publ. Co., Amsterdam, pp. 891–917.

ALLEN, C. W.
1946. The spectrum of the corona at the eclipse of 1940 October 1. Monthly Notices Roy. Astron. Soc., vol. 106, pp. 137–150.

BEARD, D. B.
1959. Interplanetary dust distribution. Astrophys. Journ., vol. 129. pp. 496–506.

BIGG, E. K.
1956. The detection of atmospheric dust and temperature inversions by twilight scattering. Journ. Meteorol., vol. 13, pp. 262–268.

BLACKWELL, D. E., and INGHAM, M. F.
1961. Observations of the zodiacal light from a very high altitude station, pts. I–III. Monthly Notices Roy. Astron. Soc., vol. 122, pp. 113–165; see also Ingham, M. F., pt. IV, pp. 157–176.

BOWEN, E. G.
1953. The influence of meteoritic dust on rainfall. Australian Journ. Phys., vol. 6, pp. 490–497.

CHAGNON, C. W., and JUNQE, C. E.
1961. The vertical distribution of submicron particles in the stratosphere. Journ. Meteorol., vol. 18, pp. 746–752.

CHANDRASEKHAR, S.
1950. Radiative Transfer. Clarendon Press, Oxford, .England, 393 pp.

COULSON, K. L.; DAVE, J. V.; and SEKERA, Z.
1960. Tables relating to radiation emerging from a planetary atmosphere with Rayleigh scattering. Univ. of California Press, Berkeley, 548 pp.

CROZIER, W. D.
1960. Black, magnetic spherules in sediments. Journ. Geophys. Res., vol. 65, pp. 2971–2977.
1961. Micrometeorite measurements: Satellite and ground level data compared. Journ. Geophys. Res., vol. 66, pp. 2793–2795.
1962. Five years of continuous collection of black, magnetic spherules from the atmosphere. Journ. Geophys. Res., vol. 67, pp. 2543–2548.

DAVIES, C. N.
1945. Definitive equations for the fluid resistance of spheres. Proc. Phys. Soc., vol. 57, pp. 259–270.

DEIRMENDJIAN, D.
1957. Theory of the solar aureole, I: Scattering and radiative transfer. Ann. Geophys., vol. **13,** pp. **286–306.**
1959. Theory of the solar aureole, 11: Applications to atmospheric models. Ann. Geophys., vol. **15,** pp. **218–249.**
1965. Note on laser detection of atmospheric dust layers. Journ. Geophys. Res., vol. **70,** pp. **743–745.**

DE JAGER, C.
1955. The capture of zodiacal dust by the earth. Mem. Soc. Roy. Sci. Liège, vol. **15,** pp. **174–182.**

DUBIN, M.
1960. IGY micrometeorite measurements. *In* Space Research, ed. by H. Kallmann-Bijl, North-Holland Publ. Co., Amsterdam, pp. **1042–1058.**

DUBIN, M., and MCCRACKEN, C. W.
1962. Measurements of distributions of interplanetary dust. Astron. Journ., vol. **67,** pp. **248–256.**

ELSÄSSER, H.
1954. Die riiumliche Verteilung der Zodiakallichtmaterie. Zeits. f. Astrophys., vol. **33,** pp. **274–285.**

FIOCCO, G., and COLOMBO, G.
1964. Optical radar results and meteoric fragmentation. Journ. Geophys. Res., vol. **69,** pp. **1795–1803.**

GIESE, R. H.
1962. Light scattering by small particles and models of interplanetary matter derived from the zodiacal light. Space Sci. Rev., vol. **1,** pp. **589–611.**

QIESE, R. H., and SEIDENTOPF, H.
1962. Optische Eigenschaften von Modellen der interplanetaren Materie. Zeits. f. Astrophys., vol. **54,** pp. **200–216.**

HEMENWAY, C. L., and SOBERMAN, R. K.
1962. Studies of micrometeorites obtained from e recoverable sounding rocket. Astron. Journ., vol. **67,** pp. **256–266.**

HIBBS, A. It.
1961. The distribution of micrometeorites/ near the earth. Jouni. Geophys. Res., vol. **66,** pp. **371–377.**

JUNGE, C. E.; CHAGNON, C. W.; and MANSON, J. E.
1961. Stratospheric aerosols. Journ. Meteorol., vol. **18,** pp. **81–108.**

LAEVASTU, T., and MELLIS, O.
1961. Size and mass distribution of cosmic dust. Journ. Geophys. Res., vol. **66,** pp. 2507–2508.

LI GOW, H. E., and ALEXANDER, W. M.
1960. Recent direct measurements of cosmic dust in the vicinity of the earth using satellites. *In* Space Research, ed. by H. Kallmann-Bijl, North-Holland Publ. Co., Amsterdam, pp. **1033–1041.**

LETTAU, H.
1951. Diffusion in the upper atmosphere. *In* Compendium of Meteorology, Boston, Amer. Meteorol. Soc., pp. **320–333.**

NEWKIRK, G. A., Jr.
1956. Photometry of the solar aureole. Journ. Opt. Soc. Amer., vol. **46,** pp. **1028–1037.**

NEWKIRK, G. A., Jr., and EDDY, J. A.
1962. Daytime sky radiance from forty to eighty thousand feet. Nature, vol. **194,** pp. **638–641.**
1963. Influx of meteor particles in the upper atmosphere of the earth as determined from stratospheric coronagraph observations. *In* Space Research 111, ed. by W. Priester, North-Holland Publ. Co., Amsterdam, pp. **143–154.**
1964. Light scattering by particles in the upper atmosphere. Journ. Atmos. Sci., vol. **21,** pp. **35–60.**

PETTERSSON, H.
1960. Cosmic spherules and meteoritic dust. Sci. Amer., vol. **202,** pp. **123–132.**

ROSEN, J. M.
1964. The vertical distribution of dust to **30** kilometers. Journ. Geophys. Res., vol. **69,** pp. **4673–4676.**

SEKERA, Z.
1956. Recent developments in the study of the polarization of sky light. *In* Advances in Geophysics, vol. **3,** ed. by H. E. Landsberg, Academic Press, New York, pp. **43–104.**

SINGER, S. F.
1961. Dust shell around the earth (abstract). Journ. Geophys. Res., vol. **66,** pp. 2560–**2561.**

THIEL, E., and SCHMIDT, R. A.
1961. Spherules from the Antarctic ice cap. Journ. Geophys. Res., vol. **66,** pp. 307–**310.**

VAN DE HULST, H. C.
1947. Zodiacal light in the solar corona. Astrophys. Journ., vol. **105,** pp. **471–488.**
1957. Light Scattering by Small Particles. J. Wiley and Sons, Inc., New York, **470** pp.

VOLZ, F. E.
1954. Die Optik und Meteorologic der atmosphärischen Trubung. Ber. Deutsch. Wetterdienstes, vol. **2,** no. **13, 47** pp.

VOLZ, F. E., and BULLRICH, K.
1961. Scattering function and polarization of skylight in the ultraviolet to the near infrared region, with haze of scettcring type **2.** Journ. Mctcorol., vol. **18,** pp. **306–318.**

VOLZ, F. E., and GOODY, R. M.
1962. The intensity of the twilight and upper atmospheric dust. Journ. Atmos. Sci., vol. **19,** pp. 385–406.

WATSON, F. G.
1956. Between the Planets. Rev. ed, Harvard Univ. Press, Cambridge, Mass., 188 pp.

WHIPPLE, F. L.
1950. The Theory of micrometeorites, I: In an isothermal ntmosphcrc. Proc. Nat. Acad. Sci., vol. 36, pp. 687–695.
1951. The theory of micro-meteorites, II: In heterothermal atmospheres. Proc. Nat. Acad. Sci., vol. 37, pp. 19–30.
1961a. The particulate contents of space. In Medical and Biological Aspects of the Energies of Space, ed. by P. Campbell, Columbia Univ. Press, New York, pp. 49–70.
1961b. The dust cloud about the earth. Naturc, vol. 189, pp. 127–128.

WRIGHT, F. W., and HODGE, P. W.
1962. Space density of dust in the stratosphere. Nature, vol. 195, p. 269.

ZACHAROV, J.
1952. Influence des Perséides sur la transparence atmosphérique. Bull. Astron. Inst. Czechoslovakia, vol. 3, pp. 82–85.

Dynamics of Orbiting Dust Particles[1]

I. I. SHAPIRO,[2] D. A. LAUTMAN,[3] and G. COLOMBO[4]

Abstract

We have studied the forces affecting the motion of small dust particles orbiting in interplanetary space. Combinations that may contribute substantially to a concentration of such dust around the earth were also analyzed. These included gravitational focusing, Jacobi capture, ejection of dust from the moon via meteor impact, and the capture of dust into long-lifetime geocentric orbits through the combined action of air drag and sunlight pressure. Our calculations indicate that, sensibly defined, an increase in flux near the earth of only about a factor of 10^2 over the interplanetary value is understandable. Even this relatively modest factor depends vitally on the assumption that a substantial fraction of the dust at the boundary of the earth's sphere of influence has a speed on the order of 1 km/sec with respect to the earth. The more reasonable choice of 3 km/sec for this speed reduces the enhancement to a factor less than 10. This result is to be contrasted with the widely aecepted deduction, based on satellite experiments and zodiacal cloud observations, that the enhancement is about 10^4. Aside from questioning the data analysis, we tire unable to offer any solution to this apparent paradox.

[1] Published as The Earth's Dust Belt: Fact or Fiction? (Pts. 1–4), Journ. Geophys. Res., vol. 71, pp. 5695–5741, 1966.

[2] Massachusetts Institute of Technology, Lincoln Labororatory, Lexington, Mass., operated with support from the U.S. Air Force.

[3] System Development Corporation, Lexington, Mass., and Smithsonian Astrophysical Observatory, Cambridge, Mass.

[4] University of Padua, Padua, Italy, and Smithsonian Astrophysical Observatory, Cambridge, Mass.

Concentration of Magnetic Dust in the Stratosphere

T. GRJEBINE [1]

The quantity of dust in the troposphere and stratosphere has previously been studied with several techniques The former studies concentrated on the relationship of dust and radioactive debris (fallout) at a time when few observations of cosmic dust were available.

The main result of these studies (Junge, Chagnon, and Manson, **1961;** Chagnon and Junge, **1961;** Junge and Manson, **1961)** has been to show that at an altitude of 20 km there is an increase in particles per unit volume of air of at least **1** order of magnitude.

Hodge and Wright **(1961)** have also shown that the concentration was variable. Many samplings and studies have been made by Friend et al. (1961), with results similar to those previously quoted. The size range of the particles was reported to be between **0.1** and **1,** and the maximum concentration was found at an altitude of about 20 km. The particle concentration was estimated by counting techniques to be about 1 particle/cm^3 or approximately 10^{-8} g/m^3; however, the study reported that the same amount of material measured by chemical techniques yields a concentration of 1.3×10^{-7} g/m^3. It is difficult to know whether this difference of **1** order of magnitude between the different techniques depends on the fact that particles smaller than **0.1** were not counted. The chemical abundances reported indicate that calcium was the main constituent (10^{-7} g/m^3), followed by phosphorus (10^{-8} g/m^3) and iron (10^{-8} g/m^3). In all cases, to the amount of the chemicals detected, the amount of the other elements should be added.

Whatever the source of the dust, it is difficult to believe that it is composed mainly of calcium. If we consider calcium as being the most easily detected element in a normal abundance of elements on the earth (Mason, **1958)** where it contributes only **1.07** percent of the total mass, then the total mass of dust should be around 10^{-5} g/m^3. We mention this point because it is typical of the discrepancy that can be introduced by comparing collections analyzed by counting techniques and total integrating collection techniques.

By an- optical counting technique Rosen **(1964)** has studied, in situ, the quantity of dust up to an altitude of **30** km. The amount at the level of maximum concentration, **20** km, is approximately 3 particles/cm^3 or a mass of about 10^{-5} g/m.^{3}

We have measured three types of collections, two made by Lambert **(1963)** with balloon-borne collectors and one by Ch. Phillipot with airplanes. These collections were planned for radioactive measurements only; hence, their use for measurements of total dust content is subject to some uncertainty and the possibility of contamination. We have performed blank experiments, however, and it appears that the risk of contamination is slight, at least for the balloon collections.

Lambert used two designs of collectors. The first design was a two-stage turbine forcing air through a paper filter. After measuring the radioactivity of the sample, we calcinated the filter and measured the magnetic attraction of the residue on a curie magnetic torsion balance. Therefore, we were following exactly the procedure as with ground collections made

[1] Centre National de la Recherche Scientifique, Centre des Faibles Radioactivités, Gif-sur-Yvette *(S.O.),* France.

240-022 O - 67----24

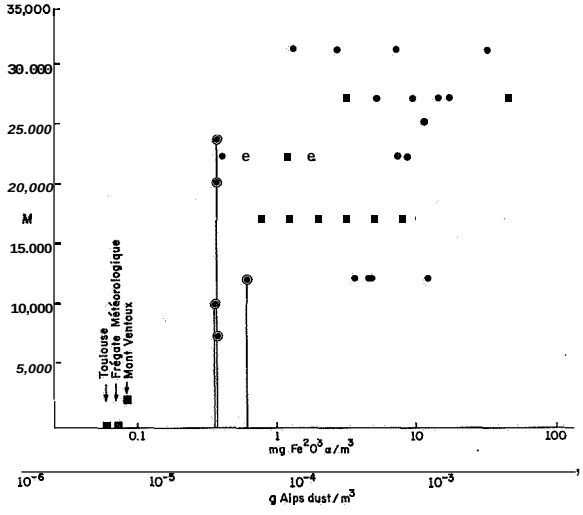

FIGURE 1.—Concentrationof magnetic dust in the stratosphere versus the altitude of collection.

- ⊙ collection made with surgical gauze; mean concentration/m³ **up** to the maximum altitude of flight.
- ● collection made with balloon air-borne turbine.
- ■ different ground collections, mean value for several months in meteorological station; ground level on mountain and sea level on meteorological ship.

with CRAPAL collectors previously reported (Grjebine, 1963, 1964).

The purpose of the calcination is to reduce the volume, but since it is not a high-temperature calcination there is not complete destruction of all the organic filter material and therefore it is not possible to establish a direct relationship between the force of magnetic attraction and sample weight. To calibrate the curie balance in terms of sample weight per cubic meter, we used a collection made on the top of Aiquille du Midi in the French Alps at an altitude of 3800 m. Comparing that sample with the Fe_2O_3 *a!* phase, we found that 1 mg Fe_2O_3 $\alpha=0.07$ mg dust; the magnetism of the sample is therefore **20** percent higher than the dust previously used to calibrate the CRAPAL collector network (Grjebine, 1963, 1964). If we assume that the magnetic susceptibility of the dust collected at **20** km is the same as the susceptibility of the Aiquille du Midi sample, we find **a** dust concentration at an altitude of 20 km of 2×10^{-4} g/m³. If the stratospheric dust is more magnetic, there would **of** course be a lower concentration in weight.

The samplings made with the turbine collectors give, for the average values for radioactive debris, results that are very similar **to** those made by other collectors up to an altitude of **20** km. In particular, they agree quite well with values reported by the Ash Can project up to this altitude; how-ever, at **30** km altitude, Lambert's samples show about 10 times the activity of the Ash Can project samples. The same difference of 1 order of magnitude appears for magnetic measurements made at **20** and **30** km. It seems likely that for altitudes greater than **20** km, Lambert's results should be decreased by an order of magnitude. It should also be pointed out that for some of Lambert's filters, which are highly magnetic, there is also a high degree of radioactivity, possibly indicating that the magnetic dust is a carrier for the radioactive debris. All these measurements are plotted against altitude in figure 1.

Only one measurement has been carried out on a filter supplied by the United States Atomic Energy Commission. This sample showed such a high magnetism that the measurement had to be made with the use of only a small part of the filter. It is not plotted on the curve (fig. 1) because the volume of air filtered was not exactly known.

The second technique used by Lambert involved an integrating collector. A surgical gauze filter was mounted on a plastic ring and was attached with a long string to a balloon. As the balloon ascended and fell, the filter swept a volume **of** air equal to twice its cross section times altitude. The efficiency of this collector for radioactive debris was about **5** percent; even with this low value a large quantity of debris and also magnetic dust was collected. The average value **of** measurements made with this technique falls between ground-level measurements such as those made at sea level (Frégate Meteorologique) and at Mont Ventoux in the French Alps and the values found at 20-km altitude from the turbine-collecting technique.

The third series of measurements made with aircraft-mounted filtering devices appears more doubtful. The average value is not greatly different from the ground-level values, but the level **of** radioactivity appears to be about an

order of magnitude less than the concentration measured at the same time and latitude by other experimenters (Machta, List, and Telegadas, 1964; Lambert, 1963). Apparently the filters did not capture all of the particles that impacted; eddy currents generated on the surface of the aircraft probably removed particles as well as deposited them. An ideal aircraft-collecting area should be from 10^3 to 10^4 times the area of the aperture admitting the air in the collector, and this was not the case for these collectors.

Conclusions

The values for stratospheric dust concentration obtained by magnetic measurements are 10 to 100 times larger than values obtained by chemical analysis methods, and a factor of 10 greater than the values from automatic optical counting techniques (10^{-5} g/m^3). These discrepancies are not exactly discrepancies, because the collection method is an integrating technique that does not discriminate with respect to particle size or shape, while other techniques usually involve a limit on size and sometimes on shape of the particles. Most of the limitations introduce a difference of about 1 order of magnitude (Grjebine, 1965).

It is difficult to decide what part of the dust collected is cosmic and what is terrestrial. It does not seem that industrial contamination can be an important contributor when one considers the large total mass of dust involved. In 1961, when the measurements were made, there had not been any volcanic activity for several years; hence this contribution is probably also negligible. The magnetic susceptibility of ground rock is quite low, so ground-rock erosion could not introduce a great error in the magnetic measurements. It also appears unlikely that any calibration errors have been introduced.

If we accept a magnetic dust density at the altitude of maximum concentration of 2×10^{-4} g/m^3 and we estimate that the stratospheric reservoir has a mean depth of 10 km, between 15- and 25-km altitude, and this reservoir is uniform around the earth, we conclude that it will contain some 10^9 tons of dust.

When comparing the magnetic dust measurements with the CRAPAL collector sample, we obtain a figure of 2×10^9 tons/year for the total accreted mass of dust. This means that the stratospheric reservoir is renewed twice each year and there is an average half-removal time of three months. These data are certainly compatible with the other sources of information we have concerning the removal time of this reservoir. For large particles, the curves published by Crozier (1962) show that peaks of the number of particles in the 5- to 10-μ range decrease within a period of about 1 month. For smaller particles, the removal time of radioactive debris from the stratosphere has been estimated at less than 2 years (Machta, List, and Telegadas, 1964; Lambert, 1963). Our measurements fall between these limits, and therefore appear to be quite reasonable, and represent mainly cosmic material.

References

CHAGNON, C. W., and JUNGE, C. E.
1961. The vertical distribution of submicron particles in the stratosphere. Journ. Meteorol., vol. 18, pp. 746–752.

CROZIER, W. D.
1962. Five years of continuous collection of black, magnetic spherules from the atmosphere. Journ. Geophys. Res., vol. 67, pp. 2543–2548.

FRIEND, J. P.; FEELY, H. W.; KREY, P. W.; SPAR, J.; and WALTON, A.
1061. The high altitude sampling prograni (HASP). Defense Atomic Support Agency, vol. 5, DASA 1300.

GRJEBINE, T.
1963. Accumulation de poussières cosmiques sur la terre. Compt. ltcnd., vol. 256, pp. 3735–3738.
1964. Study of the distribution of cosmic dust. Ann. New York Acad. Sci., vol. 119, pp. 126–142..
1965. Les poussières cosmiques. Sciences et Enseignemcnt des Sciences, vol. 35, pp. 45–55.

HODGE, P. W., and WRIGHT, F. W.
1961. The space density of atmospheric dust in the altitude range 50,000 to 90,000 feet. Smithsonian Contr. Astrophys., vol. 5, no. 14, pp. 231–238.

JUNGM, C. E.; CHAGNON, C. W.; and MANSON, J. E.
1961. Stratospheric aerosols. Jouni. Meteorol., vol. 18, pp. 81–107.

JUNGE, C. E., and MANSON, J. E.
1961. Stratospheric aerosol studies. Journ. Geophys. Res., vol. 66, pp. 2163–2182.

LAMBERT, G.
1963. Étude du comportement des aerosols radioactifs artificiels. Thèse à la Faculté des Sciences, Paris, Rapport CEA **R. 2347,** U.S.A.E.C. Translation tr. **6548,** November.

MACHTA, L.; LIST, R. **J.;** and TELEGADAS, **K.**
1964. Inventions of selected long lived radioisotopes produced during nuclear testing. U.S.A.E.C. Report HASL **142** (Health and Safety Laboratory), pp. **243–271,** New **York.**

MASON, B.
1958. Principles of Geochemistry. **J.** Wiley and Sons, Inc., New **York, 310** pp.

ROSEN, **J.** M.
1964. The vertical distribution of dust to **30** kilometers. Journ. Geophys. Res., vol. **69,** pp. **4673–4676.**

Abstract

The amount of magnetic dust in the stratosphere has been investigated by means of balloon-borne gauze filters and filters flown in airplanes. The concentration of dust is increased at an altitude of **20** km. A transformation of magnetic attraction into weight for a sample collected in the Alps at an altitude of **3800** m gives a concentration of 2×10^{-4} g/m^3 for that level. This is compatible with ground measurements of fallout of magnetic dust and residence time of dust in the stratosphere.

Role of Meteoric Dust in the Lower Ionosphere[1]

R. PARTHASARATHY[2] and D. B. RAI[2]

Abstract

The effect of the meteoric dust particles on the steady-state distribution of electrons and ions in the lower ionosphere (50 to 90 km) has been investigated. It is shown that the effective recombination coefficient obtained is higher than that obtained by ignoring the presence of dust. The expression for the effective recombination coefficient thus obtained is of the form

$$\alpha_{eff}=(\alpha_d+\lambda\alpha_i)(\eta+\gamma\lambda)+\frac{D_e+\lambda D^-}{N_e},$$

where D_e, D^+, and D^- are the dust-capture coefficients for electrons, positive ions, and negative ions, respectively; η and γ are the ratios D^e/D^+ and D^-/D^+, and the other symbols have the usual meanings. In the limit of zero dust concentration this expression reduces to the one derived by ignoring dust, i.e.,

$$\alpha_{eff}=(1+\lambda)(\alpha_d+\lambda\alpha_i),$$

since $(\eta+\lambda\gamma)$ tends to $(1+\lambda)$, while the coefficients D_e, D^+, and D^- each tend to zero.

The coefficients D_e, D^+, and D^- are derived by an extension of Natanson's theory of charging of aerosols by capture of ions. The height dependence of these coefficients comes mainly through the height distribution of the dust particles, for which Divari's results from twilight studies are utilized. It is found that only particles with a radius of the order of $\frac{1}{10}$ μ or larger contribute significantly. The recombination coefficients for the region 50 to 90 km have thus been computed and are in excellent agreement with those deduced empirically by us from the multiple-frequency (5 to 50 Mc/sec) radiowave absorption data in the auroral zone. The empirical method consisted of comparing the electron-density profile derived from the multiple-frequency radiowave absorption with the ionization-rate profile calculated from satellite-measured particle flux. The deduced recombination coefficients may occasionally be an order of magnitude larger than the coefficients obtained without taking cognizance of the dust population.

Considering the fact that dust particles of meteoric origin are always present in the lower ionosphere, it appears to be reasonably confirmed that their contribution to the steady-state distribution of electrons and ions in this region of the atmosphere is quite significant

[1] Published in Radio Sci., vol. 1, pp. 1397–1408, 1966.

[2] Geophysical Institute of the University of Alaska, College, Alas.

Infrared Optical Characteristics of Ice Spheres

W. M. IRVINE [1]

Introduction

The scattering and absorption properties of ice particles are important for the study of radiative transfer in the atmospheres of the earth and, possibly, of Venus and Mars, as well as for studies of interplanetary and interstellar dust particles. Published calculations of these parameters for infrared wavelengths are extremely limited (see the review by Feigel'son, **1964);** a number of computations have been made by Greenberg (1966), but the cross sections themselves have not been published.

The quantities that are most appropriate for describing the scattering by ice particles will depend on the given physical situation. In the present paper, values of the normalized extinction cross section (efficiency factor) Q_{ext}, the singlescattering albedo a, and the asymmetry factor $\langle\cos\theta\rangle$ are presented for spherical, homogeneous particles of radii **1.0, 4.0, '7.5, 10.0, 12.5,** and **15.0** μ for the wavelength interval $1\mu \leq \lambda \leq 150\mu$. These quantities are of particular interest in the approximate solution of problems of diffuse reflection and transmission by ice clouds, and in the study of the radiative heating of an atmosphere containing such clouds. For other studies (of the zodiacal light, for example) the angular distribution of scattered radiation would be a more relevant quantity.

Before the present results can be applied to a physical problem, it is necessary to evaluate the effeet of the simple particle model considered. The assumption of homogeneity is probably quite good for cloud crystals, but is possibly seriously wrong for interplanetary particles. An extension of the calculations to radially inhomogeneous spheres would present no computational problems, however, if a reasonable model for the variation of refractive index with radius were available (Levine and Kerker, **1963;** Levine and Olaofe, **1965).** More serious is the restriction to spherical shape; however, results of Greenberg et al. **(1963)** for scattering by spheroids and cylinders indicate that the relative magnitude of integrated quantities, such as Q_{ext} and a, will not be greatly influenced by departures from sphericity (cf. also Donn and Powell, **1963).**

Method and results

We made calculations using the Mie theory in the manner described elsewhere (Irvine, **1965).** The results are presented in figures **1** to **3.**

Values of the real part n of the index of refraction of ice were taken from Kislovskii (1959), which seems to be the best present compilation.

Values of the imaginary part n', which is related to the absorption coefficient **k** by $n' = k\lambda/4\pi$, were obtained by intercomparison of several sources for:

$1.0 \leq \lambda \leq 2.65\mu$: Reding **(1951)** (see also Hornig, White, and Reding, 1958), Ockman (1958), and Luck **(1963).**

$2.8 \leq \lambda \leq 7.5\ \mu$: Fox and Martin **(1940).**

$7.5 \leq \lambda \leq 25\ \mu$: relative values from Ockman (1958), scaled to agree with **Fox** and Martin **(1940)** at overlap.

† Harvard College Observatory and Smithsonian Astrophysical Observatory, Cambridge, **Mass.;** now at University of Massachusetts, Amherst, Mass.

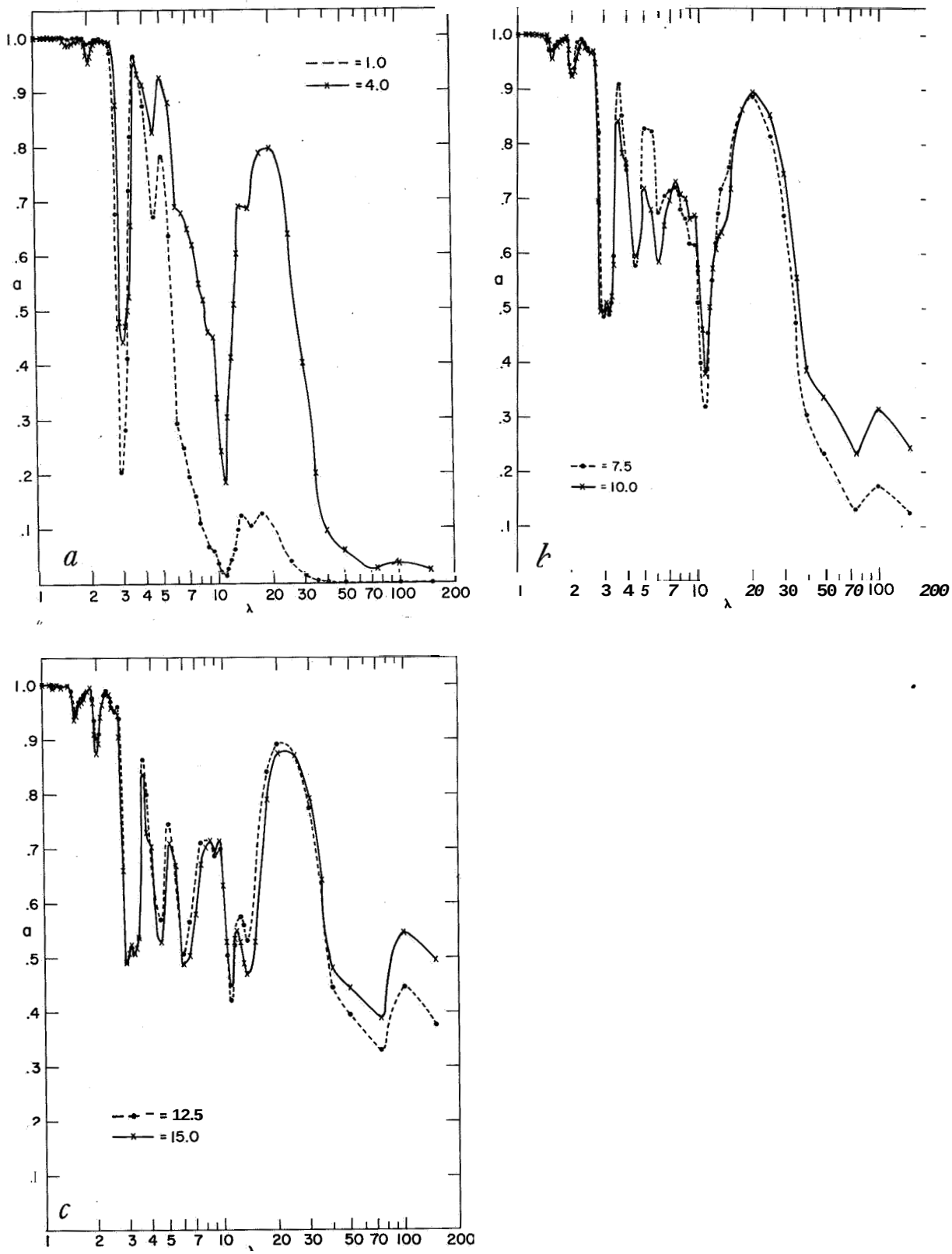

FIGURE 1.—*a*, b, *c:* Single-scattering albedo a of spherical ice particles as a function of wavelength A (in microns) for particle radii $r = 1.0$, 4.0, 7.5, 10, 12.5, 15 μ.

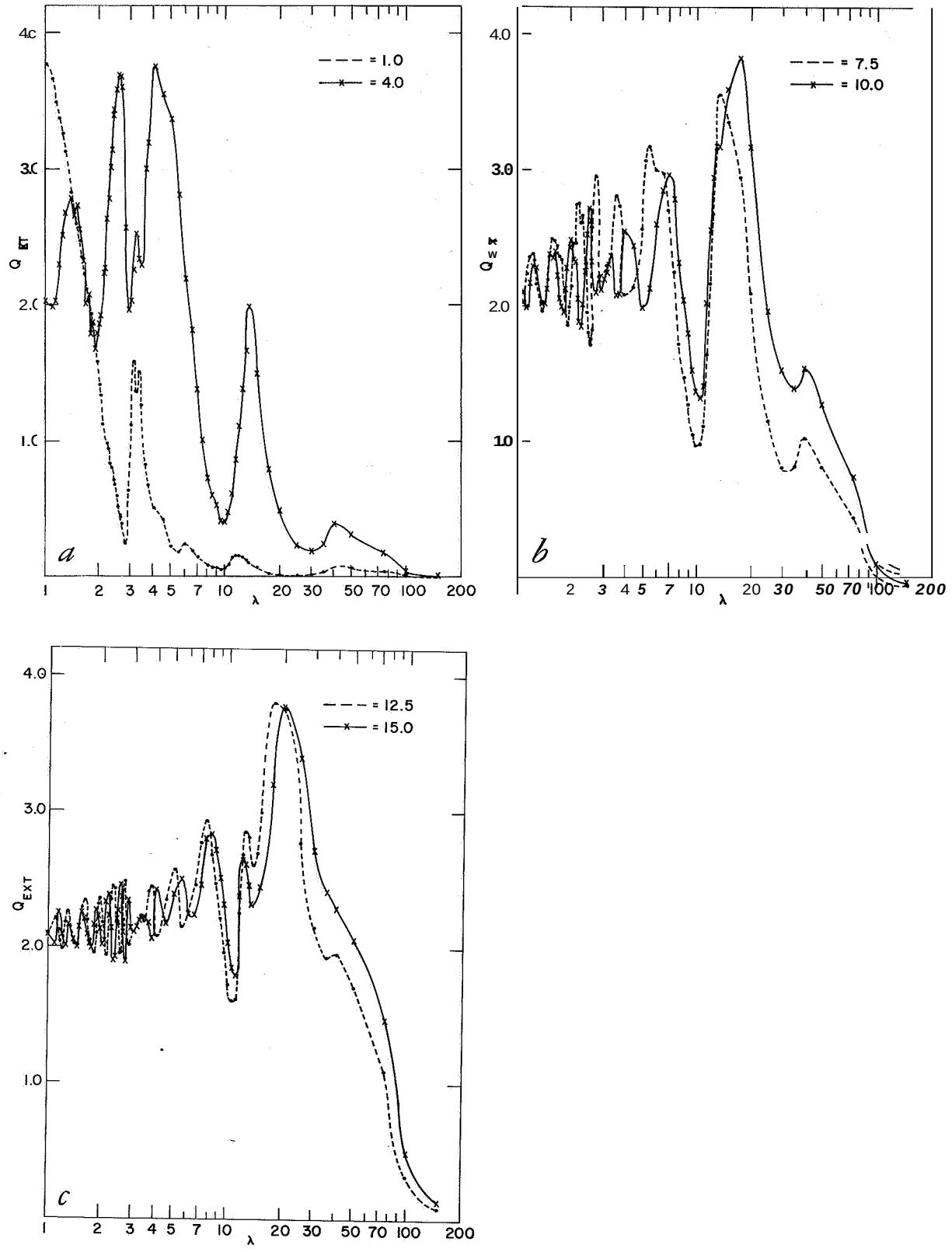

FIGURE 2.—*a*, *b*, c: Normalized extinction cross section (efficiency factor) Q_{ext} for spherical ice particles. Wavelength λ and particle radii $r = 1.0$, 4.0, 7.5, 10, 12.5, 15 are in microns.

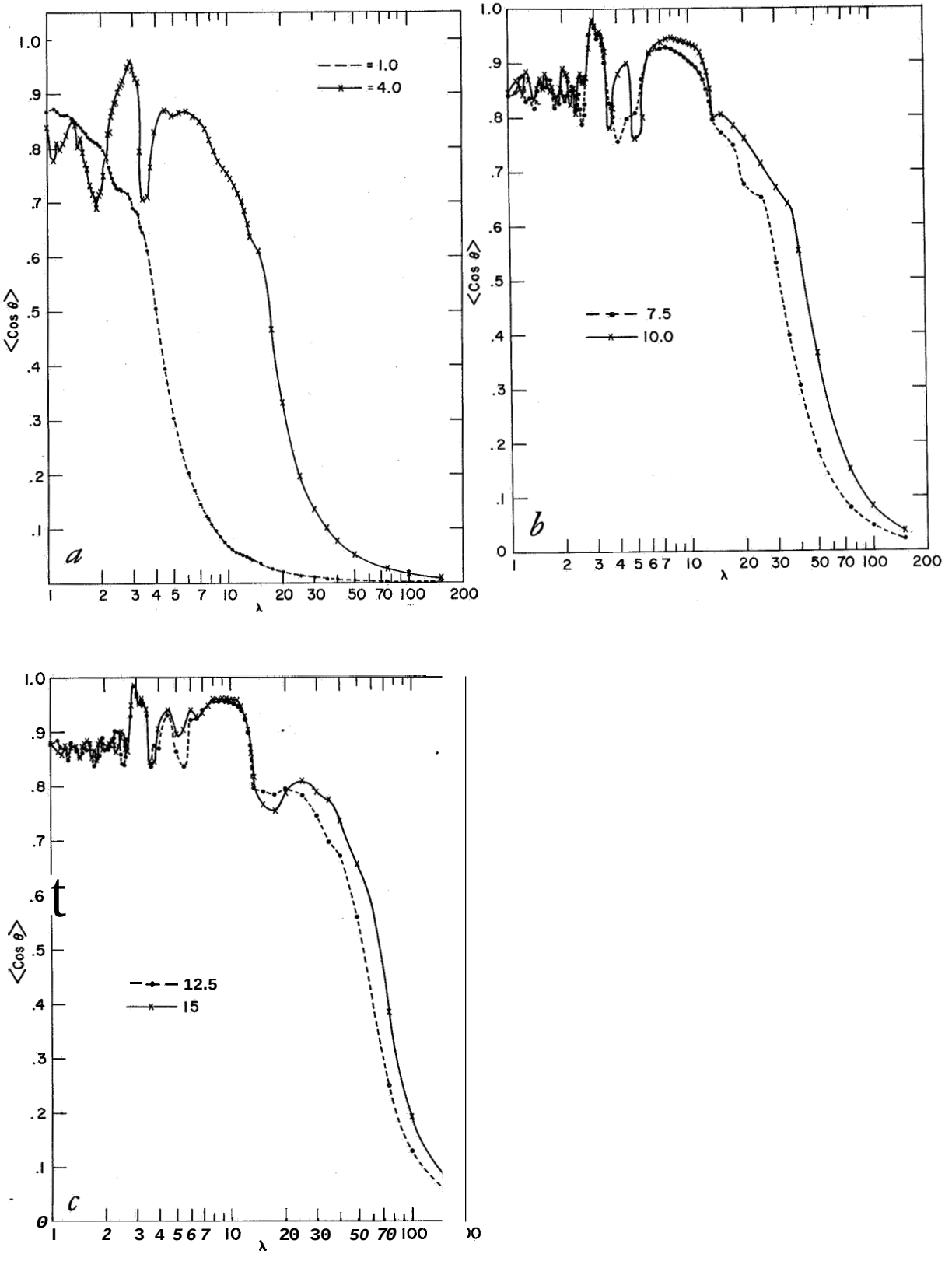

FIGURE 3.—*a, b, c:* Asymmetry factor (cos θ) of spherical ice particles. Wavelength and particle radii as in figures 1 and 2.

$25 \leq \lambda \leq 50\ \mu$: relative values from Zimmermann and Pimentel (1962), scaled to agree with Cartwright (1935) and with shorter wavelength data at overlaps.

$50 \leq \lambda \leq 150\ \mu$: Cartwright (1935).

Concentrating first on the single-scattering albedo a, we note that there are large differences in the relative strength of absorption features for the different particle radii (see figs. 1a, b, c). This indicates the possibility of using absorption spectra to determine approximate particle size in reflection from ice clouds (particularly if the clouds are thick, so that the only parameters in the approximate radiative transfer theory are a and $(\cos \theta)$).

Irvine and Pollack (in preparation) have made a comparison of the absorption spectrum (a versus λ) for water and ice. Although the curves are generally similar, the magnitudes of absorption features may be quite different, and the positions are shifted slightly. Such details may provide the possibility of differentiating between water and ice clouds in planetary atmospheres.

The spectra of Q_{ext} and $(\cos \theta)$ are more complicated (see figs. 2a, b, c; 3a, b, c) because the maxima and minima due to changes in absorption are combined with the familiar Mie theory oscillations, which arise from interference effects (see van de Hulst (1957) for Q_{ext}; Irvine (1963, 1965) for $(\cos \theta)$). The positions of the extrema are thus sensitive to the distribution of particle sizes present in a given physical situation.

Acknowledgments

I am grateful to Dr. J. B. Pollack for his evaluation of the references on the absorption coefficient of ice, to Dr. J. M. Greenberg for several helpful conversations, and to Mrs. M. Huguenin and Mrs. M. Bocchino for assisting in the computations. This work was supported in part by NASA Grant 89–60.

References

CARTWRIGHT, C. H.
1935. Extreme infrared absorption of D_2O, ice and D_2O in dioxane. Nature, vol. **136,** p. **181.**

DONN, B., and POWELL, R. S.
1963. Angular scattering from irregularly shaped particles with application to astronomy. *In* ICES Electromagnetic Scattering, ed. by M. Kerker, Macmillan Co., New York, pp. **151–158.**

FEIGEL'SON, E. M.
1964. Radiatsionnye Protessy v Sloistoobranznykh Oblakakh. Izd. "Nauka," Moscow.

FOX, J. J., and MARTIN, A. E.
1940. Investigations of infrared spectra (2.5–7.5 μ): Absorption of water. Proc. Roy. Soc. London, vol. **174A,** pp. **234–262.**

GREENBERG, J. M.
1966. The optics of interstellar grains. *In* Spectral Classification and Multicolor Photometry, ed. by K. Lodén, L. O. Lodén, and U. Sinnerstad, Academic Press, New York, pp. **291–300.**

GREENBERG, J. M.; LIND, A. C.; WANG, R. T.; and LIBELO, L. F.
1963. The polarization of starlight by oriented nonspherical particles. *In* ICES Electromagnetic Scattering, ed. by M. Kerker, Macmillan Co., New York, pp. **123–133.**

HORNIG, D. F.; WHITE, H. F.; and REDING, F. P.
1958. The infrared spectra of crystalline H_2O, D_2O and HDO. Spectrochem. Acta, vol. **12,** pp. **338–349.**

IRVINE, W. M.
1963. The asymmetry of the scattering diagram of a spherical particle. Bull. Astron. Inst. Netherlands, vol. **17,** pp. **176–184.**
1965. Light scattering by spherical particles: Radiation pressure, asymmetry factor, and extinction cross section. Journ. Opt. Soc. Amer., vol. **55,** pp. **16–21.**

KISLOVSKII, L. D.
1959. Optical characteristics of water and ice in the infrared and radiowave regions of the spectrum. Opt. Spec., vol. **7,** pp. **201–206.**

LEVINE, S., and KERKER, M.
1963. Scattering of electromagnetic spheres, when outer shell has a variable refractive index. *In* ICES Electromagnetic scattering, ed. by M. Kerker, Macmillan Co., New York, pp. **37–46.**

LEVINE, S., and OLAOFE, G.
1967. ICES–2. Proc. 2d Interdisciplinary Conf. on Electromagnetic Scattering, ed. by R. S. Stein and R. L. Rowell, Gordon and Breach, New York, in press.

LUCK, W.
1963. Beitrag zur assoziation des flüssigen. Wassers, I. Ber. Bunsenges. physik. Chem., vol. **67,** pp. **186–189.**

OCKMAN, N.
1958. The infra-red and Raman spectra of ice. Adv. Phys., vol. **7,** pp. **199–220.**

READING, F. P.
1951. The vibrational spectrum and structure of several molecular crystals at low temperature. Ph. D. Thesis, Brown Univ. Providence, R.I.

VAN DE HULST, H. C.
1957. Light Scattering by Small Particles. J. Wiley and Sons, New York, **470** pp.

ZIMMERMANN, R., and PIMENTEL, G. C.
1962. The infrared spectrum of ice temperature dependence of the hydrogen bond potential function. Proc. **Int'l.** Meeting Molec. Spectros., Bologna, **1959,** vol. **2,** pp. **726–737.**

Evidence for Extraterrestrial Particles in Polar Ice

E. L. FIREMAN[1]

The earliest method of searching for extraterrestrial particles was to examine dust collected at remote places on the earth. Our work on dust in polar ice is a natural extension of this method. The high-elevation regions of the polar ice sheets are the most remote places on the earth where contamination by terrestrial and industrial dust is minimal. The annual accumulation layers in the ice sheets provide excellent time markers for determining the deposition rate. Sufficiently large samples of material can be collected from the polar ice for examination by modern isotopic methods. These methods have been used for the past decade in meteorite studies and have not only revealed many facts about the history of meteorites but have also determined whether certain questionable objects were extraterrestrial. For example, an iron object now called the Washington County meteorite was examined about seven years ago by the meteorite curators at two large museums; they concluded that this object was terrestrial. A short time later the measurement of isotopes in this object proved that it was extraterrestrial; it was then accepted as a true meteorite. Meteorite curators now seek isotope information before deciding on the possible extraterrestrial origin of questionable objects. Our work modernizes both the earlier collection methods and the earlier methods of examination.

Collection of dust

The collection and study of a large mass of dust from the Greenland ice sheet were undertaken jointly with Mr. C. C. Langway, Jr. Several years ago we concluded that it should be possible to collect grams of extraterrestrial material from the polar ice sheets. To be more specific, an accretion rate of **500,000** tons per year for the earth gives 1 g of extraterrestrial material in 200,000 liters of ice at Camp Century, Greenland. Many million liters of ice were melted at Camp Century. This camp, maintained by the U.S. Army Research Support Group, is situated under the ice 77°10′ north latitude, 61°08′ west longitude, and at an elevation of approximately **2000** m. The mean annual precipitation is **30** cm, and the mean annual temperature is **—25"** C. The air temperature rarely rises above *0"* C during the summer.

Surface snow at Camp Century is permeable; however, at a depth of **30** m the snow is compressed into a form that is impermeable to water. Ice melted below this depth will form a subsurface lake or well. The volume of water in the well is determined by the amount of heat injected; the shape of the well is determined by the manner in which the heat is injected into the water. Since the heat conductivity into the surrounding snow and ice is low, a subsurface lake more than a million liters in volume will not freeze solid for decades.

Plate 1 is a photograph of the tunnel under the snow leading to a well where large volumes of ice either had been or were being melted. The floor of the tunnel is approximately 20 m below the surface of the snow. At the top of the well on the floor of the trench is an *A* frame that supports cables to the submersible pump, the water hose to deliver water from the bottom of the well., and the heating unit to melt ice. A schematic cross-sectional diagram of the

[1] Smithsonian Astrophysical Observatory, Cambridge, Mass.

shape of the well below the tunnel is given in figure 1. This well, which supplied the camp's entire water consumption between 20,000 and 40,000 liters per day, was made by steam melting a vertical shaft of 3 m in diameter to the impermeable snow layers at a depth of 30 to 40 m (Rodriguez, 1963). The steam-melting unit was held at this depth to form a concave-bottomed subsurface lake 20 to 30 m in diameter. The depth of the water in the lake vanes according to the rate of water withdrawn. A submersible pump, attached to the melting unit, pumps water to 5000-gallon aluminum storage tanks, which are in essence settling tanks for the particles contained in the melted ice. Our first collections were made by cleaning the particles off the bottom of the storage tanks. During the summer of 1963, when the well was 85 m deep and of the configuration shown in figure 1, we installed a filter system at the top of this well consisting of replaceable 3-μ and 0.45-μ corrugated paper cartridges mounted in a cylindrical steel housing. Several

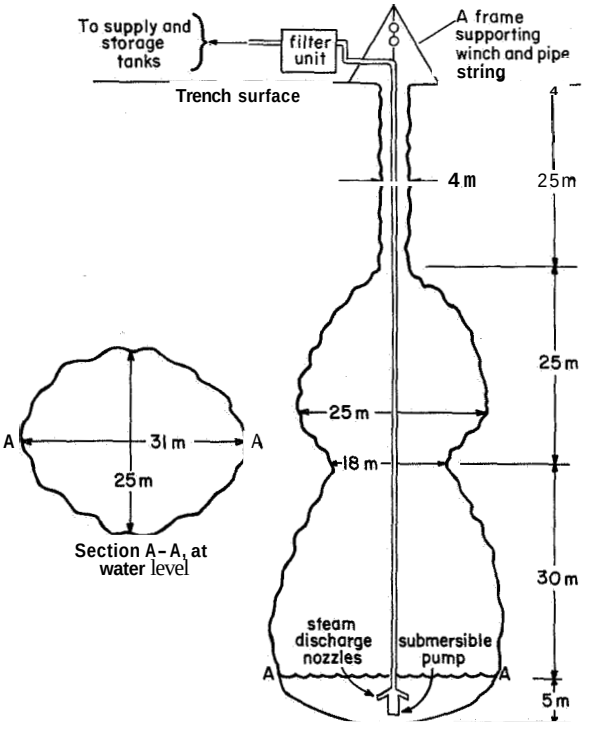

FIGURE 1.—Cross-sectional sketch of water well no. 3, Camp Century, Greenland, on July 18, 1963. Taped depth to bottom of well, 85 m.

million liters of water were filtered through these cartridges.

A new filter system was installed at the same site in the summer of 1964. In this system the water passes through Millipore filter papers, which have a very low ash content and permit an accurate determination of the weight of the collected material. Approximately 2.6×10^{-4} g of material per liter of water was collected; most of the material was organic. After the organic material was removed by ashing, the weight was 5×10^{-5} g/liter for the 8-μ paper, 6×10^{-5} g/liter for the 3-μ paper, and 7×10^{-5} g/liter for the 0.45-μ paper. The collected material contained black magnetite spherules similar to those that have been extensively studied by C. C. Langway, Jr., P. W. Hodge, F. W. Wright, and others. The black spherule content of our collections comprised about one-tenth of the total insoluble nonorganic material. Langway (1963) has estimated an accretion rate of a half-million tons per year for the earth on the basis of the black spherule content of Greenland ice. The nonorganic material collected from the melted ice consisted largely of magnetite, hematite, quartz, and feldspar. The nickel content was quite low compared to that in meteorites. A chemical analysis gave a Ni/Fe ratio of 0.012 in a light fraction (density less than 3.3) and 0.005 in a heavy fraction (density greater than 3.3). The magnesium content was also low compared to that in stony meteorites and in most terrestrial materials. The Mg/Fe ratio was approximately 0.016 in the heavy fraction, and 0.13 in the light fraction.

No large mass collection of the dissolved solids was attempted. Since some extraterrestrial material is probably dissolved, we plan to make a large collection of the soluble components and examine them for indications of extraterrestrial origin.

Isotope analysis

Isotope analysis can prove whether there is extraterrestrial material in the dust. The size of the Greenland collections made possible meaningful isotope studies. Two positive isotope indications for the presence of extraterrestrial material in the Greenland collections were found: (1) a Co^{60} radioactivity, which

appears to be due to Fe^{60}, and (2) an argon anomaly identical to that found by Merrihue (1964) in a magnetic fraction of a deep-sea sediment. The other isotopes searched for were Al^{26}, He^3, Ne^{21}, and Ar^{39}. None was found except for a small positive He^3 excess in one sample. The presence of certain isotopes and the lack of others can be explained either by the dissolution of the magnesium-containing constituents in the dust or by an unusual chemical composition.

The bombardment of small particles in space by cosmic rays, solar flares, and solar wind can modify the abundance of certain isotopes. Cosmic rays, which consist of high-energy hydrogen and helium nuclei (>1 Bev), produce by nuclear interactions a small amount of a large variety of isotopes that are lighter in mass than the bombarded element. Solar flares, which consist mainly of low-energy hydrogen and helium nuclei (<1 Bev), produce a larger amount of the isotopes that are approximately the same mass as the bombarded element. Most of the solar-flare particles (also solar-wind particles) are of such low energy that they can be implanted in the dust.

The production of the radioactive isotope Fe^{60} will be used as an example to illustrate isotope production by nuclear interactions. Helium nuclei (also tritons) interacting with iron and protons (also helium nuclei) interacting with nickel produce Fe^{60} in the following eight ways:

Reaction	*mb*	*%*	
$He^4 + Fe^{58} \rightarrow Fe^{60} + 2H$	$\sigma - 50$	0.33	(1)
$H^3 + Fe^{58} \rightarrow Fe^{60} + H$	$\sigma - 200$	0.33	(2)
$He^4 + Ni^{60} \rightarrow Fe^{60} + 4H$	$\sigma - 10$	26.2	(3)
$He^4 + Ni^{61} \rightarrow Fe^{60} + 4H + N$	$\sigma \sim 10$	1.2	(4)
$He^4 + Ni^{62} \rightarrow Fe^{60} + 2H + He^4$	$\sigma - 30$	3.7	(5)
$H + Ni^{62} \rightarrow Fe^{60} + 3H$	$\sigma - 30$	3.7	(6)
$He^4 + Ni^{64} \rightarrow Fe^{60} + 2\,He^4$	$\sigma \sim 100$	1.1	(7)
$H + Ni^{64} \rightarrow Fe^{60} + H + He^4$	$\sigma \sim 100$	1.1	(8)

The value for the cross section written after each equation is an estimated maximum value, and the percentage is the isotopic abundance of the bombarded element. Fe^{60} will be produced mainly by solar flares rather than by cosmic rays since its mass is approximately the same as that of the bombarded elements, iron and nickel. A solar-flare flux of 10^3 helium nuclei cm^{-2} sec^{-1} would produce 0.1 dpm/g of Fe^{60} by reaction (1). The other reactions would more than double the production rate estimated from reaction (1) alone. The solar-flare flux averaged over long periods is not well known. One estimate (Wasson, 1963) gives 2000 protons cm^{-2} sec^{-1} (>5 Mev). The average helium abundance in flares is also not well known. The abundance of helium in flares varies; in some flares the helium content exceeds the hydrogen content, while in most flares the reverse is true. In view of the evidence a solar-flare flux of 10^3 helium nuclei cm^{-2} sec^{-1} is not unreasonable.

Fe^{60} has been observed in the Odessa meteorite. It decays to the 5.2-year state of Co^{60}, which emits a 1.17-Mev and a 1.33-Mev gamma ray in coincidence. Roy and Kohman (1957) originally estimated the half-life of Fe^{60} to be 3×10^5 years but now (private communication) would revise this estimate to 10^5 years. On the basis of studies with a copper target, Roy and Kohman found that Fe^{60} decays to the 5.2-year Co^{60} radioactivity by way of a 10-min isomeric state. R. McCorkell (private communication), on the basis of similar studies on a copper target, found a 30-min cobalt isomer from Fe^{60}. The decay scheme for Fe^{60} based on these results is given in figure 2.

The 1.17- and 1.33-Mev coincidence gamma rays of Co^{60} were found and measured in various Greenland dust samples by the gamma-gamma coincidence method. The gamma-gamma coincidence unit used for measuring Co^{60} is described by me (Fireman, 1966). Figure 3 gives the gamma coincidence spectrum of the analyzer crystal when the trigger crystal is set at 1.25 ± 0.12 Mev for 25 g of Greenland dust (<140 mesh). In addition to the peaks at 1.17 and 1.33 Mev due to Co^{60}, there is a peak at 0.58 Mev due to Tl^{208}, probably a terrestrial contaminant. The relative heights of the Tl^{208} and Co^{60} peaks vary in different samples so that it should be possible to separate the Tl^{208}-containing minerals from the Co^{60}-containing minerals.

Since Co^{60} is a common industrial contaminant, it is necessary to show that the Co^{60} actually comes from the Fe^{60}, which can be only of extraterrestrial origin. This was done in two different ways:

1. All the cobalt was removed from the

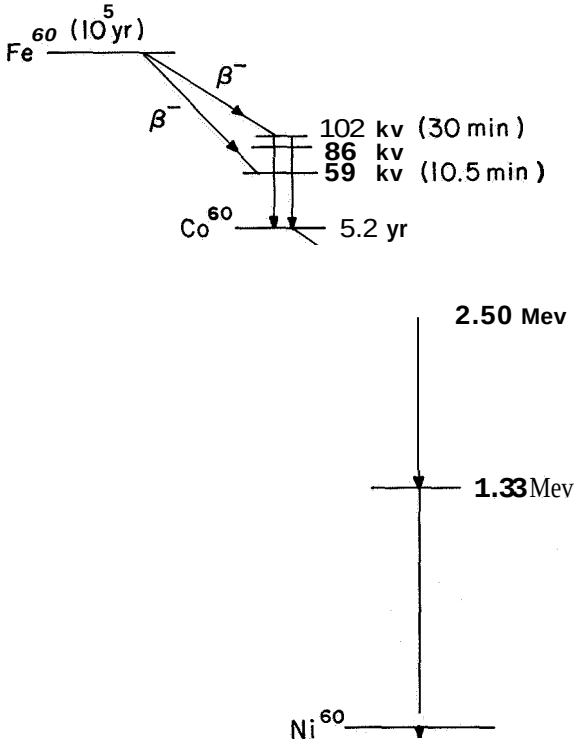

FIGURE 2.—Decay scheme for Fe^{60} ($\sim 10^5$ yr) activity.

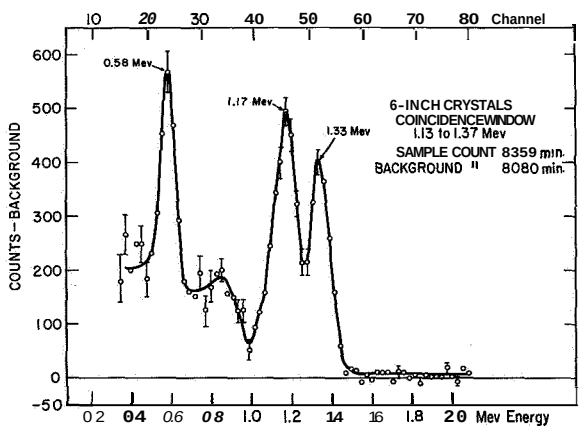

FIGURE 3.—Gamma coincidence count for 25 g of Greenland dust (<140 mesh).

iron to see whether any new cobalt activity grew in the purified iron. In this procedure it was easier to work with the short-lived rather than with the 5.2-year cobalt isotope, since the short-lived isomer reaches saturation quickly and the measurement can be repeated many times. McCorkell removed the cobalt from a Greenland dust sample, which contained 15 dpm of Co^{60}, and purified the iron. He then milked cobalt from the purified iron and counted the cobalt in a thin window. Figure 4 gives his results for four separate extractions. He observed an activity with a half-life between 25 and 40 min. In other words, McCorkell found a similar cobalt activity in cobalt milked from iron purified from Greenland dust to the one he found in iron purified from an old copper target. This indicates that the Co^{60} is due to Fe^{60}.

2. The Co^{60} activity in the Greenland dust was measured as a function of time. During 1 year of observation no decay was observed. Table 1 gives the Co^{60} in two samples of Greenland dust. A sample was collected on a 3-μ filter and showed no decay in 15 months. The other sample, which was collected from the settling tank, also showed no decay in a year. During the course of the year, however, some material was removed from this sample for mass-spectrometric measurements, and the measured activity had to be corrected accordingly. Since the 5.2-year cobalt should have decayed by approximately 20 percent during this period, the lack of decay is evidence for the Fe^{60} origin of the Co^{60} activity. We believe that it is important also to measure the buildup of the 5.2-year Co^{60} in the iron purified from both samples, and we are currently proceeding along these lines. There is approximately 0.1 dpm/g of Co^{60} in all our Greenland dust samples. There is a factor of

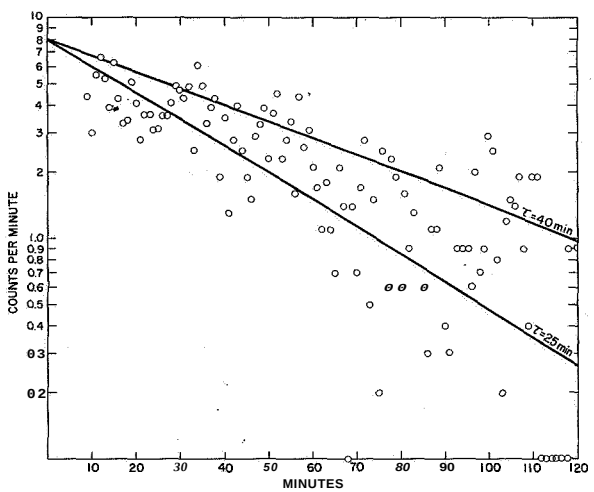

FIGURE 4.—Short-lived activity of cobalt extracted from iron purified from Greenland dust.

Sample	Weight (g)	Date counted	Water volume (liters)	Sample preparation	Counts/min 1.17+1.33 Mev	dpm/10^6 liters
3-μ filter–P9	—	May 1964	185,000	none	0.080±0.005	4.3±0.2
3-μ filter–P9	—	Aug. 1965	185,000	none	0.087±0.005	4.7±0.2
Settling tank	(34)	May 1964	$\sim 10^6$	<140 mesh	0.73 ±0.01	~7.3
Settling tank	(34)	Aug. 1964	$\sim 10^6$	<140 mesh	0.74 ±0.01	7.4
Settling tank		Sept. 1964	0.91×10^6	<140 mesh	0.64 ±0.01	7.0
Settling tank	†(25)	May 1965	0.73×10^6	<140 mesh	0.52 ±0.01	7.1
Settling tank	†(25)	June 1965	0.73×10^6	<140 mesh	0.51 ±0.01	7.0

2 higher activity in the magnetics and in the fines than in the bulk material. The Co^{60} activity is in the range of activity expected from solar-flare interactions (0.2 dpm/g). The agreement with our calculated estimate of the production rates would be fortuitous if a large percentage of the Co^{60} in our samples were due to industrial contaminants.

Another radioactive isotope that can be measured by gamma-gamma counting is Al^{26}. The half-life and decay scheme of Al^{26} are well known. Its half-life is 840,000 years, and it decays by positron emission followed by a 1.82-Mev gamma ray. No Al^{26} activity was observed in any of the collections. The Al^{26} results previously reported (Fireman and Langway, 1965) are summarized in table 2. In some of the samples the Al^{26} activity is less than one-tenth of the Co^{60} activity. Solar-flare protons interacting with magnesium in dust would produce Al^{26} by the following reaction:

$$H+Mg^{26}\rightarrow Al^{26}+N \quad \sigma\sim 250 \text{ mb, } 11\%. \quad (9)$$

Solar-flare protons interacting with aluminum and silicon would also produce Al^{26}.

These reactions should produce more Al^{26} than the Co^{60} produced by reactions (1) through (8) unless the exposure age of the extraterrestrial particles containing Mg, Al, and Si is less than 50,000 years, or unless these particles are dissolved in the water. The amount of magnesium dissolved in the mater was 10 times larger than the undissolved magnesium in the dust collection. This result leads us to believe that Al^{26} was not observed because most of the extraterrestrial magnesium components were dissolved in the water. Large mass collections of the soluble constituents are planned for the near future.

Argon-39, a radioactive isotope that would be produced mainly by high-energy cosmic rays, was not observed in the collections. The absence of Ar^{39} is not surprising because it can be lost in three ways: (1) by recoil immediately after formation, (2) by diffusion out of the small dust particles in space, and (3) by diffusion from the particles while they are heated during their passage through the atmosphere.

The stable rare-gas isotopes in dust are interesting. The He^3, Ne^{21}, and Ar^{38} isotopes are enriched if they are produced by cosmic-ray and solar-flare interactions, He^3 and Ar^{36} can also be enriched by solar-flare and solar-wind implantation; however, diffusion loss would reduce the rare-gas content. Table 3 gives the He3 and Ne^{21} contents of Greenland dust samples. The measurement on the 0.43-g sample of magnetics was made in collaboration with Dr. O. A. Schaeffer at Brookhaven National Laboratory. There was a slight He^3 excess of $(2.0\pm0.5)\times10^{-9}$ cc/g. This small excess could be implanted by one large solar flare. A similar excess of He^3 was observed by Merrihue (1964) in the magnetics from a sample of deep-sea sediment. No He^3 excess was observed in two other samples, 0.64 g and 0.50 g of fines from the settling tank (Tilles, 1965).

No Ne^{21} excess was observed. Ne^{21} would be produced only by high-energy cosmic-ray interactions and not by the other mechanisms. Furthermore, Ne^{21} could recoil out of the small-

TABLE 2.—*Al^{26}-positron activity, Ar^{39} activity, and Co^{60} activity in samples of Greenland dust*

Sample	Type	Weight (g)	Water volume (liters)	Al^{26} positron (10^{-6} dmp/l)	Ar^{39} (10^{-6} dpm/l)	Co^{60} (10^{-6} dmp/l)
Settling tank	magnetic	34	~1,000,000	≤0.3	<0.01	6.9
Settling tank	fine {140 mesh / <105 μ}	34	~1,000,000	<1.0	—	7.4
Settling tank	bulk	330	~10,000,000	<1.0	—	4.5
P_1 filter	3 μ (75%)	—	240,000	<0.4	—	—
P_2 filter	3 μ (75%)	—	190,000	<0.3	—	—
P_3 filter	3 μ (75%)	—	185,000	<3.0	—	4.5 0.2
M_1 filter	3 μ (100%)	3.6	15,000	<4.0	—	—
M_2 filter	8 μ (100%)	7.6	30,000	<2.0	—	—
Ma filter	8 μ (100%)	6.1	24,000	<2.0	—	—

TABLE 3.—*He^3 and Ne^{21} contents of Greenland samples*

Sample (wgt)	Approximate temperature	He^3 (cc STP/g)	Ne^{21}* (cc STP/g)	Ne^{20}/Ne^{22}	Ne^{22}/Ne^{21}*
Magneticsfrom 130×10^6 cm3 of ice (0.43 g)	Sampleva-porized	$(2.0\pm0.5)\times10^{-9}$	$(3\pm2)\times10^{-11}$	10.1fl.O (10.1)$_{air}$	30.5±1.0 (34)$_{air}$
Fines (<140 mesh) from settling tank (0.64 g)	500° C	$<5\times10^{-11}$	$<3\times10^{-12}$	—	—
	950° C	$<6\times10^{-11}$	$<10^{-11}$	—	—
	1050° C	$<8\times10^{-11}$	$<3\times10^{-11}$		
	1150° C	$<3\times10^{-11}$	$<2\times10^{-11}$		
	1250° C	—	—		
Fines (<140 mesh) from settling tank fraction with density >3.2 (0.50 g)	500° C	$<7\times10^{-11}$	$<2\times10^{-11}$		
	800° C	$<4\times10^{-10}$	$<10^{-10}$†		
	1000° C	$<2\times10^{-10}$	$<10^{-10}$†		
	1200° C	$<3\times10^{-11}$	$<4\times10^{-11}$		
	1350° C	$<2\times10^{-11}$	$<5\times10^{-11}$†		

*Indicates that value is for excess cosmogenic Ne^{21} relative to air neon.
†Indicates total Ne^{21} value.

sized particles and could also be lost by diffusion.

There was, however, a definite positive indication for extraterrestrial origin in the argon released at high temperature from a heavy fraction (density >3.2) of the Greenland dust. Tilles (1965) found in this sample an Ar^{36} excess similar to that found by Merrihue (1964) in the magnetics from a sample of deep-sea sediment. The Ar^{40}/Ar^{36} ratio was 230±5 in the gas released at 1200°C after 1-hour heatings ut 500°C, 800°C, and 1000°C. The atmospheric Ar^{40}/Ar^{36} ratio is 295. The Ar^{36}/Ar^{38} ratio was 5.1f0.1, identical to this ratio in air. The Ar^{36} excess is approximately 9×10^{-10} cc/g. If solar flares have an argon-to-helium ratio of approximately 10^{-4}, then dust would be subjected to a solar-flare flux of argon of approximately 0.1 cm^{-2} sec^{-1}. A 10-μ particle would then receive approximately 20×10^{-10} cc/g during a solar cycle. Since the solar argon is expected to be low in Ar^{40}, the observed Ar^{36} could be produced by solar-flare implantation during one solar cycle. In fact, the Ar^{36} excess in this respect is similar to the He^3 excess.

References

FIREMAN, E. L.
1966. Neutron exposureages of meteorites. Zeits. f. Naturforsch, vol. 21a, pp. 1138–1146.

FIREMAN, E. L., and LANGWAY, C. C., Jr.
1965. Search for aluminum-26 in dust from the Greenland ice sheet. Geochim. et Cosmochim. Acta, vol. 29, pp. 21–27.

LANGWAY, C. C., Jr.
1963. Sampling for extraterrestrial dust on the Greenland ice sheet. A.I.H.S. General Assembly, Berkeley, publ. no. 61, pp. 181–198.

MERRIHUE, C.
1964. Rare gas evidence for cosmic dust in modern Pacific red clay. Ann. New York Acad. Sci., vol. 119, pp. 351–367.

RODRIGUEZ, R.
1963. Development of glacier sub-surface water supply and sewage systems. Tech. Rep. 1737-TB, USA Engineering Research and Development Labs., Ft. Belvoir, Va.

ROY, J. C., and KOAMAN, T. P.
1957. Iron 60. Canadian Journ. Phys., vol. 35, pp. 649–655.

TILLES, D.
1965. Anomalous argon isotope ratios in particles from Greenland ice and Pacific Ocean sediments. Trans. Amer. Geophys. Union, vol. 46, p. 117.

WASSON, J. T.
1963. Radioactivity in interplanetary dust. Icarus, vol. 2, pp. 54–87.

Abstract

Sufficiently large samples of Greenland dust were collected so that isotope analysis could be made. There were definite positive indications of Fe^{60} and excess Ar^{36} and a less definite positive indication of excess He^{3}. The Fe^{60} can be explained by solar-flare interactions on iron and nickel; the Ar^{36} and He^{3} excesses can be explained by solar-flare implantation. There was no positive indication of Al^{26}, indicating that the magnesium-aluminum-silicon extraterrestrial constituents were dissolved.

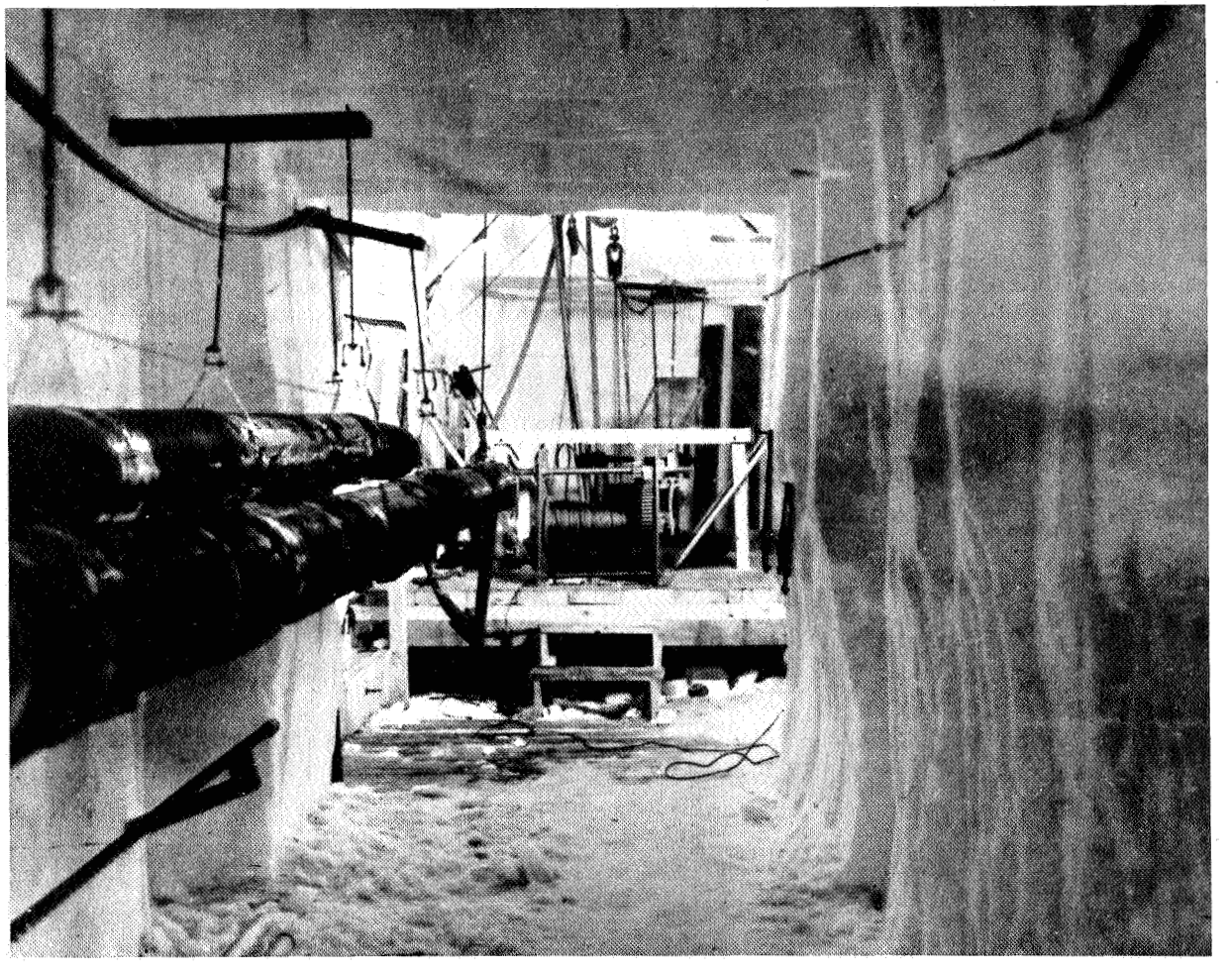

PLATE 1

Photograph of tunnel leading to water well used for camp water supply.

On Chemical Compositions of Interiors of Possibly Cosmic Particles and the Problem of Origin of Naturally Occurring Iron-Rich Spherules

P. W. HODGE [1, 2] and F. W. WRIGHT [2]

Introduction

There have been extensive attempts in recent years to identify the dust component of the influx of extraterrestrial material to the earth's surface. (For bibliographic reviews see Schmidt, **1965;** Hodge, Wright, and Hoffleit, **1961.)** Much of the effort has been expended on the study of certain iron-rich smooth-surfaced spherical particles found in a wide range of natural environments. It is not expected that all or even a very large fraction of the extraterrestrial dust accumulated by the earth should be in the form of such spherules. Their importance is due rather to their ease of location and identification, to their potential usefulness in glaciology and rock stratigraphy, and to the current controversy on their origin.

Occurrence

Iron-rich smooth-surfaced spherules, ranging in diameter from a few to 100 or more microns, occur almost everywhere on the surface of the earth. It was shown some time ago (Buddhue, **1950;** Thomsen, **1953;** Handy and Davidson, **1953;** Hoppe and Zimmermann, **1954;** Hodge and Wildt, **1958)** that the vast majority of those found in **or** near centers of population have an artificial origin. In isolated areas and in geological strata, however, spherules are found for which an artificial origin is extremely unlikely. Table 1 summarizes the various natural environments in which these spherules occur.

[1] Regularly at University of Washington, Seattle, Wash.
[2] Smithsonian Astrophysical Observatory, Cambridge, Mass.

Distinguishing characteristics of particles of known origin

SPHERULES FOUND AT METEORITE CRATERS.— We have examined spherules found in the soil at five meteorite crater locations: the Arizona crater (particles collected by J. S. Rinehart), the Sikhote-Alin craters (particles kindly supplied to the Smithsonian by **E.** L. Krinov), the Henbury craters, the Boxhole crater, and the Odessa craters. Surfaces of the Sikhote-Alin and Henbury crater spherules were smooth and shiny, but surfaces of those from the other craters were rougher, due to what we interpret as physical and chemical erosion. We have carried out chemical analyses of both the surfaces and the interiors (on polished sections) of spherules from the Sikhote-Alin and Arizona craters, and are currently analyzing spherules from the other craters. The Arizona particles, all over **100** μ in diameter, were analyzed by standard microchemical techniques, while the Sikhote-Alin particles were analyzed by the microprobe of the Advanced Metals Research Corporation, under the supervision of S. **H.** Moll. Our results show so far that spherules formed as ablation products from the molten skins of meteorites have two distinguishing characteristics: **(1)** iron-rich surfaces, often with an oxidized crust, and **(2)** nickel-rich interiors, often with a region where the nickel is about five times more abundant than elsewhere.

ARTIFICIAL METEORITE SPHERULES.—Several papers have described the artificial production of meteoritic spherules (Fechtig and Utech,

TABLE 1—*Environments in which iron-rich spherules have been found*

Location	Description	References
Atmosphere		
1. Settling at surface at isolated sites	~3 to 100 μ in size, uniform rate of deposit over large part of earth	Crozier, 1966; Hodge and Wildt, 1958; and many others
2. At 10–15 km in stratosphere	Very rare, small	Hodge, 1961; Melton (see pp. 293–299)
3. At 25 km in stratosphere	Rare, small	C. Mossop, 1963 (private communication)
4. Upper atmosphere above 80 km	Extremely rare, small	Hemenway and Soberman, 1962
Ocean sediments		
5. Magnetic fraction	Large spherules	Pettersson, 1955; Laevastu and Mellis, 1955; and many others
Ice deposits		
6. Greenland 750-yr-old ice	Relatively common	Langway, 1962
7. Antarctic 55-yr-old ice?	Relatively common	Thiel and Schmidt, 1961
8. South Pole 55-yr-old ice	Relatively common	H. Bader, 1962 (private communication)
9. Ice Island T 3, various depths	Relatively common	Stoiber et al., 1956
Sedimentary rocks		
10. Paleozoic salts	Relatively common	Mutch, 1964
11. Other sediments	Relatively common	Lougheed, 1966
Meteorite craters		
12. Sikhote-Alin	Spherules in soil and on meteorite surfaces	Krinov, 1960
13. Arizona (Canyon Diablo)	Rough spherules in soil	Nininger, 1941; Rinehart, 1958; Wright and Hodge, 1964
14. Henbury	Smooth, perfect spherules in soil	Hodge, 1965
Volcanic ash		
15. Pacific Islands	Rare, perfect spherules	Fredriksson and Martin, 1963
16. North, Central, and South America, and Hawaiian volcanoes	Rare, perfect spherules	Hodge and Wright, 1964; Wright and and Hodge, 1965a
17. Various volcanic deposits	Rare, perfect spherules	Mutch, 1964
Industrial smoke		
18. Fly ash	Spherules common	Handy and Davidson, 1953
19. City air	Spherules common	Hodge and Wildt, 1958; Hoppe and Zimmermann, 1954

1964; Schmidt, Keil, and Gault, 1965; Wright and Hodge, 1965b). Generally, when an iron-nickel source was used, the nickel was found to be concentrated toward the center of the spherule produced. We analyzed the interiors of polished sections of seven artificial spherules, three made from an iron meteorite and four from a stony-iron. Table 2 summarizes our results. We found in general that nickel and cobalt were usually more abundant in the central parts of the particle than at the surfaces, but for three of the particles, known to be formed from meteoritic material, nickel was absent throughout. Particularly for the spherules from the stony-iron meteorite, if other elements characteristic of the stony material in the meteorite (silicon, calcium, etc.) were present, neither nickel nor cobalt wits detectable in the particle.

VOLCANIC SPHERULES.—Fredriksson and Martin (1963) examined volcanic material and

TABLE 2.—*Compositions of surfaces and interiors of seven artificial meteoritic spherules (weight percent)*

	Mg	Al	Si	Ca	Ti	Cr	Mn	Fe	CO	Ni
1. Surface	—							70–75		0.1–0.2
Interior	—							67–72		0.5–1.0
2. Surface	—							70–75		
Interior	—						0.1–0.5	68–73		
3. Surface	—							65–70	~0.2	4-5
Interior	—							65–70	0.5–1.0	4-5
B. Made from Estherville mesosiderite										
1. Surface	—							68–73	~0.5	7–8
Interior	—							65–70	0.5–1.0	6–8
2. Surface	—		4–6	0.5				55–60	NO.5	4–5
Interior	—							65–70	0.5–1.0	5–6
3. Surface	—		7–8	3–4		<0.5	<0.5	40-45		
Interior	—	0.5–1.0		4–6	0.1–0.5	0.1–0.5	0.1–0.5	40–45		
4. Surface	—	6–8	20-22	7–8	<0.5	<0.5	<0.5	40–45		
Interior	—	1–2	8–10	6–8	0.1–0.5	0.1–0.5	0.1–0.5	28–33		

found that shiny magnetic spherules are a rare but always-present component of volcanic dust. We have collected and studied such spherules, derived from nine different volcanoes in various parts of the world (Hodge and Wright, 1964; Wright and Hodge, 1965a), and have confirmed Fredriksson and Martin's conclusion that iron-rich spherules occur in volcanic ejecta. Recently we have sectioned and polished two of the most perfect volcanic spherules, both from Kilauea Iki, and have found that the composition varies from place to place in the interiors of the particles (table 3 and plate 1a). However, the relative abundances of the elements do not vary greatly from place to place in the interior, or from interior to surface. In both cases, all elements tested were more abundant at the surface than in the interior. The most important conclusion from these investigations is that the characteristic chemical constitution of the volcanic spherules derived by us from surface analyses applies to the whole particle in a relative sense. That is, large amounts of aluminum, silicon, calcium, and titanium relative to iron occur throughout volcanic spherules. We are examining many more volcanic spherules to check this conclusion further.

Identification of spherules of unknown origin

METEORITIC SPHERULES.—From investigations described above, it should usually be possible to distinguish spherules derived from iron meteorites by the presence of nickel, often concentrated in an area near the center of the particle; however, it also appears possible that some iron meteorite spherules will have lost all nickel and will be almost pure iron oxide. Many of the particles found in deep-sea sediments can be identified as meteoritic from the nickel content (Fredriksson, 1956; Castaing and Fredriksson, 1958; Fechtig and Utech, 1964; Schmidt and Keil, 1966). Also, we have found that both of our two tested spherules extracted from New Mexico lake-bed sediments by Crozier have nickel in approximately the correct proportions in their interiors, although only one showed nickel at its surface.

It is much more difficult to identify any meteoritic spherules that have lost all nickel. We have found that one out of three artificially made spherules is without nickel in its interior, and that about half of the Sikhote-Alin spherules have no nickel in their interiors. These particles have about 70 percent iron by weight and virtually nothing from among the elements heavier than magnesium, except occasionally for 0.1 to 0.5 percent manganese. Many of the spherules found in isolated sites and in historical deposits also contain about 70 percent iron and 0.1 to 0.5 percent manganese and little else detectable, and some or all of these may be meteoritic (see pl. 1*b* and table 4). There are, however, roughly 10 times as many iron-

	Al	Si	Ca	Ti	Cr	Mn	Fe
Surface	13–15	28–30	14–16	1–2	—	<0.5	14–16
Interior 1	9	16	x	1.2	—	0.03	7
Interior 2	6	19	x	1.3	—	0.04	7
Interior 3	9	24	x	1.6	—	0.04	7
Interior 4	5	20	x	1.2	—	0.06	9
Interior 5	5	14	x	1.2	—	0.06	8

	Al	Si	Ti	Cr	Mn	Fc
Surface	—	5–6	<0.5	—	—0.5	60–65
Interior 1	0.1	0.1	0.7	—	0.2	68–73
Interior2	0.1	0.1	0.8	—	0.2	68–73
Interior3	0.1	0.2	0.9	—	0.2	68–73
Interior4	0.1	1.1	1.1	—	0.2	68–73
Interior5	0.1	1.1	1.2	—	0.2	68–73

manganese particles as there are iron-nickel particles, which argues against the possibility that all or even the majority of the iron-manganese particles are meteoritic.

We tentatively conclude that a small fraction, perhaps 1 to 2 percent (Hodge, Wright, and Langway, 1964), of the iron-rich spherules found in glacial deposits, sediments, and the atmosphere at isolated sites is derived from iron meteorites. Apparently a much .greater fraction of the deep-sea spherules comes from iron meteorites.

Judging from the composition of the "stony" meteoritic spherules that we have made artificially, some of the other naturally occurring spherules may be derived from stony meteorites, which are about 10 times as abundant as irons in interplanetary space. Estimates suggest that perhaps 10 percent of the spherules that we have analyzed may be such ablation products from stony meteorites. Thus, perhaps a total of 10 to 12 percent of the spherules found in isolated sites is meteoritic.

VOLCANIC SPHERULES.—Analyses of the surfaces and interiors of known volcanic spherules show that the relative abundances of iron, aluminium, silicon, calcium, and titanium are fairly characteristic and consistent. On this basis, we find that several of the spherules collected from arctic and antarctic ice are volcanic in origin. We estimate that roughly 5 percent of all Greenland ice-cap spherules can be volcanic according to their chemical composition, and their abundance relative to irregular particles confirms this estimate (Hodge and Wright, 1964).

Giovinetto and Schmidt (1965) find evidence for a much larger fraction of volcanic spherules at the South Pole. Their evidence, as yet unpublished, is based on an increase in the number of spherules found at the time of the Krakatoa eruption. Our chemical analyses of several South Pole spherules do not confirm their general conclusions, and we point out that if 5 percent of the spherules is normally volcanic, this percentage may greatly increase at the time of a violent volcanic eruption.

ORIGIN OF OTHER SPHERULES.—The majority of the spherules found in isolated sites, polar-ice deposits, and ancient sediments do not have a composition similar to that of any spherules of known origin. An industrial origin has been suggested for them by Schmidt and Fredriksson (1967), who neglect to take into account the fact that our Greenland samples are from 750-year-old ice deposits and that there was very little industrial activity anywhere in the world in the 13th century.

We believe it possible that most of these spherules of unknown origin are ablation products from cometary meteors. No other reasonable explanation has yet been proposed, and Crozier (1966) has pointed out that the

rate of fall of spherules seems to be correlated with the rate of incidence of radar meteors. It should be stated, however, that we regard the evidence concerning the origin of most of the spherules as still inconclusive. There may be some explanation that is quite different from any so far suggested.

Acknowledgment

We wish to express our gratitude to C. C. Langway, Jr., who has collaborated with us on most of the projects discussed here, to F. L. Whipple for his continuing interest, and to M. F. Comerford, who took the microphotographs reproduced here.

References

BUDDHUE, J. D.
1950. Meteoritic dust. Univ. of New Mexico Publ. in Meteoritics, no. 2, Univ. of New Mexico Press, Albuquerque, 102 pp.

CASTAING, R., and FREDRIKSSON, K.
1958. Analyses of cosmic spherules with an X-ray microanalyzer. Geochim. et Cosmochim. Acta, vol. 14, pp. 114–117.

CROZIER, W. D.
1966. Nine years of continuous collection of black, magnetic spherules from the atmosphere. Journ. Geophys. Res., vol. 71, pp. 603–611.

FECHTIG, H., and UTECH, K.
1964. On the presence or absence of nickel in dark magnetic cosmic spherules and their mechanics of origin. Ann. New York Acad. Sci., vol. 119, pp. 243–249.

FREDRIKSSON, K.
1956. Cosmic spherules in deep-sea sediments. Nature, vol. 177, pp. 32–33.

FREDRIKSSON, K., and MARTIN, L. R.
1963. The origin of black spherules found in Pacific islands, deep-sea sediments, and Antarctic ice. Geochim. et Cosmochim. Acta., vol. 27, pp. 245–248.

GIOVINETTO, M. B., and SCHMIDT, R. A.
1965. Spherules from four centuries of snow deposits at the South Pole. Trans. Amer. Geophys. Union, vol. 46, p. 116.

HANDY, R. L., and DAVIDSON, D. T.
1953. On the curious resemblance between fly ash and the meteoritic dust. Proc. Iowa Acad. Sci., vol. 60, pp. 373–379.

HEMENWAY, C. L., and SOBERMAN, R. K.
1962. Studies of micrometeorites obtained from a recoverable sounding rocket. Astron. Journ., vol. 67, pp. 256–266.

HODGE, P. W.
1961. Sampling dust from the stratosphere. Smithsonian Contr. Astrophys., vol. 5, no. 10, pp. 145–152.
1965. The Henbury meteorite craters. Smithsonian Contr. Astrophys., vol. 8, no. 8 pp. 199–213.

HODGE, P. W., and WILDT, R.
1958. A search for airborne particles of meteoritic origin. Geochim. et Cosmochim. Acta, vol. 14, pp. 126–133.

HODGE, P. W., and WRIGHT, F. W.
1964. Studies of particles for extraterrestrial origin, 2: A comparison of microscopic spherules of meteoritic and volcanic origin. Journ. Geophys. Res., vol. 69, pp. 2449–2454.

HODGE, P. W.; WRIGHT, F. W.; and HOFFLEIT, D.
1961. An annotated bibliography on interplanetary dust. Smithsonian Contr. Astrophys., vol. 5, no. 8, pp. 85–111.

HODGE, P. W.; WRIGHT, F. W.; and LANGWAY, C. C., Jr.
1964. Studies of particles for extraterrestrial origin, 3: Analyses of dust particles from polar ice deposits. Journ. Geophys. Res., vol. 69, pp. 2919–2931.

HOPPE, J., and ZIMMERMANN, H.
1954. Separation of interplanetary from industrial particles. Die Sterne, vol. 30, pp. 33–36.

KRINOV, E. L.
1960. Principles of Meteoritics. Trans. by I. Vidziunas, ed. by H. Brown, Pergamon Press, New York, 535 pp.

LAEVASTU, T., and MELLIS, O.
1955. Extraterrestrial material in deep-sea deposits. Trans. Amer. Geophys. Union, vol. 36, pp. 385–389.

LANGWAY, C. C., Jr.
1962. Some physical and chemical investigations of a 411-meter deep Greenland ice core and their relationship to accumulation. Int'l. Assoc. Sci. Hydrol. Commission of Snow and Ice, publ. 58, pp. 101–118.

LOUGHEED, M. S.
1966. A classification of extraterrestrial spherules found in sedimentary rocks and tell. Ohio Journ. Sci., vol. 66, pp. 274–283.

MELTON, C. E.
1967. Aerosol samples obtained from 9- to 12-km altitude. Smithsonian Contr. Astrophys., vol. 11, pp. 293–299.

MUTCH, T. A.
1964. Volcanic ashes compared with Paleozoic salts containing extraterrestrial spherules. Journ. Geophys. Res., vol. 69, pp. 4735–4740.

NININGER, H. H.
1941. Collecting small meteoritic particles. Pop. Astron., vol. 49, pp. 159–162.

PETTERSSON, H.
1955. Magnetic spherules and meteors. Naturwiss., vol. 42, pp. 387–388.

RINEHART, J. S.
1958. Distribution of meteoritic debris about the Ariiona meteorite crater. Smithsonian Contr. Astrophys., vol. 2, no. 7, pp. 145–160.

SCHMIDT, R. A.
1962. A survey of data on microscopic extraterrestrial particles. Contributions The Univ. of Wisc. Geophys. Polar Res. Ctr., Madison, Wisc., no. 88 (revised June 1964); NASA TN D–2719, March 1965.

SCHMIDT, R. A., and FREDRIKSSON, K.
1967. Comments. Journ. Geophys. Res. (in press).

SCHMIDT, R. A., and KEIL, K.
1966. Electron microprobe study of spherules from Atlantic Ocean sediments. Geochim. et Cosmochim. Acta, vol. 30, pp. 471–478.

SCHMIDT, R. A.; KEIL, K.; and GAULT, D. E.
1965. Electron microprobe study of a crater and ejecta produced by hypervelocity impact against a Ni-Fe target. Proc. 7th Hypervelocity Impact Symp., Tampa, Fla., vol. 5, pp. 105–121.

STOIBER, R. E.; LYONS, J. B.; ELBERTY, W. T.; and MCCREHAN, R. H.
1956. The source area and age of Ice-Island T–3. Final report under contract AF 19(604)–1075, Dartmouth College, Dept. of Geology, Hanover, N. H.

THIEL, E., and SCHMIDT, R. A.
1961. Spherules from the Antarctic ice cap. Journ. Geophys. Res., vol. 66, pp. 307–310.

THOMSEN, W. J.
1953. The annual deposit of meteoritic dust. Sky and Tel., vol. 12, pp. 147–148.

WRIGHT, F. W., and HODGE, P. W.
1964. Compositional studies of extraterrestrial particles. Ann. New York Acad. Sci., vol. 119, pp. 287–297.

1965a. Studies of particles for extraterrestrial origin, 4: Microscopic spherules from recent volcanic eruptions. Journ. Geophys. Res., vol. 70, pp. 3889–3898.

1965b. Analysis of artificial meteoritic spherules. Smithsonian Astrophys. Obs. Spec. Rep. No. 192, 10 pp.

Abstract

Iron-rich spherules, ranging in diameter from a few to over 100 μ, have been found in nature in the following environments: the atmosphere up to heights of at least 25 km, ocean sediments, arctic and antarctic ice deposits, sedimentary rocks, the soil around meteorite craters, volcanic ash, and industrial smoke. Evidence based on our investigations and those of numerous other scientists indicates that careful studies of the chemical, mineral, and physical properties of individual particles can lead to conclusions about their origins. Our recent investigation of polished sections of 23 spherules points to a clear distinction between spherules from different types of sources. Some of the naturally occurring iron-rich spherules are probably volcanic in origin and some are probably meteoritic, but the majority are unlike spherules of known origin.

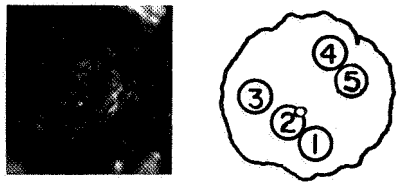

a

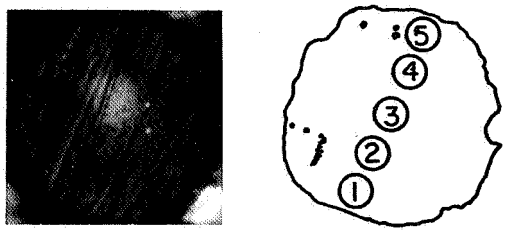

b

PLATE 1

Polished interior of a 30-μ spherule: *a*, from Kilauea Iki; *b*, from Greenland ice, with sketches of points probed.

Recovery of Magnetite Spherules from Sedimentary Rocks

T. A. MUTCH [1] and J. T. PARR [1]

Studies of possible extraterrestrial spherules contained in various types of sedimentary rocks have been undertaken. The present preparation and separation procedures result in extraction of spherules composed primarily of the mineral magnetite. While there are no chemical nor mineralogical features that point uniquely to an extraterrestrial origin, the formation and preservation of ablation droplets of this character are reasonable. By contrast, the authors can think of no terrestrial origin that adequately explains the morphology, composition, and abundance of such spherules in the sedimentary rocks under consideration. These rocks include rock salt, limestone, argillite, quartzite, and radiolarian chert. Ages range from Precambrian to Permian.

Preparation of samples involves solution or disaggregation of the rock. Since magnetite is a reasonably insoluble mineral, acids as reactive as HF can be used, providing the reaction time and pH are closely controlled. Magnetite spherules appear to undergo only limited superficial etching during this treatment. Since most silicate minerals are soluble in HF, almost any sedimentary rock can be examined by means of this preparation procedure. Less reactive acids (HNO_3, EDTA) are sufficient for disaggregation of carbonate- and sulfate-rich rocks.

Total disaggregation of a rock is a prerequisite for complete recovery of all spherules. The separation itself is effected magnetically. Consequently, extraterrestrial particles of low magnetic susceptibility, if present, are not isolated. The fact that the majority of spherules are small, less than 25 μ in diameter, means that the trapping procedure must be highly efficient. Problems in sample preparation or in magnetic separation may result in deceptively low spherule counts. Finally, before influx rates can be established, some estimate must be made regarding the depositional rate of the total rock. In all cases such estimates are tenuous.

Faced with these difficulties, one should be understandably cautious in saying anything regarding influx rates in the past as compared with those of the present. Work to date on rock salt suggests that Silurian spherule size distributions tind influx rates are similar to present dtty figures. Additionul data are needed for confirmation of this suggestion.

[1] Department of Geology, Brown University, Providence, R.I.

Fusion Crust of Iron Meteorites and Mesosiderites and Production of Cosmic Spherules

A. EL GORESY [1] and H. FECHTIG [1]

In the last few years many authors have expressed the opinion that a great part of the so-called cosmic spherules may have been produced by ablation of iron meteorites in the atmosphere. This opinion could be proved for the spherules collected during the Albatross deep-sea expedition. These spherules, investigated by Castaing and Fredriksson (1958), show iron-nickel-cobalt cores eccentrically located in the inside of magnetite spherules. The nickel content of these cores is approximately 30 percent, which is appreciably higher than the average content of nickel in iron meteorites. In the magnetite shells no nickel, or only traces of nickel, could be found.

Many of the cosmic spherules, however, do not show those cores. Instead of the cores there are holes. No nickel could be detected in these magnetite spherules.

The geochemical characteristics of iron, nickel, and cobalt in magnetite spherules have been discussed by many authors in recent years. Many arguments have been offered for and against the siderophile behavior of nickel, and its presence or absence in magnetite spherules is given as an indication of cosmic or terrestrial origin, respectively. It seemed to us very important to study, both mineralogically and with the microprobe, natural fusion crusts of some iron meteorites and stony irons, since those crusts have been formed in extremely short times under oxidizing conditions favoring the formation of magnetite and wiistite from kamacite, taenite, and troilite. The fusion crusts of the meteorites Sikhote-Alin (hexaedrite) and Pinaroo (mesosiderite) will be discussed here in detail.

It is well known that fusion crusts of iron meteorites are in general broader than those of stony meteorites because of the high heat conductivity of the metal phase compared with that of the silicates (Maringer and Manning, 1960). Ramdohr (1965) made a detailed study on this subject. In our specimens, however, the fusion crusts are not so thick as expected (they have a maximum thickness of 1 mm). Microscopic studies showed that they are formed of successive and sometimes alternating layers, and not exclusively of magnetite, as has often been mentioned.

In the Sikhote-Alin meteorite we observed the following layers:

1. An innermost layer close to the unaffected metal composed of recrystallized nickel-iron and sometimes displaying melting textures. This zone contains throughout few but finely distributed magnetite patches.

2. A magnetite-rich zone with finely disseminated metal particles. The borders between the former and this zone are not sharp, and the increase of the magnetite content from the first to the second zone is gradual. The outer boundaries of this layer do not follow the outlines of the first zone, but are strongly curved and show stalactite-like textures (pl. 1a). Under high magnification one recognizes that it is formed of alternating magnetite-rich and metal-rich thin sheets. Magnetite is sometimes locally concentrated in big patches (pl. 1a). A salient feature is the skeletal form of the magnetite indicating rapid cooling and

[1] Max-Planck-Institut für Kernphysik, Heidelberg, Germany.

crystallization from a melt (pl. 1*b*). In the interstices of the magnetite skeletons there are a large number of iron-nickel spherules of different sizes. The big metal spherules contain fine schreibersite worms intersecting the main iron-nickel mass (pl. 1b). From plate 1b it is also evident that iron-nickel is likewise disseminated in the magnetite as very fine particles (1 μ and smaller). The presence of such iron-nickel particles will surely affect the microprobe measurements and give the false impression that nickel is present in magnetite and not in the metal phase. Metal-free magnetite patches are in general very rare. This demonstrates excellently the importance of optical studies and the efficiency of first-class polishing. Microprobe measurements without careful optical studies in incident light may reveal misleading results.

3. A metal-rich zone following the complicated second zone. In texture and composition it resembles the first zone. Magnetite shows everywhere the typical skeletal form.

4. The outermost zone containing two layers: (a) An inner shell formed mainly of wustite with excellent skeletal crystals. Iron-nickel spherules are distributed in this shell, sometimes with local concentration. Wustite can be recognized from magnetite by its lower reflectivity and its dark gray color. It is likemise cubic, and hence isotropic. (b) An outer magnetite shell with typical skeletal crystals and a large number of holes of different sizes. Large iron-nickel spherules are sometimes present (pl. 1a). Magnetite also contains here fine iron-nickel particles. For microprobe measurements only those parts of magnetite must be chosen that are free of iron-nickel particles.

The points a to h, as shown in plate 1a, mere analyzed for iron, nickel, and cobalt with the microprobe. The results are given in table 1. The most interesting results are given by the nickel distribution. Both in the iron-nickel spherule (point a) and in the point b, the nickel ,content has increased up to **70** percent, which is more than a factor of 10 higher than the nickel content of the kamacite. Usually there is only a very thin layer enriched in nickel along the unaltered metallic phase of the meteorite. The magnetite itself shows

TABLE 1.—*Iron, nickel, and cobalt contents in the Sikhote-Alin fusion crust (all results are corrected for background, dead time, mass absorption, and fluorescence excitation)*

Points	Iron (%)	Nickel (%)	Cobalt (%)	Total (%)	Remarks
a	31.5	59.4	2.1	93.0	+Phosphorus
b	26.3	71.7	1.7	99.7	
c	89.9	8.1	0.6	98.6	
d	92.3	5.2	0.7	98.2	
e	53.2	5.5	0.4	59.1	+Oxygen
f	87.2	11.4	0.6	99.2	
g	66.0	0.02	0.03	66.1	+Oxygen
h	88.9	9.0	0.6	98.5	

a surprisingly high amount of nickel (point e: **5.5** percent) but, as shown in plate 1*b*, very small islands of metallic iron-nickel spherules with high nickel content are usually present. Point g, however, is located in a magnetite area where no iron-nickel islands could be seen. In this case the nickel content is **0.02** percent. The points f and h show the composition of the nonoxidized material in the neighborhood of the nickel-free magnetite area. The general result is that nickel and, to a lesser extent, cobalt migrate toward the nonoxidized parts of the melted material during an oxidation process.

In the meteorite of Pinaroo the fusion crust is mineralogically more complicated, and its composition varies laterally because of the presence of a large number of minerals that behave differently when heated, e.g., olivine, pyroxene, chromite, troilite, schreibersite, kamacite, and taenite. Olivine and pyroxene are mainly fused to a silicate glass with a relatively low thickness. Behind the fused thin silicate layer inside the meteorite, the silicates are intact and show no effects of heating. Troilite, whose melting point is considerably lower than that of silicates, has been molten and intruded between the silicates and even soaked into the fine cracks in the silicate crystals. In parts where only troilite is present it show a fluffy texture. Because of the oxidizing conditions during formation of the fusion crust, part of the troilite has been roasted to magnetite with abundant vesicles indicating escape of SO_2 vapor.

Heat has a very interesting effect on chromite in the fusion crust. In general, chromite is known as a refractory mineral. Magnetite separated during fusion overgrows the stable chromite because of the resemblance of the cell edge of both minerals. By strong and direct fusion, chromite itself shows partial breakdown into chromium-poor spinel and eskolaite (Cr_2O_3) separated as fine lamellae parallel to **(111)** of chromite. The breakdown of chromite and the eskolaite intergromth was observed for the first time by P. Ramdohr (private communication, **1965)** in fusion crusts of stony meteorites and mesosiderites. In parts where schreibersite together with taenite was captured in the fusion crust, schreibersite occurs as skeletal crystals in taenite with preferred orientation indicating separation from a metal-phosphide melt.

Where only kamacite and taenite are affected by fusion, the textures very much resemble those of Sikhote-Alin. In Pinaroo three layers (pl. 2*a*) were observed: **(1)** a nickel-rich metal layer with indication of melting following the unaltered metal; **(2)** a wustite layer with nice skeletons and a large number of very fine metal particles; **(3)** a broad magnetite zone, also with wonderful skeletal crystals (pl. **2b).** The amount of the fine iron-nickel disseminated between the magnetite skeletons varies from place to place. We also found here some big iron-nickel spherules whose size permits quantitative microprobe measurements. Magnetite is partially oxidized to hematite at the outermost layer. The fusion crust of Pinaroo is markedly intersected by tension cracks that are filled with weathering products like goethite and lepidocricite.

We carried out microprobe investigations, similar to those of Sikhote-Alin, on the fusion crust of the Pinaroo meteorite. The analyses were made at the points a to i indicated in plate 2*a*. Again the elements iron, nickel, and cobalt were measured and the results are given in table **2.** Point a gives the composition of an inner part in the unaltered meteoritic material. Point g gives the analysis of an iron-nickel spherule visible in the oxidation zone. The nickel content is **62.8** percent, which is **7** times higher than in the Ramacite phase **of** this meteorite **(8.4** percent). The points h and i

TABLE 2.—*Iron, nickel, and cobalt contents in the Pinaroo fusion crust (all results are corrected for background, dead time, mass absorption, and fluorescence)*

Points	Iron (%)	Nickel (%)	Cobalt (%)	Total (%)	Remarks
a	86.1	8.4	0.7	95.2	
b		38.8			Only nickel was measured
c		37.8			
d		40.9			
e		40.4			
f		49.5			
g	25.7	62.8	1.6	90.1	+Phosphorus
h	42.2	3.2	0.2	45.6	+Oxygen
i	52.6	0.6	0.08	53.3	+Oxygen

are in the magnetite zone. Here the nickel content is respectively **3.2** and **0.6** percent, which represents very small iron-nickel islands distributed in the oxidation zone (pl. **2b).** Surprisingly, the points b, c, d, e, and f are located in a larger area of approximately 200 $\mu \times 200$ μ with a nickel content up to 50 percent. This zone, however, turned out to be a very thin layer of nonoxidized iron-nickel alloy. In the case of a thin layer of iron-nickel metal, the electron beam of the microprobe may reach the magnetite, which is underneath the iron-nickel layer (fig. **1).** Three measurements were made with **12, 20,** and 35 kv electron energy to determine the nickel content in this area, and the result is given in table **3.** Because the penetration increases with increasing electron energies, the nickel content is highest at the lowest electron energy.

The results on the fusion crust of the Pinaroo meteorite are the same as for the Sikhote-Alin iron meteorite: very high nickel and relatively high cobalt content either in the small nonoxidized iron-nickel islands or in the outermost layer located along the unaltered metallic part **of** the meteorite.

The production **of** cosmic spherules by ablation necessarily occurs in the nonoxidized outermost zone preferably consisting of magnetite with islands **of** nickel-enriched iron-nickel alloys. So it might well be possible that magnetite spherules are produced without any nickel **or** with a nickel-rich metal core. This result is in agreement with the experiments of Fechtig and

240-022 O—67——26

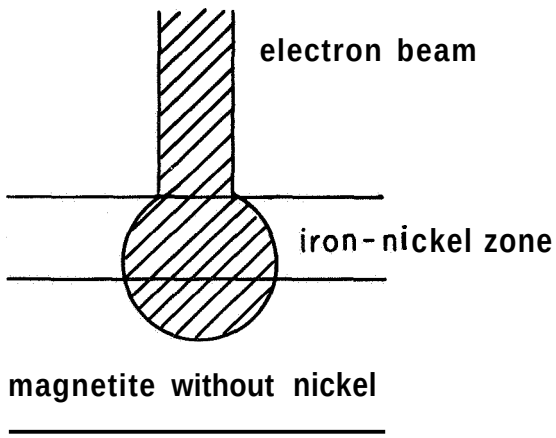

FIGURE 1.—Nickel content dependence of voltage in a thin layer.

TABLE 3.—*Nickel content dependence of voltage in a thin layer*

Voltage (kv)	Nickel (%)
12	38. 3
20	21. 0
35	17. 3

Utech **(1964)** carried out both on meteoritic material and **on** artificial iron-nickel alloys. The authors could artificially produce an oxidation crust that shows a small nickel-rich zone between the oxidized material and the non-oxidized iron-nickel alloy. The results are also in agreement with the experimental results of Schmidt, Keil, and Gault (1965), who investigated the chemical changes caused by a high-velocity impact of a small nickel-iron projectile into the same nickel-iron alloy as a target. They also observed an oxidation process, and the nickel content of the ejecta material (magnetite spherules) decreased by a factor of **10.**

The results show that the lack of nickel in the magnetite spherules is not necessarily an indication against an extraterrestrial origin. An important mineralogical fact should be taken into consideration in order to differentiate between volcanic magnetite and cosmic magnetite. It is well known that the majority of volcanic magnetites are by no means pure crystals but, in fact, are **formed** of mixed titanomagnetites, i.e., members of the complete solid-solution series magnetite-ulvospinel (Fe_2FeO_4-Fe_2TiO_4) (Ramdohr, **1960).** Many volcanic magnetites belong also to the group known as unmixed titanomagnetites, which are magnetite grains with ilmenite lamellae parallel to (111) of magnetite. Both mixed and unmixed titanomagnetites are present in nearly every volcanic rock (Ramdohr, **1940).** The titanium content may reach 20 percent in those magnetites. In questionable cases the presence of titanium can indicate a volcanic, and exclude a cosmic, origin.

References

CASTAING, R., and FREDRIKSSON, K.
1958. Analyses of cosmic spherules with an x-ray microanalyser. Geochim. et Cosmochim. Acta, vol. **14,** pp. **114–117.**

FECHTIG, H., and UTECH, K.
1964. On the presence or absence of nickel in dark magnetic cosmic spherules and their mechanics of origin. Ann. New York Acad. Sci., vol. **119,** pp. **243–249.**

MARINGER, R. E., and MANNING, G. K.
1960. Aerodynamic heating of the Grant meteorite. Geochim. et Cosmochim. Acta, vol. **18,** pp. **157–161.**

RAMDOHR. P.
1940. Die Erzmineralien in gewöhnlichen magmatischen Gesteinen. Abh. Preuss. Akad. Wiss., Math. Nat. Kl. Nr. **2,** pp. **3–43.**
1960. Die Erzmineralien und ihre Verwachsungen. Akademie Verlag, Berlin.
1965. The opsque minerals in stony meteorites. Unpublished monograph.

SCHMIDT, R. A.; KEIL, K.; and GAULT, D. E.
1965. Electron microprobe study of a crater and ejecta produced by hypervelocity impact against a nickel-iron target. Proc. 7th Hypervelocity Impact Symp., Tampa, Fla., vol. **5,** pp. **105–121.**

Abstract

Detailed mineralogical and microprobe studies have been carried out on the fusion crusts of the Sikhote-Alin and Pinaroo meteorites. The fusion crusts in the specimens studied are about 1.5 mm thick and are composed of complex metal and iron-oxide layers. The innermost layer is relatively thin and is composed mainly of recrystallized metal. This layer is followed by a magnetite-metal layer. Magnetite shows skeletal crystals, droplets, and stalactitic textures typical of crystals separating from a melt by fast cooling. Magnetite is partially intercalated by nickel-iron spherules. In the outermost layer some nickel-iron spherules were observed, as well as a thin sheet of wustite (FeO). Some of these nickel-iron spherules show eutectic intergrowth between nickel-iron and schreibersite. Other spherules are composed mainly of nickel-iron.

Microprobe measurements of the nickel-iron sphcrulcs, the magnetitc zone, and the border bctwccn the magnctitc and the unaltered meteorite have been carried out for nickel, iron, and cobalt. The results show an enrichment,, as high as 60 percent, of the nickcl in these spherules and in the outer part of the nonoxidized meteoritic material. Tho nickel content of the magnctitc in those areas in which no metallic islands can be seen is below 0.03 pcrccnt. The cobalt distribution in thcsc zones is similar to that of nickcl, but to a lcsscr cxtcnt.

The results strongly support the production of the cosmic sphcrules by ablation as far as tlicy consist of magnetite. There is, furthermore, a good agreement with similar investigations on an artificially produced oxidation crust in iron mctcoritcs and iron-nickcl alloys as rcportcd by Fcchtig and Utcch (1964).

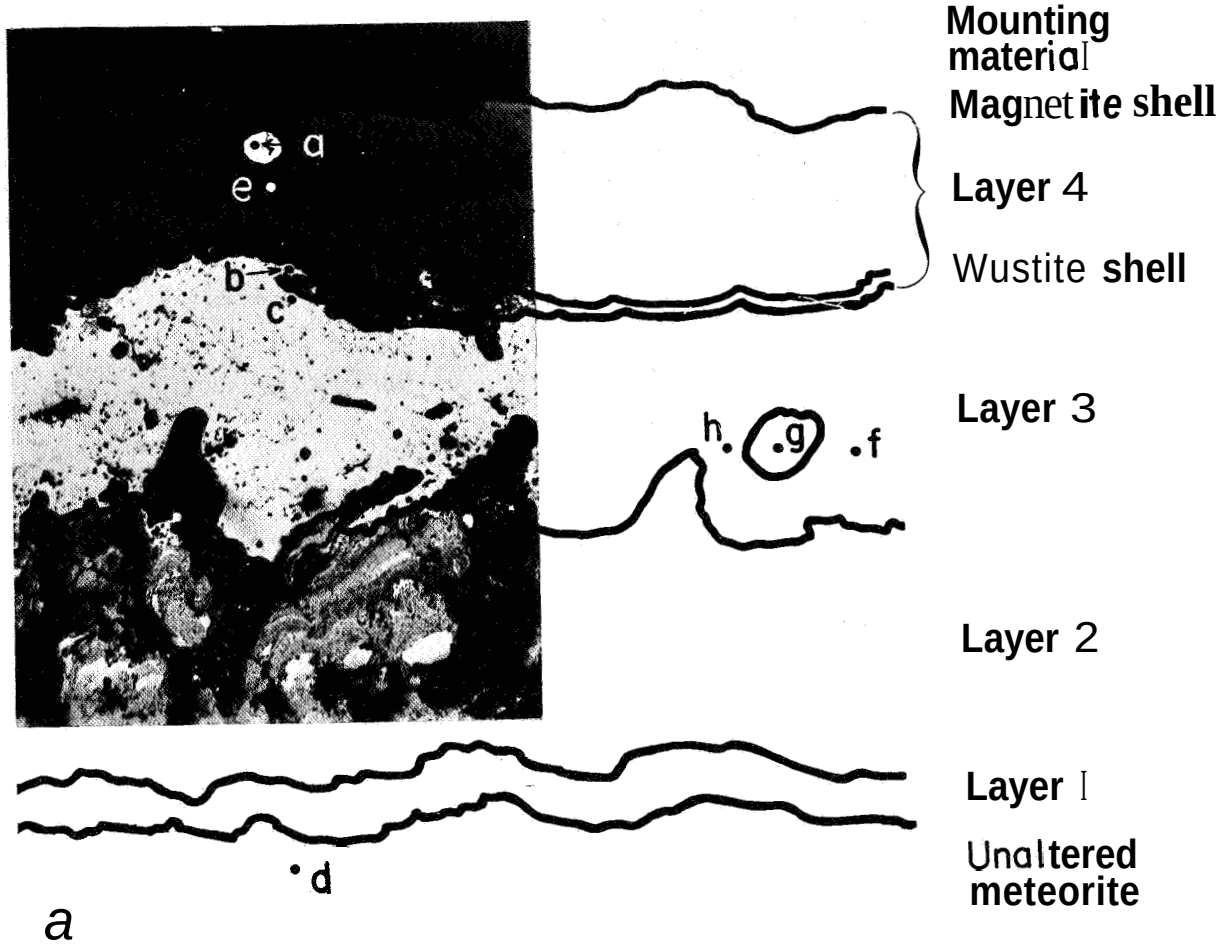

a

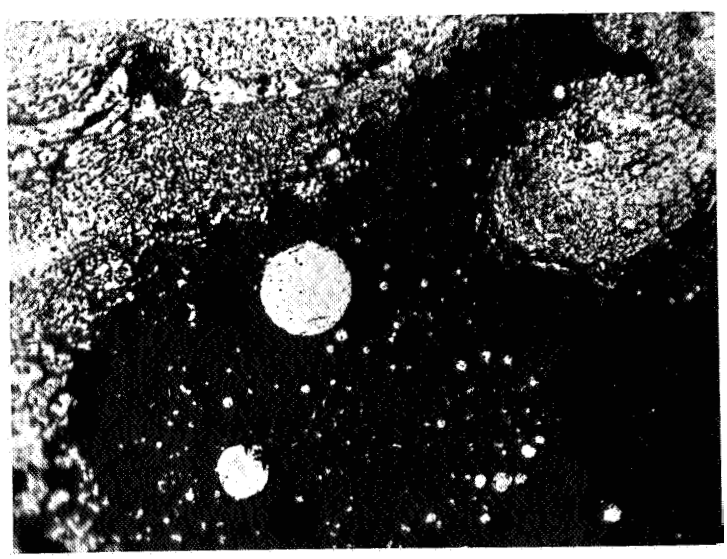

b

PLATE 1A, B

Sikhote-Alin fusion crust (magnification X 400). Skeletal crystals of magnetite (gray) with iron-nickel spherules of different sizes. The big metal spherules contain schreibersite worms (magnification X 800).

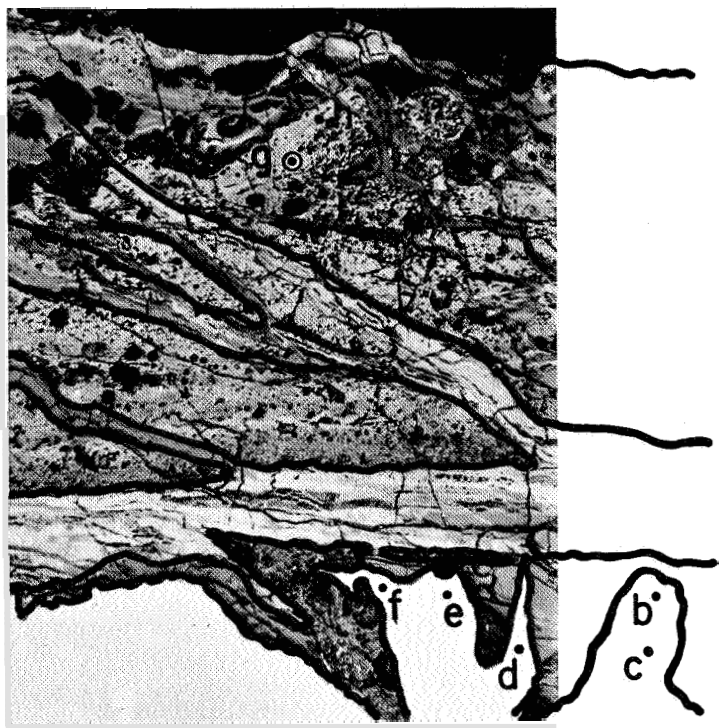

a • a

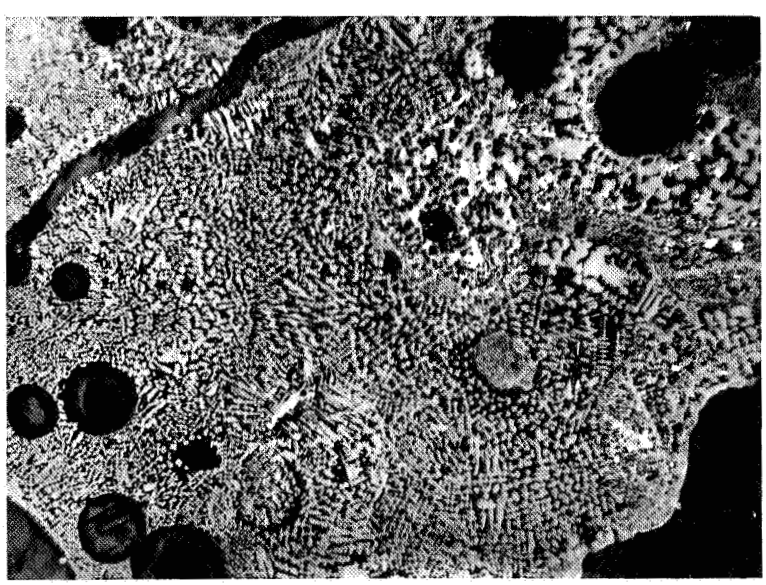

b

PLATE 2A, B

Pinaroo fusion crust (magnification X 180). Excellent skeletal magnetite crystals (light gray). Notice the presence of fine iron-nickel particles between the magnetite skeletons (the upper right part of the photograph) (magnification X 800).

Some Studies of Separated Fractions of Low Accumulation-Rate "Dust"

D. TILLES [1]

Introduction

Fine-grained material, tentatively identified as extraterrestrial in origin, has been found in deep-sea and polar deposits and studied scientifically for 90 years (see Buddhue, 1950, for a review of the early work and bibliography); however, the uncertainties in mineralogical, chemical, and morphological characteristics of possible extraterrestrial material have greatly hampered progress in these studies. Much attention has been devoted to searching out and studying "cosmic spherules"—dark magnetic iron-rich spheres, some of which have cores of metallic nickel-iron. Because of the extreme rarity of terrestrial native metallic iron, the unknown terrestrial occurrence of native metallic iron with nickel abundance greater than 1 or 2 percent, and the obvious plausibility of creation of such spherules by atmospheric ablation and oxidation of the iron-nickel meteorites, such magnetite spherules with iron-nickel cores are perhaps the only fine-grained material found on earth for which a nonterrestrial origin is almost universally accepted.

As a result of the great difficulty of definitive identification of extraterrestrial material, substantial effort has been devoted in recent years to searching for the presence of cosmic-ray-produced radioactive or stable isotopes or other stable isotope anomalies in samples suspected to contain extraterrestrial dust. Isotopes sought in sea sediments have included Cl^{36} (Schaeffer, Megrue, and Thompson, 1964), Fe^{60} (C. M. Merrihue, unpublished), Al^{26} (Lal and Venkatavaradan, 1965), and those of the noble gases (Schaeffer, Megrue, and Thompson, 1964; Merrihue, 1964; R. Bieri, private communication). Isotopes studied in particulate matter from polar ice include Al^{26} (Fireman and Langway, 1965), Ar^{39}, and Co^{60} (Fireman, DeFelice, and Langway, 1965).

Most of these searches have given negative results. The Co^{60} results, while positive, require further work to distinguish terrestrial contaminants from the daughter product of long-lived Fe^{60}. The specific activities of Al^{26} reported for two cores of sea sediment are only about twice the probable errors of the measurements.

Merrihue (1964) reported evidence of He^3 and of anomalous argon isotope ratios in gas extracted during heating of a magnetic separate of a Pacific red clay sediment. He also found evidence of anomalous neon isotope ratios. Bieri (private communication) has found much smaller argon anomalies in one Pacific sample and none in others. Schaeffer, Megrue, and Thompson (1964) found no evidence of *cosmogenic* He^3 or Ne^{21} in magnetic concentrates of sea sediments from several locations.

The work reported here was begun in the hopes of confirming the results of Merrihue and extending these results to other geographic locations and to other mineralogical concentrates. This is a progress report on continuing work.

Samples

A new magnetic separation was made by Cassidy of the same Pacific red clay previously

[1] Smithsonian Astrophysical Observatory and Harvard College Observatory, Cambridge, Mass.

studied by Merrihue. This sample, designated BBD no. 1, is from 14°05′ S latitude, 155°09′ W longitude, and was collected from the top of the sediment surface at approximately 2660 fathoms. Since no efforts were made to homogenize the dredged material, the small samples from which the different magnetic fractions were separated may represent somewhat different depths below the sediment surface.

Other measurements reported here were made on material collected by Langway in 1962 from a tank in the water-supply system of Camp Century in Greenland. The camp is located t 77°10′ N, 61'08' W at an altitude of 70000 feet, and about 145 miles from Thule. The water-supply system of Camp Century consists of steam-melted ice from the Greenland ice sheet. The particulate matter used for the studies described here was a fraction of that collected from a 20,000-liter aluminum storage tank through which an estimated 10^7 liters of melted ice had passed (Langway and Fireman, 1965). This particulate material, collected by Langway in 1962, was accumulated before Langway and Fireman installed the filter systems at the ice well. A more complete description of the Camp Century water supply has been published by Fireman and Langway (1965).

Experimental

Half-gram samples were wrapped in aluminum foil and given preliminary bakeout before commencement of runs. For the sea-sediment measurements the bakeout lasted 4 hours at 300' C; for the Greenland samples it was continued overnight at 150° C. The gas extraction and cleanup system was similar to that described by Merrihue (1964), with a revised furnace design.

The mass spectrometer was a 6-inch radius glass machine, of 60° sector, similar *to* those described by Reynolds (1956) and Schaeffer (1959). It has electron multiplier detection, but was used with no source magnet. Mass discrimination was small, and optimum source settings were essentially independent of mass.

Both spectrometer and sample system were baked out. Spectrometer sensitivity and mass discrimination were calibrated with 1/80 cc air samples (enriched with He^3), cleaned up with the sample system. The absolute amounts of gas are believed reliable to better than 40 percent.

It should be noted that, except for the He3 in the calibration spikes and the samples of rare gases extracted from the sea sediments and Greenland samples themselves, no anomalous nor nonair rare gases had previously been run in either the sample system or the spectrometer. Spectrometer memory was thus minimized, and any remote possibility of gas exchange with meteoritic or other anomalous rare-gas samples in the furnace or cleanup procedures was completely eliminated.

Complete blank runs were made at several temperatures before commencement of an actual sample run. Gases were analyzed in three fractions: helium and neon with all others condensed on charcoal with liquid nitrogen; argon released from charcoal at dry ice temperatures; and krypton and xenon released from charcoal at room temperatures.

Since it was already expected from Merrihue's work that no argon anomalies could be detected in the ratios of the total gas extracted from the magnetic fraction of sea sediments, all samples were degassed with successive l-hour heatings at increasing temperatures, with extracted gas at each temperature purified and examined with a mass spectrometer. The heating was done with a radio-frequency induction heater. Temperatures are approximate, being determined in some cases with both a thermocouple sunk in a hole in the furnace and an optical pyrometer, and in others with just the pyrometer, which looked directly down into the interior of the furnace.

Argon results

SEA SEDIMENTS.—The results on two separate magnetic samples of red clay are given in table 1. The argon released at low temperatures had an Ar^{40}/Ar^{36} ratio greater than that in air for both samples. The apparent amount of radiogenic argon is the same for the two samples, in spite of the differences in low-temperature isotopic ratios. A potassium abundance of 1.28 percent was determined by flame photometry. If we assume that all Ar^{36} in the temperature fractions with Ar^{40}/Ar^{36} ratios greater than in

TABLE 1.—Argon in magnetic *fraction* of sea sediments

Sample	Weight (g)	Approximate temperature (°C)	Ar^{40} (10^{-8} cm³ STP g^{-1})	Ar^{40}/Ar^{36}	Ar^{36}/Ar^{38}
Magnetic sea sediment − 1	0.51	500	520	472±17	4.95±0.32
		900	70	311±9	5.29±0.25
		1200	50	198±6	5.00±0.25
		1450	110	290±30	5.15±0.4
Magnetic sea sediment − 2	0.50	500	310	787±20	4.98±0.3
		950	60	358±16	4.7 ±0.6
		1200	20	194±10	4.88±0.53
	2nd cleanup	1200	30	193±12	4.85±0.5
		1400	10	239±11	5.30±0.5

air is in fact air argon, we can calculate an apparent potassium-argon age of about 40×10^6 years for these samples.

All Ar^{36}/Ar^{38} ratios were consistent with air ratios.

The 1200° C fractions of argon from both samples had Ar^{40}/Ar^{36} ratios less than 200, and the ratio for the 1400° C fraction of one of the samples was about 240—still well below the air ratio of 295.

The minimum observed value of Ar^{40}/Ar^{36}, which was 193±12, is slightly higher than the value of 172±5 observed at 1400° C by Merrihue (1964), but our samples were a quarter the size of Merrihue's, and hence the relative contribution of blank air argon to our measurements is probably larger. Also, the efficiency of separation for the two independent magnetic concentrations may be different.

As a check on the possibility that our mass 36 peak included a contribution from something other than argon (which could cause a spuriously low Ar^{40}/Ar^{36}), the 1200° C fraction of one of the samples was recondensed onto charcoal at liquid nitrogen temperatures and was stored overnight while the spectrometer was thoroughly pumped out. It was then given a complete second cleanup over hot titanium foil that had been degassed again at high temperature while being pumped on. Following this second cleanup, the sample was readmitted to the spectrometer and remeasured. Within the limits of error no change in ratios was observed.

Our results for these measurements are compared in figure 1 with those of Merrihue. The agreement is considered satisfactory, particularly in view of our smaller sample size. These results confirm the anomalously low Ar^{40}/Ar^{36} previously reported by Merrihue for a similar sample.

GREENLAND DUST.—Encouraged by the good agreement for the argon anomalies in the sea sediments, we next turned to Greenland dust. We initially studied the gases released from a bulk sample that was untreated except for being sieved to pass a 140 mesh screen. About an order of magnitude more argon was found in this material than in the magnetic sea sediments, and Ar^{40}/Ar^{36} ratios of nearly 5000 were measured. The argon was enriched in radiogenic Ar^{40} at all temperatures of release (table 2). A potassium determination of 0.64 percent when combined with the argon measurements gave an apparent potassium-argon age of about 2.7×10^9 years.

Since this value (with its associated uncertainties) seemed well within the possible age range for Canadian shield rocks, and since there are immense exposures of these rocks that could provide a source for windblown mineral grains, it was decided to try to remove the potassium-bearing material with a density separation. A sample was centrifuged in methylene iodide of density 3.2 g/cm³. About one-fifth of the sample sank at this density. The heavy fraction was recentrifuged and was then subjected to the same kind of gas extraction, purification,

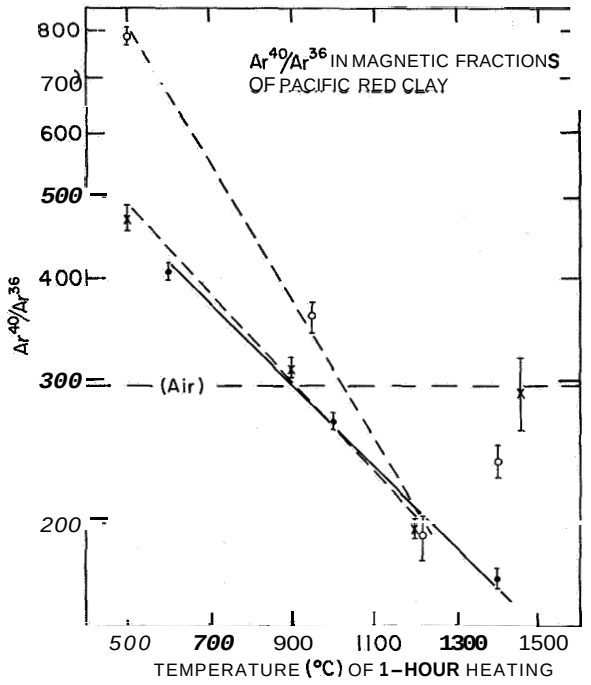

FIGURE 1.—Ar^{40}/Ar^{36} ratios in gas released from magnetic separates of Pacific red clay during successive 1-hour heatings. The solid line and black circles are the measurements of Merrihue (1964).

TABLE 2.—*Argon in unseparated Greenland material—1 (<140 mesh)*

Approximate temperature	Ar^{40} (10^{-8} cm³ STP g^{-1})	Ar^{40}/Ar^{36}
	7000	945
	5200	3340
1050	1400	4700
1150	200	2050
1250	40	1250
1650	125	400

and mass spectrometry as were the sea-sediment samples.

The concentrations of Ar^{40} before and after the density separation are given in figure 2. The argon isotope ratios found in the dense fraction are given in table 3 and figure 3. The 1200° C fraction released argon with Ar^{40}/Ar^{36} of 228 ± 5. After a complete second cleanup this ratio was 232 ± 5, identical to the previous value within errors. The Ar^{36}/Ar^{38} ratio of this temperature fraction was 5.21 ± 0.08.

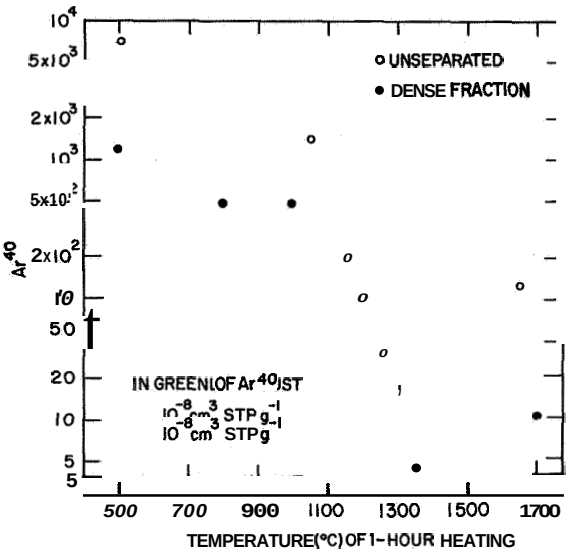

FIGURE 2.—Amounts of Ar^{40} in gas released from Greenland dust during successive 1-hour heatings (10^{-8} cm³ STP g^{-1}). Open circles: unseparated. Solid points: fraction with density greater than 3.2.

TABLE 3.—*Argon in Greenlandmaterial—8 (density > 3.2)*

Approximate temperature (°C)	Ar^{40} (10^{-8} cm³ STP g^{-1})	Ar^{40}/Ar^{36}	Ar^{36}/Ar^{38}
500	1200	320f 15	
800 [a, c]	480	576±43	4.9 ±0.6
1000	480	471± 19	—
1200 [a]	—	238± 15	4.98f0.4
1200 [b]	96	228± 5	5.05±0.15
1200 [c]	101	232± 5	5.21f0.08
1350 [d]	6	308±28	4.5 ±1.2
1700	~10	350±30	—

[a] small aliquot (—10 percent) of gas release for ratios;
[b] Rest of gas release;
[c] Rerun on mass spectrometer after overnight *storage* and complete additional cleanup;
[d] This is lower than typical blanks at these temperatures.

The same kind of anomalous Ar^{40}/Ar^{36} ratio was therefore observed for the dense Greenland material as for the magnetic sea sediments, and at the same temperature. Although the ratio was not so low as observed in the magnetic sea sediments, the apparent concentration of excess Ar^{36} and Ar^{38} is somewhat higher.

The measured potassium abundance of this dense fraction was 0.14 percent, giving an

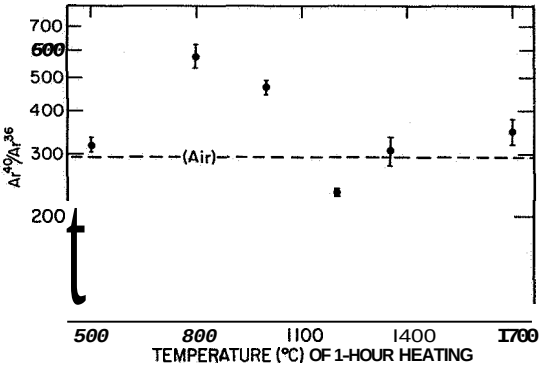

FIGURE 3.—Ar^{40}/Ar^{36} ratios in gas released from Greenland dust fraction with density greater than 3.2 during successive 1-hour heatings.

apparent potassium-argon age for this material of about a billion years.

Other rare gases

No evidence of anomalous Xe^{129} was found. Upper limits for He^3 and Ne^{21} were also determined. The He3 values are given in table 4. These upper limits are consistent with those determined by Schaeffer, Megrue, and Thompson (1964). The Ne^{21} upper limits found in the magnetic fraction of the sea sediment were consistent with measured amounts found by Merrihue at comparable release temperatures. The He^3 upper limits are much lower than the values reported by Merrihue for comparable temperatures of release from the magnetic fraction of the Pacific red clay. The reason for this disagreement is not clear. Our upper limit is essentially determined by HD+ from hydrogen not completely cleaned up by titanium. Our preliminary bakeout of the magnetic sea sediments lasted for 4 hours at 300° C; Merrihue's extended over 15 hours but at only 150° C. However, Merrihue found He^3 released after an hour at 600° C, and twice as much He^3 after an hour at 1000° C. Since an hour at 600° C had not released most of the He^3 from his sample, it is not expected that 4 hours at 300° C would have done so from ours. There may be real variations of He^3 abundance from sample to sample, although no large differences in argon anomalies were found in the same samples.

TABLE 4.—*Upper limits for He8*

Sample	Weight (g)	Approximate temperature (°C)	He^3 (cm^3 STP g^{-1})
Magnetic sea sediment – 1	0.51	500	$<10^{-10}$
		900	$<8\times10^{-11}$
		1200	$<8\times10^{-11}$
		1450	$<10^{-9}$
Magnetic sea sediment – 2	0.50	500	$<10^{-10}$
		950	$<5\times10^{-11}$
		1200	$<3\times10^{-11}$
		1400	$<4\times10^{-11}$
Greenland– 1	0.64	500	$<5\times10^{-11}$
		950	$<6\times10^{-11}$
		1050	$<8\times10^{-11}$
		1150	$<3\times10^{-11}$
		1250	—
Greenland – 2 (density >3.2)	0.50	500	$<7\times10^{-11}$
		800	$<4\times10^{-10}$
		1000	$<2\times10^{-10}$
		1200	$<3\times10^{-11}$
		1350	$<2\times10^{-11}$

Measurements of He^4 and Ne^{20} in the unseparated Greenland material and the dense Greenland fraction are given in table 5.

In the gas released at 500° C from the dense Greenland fraction, a He^4/Ne^{20} ratio of about 420 was found. This is similar to the estimated cosmic-abundance ratio and to the values observed in many gas-rich or "primordial gas" meteorites; however, the contribution to this ratio of radiogenic helium released at this temperature is not known.

The apparent potassium-argon age of the dense fraction is much less than the age of the total sample. Yet the He^4 concentration at the lowest temperatures is higher in the dense fraction than in the total sample, and the total He^4 concentrations are similar. Either there is much more uranium and thorium in the dense fraction than in the total sample, or there is nonradiogenic helium in the dense fraction. The former is possible, since minerals such as zircon are resistive, dense, and high in uranium and thorium concentrations; however, no evidence of such minerals was seen in the X-ray powder pictures. The latter

TABLE 5.—*He^4 and Ne^{20} in Greenland material (em3 STP g^{-1})*

Sample	Temperature (° C)	He^4	Ne^{20}	He^4/Ne^{20}
Greenland– *1*	*500*	*3. 3 x 10^{-6}*	*1. 7×10^{-8}*	*194*
	950	*2. OX 10^{-6}*	*2×10^{-8}*	*100*
	1050	*< 2 x 10^{-8}*	*1×10^{-8}*	*<2*
Greenland – *2* (ρ>3.2)	*500*	*5. 2×10^{-6}*	*1. 2×10^{-8}*	*420*
	800	*9. 4×10^{-7}*	*7. OX 10^{-8}*	*13*
	1000	*TX 10^{-8}*	*7×10^{-8}*	*1*
	1200	*<1×10^{-8}*	*5 x 10^{-8}*	*<0. 2*

explanation seems more probable, but can only be verified by uranium and thorium measurements.

Similar ratios of He^4/Ne^{20} for the magnetic sea sediments are suspect, since an order of magnitude more high temperature He^4 was found in the first of the two samples than in the second. The second sample, loosely wrapped in aluminum foil, was in a side arm of the furnace during the gas extractions from the first sample, and was subjected to intense radio-frequency discharge. It is possible that such discharge may have released gas prematurely from the second sample and allowed it to be measured as part of the gas from the first sample. This may also explain the observed increase in argon concentration found for the highest release temperature of the first magnetic sea-sediment sample measured. Such an increase was not observed for the second sample. The possibility of such loss also unfortunately weakens the reliability of the He^3 measurements in the second sea-sediment sample, although it cannot have affected the measurements in the first sample.

Merrihue found at 600° C a ratio for He^4/Ne^{20} of **470,** in a magnetic fraction of sea sediment, similar to that observed at 500° C in our dense Greenland fraction. He also found in the gas released at **600'** C and 1000' C more of both He^4 and Ne^{20} in the magnetic fraction of the red clay than in the nonmagnetic fraction.

Too few samples have as yet been studied to provide a strong demonstration of the presence of excess He^4 and Ne^{20}. For both the sea sediments and Greenland samples, however, there is an indication of the presence of higher concentrations of He^4 and Ne^{20} in the dense or magnetic material, and the observed ratio of these two isotopes in the lowest gas release temperature is similar to the "cosmic" ratio.

Determination of potassium-argon and uranium-helium ages in high-purity mineral concentrates should help distinguish radiogenic helium from any excess helium that may be present.

Mineralogy of samples containing anomalous argon

Considerable effort has been devoted to determining the mineralogical composition of the samples in which anomalous argon isotope ratios have been observed. Mineralogical data may help to explain the present observations, and are in any case essential for further, more complete concentration of individual mineral fractions, which are required for future mass spectrometric investigations.

W. A. Cassidy has estimated (private communication) that the abundance of the magnetic material that he separated with a hand magnet from the Pacific red clay is at least 4 percent of that sample, with some additional material still being removed with further separations. We have made X-ray diffraction studies of several size fractions of material separated magnetically from another aliquot of this same barrel dredge. We performed the size separations by settling in 0.002 N NH_4OH, and the magnetic separations by using a Frantz Ferro-filter and varying field-strength hand magnets.

X-ray diffraction powder photographs indicate that the Ferro-filter and Cassidy's hand-magnet separations give crudely similar separation efficiencies and roughly the same assemblage of minerals, which includes magnetite,

ilmenite, augite, phillipsite, hypersthene, and some glassy material. There is no evidence of any major difference in mineral abundances between a coarse-grained magnetic fraction (5 to 60 μ for magnetite density) and a very fine-grained magnetic fraction (less than 1.5 μ for magnetite density).

Essentially all of the dense Greenland fraction appears, from X-ray diffraction studies, to be magnetite and hematite; the sample is highly magnetic.

The one mineral apparently common to anomalous argon-bearing samples from both Greenland and the Pacific is magnetite. It seems probable that the anomalous argon must be present in magnetite from both locations. However, our current data do not exclude its presence in more than one mineral, or in minerals undetectable in X-ray studies of the present concentrates. Mass spectrometry on much purer mineral concentrates will be required to verify these possibilities.

Furthermore, the lack of detection of anomalous argon in nonseparated bulk samples of these materials cannot be considered as evidence for its nonpresence in nonmagnetic fractions, for the only nonmagnetic or bulk samples studied to date have in all cases been assemblages of minerals including a much larger total of radiogenic argon, which would tend to mask any of the kind of anomalous argon isotope ratios so far found in the magnetic or dense fractions. Here again, more extensive mineral separations are required.

Discussion

The only confirmed isotope anomalies in fine-grained material suspected to include an extraterrestrial component are the apparent presence of excess Ar^{36} and Ar^{38} released at high temperatures. The minimum amount of excess Ar^{36} can be calculated by assuming that if the Ar^{40}/Ar^{36} ratio is observed to be greater than that in air, the argon is a mixture of contemporary air argon and radiogenic argon from decay of potassium, and if the Ar^{40}/Ar^{36} ratio is observed to be less than that in air, the argon is a mixture of contemporary air argon and excess Ar^{36} and Ar^{38}, with no radiogenic Ar^{40}. Minimum amounts of excess Ar^{36}, derived in this way, are given in table 6. All observed ratios of Ar^{36} to Ar^{38} are consistent with air ratios.

It is seen that the apparent minimum concentrations of excess Ar^{36} are similar for the magnetic fractions of the Pacific red clay and for the dense fraction of Greenland dust. This approximate agreement of measurements on samples collected from two extremely different environments and from two very distant locations on the earth's surface suggests that we are dealing with a worldwide phenomenon. The most obvious similarity in these separate collections is that both come from locations of very low total accumulation rate of dust, sediment, and debris from all terrestrial and extraterrestrial sources combined.

The accumulation rates in the red clay areas of the South Pacific are of the order of 1 mm of sediment per 1000 years (Sackett, 1964; Goldberg and Koide, 1962) corresponding to about 2×10^{-4} g cm^{-2} yr^{-1}, so that if the measured magnetic fraction had an abundance of 4 percent it would have an accumulation rate of the order of 8×10^{-6} g cm^{-2} yr^{-1}.

The Greenland tank collection corresponds to a total accumulation of 1.5×10^{-6} g cm^{-2} yr^{-1} (Langway and Fireman, 1965), although this is a minimum value since the overall collection efficiency is not known. The corresponding minimum accumulation rate for the dense Greenland fraction is 3×10^{-7} g cm^{-2} yr^{-1}.

Both the magnetic Pacific and dense Greenland materials are, of course, mixtures of unknown proportions of terrestrial and extraterrestrial materials.

TABLE 6.—*Minimum Ar^{36} excess per gram* (units: 10^{-10} cm^3 STP g^{-1})*

Sample	Concentration	Reference
Sea sediments (magnetic fraction)	7	Merrihue
Sea sediments (magnetic fraction)	8	This work
Sea sediments (magnetic fraction)	6	This work
Greenland dust (dense fraction)	9	This work

*Assuming (1) all Ar^{40} is air whenever Ar^{40}/Ar^{36} < air ratio; (2) no excess Ar^{38} whenever Ar^{40}/Ar^{36} > air ratio.

Since all of the identified minerals in the anomalous samples measured are of widespread occurrence on the earth's surface, and since the argon isotope ratio has probably changed with time both within the earth and in the earth's atmosphere, the question of whether these observed argon anomalies are terrestrial or extraterrestrial in origin must be critically examined. The lack of confirmation of the presence of He^3 underlines the importance of such an examination.

There are, in principle, four ways in which samples of anomalous rare gas with isotope ratios different from those of the present atmosphere might be produced or incorporated into terrestrial rocks or minerals: **(1)** radioactive decay: e.g., He^4 and Ar^{40}, fission xenon; *(2)* nuclear reactions: e.g., of neutrons, alpha particles, cosmic rays; **(3)** trapping of a sample of ancient atmosphere; and **(4)** solidification in the presence of gases from incomplete outgassing of the interior of the earth itself.

We will not discuss **(1)** and **(2)** further here as they do not appear capable of accounting for the observed anomalous argon.

If the atmospheric Ar^{40}/Ar^{36} ratio has increased as a function of time, then a sample of an ancient terrestrial atmosphere would have Ar^{40}/Ar^{36} lower than the contemporary value. If sedimentary material had cemented together in the presence of atmospheric gases sufficiently tightly so that it did not lose its trapped-gas content, and had then melted at depths in the earth at high temperature, again in a gas-tight environment, some minerals might have incorporated samples of the rare gases in an ancient atmosphere; however, this model places severe constraints on the age of the minerals in the sediments and on their potassium content. The minerals will contribute excess radiogenic Ar^{40}, which will be mixed with the ancient atmosphere before solidification from the melt, thus masking any lower-than-contemporary Ar^{40}/Ar^{36} ratios. It also places severe constraints on the inherited argon from within any other part of the gas-tight region of magma.

An alternative possibility for sampling an ancient atmosphere may be submarine extrusive vulcanism at great depths in the oceans. This process would solidify minerals in contact with very high hydrostatic pressures, and the argon dissolved in the ocean (Bieri, Koide, and Goldberg, **1964**), which would be in equilibrium with the argon in the atmosphere, might be forced into solidifyingmineral lattices. Samples of ancient deep-seated submarine extrusive rocks, if obtainable, might enable us to investigate this problem. At present this explanation seems unlikely because of the findings of the anomalies in material from Greenland. With the known great difficulty in finding or obtaining samples of truly ancient submarine rocks, the surface of the ice in Greenland appears an unlikely place to discover such samples.

There exists in principle another way of eliminating some terrestrial origins for the argon anomalies. Let us assume that the ratio of Ar^{40}/Ar^{36} in the atmosphere or in the ocean is a function of time, given by the ratio of the independent functions of time describing $Ar^{40}(t)$ and $Ar^{36}(t)$. Then

$$\frac{\frac{Ar^{40}}{Ar^{36}}(t_1)}{\frac{Ar^{40}}{Ar^{36}}(t_0)}=\left[\frac{Ar^{40}(t_1)}{Ar^{40}(t_0)}\right]\left[\frac{Ar^{36}(t_0)}{Ar^{36}(t_1)}\right].$$

If we denote present time by t_1 and the time of solidification of an old mineral by t_0, we have the ratio R:

$$R=\frac{295}{\frac{Ar^{40}}{Ar^{36}}(t_0)}=\frac{Ar^{40}]_{4.5\times10^9\ yrs}}{Ar^{40}]_{t_0}}\times\frac{Ar^{36}]_{t_0}}{Ar^{36}]_{4.5\times10^9\ yrs}}.$$

If we assume that Ar^{40} is outgassed on the average fairly rapidly after its formation from K^{40}, we can use the K^{40} decay constant as a degassing rate as well, and have

$$\frac{Ar^{40}]_{4.5\times10^9}}{Ar^{40}]_{t_0}}=\frac{1-e^{-\lambda(4.5\times10^9)}}{1-e^{-\lambda t_0}}=\frac{1-e^{-\lambda(4.5\times10^9)}}{1-e^{-\lambda(4.5\times10^9-T)}},$$

where T is the contemporary potassium-argon age corresponding to solidification at t_0.

The time dependence of Ar^{36} is a function of the history of the atmosphere assumed. Two reasonable limits may be: **(I)** constant from some time early in the earth's history (Suess, **1949**), and **(11)** increasing linearly with time (Tilles, **1965**).

We have, then, for these two cases,

$$\text{(I)} \qquad \frac{Ar^{36}]_{t_0}}{Ar^{36}]_{4.5\times10^9\ \text{yrs}}}=1$$

$$\text{(II)} \qquad \frac{Ar^{36}]_{t_0}}{Ar^{36}]_{4.5\times10^9\ \text{yrs}}}=\frac{t_0}{4.5\times10^9},$$

and assembling these factors we get

$$\text{(I)} \quad R-\frac{1-e^{-\lambda(4.5\times10^9)}}{1-e^{-\lambda(4.5\times10^9-T)}}$$

$$\text{(II)} \quad R=\left[\frac{1-e^{-\lambda(4.5\times10^9)}}{1-e^{-\lambda(4.5\times10^9-T)}}\right]\left[\frac{4.5\times10^9-T}{4.5\times10^9}\right].$$

Although these expressions are dependent on the model of outgassing of Ar^{40} assumed, they are not critically so for young potassium-argon ages and can be modified to take account of more realistic models.

If we now consider a mineral of potassium-argon age T that incorporated a sample of terrestrial atmospheric or oceanic argon in its structure when it crystallized, we can calculate the value of Ar^{40}/Ar^{36} expected for this "inherited" argon. If this ratio agrees with the observed ratio of the anomalous component, this type of terrestrial origin is supported.

Let us use the apparent potassium-argon age (10^9 years) of the dense Greenland fraction to demonstrate this calculation. By substituting and solving, we have for (I), $R=1.09$ and for (II), $R=0.85$. The observed value for $R=295/232=1.33$ at 1200° C for this sample.

A more striking case is that of the magnetic fraction of the sea sediment with a potassium-argon age of about 40 million years. In this case, for both (I) and (II) the model value of R is within a percent of unity. Yet the observed value is $R=295/195=1.51$. This difference is larger than the uncertainties in model atmospheric ratios, or potassium-argon age determinations. It also shows no correlation of magnitude of anomaly with apparent potassium-argon age.

Several of the uncertainties that might affect the comparison of model and observed ratios will increase the discordancy. These include the following: (1) any radiogenic Ar^{40} that is released at the temperatures where the anomalous argon is observed (the rapidly decreasing Ar^{40} concentrations as the temperature of release is raised suggest that this may well be significant and may reduce the apparent Ar^{40}/Ar^{36} anomaly from the actual); (2) any dilution by contemporary air blanks; and (3) any inherited excess Ar^{40}, such as is found in beryls, pyroxenes, etc., will also, of course, reduce the magnitude of the apparent anomaly.

Thus, this type of analysis argues against an inherited terrestrial origin for these anomalies. It is possible, however, that part of the potassium in the magnetic sea sediment is in ("zero-age" terrestrial minerals in the surface sediments (phillipsite, for example) and that the real potassium-argon age of that fraction of the sample containing the anomalous argon is older. In such a case the usefulness of the above analysis is reduced.

Samples of terrestrial rocks that have inherited significant amounts of their initial complement of cosmic gases are currently unknown. Measurements of terrestrial rocks (Butler, Jeffery, and Reynolds, 1963) suggest that primordial xenon has been at least substantially outgassed from the earth. Argon would be expected to be more completely outgassed than xenon.

Terrestrial natural gases are enriched in Ar^{40} relative to air (Zartman, Wasserburg, and Reynolds, 1961; Wasserburg, Mazor, and Zartman, 1963; Clarke and Thode, 1964). Certain minerals have been found to inherit excess argon (Aldrich and Nier, 1948; Damon and Kulp, 1958; Hart and Dodd, 1962). These include beryl, cordierite, tourmaline, and pyroxenes. All evidence to date indicates that the inherited argon is highly enriched in radiogenic Ar^{40}; however, only total gas has usually been measured, and not that released as a function of temperature.

Through investigations of argon in fluid inclusions in quartz and fluorite Rama, Hart, and Roedder (1965) and Lippolt and Gentner (1963) also have found gas with Ar^{40}/Ar^{36} ratios greater than in air.

Keevil, Joliffe, and Larsen (1942) and Cherdyntsev (1961) have reported evidence of inherited excess helium in some terrestrial magnetite samples. Argon has not yet been

studied in known terrestrial magnetites; we are planning such studies.

The arguments against terrestrial origin of the anomalies can be summarized as follows:

1. No terrestrial samples with Ar^{40}/Ar^{36} ratios less than in contemporary air have ever been observed.

2. Terrestrial samples known to be rich in excess or inherited argon are generally also rich in radiogenic argon, with high Ar^{40}/Ar^{36} ratios.

3. Tentative comparison of potassium-argon ages of minerals containing anomalous Ar^{40}/Ar^{36} with model atmospheric ratios leads to differences.

However, further experimental studies of known terrestrial samples with differential gas release as a function of temperature are desirable.

We consider next extraterrestrial mechanisms of origin. No conclusive evidence for the presence of cosmic-ray or energetic solar-flare particle-produced spallation isotopes in these anomalous samples has been found to date. The Ar^{36}/Ar^{38} ratio in the 1200° C dense Greenland fraction can be used to place an upper limit on the amount of cosmogenic argon in the sample with the highest measured amount of anomalous gas. The limit is less than 1 percent of the total Ar^{36} released at 1200° C, or less than 4×10^{-11} cm^3 STP g^{-1}. This is lower by a factor of 10^2 to 10^4 than the amounts of spallation argon found in iron meteorites, and is consistent with the lack of any positive evidence in this work and in that of Schaeffer, Megrue, and Thompson (1964) for the presence of spallation He^3 or Ne^{21}.

Since much of the spallation argon in fine-grained material will be produced by energetic particles interacting with iron, its production rate in small particles exposed to solar flares is probably not radically different from that in meteorites exposed to cosmic rays. We then make three extreme assumptions:

1. There has been no loss of spallation argon by diffusion or recoil.

2. All of the dense Greenland material is extraterrestrial.

3. The density of the individual particles before atmospheric entry was 8, and their composition was pure iron.

With these assumptions and our argon measurements we can calculate an upper limit for the exposure time of the dust and compute an average-sized particle corresponding to a Poynting-Robertson limited lifetime.

The calculated exposure time is 0.1×10^6 years; for material spiraling in from 3 a.u. this lifetime, if limited by the Poynting-Robertson effect, corresponds to an average size of 20 μ. It is also of interest to note that this is roughly the size below which dense grains can enter the atmosphere without melting, and above which they will melt and ablate. Thus, larger grains, which would have longer lifetimes in space and greater concentrations of spallation-produced gases, will not be expected to survive entry intact and will probably be degassed during atmospheric entry.

The calculation is in a sense an academic one, since the assumptions, while as precise as any others that might be made at this time, are certainly unrealistic; however, it does serve to demonstrate that the lack of cosmogenic argon is not an extraordinary surprise, and serves also as a useful reminder of the expected difficulty of searching for long-lived radioactive isotopes in the probably briefly exposed dust grains.

Merrihue (1964) suggested the possible contributions of stopped solar-wind or solar-flare ions to the gas content of extraterrestrial dust. I have noted that if small particles are exposed in space for lifetimes limited by the Poynting-Robertson effect, they will accumulate, embedded in their surfaces, an amount of solar gas per gram that is independent of density or of size distribution (Tilles, 1965).

For material arriving at the earth from a distance of A_0 a.u., and assumed bombarded by a radially decreasing solar-wind flux of W_0 atoms cm^{-2} yr^{-1} at 1 a.u., this concentration is $10^7 W_0 \ln A_0$ atoms per gram. Estimates for solar-wind flux, argon abundance in solar wind, and dust-grain origin give about 5×10^{-3} cm^3 $Ar^{36} + Ar^{38}$ per gram of extraterrestrial dust. This concentration is 10^7 times that observed. A combination of circumstances may account for this factor:

1. We may be measuring material heady diluted with terrestrial contaminants.

2. Solar-wind atoms will mainly be very shallowly embedded and may be almost entirely lost during atmospheric-entry heating. Only some kind of high-temperature Maxwellian tail of the initial distribution may remain to be released at temperatures of 1000° C or above.

3. If the present grains had any coating of volatile or organic material while in space, the stopped solar-wind atoms would almost entirely be in this coating, which may be vaporized or burned coming into the atmosphere.

4. The surfaces of grains may have been slightly etched during storage in the ocean or water tank prior to sample collection.

5. Gas may be lost from grain surfaces by sputtering in space, or by diffusion either in space or during terrestrial storage and prebake of experiment.

6. Our derived minimum values may significantly underestimate the excesses of Ar^{36} and Ar^{38} present.

7. The lifetimes of small particles in space may be limited by other perturbations than the Poynting-Robertson effect, and may be much shorter than calculated (Shapiro, Lautman, and Colombo, see p. 359).

8. The grain surfaces, which are expected to be highly reduced in space by solar-wind protons, may lose most or all of their shallowly implanted rare gases on oxidation during atmospheric entry or terrestrial storage.

For all of these reasons, the disagreement between estimated source intensity and measured values cannot be used as evidence against the existence of the solar-wind atmospheric source, although it does suggest that the solar wind is probably not the source of the noble gas anomalies in dust observed to date.

It is of interest to note that with an extraterrestrial dust influx rate of 2×10^{-7} g cm^{-2} yr^{-1} averaged over the earth's surface for 4.5×10^{9} years, solar wind embedded in small grains appears capable of providing for one-fifth of the present atmospheric Ar^{36} and Ar^{38} abundances (Tilles, 1965). However, this calculated figure assumes no loss in space, which is certainly unrealistic. Sputtering alone may result in important losses for grains of micron size and larger, with the fraction of gas retained inversely proportional to density and radius of grains.

As an alternative to a solar-wind source, stopping of solax-flare ions, as has been observed with satellite material in the cases of He^3 and H^3 (Schaeffer and Zähringer, 1962; Fireman, DeFelice, and Tilles, 1961; Tilles, DeFelice, and Fireman, 1963), might also provide Ar^{36} and Ar^{38} excesses.

Solar-flare ions, having much higher energies than solar-wind ions, will be stopped more deeply and uniformly in grains in space. They are thus more likely to be observed at high release temperatures.

Lal and Venkatavaradan (1965) have recently found Al^{26} in sea sediments. They conclude that cosmic-ray spallation of atmospheric argon, ablation of chondrite meteorites, and galactic cosmic rays bombarding extraterrestrial dust are all inadequate to account for the observed activity of Al^{26}. They calculate, however, that if: (1) 10^4 tons/day of extraterrestrial dust falls on earth, (2) this dust has chondrite composition, and (3) the dust particles are in space long enough for the establishment of secular equilibrium concentrations of Al^{26}, then a flux of 20 solar-flare protons cm^{-2} sec^{-1} averaged over the dust particles' orbits and having an energy >10 Mev would account for the observed Al^{26} activities. To the extent that the average lifetimes in space are in fact shorter, this flux is increased.

If the ratio of argon to protons in the flare stream is 2×10^{-6}—an assumed cosmic abundance we have used already (Tilles, 1965)—then the observed excess Ar^{36} and Ar^{38} in the anomaly-bearing samples of sea sediment and Greenland dust can be accounted for by the stopping of the same intensity of solar-flare ions as is required to produce the Al^{26} by spallation.

We can state this same fact in another way. The 20 flare protons cm^{-2} sec^{-1} required by Lal and Venkatavaradan is a flux lower by 10^7 than the expected solar-wind flux at 1 a.u. But our anomalous Ar^{36} and Ar^{38} concentrations are themselves lower by a factor 10^7 than that expected from the solar-wind source.

Of course, because of terrestrial dilution, uncertainty in dust lifetimes in space, and the possibility of gas loss, the precision of this agreement is certainly fortuitous. Nevertheless, both the amount and observed release temperatures of the anomalous argon, and to

a first approximation the He^4 and Ne^{20} also, seem in much better agreement with what is expected for stopped solar-flare ions[2] than for stopped solar-wind ions.

Finally, it is possible that extraterrestrial material such as cometary matter may have incorporated rare gases into its structure during its early history of condensation and solidification (Urey, 1952a, b).

Thus there seem to be plausible explanations for the argon anomalies if the samples contain extraterrestrial material. No terrestrial origins seem probable.

The only mineral found with X-ray diffraction in both kinds of anomalous samples is magnetite. It is of interest to suggest that magnetite is a plausible form in which to expect extraterrestrial iron. Magnetite is abundant in Renazzo, a meteorite suggested by Wood (1963) to be very primitive, and magnetite (or trevorite) is a major constituent of Type I carbonaceous chondrites (Mason, 1962). Magnetite spherules, believed to be extraterrestrial, are often suggested to be the result of atmospheric ablation of meteoritic metal. It is possible that magnetite may be the stable chemical form of iron in a suitably fractionated solar gas (Studier, Hayatsu, and Anders, 1965) at low temperatures, which might be typical of the environment from which comets formed. In such a case magnetite ablation spherules might be only a small fraction of the extraterrestrial magnetite arriving at the earth.

If it can be conclusively demonstrated that the argon anomalies are not terrestrial in origin, these anomalies then provide a delicate probe for investigations elucidating the detailed physical and chemical characteristics of extraterrestrial dust on earth, and perhaps indirectly, of comets.

Summary

We have confirmed the argon anomalies reported by C. M. Merrihue for a magnetic fraction of Pacific red clay in other samples of this barrel dredge of sediment. We have found similar argon anomalies in a dense sample of particulate matter from Greenland. There is no evidence of cosmogenic He^3 or Ar^{38} in these samples. The only mineral detected in samples from both environments is magnetite. Comparison of model atmospheric argon ratios with observed anomalous ratios and potassium-argon ages argues against a terrestrial explanation for the anomalies. The presence of extraterrestrial dust is probably the explanation of the anomalies, and there exist several mechanisms to account for anomalous argon in extraterrestrial material.

Acknowledgments

I am deeply indebted to Dr. Craig M. Merrihue for many helpful discussions and for technical assistance. His pioneering work in this field opened many new possibilities. His recent death is a very great personal tragedy for those who knew him, and a major scientific loss. I should also like to thank Drs. W. A. Cassidy and C. C. Langway, Jr., for providing samples, and Dr. O. A. Schaeffer for assistance in the construction of our mass spectrometer. Dr. G. Arrhenius provided invaluable guidance in mineralogy of sea sediments, and many stimulating comments. I also thank Mrs. U. B. Marvin, who assisted in some of the X-ray work, and R. Werby, who did the potassium analyses. Financial assistance was provided by the National Science Foundation, Grant G–16067.

References

ALDRICH, L. T., and NIER, A. O.
1948. The occurrence of helium-3 in natural sources of helium. Phys. Rev., vol. 74, pp. 1590–1594.

BIERI, R.; KOIDE, M.; and GOLDBERG, E. D.
1964. Noble gases in sea water. Science, vol. 146, pp. 1035–1037.

BUDDHUE, J. D.
1958. Meteoritic Dust. University of New Mexico Press, Albuquerque, 102 pp.

BUTLER, W. A.; JEFFERY, P. M.; and REYNOLDS, J. H.
1963. Isotopic variations in terrestrial xenon. Journ. Geophys. Res., vol. 68, pp. 3281–3291.

CHERDYNTSEV, V. V.
1961. Abundance of Chemical Elements. English ed., trans. by W. Nichiporuk, University of Chicago Press, Chicago, 304 pp.

CLARKE, W. B., and THODE, H. G.
1964. Isotopic anomalies in xenon from meteorites and xenon from natural gases. *In* Isotopic and Cosmic Chemistry, ed. by H. Craig, S. L. Miller, and G. J. Wasserburg, North-Holland Publ. Co., Amsterdam, pp. 471–515.

[2] This source is more fully discussed by the author in a paper in preparation. Note added in proof: This paper has since been published in Science, vol. 163, pp. 981–984, 1966.

DAMON, P. E., and KULP, J. L.
1958. . Excess helium and argon in beryl and other minerals. Amer. Mineral., vol. 43, pp. 433–459.

FIREMAN, E. L.; DEFELICE, J.; and LANGWAY, C. C., Jr.
1965. Greenland dust: Radioactivity studies (abstract). Trans. Amer. Geophys. Union, vol. 46, p. 117.

FIREMAN, E. L.; DEFELICE, J.; and TILLES, D.
1961. Solar flare tritium in a recovered satellite. Phys. Rev., vol. 123, pp. 1935–1936.

FIREMAN, E. L., and LANGWAY, C. C., Jr.
1965. Search for aluminum-26 in dust from the Greenland ice sheet. Geochim. et Cosmochim. Acta, vol. 29, pp. 21–27.

GOLDBERG, E. D., and KOIDE, M.
1962. Geochronological studies of deep sea sediments by the ionium and thorium method. Geochim. et Cosmochim. Acta, vol. 26, pp. 417–450.

HART, S. R., and DODD, R. T., Jr.
1962. Excess radiogenic argon in pyroxenes. Journ. Geophys. Res., vol. 67, pp. 2998–2999.

KEEVIL, N. B.; JOLIFFE, A. W.; and LARSEN, E. S.
1942. The distribution of helium and radioactivity in rocks. Amer. Journ. Sci., vol. 240, pp. 831–846.

LAL, D., and VENKATAVARADAN, V. S.
1965. Low-energy protons: Average flux in interplanetary space during the last 100,000 years. Science, vol. 151, pp. 1381–1384.

LANGWAY, C. C., Jr., and FIREMAN, E. L.
1965. Greenland dust: Large-volume collections and microscopic studies (abstract). Trans. Amer. Geophys. Union, vol. 46, pp. 116–117.

LIPPOLT, H. J., and GENTNER, W.
1963. K-Ar dating of some limestones and fluorites (examples of K-Ar ages with low Ar-concentrations). *In* Radioactive Dating, IAEA, Vienna, pp. 239–244.

MASON, B.
1962. Meteorites. J. Wiley and Sons, New York, 274 pp.

MERRIHUE, C. M.
1964. Rare gas evidence for cosmic dust in modern Pacific red clay. Ann. New York Acad. Sci., vol. 119, pp. 351–367.

RAMA, S. N. I.; HART, S. R.; and ROEDDER, E.
1965. Excess radiogenic argon in fluid inclusions. Journ. Geophys. Res., vol. 70, pp. 509–511.

REYNOLDS, J. H.
1956. High sensitivity mass spectrometer for noble gas analysis. Rev. Sci. Instr., vol. 27, pp. 928–934.

SACKETT, W. M.
1964. Measured deposition rates of marine sediments and implications for accumulation rates of extraterrestrial dust. Ann. New York Acad. Sci., vol. 119, pp. 339–346.

SCHAEFFER, O. A.
1959. High sensitivity mass spectrometry of the rare gases. Brookhaven Nat. Lab., no. 581 (T–161), 12 pp.

SCHAEFFER, O. A.; MEGRUE, G.; and THOMPSON, S. O.
1964. Experiments to test the presence of cosmogenic nuclides in ocean sediments. Ann. New York Acad. Sci., vol. 119, pp. 347–350.

SCHAEFFER, O. A., and ZÄHRINGER, J.
1962. Solar flare helium in satellite materials. Phys. Rev. Letters, vol. 8, pp. 389–390.

SHAPIRO, I. I.; LAUTMAN, D. A.; and COLOMBO, G.
1967. Dynamics of orbiting dust particles (abstract). Smithsonian Contr. Astrophys., vol. 11, p. 359.

STUDIER, M. H.; HAYATSU, R.; and ANDERS, E.
1965. Organic compounds in carbonaceous chondrites Science, vol. 149, no. 3691, pp. 1455–1459.

SUESS, H. E.
1949. Die Häufigkeit der Edelgase aus der Erde und im Cosmos. Journ. Geol., vol. 57, pp. 600–607.

TILLES, D.
1965. Atmospheric noble gases: Solar-wind bombardment of extra-terrestrial dust as a possible source mechanism. Science, vol. 148, pp. 1085–1088.

TILLES, D.; DEFELICE, J.; and FIREMAN, E. L.
1963. Measurements of tritium in satellite and rocket material 1960–1961. Icarus, vol. 2, pp. 258–279.

UREY, H. C.
1952a. The Planets: Their Origin and Development. Yale University Press, New Haven, Conn., 245 pp.
1952b. Condensation processes and the origin of the major and terrestrial planets. *In* L. Farkas Memorial Volume, ed. by A. Farkas and E. Wigner, Res. Counc. of Israel, Spec. Publ., no. 1, Jerusalem, pp. 3–12.

WASSERBURG, G. J.; MAZOR, E.; and ZARTMAN, R. E.
1963. Isotopic and chemical composition of some terrestrial natural gases. *In* Earth Science and Meteoritics, ed. by J. Geiss and E. D. Goldberg, North-Holland Publ. Co., Amsterdam, pp. 219–239.

WOOD, J. A.
1963. On the origin of chondrules and chondrites. Icarus, vol. 2, pp. 152–180.

ZARTMAN, R. E.; WASSERBURG, G. J.; and REYNOLDS, J. H.
1961. Helium, argon, and carbon in some natural gases. Journ. Geophys. Res., vol. 66, pp. 277–306.

Abstract

Anomalous isotope ratios have been found in argon released at 1200° C (following successive heatings at lower temperatures) from magnetically separated fractions of a Pacific red clay sea sediment and from a density separated ($\rho > 3.2$) fraction of Greenland dust. The minimum values of Ar^{40}/Ar^{36} found in the sea sediment were 198 ± 6 and 194 ± 10 and in the Greenland material 230 ± 5. Ratios of Ar^{36}/Ar^{38} were consistent with air ratios, with a value of 5.21 ± 0.08 for the Greenland temperature fraction containing the greatest amount of anomalous argon. Amounts of excess Ar^{36}, relative to air, varied from 5 to 10×10^{-10} cm^3 STP g^{-1}. The measurements confirm Merrihue's earlier argon results on the Pacific red clay, and extend them to material from Greenland, demonstrating that the argon anomalies are a worldwide phenomenon. No evidence of cosmic-ray or solar-%re-produced spallation argon nor of solar-wind or solar-flare-imbedded He^3 was observed. X-ray studies indicate that the one mineral detectable in both Pacific and Greenland anomaly-bearing samples is magnetite. Arguments against a terrestrial origin for the argon anomalies are presented, and possible extraterrestrial mechanisms that might account for them are reviewed.

U.S. GOVEWMENT PRINTING OFFICE :1967—O-240-022